VDE VERLAG

GMM-Fachbericht **110**

ACTUATOR 2024

International Conference and Exhibition on New Actuator Systems and Applications

ACTUATOR 24

GMM Conference
June 13 – 14, 2024 in Wiesbaden

VDE VDI GMM

GMM-Fachbericht **110**

ACTUATOR 2024

International Conference and Exhibition on New Actuator Systems and Applications

GMM Conference
June 13-14, 2024 in Wiesbaden

Organizer:
VDE VDI-Society Microelectronics, Microsystems and Precision Engineering (GMM)

Dr. Ronald Schnabel, VDE e.V. GMM Branch

VDE VERLAG GMBH

Cover picture: © Michael Gareis, TU Berlin – Olena/stock.adobe.com

Bibliographic Information of the German National Library
The German National Library lists this publication in the National Bibliography;
detailed bibliographic data are available on the Internet at **https://portal.dnb.de/**.

ISBN 978-3-8007-5894-4 (CD-ROM)
ISBN 978-3-8007-5895-1 (E-Book)
ISSN 1432-3419

© 2024 VDE VERLAG GMBH · Berlin · Offenbach, Bismarckstraße 33, 10625 Berlin
www.vde-verlag.de

All rights reserved. Any utilization in breach of the strict limits of copyright law, without the prior approval of the publisher, is prohibited. Reproductions of common names, brand names, trademarks etc. in this publication are not subject to the acceptance that these names could be regarded as free or could be used by anyone, even without particular marking, in the sense of the trademark and brand protection legislation. Publication does not imply that the solutions described are not protected by intellectual property rights (e.g. patents and utility models). The publisher assumes no liability for the correctness and practicability of the programs, circuits, and any other arrangements and instructions published, nor for the correctness of the technical content of this publication. The up-to-date valid versions of the relevant statutory and official regulations and technical regulations (e.g. VDE body of regulations) have to be respected.

CD Production: DMS – Disk Media Service, Berlin
Produced in Germany

Welcome to the new ACTUATOR Conference 2024

The ACTUATOR Conference 2024 –may we inform you ...
ACTUATOR is a major biennial event bringing together leading experts, suppliers and users in the field of new actuators from all over the world. The invitation to attend ACTUATOR is aimed at executives and researchers from industrial companies as well as institutes, colleges and universities who are interested in the transfer of R&D results into innovative actuator applications and drive technologies.

ACTUATOR 2024 – together with you on an international stage
With about 200 participants from more than 20 countries, the International Conference on New Actuator Systems and Applications has been the most important place to meet leading international specialists, to share their expertise and to start business co-operations in the field of new actuator technologies.

ACTUATOR – the key forum for actuators
based on smart materials and micro technologies as well as their applications in all areas of engineering for thirty years now. Over the years, a huge variety of excellent ideas and results have been reported. A lot of them have been raised from vision to mass product. Among the success stories you will find established applications of new actuators, in their use in fuel injection, adaptive shock absorbers, nanopositioning, precision engineering like camera lenses and other applications of miniaturized drives.

New product generations
In this way, ACTUATOR has launched the realization of new product generations with outstanding compactness and high performance properties which so far have not been achieved in conventional technologies.

The Exhibition
The Exhibition on New Actuator Systems and Applications will present components, system approaches and applications of smart actuators and low-power electromagnetic drives based on conventional (electromagnetic) and innovative working principles (new actuators), and associated subjects. The range of topics also includes measurement techniques, control concepts and circuits, driver components and units, system integration, layout and simulation tools etc.

ACTUATOR 2024 Steering Committee
Manfred Kohl, Jürgen Maas, Salvador Pané i Vidal, Herbert Shea, Emmanuel Vander Poorten, Ulrike Wallrabe, Yoko Yamanishi

Program Committee

Steering Committee Members

Kohl, Manfred | Karlsruher Institut für Technologie, Germany
Maas, Jürgen | Technische Universität Berlin, Germany
Pané i Vidal, Salvador | Swiss Federal Institute of Technology (ETH) Zurich, Switzerland
Shea, Herbert | Ecole Polytechnique Fédérale de Lausanne (EPFL), Switzerland
Vander Poorten, Emmanuel | Katholieke Universiteit Leuven, Heverlee, Belgium
Wallrabe, Ulrike | University of Freiburg, Department of Microsystems Engineering – IMTEK, Germany
Yamanishi, Yoko | Kyushu University, Japan

Program Committee Members

Biedermann, Miriam | Bürkert Werke GmbH & Co. KG, Karlsruhe, Germany
Chikhaoui, M. Taha | Université Grenobles-Alpes, France
Choi, Seung-Bok | The State University of New York, Korea (SUNY Korea), Incheon, South Korea
Claeyssen, Frank | CEDRAT Technologies S.A., Meylan, France
Goldasz, Janusz | BWI Beijing West Industries Technical Center Kraków, Poland
Henke, Markus | Technische Universität Dresden, Germany
Jager, Edwin | Linköping University, Sweden
Kanda, Takefumi | Okayama University, Japan
Krippner, Peter | Bürkert Werke GmbH & Co. KG, Karlsruhe, Germany
Lötters, Joost | Bronkhorst High-Tech B.V., Ruurlo, Netherlands
Maas, Jürgen | Technische Universität Berlin, Germany
Manfredi, Luigi | University of Dundee, Great Britain
Marienfeld, Peter | Contitech Vibration Control GmbH, Hannover, Germany
Merlo, Sabina | University of Pavia, Italiy
Monner, Hans Peter | German Aerospace Center (DLR), Braunschweig, Germany
Morishima, Keisuke | Osaka University, Yamadaoka, Japan
Morita, Takeshi | The University of Tokyo, Japan
Müller, Bert | University of Basel, Switzerland
Nienhaus, Matthias | Universität des Saarlandes, Saarbrücken, Germany
Pagounis, Emmanouel | ETO MAGNETIC GmbH, Stockach, Germany
Perret, Jérôme | Haption GmbH Aachen, Germany
Pertsch, Patrick | PI Ceramic GmbH, Lederhose, Germany
Pott, Peter | University of Stuttgart, Germany
Preumont, André | Université libre de Bruxelles, Belgium
Price, Aaron | The University of Western Ontario, Canada
Renaud, Pierre | Institut National des Sciences Appliquées Strasbourg INSA, Strasbourg, France
Seelecke, Stefan | Universität des Saarlandes, Saarbrücken, Germany
Takasaki, Masaya | Saitama University, Japan
Uchino, Kenji | The Pennsylvania State University, USA
Ugurlu, Barkan | Ozyegin University, Çekmeköy - Istanbul, Turkey
Vergani, Giorgio | SAES Getters S.p.A., Lainate, Italy

Content

Functional test of a training device for moving fingers and wrist joints using soft pneumatic actuator 1
Masaki Todo, Hironari Taniguchi, Daigo Ishii
Graduate School of Robotics and Design, Osaka Institute of Technology, Japan

Control of Magnetorheological Fluid Brake for Medical Ergometers based on Cycling Model 5
Abd Elkarim Masoud, Valentin Schreiner, Jürgen Maas
Technical University Berlin, Mechatronic Systems Lab, Germany

Design, manufacturing and control of a non-magnetic pneumatic linear stepper actuator with inchworm kinematics 9
Timothée Portha[1], Laurent Barbé[1], François Geiskopf[1], Jonathan Vappou[1], Paolo Cabras[1,2], Pierre Renaud[1]
[1]*Université de Strasbourg, INSA Strasbourg, CNRS, INSERM, ICube, Strasbourg, France,*
[2]*IGT, Image Guided Therapy, Pessac, France*

An electrokinetic lab-on-CMOS DNA detection system for sample-toresult diagnostic applications ... 13
Lewis Keeble[1], Arthur Jaccottet[1], Daryl Ma[1], Jesus Rodriguez-Manzano[2], Pantelis Georgiou[1]
[1]*Department of Electrical and Electronic Engineering, Imperial College London, UK*
[2]*Department of Infectious Diseases, Imperial College London, UK*

Characteristics of Resonance Type Piezoelectric Motors Made with Textured Piezoceramics Material 17
Burhanettin Koc[1], Bülent Delibas[1], Safakcan Tuncdemir[2], Ahmet Erkan Gürdal[2], Franz Schubert[3]
[1]*Physik Instrumente (PI) GmbH & Co. KG, Karlsruhe, Germany*
[2]*QorTek, Inc., Linden, PA, USA*
[3]*PI Ceramic GmbH, Lederhose, Germany*

Study on Miniaturization of a Pump Using Ultrasonic Transducer and Opposing Surface 21
Masaya Takasaki, Yuki Nakasuji, Yuji Ishino, Takeshi Mizuno
Saitama University, Japan

Low voltage (Bi, Sc)(Pb, Ti)O3 based piezoelectric multilayer actuators for high temperature applications 23
Runjiang Guo, Qingbin Meng, Renlong Gao, Cary Zhang
Thorlabs Optical Electronic Technology (Shanghai) Co., Ltd., Shanghai, China

High-Accuracy Alignment of integrated Optical Components utilizing Ferroelectric Shape-Memory Actuators 27
Zijian Chen[1,2], Jens Twiefel[1,2], Jörg Wallaschek[1,2]
[1]*Leibniz University Hannover, Institute of Dynamics and Vibration Research, Garbsen, Germany*
[2]*Leibniz University Hannover, Cluster of Excellence PhoenixD, Hannover, Germany*

Audio Frequency Actuation of SMA Wires 31
Arif Kazi[1], Lukas Buser[1], Maximilian Schmitt[1], Max Karch[1], Markus Köpfer[2]
[1]*Aalen University of Applied Sciences, Aalen, Germany*
[2]*Actuator Solutions GmbH, Gunzenhausen, Germany*

Investigation of the localized twinning behavior of magnetic shape memory alloys using digital image correlation 35
Robert Courant, Jürgen Maas
Technische Universität Berlin, Germany

Actuation properties of a magnetic shape memory element prepared by laser ablation.....40
Andrey Saren, Aditya Kumthekar, Ville Laitinen, Kari Ullakko
Material Physics Laboratory, Lappeenranta-Lahti University of Technology LUT, Finland

Optimization and Investigation of Radial-flux Permanent Magnet Micromotor Utilizing MEMS 3D Solenoid Coils with Iron Core.....44
Kaibo Lei, Haiwang Li, Tiantong Xu, Yuying Wu, Kaiyun Zhu, Yanxin Zhai
Beihang University, Beijing, China

Directional Anisotropy in Smart Magnetic Actuation.....48
Dharmi Chand, S M Srinivasan
Indian Institute of Technology Madras, Chennai, India

Optimized high-efficiency MICA actuators for space compressors.....51
Xavier De Lepine, Frank Claeyssen, Francois Barillot, Patrick Meneroud, Aurore Loubet, Timotéo Payre, Nicolas Bourgeot, Olivia Stadler, David Ferris, Jocelyn Rebufa, Arnaud Barnique, Gérald Aigouy, Hélène Rouxel
Cedrat Technologies, Meylan, France

-Push, Push, Push- Direct writing of magnetic micro actuators.....55
Nicolas Geid, Eleonora Galli, Jürgen Rühe
(IMTEK), Universität Freiburg, Germany

Development of microbubble shock wave reflection needle-free injection.....57
Yibo Ma[1], Wenjing Huang[2], Naotomo Tottori[1], Yoko Yamanishi[1]
[1]Bio-medical Fluid Engineering Laboratory, Mechanical engineering, Kyushu University, Fukuoka, Japan
[2]Kindai University Technical College, Mie, Japan

Computational Study of Fluid Flow in Multi-Stage Pinch Mode MR Valves.....60
Janusz Gołdasz[1], Bogdan Sapinski[2], and Michal Kubik[3]
[1]Cracow University of Technology, Krakow, Poland
[2]AGH University of Krakow, Krakow, Poland
[3]Brno University of Technology, Brno, Czech Republic

Rheological properties of abrasive magnetorheological fluids for immersed tumbling processes.....64
Fabian Sordon[1], Christian Lahoda[2], Eckart Uhlmann[2,3], Jürgen Maas[1]
[1]Mechatronic Systems Lab EMK, Technische Universität Berlin, Berlin, Germany
[2]Technische Universität Berlin, Institute for Machine Tools and Factory Management, Berlin, Germany
[3]Fraunhofer Institute for Production Systems and Design Technology, Berlin, Germany

Utilization of Sedimentation in Magnetorheological Fluids for Online Rotor Balancing.....68
Valentin Schreiner, Jürgen Maas
Technische Universität Berlin, Fachgebiet Elektromechanische Konstruktionen, Berlin, Germany

Innovative Fin Ray gripper with integrated SMA actuator wires 72
Shivaani Anitha Sivakumar[1,2], Yannik Goergen[1], Tom Gorges[1], Gianluca Rizzello[2], Paul Motzki[1,2]
[1]ZeMA – Center for Mechatronics and Automation Technology, Depart. Smart Material Systems, Saarbruecken, Germany
[2]Saarland University, Depart. Systems Engineering, Saarbruecken, Germany

Development of an integrated foil-based sensor for position sensing of magnetic shape memory alloy actuators 76
Patrick Fleischmann[1], René Schnetzler[2], Bernd Gundelsweiler[1]
[1]Institute of Design and Production in Precision Engineering, University of Stuttgart, Germany
[2]ETO GRUPPE TECHNOLOGIES GmbH, Stockach, Germany

Flux control in magnetic circuits using variable reluctance of magnetic shape memory alloys 80
Marco Hutter, Bernd Gundelsweiler
Institute of Design and Production in Precision Engineering, University of Stuttgart, Germany

Investigation of the influencing factors in the production of Shape Memory alloy wire bending actuators for integration in micro-electromechanical systems 84
Andreas Erben[1], Kenny Pagel[1], Daniel Hoffmann[2], Andrea Böhm[1], Welf-Guntram Drossel[1]
[1]Fraunhofer Institute for Machine Tools and Forming Technology IWU, Dresden, Germany
[2]Hahn-Schickard Gesellschaft, Villingen-Schwenningen, Germany

Analysis of the controller and damping behavior of an electrodynamic actuator system for an 11 kW two-pole induction motor on an elastic steel frame foundation 86
Raimund Wachter[1], Ulrich Werner[2], Hans-Georg Herzog[3], Christian Bauer[4]
[1]ELSYS - Institute for Power Electronic Systems, Nuremberg Institute of Technology, Germany
[2]Faculty EFI, Nuremberg Institute of Technology, Germany
[3]Technical University of Munich (TUM), Garching, Germany
[4]IN HVM HVM, Innomotics GmbH, Nuremberg, Germany

Design of a range of attachable Lorentz force actuators adapted to different active damping applications.....90
Alexander Pena-Sevillano[1], Iker Mancisidor[1], Rafa Barcena[2], Inaki Laka[1], Jokin Munoa[1]
[1]Dynamics & Control, Ideko, Elgoibar, Spain
[2]Mechanical Engineering Department, University of Basque Country (UPV-EHU), Bilbao,Spain

Development of a compact jumping lunar rover driven by shape memory alloy actuators 94
Yuki Oka, Hironari Taniguchi, Taichi Izumi, Koki Yura
Osaka Institute of Technology, Japan

Performance Optimization of an SMA-Actuated Camera Gimbal.....98
Alexander Schwegler[1], Dennis Niklas[1], Tobias Schumm[2], Arif Kazi[1]
[1]Aalen University of Applied Sciences, Aalen, Germany
[2]Actuator Solutions GmbH, Gunzenhausen, Germany

Magnetic Fast Steering Mirror for Inter-satellites and Feeder Link Optical Communication 102
Etienne Betsch, Augustin Bedek, Nicolas Bourgeot, Arnaud Barnique, Patrick Meneroud, Hugo Grardel, Pierre Personnat, Théo Simon, Marc Fournier, Sylvain Chardon, Gérald Aigouy, Xavier De Lepine, Frank Claeyssen
CEDRAT TECHNOLOGIES, Meylan, France

Self-sensing in spring-loaded SMA actuators using artificial neural networks.....108
Krunal Koshiya[1], Vladimir Naumov[1], Tom Gorges[1], Gianluca Rizzello[2], Paul Motzki[1,2]
[1]ZeMA – Center for Mechatronics and Automation Technology, Depart. Smart Material Systems, Saarbrücken, Germany
[2]Saarland University, Depart. Systems Engineering, Saarbrücken, Germany

The Effects of Training on Electro-Thermo-Mechanical Actuation and Sensing Characteristics of NiTi Actuator Wires.....112
Joshua Mayer[1], Dominik Scholtes[1,2], Tom Gorges[1], Gianluca Rizzello[2], Paul Motzki[1,2]
[1]Smart Material Systems, Center for Mechatronics and Automation Technology - ZeMA gGmbH, Saarbruecken, Germany
[2]Saarland University, Department of Systems Engineering, Saarbruecken, Germany

Precision Atmospheric Pressure Driven Actuator controlled by Self-Sensing Electro-Magnetic Valve.....116
Yahui Zhang, Bintang Yang
School of Mechanical Engineering, Shanghai Jiao Tong University, China

MULTISTABLE MAGNETIC LIFT ACTUATION UNDER VARIABLE LOADS 120
Pascal M. Weber, Yannik T. Rüde, Ulrike Wallrabe
IMTEK – Department of Microsystems Engineering, University Freiburg, Germany

Model Order Reduction Augmented by a Neural Network for a Nonlinear Electrostatic Microactuator 124
Arwed Schütz[1], Lars Nolle[1,2], Tamara Bechtold[1]
[1]*Jade University of Applied Sciences, Wilhelmshaven, Germany*
[2]*German Research Centre for Artificial Intelligence, Oldenburg, Germany*

Optimized Feedforward Control of a Multistable Magnetic Actuator 128
Michael Olbrich[1], Pascal Weber[2], Ulrike Wallrabe[2], Christoph Ament[1]
[1]*University of Augsburg, Chair of Control Engineering, Germany*
[2]*University of Freiburg, Department of Microsystems Engineering (IMTEK), Germany*

Natural Rubber Foil-Based Elastocaloric Cooling 132
Carina Ludwig[1], Jan Leutner[2], Oswald Prucker[2], Jürgen Rühe[2], and Manfred Kohl[1]
[1]*Institute of Microstructure Technology (IMT), Karlsruhe Institute of Technology (KIT), Germany*
[2]*Department of Microsystems Engineering (IMTEK), University of Freiburg, Germany*

A Dielectric Elastomer based Miniaturized Soft Planar Microactuator 136
Simon Holzer, Bhawnath Tiwari, Stefania Konstantinidi, Yoan Civet, Yves Perriard
Integrated Actuators Laboratory (LAI), Ecole polytechnique fédérale de Lausanne (EPFL), Neuchâtel, Switzerland

Investigation of the influence of fiber reinforcement onto electro-active strain and force in uniaxial DEAs 140
Stefania Konstantinidi[1], Markus Koenigsdorff[2], Simon Holzer[1], Johannes Mersch[3], Thomas Martinez[1], Yoan Civet[1], Gerald Gerlach[2], Yves Perriard[1]
[1]*Integrated Actuators Laboratory (LAI), Ecole polytechnique fédérale de Lausanne (EPFL), Neuchâtel, Switzerland*
[2]*Institute of Solid-State Electronics, Faculty of Electrical and Computer Engineering, Dresden University of Technology (TUD), Dresden, Germany*
[3]*Institute of Measurement Technology, Faculty of Mechatronics, Johannes Kepler University Linz, Austria*

Tubular Dielectric Elastomer Transducer with Hydrostatic Force Transmission 144
Tim Krüger, Jürgen Maas
Mechatronic Systems Lab, Technische Universität Berlin, Germany

Design and Fabrication of a Five-Fingered Soft Robotic Hand with Embedded SMA Actuator and Piezoresistive Flexible Sensor 148
Racha Benarrait[1], Monika Leester-Schäde[1], Frederic Lamarque[2], Andreas Dietzel[1]
[1]*Institut fûr Mikrotechnik, Technische Universität Braunschweig, Germany*
[2] *Université de Technologie de Compiègne, (Mechanics energy and electricity), France*

Fabrication of pneumatic soft fingers taking into account material/ process/design interaction 151
Baptiste Kraehn[1], Thibault Delrieu[2], Laurence Meylheuc[1], Pascal Seguin[2], Jean-Pierre Gazeau[2], Olivier Piccin[1]
[1]*ICube, INSA Strasbourg, France*
[2]*Pprime Institute, Poitiers University, France*

Soft aquatic robot using shape memory actuators based on an octopus jellyfish to improve water quality in aquariums 155
Yoshiaki Fujiwara, Hironari Taniguchi, Teppei Ueda,
Graduate School of Robotics and Design, Osaka Institute of Technology, Japan

Development of a soft avatar robot using soft pneumatic actuators for an exhibition hall.....159
Yuki Hirano[1], Hironari Taniguchi[1], Hideaki Kokubu[1], Ryo Kawabata[1], Yuki Tanaka[1], Shinji Miura[2]
[1]Department of Robotics, Faculty of Robotics and Design, Osaka Institute of Technology, Japan
[2]Department of Design and Architecture, Faculty of Robotics and Design, Osaka Institute of Technology, Japan

Integrated Force Sensing Technology for Twisted String Actuation Using Conductive Yarns.....163
Giuliano A. Giacoppo, Sina Öztürk, Peter P. Pott,
Institute of Medical Device Technology, University of Stuttgart, Germany

Direct writing of multilayer multistimuli micro-actuators.....167
Eleonora Galli[1], Nicolas Geid[1,2], and Jürgen Rühe[1,2]
[1]IMTEK, Universität Freiburg, Germany
[2]FIT, Universität Freiburg, Germany

Rate Dependent Prandtl-Ishlinskii (RDPI) Model based motion compensation of Mitraclip® Delivery System.....169
Syed Zain Mehdi, Mouloud Ourak, Emmanuel Vander Poorten
Department of Mechanical Engineering, KU Leuven, Belgium

Light-controlled mechanisms based on photomobile polymers for seamless integration in demanding environments.....173
Mathieu Thomachot, Jolan Gauthier, Patrick Meneroud, Sylvain Duc, Frank Claeyssen
Guillaume Mansuy Cedrat Technologies, Meylan, France

An inchworm using piezoelectric actuators and electromagnets with MR fluid 179
Takeshi Inoue, Hayata Takashima, Akihiro Torii, Suguru Mototani, Kae Doki
Aichi Institute of Technology, Toyota, Japan

A Flow Control Valve using Piezoelectric Vibrator for Hydraulic Soft Actuators 182
Takefumi Kanda[1], Kou Hashimoto[1], Yuma Mizokuchi[1], Yusuke Ota[1], Shuichi Wakimoto[1], Daisuke Yamaguchi[1], Koichi Suzumori[2], Hiroyuki Nabae[2]
[1]Okayama University, Japan
[2]Tokyo Institute of Technology, Japan

The Application of Piezoelectric-Driven Actuators in Bone Conduction Devices 184
Julia Lieber[1], Alexander Reininger[2]
[1]MED-EL, Innsbruck, Austria
[2]Linz Center of Mechatronics, Linz, Austria

Piezoelectric Spindle Drives.....188
Alexej Wischnewski
Physik Instrumente (PI) GmbH & Co KG, Karlsruhe, Germany

A wideband vibration energy harvester with integrated energy management designed for harsh environment.....192
Timotéo Payre, Nabil Bencheikh, Clément-Joseph Galteau, Alexandre Pagès, Guillaume Mansuy, Boris Laluc
Cedrat Technologies SA, Meylan, France

Material Properties of Hard and Soft Piezoelectric Ceramics at Cryogenic Temperatures 195
Burhanettin Koc[1], Jan Homberg[1], Sebastian Schlack[2]
[1]Physik Instrumente (PI) GmbH & Co. KG, Karlsruhe, Germany
[2]PI Ceramic GmbH, Lederhose, Germany

HASEL-Actuated Pneumatic Valve for Image Guided Robotic Systems 199
Fabian Sadi, Jan Holthausen
Mannheim Institute for Intelligent Systems in Medicine (MIISM), Mannheim, Germany

Improving dynamic accuracy of closed loop bandwidth of piezo mechanisms with advanced contro laws and embedded eddy current position sensors 203
Clément Cote, Alexandre Pagès, Olivier Sosnicki, Mathieu Castruccio, Timoteo Payre, Guillaume Mansuy, Xavier De Lepine,
Cedrat Technologies, Meylan, France

Measurement of the High-Power Quality Factor for Piezoelectric Transducers Based on the Electrical Harmonic Steady-State Response 207
Alexej Wischnewski
Physik Instrumente (PI) GmbH & Co. KG, Karlsruhe, Germany

Inertial & Inchworm piezoelectric motors: Design and Motorization selection key aspects 211
Nabil Bencheikh, Nicolas Bourgeot, Alexandre Pagès, Gérald Aigouy, Jocelyn Rebufa, Etienne Betsch, Frank Claeyssen
Cedrat Technologies, Meylan, France

Targeted acoustic positioning of various objects 215
Alexander Backer, Sandro Krempel, Benedikt Stromer, Klaus Stefan Drese
Institute of sensor and actuator technology, University of applied sciences Coburg, Germany

Investigations of additively manufactured SMA high-load actuator elements 219
Andrea Böhm[1], Christian Weck[2], Andreas Hofer[1], Kenny Pagel[1], Welf-Guntram Drossel[1]
[1]*Fraunhofer Institute for Machine Tools and Forming Technology IWU, Dresden, Germany*
[2]*Fraunhofer Institute for Manufacturing Technology and Advanced Materials IFAM, Bremen, Germany*

Modular Gripping Mechanism for Collaborative Robotic Endoscopic Lumbar Decompression (ELD) surgery 221
Giovanni Battista Regazzo[1], Ayoob Davoodi[1], Yuyu Cai[1], Fabio Carrillo[2], Christoph J. Laux[3], Philipp Fürnstahl[2], Emmanuel Vander Poorten[1]
[1]*KU Leuven, Department of Mechanical Engineering, Robot-Assisted Surgery Group (RAS), Leuven, Belgium.*
[2]*Research in Orthopedic Computer Science (ROCS), University Hospital Balgrist, University of Zurich, Switzerland.*
[3]*University Spine Center Zurich, University Hospital Balgrist, University of Zurich, Switzerland.*

Custom Voice Coil Actuator for flexure-based electromechanical RF switch 223
Daniel Grivon
CSME, Neuchâtel, Switzerland

Modelling of an ice protection system based on icephobic and piezoelectric technologies, for WT demonstration 225
Luigi Mangiacrapa[1], Nadine Rehfeld[2], Filomena Piscitelli[1], Salvatore Ameduri[1], Antonio Concilio[1], Giuseppe Mingione[1]
[1]*Centro Italiano Ricerche Aerospaziali, CIRA, Capua, Italy*
[2]*Fraunhofer-Institut für Fertigungstechnik und Angewandte Materialforschung IFAM, Bremen, Germany*

Easy access to smart materials data and models using an ontologybased data and model access approach 229
Robert Courant[1], Jana Mertens[1], Mena Leemhuis[2], Özgür Özçep[2], Martin Dahlmann[3], Sebastian Stark[4], Andrea Böhm[5], Kenny Pagel[5], Maximilian Hinze[7], Daniel Pinkal[6], MichaelWegener[6], MartinWagner[7], Holger Neubert[4], Thomas Sattel[3], Jürgen Maas[1]
[1]Technische Universität Berlin, Germany
[2]University of Lübeck, Germany
[3]Technische Universität Ilmenau, Germany
[4]Fraunhofer Institute for Ceramic Technologies and Systems IKTS, Dresden, Germany
[5]Fraunhofer Institute for Machine Tools and Forming Technology IWU, Dresden, Germany
[6]Fraunhofer Institute for Applied Polymer Research IAP, Potsdam, Germany
[7]Technische Universität Chemnitz, Chemnitz, Germany

Design and simulation of negative-stiffness thermoplastic biasing mechanism for dielectric elastomer actuators 233
Saverio Addario[1], Alberto Priuli[1], Jonas Hubertus[3], Günter Schultes[3], Stefan Seelecke [1,2], Gianluca Rizzello[1]
[1]Saarland University, Department of Systems Engineering, Saarbrücken, Germany
[2]Smart Material Systems, Center for Mechatronics and Automation Technology - ZeMA gGmbH, Saarbrücken, Germany
[3]Department of Sensors and Thin Films, University of Applied Sciences of Saarland, Saarbrücken, Germany

Miniaturization of HASEL Actuators for Next-Generation Applications 237
Ashwani Sharan Tripathi[1], Chen Jiao[1], Andreas Lars Peter Hubracht[2], Georgi Paschew[1], Uwe Marschner[1], E.-F. Markus Henke[1,3], Jürgen Maas[2], and Andreas Richter[1]
[1]Institute of Semiconductors and Microsystems, Technische Universität Dresden, Germany
[2]Mechatronic Systems Lab, Technische Universität Berlin, Germany
[3]Biomimetics Lab, Auckland Bioengineering Institute, The University of Auckland, New Zealand

Miniaturized Dielectric Elastomer Switch with the Potential as Bricks of Cooperative Multi-Actuator System 241
Chen Jiao[1], Ashwani Sharan Tripathi[1], Andreas Hubracht[2], Uwe Marschner[1], Jürgen Maas[2], Andreas Richter[1], E.-F. Markus Vorrath[1,3]
[1]Institute of Semiconductors and Microsystems, Technische Universität Dresden, Germany
[2]Mechatronic Systems Lab, Technische Universität Berlin, Germany
[3]Biomimetics Lab, Auckland Bioengineering Institute, The University of Auckland, New Zealand

A bistable pneumatic actuator based on flexible metamaterials 245
Anagha Navale, Ritika Gupta, Hugo de Souza Oliveira, Viacheslav Slesarenko, Edoardo Milana
University of Freiburg, Germany

Axially Distributed Fluidic Actuators for Steerable Minimally Invasive Surgical Device Applications 249
Bob Lathrop, Mouloud Ourak, Emmanuel Vander Poorten
Department of Mechanical Engineering, KU Leuven, Belgium

A toolchain for deployment of concentric tube continuum robots as curved cannulae in stereotactic neurosurgery 252
Julian Mühlenhoff[1], Matthias K. Hoffmann[2], Dörthe Keiner[3], Mohamed Henia[3], Joachim Oertel[3], Kathrin Flaßkamp[2], Thomas Sattel[1]
[1]Mechatronics Group, Technische Universität Ilmenau, Germany
[2]Systems Modeling and Simulation, Saarland University, Germany
[3]Department of Neurosurgery, Saarland University Medical Center and Faculty of Medicine, Homburg, Germany

Inverse pneumatic artificial muscles with implantable vascular graft 256
Laura Galassi[1,2], Lucrezia Lorenzon[1,2], Matteo Cianchetti[1,2]
[1]The BioRobotics Institute, Scuola Superiore Sant'Anna, Pisa, Italy
[2]Department of Excellence in Robotics & AI, Scuola Superiore Sant'Anna, Pisa, Italy

An origami-based fluidic actuator for Minimally Invasive Surgery 260
Le Gall Alexia, Dangel Théo, Chen Zixi, Cianchetti Matteo
Scuola Superiore Sant'Anna, Italy

Biomimetic Hygromorphic Actuator Systems 263
Jürgen Rühe
University of Freiburg, IMTEK, Freiburg, Germany

Development of a 3D-Bendable soft Robotic Segment actuated by Rolled Dielectric Elastomer Actuators.....266
Julian Kunze[1], Giovanni Soleti[2], Daniel Bruch[2], Gianluca Rizzello[2], Paul Motzki[1,2]
[1]ZeMA - Center for Mechatronics and Automation Technology, Depart. Smart Material Systems, Saarbrücken, Germany
[2]Saarland University, Depart. Systems Engineering, Saarbrücken, Germany

Integrated manufacturing of small-scale dielectric elastomer transducers with rigid structures 269
Andreas Hubracht[1], Albert Thelemann[1], Chen Jiao[2], Ashwani Sharan Tripathi[2], Uwe Marschner[2], Andreas Richter[2], E.-F. Markus Vorrath[2], Jürgen Maas[1]
[1]Mechatronic Systems Lab, Technische Universität Berlin, Germany
[2]Institute of Semiconductors and Microsystems, Technische Universität Dresden, Germany

Miniature Piezo Fast Steering Mirror for Optical Communication in NanoSats and CubeSats.....273
Sylvain Chardon, Timotéo Payre, Mathieu Thomachot, Hugo Grardel, Yann Quentel, Gérald Aigouy, Frank Claeyssen
Cedrat Technologies, Meylan, France

Transient response control of the ultrasonic motor with adaptive frequency sweep 277
Tatsuki Sasamura[1], Norio Sashida[3] and Takeshi Morita[1,2]
[1]Graduate School of Frontier Sciences, The University of Tokyo, Japan
[2]Graduate School of Engineering, The University of Tokyo, Japan
[3]SHINSEI CORPORATION, Tokyo, Japan

Micro magnetomechanical systems (MAMS) 281
Kari Ullakko, Ville Laitinen, Andrey Saren, Hu Hao, Aditya Kumthekar, Meysam Inally
Material Physics Laboratory, Lappeenranta-Lahti University of Technology LUT, Finland

Chemofluidics – an autonomous Lab-on-Chip concept based on smart material components.....283
Andreas Richter[1], Mario Menschikowski[2], Markus Friedemann[2], Denise Gruner[1,2], Anthony Beck[1], Mohammed Sahadha[1], Franziska Obst[1], Paula Kalenczuk[1], Stefan Grünzner[1], Alexander Kutscher[1], Andreas Voigt[1], Uwe Marschner[1]
[1]Institute of Semiconductors and Microsystems, Technische Universität Dresden, Germany
[2]Institute of Clinical Chemistry and Laboratory Medicine, University Hospital Dresden, Germany

Adaptive Hydrogel Microactuators 285
H.B. Duc Tran, Christoph A. Spiegel, Eva Blasco
Institute of Organic Chemistry (OCI), Heidelberg University, Germany & Institute for Molecular Systems Engineering and Advanced Materials (IMSEAM), Heidelberg University, Germany

In-Plane Bistable Microdevice in Silicon Technology 287
Gowtham Arivanandhan[1], Maximilien Kiegerl[1], Elaheh Akbarnejad[2], Zixiong Li[1], Alfred Ludwig[2], Manfred Kohl[1]
[1]Institute of Microstructure Technology, Karlsruhe Institute of Technology (KIT), Karlsruhe, Germany
[2]Institute for Materials, Ruhr University Bochum (RUB), Bochum, Germany

Development of a Re-Programmable Micro Origami Device 289
Vincent Gottwald, Lena Seigner, Manfred Kohl
Institute of Microstructure Technology, Karlsruhe Institute of Technology (KIT), Karlsruhe, Germany

-Hold it together- Micro-actuator latching mechanism 291
Martin Heyer, Jürgen Rühe

Functional test of a training device for moving fingers and wrist joints using soft pneumatic actuator

Masaki Todo, Hironari Taniguchi, and Daigo Ishii
Graduate School of Robotics and Design, Osaka Institute of Technology
1-45, Chayamachi, Kitaku, Osaka, Japan

Abstract

In this study, we developed a finger and wrist motion support device for preventing joint contracture using a slide table that can adjust to the size of the user's hand and a pneumatic soft actuator whose length can vary. By directly applying the pneumatic soft actuator to the hand, flexion and extension movements are performed at each joint to prevent contracture. To investigate the performance characteristics of the actuators used in the prototype device, experiments measuring force generation were conducted. The experiments revealed that the box-type actuator ceased to increase its generated force when it approached a certain distance, while the laminated-type actuator, which inflated in a fan-shaped manner, increased linearly. This result is attributed to the fact that the box-type actuator allows force to escape from surfaces other than the contact surface and the fixed surface. Additionally, the operation of the device was verified with one male participant in his twenties. The flexion motion achieved a success rate of around 90% of the target value, but the wrist extension motion resulted significantly lower compared to other movements.

1 Introduction

Joint contractures, resulting in decreased joint range of motion, occur when joints remain immobile due to accidents, illness, or aging. Improving joint range of motion (ROM) through physical therapy is expected to prevent joint contracture. However, the shortage of physical therapists who provide ROM training has become a concern in the nursing and welfare fields in recent years. The joints of the fingers and wrists are crucial for grasping and carrying objects in daily life, and devices have been developed to provide rehabilitation in place of physical therapists [1-2]. Among them, many glove-type devices designed to be worn on the hand have been developed [3-4]. Some devices have increased tensile strength compared to conventional pneumatic bellows actuators by employing an actuator that pulls a cable passing through the center of the bellows [5], some use a servomotor to pull a fishing line to bend the fingers and a rubber band to return the fingers to an extended state [6], and some use a device made of airbags to maintain finger extension [7].

This research group has been developing a device that provides motion support by directly acting on joints using a pneumatic soft actuator formed by crimping aluminum film into a bag or box shape and covering it with canvas [8-10]. Previous devices have not been able to bend the flexion and extension of the MP joints and wrist joints to the reference range of motion for each joint. In this study, we investigated a mechanism for the linear movement of the slide stand and an actuator that corresponds to the size of the user's hand, and revised the device with the aim of enabling movement of both the MP joints and the wrist joints to the reference range of motion. Additionally, force measurement experiments of the actuator were conducted to investigate its characteristics. A user trial was conducted with one male participant in his twenties to verify the device's operation. This paper reports on the structure of the device, the method of movement, force measurement experiments of the actuator, and the operation check of the device.

2 Training device for moving fingers and wrist joints

2.1 Design

Figure 1 illustrates the structure of the finger and wrist joint motion support device. The main unit is 250 mm wide, 650 mm deep, and 353 mm high, and consists mainly of pneumatic soft actuators (1) to (4), a slide stand (shown in blue), and an arm rest (shown in green). The fixation actuator (1) holds the wrist and the back of the hand from above to prevent the arm from moving during each movement. The wrist joint extension actuator (2) and the MP joint extension actuator (3) are used for each extension movement, and these two actuators are housed inside the slide stand. The flexion actuator (4) is used for flexion of the MP joint and wrist joint, and by changing the position of the slide stand, both flexion movements can be performed with a single actuator.

In addition, the actuator for wrist joint extension in (2) of this device has a canvas band on each of the bag-type actuators, and the tip of this band is fixed as shown **Figure 2**. When compressed air is applied to the actuator, the tip of the arm rest presses down on the band, causing the sliding platform to move. This movement changes the axis of rotation of the stacked actuators, which expand in a fan shape. As the axis of rotation moves, the length of the actuator from the axis of rotation changes, allowing the actuator to accommodate different palm lengths for different users.

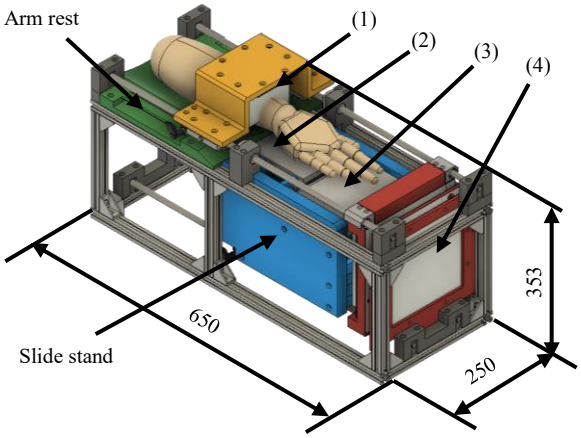

Figure 1 Training device for moving fingers and wrist joints using soft pneumatic actuators

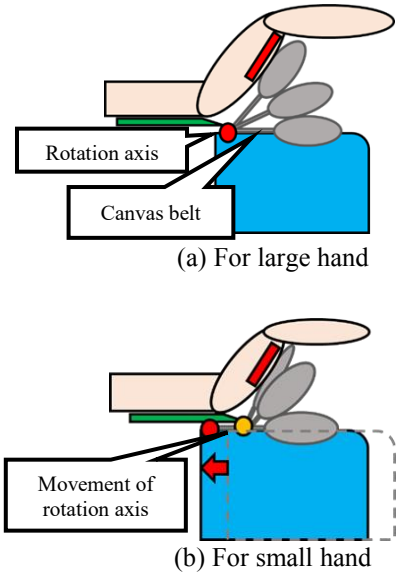

Figure 2 Movement of rotation axis

2.2 Working method

We explain the method of exercising the fingers and wrist joints using this device. The device is designed to flex and extend the MP joints and wrist joints up to the reference range of motion of the four fingers except for the thumb. First, the arm and the slide stand are positioned. With the slide stand fully retracted under the arm rest, the arm is inserted with the back of the hand facing upward, and stopped at the position where the wrist joint is fully flexed as shown in **Figure 3**. Then, fix the wrist with the fixation actuator (1) and pull out the slide stand so that the border between the actuators (2) and (3) inside the slide stand aligns with the MP joint. From this state, compressed air is applied to the wrist joint extension actuator (2) to perform wrist joint extension, and the air is applied to the MP joint extension actuator (3) to perform MP joint extension while holding the back of the hand with the fixation actuator (1) as shown in **Figure 4**. The MP joint flexion motion is performed by applying air to the actuator (4) while moving the slide stand with the four fingers flexed, and by applying air to the actuator (4) when the slide stand is completely retracted and the wrist joint is bent as shown in **Figure 5**.

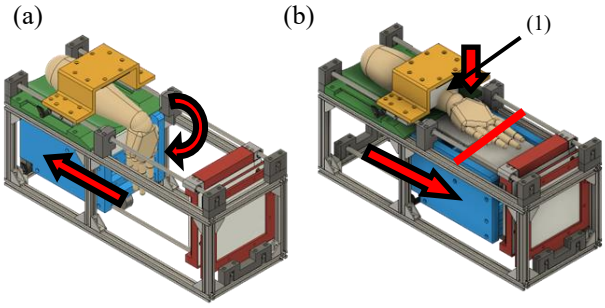

Figure 3 Positioning for (a) wrist and (b) finger joints

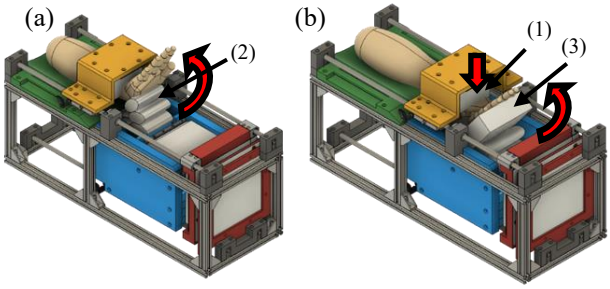

Figure 4 Extension movement for (a) wrist and (b) finger joints

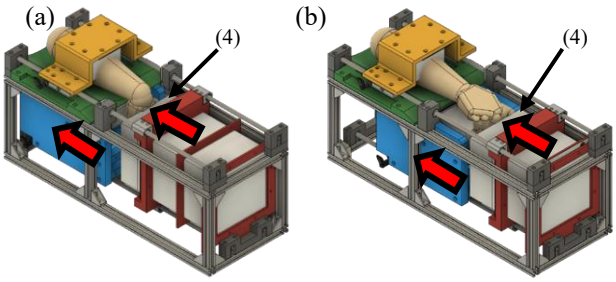

Figure 5 Flexion movement for (a) wrist and (b) finger joints

2.3 Generated force of soft actuator

To investigate the characteristics of soft actuator used in the prototype device, force generation measurement experiments were conducted for each actuator. The distance from the digital force gauge to the fixed surface of the actuator was varied in the case of a box-type actuator, and the angle was varied in the case of a stacked actuator. The generated force was measured three times at each position, and the average value was recorded. Under the test conditions, the applied air pressure was fixed at 20 kPa, and a 3D printer was used to fabricate rectangular plates of the size of each part of the hand and fingers as fixture to be attached to the digital force gauge.

Below are the experimental results and discussion. First, **Figure 6** shows the force generated when the back of the hand is held by the fixing actuator (70 × 70 × 90 mm box-type actuator) using a fixture (70 × 80 mm) on the dorsum of the hand. The force generated increased linearly as the distance from the fixation surface approached from 80 to

50 mm, with a maximum force of 177.5 N at the 50 mm position. It is believed that the force escaped from the front, back, left, and right surfaces other than the actuator contact surface.

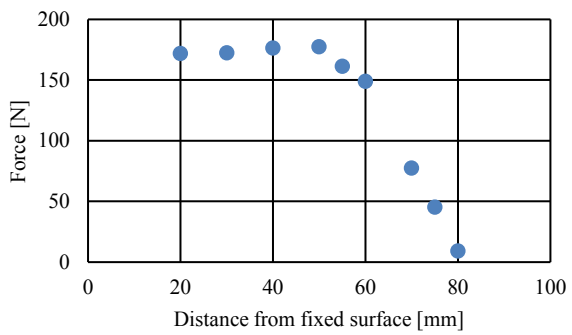

Figure 6 The force generated when the back of the hand is held by the fixing actuator (70 × 70 × 90 mm box-type actuator)

Figure 7 shows the force generated during wrist joint extension motion. The palm fixture (80 x 100 mm) on an actuator for wrist joint extension, which is stacked actuator with a 70 x 70 mm bag-type actuator at the top. The experimental results showed that, unlike the box actuator, the force generated increased linearly even when the digital force gauge was brought close to a position up to 10 degrees from the fixed surface, and the maximum force generated was 62.9N at the 10-degree position. We considered that the stacked actuator, which uses a bag-type actuator, expands only in the vertical direction, making it difficult for the force to escape in the front-back and left-right directions, compared to a box-type actuator. The force at 70 degrees, which is within the reference range of motion, was 4.0 N, indicating safety.

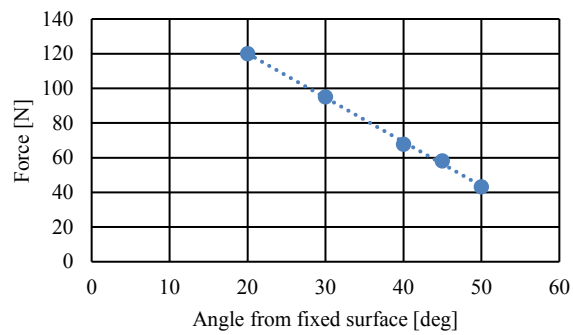

Figure 7 The force generated during wrist joint extension motion

Finally, **Figure 8** shows the force generated during MP joint extension motion. The hand fixture (80 x 100 mm) is used on the MP joint extension actuator, which is stacked actuator with a box-type actuator with a contact surface of 95 x 130 mm at the top. The experimental results showed that, as with the wrist joint extension actuator, the force increased linearly as the angle from the fixation surface was approached, with a maximum force of 120.0 N generated at the 20-degree position. Additionally, at the position corresponding to the reference range of motion, which is 45 degrees, the force was 58.0 N.

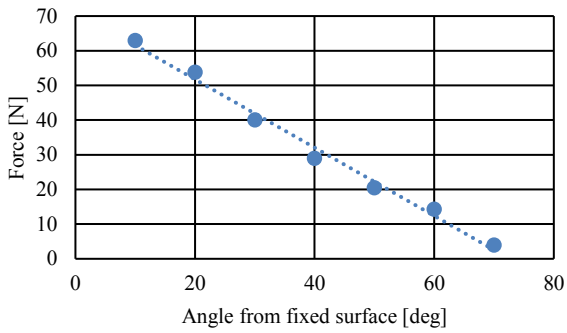

Figure 8 The force generated during MP joint extension motion

3 Movement test

The functionality of the device was then verified with a male participant in his 20s. First, the range of motion of each joint in the participant's left hand was measured with a goniometer before using the device. Next, each extension and flexion movement were performed after positioning of the arm and slide table as described in Section 2.2. The movement angles were measured with a goniometer and the joint range of motion (measured angle) measured before using the device was used as the target angle and compared with the experimental results. Extension and flexion movements were performed three times each, and the average value was used as the measurement result. The pressure applied to each actuator was set at 20 kPa. This study was conducted with the approval of the Ethics Committee for Life Science Experiments at Osaka Institute of Technology (approval number: 2023-54). **Figure 9 and 10** show the measurement angles and a photograph of the experiment.

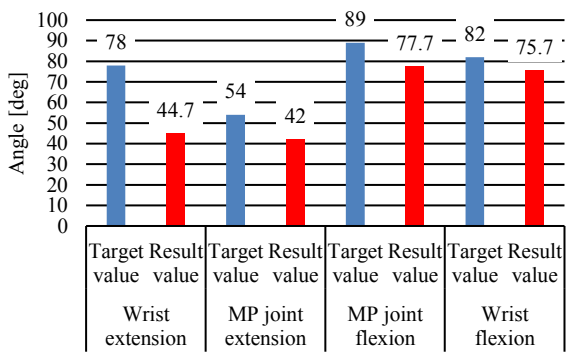

Figure 9 Target values (measurement angles before using the device) and result values

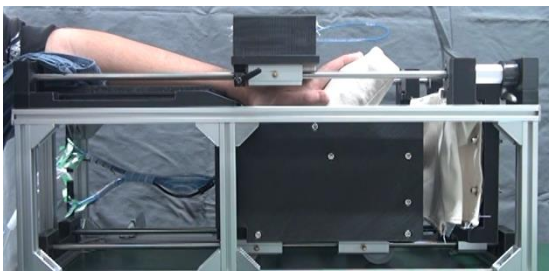

Figure 10 Movement test with MP joint extension

As a result, the MP joint flexion reached 77.7 degrees against the target value of 89 degrees, and the wrist flexion reached 75.7 degrees against the target value of 82 degrees, achieving approximately 90% of the target values. On the other hand, wrist extension fell short by 44.7 degrees of the target value of 78 degrees, which is more than 30 degrees. We considered that it was difficult for the subject to perform within a range where they did not feel pain with the fixation actuator, and if the fixation was not painful, the arm was pushed by the actuator toward the body during the extension movement, causing the wrist joint to shift its position.

4 Conclusions

In this study, we proposed the hand and wrist joints motion support device using soft actuators. The device includes a slide stand that supports the hand while incorporating an actuator for extension, and an actuator whose length changes depending on the position of the slide stand, designed to accommodate the size of the user's hand. We tested the operation of the device with a male participant in his 20s. The results showed that the flexion movement achieved approximately 90% of the target value, but the wrist joint extension movement was significantly lower than the other movements. In the future, we plan to improve the actuators, especially the fixation actuator, and to control each movement using sensors.

5 Acknowledgement

The authors gratefully acknowledge funding by the Japan Keirin Autorace Foundation (JKA) through its promotion funds from AUTORACE.

6 Literature

[1] Prem Kumar Mathavan Jeyabalan, Aravind Nehrujee, Samuel Elias, M. Magesh Kumar, S. Sujatha, and Sivakumar Balasubramanian, : Design and Characterization of a Self-Aligning End-Effector Robot for Single-Joint Arm Movement Rehabilitation. Robotics 2023, 12(6), 149, 2023.

[2] Vicenç Punsola-Izard, Aroa Casado, Nuria Carnicero, Elena Ozaes-Lara, Judit Mendieta-Zamora, Gemma Romera-Orfila, Karen S. Schultz, and Manuel Llusà, : A Comparison between Two Intervals of Daily Total End Range Time for Treatment of Proximal Interphalangeal Joint Flexion Contracture Using an Elastic Tension Digital Neoprene Orthosis. J. Clin. Med. 2023, 12(5), 1987, 2023.

[3] Rami Alhamad, Nitin Seth, and Hussein A. Abdullah, : Initial Testing of Robotic Exoskeleton Hand Device for Stroke Rehabilitation. Sensors 2023, 23(14), 6339, 2023.

[4] Fanye Meng, Chang Liu, Yu Li, Hao Hao, Qishen Li, Chenyi Lyu, Zimo Wang, Gang Ge, Junyi Yin, Xiaoqiang Ji, and Xiao Xiao, : Personalized and Safe Soft Glove for Rehabilitation Training. Electronics 2023, 12(11), 2531, 2023.

[5] Dehao Duanmu, Xiaodong Li, Wei Huang, and Yong Hu, : Soft Finger Rehabilitation Exoskeleton of Biomimetic Dragonfly Abdominal Ventral Muscles: Center Tendon Pneumatic Bellows Actuator. Biomimetics 2023, 8(8), 614, 2023.

[6] Ebenezer Raj Selvaraj Mercyshalinie, Akash Ghadge, Nneka Ifejika, and Yonas Tadesse, : NOHAS: A Novel Orthotic Hand Actuated by Servo Motors and Mobile App for Stroke Rehabilitation. Robotics 2023, 12(6), 169, 2023.

[7] Gregory Jackson, and Hussein A. Abdullah, : Development and Testing of a Soft Exoskeleton Robotic Hand Training Device. Sensors 2023, 23(20), 8395, 2023.

[8] Hironari Taniguchi, Yusuke Naito, : Hand Rehabilitation Device to Prevent Contracture for Finger Joints using Pneumatic Soft Actuators. International Journal of Innovations in Engineering and Technology (IJIET), ISSN: 2319 – 1058, 2014.

[9] R. Aoyama, H. Taniguchi, : A Proposal for ROM Device to Prevent Contractures of the Thumb Joint Using Pneumatic Soft Actuators. ACTUATOR2018, p.607-611, 2018.

[10] Hiro Okamoto and Hironari Taniguchi, : Development of Pneumatic Exercise Device for the Range of Motion in the Ankle Joint. 2022 IEEE/SICE International Symposium on System Integration (SII), 585-589, 2022.

Control of Magnetorheological Fluid Brake for Medical Ergometers based on Cycling Model

Abd Elkarim Masoud, Valentin Schreiner and Jürgen Maas
Technical University Berlin, Mechatronic Systems Lab, Hardenbergstraße 36, 10623 Berlin, Germany,
Email: Abdelkarim.Masoud@emk.tu-berlin.de

Abstract

Bicycle ergometers offer a convenient means of exercise independent of outdoor conditions, finding application not only in sport and leisure but also in medical diagnostics and rehabilitation. Existing models predominantly employ eddy current brakes, necessitating additional components like planetary gearboxes and flywheels to compensate for speed-dependent torque. Magnetorheological fluid (MRF) brakes represent a promising alternative, offering precise torque adjustment regardless of speed. This paper presents a control scheme of an MRF-based ergometer optimized for medical rehabilitation and competitive sports. A brief overview of MRF-based actuators provides the foundation for discussing the ergometer's implementation, control system, and experimental validation. A cascaded control system was design, in which a low level control strategy optimizes the torque adjustment, utilizing dynamic feedforward and nonlinear compensation structure. And a high level control is used, to accurately replicate real-world driving behavior of a bicycle in a Hardware-in-the-Loop (HiL) test bench. Finally, experimental results demonstrate the effectiveness of the developed MRF-based ergometer, offering precise control and realistic driving behavior.

1 Introduction

Bicycle ergometers provide the opportunity to exercise independently of the environment. As well as being used for sport and leisure, they are consequently also used in medical performance diagnostics and rehabilitation medicine. The powertrains of commercially available models are almost exclusively based on eddy current brakes [1]. As the torque of eddy current brakes is highly dependent on the speed [2], planetary gearboxes and belt drives are usually used in the drive train. In addition, a flywheel is usually used on the fast-rotating shaft to compensate for the torque that drops off at standstill. The incorporation of flywheels introduces complexities, increases production costs enormously, and expands the dimensions of the braking system. Addressing these drawbacks and aiming to preserve optimal dynamics, a promising alternative represents the utilization of brakes based on magnetorheological fluids (MRF). Classified as smart materials, MRFs allow for the manipulation of specific material properties through the effect of a magnetic field, enabling the realization of brakes with precise and finely adjustable braking torque. The generated braking torque by MRF brakes remains nearly independent of rotational speed within the relevant range for ergometers, as substantiated by previous studies [3, 4]. By eliminating supplementary components like gears or drive belts, MRF brakes contribute to cost reduction and a more compact installation footprint. In contrast to eddy current brakes, magnetorheological brakes allow torque to be adjusted almost independently of speed and provide the rated torque even at standstill. This obviates the need for previously employed physical components like flywheels, as their effects can be emulated through MRF brakes. Additionally, the speed-independent resistance torque facilitates precise regulation of the power exerted by the patient, offering significant rehabilitation benefits.

The system proposed in [5] consequently utilize this approach as a direct drive. The T-drum design used provides high torque density with long service life and good controllability. The low moment of inertia of the developed system, which acts directly on the driveshaft without a gearbox, results in a highly dynamic system. This presents a particular challenge for use in a bicycle ergometer, but in combination with the Hardware-in-the-Loop system presented in this contribution, also offers a great degree of freedom and thus new possibilities for training as well as rehabilitation medicine.

This paper outlines the development of a controllable MRF-based ergometer tailored for application in medical rehabilitation and competitive sports. The initial section provides a succinct overview of the working principle of the MRF-based actuator, laying the groundwork for the subsequent discussion on the implementation of the actuator and of required moment- and position-sensors into an ergometer. The next focal point of the paper resides in the presentation of the ergometer's control system. An energy-based model of a bicycle is formulated to facilitate the real-time adaptation of driving resistance parameters, including roll resistance, bicycle inertia, and gears. The paper concludes with the implementation and validation of the control algorithm through representative experimental investigations, underscoring the practical applicability and efficacy of the developed MRF-based ergometer.

2 Ergometer based on MRF actuator (HiL System)

The developed system in [5] is intended to replace a currently used eddy current brake in a space-neutral manner, while reducing the need for additional components. This limits both the axial and radial installation space. Figure 1 shows the actuator design and measured torque behaviour versus coil current. The rotational speed during the experiment was set to 10 rpm, so that the influence of viscosity is negligible. The brake is able to generate a maximum resistance torque of up to 90 Nm at a maximum rotational

speed of 180 rpm. In order to enable training at very low resistance values, the no-load torque must be as low as possible. The relationship between the measured torque and current is nonlinear and is denoted by $\mathcal{N}$.

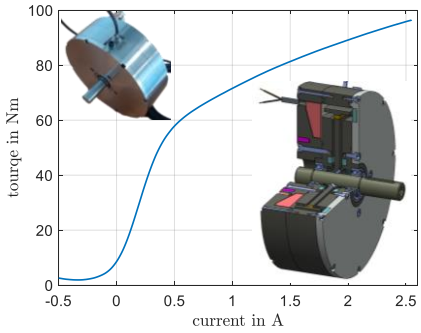

Figure 1 Actuator design and experimentally obtained torque-current-characteristic used in this work as presented in [5].

In Figure 2, the MRF ergometer with the HiL system is depicted. By energizing the MRF actuator, a braking torque is generated when pedaling, which can be adjusted depending on the current *i*.

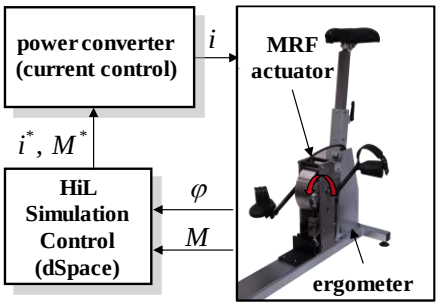

Figure 2 HiL structure of the MRF Ergometer.

For position φ and torque M measurements, a high-resolution incremental encoder and a strain gauge-based torque sensor are used. Parameterization of the controllers and initialization of the set-point values as well as the recording and displaying of measurement signals are preformed using the HiL system of dSPACE. The sensor data is recorded in dSpace, and a desired current i^* or torque M^* is specified. The goal is to implement control algorithms that can closely replicate real driving behavior.

3 Torque control of the MRF actuator (low level control)

To achieve the best possible performance of the MRF ergometer, the braking torque must be adjusted as fast as possible to follow the typical load profile for a bicycle. In Figure 3, the structure of the torque control is depicted, which used as inner control loop for the outer high-level control.

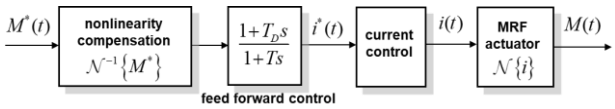

Figure 3 Torque control for an improved transient torque response.

The time delay due to the dynamic behavior of the coil current is determined by the inductance and the winding resistance of the coil and is minimized by using a PI-control current controller. The control parameters of the current control were adjusted according to the inductance and resistance of the rotary actuator and optimized with respect to maximum dynamics. The remaining time delay of the controlled current can be neglected, as long as a certain gradient of the reference current is not exceeded. Furthermore, the propagation speed of the magnetic field inside the magnetic circuit is affected by eddy currents and thus the transient response of the generated torque is mainly delayed by it [7, 8]. To maximize the dynamics, a dynamic feedforward control using a PD-T_1 element has been implemented. During transition phase, the time gradient of the current is maximally specified to obtain a fast torque response. Finally, for a linear torque control, the inverse of the measured nonlinearity $\mathcal{N}^{-1}$ is determined and placed at the beginning of the control structure. In Figure 4, the measurement results for torque and current measurement with and without feedforward control are illustrated.

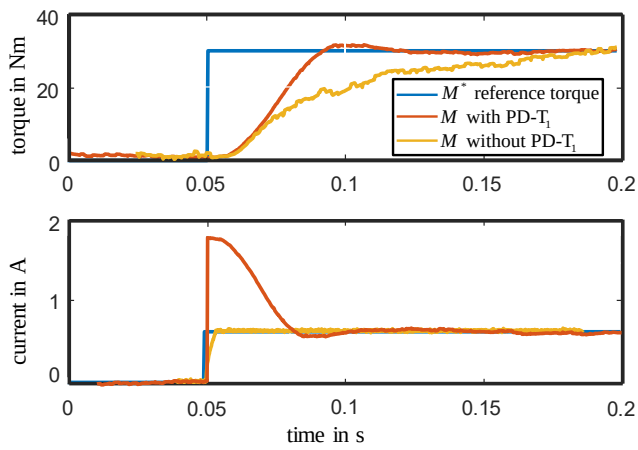

Figure 4 Torque and current responses of the MRF actuator with and without feed forward control.

For a desired torque step of 30 Nm, the total settling time has been reduced from 70 ms to approximately 30 ms with the feed forward control. In the current signal, it can be observed that the current rise is quite large in order to compensate for the effects of eddy currents. As described in [8], changing the shape of the magnetic circuit or changing the material could offer possibilities to even further improve the dynamics.

4 Model based control of the Ergometer (high level control)

4.1 Specification of a harmonic torque profile

To replicate real driving behavior, the goal is to specify a harmonic load profile where the offset M_0, amplitude $\hat{M}$, and phase α can be adjusted. This phase is determined by the measured position of the pedal and a shift that can be used to compensate for phase shift and adjust the dead center. Thus, a typical load profile for a bicycle is described in the ergonomic study [6] as follows:

$$M^*(\varphi) = M_0 + (\hat{M} - M_0)\sin(2\cdot\varphi + \alpha) \qquad (1)$$

In this case, the phase α was adjusted to set the minimum torque at the dead center. Depending on the pedal angle, the torque was then adjusted to the low level torque control according to Figure 1. In Figure 5, the measurement result of the torque profile for a cadence of approximately 60 rpm is depicted.

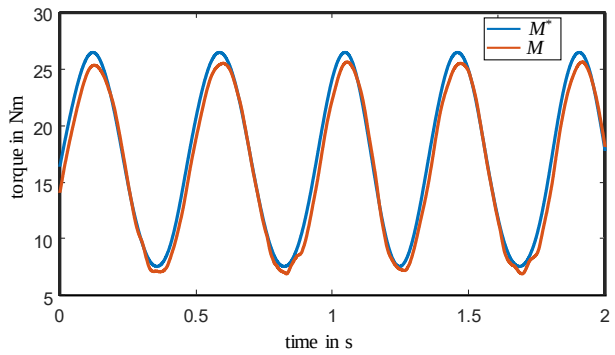

Figure 5 Experimental results for the harmonic torque profile in accordance to Eq. (1) by using the control in Fig 3.

Thus, a harmonic torque profile can be specified without significant time delay or control errors. There is still a slight phase shift, which is dependent on speed and could not be completely compensated despite accounting for dead time. However, when a harmonious torque profile is specified, the natural, smooth rotation that we are used to from cycling is only achieved to a limited extent. Depending on body structure, different individuals introduce different torque profiles (e.g., due to varying height, left/right leg muscle), resulting in the natural torque profile not being ideally harmonic as assumed in Eq. (1). Controlling the specified torque profile dependent on angle doesn't achieve an ideally natural driving behavior, as each individual generates a different load profile.

4.2 Control with an energy-based approach

The torque profile of the MRF actuator should be able to adapt to the individual torque profile of a driver. To adjust the desired driving behavior, the outer high-level control structure shown in Figure 6 is proposed.

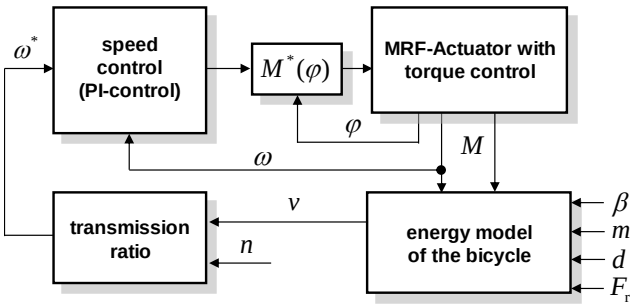

Figure 6 Control structure of the MRF ergometer based on speed control and energy model.

The reference variable is not torque but rather the angular velocity of the pedal ω^* generated by the bicycle model. The speed controller ensures that the desired torque $M^*(\varphi)$ automatically adjusts given the pedal speed. The desired speed ω^* is determined from an energy-based (kinetic energy) bicycle model as follow:

$$\frac{\mathrm{d}\mathcal{U}_{\mathrm{kin}}}{\mathrm{d}t} = P_{\mathrm{m}} - P_{\mathrm{r}} - P_{\mathrm{g}} - P_{\mathrm{w}}, \text{ with}$$
$$\mathcal{U}_{\mathrm{kin}} = \frac{1}{2} m \cdot v^2,\ P_{\mathrm{m}} = M\omega,\ P_{\mathrm{r}} = F_{\mathrm{r}} v, \qquad (2)$$
$$P_{\mathrm{g}} = v \cdot mg\sin(\beta),\ P_{\mathrm{w}} = F_{\mathrm{w}} \cdot v,\ F_{\mathrm{w}} = d \cdot v^2$$

Where U_{kin} represents the kinetic energy of the bicycle with the velocity v, P_{m} is the supplied mechanical power, P_{r} is the power of rolling resistance F_{r}, and P_{g} is the power of the resistance due to the gradient of the road β, P_{w} is the power due to wind resistance. The mass in Eq. 2 includes the mass of bike and rider as well as the transformed moment of inertia J_{w} of both wheels.

$$m = m_{\mathrm{Rider}} + m_{\mathrm{Bike}} + 2\frac{J_{\mathrm{w}}}{r^2}, \text{ with}$$
$$m_{\mathrm{Rider}} = 68\,\mathrm{kg},\ m_{\mathrm{Bike}} = 10\,\mathrm{kg},\ J_w = 0{,}26\,\mathrm{kg\,m^2} \qquad (3)$$

By integrating Eq. 2, considering the supplied and dissipated powers, the kinetic energy is evaluated in real-time, from which the velocity

$$v = \sqrt{\frac{2\mathcal{U}_{\mathrm{kin}}}{m}} \qquad (4)$$

is estimated. Furthermore, the bicycle speed v enters the speed control as the desired speed

$$\omega^* = \frac{1}{r\,n} v, \qquad (5)$$

with a wheel radius r and a transmission factor n, allowing gears to be represented in addition to the bicycle model parameters. For the validation of the control structure, two test runs are depicted in Figures 7 and 8. Table 1 lists realistic parameters used in the experiments.

Parameter	r	n	m	F_{r}	β
Value	36 cm	1-3	80 kg	2.4 N	0-10°

Table 1 Parameters to emulate the cycling behaviour.

In the first experiment (Figure 7), an acceleration test is conducted on a slope with β=0, with gear shifts n from 1 to 3 (red line). During the experiment, pedaling does not generate a constant harmonic torque profile (black lines),

which also occurs during natural cycling. By observing the averaged power, it can be noted that with each gear upshift it increases, leading to continuous acceleration of the emulating bicycle system.

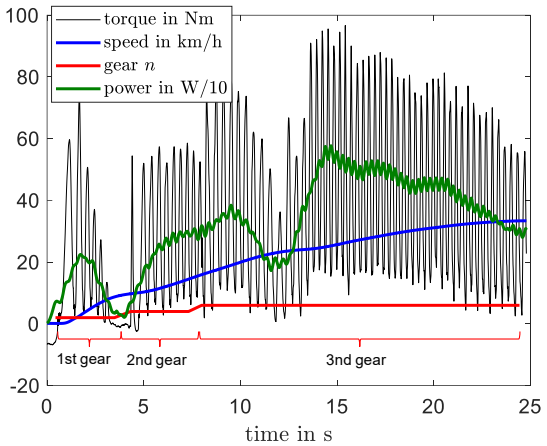

Figure 7 Experimental results of the model-based bicycle HiL-system in case of acceleration during gear upshifts.

In the second experiment, the road gradient β is varied, and the cycling behavior during this variation is examined. After an acceleration phase, approximately 20 seconds during the first experimental phase, the road gradient is set to 7°. Due to the gravitational force acting on the mass m, the bicycle decelerates, and the virtual speed visibly decreases. After approximately 50 seconds, the road returns to being flat (β=0), the torque on the MRF actuator is reduced, and the system accelerates again. When riding downhill in the range of 70 s, it can further be observed that the bike continues to accelerate as the rider pushes for top speed.

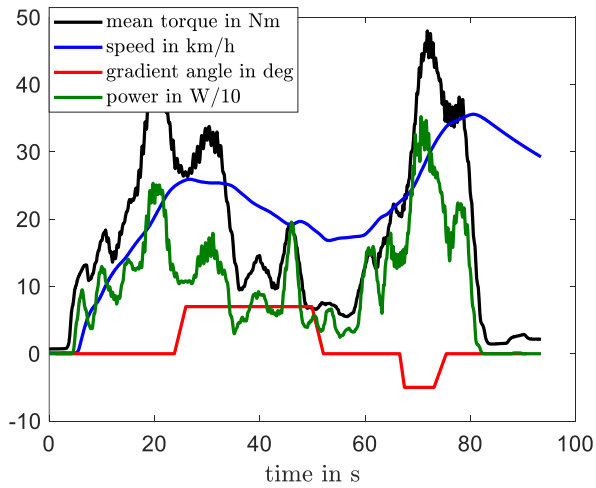

Figure 8 Experimental results of the model-based bicycle HiL-system when varying the road gradient.

5 Conclusion

The development of MRF-based ergometers offers a promising alternative to traditional eddy current brakes in bicycle ergometer design. By leveraging MRF technology, these ergometers provide precise and independent torque adjustment, eliminating the need for supplementary components like flywheels and reducing production costs. The integration of MRF actuators and advanced control systems enables the realization of highly dynamic ergometers tailored for medical rehabilitation and sports training. Through representative experimental investigations, the versatility and practical applicability of the developed MRF-based ergometer have been demonstrated, underscoring its potential for enhancing performance and facilitating precise control in different applications. This research opens new avenues for future advancements in ergometer design and contributes to the advancement of medical rehabilitation and competitive sports training.

6 Acknowledgments

This contribution is accomplished within the project "RotAktor", funded by the Federal for Economic Affairs and Energy (BMWi) of Germany under grant number KK5125801RU0.

7 Literature

[1] Vandewalle, H. and Driss T., Friction-loaded cycle ergometers: Past, present and future, Cogent Engineering, 1029237, 2015.

[2] Sharif S., Faiz J., Sharif K., Performance analysis of a cylindrical eddy current brake, IET Electric Power Applicat., Vol. 6 Issue 9, 661 – 668, 2012.

[3] Maas, J., Güth, D., Wiehe, A., MRF-actuator concepts for HMI and industrial applications, SPIE Smart Structures/NDE, 7977, p. 7977-14, 2011.

[4] Ayraam, M., et al., Portable smart wrist rehabilitation device driven by rotational MR-fluid Brake actuator for telemedecine applications, IEEE/RSJ Intern. Conf. on Intelligent Robots and Systems, 2008.

[5] Masjosthusmann, L., Schreiner, V., Tschersich, J., Baumann, F., Neumann, L., & Maas, J., Development of a precisely controlled magnetorheological fluid brake for medical ergometers, ACTUATOR 2022.

[6] Saeed, D. F. et al., Prediction of crank torque and pedal angle profiles during pedaling movements by biomechanical optimization, MEDICAL AND BIO-ENGINEERING APPLICATIONS, 2014.

[7] Wiehe, A.; Maas, J.: Control Based Optimization of the Dynamic Behavior of MR Actuators. 12th International Conference on New Actuators - ACTUATOR 2010, pp. 817-820, 2010.

[8] Strecker, Z.; Jeniš, F.; Kubík, M.; Macháček, O.; Choi, S.B. Novel Approaches to the Design of an Ultra-Fast Magnetorheological Valve for Semi- Active Control. Materials 14, 2021.

Design, manufacturing and control of a non-magnetic pneumatic linear stepper actuator with inchworm kinematics

Timothée Portha[1], Laurent Barbé[1], François Geiskopf[1], Jonathan Vappou[1], Paolo Cabras[1,2], Pierre Renaud[1]
[1]Université de Strasbourg, INSA Strasbourg, CNRS, INSERM, ICube, Strasbourg, France,
timothee.portha@etu.unistra.fr
[2]IGT, Image Guided Therapy, Pessac, France

Abstract

Over the past decades, pneumatic actuation has emerged as an interesting solution for Magnetic Resonance Imaging (MRI)-compatible robotics. In this paper, a pneumatic linear stepper motor that enables to position medical devices is presented. The proposed actuator is based on inchworm kinematics, and it is composed of three main active chambers: two grippers and one extension chamber. The first part of the paper presents the design and manufacturing of the three components based notably on additive manufacturing of elastomers and rigid polymers, and then the control strategy is described. Experimental results show the MR compatibility as well as the effectiveness of the actuator, especially in terms of achievable speeds through the control of the extension chamber. Testing of the actuator also confirms the interest for the application, with possible evolutions to widen its field of application.

1 Introduction

In the medical field, robotics has proved its worth in a wide range of applications. Robotics applied to image-guided interventions are of particular interest for tasks such as needle positioning [1] and HIFU (High Intensity Focused Ultrasound) probe positioning [2], that relies on MRI to monitor the procedure and to position the device. This imposes strong design constraints on the robotic system in terms of compactness, magnetic susceptibility and MR-compatibility of any active component in the robot, i.e. sensors and actuators. Polymer materials and fluidic actuation have thus been primarily used [3]. Several actuators have been proposed, many of them using pneumatic energy. Several designs of stepper motors can be found, but solutions for linear actuation are still limited. One solution of great interest, proposed in [4], generates force and linear step-by-step displacement through the relative motion of racks. Nevertheless, generated force and relative motion are strongly dependent, and friction inherent to the kinematic principle has to be managed. Another solution, proposed in [5], relies on inchworm kinematics to enable needle positioning. A continuous elongation of a central pneumatic chamber is responsible for needle motion. Pneumatic grippers are integrated to generate the inchworm kinematics and obtain unlimited range of motion. Here, friction is being used to allow for a correct grasping of the needle, i.e. the moving element. Possible sliding limits the achievable precision in terms of position and force transmission.

2 Proposed actuator's design

2.1 Structure and working principle

A linear stepper actuation unit is thus proposed with a specific design. It is intended to position a HIFU probe in the MRI tunnel. Using inchworm kinematics with rigid obstacles seems promising to achieve positioning control in open loop, without any sensor in the MRI field, while guaranteeing the amplitude of the steps. We applied this approach with a target resolution below 2 mm, to be compatible with the typical MR image resolution used for HIFU ablations monitoring protocols. In addition, the actuation unit needs to be compact and controlled remotely, since the pneumatic control cabinet must be connected using 10-m long pneumatic tubing. The actual actuation unit is shown mounted on two guiding rods in **Figure 1** and its different components are represented schematically in **Figure 2**. The sequence of inchworm kinematics is depicted in **Figure 3**.

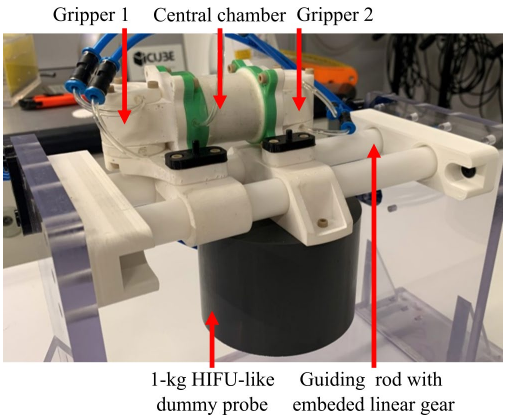

Figure 1 - The prototype of linear stepper actuator.

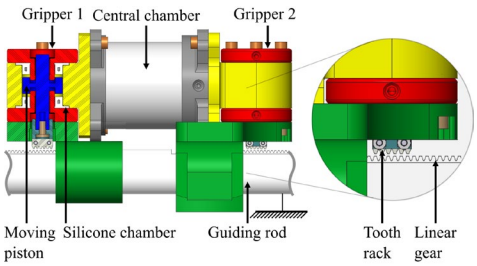

Figure 2 - CAD drawing of the actuation unit.

In **Figure 3**, the use of rigid obstacles for transmission is illustrated. Using three pneumatic elements, two grippers and a central chamber, it is possible to generate the linear motion. The central chamber exerts the axial force and modifies the distance between the grippers.

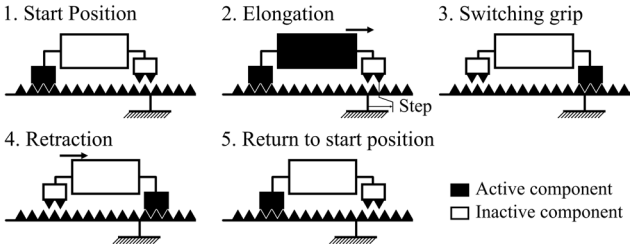

Figure 3 – Actuation sequence of the inchworm kinematics.

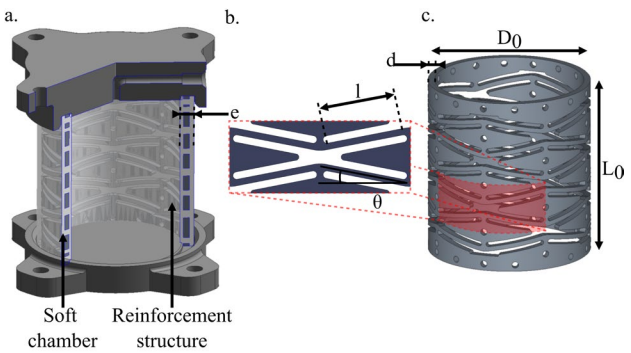

Figure 4 – a. 3D CAD view with partial section of a gripper. b. Unit pattern of the reinforcement structure. 3D CAD view of the reinforcement structure.

2.2 Central chamber

The central chamber is designed as a 1-way piston composed of an inflatable chamber reinforced with a truss structure. This reinforcement structure aims to favor the axial elongation of the pneumatic chamber. The design of the central chamber is presented in **Figure 4**. The reinforcement truss structure consists in a repetition of an inverted honeycomb pattern (**Figure 4.b**). This pattern is inspired by the one introduced in [6], allowing motion through the bending of beams of length l from an initial angle θ. This pattern is repeated N_v and N_c times, respectively along the length of the structure and its circumference. The thickness of the structure is denoted by d. In order to satisfy the need for compactness, the diameter of the central chamber is fixed to 35 mm. The values of the parameters are set to obtain an elongation at least twice the requested resolution, i.e. $(\theta, d, N_c, N_v) = (11°, 1.5\,mm, 4, 3)$. With such values, the theoretical elongation following models introduced in [6] is equal to 4.4 mm, for an internal pressure of 0.6 bar. Under this internal pressure, a theoretical force of 48 N is developed by the chamber.

2.3 Grippers

The grippers are designed to clench on a standard linear rack in order to maintain one side of the actuator and transmit the force generated by the central chamber. The pitch of the rack is chosen to be equal to 1.57 to be compatible with the desired resolution. The pressure angle is equal to 20°, leading to a teeth height of 0.77 mm. To favor the dynamics of both the opening and the closing of the piston, a bi-directional actuation is chosen for the grippers. The design of the grippers is shown in **Figure 5**. The piston of each gripper is set in motion through the inflation of two toric pneumatic chambers. The use of chambers reduces the constraints related to the design of an airtight cavity to generate motion and to avoid the friction generated by a gasket-based solution. The pneumatic chambers as well as the central piston are encased in a 3D printed outer envelope guiding axially the deformation of the pneumatic chambers and the displacement of the piston.

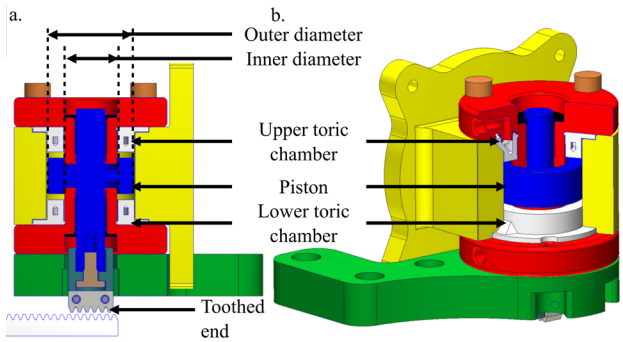

Figure 5 – a. CAD Section of a gripper. B. 3D view with partial section of a gripper.

The grippers need to develop a force sufficient to maintain the unit in place under the force developed by the central chamber, with a coefficient of security equal to 2. The outer and inner diameters of the piston are therefore respectively set to 17.1 mm and 12.5 mm. The amplitude of the motion of the piston was set to be equal to 1 mm, sufficient to clench on the linear rack. An internal pressure of 3.5 bar is thus set when inflating the pneumatic chambers. Finally, the gripper's dimensions are chosen to be within the same order as those of the central chamber, allowing an easier implementation while satisfying the need of compactness.

3 Manufacturing

In order to implement these active elements with the required dimensions while satisfying the constraint of low magnetic susceptibility, specific manufacturing strategies have been considered.

3.1 Central chamber

In order to have precise control of the pattern geometry, the reinforcement truss structure was machined from a raw cylinder of PVC, using a five axis CNC-milling machine. This structure was encompassed in a bi-component silicone rubber (RTV 3428) using overmolding technique. The resulting overmolded truss structure was then attached to sealing parts maid in resin using Polyjet process (VeroWhite, Stratasys) as shown in **Figure 6**.

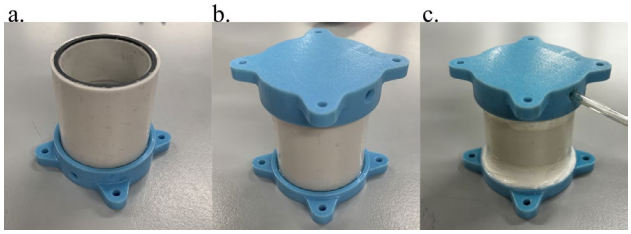

Figure 6 – a., b. Overmolded structure attached to structural ends caps in resin in blue. c. Sealed central chamber, air-input tube (internal diameter: 3 mm).

3.2 Grippers

The structural elements of the grippers were 3D printed using SLA process (Resin 10k, FormLabs), given the resolution of the process (25 µm, Form3BL, FormLabs). The toothed components are of standard geometry and made of POM. To manage the specific shape of the toric chambers, 3D printing of silicone by extrusion was adopted. The chambers are obtained using single-component moisture-cure silicone rubber (A8 Pro, Würth). The printing is achieved using a proprietary platform [7] composed of a Tobeca 3 (Tobeca Sarl) FDM printer adapted to host a vipro-HEAD 5 (ViscoTec GmbH). This printing head allows the 3D printing of soft materials, silicone rubber in our case, to form a pneumatic chamber with an airtight cavity as shown in the time lapse in **Figure 7**. Nozzle diameter for printing is 0.4 mm.

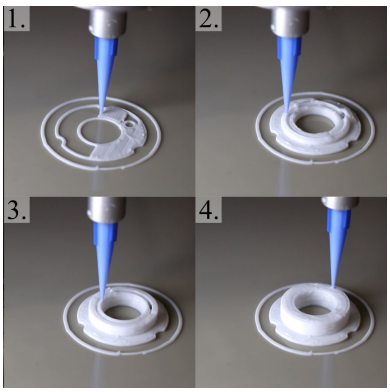

Figure 7 – Timelapse of the 3D printing of a toric chamber.

Before the complete assembly of the actuator, the piston motion was characterized to verify the amplitude of the opening and closing motion of the gripper. These initial tests showed the dimension's variability due to the SLA and silicone printing process required an update of the gripper dimensions, as the gripper range was too large. The dimensions of the moving piston were then adjusted to satisfy the 1 mm stroke of the moving piston with a correct gripping on the linear rack.

3.3 Guiding elements

The two guiding rods visible in **Figure 1** were machined from raw POM to obtain desired 20 mm diameter and to host the linear rack which was attached afterward. The two guiding parts connecting the actuation unit to the guiding rods were 3D printed using SLA process (Resin 10k, Formlabs) and the guiding surfaces were re-machined to the desired 20 mm diameter.

4 Control

An actuation sequence for inchworm kinematics has been developed. This sequence aims at managing the sequential activation of each pneumatic component in the unit. The velocity of the actuator is correlated to the synchronization of the pressurization of each chamber and the dynamics of the central chamber elongation. The originality of the proposed sequence is to exploit the achievable dynamics of the central chamber to perform the elongation and gain time in the inchworm sequence. In other words, the central chamber is designed to provide an elongation greater than the step motion, which equals the rack pitch. Instead of achieving the motion in quasi-static conditions, the inchworm sequence is adapted to improve dynamics: as illustrated in **Figure 8**, with two steps added between the steps 2 and 3 and between the steps 4 and 5 from **Figure 3**. The grippers are closed while the central chamber is still elongating to lower the sequence cycle time.

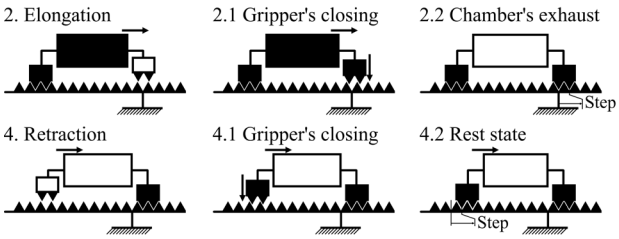

Figure 8 – Modifications applied to the steps 2 and 4 of the inchworm sequence.

This means that the activations of grippers need to be finely synchronized accordingly to ensure the translation amplitude, while the component response times are impacted by the long length of transmission lines. To ensure the translation amplitude, the gripper has to be in a closed state when the central chamber's elongation is within an interval that was defined as 85% to 115% of the step size. The response times of the pneumatic elements were identified experimentally to tune the synchronization [8]. We could observe the existing compromise between the central chamber's pressure and the temporal interval for which the central chamber's elongation lies between 85% and 115% of a step. Indeed, for the elongation, this interval is [322 ms; 580 ms] for 0.6 bar, while it drops to [213 ms; 270ms] for 0.8 bar. As a result, the sequence is performed with a pressure of 0.6 bar for the central chamber.

5 Validation

5.1 MRI compatibility

First, we evaluated the potential artifacts in MRI images resulting from the actuator. The system represented in **Figure 1** was placed in a 1.5 T MRI scanner (MAGNE-

TOM Aera, Siemens Healthineers, Erlangen, Germany). A 128-element spherical HIFU transducer (Imasonic, France, 1 MHz central frequency, 60 mm natural distance) was mounted on the actuator (**Figure 8.a**.). **Figure 8.b** shows an MRI image obtained using a T2-weighted Turbo Spin Echo sequence. One can see that the actuator is not visible on the MRI image and that no perturbation is present in the phantom gel requiring to be monitored during the HIFU procedure. MR-compatible markers were used to localize the MRI plane containing the transducer.

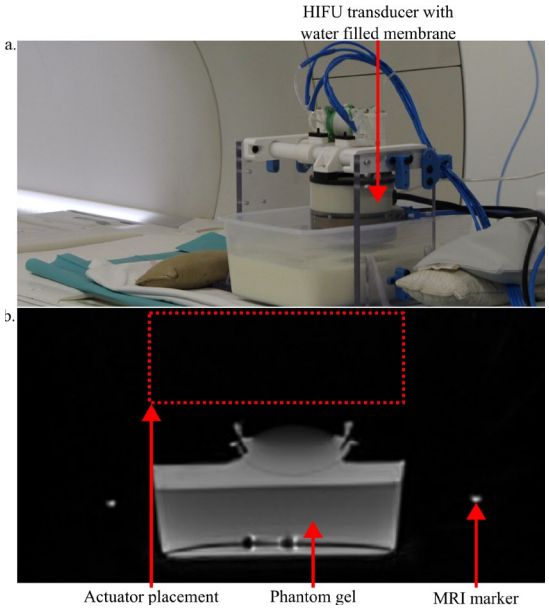

Figure 8 – a. The setup inserted in the MRI. b. MRI magnitude image of the actuator holding a HIFU transducer.

5.2 Motion validation

Second, an experimental evaluation with a 1-kg HIFU-like dummy probe was carried out with the setup presented in **Figure 1**, using the activation sequence determined in section 4. It is shown that the actuation sequence can be adjusted to modulate the average speed. Average velocities are obtained in the range of 0.2 to 0.8 mm/s. The mean positioning error was assessed for 0.4 and 0.8 mm/s after each step and does not exceed 0.1 mm and no step was missed during motion. These positioning errors are satisfactory and acceptable considering the typical MRI resolution of 2 mm.

6 Discussion

In this article, we have presented the design, manufacturing and control of a new linear stepper actuator for the positioning of medical devices, in our case a HIFU transducer, inside an MRI scanner. The presented design and manufacturing process of this actuator satisfy the requirements in terms of MR-compatibility, as demonstrated experimentally inside the MRI.

The positioning errors were estimated for speeds between 0.2 and 0.8 mm/s during the system's motion while being supplied though 10 m long transmissions with an adapted sequence. Since these errors are deemed to be satisfactory compared to the MRI typical resolution, all the constraints related to the application are thus satisfied.

As perspectives of the presented work, other velocities could be obtained by adjusting the design of the active components. These modifications could allow adapting the actuator to different applications requiring different speeds, resolutions or developed forces. Indeed, by reducing the diameter of the central chamber, the compactness could be further improved, and the elongation speed increased. Furthermore, modifying the rack's pitch directly impacts the achievable resolution. As a second perspective, the implementation of other control strategies, through the integration of a position sensor, could be considered. By handling the compatibility of this position sensor, this integration could potentially improve the control of the elongation of the central chamber with a closed-loop control law, as well as improving the synchronization of the pneumatic elements.

Literature

[1] R. Monfaredi, K. Cleary, and K. Sharma, "MRI Robots for Needle-Based Interventions: Systems and Technology," Annals of biomedical engineering, vol. 46, pp. 1479–1497, Oct. 2018.

[2] P. Cabras, P. Auloge, F. Bing, P. P. Rao, S. Hoarau, E. Dumont, A. Durand, B. Maurin, B. Wach, L. Cuvillon, E. Breton, A. Gangi, and J. Vappou, "A new versatile MR-guided high-intensity focused ultrasound (HIFU) device for the treatment of musculoskeletal tumors," Scientific Reports, vol. 12, p. 9095, May 2022.

[3] R. Gassert, A. Yamamoto, D. Chapuis, L. Dovat, H. Bleuler, and E. Burdet, "Actuation methods for applications in MR environments," Concepts in Magnetic Resonance Part B: Magnetic Resonance Engineering, vol. 29B, no. 4, pp. 191–209, 2006.

[4] V. Groenhuis and S. Stramigioli, "Laser-Cutting Pneumatics," IEEE/ASME Transactions on Mechatronics, vol. 21, pp. 1604–1611, June 2016.

[5] A. Pfeil, L. Barbé, B. Wach, A. Bruyas, F. Geiskopf, M. Nierenberger, and P. Renaud, "A 3D-Printed Needle Driver Based on Auxetic Structure and Inchworm Kinematics," American Society of Mechanical Engineers Digital Collection, Nov. 2018.

[6] F. Schmitt, O. Piccin, B. Bayle, P. Renaud, and L. Barbé, "Inverted Honeycomb Cell as a Reinforcement Structure for Building Soft Pneumatic Linear Actuators," Journal of Mechanisms and Robotics, vol. 13, p. 011020, Feb. 2021

[7] L. Mosser, L. Barbé, L. Rubbert and P. Renaud. "ROS2 for soft materials additive manufacturing," ROSConFr, June 2023

[8] T. Portha, L. Barbé, F. Geiskopf, J. Vappou and P. Renaud, "A non-magnetic dual-mode linear pneumatic actuator: initial design and assessment", 2024 IEEE International Conference on Robotics and Automation (ICRA), *to be published*

An electrokinetic lab-on-CMOS DNA detection system for sample-to-result diagnostic applications

Lewis Keeble[1] (l.keeble18@imperial.ac.uk), Arthur Jaccottet[1], Daryl Ma[1], Jesus Rodriguez-Manzano[2], Pantelis Georgiou[1]
1 –Department of Electrical and Electronic Engineering, Imperial College London, London, UK
2- Department of Infectious Diseases, Imperial College London, London, UK

Abstract

A lab-on-CMOS DNA detection system was designed with an array of pH sensors and an electrode array, created using standard top-metal and passivation openings, that can carry out electrokinetic sample preparation. To test the concept, electrokinetic trapping of DNA was successfully carried out using two gold-plated CMOS bond-pads as electrodes. This is the first instance of electrokinetic trapping of DNA on-CMOS and the first use of standard CMOS passivation openings for electrokinetics. The aim is to create a truly sample-to-result and entirely CMOS-based diagnostic device for increased speed, robustness, and accessibility.

1 Motivation

Producing rapid, accessible, and robust diagnostic devices is key to limiting the spread of infectious diseases [1]. Yet, many devices are not truly sample-to-result, with sample preparation conducted externally to the device. This increases the time-to-result, the burden on users, and the likelihood of incorrect results from contamination or incorrect usage.

Electric field interactions can be leveraged to conduct various sample preparation procedures, such as cell lysis [2], sample purification [3], concentration [4], mixing [5], pumping [6], and transport [7] for a range of targets. These interactions are ideally suited to implementation on CMOS, allowing combination with integrated circuitry and on-chip sensors, which promises greater functionality.

The vision is to create an electrokinetic lab-on-CMOS diagnostic device that can detect DNA and conduct the full sample-to-result pipeline on-chip.

2 Approach

A 502x571µm microchip was designed in 65nm CMOS (TSMC), the layout of which can be seen in Figure 1. A 4x2 array of 32µm electrodes separated by 32µm was created using top-metal and passivation openings. To minimise the number of DRC violations that needed waiving from the electrode design, a structure mimicking that of a standard circuit-under-pad bond-pad was used. This consists of chamfered squares of M8, M9, and AP (redistribution layer) metal layers, a via array connecting M8 and M9 (Via8), and a passivation opening connecting M9 and AP (CB). An octagonal passivation opening was added in the CB2 passivation opening layer to expose the underlying AP metal layer and produce an electrode with the desired shape. An octagon was chosen as the closest match to the circular quadropole arrays used in the literature that could be implemented in a commercial CMOS process [3]. The electrodes were `hard-wired' to bond-pads, allowing higher voltages to be applied for electrokinetic actuation, beyond the 1.1V input [8].

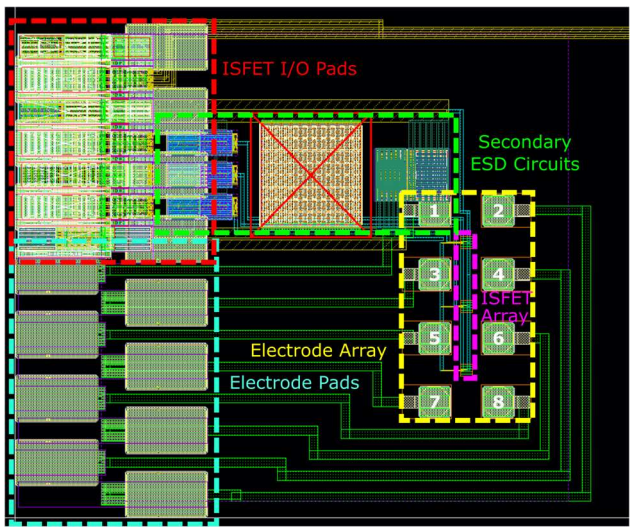

Figure 1: Top level layout of a 65nm CMOS microchip for electrokinetic sample preparation. The numbers of the electrodes are used in defining the polarisation patterns.

The electrodes allow six different polarisation patterns, shown in table 1, that enable the following functions:

1) **Cell lysis:** DC electroporation will be used to breakdown cellular membranes with electric fields and release nucleic acids for testing [2].
2) **Sample concentration:** Positive dielectrophoresis (pDEP) will be used to trap more DNA as the sample flows through the

Electrode	Lysis	Trapping	Purification	Transport	Pumping	Mixing
1 2	+ +	+ -	+ -	0° 0°	+ +	+ +
3 4	+ +	+ -	- +	90° 90°	+ +	- -
5 6	+ +	+ -	+ -	180° 180°	- -	+ +
7 8	+ +	+ -	- +	270° 270°	f f	- -

Table 1: Polarisation patterns of the electrodes corresponding to figure 1 for different electrokinetic interactions. + and - indicate positive and negative polarities respectively, f represents a floating electrode, and values in degrees represent phases of a sinusoidal voltage.

system, increasing the concentration of targets for testing [4].

3) **Sample purification:** Electric quadropoles will attract DNA to electrode edges through pDEP and cells to the centre through negative DEP (nDEP). The cells held weakly by nDEP will be removed by fluid flow [3]. This will reduce the inhibition of amplification reactions from cellular materials.

4) **Target transport:** Travelling-wave DEP will use a sinusoidal voltage with a 90° phase shift between adjacent electrodes to move target molecules within a solution [7].

5) **Fluid pumping:** Asymmetrical AC electroosmosis (ACEO) will be used to pump fluid [6].

6) **Sample mixing:** Chaotic fluid vortices will be induced through ACEO to mix samples [5].

Three ion-sensitive field-effect transistors (ISFETs) are placed at the centre of the electrode array, with external connections to take readings using a semiconductor analyser. The ISFETs have 12µmx12µm top-metal floating gates connected with a via stack to the gate of the underlying transistor. The electrode array will also be used to form an on-chip, three-electrode system, with working, counter, and reference electrodes, for impedance sensing via an off-chip analyser [9]. A high-level representation of the system is illustrated in Figure 2.

Detection of DNA is enabled through a loop-mediated isothermal amplification reaction. As the reaction progresses, protons are produced that can be detected by the ISFETs [10]. Concurrently, as the concentration of DNA in the sample increases, a decrease in impedance will occur [11]. Combined pH-impedance detection of DNA offers advantages such as increased dynamic range and faster time-to-positive and will provide greater insight into reaction dynamics [12].

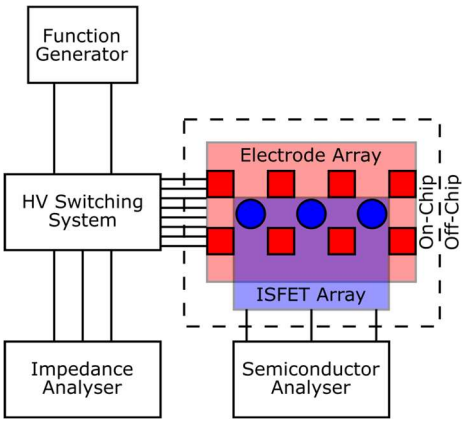

Figure 2: A high-level system diagram for the electrokinetic lab-on-CMOS

The standard CMOS metallisation is an aluminium-copper alloy that has low electrochemical stability. To prevent electrolysis upon application of voltages to the electrodes, zincation followed by an electroless nickel, immersion gold (ENIG) plating process will be conducted. An Ag/AgCl quasi-reference electrode will be created for both ISFET and impedance sensing systems by electroplating and chlorinating silver [13]. To increase the efficiency of the electrokinetic sample preparation, two-photon polymerisation and thermal processing will be used to fabricate 3D carbon electrodes on the top-metal [14].

To test the feasibility of using standard CMOS top-metal and passivation openings to conduct electrokinetic actuation, two ENIG-plated bond-pads of a 0.18µm CMOS microchip were used to trap DNA via DEP, one of which is imaged in Figure 3. ENIG plating (Technic UK EN AT6500, Metalor SuperMex) is preceded by zincation of the bondpads (Technic UK EN Zincate), with the process described in [13]. The 40pM 45kbp λ-DNA was

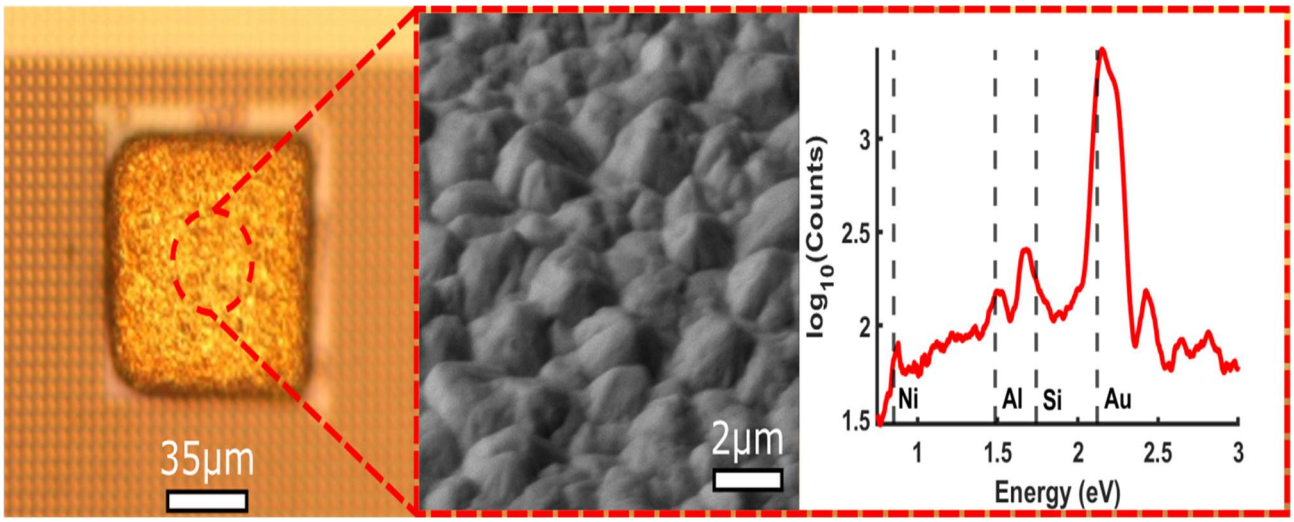

Figure 3: Optical **(left)** and SEM **(middle)** images of the ENIG-plated bond-pad, with EDX **(right)** analysis of the surface.

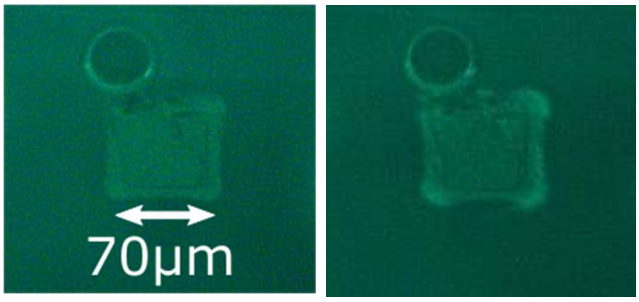

Figure 4: A fluorescence image of an ENIG-plated bond-pad in 40pM λ-DNA before **(left)** and after **(right)** a 4V, 500Hz electric field is applied.

stained with YOYO-1 at a ratio of 10 base-pairs:1 dye molecule and was viewed with a Zeiss AxioZoom V16 upright fluorescence microscope. An Agilent 33522A function generator was used to provide voltages to the two bond-pads with a 180º phase shift between them.

Results

With a 4V, 500Hz voltage applied to the bond-pads, DNA was trapped at the electrode edges, as can be seen in Figure 4. The fluorescence intensity profiles contained in Figure 5 indicate that the concentration of DNA at the electrode corners has been doubled by electrokinetic trapping. This is the first demonstration of DNA electrokinetic trapping on-CMOS and the first use of standard CMOS passivation openings for electrokinetics.

The strength of electrokinetic trapping is lessened by the curved edges and large thickness, in the order of 1µm, of the electroplated electrode, both of which reduce the electric field intensity. In future experiments, the ENIG-plating time will be shortened to keep metallisation just below the level of the passivation and avoid the bump profile.

Once the electric field was turned off, the DNA drifted away from the electrode, apart from in some areas, which may be caused by imperfections in the immersion gold coating causing DNA to bond to the underlying metal. This theory is supported by the slow generation of bubbles, which can be noted in Figure 4. An improvement in the quality of the gold plating must be achieved or 3D carbon electrodes must be fabricated for long-term usage.

Future Work

After conducting CMOS post-processing and individually testing and verifying each of the functionalities discussed previously, the ultimate aim is to conduct a full, sample-to-result process on the microchip, with electrokinetic sample preparation and electrochemical detection of an amplification reaction.

In the next iteration of this microchip, impedance sensing circuits and ISFET readout will both be moved on-chip and combined with analogue-to-digital conversion and mixing for data output to improve performance and increase compactness of the system. Importantly, testing from this microchip will determine whether a switching

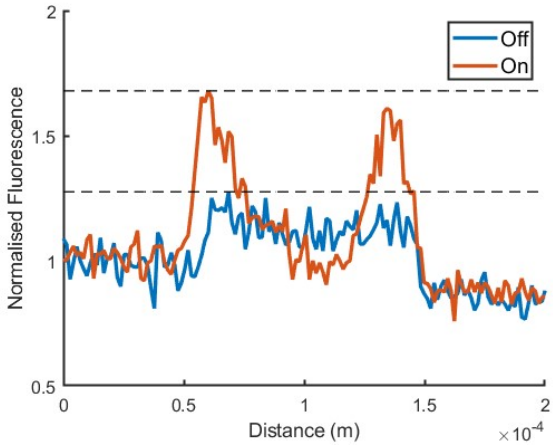

Figure 5: Fluorescence intensity profiles along the edge of the ENIG-plated bond-pad for the images in Figure 4.

system can be implemented on-chip to change between the six electrokinetic polarisation patterns and impedance sensing. If this is possible, the system will benefit from extreme modularity and reconfigurability. The vision is to have a large sensor-actuator array where subgroups of electrodes can be assigned different functions to perform within the sample-to-result pipeline. This could allow for the multiplexing of reactions on-chip with multiple results obtained from a single sample.

Conclusion

In this paper, a novel microchip was designed with a sensor-actuator array to provide a proof-of-concept for an electrokinetic lab-on-CMOS diagnostic. The design was supported by experiments which carried out electrokinetic DNA trapping using CMOS top-metal electrodes for the first time.

References

[1] O'Neill, J. (2015). Review on Antimicrobial Resistance: Rapid Diagnostics, *Wellcome Trust*

[2] Punjiya, M., Mocker, A., Napier, B., Zeeshan, A., Gutsche, M., & Sonkusale, S. (2020). CMOS microcavity arrays for single-cell electroporation and lysis. *Biosensors and Bioelectronics*, *150*

[3] Sonnenberg, A., Marciniak, J. Y., Krishnan, R., & Heller, M. J. (2012). Dielectrophoretic isolation of DNA and nanoparticles from blood. *ELECTROPHORESIS*, *33*(16), 2482–2490.

[4] Velmanickam, L., Bains, M., Fondakowski, M., Dorsam, G. P., & Nawarathna, D. (2018). iLluminate-miRNA: Paradigm for high-throughput, low-cost, and sensitive miRNA detection in serum samples at point-of-care. *Journal of Physics D: Applied Physics*, *52*(5), 55401.

[5] Ng, W. Y., Goh, S., Lam, Y. C., Yang, C., & Rodriguez, I. (2009). DC-biased AC-electroosmotic and AC-electrothermal flow mixing in microchannels. *Lab on a Chip, 9,* 802-809

[6] Loucaides, N., Ramos, A., & Georghiou, G. E. (2012). Configurable AC electroosmotic pumping and mixing. *Microelectronic Engineering*, *90*, 47–50.

[7] Chan, Y. S., & Lee, C. Y. (2022). A Programmable Bio-Chip with Adaptive Pattern-Control Micro-Electrode-Dot-Array. *IEEE Transactions on Circuits and Systems II: Express Briefs*, *69*(11), 4513–4517.

[8] Ismail, Y. (2015). High-Voltage Generation and Drive in Low-Voltage.

[9] Ma, D., Ghoreishizadeh, S. S., Georgiou, P. (2020). Dapper: A Low Power, Dual Amperometric and Potentiometric Single-Channel Front End. *2020 IEEE International Symposium on Circuits and Systems (ISCAS)*, 1-5

[10] Toumazou, C. *et al*. (2013). Simultaneous DNA amplification and detection using a pH-sensing semiconductor system. *Nature Methods*, *10*, 641–646.

[11] Salm, E., Zhong, Y., Reddy, B., Duarte-Guevara, C., Swaminathan, V., Liu, Y.-S., & Bashir, R. (2014). Electrical Detection of Nucleic Acid Amplification Using an On-Chip Quasi-Reference Electrode and a PVC REFET. *Analytical Chemistry*, *86*(14), 6968–6975.

[12] Wang, Z., Keeble, L., Moser, N., Lande, T. S., & Georgiou, P. (2021). A Dual-Sensing CMOS Array for Combined Impedance-pH Detection of DNA with Integrated Electric Field Manipulation. 2021 IEEE International Symposium on Circuits and Systems (ISCAS), 2021-May, 1–5. https://doi.org/10.1109/ISCAS51556.2021.9401548

[13] Keeble, L., Jaccottet, A., Ma, D., Rodriguez-Manzano, J., & Georgiou, P. (2023). An Electroplated Ag/AgCl Quasi-Reference Electrode Based on CMOS Top-Metal for Electrochemical Sensing. *Electrochimica Acta*.

[14] Haque, M. A., Lavrik, N. v, Hedayatipour, A., Hensley, D., Briggs, D. P., & Mcfarlane, N. (2020). Carbonization of 3D printed polymer structures for CMOS-compatible electrochemical sensors. *J. Vac. Sci. Technol. B*, *38*, 52203.

Characteristics of Resonance Type Piezoelectric Motors Made with Textured Piezoceramics Material

Burhanettin Koc, Physik Instrumente (PI) GmbH & Co. KG, Karlsruhe, Germany (b.koc@pi.de)
Bülent Delibas, Physik Instrumente (PI) GmbH & Co. KG, Karlsruhe, Germany (b.delibas@pi.de)
Safakcan Tuncdemir, QorTek, Inc., Linden, PA, USA (stuncdemir@qortek.com)
Ahmet Erkan Gürdal, QorTek, Inc., Linden, PA, USA (egurdal@qortek.com)
and
Franz Schubert, PI Ceramic GmbH, Lederhose, Germany (f.schubert@piceramic.de)

Abstract

Common material for resonance drive type (ultrasonic) motors are made with hard type piezoelectric ceramics (Hard PZT), which have very low dielectric loss and high mechanical quality factor around 2000. On the other hand, their piezoelectric charge constants are inferior to soft type piezoelectric ceramic materials. Unavailability of a Hard PZT with high piezoelectric charge constant has been one of the limiting factors in ultrasonic motor designs. A newly developed PMN-PZ-PT based textured piezoelectric ceramic material (TX101) enables a new design space for ultrasonic motors by providing a hybrid solution with a high piezoelectric charge constant even larger than common soft type piezoelectric ceramics and semi hard type characteristics with low dielectric loss and relatively high mechanical quality factor of around 500. We evaluated two resonance type of piezoelectric motors made with this textured piezoelectric material.

1 Introduction

Texturization is a viable approach to enhancing the performance of piezoelectric ceramics. Piezoelectric coefficients of textured ceramics are 2-3 factor higher than the ones produced with polycrystalline PZTs. Despite having a higher hysteresis in the strain-field, textured ceramics have been reported similar piezoelectric properties compared to single crystal piezoelectric materials [1]. Zate T.T. et al. [2] presented a textured ceramic with increased piezoelectric properties and curie temperature by using CuO as a dopant in the matrix powder and modifying the sintering process. Multilayer piezoelectric actuators using textured PMN-PIN-PT with a layer thickness of 36 µm were presented as cost-effective alternative for the replacement of single crystal materials [3]. Tetik C. H. S. et al. developed a lead-free sodium bismuth titanate based textured piezoelectric ceramic by using templated grain growth and tape casting [4].

Our technical approach here where we investigate the performance benefits of textured piezoceramics in piezoelectric motors is one-to-one replacement of the stator element of a motor with a mature design and with successful track record in various nano positioning applications. Our tests and characterizations aimed to evaluate if the stator made of the new material can meet the anticipated specifications, as well as to identify performance benefits, such as increased force, a greater range of velocity, improved controllability, and so forth.

We evaluated two motor types. First is single mode excitation (resonance) type and the other is multi-mode excitation type. Both stators are manufactured with the textured piezoelectric material (TX101) and traditional hard PZT material (H-PZT).

2 Piezoelectric Motor Structures

2.1 Single Mode Resonance Type (Type-I)

The Type-I stator is manufactured under a trade name of "PIline®" by PI Ceramic (PIC). The stator is a rectangular piezoelectric plate with two primary surfaces where metallization electrodes are applied. The plate has a certain length to width ratio. The first and second electrodes (active electrodes) on one major surface split the plate into two equal portions, whereas the electrode on the opposite side completely covers the second major surface (common electrode). A pusher is attached at the centre of a long, side-surface (Figure 1a).

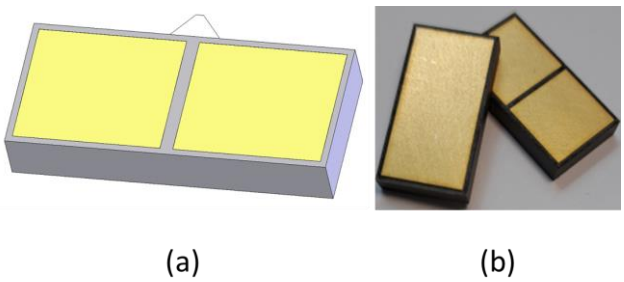

Figure 1 a) CAD Model of the stator for Type-I motor. b) Manufactured stators with the textured piezoelectric material (TX101) with the dimension of 18x9.5x3 mm^3.

The operating principal of the Type-I stator: When one electrode is electrically excited with a sinusoidal signal around the main operating mode, leaving the other electrode floating, a planar mode on the excited half side is

generated. Figure 2a shows the behaviour of the stator simulated using GID-ATILA finite element analysis (FEA) software when the stator is made with conventional hart PZT based ceramics. Further simulation snapshots show that maximum displacement is at the tip of the friction coupler (Figure 2b).

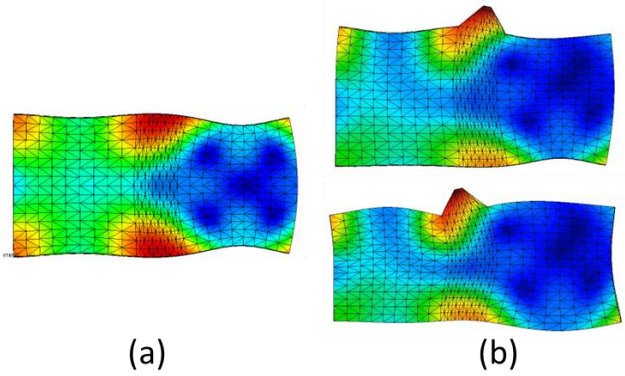

Figure 2 Behavior of the Type-I stator simulated using GID-ATILA software. a) A radial or planar mode on the electrically driven half is excited. b) Deformed states of the stator. The maximum displacement is at the tip of the friction coupler.

When the same structure is simulated with FEA software using TX101 material data [7], we observed a different characteristic of the excited mode compared to our analysis with a H-PZT. The excited section expands and shrinks in width direction. The maximum displacements are at the side surfaces of the excited section (Figure 3); whereas the maximum displacement in H-PZT stator is at the tip of the friction coupler (Figure 2). This uncommon behavior is maintained for different length to width aspect ratios.

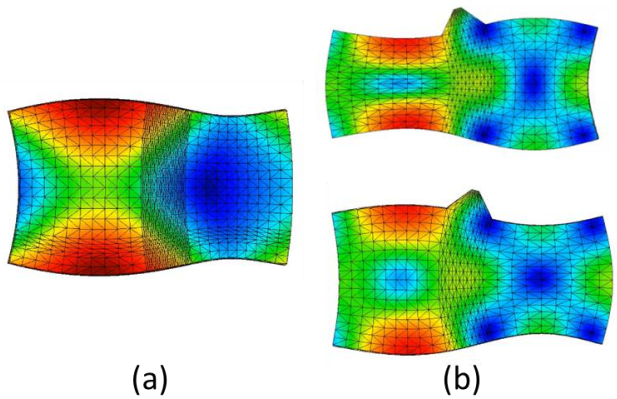

Figure 3 Behavior of the Type-I stator simulated using GID-ATILA software, when the material is TX101. a) The largest deformation is at the middle parts of the excited side surfaces. b) After the attachment of the friction coupler, the behavior is maintained.

Further investigating this uncommon behaviour of textured piezoceramic made stators at resonance mode, we noticed that dominant deformation in electrically excited section of the stator is in width direction. This cause largest deformation to occur in 1/4th of the excited section unlike to occur at the fiction couple which is attached at half length . This behaviour would be attributed to very small compliance value (s_{12}^E) of the TX101 textured piezoceramics. For standard PZT based polycrystal piezoelectric ceramics, the compliance values at the off-diagonal sections (s_{12}^E, s_{13}^E) have negative signs and their values are close to each other. However, for the textured piezoelectric ceramic (TX101), s_{12}^E has a small and positive value which explains the uncommon large deformation in width direction [7].

2.2 Multi-Mode Resonance Type (Type-II)

The second motor (Type-II) is a multi-mode excitation type, where the excited modes are first longitudinal and second bending modes (L1B2) of a rectangular plate [6]. Conductive electrodes on top and bottom surface of a rectangular piezoelectric plate divide the plate into two sections in length and in width directions, respectively. When both top and bottom surface electrodes of the piezoelectric plate are excited by two sinusoidal signals with a phase difference of 90 degrees, the first longitudinal and the second bending modes couple and move the friction coupler, which is attached at one end surface, in an elliptical trajectory (Figure 4a).

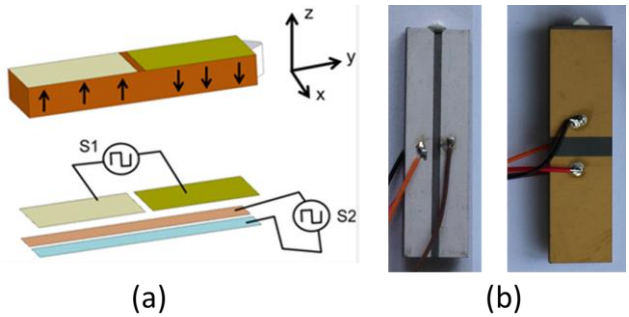

Figure 4 a) CAD Model of the stator for Type-II motor and driving the surface electrodes with signal 1 (s1) and signal 2 (s2), b) Manufactured stators with the textured piezoelectric material (TX101) and traditional hard PZT material.

Magnitudes of the impedance spectra for both stators are seen in Figure 5. Even though the size of the stators is identical (30x8x2 mm^3), the stator made with TX101 material has lower first and second mode resonance frequencies due to higher compliance. For both stators, independently excited 1st longitudinal (L1) and 2nd bending (B2) modes are close enough that during operation of the motor, these modes couple to generate elliptical motion on the stator which contribute for the movement of the slider.
By driving the stators with burst sinusoidal signals at 40 and 80 V near to their resonance frequencies, peak to peak vibration velocities of both stators were also measured in longitudinal direction (Figure 6). For the stator made with the traditional hard PZT material (H-PZT), magnitudes of the vibration velocities are larger but in a narrow frequency range. On the other hand, vibration velocities spread over a wider frequency range at a smaller magnitude for the stator made with the textured piezoelectric material (TX101).

For Type-II motors, it is desirable that first longitudinal and the second bending modes to be coupled. In such a case, having semi-hard characteristics is an advantage to spread the vibration velocity over a wider frequency range.

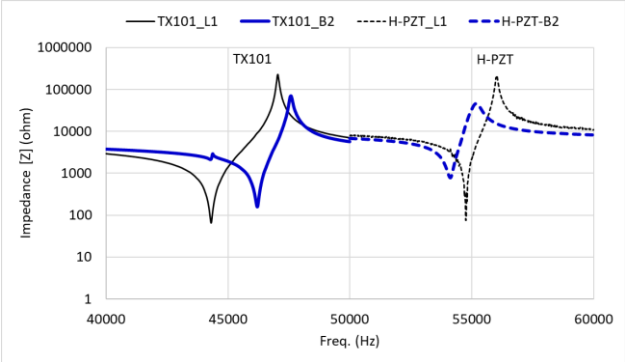

Figure 5 a) Magnitudes of the impedance spectra for both stators made with the textured piezoelectric material (TX101) and traditional hard PZT material (H-PZT). For the stator made with TX101, 1st longitudinal (L1) and 2nd bending (B2) modes are about 10 kHz lower.

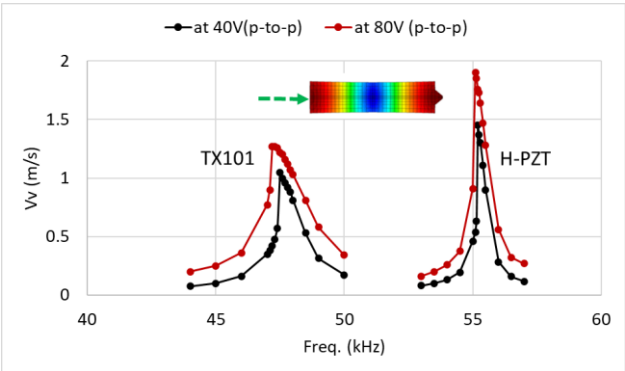

Figure 6 Peak to peak vibration velocities around the resonance frequencies of the stators

Figure 7 shows the magnitudes of the displacements at off-resonance frequencies when the stators were operated with sinusoidal signals at 80V. The displacements at each frequency were calculated from measured vibration velocity values.

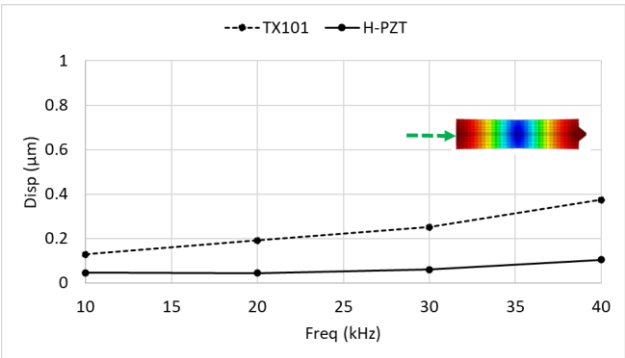

Figure 7 Magnitudes of peak-to-peak displacements in length direction calculated from the measured vibration velocity at off-resonance frequencies.

2.3 Type-II Motor Characteristics

Both stators were characterized with identical fixtures in identical test conditions including their holding boundary conditions and pressing force values. The identical test fixtures shown in Figure 8 have integrated position sensors which can measure the slider position with 10 nm resolution.

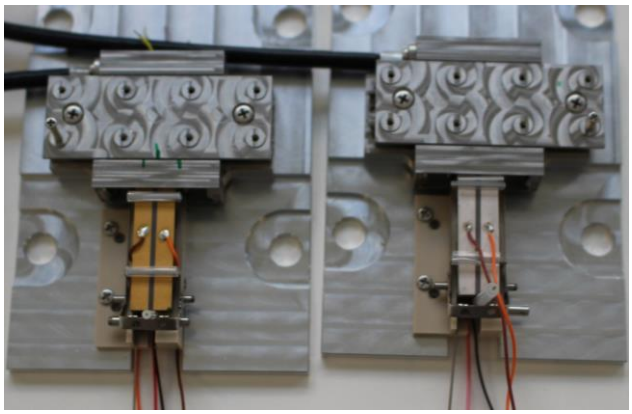

Figure 8 The prototyped piezoelectric motors with textured piezoceramics (left) and with a traditional hard PZT material (right), shown while assembled to the test fixtures.

Slider positions for both stators were measured while driving the motor near to their corresponding resonance frequencies. Figure 9 shows the slider position with step movements and the corresponding slider velocity in both directions for the stator made with the textured piezoelectric material (TX101). The motor was operated at 45 kHz with 160 V. Each step corresponds to a driving amount of 1000 pulses (about 22 millisecond driving time). Slider velocity in both directions can exceed 200 mm/s.

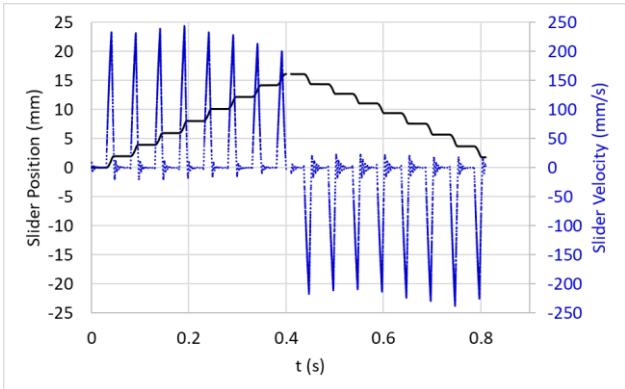

Figure 9 Slider position with step movements and the corresponding slider velocity in both directions for the stator made with the textured piezoelectric material (TX101)

Figure 10 shows the slider position with step movements and the corresponding slider velocity in both directions for the stator made with the traditional hard PZT material (H-PZT). The motor was operated at 55 kHz with 160 V. The step movements were generated with open loop drive so a velocity difference is visible.

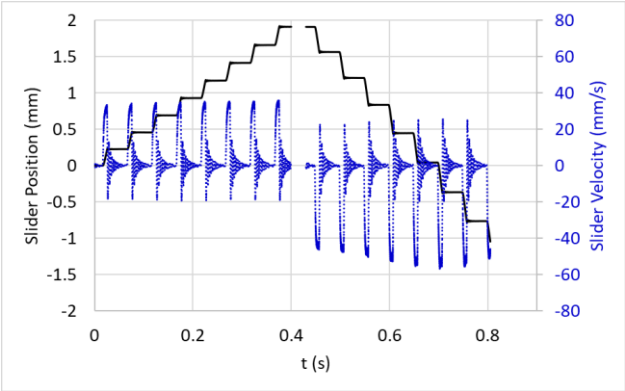

Figure 10 Slider position with step movements and the corresponding slider velocity in both directions for the stator made with traditional hard PZT material (H-PZT)

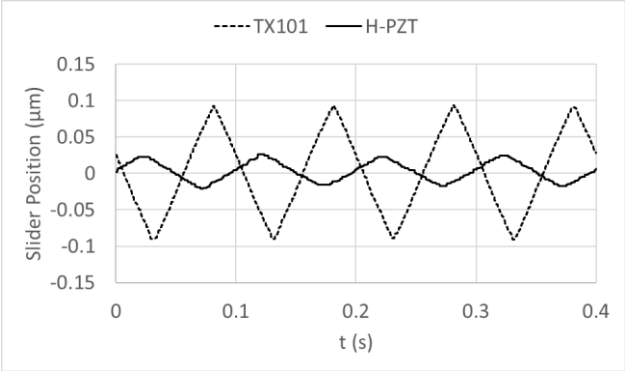

Figure 11 Slider positions when the stators were excited with a triangular signal with a peak-to-peak magnitude of 160 V at 100 Hz

In a resonance type (ultrasonic) motor, movement of a slider starts after vibration level reaches above a certain threshold value. In order to generate the vibration level above a certain threshold value, driving voltage on the piezoelectric vibrating element should be above a threshold voltage value. In general, due to the frictional nonlinearities, there is non-linear characteristics at the low-velocity region. The nonlinearity of velocity against input driving voltage can be improved (or bypassed) by operating the vibrating element with an analogue signal. A triangle waveform at low frequency can verify the controllability of a slator position with an analogue signal. Since a stator and a slider are in contact; when the stator generates a tangential displacement, the slider would also make the same movement. This low frequency driving method, which is also called as analogue drive, is employed to compensate above mentioned low-velocity non-linearities. Slider position is controlled by an analogue voltage. As normal and tangential displacements in the stator can be independently controlled [6], a triangular signal was applied to the stator to generate a tangential deformation at 100 Hz. At this low frequency, the slider of the motor was moving together with the tip of the friction coupler. Figure 11 shows the slider positions for both test stages when the stators were operated at 100 Hz with a peak-to-peak signal magnitude of 160V. The higher piezoelectric charge constants of textured piezoceramics play an important role for longer range position control of a slider at low-velocities.

3 Conclusion

Textured piezoelectric ceramic material emerges as a superior material choice for multi-mode excitation type piezoelectric motors as we have observed improved mechanical output characteristics without the sign of self-heating or deviation in drive characteristics at high frequency. We can conclude that one-to-one replacement of the material of vibrating stator is not a suitable approach for all ultrasonic motor types. When making a vibrating stator using a new piezoelectric material for a nano-positioner, actuated by a resonance type piezoelectric motor, the vibrating stator structure needs to be designed accordingly. With the improved piezoelectric coupling properties with moderately high mechanical quality factor, the textured piezoelectric ceramic (TX101) has the flexibility to be used in structures that have lower resonance modes. Such motor can be operated not only according to resonance drive principal with sinusoidal signal waveforms, but also via inertial drive principal with sawtooth signal waveforms.

4 Literature

[1] Messing, G. L., et al., "Templated grain growth of textured piezoelectric ceramics", Critical Reviews in Solid State and Materials Sciences, 29, 2, pp. 45-96, 2004.

[2] Zate, T. T., et al., “Textured Pb(Mg1/3Nb2/3)O3 −Pb(In1/2Nb1/2)O3 −PbTiO3 ceramics with enhanced piezoelectric properties and high Curie temperature prepared by low-temperature sintering”. Sensors and Actuators A: Physical, 366, 2024.

[3] Zate, T. T., et al., “Development of Textured 0.37 PMN-0.29 PIN-0.34 PT Ceramics-Based Multilayered Actuator for Cost-Effective Replacement of Single Crystal-Based Actuators”. J. Korean Inst. Electr. Electron. Mater. Eng., 36.4, pp. 362-368, 2023.

[4] Coban Tetik, H. S., et al., Development of textured lead-free NBT-based piezoelectric materials in a matrix, synthesized by an alternative route, via templated grain growth. J Mater Sci: Mater Electron 34, 324, 2023.

[5] Wishnewskiy, W.; Kovalev, S.; Vyshnevskyy, A. A New Ultrasonic Piezoelectric Actuator for Nanopositioning. In Proceedings of the 9th International Conference on New Actuators, Bremen, Germany, 14–16 June 2004; pp. 118–122.

[6] Koc, B.; Thelen, M. An Ultrasonic Motor using Independently Driven Surface Electrodes of a Piezoelectric Plate. In Proceedings of the 13th International Conference on New Actuators, Bremen, Germany, 13–15 June 2014; pp. 214–217.

[7] Qortek Inc. [Online] https://qortek.com/technologies/textured-piezoceramics/ Accessed on April 30, 2024.

Study on Miniaturization of a Pump Using Ultrasonic Transducer and Opposing Surface

Masaya Takasaki, Yuki Nakasuji, Yuji Ishino, Takeshi Mizuno
Saitama University, Shimo-Okubo 255, Sakura-ku, Saitama, 3388570, Japan
masaya@ieee.org

Abstract

Previously, we found an occurrence of pump effect when an opposing block faces an ultrasonically vibrating surface with a small gap. To observe the effect, an experimental setup with an ultrasonic transducer and a block was prepared. The ultrasonic transducer had a hole to provide the path for fluid flow and the opposing surface was a tapered end of an aluminum cylinder. According to the measurement results of a gauge pressure in the hole, when circumference of the opposing block is tapered, air was discharged from the gap of two surfaces. On the other hand, when center of the block is tapered, fluid was sucked into the gap. In this research, miniaturization of the pump was discussed. By selecting higher frequency for the transducer, total size of the pump can be reduced. A Langevin type ultrasonic transducer whose resonant frequency was 58 kHz was applied.

1 Introduction

Recently, application of ultrasonic vibration is covering pump. [1]-[3] In these developments, liquid was tried to transport by the pumps. Previously, an occurrence of pump effect was found in an experimental setup consisting of a Langevin type ultrasonic transducer and an opposing metal block whose surface was tapered[4].

With the ultrasonic vibration, air in the gap between vibrating surface and opposed surface can be pressurized and guided by the tapered surface into a hole equipped in the transducer, as shown in Fig.1 (a). In this case, the tapered shape was equipped in the center of the opposing surface as shown in the figure. This type of the surface is called “valley type.” On the other hand, when the ultrasonic vibration was applied with the opposing surface with circumference tapered shape as shown in Fig. 1 (b), air in the hole was pulled out to the atmosphere. This type of air flow direction could be switched by changing the tapered shape. Thanks to squeeze film effect, no component slides in the setup. Therefore, long life time can be expected for the pump under this principle.

In this paper, miniaturization of the ultrasonic pump is reported. Higher frequency was selected as driving frequency for longitudinal vibration mode. As a result, size of whole experimental setup can be reduced.

Experimental Setup

An experimental setup was built as shown in Fig. 2. A bolt-clamped Langevin transducer whose diameter was 15 mm and was coupled with a horn which had a hole inside to guild pumped fluid. The horn was supported by a frame at the vibration node of it. The resonance frequency of the transducer was 58 kHz. Total length of the coupled transducer was 80 mm. As a result, the volume of the ultrasonic transducer was 1/8 as that of the previous ultrasonic transducer whose resonance frequency was 28 kHz. The opposing aluminum block was supported by a leaf spring with strain gauges. With this structure, the block was pressed to the transducer and the pressing force could be monitored during the following experiments. Referencing the monitored force, parallelism between vibration surface and opposing surface was arranged. The outlet of the hole in the horn was connected to a pressure sensor, flow rate sensor and a throttle valve. Adjusting the valve, the load given to the pump was changed.

The opposing blocks were newly fabricated for the following experiments. Diameter of the blocks was 15 mm, same as that of the ultrasonic transducer. Taper angle

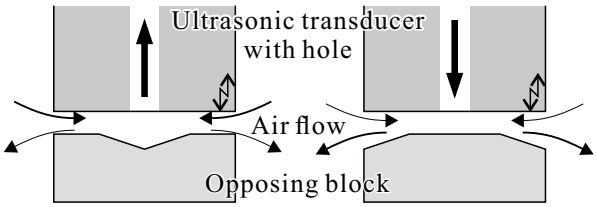

(a) Valley type (b) Mountain type

Figure 1 Pump effect in the gap between ultrasonically vibrating surface and opping surface.

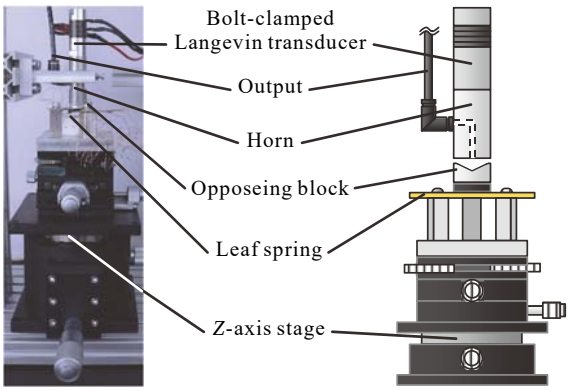

Figure 2 Experimental setup for observation of pump effect with miniaturized components

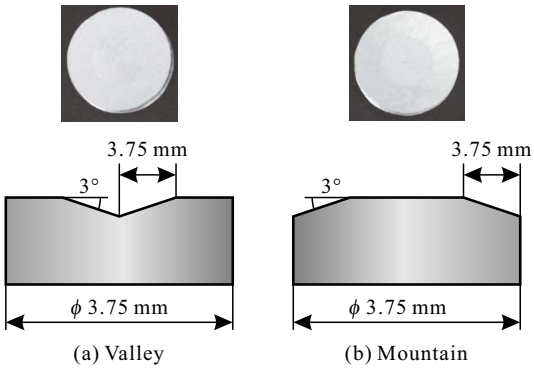

Figure 3 Fabricated opposing blocks

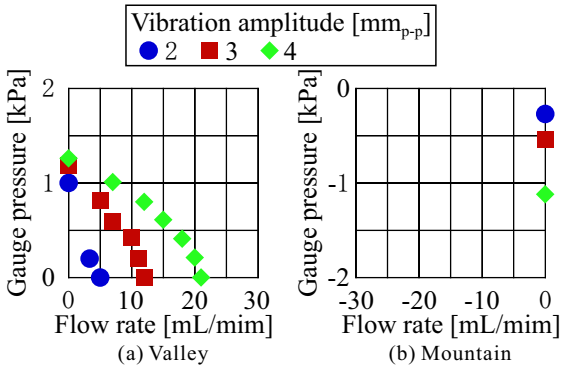

Figure 4 Relationship between flow rate and gauge pressure

for both the valley type and mountain type was 3 deg. The diameter of the opposing surface was half as that of the surface in the previous research. Therefore, pressing force was arranged to 0.25 N, which was quarter of that in the previous research. Vibration amplitude was set as half as that of previous research experiments, because frequency in this research was twice as that of previous investigation. With these conditions, the following observation experiments were carried out.

2 Observation of Pump Effect

For the observation of the pump effect, positive flow direction was defined as the direction from the atmosphere around the opposing block into the hole in the horn. Adjusting the valve, pressure and flow rate in the output port was recoded. The observation results were plotted on Fig. 4. Positive flow was observed in the case of mountain type opposing furface, as shown in Fig. 4 (a). With larger vibration amplitude, higher pressure and larger flow tare was observed. This tendency was similar to those of our previous investigations. Then, negative flow was observed with valley type opposing furface, as shown in (b) of the figure.

For both type of opposing surface, maximum pressure and flow rate were smaller than those of previous observation where resonance frequency of the ultrasonic transducer was 28 kHz. In case of mountain type opposing surface, no flow was induced while the valve was opened.

3 Conclusion

For the pump consisting of a Langevin type ultrasonic transducer and an opposing surface, miniaturization was considered by applying higher driving frequency. Experimental setup was fabricated with 58 kHz Langevin transducer. As a result of experimental observation of pump effect, pump effect was induced. On the other hand, maximum pressure and maximum flow rate were smaller than those of previous observation.

4 Literature

[1] C. Yun, et al., “An Ultrasonic Suction Pump with No Physically Moving Parts,” Japanese Journal of Applied Physics, Vol. 43, No. 5B, pp.2864-2868, 2004.

[2] M. Nishikawa, et al., “An Ultrasonic Suction Pump with No Physically Moving Parts,” Proc. JSPE Spring Meeting, pp. 103-104, 2008. (in Japanese)

[3] T. Nakanishi, et al., “Ultrasonic Pump using Pressure Difference of Micro-Cavitation,” Proc. JSME Fluids Engineering Conference, pp. 157-158, 2010. (in Japanese)

[4] H. Shinada, et al., “Pump using Ultrasonic Transducer and Opposing Surface (1st report: Observation of Pump Effect),” Trans. JSME, Vol. 83, No. 845, pp. 1-7, 2017. (in Japanese)

Conference Focus: Piezoelectric actuators /Piezoelectric motors

Application: **oral**

Low voltage (Bi, Sc)(Pb, Ti)O_3 based piezoelectric multilayer actuators for high temperature applications

Runjiang Guo, Qingbin Meng, Renlong Gao, Cary Zhang
Thorlabs Optical Electronic Technology (Shanghai) Co., Ltd., Shanghai, China, Rguo@thorlabs.com

As the PZT (Pb(Zr, Ti)O3) ceramics has long been studied for decades, the PZT related materials are widely applied in many products such as piezoelectric actuators, linear motors and so on. However, one drawback for PZT is its relative low curie temperature. Therefore the conventional PZT products can only be applied at relatively low temperature (<150℃). A new kind of piezoelectric materials with high curie temperature and depolarization temperature BSPT ((Bi, Sc)(Pb, Ti)O3) can be used to solve this problem. In this work, the piezoelectric actuator chip made by BSPT materials can work at 250℃ without performance degradation. The multilayer technology is also introduced to reduce the operation voltage down to 150V, while can be even down to 45V. The manufactured BSPT actuator chip with multilayer structure can achieve the stroke of as high as 4 µm at external voltage of 150V which is higher than other single layer products. When we stack three or more BSPT chips together, the BSPT stack actuator can even achieve the stoke of more than 10 µm. As the chemical activity of Pt is much lower than that of Ag and Pd, we use Pt inner electrode instead of Ag/Pd inner electrode to enhance the stability and the lifetime of BSPT actuators, which indicates that our product can also work at extreme environment. In brief, our research provides a new idea in the high temperature piezoelectric motion control applications such as high temperature gas valve, glue dispensing device, nano or micro positioner and so on.

Introduction

Since the discovery of piezoelectric effect in year of 1883, piezoelectric ceramics have found wide applications in various products such as piezoelectric actuators, linear motors and so on[1,2]. PZT (Pb(Zr,Ti)O_3), a conventional piezoelectric material, has been extensively studied for its exceptional properties over several decades. However, one limitation of PZT is its relatively low Curie temperature (approximately 340°C). Consequently, for the soft PZT ceramics used in our piezoelectric actuator, depolarization may occur at around 130°C, which hampers their further utilization particularly in high temperature applications.[3-5]

To solve this problem, researchers are actively seeking alternative materials with higher Curie temperatures. Among all the piezoelectric materials, BSPT ((Bi, Sc)(Pb, Ti)O_3) emerges as a promising candidate due to its remarkable Curie point of up to 450°C. Therefore, BSPT can be tailored specifically for high temperature application. [6-8]

Therefore, based on the above analysis, we fabricated the multilayer piezoelectric actuator chip using the BSPT material as the ceramic effective layer. In this work, the as-fabricated chip demonstrated stable performance at 250°C without any noticeable degradation. Compared with the conventional single layer ceramic, the implementation of multilayer technology significantly enhanced the apparent d_{33} value of BSPT ceramics while reducing the operating voltage. Consequently, our manufactured BSPT actuator chip with a multilayer structure achieved an impressive stroke subjected to an external voltage of 150V, surpassing that achievable by conventional PZT materials.

It is worth noting that we use Pt as the inner electrode instead of the conventional Ag/Pd electrode. Due to its significantly lower chemical activity compared to Ag and Pd, the stability and lifetime of BSPT actuators are greatly enhanced, indicating their ability to operate reliably in extreme environments without the risk of leakage or failure. In addition, by introducing Pt into the multilayer ceramics, we have successfully reduced the grain size of BSPT to an optimal grain size which can exhibit the best piezoelectric property[9-11]. In summary, our BSPT actuator chip exhibits promising potential for high-temperature piezoelectric motion control applications such as high-temperature gas valves, glue dispensing devices, nano or micro positioners, etc.

Design of BSPT actuator chip

The BSPT ceramic powder and thin films are made in house. The piezoelectric constant d_{33} reaches a remarkable value of 475 pC/N, which closely approximates the conventional PZT ceramics, thereby indicating the exceptional piezoelectric properties exhibited by the BSPT ceramics.

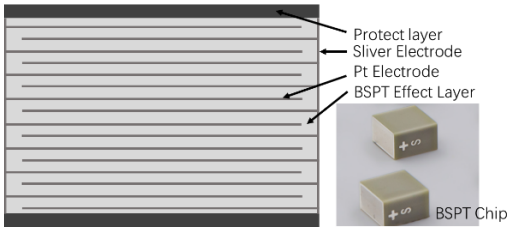

Figure 1 The structure illustration and the product photos of BSPT multilayer ceramic of BSPT multilayer ceramic chip.

The BSPT piezoelectric actuator is constructed using a multilayer structured ceramics with interdigitated electrode, as depicted in Fig.1. The ceramic structure is comprised of three distinct layers, wherein the upper- and lower-layers function as protective coatings with a thickness of 300µm each, while the middle layer consists of BSPT thin film. The manufacturing process involves stacking and bonding 49 sheets of BSPT film together, followed by application of platinum paste to create a multi-layered ceramic structure. Fig.1 also shows photograph of multilayer BSPT piezoelectric actuator chip with the external dimensions of 5.0mm*5.0mm*3.0mm.

Result and discussion

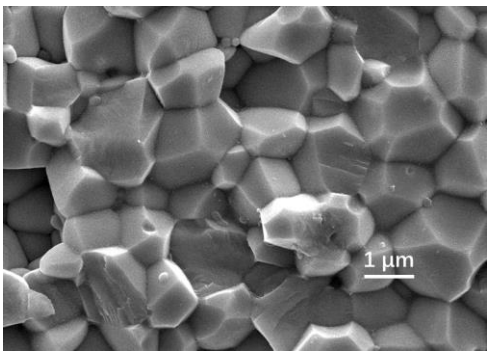

Figure 2 The SEM morphology of BSPT multilayer ceramic chip.

The cross-sectional morphology of BSPT ceramic is observed by SEM and shown in Fig.2. As the effective layer thickness for a single BSPT ceramic layer is approximately 50 µm. Consequently, when the BSPT chip is working at a voltage of 150V, the equivalent electric field reaches up to as high as 3000 kV/m, which is 50% higher than that in those conventional piezoelectric chips with a thicker effective layer. As shown in Fig.2, the grain size of BSPT is about 2 µm. The previous report demonstrated that the optimal size for BSPT ceramics is 1µm, and the closer the particle size approaches 1µm, the enhanced performance of the ceramics can be observed.

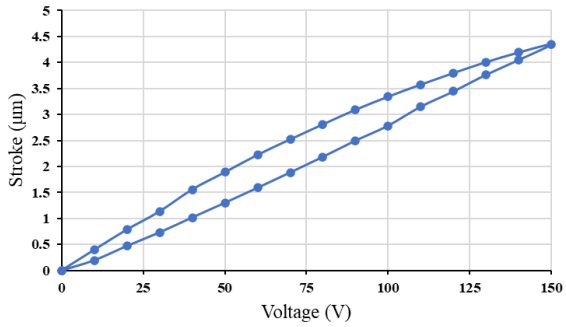

Figure 3 The stroke of BSPT chip under the working voltage of 150V at room temperature.

In this work, the stroke hysteresis loop of BSPT chip under a working voltage of 150V is presented in Fig.3. Due to its high working electric field, the BSPT chip can achieve a stroke of as high as 4.24 µm at external voltage of 150V, which is equivalent to 1.4‰ in total and higher than the stroke of piezoelectric actuator chip made by PZT (3.6 µm). Furthermore, based on calculations from the hysteresis loop, the hysteresis value of BSPT (10%) is lower than the required standard (15%), indicating that it could be considered as a promising candidate for piezoelectric actuator chips.

The stroke of BSPT at various temperatures (ranging from 30°C to 275°C) is measured and depicted in Fig.4(a), considering its intended application under high temperature conditions. Additionally, the hysteresis loop of BSPT at three distinct temperatures (room temperature, 200°C, and 250°C) is illustrated in Fig.4(b). As shown in Fig.4 (a) and (b), the displacement performance of BSPT increases with the rise in temperature at first, reaching its peak at 200°C. However, as the temperature continues to increase to 275°C, the performance of BSPT decreases again, exhibiting a trend of initial increase followed by decline. Stability is another important property for piezoelectric actuator chip. Fig.4 (c) illustrates the stroke repeatability of BSPT at 250°C, demonstrating that even after 1000 cycles, the BSPT chip retains its piezoelectricity and maintains a stable stroke of over 3.5 µm. This indicates that the BSPT can operate continuously and reliably in high-temperature environments.

Table 1 The electrical properties of BSPT chip with different electrode

Electrode material	Capacitance (nF)	DF (%)	d33 (pC/N)	Stroke (μm)	Hysteresis	Fs (KHz)	Phase angle (°)	Zr (mΩ)
Pt	258.26	3.85%	20200	4.24	<15%	364	70.01	499
Ag/Pd	145.98	3.87%	14180	2.81	<15%	369	67.66	719

The electrical properties for BSPT are measured and summarized in Tab.1. Notably, the d_{33} value of the BSPT chip exceeds 20000 pC/N, which is equivalent to that of conventional PZT ceramic. The capacitors of BSPT also reaches to 260 nF, which is also very close to that of PZT ceramics.

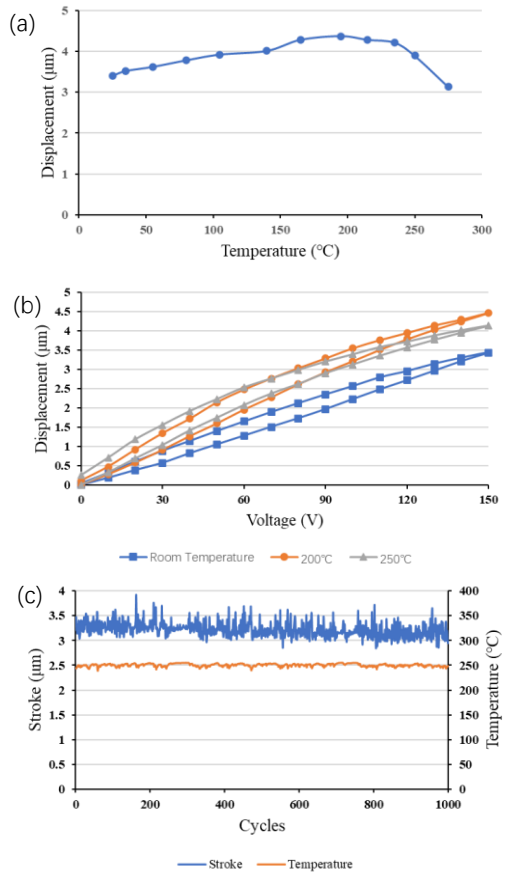

Figure 4 (a) the displacement at 150V and (b) the hysteresis plots at various temperatures, (c) the repeatability of BSPT at 250°C

In contrast to conventional actuator chip using Ag/Pd as the internal electrode, we utilize Pt due to its inert chemical properties in this study. For comparison purposes, we also fabricated a BSPT chip with an Ag/Pd internal electrode. The electrical property of BSPT with Ag/Pd electrode is measured and listed in Tab.1 and the stroke hysteresis loop of BSPT with Ag/Pd electrode is shown in Fig.5(a). It is evident from these results that the piezoelectric properties of the BSPT chip with an Ag/Pd electrode are significantly inferior compared to those with a Pt electrode. Furthermore, the BSPT chip with an Ag/Pd electrode exhibits substantial leakage current and limited DC lifetime when compared to its counterpart using Pt as the internal electrode. Two primary reasons account for these observations. Firstly, owing to its lower chemical reactivity relative to Ag and Pd, Pt effectively inhibits ion migration within ceramics, thereby reducing the risk of ceramic leakage and failure. Secondly, employing Pt as the electrode leads to a considerably smaller grain size in BSPT ceramics than when using Ag/Pd electrodes. Although no direct literature has been found to support this, Pt has indeed had a significant impact on grain size in our hundreds of observations. Previous research has demonstrated that optimal grain size for BSPT ceramics is approximately 1 μm; however, at a grain size of around 1 μm, they exhibit superior piezoelectric performance. As shown in Fig.5 (b), the grain size of BSPT ceramic using Ag/Pd as electrodes is 5-8 μm, which is much higher than that using Pt as electrodes. However, as shown in Fig.2, when utilizing Pt as the inner electrode material for BSPT chips, their grain size approaches approximately 2 μm – precisely within this optimal range. Based on these two factors mentioned above, we adopt Pt as our choice for achieving high-performance and highly stable chips.

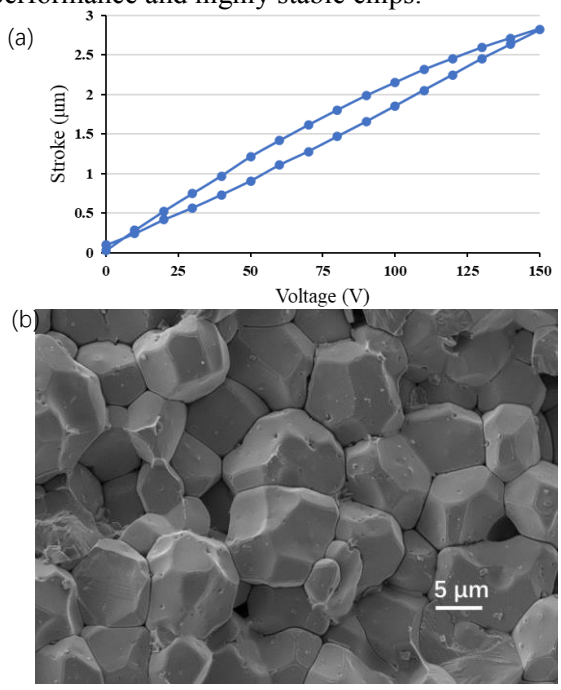

Figure 5 (a) the stroke and (b) SEM morphology of BSPT chip using Ag/Pd as electrodes

We adhere three single BSPT chips together to fabricate the BSPT piezoelectric stack, as shown in Fig.6 (a) with external dimensions of 5.0*5.0*3.0 mm^3. The stroke hysteresis loop for the BSPT stack is presented in Fig. 6(b), indicating a stroke of 10 µm. It will be an excellent candidate for applications such as high-temperature gas valves, glue dispensing devices, and nano/micro positioners.

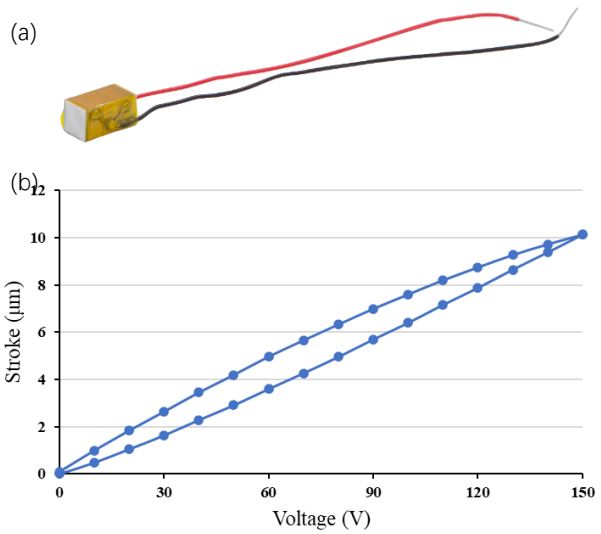

Figure 6 (a) product photo and (b) the stroke curve of BSPT stack stacked by three BSPT chips.

Conclusion

In this report, we fabricate the piezoelectric actuator chip made by BSPT material and using the Pt as the inner electrode. Owing to its high curie point, the BSPT can be applied at higher temperature than other conventional PZT materials. As shown in this report, the as fabricated BSPT actuator chip can achieve the stroke of as high as 4 µm at external voltage of 150V. When we stack three or more BSPT chips together, the BSPT stack actuator can even achieve the stoke of more than 10 µm. In addition, the BSPT chip can work at 250°C for a long time without performance degradation. Apart from its excellent property, the introduction of Pt can also enhance its piezoelectric properties and stability. In summary, our BSPT actuator chip exhibits promising potential for high-temperature piezoelectric motion control applications such as high-temperature gas valves, glue dispensing devices, nano or micro positioners, etc.

Reference

[1] Z. Zhang, J. Xu, J. Xiao, et al., Simulation and analysis of the PMN-PT based phased array transducer with the high sound velocity matching layer, Sens. Actuator A Phys. (313) (2020), 112195.

[2] Z. Zhang, J. Xu, L. Yang, et al., Design and comparison of PMN-PT single crystals and PZT ceramics based medical phased array ultrasonic transducer, Sens. Actuator A (283) (2018) 273–281

[3] K. Rymantas, V. Algirdas, S. Reimondas, et al., High temperature ultrasonic transducers for imaging and measurements in a liquid Pb/Bi eutectic alloy, IEEE Trans. Ultrason. Ferroelectr. Freq. Control. (52) (2005) 525–537.

[4] S. Zhang, F. Yu, Piezoelectric materials for high temperature sensors, J. Am. Ceram. Soc. (94) (2011) 3153–3170.

[5] B. Noheda, D.E. Cox, G. Shirane, et al., A monoclinic ferroelectric phase in the Pb (Zr1-xTix)O3 solid solution, Appl. Phys. Lett. (74) (1999) 2059–2061

[6] R. E. Eitel, C. A. Randall, T. R. Shrout, P. W. Reherig, W. Hackenberger and S. E. Park. New High Temperature Morphotropic Phase Boundary Piezoelectrics Based on Bi(Me)O3–PbTiO3 Ceramics. Jpn. J. Appl. Phys. (40) (2001) 5999~6002

[7] R.E. Eitel, C.A. Randall, T.R. Shrout, S.-E. Papk, Preparation and characterization of high temperature perovskite ferroelectrics in the solid-solution (1-x)BiScO3-xPbTiO3, Jpn. J. Appl. Phys. (41) (2002) 2099–2104.

[8] R.E. Eitel, S.J. Zhang, T.R. Shrout, et al., Phase diagram of the perovskite system (1-x)BiScO3-xPbTiO3, J. Appl. Phys. (96) (2004) 2828–2831.

[9] T. Zou, Study on preparation and size effect of fine grain high temperature BiScO3-PbTiO3 ceramic. (2009, Doctoral dissertation, Tsinghua University).

[10]H. Wang, Preparation and grain size effect of (1-x)BiScO3-xPbTiO3 piezoelectric ceramics. (2009, Doctoral dissertation, China University of Geosciences).

[11] W. R. Buessem, L. E. Cross, A. K. Goswami, Phenomenological Theory of High Permittivity in Fine-Grained Barium Titanate. J. Am. Ceram. Soc. (49) (1966) 33-36.

High-Accuracy Alignment of integrated Optical Components utilizing Ferroelectric Shape-Memory Actuators

Zijian Chen[1,2], Jens Twiefel [1,2] and Jörg Wallaschek [1,2]
[1] Leibniz University Hannover, Institute of Dynamics and Vibration Research, Garbsen, Germany
[2] Leibniz University Hannover, Cluster of Excellence PhoenixD, Hannover, Germany
chen@ids.uni-hannover.de

Abstract

High-precision alignment of optical elements is crucial for the development and manufacture of highly integrated optical systems. Controlled ferroelectric actuators, known for their unlimited displacement resolution, are ideal for such precise alignment tasks. Traditionally, such actuators are driven unipolarly along the predetermined delivery state polarization direction and require a constant voltage level to maintain the alignment, which is impractical for long-term applications. This paper presents a novel approach for harnessing the ferroelectric shape-memory effect through intentional manipulation of ferroelectric material polarization, thereby enabling control over its remanent strain. This remanent strain maintains without external power supply, presenting an ideal solution for long-term alignment tasks. Furthermore, this technique allows the readjustment of the optical components in response to aging, drifting, disturbance or changes in tolerance.

Keywords: Ferroelectric Shape-Memory, High-Accuracy Alignment, Integrated Optical Systems

1 Introduction

In integrated optical systems, a misalignment of components, even in the nanometer range, can significantly impair the performance, functionality, and reliability. Thereby, assembly and calibration are important tasks that need to be performed with high effort, even with high-precision assembly equipment. Our strategy aims to integrate an actuator within the optical system itself, which allows the actuator to perform the final, precise adjustments required for optimal alignment. In addition, the integrated actuator offers the advantage that readjustments can be undertaken during the product's service life, thus extending the system's durability and performance. An illustrative application of this technique is the alignment of laser diodes with optical wave guides (see **Figure 1**).

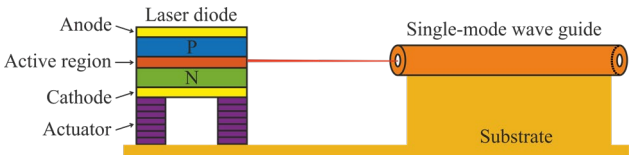

Figure 1: Alignment of a laser beam to a single-mode wave guide

This scenario presents a significant challenge due to the stringent requirements to align the laser beam − emitted from the edge of a laser diode's active region − into a narrow core of the single-mode wave guide, often less than 9 microns in width. Ferroelectric actuators, renowned for their high displacement resolution, are an ideal option. Nonetheless, it's also significant that once the laser beam is aligned, its position is maintained. The conventional use of such actuators is hindered by their need for constant voltage offset to maintain alignment, a constraint that our novel method aims to overcome. This paper introduces a novel approach of utilizing the ferroelectric shape-memory effect (first presented by [1]), which exploits intentional manipulation of ferroelectric material polarization in order to harness the remanent strain for alignment purposes. In addition, a close-loop control system can be implemented without high effort, utilizing the transmitted laser energy as feedback.

2 Methodology

Ferroelectric materials are, in most cases, polycrystalline sintered ceramics whose main characteristic is the modification of domain polarizations by applying a corresponding electric field. **Figure 2** shows the measured strain vs. electric field strength curve of a soft PZT (SP505) and the schematic representation of its domain orientations in different polarization states.

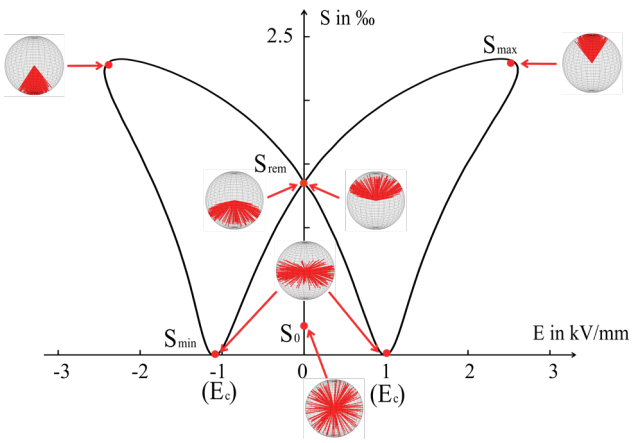

Figure 2: Measured strain vs. E-field strength curve of a soft PZT with schematic representation of its domain polarizations

Freshly sintered PZTs exhibit spontaneous polarization and has a strain of S_0. Normally, they will be poled during

manufacturing by a strong electric field to obtain macroscopic polarization and strain (S_{max}) throughout the entire component. After removing the electric field, a certain level of polarization and strain remains (S_{rem}), which are so called remanent polarization and strain. The central idea of the novel approach is to harness this remanent strain for alignment purposes. To achieve that, two methods of electrical manipulation of domain polarisation are presented in **Figure 3**. For better understanding, it should be noted that the PZT-sample's initial polarization state is in the +Z-direction and its strain in this +Z-direction is used for the alignment.

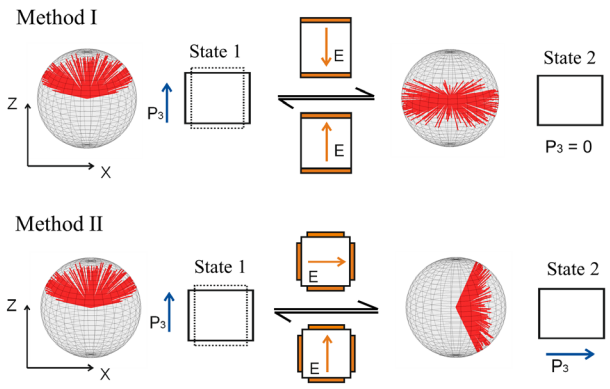

Figure 3: Two methods of electrical manipulation of domain polarisation

In method one, the electric field is applied parallel or antiparallel to the initial polarization state. The polarization of the sample switches between two states. In state one, domain polarization strives to align as much as possible with the applied electric field, resulting in the maximal remanent strain (approximately S_{rem}). In state two, the domain polarization orients away from the +Z-direction, achieving the minimal remanent strain, which is similar to the case when the coercive electric field (E_c) is applied. In this method, the electric field strength is limited to be below E_c to ensure that the macroscopic polarization of the sample either remains in the +Z-direction or approaches the minimum in the Z-direction (towards S_{min}). This prevents unintended elongation of the PZT-sample with the antiparallel electric field. In method two, the electric field is applied perpendicular to the current polarization state. This can cause the macroscopic polarization to alternate between the +Z- and +X-directions. Considering only the strain along the +Z-direction, in state one, the remanent strain is at its highest (approximately S_{rem}). In state two, the perpendicular electric field induces a switch in domain polarization towards the +X-direction, which results in a reduction of the remanent strain along the +Z-direction. As the strength of this perpendicular electric field exceeds E_c, the remanent strain along +Z-direction can be effortless reduced to its minimum (approximately S_{min}). In the following section 3, the validation of the first method is carried out, including the design of driving signals. Section 4 introduces a novel electrode configuration that allows the application of a perpendicular electric field for the implementation of method two.

3 Experiments based on method I

3.1 Design of the operating signal

For validation of method one, an electric field is applied parallel or antiparallel to the PZT-sample's initial polarisation state and not exceeding E_c. When the remanent strain is used for high-precision alignment, it's crucial that the remanent strain can be adjusted in the smallest steps possible, thereby, maximizing the actuator's displacement resolution. However, if the poling holding time of the PZT-component exceeds the necessary duration, it may lead to large jump in remanent strain, reducing the displacement resolution of the actuator. In that case pulse singles are employed, similar to [2]. The experiment utilizes a multilayer piezoelectric actuator composed of SP505 (a type of soft PZT material from CeramTec), a Laser-Doppler-Vibrometer (with displacement decoder DD-900 from Polytech) for displacement measurements. The operating signal was produced with an arbitrary waveform generator from National Instruments. To amplify the signal, a high-speed amplifier from NF Corporation was used.

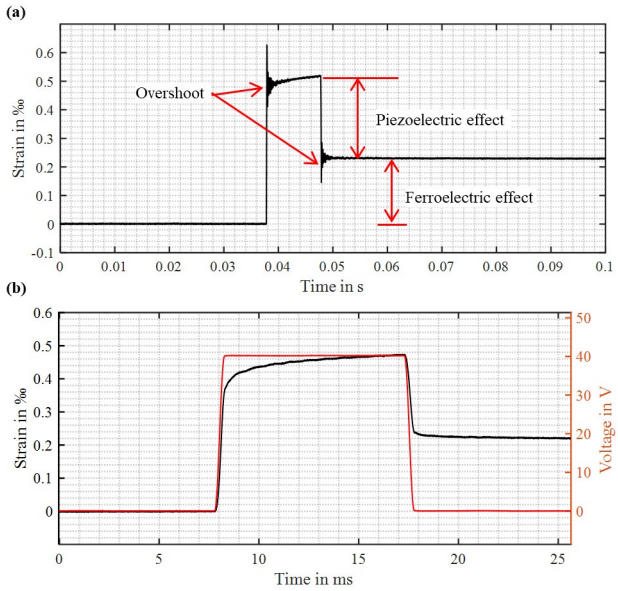

Figure 4: Strain response of multilayer actuator. **(a)**: To a pulse signal, **(b)**: To a modified pulse signal.

Figure 4 (a) shows the strain response of the actuator to a pulse signal with 40 V for ten milliseconds. The observed strain results from two distinct processes: the shift of central ions, attributed to the piezoelectric effect, and the switching of domains, identified as the ferroelectric effect. After withdrawal of voltage, the strain associated with the piezoelectric effect reverses, whereas the strain related to the ferroelectric effect partly remains. A rapid increase in voltage can cause an uneven distribution of mechanical stresses across the multilayer actuator, increasing the risk

of its failure. Additionally, a notable overshoot is observed. Therefore, the modification of the pulse signal is necessary to minimize the undesired overshoot and improve the actuator's performance.

In terms of overshoot minimization, the rising and falling edges are modified [3]. Two different shapes are discussed in this paper i.e., the ramp shape and the sinusoidal shape. For calculating the signal rising time, the frequency response of the actuator, including its mounting periphery, is measured. An undamped single degree of freedom system is built based on its dominant resonance frequency, and its equation of motion is transferred into Laplace domain and then further multiplied with the excitation signals, i.e., ramp-shaped and sinusoidal-shaped step signal. Their products in Laplace domain are transferred back to time domain to determine the time at which the velocity is zero, i.e. the displacement is at its largest. This calculated time is the desired rising time. The results show that the ramp-shaped signal has a shorter rising time, but can excite higher vibration modes of actuator due to its sharp change in slope at turning point. Thereby, the sinusoidal-shaped signal is selected. Its final shape is a half cosine curve, in order to smoothen both turning points of the signal. **Figure 4 (b)** shows the strain response of the actuator to the modified pulse signal. The large overshoot is minimized. However, slight oscillations can be observed, which is due to the fact that the rising time is calculated based on an undamped system, as opposed to the actual system with damping from the actuator itself and the mounting periphery. The velocity of the damped system at the calculated rising time is not zero and thus the slight oscillation occurs.

3.2 Results

Based on the modified operating signal, the multilayer actuator is excited with several rising and sinking pulse signals, each having a duration of ten milliseconds. The voltage of the highest pulse is 100 volts, which induces an electric field strength equal to E_c. **Figure 5** shows that with the help of the rising pulse signals, the strain of the actuator increases gradually from a start position, here defined as zero. With the sinking pulse signals, the strain can return to zero.

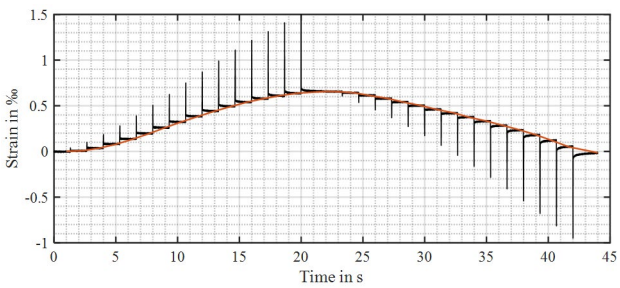

Figure 5: Strain response of the multilayer piezoelectric actuator to modified rising and falling pulse signals

As discussed in section 2, to prevent the polarization of PZT-components from opposing the actuation direction, the electric field strength induced by the negative pulse signal is limited to $-E_c$. In addition, in order to precisely control the remanent strain, the pulse width also needs to be maintained in a few milliseconds. These two constraints increase the difficulty of utilizing the full strain range from S_{min} to S_{rem}. It should be noted that applying a higher pulse with negative polarity for extended duration (e.g., applying an electric field around $-E_c$ for several seconds) can further reduce the remanent strain as shown in **Figure 5**. However, to accurately and completely minimize the remanent strain, the exact duration and magnitude of this pulse must be determined based to the polarization state of the PZT-components, which is challenging without additional measurements. This increase the effort of developing a control system that fully harnesses available remanent strain. To address these challenges, a novel actuator design is proposed.

4 Novel actuator design

4.1 Operation principle

In the proposed novel configuration, the second method is utilized, in which an electric field is applied perpendicular to the current polarisation state of the PZT-component. **Figure 6** shows the structure of a single layer, which can be built into a bender or multilayer actuators. Interdigital electrodes (IDEs) are placed on both upper and lower surface of the single actuator layer [4]. Positive and negative electrodes are connected with long, thin conductors with a relatively high resistivity, e.g. constantan or platinum. The shape is similar to the structure of strain gauge sensor in order to obtain a high electric resistance, which produces a gradual decrease in the electric potential from a high level to zero. This impacts the electric field significantly, as shown in **Figure 6 (a)** and **(b)**.

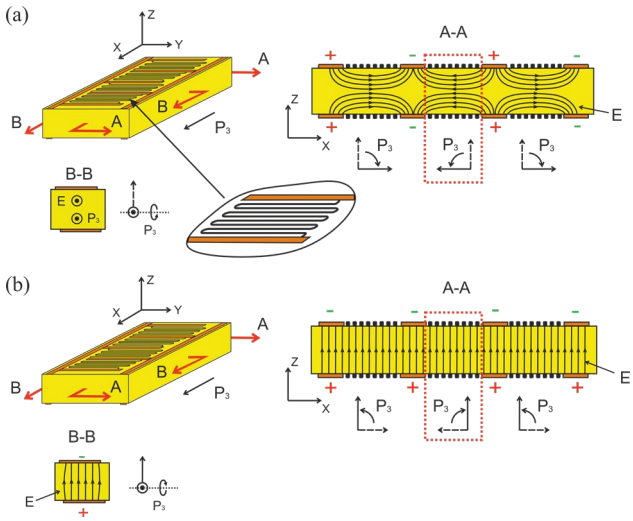

Figure 6: Single layer of the novel actuator design. **(a)**: actuation mode (domain switching from Z to X); **(b)**: remanent strain reduction mode (domain switching from X to Z).

The operating principle is shown in **Figure 6**. The actuation mode is illustrated in **(a)**, where a certain voltage is applied to the adjacent positive and negative electrodes on

one surface of the PZT-layer. Within the region between these electrodes (exemplary marked with red dotted box), the electric field lines run parallel and switch the domain polarization into X-direction, which is the actuation direction. This new orientation causes the PZT-layer elongate in this direction. The resistance of the conductor leads to a gradual decrease in the applied voltage along its length, which results in a smaller electric potential difference between adjacent parts of the conductor. This reduction of electric potential helps to prevent the electric field lines from bending. **(b)** depicts the remanent strain reduction mode, where a voltage is applied across electrodes located on the upper and lower surfaces of the PZT-layer. This means that the electrodes on one surface and the conductor between them have the same electric potential. In this case, the area between the two opposite conductors (exemplary marked with red dotted box) receives sufficient high electric field strength to switch the domain polarization from the X direction back to the Z direction. This switching process contributes to a reduction in remanent strain in X-direction, i.e., actuation direction.

4.2 Numerical simulation

Figure 7 shows the simulated distribution of the electric field lines within this novel actuator configuration in Ansys Maxwell. The selected ferroelectric material is SP505, which has a thickness of 100 microns. The distance between adjacent electrodes on one surface is 105 microns, and the width of each electrode is 50 microns. The conductor connecting the electrodes has a thickness of 5 microns. In addition, a voltage of 10 volts is applied. Due to the presence of the conductor, the electric field lines remain parallel between electrodes (marked with black box) in actuation mode, with a strength of approximately 1×10^5 V/m. In the meanwhile, the electric field strength in this region is increased in remanent strain reduction mode, which is similar to the electric field strength between two plates (1×10^5 V/m).

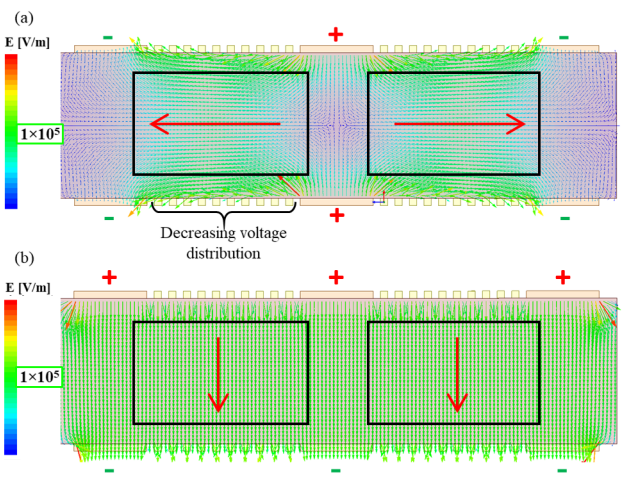

Figure 7: Simulated distribution of the electric field lines. **(a)**: actuation mode; **(b)**: remanent strain reduction mode.

In terms of operating signals, for actuation mode, the signal is the modified pulse signals as discussed in section 3. For remanent strain reduction mode, the perpendicular electric field can also be applied utilizing pulse signals for the fine-tuning of remanent strain. Additionally, to exploit the full strain range from S_{min} to S_{rem}, the electric field strength induced by pulse signals can exceed E_c. Contrary to method one, at this point, there is no concern about the domain polarization reversing opposite to the actuation direction. Thus, the design of a control system is simplified.

5 Conclusion

This paper introduces a novel approach that employs ferroelectric shape memory effect for the high-accuracy alignment of highly integrated optical components. The remanent strain can be precisely adjusted by applying pulse signals with a duration in the range of a few milliseconds. The overshoot and uneven mechanical stress across the actuator are reduced by modifying the edges of the pulse signal. For method two, in which the electric field is applied perpendicular to the current polarization state of the ferroelectric component, a novel configuration is introduced. Its key advantage is the ability to apply an electric field stronger than E_c, which significantly enhance the reduction of remanent strain. Thus, the usable remanent strain for alignment purposes is increased without a complex control system. This method can be implemented using a single layer of ferroelectric material sandwiched between interdigitated electrodes (IDEs). A pair of positive and negative IDEs are connected with long, thin conductors. This guarantees an adequate electric field for reducing remanent strain without bending the electric field lines and thus decreasing the electric field strength for actuation mode.
In the example (see **Figure 1**), when fully utilizing 1.3 ‰ remanent strain of the material SP505 for actuation, an actuator as small as 7 millimeters is sufficient for the 9-microns stroke required for aligning a laser beam with a single-mode wave guide.

6 Literature

1. Morita, T.; Kadota, Y.; Hosaka, H. Shape Memory Piezoelectric Actuator. *Applied Physics Letters* **2007**, *90*, 082909, doi:10.1063/1.2709985.
2. Reiser, J.; Marth, H. PIRest Technology – How to Keep the Last Position of PZT Actuators without Electrical Power.; VDE VERLAG GMBH · Berlin · Offenbach, Germany, June 25 18AD; pp. 75–78.
3. Henke, A. *Modellbildung, Simulation und Optimierung piezoelektrischer Stellsysteme*; HNI: Paderborn, 2001; ISBN 3-935433-05-0.
4. Liu, H.; Zhong, J.; Lee, C.; Lee, S.-W.; Lin, L. A Comprehensive Review on Piezoelectric Energy Harvesting Technology: Materials, Mechanisms, and Applications. *Applied Physics Reviews* **2018**, *5*, 041306, doi:10.1063/1.5074184.

Audio Frequency Actuation of SMA Wires

Prof. Dr.-Ing. Arif Kazi, Aalen University of Applied Sciences, Aalen, Germany
Lukas Buser B. Eng., Aalen University of Applied Sciences, Aalen, Germany
Maximilian Schmitt B. Eng., Aalen University of Applied Sciences, Aalen, Germany
Max Karch B. Eng., Aalen University of Applied Sciences, Aalen, Germany
Dipl.-Ing. Markus Köpfer, Actuator Solutions GmbH, Gunzenhausen, Germany

Abstract

The shape memory effect in nickel-titanium-based shape memory alloys (SMA) is due to a crystallographic reversible phase transformation between the low-temperature martensitic and the high-temperature austenitic phase of the material. Actuation frequencies of SMA wires are typically limited to a few Hertz, primarily due to the time required for cooling. Thus, not many are aware that SMA wires can also generate forces at audio frequencies of up to several thousand Hertz. This paper systematically investigates the factors that influence the ability of SMA wires to generate forces at high operating frequencies. Preliminary experimental results show that mean SMA wire stress and temperature, current amplitude, and frequency all have a significant impact on force amplitude. Measured force amplitudes varied between 10 mN at an actuation frequency of 100 Hz down to 0.2 mN at 7.5 kHz.

1 Introduction

In recent years, actuators using nickel-titanium-based shape memory alloys (SMA) have gained prominence in various application fields, including automotive, aerospace, medical devices, and consumer electronics [1-4]. The main advantages of SMA actuators are their high energy density, ease of miniaturization, and noiseless operation. The actuator dynamics can be improved by increasing the surface-to-volume ratio of the SMA element. However, even for very thin SMA wires, the actuation frequencies are usually limited to a few Hertz.

[5] took the optimization of the surface-to-volume ratio to an extreme. The researchers demonstrated that 1 µm thick SMA structures fabricated by focused ion beam milling can be excited by a UV laser at up to 1.6 kHz. However, also standard SMA wires can be operated at audio frequencies well above 1 kHz by applying high-frequency electrical pulses [6, 7]. This may seem rather surprising given the fact that phase transformation processes in the material typically require temperature changes of several Kelvin. The audio frequency mode of operation may open up a whole new field of applications for SMA actuators and active sensors working in resonance [8].

Although SMA wire audio frequency experiments were reported already more than 15 years ago, no systematic studies investigating the optimum conditions for SMA audio frequency operation are known. As a starting point for the design of future resonance mode SMA devices, this study aims to provide comprehensive and quantitative data regarding the operating conditions that maximize the actuation of SMA wires at audio frequencies.

2 Scope of Experiments

2.1 Input Variables

Shape memory alloys can be regarded as materials that change their mechanical properties with their temperature. Therefore, the operating point of an SMA wire is characterized by its mean temperature, stress, and strain. Reflecting the load limits to which the SMA wire can be operated safely under standard conditions, the stress level was to be varied between 100 and 400 MPa.

Both the mean temperature and the temperature variation of the SMA wire that is undergoing audio frequency operation depend on the electrical current heating the wire. Sinusoidal currents with variable frequencies, amplitudes, and bias were to be applied, with maximum frequencies of at least 5 kHz. Maximum currents should be sufficient to transform the SMA wire into full austenite.

Recent experimental evidence in the authors' lab suggests that dynamic force amplitudes will be more pronounced when the SMA wire is working against a high load stiffness. It was therefore decided that the experimental setup should be designed to be as stiff as possible, but should also incorporate the means to change the stiffness that the SMA wire experiences during audio frequency operation.

2.2 Target Variables

As a measure of the manifestation of audio frequency operation, dynamic changes in stress and strain of the SMA wire can be used. Stress and strain amplitudes are interrelated through the load stiffness against which the SMA wire is working. The dynamic force amplitude was selected as the target measurement parameter. With the diameter of the SMA wire and the known load stiffness, the stress and strain amplitudes can be determined.

Previous experiments indicated that during audio frequency operation, lengthening of the SMA wire may occur. This could affect measurement results and might also pose a challenge for the design of audio-frequency SMA devices. Thus, the SMA wire length was also to be monitored.

3 Experimental Setup

For the experiments, a setup was developed that comprises four subsystems (see **Figure 1**).

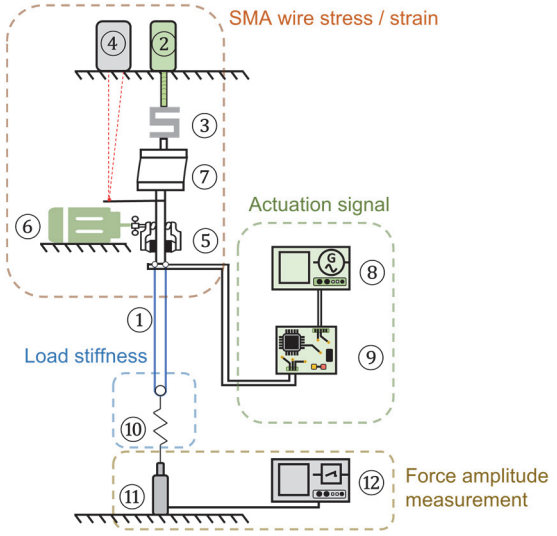

Figure 1 Schematic of the experimental setup.

3.1 SMA wire stress / strain

The first subsystem of the experimental setup is used to set the stress level of the SMA wire before the start of audio frequency operation. The position of the upper fixation point of the SMA wire ① can be adjusted by means of a linear actuator (Nanotec LGA42, ②). SMA wire stress is controlled by means of strain gage-based force sensor (ME Messsysteme KD40s 10N, ③) mounted on the slider of the linear actuator. The SMA wire strain is recorded using a laser triangulation sensor (Micro-Epsilon optoNCDT ILD1320-25, ④) with the sensor target placed at the movable fixation point of the SMA wire.

To ensure high load stiffness during audio frequency operation, a motorized brake system was conceived which serves to decouple the compliant force sensor and the linear actuator from the SMA wire. The brake comprises a centering vise ⑤ that can be opened and closed via a DC motor ⑥. The centering vise applies a clamping force of several kilonewtons to a steel block to which the SMA wire is fixed. To protect the force sensor from high forces when closing the brake, a flexure beam guide ⑦ is placed between the steel block and the force sensor.

3.2 Actuation signal

The actuation signal is provided by a programmable signal generator (R&S HM8150, ⑧) that allows for a free adjustment of signal type, frequency, amplitude, and bias. The actuation signal from the signal generator serves as the reference signal for the output current of the subsequent analogue power electronics ⑨. The power electronics is an in-house development and has a proven track record in the authors' laboratory.

3.3 Load stiffness

The load stiffness the SMA wire will experience during audio frequency actuation is varied by short exchangeable lengths of thin metal tube ⑩ mounted between the lower end of the SMA wire and its fixation point. Due to the low mass of the compliant tube elements, the resonance frequencies are well above the frequency range of interest.

3.4 Force amplitude measurement

One of the main challenges was the measurement of small high-frequency force variations on top of the large static force generated by the SMA wire. The sensor system was also to be very stiff in order not to reduce the overall stiffness of the experimental setup.

A solution satisfying these requirements was identified in a piezoelectric force sensor (Kistler 9217A, ⑪). In conjunction with the appropriate measurement amplifier (Kistler 5018A1000), the sensor provides a force sensitivity of 200 V/N and a resonance frequency above 20 kHz. The sensor stiffness is specified at 15.000 N/mm. The analog sensor signal is recorded and stored by a digital oscilloscope (Keysight DSOX2002A, ⑫) with a bandwidth of 70 MHz.

In the end, the experimental setup was shielded from moving air by a PMMA cover. **Figure 2** shows a photograph of the final setup.

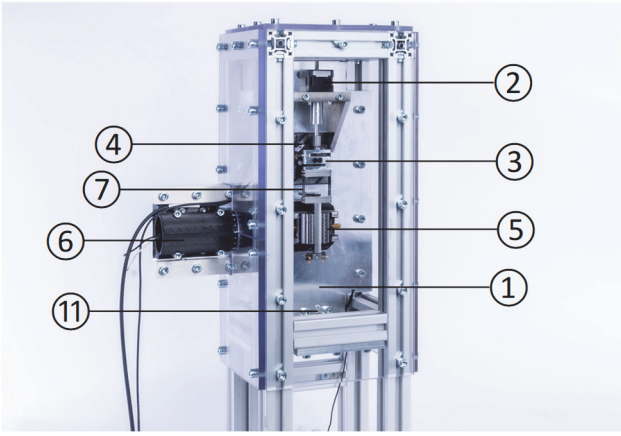

Figure 2 Finalized experimental setup.

4 Experimental procedure

The experiments used 76 µm diameter Smartflex® SMA wires with a length of 150 mm. All wires were subjected to a run-in procedure of 1500 full transformation cycles at a load of 200 MPa to make sure that residual elongation would not affect measurement results. The wires were mounted in a U-shaped configuration (see **Figure 1**), which doubled the generated force.

The behavior of SMA wires is strongly non-linear and displays a pronounced hysteresis. Therefore, the loading history of the SMA wire under test needs to be carefully controlled. Every experimental run started with the power electronics providing a constant DC current to establish the operating temperature of the SMA wire. The force on the wire was increased until the desired stress level was reached; then the brake was closed. As soon as the sinusoidal audio frequency signal was started, the bias current was reduced to maintain constant heating power.

The audio frequency measurement lasted 25 s, after which the brake was opened, the SMA wire tension was relieved, and the current reduced to zero. After each experimental run, wire elongation was monitored by measuring the length of the wire with the laser triangulation sensor ④ at a high ('austenitic') current of 180 mA and a low stress level of 75 MPa.

The software controlling the experimental setup allows conducting the experimental runs in a highly automated manner. Manual intervention is only needed for varying the load stiffness by exchanging the compliant metal tube or for exchanging the SMA wire under test.

5 Verification and Validation

Implementation of the experimental setup was followed by an in-depth verification of its properties. Closing of the brake showed to change the stress in an austenitic SMA wire by less than 7 MPa. For a closed brake, a stiffness of the upper fixation point of the SMA wire of more than 70000 N/mm was measured. With the piezoelectric sensor and appropriate filtering, force amplitudes down to 0,1 mN could be measured. Ten consecutive experimental runs under identical conditions showed a variance of SMA wire length measurements of 7 µm. Frequency sweeps of the actuation signal between 100 and 7500 Hz did not show any signs of resonances in the setup.

Lengthening of the SMA wire was investigated under worst case conditions, i.e. for a maximum wire stress of 400 MPa, a high DC current of 180 mA and a current amplitude of 75 mA. The duration of the audio frequency excitation was increased to 60 s per experimental run, and a total of 128 runs were conducted. After two hours of operation at a frequency of 100 Hz (i.e. a total of 768,000 cycles), no lengthening of the SMA wire was observed. However, measured force amplitudes had decreased by more than 30% in a roughly exponential fashion (see **Figure 3**).

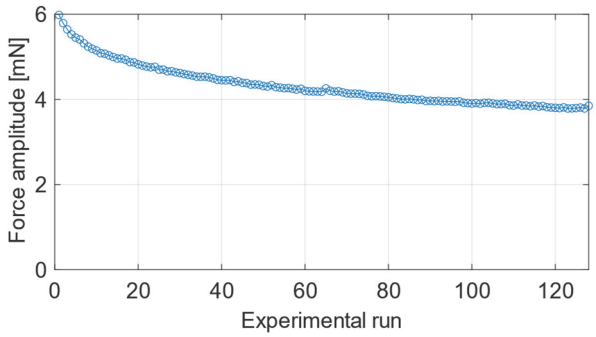

Figure 3 SMA force amplitude over experimental runs.

Clearly, force amplitudes that decrease with the number of cycles should not corrupt experimental results. Therefore, the audio frequency experiments were conducted with SMA wires that had already seen ~70 experimental runs. The factors influencing the decrease of force amplitudes will be analyzed in future experiments.

6 Audio Frequency Experiments

6.1 DoE on input variables

For a systematic screening of the input variables, a statistical Design of Experiment (DoE) was planned. A D-optimal design was used, as this allows to define a different number of levels for each factor (i.e. input variable) as well as conditions for the combination of levels. In the DoE, the following input variables and levels were considered:

- SMA wire stress (100/400 MPa)
- Actuation frequency (100/500 Hz)
- Current amplitude (35/75 mA)
- DC current (100/180 mA)

The DC current applied to the SMA wire before audio frequency operation relates to its mean temperature. The low current value will maintain a mainly martensitic SMA wire condition, while the high value will create a mainly austenitic condition.

In the experiment, only the maximum stiffness of the experimental setup was used. A number of 72 experimental runs was predicted to deliver a statistical power of 94%. **Figure 4** shows the resulting P-values for the main factors and their first-order interactions.

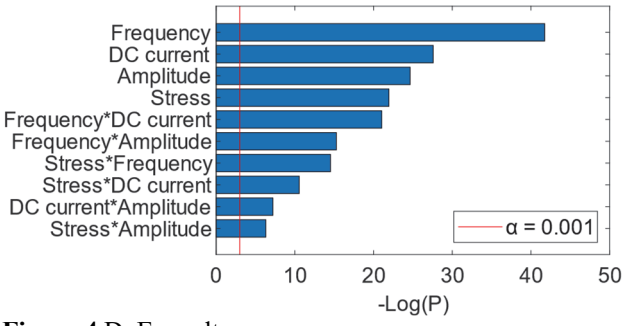

Figure 4 DoE results.

The results of the DoE show that the main factors and their interactions all had a statistically highly significant impact on the force amplitude. Subsequent experiments investigated the main factors in more detail.

6.2 Effect of SMA wire stress

To analyze the impact of SMA wire stress on the force amplitude, the mean stress was set to 13 different levels (at a frequency of 100 Hz, a DC current of 180 mA and a current amplitude of 75 mA). **Figure 5** shows the resulting force amplitudes.

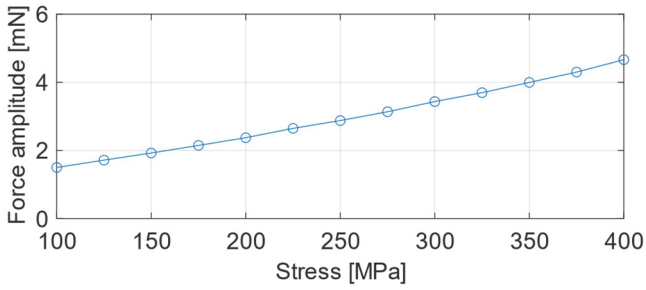

Figure 5 Impact of SMA wire stress.

Not surprisingly, higher mean wire stress produced higher force amplitudes. The relation between the two variables appeared to be rather linear.

6.3 Effect of current bias and amplitude

The next set of experimental runs investigated the effect of both current bias and amplitude at the same time. The DC current was set to 27 different levels, with the amplitude 80% of DC current (at a frequency of 100 Hz and a stress of 200 MPa). **Figure 6** shows the results.

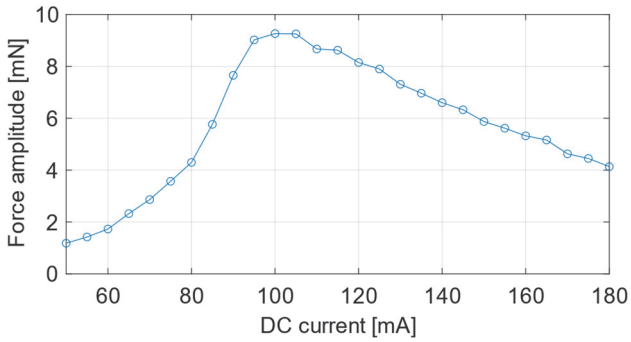

Figure 6 Impact of current bias and amplitude.

The force amplitudes reached a maximum for DC currents of ~100 mA (i.e. a current amplitude of 80 mA at a bias of 82.5 mA). This indicates that the phase composition of the wire may have a major impact on the force amplitudes.

6.4 Effect of actuation frequency

The DoE found actuation frequency to be the most significant factor. To investigate its impact more closely, the frequency was set to 59 different values. During the experimental runs, the SMA wire stress was at 200 MPa, while the DC current was set to 100 mA and the current amplitude was set to 80 mA. **Figure 7** shows the outcome of this experiment.

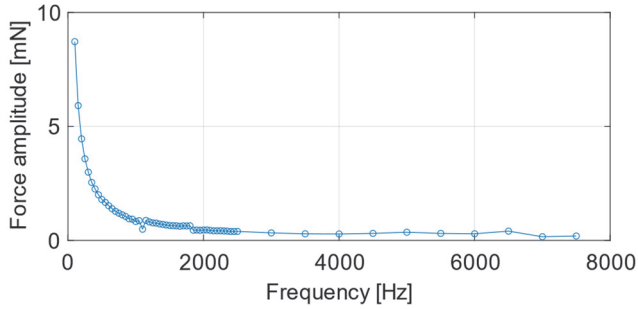

Figure 7 Impact of actuation frequency.

Up to approx. 2.5 kHz, higher frequencies produced lower force amplitudes. This can be explained by reduced heating and cooling times, which results in lower temperature amplitudes. Interestingly, frequencies above 2.5 kHz produced constant force amplitudes of 0,29 mN, which can hardly be explained by thermal effects. This high-frequency effect requires closer investigation.

7 Conclusion and Outlook

This study investigates the impact of different operating points, actuation frequencies and amplitudes on the audio frequency operation of SMA wires. At frequencies well above 100 Hz, SMA wires can hardly be expected to generate significant displacements. Yet, their high force generation capability still allows them to produce force amplitudes of several mN when working against stiff environments. This may be sufficient to drive SMA devices working in resonance.

The preliminary results presented in this paper show that mean SMA wire stress and temperature, current amplitude, and frequency all had a statistically significant impact on force amplitude. Force amplitudes increased with wire stress, while reaching a pronounced maximum for a certain current bias and amplitude. Force amplitudes generally dropped as actuation frequency increased. However, at frequencies above 2.5 kHz, force amplitudes remained surprisingly constant. Force amplitudes of 0.2 mN were still measured at actuation frequencies of 7.5 kHz.

Future work will investigate this high-frequency effect in more detail. In addition, the factors influencing the decrease of force amplitudes over the number of cycles will be explored as well as the dependency of force amplitudes on load stiffness and SMA wire diameter.

8 Acknowledgements

The authors thank the German Ministry of Education and Research (BMBF) for funding this work within the context of the project *SMArtMed* (grant no. 13FH080KX1).

9 References

[1] S. Shreekrishna, R. Nachimuthu, V.S. Nair; *A review on shape memory alloys and their prominence in automotive technology*. Journal of Intelligent Material Systems and Structures, Vol. 34, No. 5, Mar. 2023.

[2] G. Costanza, M.E. Tata; *Shape memory alloys for aerospace, recent developments, and new applications: A short review*. Materials, Vol. 13, No. 8, Apr. 2020.

[3] J.W. Sohn, G.W. Kim, S.B. Choi; *A state-of-the-art review on robots and medical devices using smart fluids and shape memory alloys*. Applied Sciences, Vol. 8, No. 10, Oct. 2018.

[4] A. Schwegler, D. Niklas, T. Schumm, A. Kazi; *Performance Optimization of an SMA-Actuated Camera Gimbal*. 19th International Conference and Exhibition on New Actuator Systems and Applications (Actuator 2024), Wiesbaden, June 13-14, 2024.

[5] H.T. Lee, M.S. Kim, G.Y. Lee, C.S. Kim, S.H. Ahn: *Shape Memory Alloy (SMA)-Based Microscale Actuators with 60% Deformation Rate and 1.6 kHz Actuation Speed*. Small, Vol. 14, No. 23, May 2018.

[6] Y.H. Teh; *Fast, Accurate Force and Motion Control of Shape Memory Alloy Actuators*. Ph.D. Thesis, Dept. Information Engineering, The Australian National University, Canberra, Australia, Oct. 2007.

[7] Y.H. Teh, R. Featherstone; *Experiments on the Audio Frequency Response of Shape Memory Alloy Actuators*. Proc. Australasian Conf. Robotics & Automation, Sydney, Australia, Dec. 5–7, 2005.

[8] D. Fehrenbach, F. Witt; *Antrieb für einen Vibrationssensor, Vibrationssensor und Verwendung von Formgedächtnismaterialien als Antriebselement in Vibrationssensoren sowie Verfahren zum Antrieb eines Vibrationssensors.* Deutsches Patent DE102020130558 A1, Mai 19, 2022.

Investigation of the localized twinning behavior of magnetic shape memory alloys using digital image correlation

Robert Courant[a] and Jürgen Maas[a]
[a]Technische Universität Berlin, Berlin, Germany

Abstract

In this work, we present an approach to model the hysteretic response of magnetic shape memory alloys (MSMA) to contracting and elongating loads using predefined bands over the length of the sample, motivated by the twinning stress of individual twin bands. To observe the twinning behavior of identified sections, optical images of MSMA samples are recorded under mechanical excitation and processed using digital image correlation (DIC). Several fitted models to predict the bands response to more complex inputs including inner hysteresis loops are derived, parameterized and compared with experimental results.

1 Introduction

Magnetic shape memory alloys (MSMA) are smart materials showing a significant stroke under mechanical and magnetic loads. Their actuation mechanism is based on the reorientation of martensite twin variants due to the high magneto-crystalline anisotropy, with a higher magnetic permeabilty along the shorter, so-called magnetic easy axis compared with the hard axes [1]. The energy difference between the possible lattice orientations creates a driving force towards a reorientation [2] as illustrated in **Figure 1**. These driving forces have to overcome a threshold – the material inherent twinning stress σ_{tw} – to induce a reorientation along diagonal twin boundaries [3]. In previous work [4, 5], we showed that to model the inhomogenious magnetic field distribution within MSMA elements in intermediate switching states, homogenization over the entire element is not sufficient. Instead, a localized consideration of the twinning stress is required. However, the corresponding twinning stress distribution is typically unknown [6]. Digital image correlation (DIC) offers a solution, allowing the in-situ optical determination of local strains [7].

In this work, we use optical images of an MSMA element and process them using DIC to identify the local twinning stress distribution, using a simple excitation as described in section 2. Motivated by a model of idealized, equally distributed twin bands presented in section 3, several possible models to simulate the response of the investigated bands under complex excitations are derived in section 4. The model parameters can be identified using information from only the outer hysteresis loop in section 5 and the model results are validated with representative experimental results in section 6.

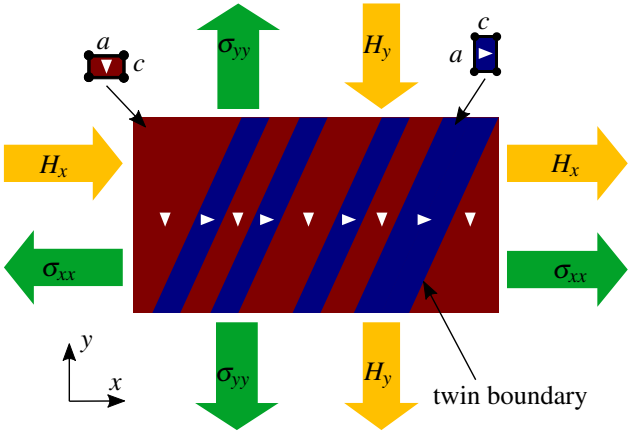

Figure 1 MSMA element with differently oriented domains (red domains denote a vertical easy axis, blue domains indicate a horizontal easy axis) separated by twin boundaries under magnetic and mechanical loads.

2 Experimental setup

For the experiments, a standard MAGNETOSHAPE® MSMA element with the dimensions 15 mm x 3 mm x 2 mm provided by ETO MAGNETIC GmbH with glued fixtures is used under mechanical compressive and tensile loads. The optical images are recorded using an Allied Vision Alvium 1800 U-500m industrial camera and then post-processed using the DIC algorithm from [8], resulting in images like in **Figure 5** (a). The used camera's resolution is not sufficient to capture single twin bands. Therefore each processed band from the DIC, called **DIC band** in this work, has to be assumed to consist of multiple twin bands. Consequently, we need to derive a model for the DIC bands that captures the behavior of multiple twin bands.

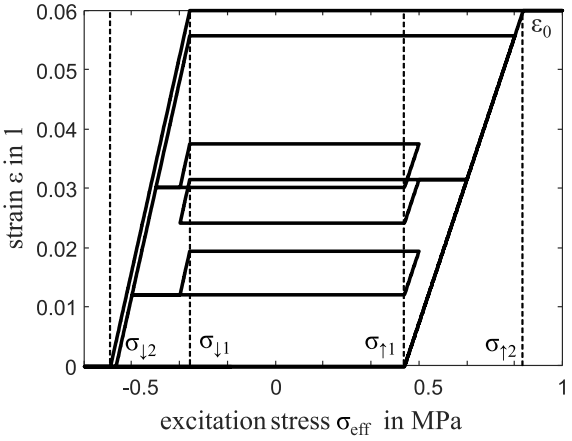

Figure 2 Calculated response of an ideal MSMA element consisting of elementary hysterons according to eq. (1) with asymmetric equal twinning stress distribution $\sigma_{\mathrm{tw}\downarrow}$ between $\sigma_{\downarrow 1}$ and $\sigma_{\downarrow 2}$ and $\sigma_{\mathrm{tw}\uparrow}$ between $\sigma_{\uparrow 1}$ and $\sigma_{\uparrow 2}$, maximum strain ε_0, split up view in **Figure 3**.

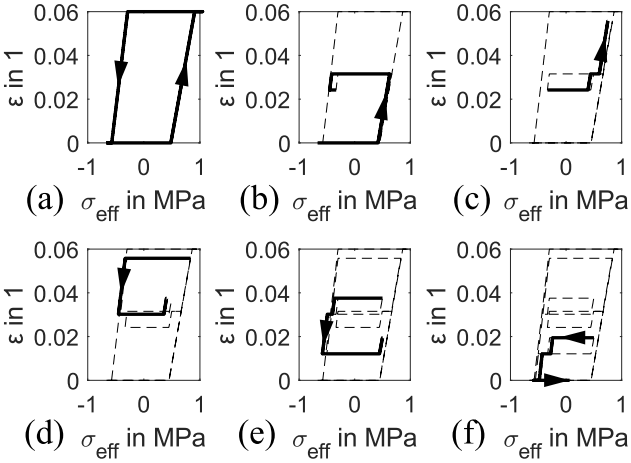

Figure 3 Sequence of intermediate results of the calculated response shown in **Figure 2** with previous path dashed and added sections solid: (a) outer up and down cycle, (b) inner up-down, (c) only up out of the minor loop, (d) inner down-up, (e) further inner down-up, (f) down out of the inner loop.

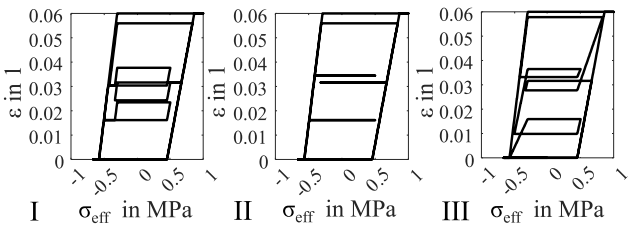

Figure 4 Comparison of the introduced models for the excitation from **Figure 2**: I model with steps yielding the exact same results, II hardening type model without filler inner loops, III model with adapted slopes.

3 Model motivation

Our goal is to introduce a simplified model of each DIC band consisting of multiple twin bands. Following the threshold approach from [3], each twin band needs to be assigned a twinning stress. Preliminary studies showed a difference in the reorientation for compression compared to elongation. It can be observed in experimental results that MSMA samples are easier to compress than to elongate. This tension-compression asymmetry on a macroscopic level has been discussed in [7] and might be caused by the low symmetry of their martensite habit planes with respect to the parent austenite phase. To accommodate for this behavior, a model with separate compressive and tensile twinning stresses $\sigma_{\mathrm{tw}\downarrow}$ and $\sigma_{\mathrm{tw}\uparrow}$ for each twin band is proposed. Each band can be viewed as an elementary hysteron $\hat{\gamma}_{\alpha\beta}[u(t)]$ with $\alpha = \sigma_{\mathrm{tw}\uparrow}$ and $\beta = \sigma_{\mathrm{tw}\downarrow}$ in a Preisach model [9]:

$$f(u(t)) = \iint_{\alpha>\beta} \mu(\alpha,\beta)\hat{\gamma}_{\alpha\beta}[u(t)]\,\mathrm{d}\alpha\,\mathrm{d}\beta. \qquad (1)$$

To illustrate this theoretical behavior, we assume a simple equal distribution of twinning stresses $\sigma_{\mathrm{tw}\uparrow}$ and $\sigma_{\mathrm{tw}\downarrow}$ between a start $\sigma_{\downarrow 1}$ and an end $\sigma_{\downarrow 2}$ as used in hardening type models like [10]. To qualitatively include the asymmetry, we increase the tensile twinning stresses $\sigma_{\mathrm{tw}\uparrow}$ between $\sigma_{\uparrow 1}$ and $\sigma_{\uparrow 2}$ proportionally by 50%.

The resulting calculated global behavior for a complex mechanical excitation showing different outer and inner hysteresis loops is depicted for the full signal in **Figure 2** and split into sections in **Figure 3**. The outer hysteresis loop follows directly the twinning stress distribution. Additionally, it becomes evident, that, independent of the strain history, the movement always starts at $\sigma_{\uparrow 1}$ for increasing excitation and $\sigma_{\downarrow 1}$ for decreasing excitation and the slope between $\sigma_{\uparrow 1}$ and $\sigma_{\uparrow 2}$ and $\sigma_{\downarrow 1}$ and $\sigma_{\downarrow 2}$ respectively remains constant. The reason for this is, that in this model with a fixed factor between the directions, the band with the lowest twinning stress in one direction is also the easiest in the other and can therefore always be switched first, regardless of the load history. For some detailed loops in **Figure 3**, a step can be observed. The first movement only occurs, until the past extremum in that direction has been reached. This complies with the Preisach characteristics being dependent on past extrema, with the wipeout property limiting the number of the important ones to the dominant extrema [11].

4 Hysteresis model of DIC bands

Following the considerations before, we model the outer hysteresis loop of each DIC band number $_i$ as a rhomboid defined by $\sigma_{\uparrow 1,i}$, $\sigma_{\uparrow 2,i}$, $\sigma_{\downarrow 1,i}$, $\sigma_{\downarrow 2,i}$ and $\varepsilon_{0,i}$ as introduced in **Figure 2**. This outer loop is perfect for an equal twinning stress distribution inside the DIC band and a good approximation otherwise. Based on these five parameters for the outer loop, three different models for the strain ε_i including inner loops of each DIC band are set up, depicted in **Figure 4** for the excitation from **Figure 3**. For easier reading, the indizes $_i$ have been omitted from the following equations.

An obvious choice labeled as **model I** is to directly use the Preisach model of equally distributed twin bands according

to eq. (1) as described before, producing steps dependent on the complex load history.

Model II follows the well known hardening models like used in [10], simply holding the output strain of each DIC and constant between the two slopes of the rhomboid. Therefore, it cannot replicate filled inner loops. The following implementation of the modeled output strain ε uses the input stress σ_{eff} and the stored output strain ε_{old} from the last load step. For increasing σ_{eff}, the output strain is $\varepsilon_i(\varepsilon_{\text{old}}, \sigma_{\text{eff}}) = \max(\varepsilon_{\text{old}}, \varepsilon_{\uparrow}(\sigma_{\text{eff}}))$ with

$$\varepsilon_{\uparrow}(\sigma_{\text{eff}}) = \begin{cases} 0 & \text{, for } \sigma_{\text{eff}} \leq \sigma_{\uparrow 1} \\ \varepsilon_0 \frac{\sigma_{\text{eff}} - \sigma_{\uparrow 1}}{\sigma_{\uparrow 2} - \sigma_{\uparrow 1}} & \text{, for } \sigma_{\uparrow 1} < \sigma_{\text{eff}} < \sigma_{\uparrow 2} \\ \varepsilon_0 & \text{, for } \sigma_{\text{eff}} \geq \sigma_{\uparrow 2} \end{cases} . \tag{2}$$

For decreasing σ_{eff}, the strain can be calculated as $\varepsilon_i(\varepsilon_{\text{old}}, \sigma_{\text{eff}}) = \min(\varepsilon_{\text{old}}, \varepsilon_{\downarrow}(\sigma_{\text{eff}}))$ with

$$\varepsilon_{\downarrow}(\sigma_{\text{eff}}) = \begin{cases} 0 & \text{, for } \sigma_{\text{eff}} \leq \sigma_{\downarrow 1} \\ \varepsilon_0 \frac{\sigma_{\text{eff}} - \sigma_{\downarrow 2}}{\sigma_{\downarrow 1} - \sigma_{\downarrow 2}} & \text{, for } \sigma_{\downarrow 2} < \sigma_{\text{eff}} < \sigma_{\downarrow 1} \\ \varepsilon_0 & \text{, for } \sigma_{\text{eff}} \geq \sigma_{\downarrow 1} \end{cases} . \tag{3}$$

In both cases, $\varepsilon_{\text{old}} = \varepsilon$ is stored for the next load step.

An additional investigated **model III** for the DIC bands lies in between the two previous models. The movement starts at $\sigma_{\uparrow 1}$ and $\sigma_{\downarrow 1}$ like the Preisach model but the slope is adapted to always end at $\sigma_{\uparrow 2}$ and $\sigma_{\downarrow 2}$ respectively. For cases with $\sigma_{\uparrow 1} < \sigma_{\downarrow 1}$, this rule would produce a discontinuity on load reversal. To avoid this, a linear interpolation between $\sigma_{\uparrow 1}$ and $\sigma_{\downarrow 1}$ is used for the start of the slope in both directions in those cases. A possible implementation uses the previous minimum and maximum reached strains $\varepsilon_{\min}$ and $\varepsilon_{\max}$, respectively.

For increasing excitation σ_{eff}, the output strain is

$$\varepsilon_i(\sigma_{\text{eff}}, \varepsilon_{\min}) = \begin{cases} \varepsilon_{\min} & \text{, for } \sigma_{\text{eff}} \leq \sigma_{\uparrow 1} \\ \varepsilon_{\min} + (\varepsilon_0 - \varepsilon_{\min}) \frac{\sigma_{\text{eff}} - \sigma_{\uparrow 1}}{\sigma_{\uparrow 2} - \sigma_{\uparrow 1}} & \text{, for } \sigma_{\uparrow 1} < \sigma_{\text{eff}} < \sigma_{\uparrow 2} \\ \varepsilon_0 & \text{, for } \sigma_{\text{eff}} \geq \sigma_{\uparrow 2} \end{cases} , \tag{4}$$

with the unchanged $\varepsilon_{\min}$ and a new $\varepsilon_{\max} = \varepsilon(\sigma_{\text{eff}}, \varepsilon_{\min})$ stored for the next load step. For decreasing σ_{eff}, the strain can be modeled by

$$\varepsilon_i(\sigma_{\text{eff}}, \varepsilon_{\max}) = \begin{cases} 0 & \text{, for } \sigma_{\text{eff}} \leq \sigma_{\downarrow 2} \\ \varepsilon_{\max} \frac{\sigma_{\text{eff}} - \sigma_{\downarrow 2}}{\sigma_{\downarrow 1} - \sigma_{\downarrow 2}} & \text{, for } \sigma_{\downarrow 2} < \sigma_{\text{eff}} < \sigma_{\downarrow 1} \\ \varepsilon_{\max} & \text{, for } \sigma_{\text{eff}} \geq \sigma_{\downarrow 1} \end{cases} , \tag{5}$$

with a new $\varepsilon_{\min} = \varepsilon(\sigma_{\text{eff}}, \varepsilon_{\max})$ and the unchanged $\varepsilon_{\max}$ stored for the next load step.

As mentioned before, bands with $\sigma_{\uparrow 1} < \sigma_{\downarrow 1}$ have to be adjusted. Instead of $\sigma_{\uparrow 1}$ and $\sigma_{\downarrow 1}$, $\sigma'_{\uparrow 1}$ and $\sigma'_{\downarrow 1}$ have to be used in eq. (4) and eq. (5) according to

$$\sigma'_{\uparrow 1} = \frac{\varepsilon_{\min}}{\varepsilon_0} (\sigma_{\downarrow 1} - \sigma_{\uparrow 1}) \tag{6}$$

$$\sigma'_{\downarrow 1} = \frac{\varepsilon_{\max}}{\varepsilon_0} (\sigma_{\downarrow 1} - \sigma_{\uparrow 1}). \tag{7}$$

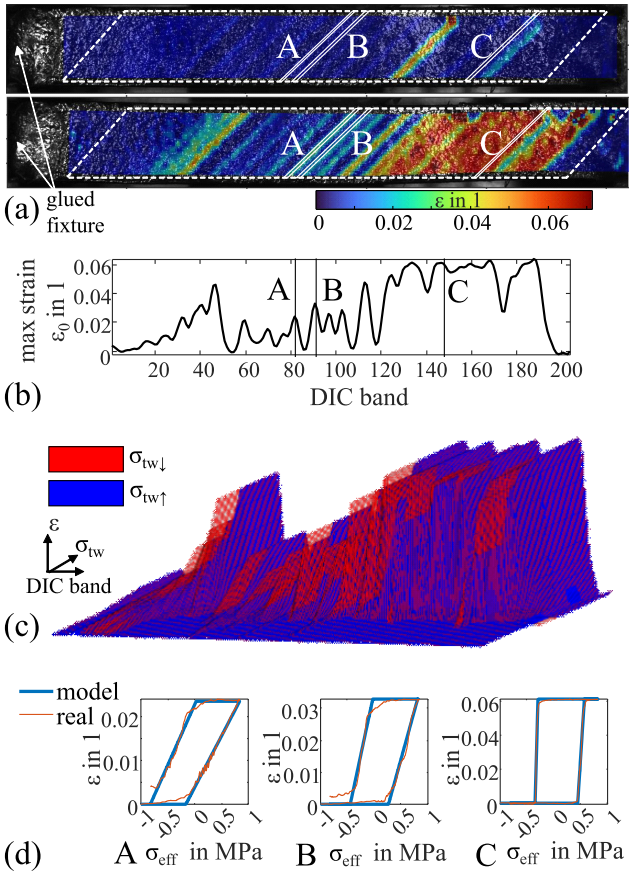

Figure 5 (a) DIC images of MSMA element at low and high tensile stress with corresponding color-coded strain, red domains are elongated and have a vertical shorter lattice axis, blue domains indicate a horizontal shorter axis, highlighted bands A, B and C, (b) identified maximum strain ε_0 over the length of the element separated in 200 bands, (c) 3D visualization of the limiting surfaces of the identified hysteresis for all bands with the twinning stress in depth direction, (d) experimental strain ε of the outer hysteresis loop identified via DIC and model for the highlighted bands A, B and C.

To model the behavior of the entire MSMA element, all the $N = 200$ individual DIC bands have to be summed up

$$\bar{\varepsilon} = \frac{1}{N} \sum_{i=1}^{N} \varepsilon_i \tag{8}$$

5 Identification

Each model uses the same five parameters for each DIC band. They are identified from the optically investigated strain of only one outer hysteresis loop excitation with the tensile stress limited by the glued fixture. **Figure 5** (a) depicts two exemplary images of the identified color-coded axial strain ε, limited to the range $(0, 0.07)$, at low and high tensile stress. The full sample's overall elongation between the two states becomes apparent on the right, while it is fixed on the left. The left area is not part of the identification, because the glued fixture affects the lighting and cannot elongate anyway. The 2D strain is averaged inside

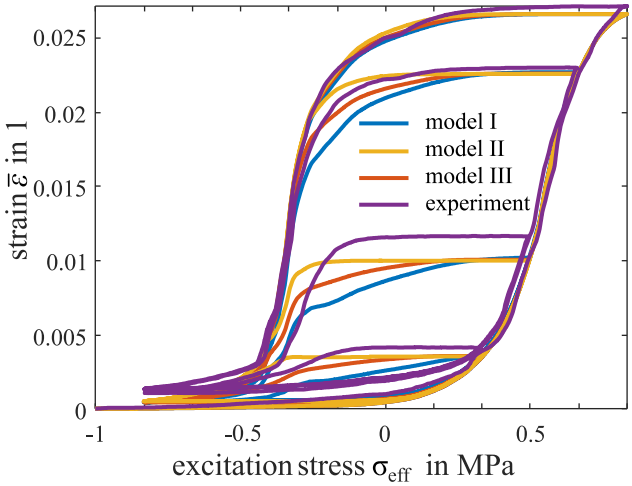

Figure 6 Calculated and experimental results for the movement of the entire MSMA element consisting of the 200 DIC bands, all using the same color legend: model I with steps, model II hardening type, model III with adapted slopes, experimental results.

of 200 predefined diagonal bands to generate 200 concentrated values for each captured load step. For the highlighted bands A, B and C, **Figure 5** (d) shows this experimental strain identified via DIC and the corresponding fitted model and **Figure 5** (b) depicts the fitted maximum strain ε_0 for all bands. **Figure 5** (c) visualizes the limiting surfaces of the hysteresis based on the rhomboid shape from the five parameters for each band. It can be seen in **Figure 5** (c) and (d), that the outer hysteresis curve of some bands like A has a rather shallow slope in both directions, indicating the averaging over multiple twin bands, while bands like C are really steep, getting close to the ideal hysteron shape of a single twin band.

6 Validation

For experimental validation, three additional inner loops were recorded and post-processed in the same way as the identification signal to obtain time series data for all 200 bands. **Figure 7** depicts the results for the bands A, B and C according to **Figure 5** (a) with the strain identified from the experiment IV compared to the strain calculated from the three models I-III for the same excitation. **Figure 7** (a) shows the MSMA strain under mechanical excitation for a band exhibiting a shallower slope with $\sigma_{\uparrow 1} < \sigma_{\downarrow 1}$, the special case in model III, **Figure 7** (b) is still shallow, but features $\sigma_{\uparrow 1} > \sigma_{\downarrow 1}$, and **Figure 7** (c) exhibits a an almost step-wise twinning stress distribution. For shallower gradients the differences are more apparent, while for steeper gradients the models converge.

Figure 6 shows the strain for the entire element summarized over all bands. In the steep areas, a slight model deviation in stress has an big impact on the strain after load reversal, exaggerating the difference between model and experiment. It becomes apparent from both the total and the individual strains, that model I with the steps has the largest deviations from the experimental results, model II

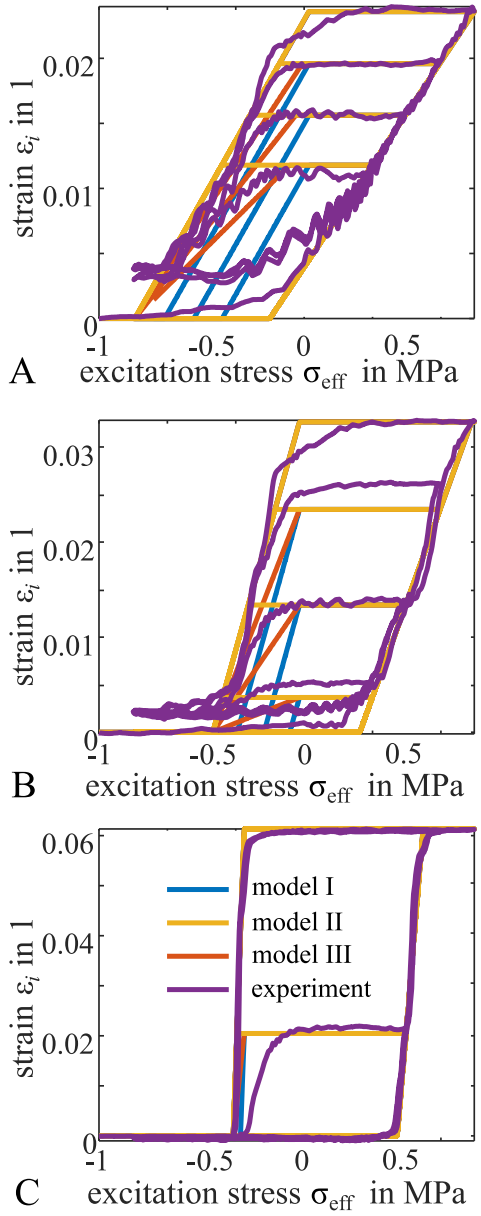

Figure 7 Calculated and experimental results for the three DIC bands A, B and C according to **Figure 5**, all using the same color legend: model I with steps, model II hardening type, model III with adapted slopes, experimental results.

retains a constant output for too long after load reversal, while model III with the adapted slopes yields the best compromise, although it lacks an obvious microstructural foundation.

7 Conclusion

In this work, we presented a framework to identify localized hysteresis parameters from optical images of an MSMA sample with limited resolution processed using DIC. Three differently defined models for the inner hysteresis using the same parameter set were compared with experimental results. For the investigated excitation, the model with adapted slopes matches the experimental re-

sults best. More experiments with different excitations including more complex inner loops and MSMA elements are required to further assess and refine the approach. It has to be noted, that the model does not account for the interaction of neighboring bands, e. g. due to transverse contraction. This means additionally, that the approach is currently only suitable for fine twinned samples while coarse twins might be possible to be simulated with the suggested integration interactions. To truly investigate the individual twin bands, a higher resolution is required.

8 Acknowledgements

We would like to thank M. Laufenberg of ETO MAGNETIC GmbH for providing samples.

9 Literature

[1] E. Pagounis, R. Chulist, M. J. Szczerba, and M. Laufenberg. Over 7% magnetic field-induced strain in a Ni-Mn-Ga five-layered martensite. *Applied Physics Letters*, 105(5):052405, August 2014. ISSN 0003-6951. URL https://doi.org/10.1063/1.4892633.

[2] R. C. O'Handley. Model for strain and magnetization in magnetic shape-memory alloys. *Journal of Applied Physics*, 83(6):3263–3270, March 1998. ISSN 0021-8979. URL https://doi.org/10.1063/1.367094.

[3] A. A. Likhachev and K. Ullakko. Magnetic-field-controlled twin boundaries motion and giant magneto-mechanical effects in Ni–Mn–Ga shape memory alloy. *Physics Letters A*, 275 (1):142–151, October 2000. ISSN 0375-9601. doi: 10.1016/S0375-9601(00)00561-2. URL https://www.sciencedirect.com/science/article/pii/S0375960100005612.

[4] R. Courant and J. Maas. Fully coupled multiphysics simulation model of magnetic shape memory actuators. In *ACTUATOR 2021; International Conference and Exhibition on New Actuator Systems and Applications*, pages 1–4, February 2021. URL https://ieeexplore.ieee.org/document/9400583.

[5] R. Courant and J. Maas. Fully coupled simulation of magnetic shape memory alloys under elongating and contracting perpendicular magnetic fields. In *ACTUATOR 2022; International Conference and Exhibition on New Actuator Systems and Applications*, pages 1–4, June 2022. URL https://ieeexplore.ieee.org/abstract/document/9899232.

[6] F. Ehle, P. Neumeister, E. Haufe, and H. Neubert. Magnetic characterization of ferromagnetic shape memory components under defined mechanical loading. *Shape Memory and Superelasticity*, 6(1):10–23, January 2020. ISSN 2199-3858. doi: 10.1007/s40830-020-00266-2. URL https://link.springer.com/article/10.1007/s40830-020-00266-2.

[7] G. J. D'Silva, H. Feigenbaum, and C. Ciocanel. Strain Field in Ni2MnGa Magnetic Shape Memory Alloys with Different Twin Densities under Combined Tensile and Magnetic Loading. *Smart Materials and Structures*, 2023. ISSN 0964-1726. doi: 10.1088/1361-665X/acfd6f. URL http://iopscience.iop.org/article/10.1088/1361-665X/acfd6f.

[8] J. Yang and K. Bhattacharya. Augmented Lagrangian Digital Image Correlation. *Experimental Mechanics*, 59(2):187–205, February 2019. ISSN 1741-2765. URL https://doi.org/10.1007/s11340-018-00457-0.

[9] R. Courant and J. Maas. Bridging the scales between twin level and component level models of magnetic shape memory alloys. In *ASME 2022 Conference on Smart Materials, Adaptive Structures and Intelligent Systems*. American Society of Mechanical Engineers, sep 2022. URL https://doi.org/10.1115/smasis2022-91681.

[10] B. Kiefer and D.C. Lagoudas. Modeling the Coupled Strain and Magnetization Response of Magnetic Shape Memory Alloys under Magnetomechanical Loading. *Journal of Intelligent Material Systems and Structures*, 20(2):143–170, January 2009. ISSN 1045-389X. URL https://doi.org/10.1177/1045389X07086688.

[11] I. D. Mayergoyz. *The Classical Preisach Model of Hysteresis*. Springer New York, 1991. ISBN 9781461230281. URL https://link.springer.com/book/10.1007/978-1-4612-3028-1.

Actuation properties of a magnetic shape memory element prepared by laser ablation

Andrey Saren, Aditya Kumthekar, Ville Laitinen, Kari Ullakko
Material Physics Laboratory, Lappeenranta-Lahti University of Technology LUT, Lappeenranta 53850, Finland
E-mail address: andrey.saren@lut.fi

Abstract

We used laser ablation (LA) technique to prepare an actuating element from a single crystal of 10M $Ni_{50}Mn_{28}Ga_{22}$ magnetic shape memory (MSM) alloy, and characterized its structural, magnetic and mechanical properties at ambient temperature. The LA cutting stabilized a fine twin structure with type 1 twins and a twin bilayer width of 25 µm on average. The measurements revealed a magnetic-field-induced strain of 4.5% and a magnetostress of 2.7 MPa in saturating fields. The sample exhibited a twinning stress of 1.02 MPa which was 7% more when compared to an electropolished LA-untreated crystal with fine twins of type 1. We attribute the slight increase of the twinning stress and a moderate increase of the stress-strain loop slope to surface defects generated by LA-cutting. In high-rate pulsed magnetic actuation, the sample demonstrated peak actuation velocities of about 4 m/s in both contraction and elongation modes. Our results demonstrate LA as a promising method for manufacturing actuating elements from MSM alloys, without the need for additional post-processing.

1 Introduction

Magnetic shape memory (MSM) Ni-Mn-Ga-based alloys are promising actuating materials due to the unique combination of a large strain 6-12% [1,2] and fast response to magnetic field [3]. In these compounds, the magnetically actuated shape change, which is called the MSM effect, is related to the motion of twin boundaries (TBs) connecting differently oriented twin variants.

In MSM-based applications, the control of TBs is important. First, TBs should be present in the MSM material, as new TBs generation is not possible by a magnetic field alone. Next, TBs may disappear when full reorientation of the crystal lattice occurs. Several methods are known for stabilizing type 1 TBs via different surface treatments, *e.g.*, by surface damage using abrasive particles [4], coating with hard TiN and soft elastomer [5], ion implantation by Nb ions [5], diamond-like carbon coating [6], and shot peening [7]. Fatigue life can be remarkably improved by creation of surface defects, which may stabilize a dense twinned microstructure [4,7]. Surface damage, however, increases twinning stress (TS) and decreases magnetic-field-induced strain (MFIS) [4].

Recently, laser ablation (LA) was used for fabricating a microdevice prototype from a single crystal of 10M Ni-Mn-Ga [8]. Unlike the commonly used cutting methods, such as spark eroding or wire cutting, which usually require additional surface treatments to reduce surface stresses introduced during cutting, LA can be applied without post-processing treatments when approaching the so-called 'cold ablation' regime. In addition, LA allows to create complex geometries and provides faster cutting.

In the present research, we characterized the structure and magneto-mechanical properties of an actuating element, cut from a single crystal of 10M Ni-Mn-Ga alloy using LA technique.

2 Experimental

2.1 Alloy characterization

The target sample was machined from a single crystalline bar (with 20×2.4×0.9 mm^3 dimensions) of 10M $Ni_{50}Mn_{28}Ga_{22}$ alloy (AdapatMat Ltd.), with the following lattice parameters in the cubic coordinates of the parent austenite: a=5.981, b=5.943, c=5.605±0.002 Å, and γ=90.38±0.01° (x-ray diffraction was performed using PANalytical Empyrean diffractometer with Cu tube, λ = 0.15406 nm, at ambient temperature). Maximum transformation strain, calculated from the lattice parameters, is 6 %. The martensitic phase transformation temperatures, T_A and T_M, and the Curie temperature, T_C, were determined as follows: T_A=332, T_M=323, and T_C=373±1 K. Magnetization curves for easy and hard directions were measured at 298 K, from which saturation magnetization and anisotropy field yielded 0.67 T and 530 kA/m, respectively. Using these values, the anisotropy energy, K_U, was estimated at 180 kJ/m^3, and the maximum magnetic-field-induced stress, $\sigma_{mag}=K_U/(1-c/a)$, at 2.9 MPa.

2.2 Laser ablation

Prior to LA-cutting, the initial Ni-Mn-Ga bar was electropolished. A femtosecond pulsed width laser micromachining setup described in [8,9], based on the Satsuma HP laser (Amplitude Systems), was used to machine the target sample. The laser produced a near-Gaussian beam with a 1030 nm wavelength, converted to a 515 nm wavelength by a second-harmonic generation module. During cutting, the sample was heated above T_C. To achieve a deep cutting of 0.9 mm and sufficiently high surface quality in terms of surface roughness and geometrical accuracy, a four-layer scanning strategy and optimized process parameters were applied based on the studies presented in [8,9], with the

following parameters: a hatch distance of 0.01 mm, a power of 3.6 W, a pulse width of 400 fs, a scanning speed of 500 mm/s, and a repetition rate of 71 kHz. The machining was performed until the target sample was completely cut away from the initial bar. To remove residual powder contaminants, the sample was cleaned in an ultrasonic acetone bath for 15 min at ambient temperature.

2.3 Stress-strain, magnetostress and high-rate magnetic actuation measurements

A homemade stress-strain setup, described in [10], was used to measure stress-strain loops of the LA-cut sample and an untreated crystal. In magnetostress measurements, a custom-made electromagnet was used in a pulsed mode during straining, with precautions to avoid the magnetic field influence on the stress measurements, see [10]. In high-rate pulsed magnetic actuation experiments, a laser Doppler vibrometer (LDV) based setup was used, which is described in [11]. Magnetic field pulses of different amplitudes and a duration of 150 µs were applied to the sample, causing it to contract or elongate.

3 Results

3.1 The geometry and surface of the sample

The LA-cut sample had a shape close to prismatic with a length of 6 mm and a height of 0.85 mm on average, see **Figure 1a**. The width of the top and bottom faces (non-treated by LA) was 0.66 and 1.2 mm, respectively. The cross-section was close to trapezoid with an area of 0.8 mm^2. The difference in the top and bottom widths and sidewall angles of about 10-17° are a result of laser ablation process when used for a deep cutting [8], due to the Gaussian profile of the laser beam which is intense at the center and weaker at the circumference. This effect is also amplified by the decrease of reflectivity due to the incidence angle variation on the sidewall leading to lower efficiency for material removal on the walls.

Above mentioned phenomena are also the reasons for generation of brush like structures at the sidewalls. It was shown in [8] that after a certain number of passes, cone-shaped microstructures developed on the side walls of the LA-treated material. Although most of the cones were removed from the machining area after additional passes, some conical structures near the sidewall of the specimen remained and this caused a brush like edge at the bottom.

At ambient temperature the LA-cut sample exhibited a fine two-variant laminated structure consisting of type 1 twins, in which the variants differed in the orientation of the easy *c*-axis (**Figure 1b**). The twin bilayer width was 25 µm on average.

3.2 MFIS in a static field

To evaluate the MFIS value, a static magnetic field of 0.8 T was applied to the sample in two different directions: along the largest dimension and perpendicular to the top and bottom facets. The maximum MFIS value, measured from the sample's length variation, was 4.5 %.

Figure 1c shows redistribution of twin variants on the bottom facet caused by field application in two perpendicular directions. A local MFIS, calculated from the fractions occupied by the differently oriented variants and averaged over a width of about ten twin bilayers, reached 5 % [10].

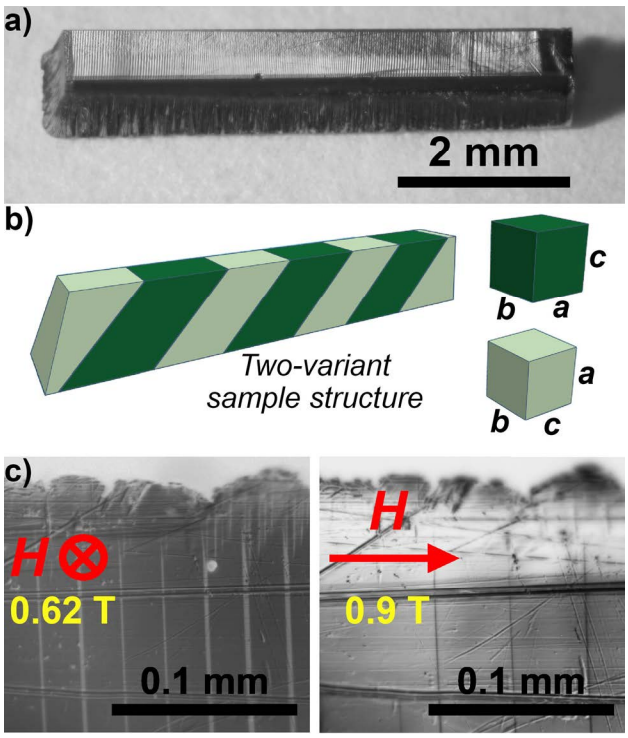

Figure 1 (a) Photo image of the LA-cut sample. (b) A schematic of the laminated two-variant sample structure. (c) Optical micrographs with DIC contrast showing redistribution of twin variants caused by a static magnetic field application across (left image) and along (right image) the sample. Darker stripes correspond to the dark green variant in (b).

3.3 Stress-strain loops and magnetostress

A set of stress-strain loops measured for LA-cut sample at different strain amplitudes are presented in **Figure 2a**. The measurements revealed a TS of 1.02 MPa (calculated as half the height of the stress-strain loop at half the maximum strain) and an average loop slope of 0.46 MPa/%. For a comparison, in the untreated crystal with polysynthetic type 1 twins created by bending, the TS value was 0.95 MPa and the slope was 0.3 MPa/%, see **Figure 2b**. The force spikes visible in the latter curve correspond to TBs jumps and TB annihilation events.

The LA-cut sample exhibited a magnetostress of 2.7±0.1 MPa when placed in a perpendicular magnetic field of 0.82 T during straining. When compared to the theoretical σ_{mag} of 2.9 MPa, this value is 7 % lower, which is most likely due to a deviation of the sample axis and the magnet axis from [100] and [001] crystallographic directions, respectively [10].

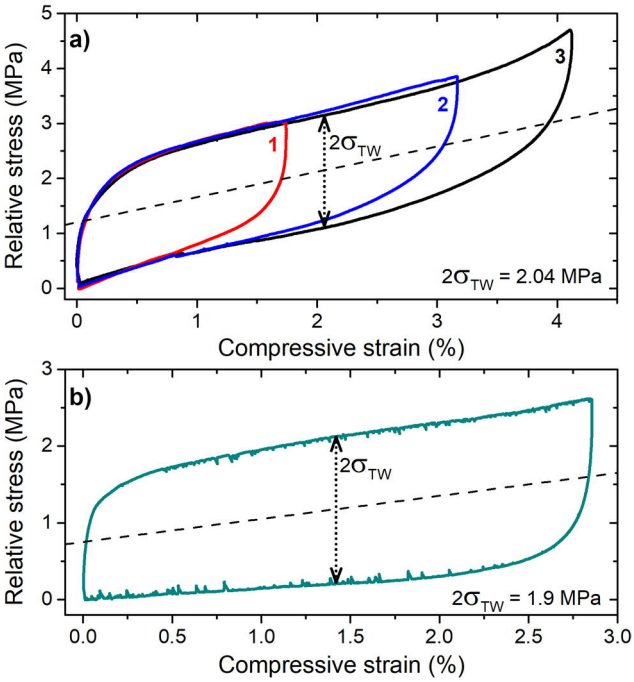

Figure 2 (a) Stress-strain loops measured for the LA-cut sample at different strain amplitudes. The strain was calculated for the unconstrained, 4 mm in length, part of the sample. The dashed line indicates an average loop slope of 0.46 MPa/%. (b) Stress-strain loops measured for LA-untreated crystal of 14 mm in length with polysynthetic fine twins of type 1 created by bending. The dashed line indicates an average loop slope of 0.3 MPa/%.

3.4 High-rate pulsed magnetic actuation

In the high-rate actuation experiments, a Helmholtz coil was used to generate magnetic field applied along or perpendicular to the sample causing it to contract or elongate, respectively. The initial state of the sample was set, correspondingly, to the elongated or contracted one by applying a 0.8 T static magnetic field. The sample was glued to a rigid support on one end, and LDV registered the sample's actuation velocity by directly measuring the velocity of its free end during the field pulse application. The results of these experiments are presented in **Figure 3**. Under saturating fields, actuation velocity can reach 4 m/s. Actuation acceleration at the beginning of the field pulse, calculated from the velocity data, reached values of 4.7×10^5 and 2×10^5 m/s^2 in contraction and elongation modes, respectively.

4 Discussion

The presented data shows that LA stabilized fine type 1 twins in the studied sample. Presumably, the surface defects, originated from the LA process, act as pinning points for TBs, similarly to other surface treatments. The stabilized TB pattern allows for repeatable smooth actuation visible in stress-strain characteristics whereas non-stabilized TBs in the untreated crystal exhibit jumps and finally annihilate.

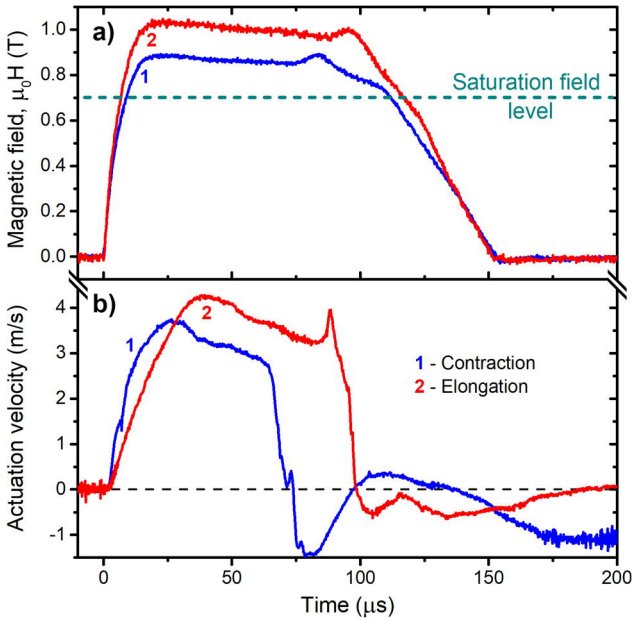

Figure 3 High-rate actuation of the LA-cut sample by a pulsed magnetic field. (a) Applied magnetic field pulses in contraction (curve 1) and elongation (curve 2) modes. (b) Temporal dependencies of actuation velocity in contraction and elongation modes.

However, surface damage decreases TB mobility and MFIS, and, finally, the energy efficacy. Importantly, the TBs stabilization by LA had moderate effects on MSM performance: the MFIS was decreased to 4.5 %, and the TS was increased only by 7 %. The TS value and the stress-strain loop slope have the largest influence on the energy transfer efficacy during magnetic actuation. **Table 1** summarizes the accessible literature data and the present results concerning the TS, the slope, and the MFIS in 10M Ni-Mn-Ga samples with stabilized fine type 1 twin structures. It is seen that LA cutting provides the lowest TS increase, when compared to the untreated crystal, while maintaining a large MFIS and a moderate slope.

In the high-rate magnetic actuation experiments, the LA-cut sample exhibited peak contraction and elongation velocities of about 4 m/s at saturating fields, and accelerations of $(2\text{-}4.7)\times10^5$ m/s^2. These values are significantly larger when compared to single type 1 TB motion in 10M martensite of Ni-Mn-Ga [12,13]. *E.g.*, actuation velocity values of 4 m/s are about 15 times larger when compared to a single type 1 TB motion. In addition, according to [13], for type 1 TBs, TS has a strong dependence on the TB velocity, limiting the TB velocity below 5 m/s, and correspondent actuation velocity below 0.3 m/s. The large actuation velocity values observed in LA-cut sample are due to the collective motion of numerous TBs. Indeed, taking into account the bilayer width of 25 µm, one can estimate the number of TBs in the sample to be more than 400.

Roughly, to produce 4 m/s actuation velocity, the velocity of an individual TB, V_{TB}, can be estimated as follows: $V_{TB} \approx 4\ m/s\ /\ 400\ /\ (1\text{-}c/a) = 0.17\ m/s$. This value is more than an order smaller than the maximum TB velocities reported in [12,13]. Thus, the energy efficiency remains high even at high actuation rates thanks to numerous twins stabilized by LA.

Table 1 Comparison of the stress-strain loop parameters and MFIS for stabilized fine type 1 twin structures by different surface treatments in 10M Ni-Mn-Ga

Source	Surface treatment	Average twin width, µm	TS of the treated / untreated sample, MPa	Slope of the stress-strain curve, MPa/%	MFIS, %
[5]	Coating with hard TiN	15	– / 1.2	–	1
[5]	Nb^+ ions implantation	40	1.5 / 0.7	0.37	4.5
[6]	Diamond-like coating	13	0.55 / 0.37	0.53	4
[7]	Shot peening with 100 µm SiO_2	–	– / –	–	5
Present work	Laser ablation	25	1.02 / 0.95	0.46	4.5

5 Conclusion

In conclusion, the present research demonstrates laser ablation as a promising method for manufacturing actuating elements from MSM alloys without the need for additional post-processing. LA-generated surface defects stabilize a fine twin structure with type 1 TBs, while having a moderate effect on the TBs mobility.

6 Acknowledgements

This work was supported by the Strategic Research Council of Finland (grant number 313349), the Research Council of Finland (grant numbers 325910 and 349579) and the AMBI (Analytics based Management for Business and Manufacturing Industry) research platform of Lappeenranta-Lahti University of Technology LUT.

7 Literature

[1] Murray, S.: Marioni, M.: Allen, S.: O'Handley, R.: Lograsso, T.: 6% magnetic-field induced strain by twin-boundary motion in ferromagnetic Ni–Mn–Ga. Appl. Phys. Lett. 77 (2000) 886–888

[2] Sozinov, A.: Lanska, N.: Soroka, A.: Zou, W.: 12% magnetic field-induced strain in Ni-Mn-Ga-based non-modulated martensite. Appl. Phys. Lett. 102 (2013) 021902

[3] Saren, A.: Nicholls, T.: Tellinen, J.: Ullakko K.: Direct observation of fast-moving twin boundaries in magnetic shape memory alloy Ni-Mn-Ga 5M martensite. Scripta Mat. 123 (2016) 9–12

[4] Chmielus, M.: Witherspoon, C.: Ullakko, K.: Müllner, P.: Schneider, R.: Effects of surface damage on twinning stress and the stability of twin microstructures of magnetic shape memory alloys. Acta Mat. 59 (2011) 2948–2956

[5] Ullakko, K.: Chmielus, M.: Müllner, P.: Stabilizing a fine twin structure in Ni–Mn–Ga samples by coatings and ion implantation. Scripta Mat. 94 (2015) 40–43

[6] Musiienko, D.: Smith, A.R.: Saren, A.: Ullakko, K.: Stabilization of a fine twin structure in Ni–Mn–Ga by a diamond-like carbon coating. Scripta Mat. 106 (2015) 9–12

[7] Zhang, H.: Armstrong, A.: Müllner, P.: Effects of surface modifications on the fatigue life of unconstrained Ni-Mn-Ga single crystals in a rotating magnetic field. Acta Mat. 155 (2018) 175-186

[8] Kumthekar, A.: Laitinen, V.: Ullakko, K.: Effects of machining parameters on Ni-Mn-Ga-based alloys for fabrication of multifunctional micro devices using femtosecond pulse width laser. IOP Conf. Ser.: Mater. Sci. Eng. 1296 (2023) 012040

[9] Kumthekar, A.: Laitinen, V.: Namvari, M.: Ullakko, K.: Micromachining of functional Ni-Mn-Ga single crystals using femtosecond pulsed laser. CIRP J. Manuf. Sci. Technol. 49 (2024) 56–61

[10] Saren, A.: Kumthekar, A.: Laitinen, V.: Ullakko, K.: Characterization of a magnetic shape memory actuating element manufactured by laser ablation. Scripta Mat. 244 (2024) 116006

[11] Saren, A.: Laitinen, V.: Vinogradova, M.: Ullakko, K.: Twin boundary mobility in additive manufactured magnetic shape memory alloy 10M Ni-Mn-Ga. Acta Mat. 246 (2023) 118666

[12] Saren, A.: Musiienko, D.: Smith, A.R.: Ullakko, K.: Pulsed magnetic field-induced single twin boundary motion in Ni–Mn–Ga 5M martensite: a laser vibrometry characterization. Scripta Mat. 113 (2016) 154–157

[13] Saren, A.: Ullakko, K.: Dynamic twinning stress and viscous-like damping of twin boundary motion in magnetic shape memory alloy Ni-Mn-Ga. Scripta Mat. 139 (2017) 126–129

Optimization and Investigation of Radial-flux Permanent Magnet Micromotor Utilizing MEMS 3D Solenoid Coils with Iron Core

Kaibo Lei, Haiwang Li, Tiantong Xu*, Yuying Wu, Kaiyun Zhu and Yanxin Zhai
Beihang University, Beijing 100191, China

Abstract

This paper optimizes the radial-flux permanent magnet micromotor used in high power-density micro-actuators. There are some urgent problems found in actual manufacturing of the micromotor. Therefore, we analyze the problems and optimize the design of the micromotor. Then we calculate and simulate the optimized micromotor. For the optimized micromotor, we show the manufacturing advantages of easier processing and application, and we show the better performance. The diameter of the micromotor is 20 mm, and the height is 2mm. The operating temperature reaches 88 °C. The iron core magnetic density is close to the saturation of 1.8 T, which reflects the high iron core utilization rate. The optimized micromotor increases the rated torque of 174.6% and the total efficiency of 44.3%.

1 Introduction

Electromagnetic (EM) micromotors with permanent magnets (PMs) have attracted considerable attention owing to their application potential as high power-density micro-actuators to actuate micro pumps, micro propellers and micro manipulators [1]. In the field of micromanufacturing, in order to pursue simple structure and convenient processing, most permanent magnet micromotors use planar coils [2,3]. At present, the magnetic circuit design of the developed permanent magnet micromotor usually chooses the axial magnetic circuit [4]. Under this layout, the permanent magnet can only be on the upper or lower side of the planar coil, which is conducive to the processing of the permanent magnet and ensures high speed [5]. However, iron cores of planar coils are placed outside the coils, which is not conducive to reducing the magnetic leakage and increasing the inductance density. To solve these problems, we extended research on three-dimensional (3D) solenoid coils with iron core fabricated by micro electro-mechanical system (MEMS) processes, and we applied the 3D coils to PM micromotors in a previous study [6] (called the prototype micromotor). However, there are some urgent problems found in actual manufacturing. To improve application possibility and electromagnetic performance, we optimize and investigate the prototype micromotor in this paper.

2 Design

Owing to the frontier and complexity of the micromanufacture process, the prototype micromotor was very easy to be damaged during the manufacturing and testing process, which in turn affects the stability and accuracy of the test. Therefore, we optimize the micromotor from three aspects: process, structure and simulation design.

In terms of the process, the most prominent problems are as follows: The first is the shape. The shape of the prototype micromotor is hexagonal, which will be damaged due to stress concentration during processing, thus damaging the entire silicon substrate coil. Especially for the key process of surface flattening, when chemical mechanical polishing (CMP) is used to realize the flattening, the corners of the micromotor will be affected by a large impact force, so that the whole micromotor will be broken. Secondly, it is the electrical connection problem of the micromotor. The prototype micromotor has more pins, and each group of coils has import pins and export pins. Therefore, the lead is complex, and it is easy to damage the micromotor when welding. After repeated testing, the lead will continue to shake, the weld will become very loose, resulting in the instability of the power.

The optimized micromotor is shown (**Figure 1**). To avoid stress concentration and improve success rate of the process, we changed the hexagonal shape of the micromotor to the circular shape, which reduced the possibility of breakage during thinning or bumping. To solve the problem of electrical connection of the micromotor in practical application, we integrated the neutral point and the electrical connection between each set of coils into the MEMS fabrication of coils. For the stability of the electric connection, the pin size was enlarged, which did not increase the size of the micromotor.

In terms of the structure, the prototype micromotor has 15 turns in each coil, and the distance between the center and the side of the hexagon in the axial view is 9.65 mm, and the total area is 322.6 mm^2. The optimized micromotor further staggers the holes of the coil in the width direction, which reduces the diameter of the vertical wire from 100 μm to 90 μm. Under the condition that the distance between the holes and the holes is essentially unchanged, realizing a number of 20 turns per coil with a radius of 9 mm and a total area of 254.3 mm^2. Its structure is more compact and can enhance the power density of the motor. The change of coils is shown (**Figure 2**).

In terms of the simulation design, the prototype micromotor only adopts the electromagnetic design-based method of the conventional motor, and ignores the heat transfer design. The optimized micromotor was designed by combining the electromagnetic theoretical design, electromagnetic simulation, and electromagnetic-thermal coupling analysis, design, and optimization. Firstly, the structural parameters

of the stator and the primary structural parameters of the rotor are determined by electromagnetic theoretical calculation. Secondly, the preliminary static strength simulation and heat transfer simulation were carried out, and the overall working temperature of the micromotor was determined to be 86 ℃, the winding temperature was slightly higher to 88.71 ℃, and the total heating power in the micromotor was 2.83 W. Thirdly, electromagnetic simulation and optimization were performed to determine the final structural parameters of the rotor. Based on this, electromagnetic thermal coupling simulations can be carried out. Fourthly, taking 88.71 ℃ as the reference temperature of copper resistivity, the calculated resistivity is 2.131×10^{-8} Ω·m, which is set as the resistivity of the winding in the electromagnetic simulation. The electromagnetic simulation is carried out, and the average copper loss power of the winding and the iron core iron loss power are obtained. Fifthly, the average copper loss power of the winding, the iron loss power of the iron core considering stray loss and the iron loss power of the permanent magnet are set as the uniform heat sources respectively as the internal heat sources of the winding, the iron core and the permanent magnet in the heat transfer simulation. The steady-state heat transfer simulation is carried out to obtain the temperature field of the whole machine. Sixth, the obtained temperature field is compared with the previous temperature distribution. If the error is large, the input voltage of the external circuit of the electromagnetic simulation is modified, and the above process is repeated until the temperature field distribution error is acceptable, so as to obtain the performance of the optimized micromotor.

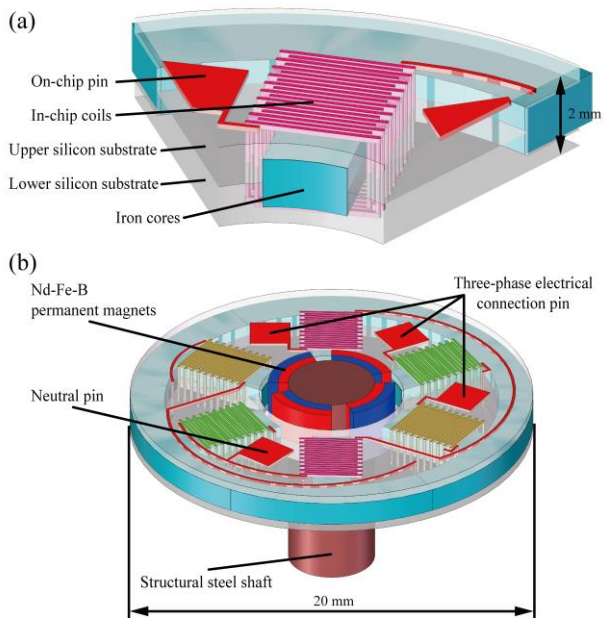

Figure 1 (a) Details of one group of 3D iron-core MEMS silicon-embedded coils, and the thickness is 2mm. (b) The overall structure of the optimized micromotor, which contains a six-slot stator made of single-crystal silicon substrates and a four-pole rotor.

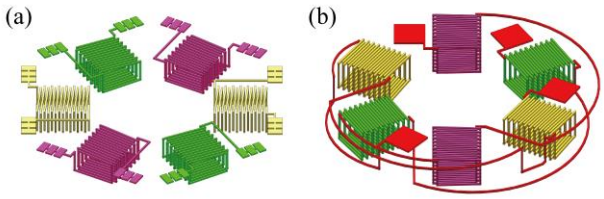

Figure 2 Change the coils from (a) to (b).

3 Results

After several iterations of simulation optimization, when the average current in a state angle is 1.23 A (ignoring the current fluctuation caused by commutation), the power obtained by electromagnetic simulation is processed and input into heat transfer simulation as the internal heat source condition, and the temperature field error is the smallest. As is shown (**Figure 3**). The average temperature of the winding is 88.43 ℃ (originally calculated as 88.71 ℃, error 0.08%). The average temperature of winding and silicon substrate is 88.42 ℃ (originally calculated as 88.70 ℃, error 0.08%). The average temperature of core is 84.92℃ (originally calculated as 86.68℃, error 0.5%). In addition to the temperature field error, the error of the winding resistivity is very small (the error of the resistivity between 88.43℃ and 88.71℃ is 0.7%).

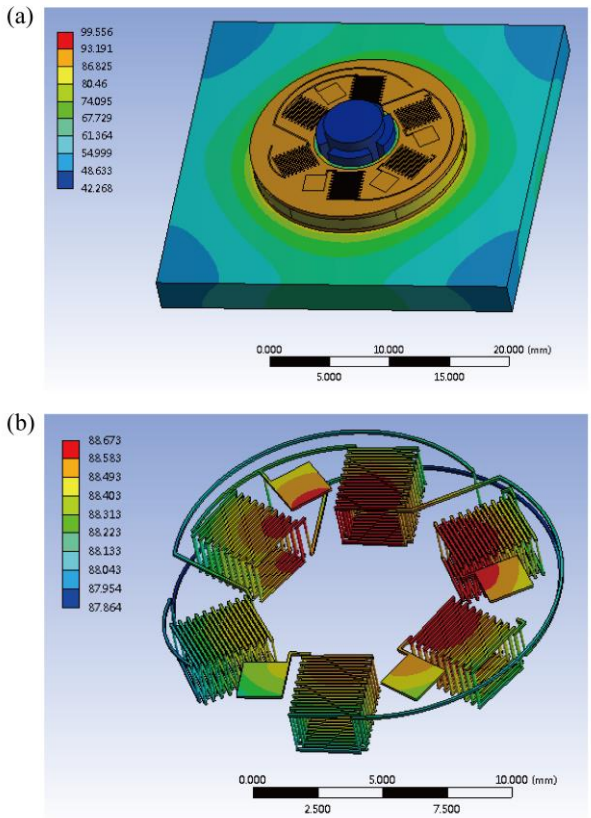

Figure 3 (a) The overall temperature field distribution of the optimized micromotor during operation. (b) The winding temperature field distribution of the optimized micromotor during operation.

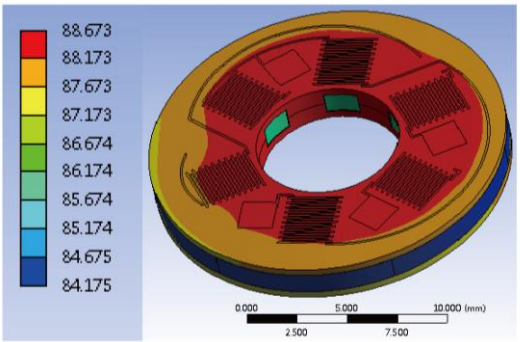

Figure 4 Temperature distribution during micromotor operation (°C).

The "burn out" failure mode of the micromotor is quite different from traditional large motors. When we optimize the temperature field simulation of the micromotor, we consider the "burn out" failure mode. When the temperature increases, it will cause the expansion of silicon and copper materials. Because the difference between the thermal expansion coefficient of the two materials is huge (silicon is $2.8\times10^{-6}K^{-1}$ (80°C), copper is $17\times10^{-6}K^{-1}$ (80°C)), it will cause the expansion stress between each other. The higher the temperature, the greater the expansion stress. When the expansion stress is too large, it will break silicon-embedded coils, which makes the micromotor "burn out". The overall operating temperature of the optimized micromotor is above 84 °C, and the maximum temperature can reach 88 °C. The specific temperature distribution is shown (**Figure 4**).

The magnetic density distribution on the central surface of the optimized micromotor is shown (**Figure 5**). The higher position of the iron core magnetic density is the tooth portion, which is primarily distributed between 1.6 T and 1.9 T, which is close to the saturation magnetic density of the iron core Bs=1.8 T, and the iron core utilization rate is high. Some positions are oversaturated, which will cause low efficiency and high loss of the materials at these positions under alternating magnetic field. However, the copper loss of the motor is much greater than the iron loss, so the iron loss does not affect the overall performance.

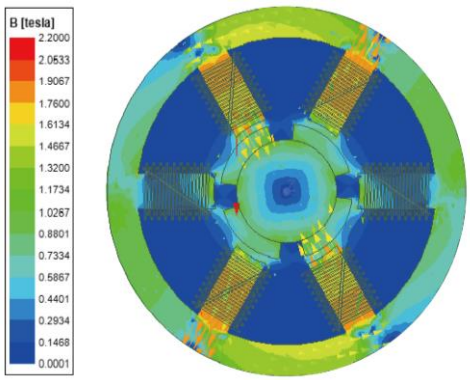

Figure 5 Magnetic flux density distribution in the center plane.

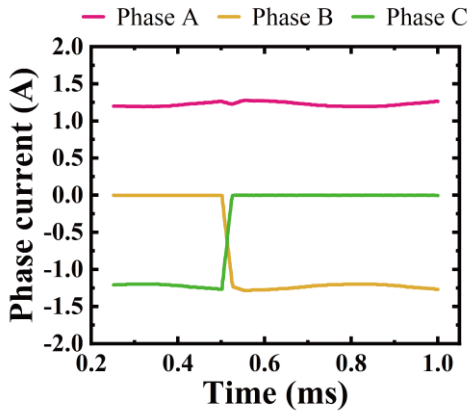

Figure 6 Three-phase current waveform.

Based on the phase which is always on, the average current in a state angle is 1.23A. The influence of commutation fluctuation is small. The three-phase current waveform is shown (**Figure 6**). In order to show the current change in the commutation process, the abscission is taken from a state angle plus half of the state angle before commutation, a total of 1.5 state angles (0.25ms-1ms). It can be seen that, the current in one state angle is relatively stable and fluctuates only during commutation.

The torque waveform in 1.5 state angles is shown (**Figure 7**). The rated torque is the average torque in one state angle, which is 658.7μN·m. The standard deviation of the torque is 85.4μN·m, so the comprehensive torque is 573.3μN·m. The torque ripple is 13%.

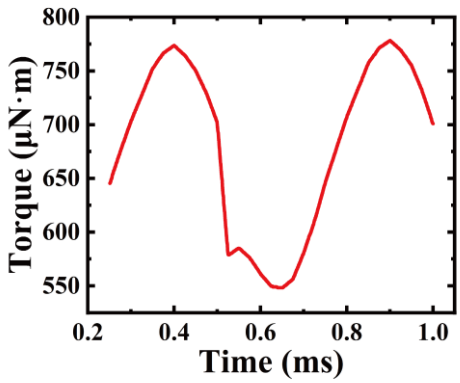

Figure 7 Torque waveform.

By analyzing the electromagnetic and thermal coupling phenomenon of micromotor, combining with the numerical simulation ideas and methods proposed by the actual situation of MEMS permanent magnet micromotor, which are different from the conventional scale motor, the three-dimensional electromagnetic and thermal coupling simulation is established and carried out. Through parametric scanning and data analysis, on the basis of the optimized structural design scheme, the structural parameters of the rotor are optimized to obtain the final structural size. Taking the temperature limit as the design goal, the corresponding performance parameters are simulated as the estimated performance of the rated operating point. At the

rated speed of 10000 rpm, the optimization and comparison performance of the micromotor are shown in **Table I**.

Table I Comparison of micromotor simulation results before and after optimization.

Parameter	Before optimization	After optimization	Degree of improvement
No-load air gap flux density/T	0.737	0.782	6.1%
Rated air gap flux density/T	0.69	0.72	4.3%
Rated operating temperature/°C	65	84	29.2%
Rated winding operating temperature/°C	69	88.43	28.2%
Rated voltage/V	2.45	3.34	36.3%
Rated current/A	1	1.23	23.0%
Rated speed /rpm	10000	10000	—
Rated torque /mN m	0.240	0.659	174.6%
Torque constant /(N m/A)	2.40×10^{-4}	5.36×10^{-4}	123.3%
Rated input power/W	2.45	4.11	67.8%
Rated electro-magnetic power/W	0.251	0.6	139.0%
Rated output mechanical power/W	0.15	0.362	141.3%
Total efficiency	6.1%	8.8%	44.3%

The optimized micromotor improves the magnetic flux density at the air gap. For the design of permanent magnet motor, the axial length of Nd-Fe-B permanent magnets is generally equal to the length of the armature to ensure that the air gap magnetic density is large, and the remanence of ferrite permanent magnet is small, so the axial length of ferrite permanent magnet is often slightly longer than the length of armature. The motor belongs to the very micro motor, the overall size of the permanent magnet of the motor is far smaller than that of the conventional permanent magnet motor, the small size of the permanent magnet is difficult to magnetize, magnetic slightly lower than the standard value. Although the length of the armature of this motor is very short and lengthening the permanent magnet will lead to a decrease in the utilization of the permanent magnet, lengthening the permanent magnet can improve the energy density. Therefore, under comprehensive consideration, the axial length of the permanent magnet used in this motor is longer than the length of the armature. After simulation analysis, a circle in the air gap is taken on the center surface of the armature to read the value of air gap magnetic density. At different rotor positions, the air gap magnetic density is not the same, and the magnetic density is greater when the center angle is 30°. Therefore, the rotor position was selected as 30° electrical angle to calculate the average air-gap magnetic density in the positive area of the permanent magnet (within 66° of the polar arc angle).

4 Conclusions

In this paper, the radial-flux permanent magnet micromotor manufactured by MEMS process is optimized. Combined with the electromagnetic thermal coupling method, considering the realizability of the process, the performance improvement of the micromotor is realized. The diameter of the optimized micromotor is 20 mm, and the height is 2 mm. The operating temperature reaches 88 °C. The iron core magnetic density is close to the saturation of 1.8 T, which reflects the high iron core utilization rate. The optimized micromotor increases the rated torque of 174.6% and the total efficiency of 44.3%.

5 Literature

[1] O. Cugat, et al.: Magnetic micro-actuators and systems (MAGMAS). IEEE, 2003, pp. 3607–3612.

[2] M. Nienhausa, et al.: Design and realization of a penny-shaped micromotor. Design, Test, and Microfabrication of MEMS and MOEMS., 1999, pp. 592–600.

[3] Ding X , et al.: Improved differential-evolution based optimization design of an axial flux MEMS micromotor. International Journal of Applied Electromagnetics and Mechanics, 2017, pp. 645-661.

[4] S. Merzaghi, et al.: Development of a Hybrid MEMS BLDC Micromotor. IEEE, 2011, pp. 3–11.

[5] O. Cugat, et al.: Novel magnetic micro-actuators and systems (MAGMAS) using permanent magnets. Sensors Actuators, A Phys., 2006, pp. 265–269.

[6] Z. Tao, et al.: A Radial-Flux Permanent Magnet Micromotor with 3D Solenoid Iron-Core MEMS In-Chip Coils of High Aspect Ratio. IEEE, 2020, pp. 1090–1093.

Directional Anisotropy in Smart Magnetic Actuation

Dharmi Chand and S M Srinivasan

Department of Applied Mechanics and Biomedical Engineering, Indian Institute of Technology Madras, Chennai, 600036, Tamil Nadu, India

Email address: am19d014@smail.iitm.ac.in, mssiva@iitm.ac.in

Abstract

Magnetoactive shape morphing soft magnetic materials (MASMA) are comprised of a soft polymer matrix impregnated with magnetic particles that display multifunctionality in the magnetic field. The arrangement and magnetization direction of the magnetic particles in the polymer matrix play a pivotal role in defining the deformation direction and actuation capacity. The traditional molding fabrication technique of shape programming is a tedious and complex process, and the requirement of a specifically shaped mold limits the applications of the MASMA. A particle arrangement pattern responsible for the generation of different shapes is studied, and thus, a pattern-mimicking strategy is developed to generate the desired shape to eradicate the need for a mold. The actuator generates the required shape in the magnetic field due to the magnetostriction effect. Results show that we can generate many shapes by controlling the direction of the magnetic moment by arranging the magnetic brick units in different arrangements.

1 Introduction

Shape morphing soft materials are capable of generating programmed shapes in response to various stimuli such as light[1], pH[2], heat[3], magnetic[4], [5], [6], [7], [8] and electric fields[9]. These smart soft materials are made of a flexible matrix infused with a stimuli reactant material and have a wide range of applications in soft robotics, biomedical, and other engineering. Among all the stimuli, a magnetic field offers more precise and untethered control over the functionality of such smart materials[10]. The magnetic field is safe for biological beings and provides multidirectional remote control in confined spaces[11], [12].

MASMA is comprised of micro/nano magnetic particles infused in a soft polymer matrix. Based on the magnetic properties of the infused particles (hard or soft), the complexity of shape programming in MASMA can be controlled[13]. Upon application of a magnetic field, hard magnetic particles get polarized and thus can generate programmed shapes attraction and repulsive forces[4], [14]. However, soft magnetic particles align and form a chain structure when applying external magnetic force [5]. The chain structure is retained once the soft material is cured or polymerized. When this cured polymer composite is kept in a magnetic field, it generates various deformations depending on the direction of the magnetic moment of these chains. The width and length of these chains depend on the intensity of the applied field, and the density of chains depends on the amount of magnetic particles in the polymer matrix.

Researchers have been trying to utilize this chain arrangement of soft magnetic particles to generate various shapes and deformations in soft polymers[4], [8], [10]. A mold of a specified shape and size is required to program the magnetic material for a specific shape[10]. When programming for a specific shape, the magnetic particles form a chain structure in various directions depending on the mold's shape. A careful evaluation of such programmed shapes can reveal the anisotropic arrangement of such particle chains in various shapes. However, the requirement of mold limits the application of such advanced material in various fields. Hence, a moldless method is required where this anisotropic arrangement of particles can be controlled to program the materials for various shapes.

The current study is focused on studying the anisotropic arrangement of magnetic particles in various mold-programmed shapes and utilizing the same arrangement to program the material for a specific shape without employing any mold. A brick-mortar masonry approach is utilized here, where bricks can be assembled in various configurations to generate various shapes. The brick is infused with magnetic particle chains aligned at various angles and alignments. As per the required shapes, these bricks can be configured appropriately and glued together to generate the desired shape without employing the mold. Some simple shapes are generated using this method and tested for their shape-generation capabilities.

2 Experimental Section

2.1 Materials

The soft magnetic actuator in this study comprises a soft silicon matrix infused with soft magnetic particles. The liquid silicon rubber (LSR-2) with shore hardness A 15 is procured from Chemzest Technoproducts Pvt. Ltd India. The magnetic particles used in this study are carbonyl iron particles with 6-micron APS procured from Aritech Chemazone. The magnetic particles are soft magnetic and have very low remanance magnetization.

2.2 Brick fabrication

The magnetic brick is fabricated by mold casting and magnetic programming. The current study uses a simple 3D printed rectangular mold (of dimensions 8mm×2mm×1mm). The magnetic material is prepared by mixing Iron particles with liquid silicon rubber (procured from Chemzest Technoproducts Pvt. ltd India) in 1:1 w/w proportion. Appropriate curing hardener for liquid silicon is added to this composite mix. After mixing thoroughly, this composite mix is poured into the brick mold, and the mold is then kept in the uniform magnetic field (UMF) at various angles (0°, 10°, 20° etc.) until the curing is done. Once the curing is done, the brick blocks are removed from the mold and vacuumed for an hour to remove any gas. The brick blocks are then tested for alignment angles and maximum deformation in an external magnetic field. A set of bricks with various alignments is prepared and stored, and thus, a library of brick units is created. As per the requirement, bricks with desired alignments are taken from the library to fabricate the magnetic actuator with various shapes.

2.3 Fabrication of Actuator with Various Shapes

The actuators with various shape-morphing capabilities are fabricated using magnetic brick blocks. For this, magnetic bricks with chain alignments are packed together, as shown in Figure 1, forming long particle chain structures along the actuator's length, generating an anisotropic structure. This arrangement of bricks is glued together using silicon and hardener mix. Once the silicon and hardener mix is cured, the brick units are glued with each other and form a single actuator body.

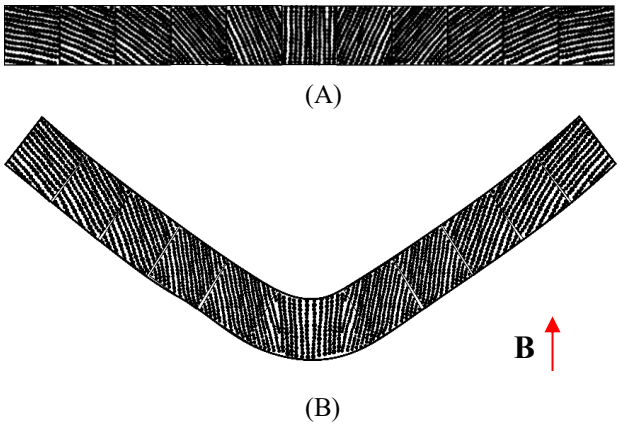

Figure 1: (A) Particle chain arrangement in initial sate; (B) Actuat-ed state in magnetic field

The alignment of particle chain in bricks defines the anisotropic particle chain arrangement in the actuator which generates directional moment when an external magnetic field is applied. As seen in Figure 1 (B) the actuator generates an actuated shape when kept in magnetic field. Similarly, various shapes can be generated by carefully controlling the chain anisotropy in the actuators.

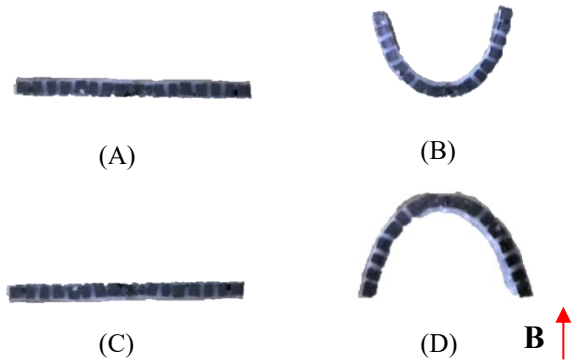

Figure 2: (A) U-shaped actuator in the initial state; (B) U-shaped actuator in the final state in the magnetic field. (C) Inverted U-shaped actuator in the initial state; (D) Inverted U-shaped actuator in the final state in the magnetic field.

Fig 1 depicts the chain alignment required to generate a U shape in an actuator, and Fig. 2 shows an actuator prepared following a similar particle chain alignment. As shown in Figure 2, when kept in a magnetic field, the actuator generates a programmed shape following the particle chain alignment. Similarly, an N-shaped actuator is also fabricated and tested for shape generation (Figure 3). The shape's deformation and curvature can be controlled by controlling the chain alignment configuration along the length.

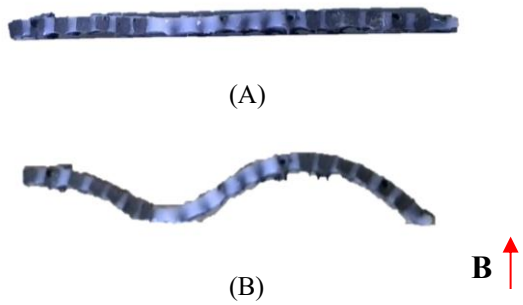

Figure 3: N-shaped actuator: (A) Initial state; (B) Final State

3 Results and Discussion

The shape morphing actuators fabricated using the brick-mortar masonry technique can generate the desired shape without employing the mold-shaped programming technique. The actuators are tested for shape-morphing ability in the magnetic field, and the results are plotted in non-dimensional form (Figure 4). In Figure 4, the deformation of the U-shaped actuator is non-dimensionalized with respect to its length and is plotted against the magnetic field. We can see that initially, the change in shape is very slow, but then there is a sudden increase in deformation due to the magnetostriction effect. Once the actuator reaches its maximum deformation or attains the programmed shape, there will be no further change in shape, and it will reach the saturation deformation level.

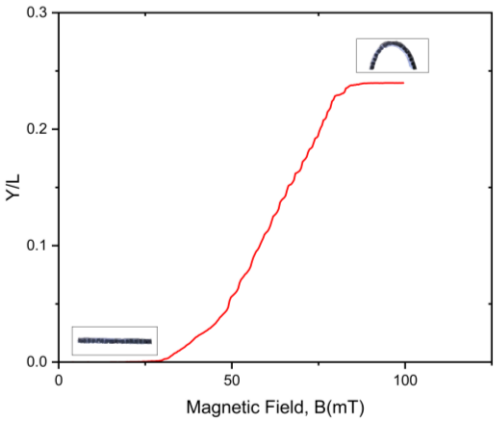

Figure 4: Deformation characterization of the actuator with change in magnetic field.

4 Conclusions

This study shows that we can generate many shapes by controlling the anisotropic arrangement of the magnetic particle chains in the soft matrix. By directionalising the anisotropic alignment of the magnetic particle chains in the matrix, we can control the localized magnetic moment and torque in the matrix, and thus, any desired shape can be generated following this method. The brick-mortar masonry approach of shape programming discussed in this current study paves the way for moldless programming techniques and opens the way towards the development of additive manufacturing for shape programming.

We are currently working on the development of such a device for the additive manufacturing shape-programmed magnetic actuators.

5 Literature

[1] Y. Huang, Q. Yu, C. Su, J. Jiang, N. Chen, and H. Shao, "Light-Responsive Soft Actuators: Mechanism, Materials, Fabrication, and Applications," *Actuators*, vol. 10, no. 11, Art. no. 11, Nov. 2021, doi: 10.3390/act10110298.

[2] "Dual pH-Responsive Hydrogel Actuator for Lipophilic Drug Delivery | ACS Applied Materials & Interfaces." Accessed: May 07, 2024. [Online]. Available: https://pubs.acs.org/doi/full/10.1021/acsami.9b21713

[3] Y. Dai, T. Qu, H. Zang, and C. Liu, "Soft actuators driven by humidity and temperature based on plant parchment," in *2019 WRC Symposium on Advanced Robotics and Automation (WRC SARA)*, Aug. 2019, pp. 228–234. doi: 10.1109/WRC-SARA.2019.8931804.

[4] N. Bira, P. Dhagat, and J. R. Davidson, "A Review of Magnetic Elastomers and Their Role in Soft Robotics," *Front. Robot. AI*, vol. 7, p. 588391, Oct. 2020, doi: 10.3389/frobt.2020.588391.

[5] S. R. Mishra, M. D. Dickey, O. D. Velev, and J. B. Tracy, "Selective and directional actuation of elastomer films using chained magnetic nanoparticles," *Nanoscale*, vol. 8, no. 3, pp. 1309–1313, 2016, doi: 10.1039/C5NR07410J.

[6] Y. Alapan, A. C. Karacakol, S. N. Guzelhan, I. Isik, and M. Sitti, "Reprogrammable shape morphing of magnetic soft machines," *Science Advances*, vol. 6, no. 38, p. eabc6414, Sep. 2020, doi: 10.1126/sciadv.abc6414.

[7] M. M. Schmauch, S. R. Mishra, B. A. Evans, O. D. Velev, and J. B. Tracy, "Chained Iron Microparticles for Directionally Controlled Actuation of Soft Robots," *ACS Appl. Mater. Interfaces*, vol. 9, no. 13, pp. 11895–11901, Apr. 2017, doi: 10.1021/acsami.7b01209.

[8] J. Kim, S. E. Chung, S.-E. Choi, H. Lee, J. Kim, and S. Kwon, "Programming magnetic anisotropy in polymeric microactuators," *Nature Mater*, vol. 10, no. 10, Art. no. 10, Oct. 2011, doi: 10.1038/nmat3090.

[9] Z. Ma and D. Sameoto, "A Review of Electrically Driven Soft Actuators for Soft Robotics," *Micromachines*, vol. 13, no. 11, Art. no. 11, Nov. 2022, doi: 10.3390/mi13111881.

[10] Y. Kim and X. Zhao, "Magnetic Soft Materials and Robots," *Chem. Rev.*, vol. 122, no. 5, pp. 5317–5364, Mar. 2022, doi: 10.1021/acs.chemrev.1c00481.

[11] K. E. Peyer, L. Zhang, and B. J. Nelson, "Bio-inspired magnetic swimming microrobots for biomedical applications," *Nanoscale*, vol. 5, no. 4, pp. 1259–1272, 2013, doi: 10.1039/C2NR32554C.

[12] S. Fusco *et al.*, "Self-folding mobile microrobots for biomedical applications," in *2014 IEEE International Conference on Robotics and Automation (ICRA)*, May 2014, pp. 3777–3782. doi: 10.1109/ICRA.2014.6907406.

[13] A. K. Bastola and M. Hossain, "The shape – morphing performance of magnetoactive soft materials," *Materials & Design*, vol. 211, p. 110172, Dec. 2021, doi: 10.1016/j.matdes.2021.110172.

[14] B. D. Cullity and C. D. Graham, *Introduction to magnetic materials*, 2nd ed. Hoboken, N.J: IEEE/Wiley, 2009.

Optimized high-efficiency MICA actuators for space compressors

Xavier De Lepine, Frank Claeyssen, Francois Barillot, Patrick Meneroud, Aurore Loubet, Timotéo Payre, Nicolas Bourgeot, Olivia Stadler, David Ferris, Jocelyn Rebufa, Arnaud Barnique, Gérald Aigouy, Hélène Rouxel, Cedrat Technologies, Meylan, France

Abstract

Moving Iron Controllable Actuators MICA™ are magnetic linear actuators from CEDRAT TECHNOLOGIES (CTEC) that find interests in applications requiring high-force density and low heating. Because of these attractive performances, some space applications such as ZBO Gas compressors and Pulse Tube Cryocooler are considering their use in operational missions. However, this last application requires the demonstration of additional features, notably a high efficiency, a long lifetime and a good force homogeneity to minimize the generation of exported micro-vibrations. To fulfil these additional features, CTEC has developed an optimised MICA following the specifications of the Pulse Tube Cryocooler (PTC) of AIR LIQUIDE. The paper will present the performance progresses obtained on this customized MICA, from modelling prediction to lab tests of Engineering Models.

1 Introduction

The MICA™ (Moving Iron Controllable Actuator) is a CEDRAT TECHNOLOGIES (CTEC) proprietary actuator magnetic design concept, based on a polarized variable reluctance principle. This concept has been de-scribed in previous CTEC publications [1] and [2] as well as its advantages, a high-force density and low heating.

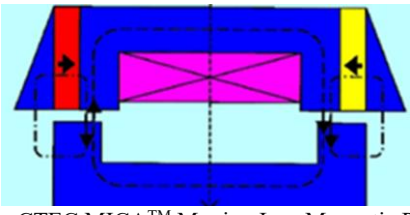

Figure 1: CTEC MICA™ Moving Iron Magnetic Principle

Because of these attractive performances, some space applications such as Gas compressors for Zero-Boil-Off (ZBO) [3] and Pulse Tube Cryocooler (PTC) are considering their use in operational missions such as Lunar Orbital Platform-Gateway (LOP-G) and future satellites of earth observation. In both cases, the MICA™ is used at resonance in linear oscillation to compress a gas. This has been demonstrated in [3] showing good efficiency.

AIR LIQUIDE ADVANCED TECHNOLOGIES (ALAT) requested for the PTC application of more demanding actuator performances [4], in particular a long lifetime, a high efficiency and low levels of micro vibrations. This new actuator would provide, in theory, about 6W cooling power in [50K-60K] range as requested.

At first, MICA™ was assessed by ALAT in Phase 1 (Gen.1.1) [4]. It was deemed promising but not satisfying. Therefore, ALAT ordered to CTEC a new MICA™ in Second Phase, with the objective to cover high power efficiency, low exported micro-vibrations, and extra-long lifetime.

The work presented in this article shows the approach that has been conducted to achieve this goal.

2 Optimization framework

2.1 Performance assessment

MICA™ actuators dedicated to compressor applications must address several topics that can be contradictory: High efficiency is needed to save power in operation, a smoothed behaviour is needed to minimize parasitic forces and extra-long operation lifetime ([5], [6]) is required to reduce maintenance to the minimum.

Nevertheless, the very principle of MICA™ actuators rely on the magnetic field concentrated in the radial airgap to produce axial force. This approach allows significant force density at the cost of non-linear behaviour along the axis direction. Consequently, the magnetic designer must find the best compromise between the homogeneity along axial displacement and the maximum force to achieve. In fact, the homogeneity of the actuator is strongly related to its parasitic micro-vibrations, while a large force maximizes efficiency.

Additionally, an extra-long operation lifetime is easier to achieve with soft guiding blades, while it is recommended to have stiff guiding blades to reject radial vibrations. For this purpose, a strategy based on flexible blades [7] has been adopted.

Therefore, the optimization approach consists in taking into consideration all these parameters to achieve the best solution.

2.2 Modelling framework

Several tools have been developed to monitor the relevant parameters of the actuator performance: the input/output power (magnetic, fluidic & mechanical coupled models), the parasitic force (axial and radial), the flexible bearings lifetime, etc.

The Figure 2 presents the electromechanical model of the system that was used to estimate the overall performance of the system, including the mechanical parts, the magnetic parts, and the fluidic parts.

The mechanical parts are modelled with a linear stiffness (K_b) and a viscous damper (C_b), the latter to express the structural damping due to fixation.

The magnetic components are considered through the magnetic stiffness (K_b) and the force factor (K_m), that act on both mechanical and electrical domains. Besides, eddy currents that develop either in the statoric part of the actuator or in the moving part of the actuator are captured with $R_{EC}(\omega)$ and $C_{EC}(\omega, x)$, respectively.
Similarly, the compression chamber was modelled with a mechanical stiffness $K_{gas}(\omega, x)$ and a viscous damper $C_{gas}(\omega, x)$.

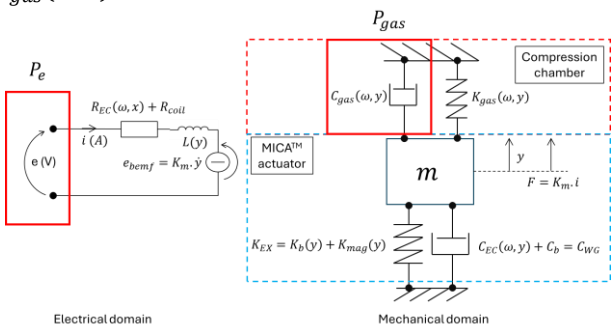

Figure 2: Electro-fluid-mechanical model

The input electrical power is called P_e, while the output mechanical power dissipated in gas is called P_{gas}. The latter is the useful power for the purpose of compression.

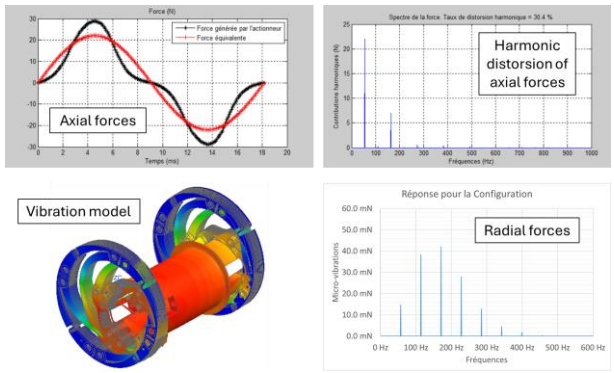

Figure 3: Multiphysics tools used for design and optimization

2.3 Trade-off and results of the optimization process

Two key components are central in the optimization process: the flexible bearings and the magnetic circuit.
The flexible bearings must be designed to meet several requirements that can be contradictory, sometimes. In fact, they are built such that they must withstand extra-long lifetime (about 10 years of continuous working conditions), while limiting the exported radial parasitic forces due to magnetic excitation. The first implies low mechanical stresses in axial direction, while the second implies a quite large radial stiffness so that the moving part of the actuator works as a high pass filter with regard to inner magnetic forces generated by the actuator itself.

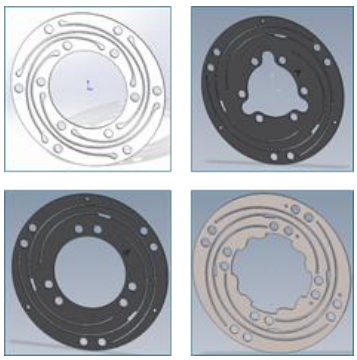

Figure 4: A few examples of bearing designs

Similarly, the magnetic circuit must be carefully designed to achieve several targets: a large actuation force for a given current at zero displacement (to maximize efficiency at the resonant frequency), axial force homogeneity to minimize axial harmonics (to minimize axial parasitic forces when two actuators must work in back-to-back setup), low sensitivity to mechanical tolerances to insure repeatability between units, and more importantly, low parasitic radial forces for a given eccentricity to reduce micro-vibrations.

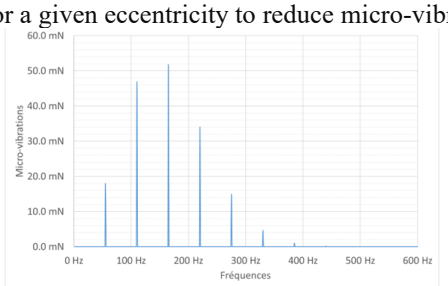

Figure 5: Estimated exported micro-vibration forces

To find the best compromise, a strategy based on local magnetic saturations shaped on specific design indicators was adopted. In Figure 5, an estimation of the exported micro-vibrations is shown, while Table 1 shows a few intermediate results that were obtained during this iterative process. Results are given for 10A 0-p nominal current.

	Phase 1 (Gen.1.1)	Gen2.1	Final (PTC)
Stroke	± 5mm	± 5mm	± 5mm
Axial homogeneity @±5mm	58%	86%	76%
Force @ 10A	~180 N	130 N	~200N
Rad. mag. Stiff. (N/mm)	-540	-190	-420
Outp. mech. Pwr. (W)	130	70	150
Sens mech. Tol. (*)	High	Low	Low
Axial stiff.	Non-linear	Non-linear	<1.8N/mm
Mass of Mag. Act. part	1.3 kg	1.0 kg	1.4 kg

Table 1: Models obtained during optimization process

3 Experimental results

3.1 Setup

Several experimental setups were designed to investigate the main characteristics of the sub-components: the magnetic circuit, the flexible bearings alone, the axial and radial dynamics, the output power, etc.
In Figure 6 are presented three strategic setups that validate the magnetic circuit in static and dynamics, the flexible bearings lifetime characteristics and the radial dynamics.
For the validation of the flexible bearings, an approach similar to [7] was adopted, in which the units were tested at stroke larger than the nominal stroke. More details are given in chapter 3.2.1.

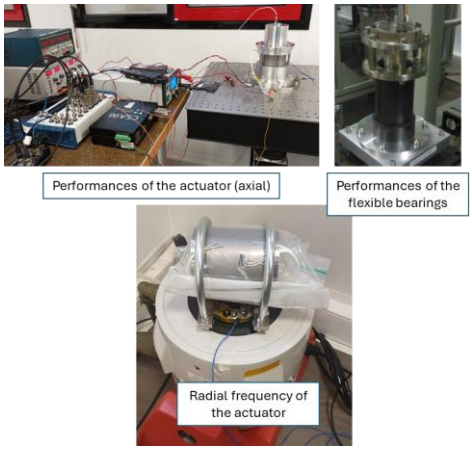

Figure 6: Experimental setups to validate the performances of the system

The former setup was designed to demonstrate the capacity of the actuator to achieve the requirements in terms of: frequency, power, stroke, as defined by the specification. The challenge is to insure that the stiffness and damping coefficients of the compression chamber (K_{gas} and C_{gas}, respectively) would match to the requirement at the right stroke (Figure 7 shows the non-linear behaviour of the chamber).
Additionally, a specific setup was needed to collect useful information about the performance of the flexible bearings in terms of lifetime. To achieve this goal, a voice-coil was used to impose an axial displacement that were much larger than the nominal stroke to apply stresses above the Wöhler curve. With this approach, it becomes possible to obtain useful experimental data regarding theoretical information that exist in literature. In fact, as the objective for the project is to achieve more than 10 years in continuous operation, it cannot be achieved during a standard project, which usually last about 1 year or two. More details about this setup and the philosophy behind it are presented in §3.2.1.
The last picture shows a shaker owned by CTEC that was used in this project to identify the radial frequency of the actuator. This result is important as it includes the radial stiffness of the flexible bearings, the magnetic stiffness of the magnetic circuit, as well as the mobile part of the actuator (rotor). The result of this test has an immediate impact on the exported forces rejection capacity of the actuator.

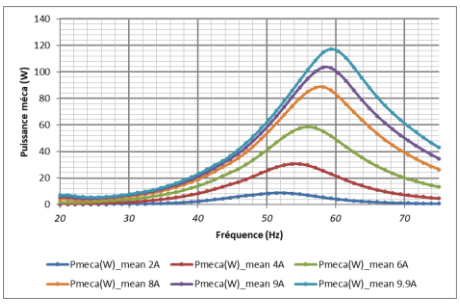

Figure 7: Output power (P_{gas}) vs input excitation current

3.2 Performances

In this chapter, the main performances of the actuator are presented. They include the results of the flexible bearings in lifetime and the performances in terms of power, efficiency, frequency, etc.

3.2.1 Fatigue performance

The philosophy adopted for the lifetime analysis of the flexible bearings was to evaluate how far the actual bearing were from the theoretical Wöhler curve. This approach allows to obtain useful information about the capacity of the bearing to sustain extra-long working time (more than 10 years of continuous working conditions) during a standard project.

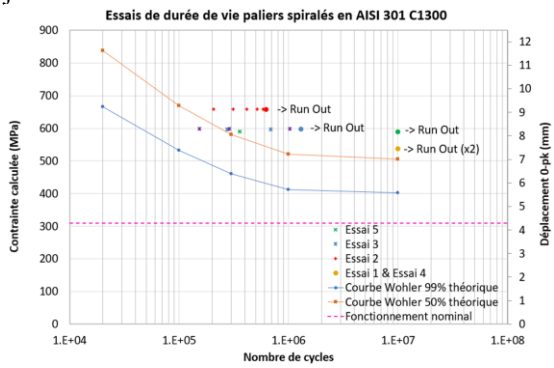

Figure 8: Results of lifetime tests of flexible bearings

In practice, the flexible bearing is excited such that the stresses are above the theoretical Wöhler curves provided in literature until breakdown. A few tens of components were tested, and the results were all encouraging: most pieces broke above the 50% Wöhler curve, which tends to show that the bearings can work according to the requirements. In fact, the dotted line shows the nominal stress seen by the bearings in working conditions.

3.2.2 Exported micro-vibration forces

Tests conducted by the customer showed good correlation between the estimated forces (Figure 5) and measured ones. A typical max level is below 50mN, which is the level announced by NG cryocoolers with similar power [8].

3.2.3 Dynamic performance

The performances of the new MICA™ actuator have been measured for three units (2xEMs + 1xEQP, they are visible on Figure 9) for the needs of the project. The outcome results could then provide a first feedback of the repeatability of the manufacturing process.

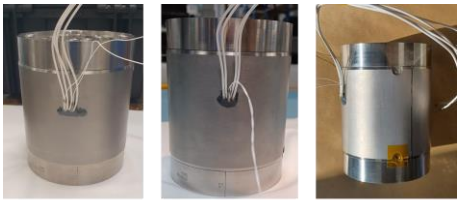

SN02 SN03 SN06

Figure 9: Units produced during the project

The performance evidenced in the following are : the output power P_{gas} (useful for the compression process), the input electrical power P_e, the efficiency P_{gas}/P_e, the displacement x, and the power factor $\cos\phi$, with $\phi = \arg(i/e)$.
Figure 10 shows the comparison between the performances of three units. The differences between the units lie within the measurement errors, which tends to show that the manufacturing process is robust and repeatable.

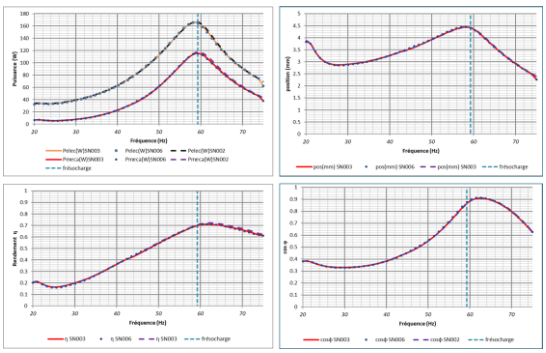

Figure 10: Comparison between the performances of three units

Main parameters are listed in Table 2.

Parameters	SN06	SN03	SN02	% dev.
$f_{réso}$	$59Hz$	59Hz	59.3Hz	0.5%
Current	$9.9A$	9.9A	9.9A	0%
Voltage	$38.4V$	38.9 V	$39.4V$	2.6%
Y_0	$4.4mm$	4.4mm	4.4mm	0%
P_{gaz}	$115W$	115W	115W	0%
P_e	$164W$	165W	165W	0.6%
$\cos\phi$	0.88	0.86	0.87	2%

Table 2: Performance comparison between units

4 Conclusions

This works shows that MICA™ technology is clearly relevant for compressors in space applications, either in terms of power efficiency, lifetime and exported micro-vibration forces. These performances were obtained after a multivariable optimization procedure (magnetic, electrical, mechanical, vibrations, etc.), and all indicators were improved, at least in theory, when compared to the initial proposal provided by CTEC in First phase.
Additionally, the theoretical tools were validated with experimental results in most key parameters: power, guiding blades lifetime and exported micro-vibrations. Those results have been reached for three units within a range smaller that 3% in all parameters, which consolidates the manufacturing process in terms of quality and repeatability.

5 Acknowledgement

The authors gratefully thank AIR LIQUIDE ADVANCED TECHNOLOGIES Sassenage (F) and CNES Toulouse (F) for supporting these works.

6 Literature

[1] F. Claeyssen, G. Magnac, O. Sosnicki, "Moving Iron Controllable actuator", ACTUATOR 2008, 9-11 June 2008, C3.3, pp. 445 – 448, Messe Bremen

[2] G. Aigouy, X. De Lepine, P. Meneroud, MICA20CS Proof mass actuator – Conf. ACTUATOR 2022 29-30 June 2022, Darmstadt, DE, VDE VERLAG · Berlin

[3] P. Meneroud, S. Rowe, G. Aigouy, Design of a 2 stages compressor for mobility applications, using compact and efficient Moving Iron Controllable Actuators, Conf. ISEF 2019, Nancy Fr, 29-31 Aug .2019 – Proc P2-B-2

[4] P.O. Mine, Air Liquide Pulse Tube Cryocooler Compressor Development (DEMO 0) and Test Results, 8th European Space Cryogenics Workshop 2023, 5-7 June 2023, Noordwijk, NL

[5] F. NOVÝ, O. BOKŮVKA, L. TRŠKO, M. CHALUPOVÁ, Ultra high cycle fatigue of materials, Dpt of Materials Engineering, University Of Zilina in Zilina, Annals of the Faculty of Mechanical Engineering Hunedoara, Romania - International Journal of Engineering, 2012.

[6] W. Illg, C. B. Castle, Fatigue of four stainless steels and three titanium alloys before and after exposure to 550° f (561° k) up to 8800 hours, NASA, Clearinghouse for Federal Scientific and Technical Information, Jul. 1965.

[7] H. Dang, High Efficiency Pulse Tube Cryocoolers for Aerospace Applications, Shanghai Institute of Technical Physics, Chinese Academy of Sciences, Shanghai 200083, China, Advances in Cryogenic Engineering, AIP Conf. Proc. 1573, 378-385, 2014; doi: 10.1063/1.4860726

[8] Northrop Grumman High Efficiency Cryocoolers for space, 2024, https://cdn.prd.ngc.agencyq.site/-/media/wp-content/uploads/Northrop-Grumman-Cryocoolers-Datasheet.pdf

-Push, Push, Push-
Direct writing of magnetic micro actuators

Nicolas Geid, Eleonora Galli, Jürgen Rühe, Labor für Chemie und Physik von Grenzflächen, Institut für Mikrosystemtechnik (IMTEK), Universität Freiburg, Georges-Köhler-Allee 103, 79110 Freiburg, Germany
nicolas.geid@imtek.de

Abstract

In this contribution we discuss the combination of two photon lithography (2PL) and C,H insertion crosslinking (CHic) for the generation of magnetic micro actuators. The structures are written in a solid pre-polymer which contains a small number of photoreactive groups for photocrosslinking in the focus of the 2PL laser. The material is also filled with magnetic nanoparticles which later on makes the microstructures responsive to a dynamic magnetic field. We will show how complex actuators can be generated. The actuators can be spread out over a fairly large field an almost all structures that were generated also react to the magnetic stimulus. This makes them perfect candidates for use in microfluidic systems e.g. to transport liquids.

1 Introduction

Magnetic micro actuators are becoming increasingly important in the field of microfluidics. For example, pumping liquids in the microlitre range is one of the main tasks in lab-on-a-chip applications.[1] The stimulation or mechanical manipulation of cells is also an area that is receiving a lot of attention. To date, mask-based or template-based methods have been used to fabricate such actuators.[2,3,4] However, these methods are limited when applications require a more indi-vidual design of complex structures.

2 Two-Photon crosslinking

Our study introduces a novel method for direct writing of magnetic micro actuators using two-photon lithography. This technique involves a photochemical reaction triggered by a femtosecond laser through the nearly simultaneous absorption of two photons.
The reaction occurs at a high laser intensity specifically around the focal point (voxel; volume and pixel), enabling direct writing in all three spatial directions, voxel by voxel. The photochemical reaction at the core of our approach is termed C,H insertion crosslinking (CHic). The starting material is a copolymer containing a main functional group (n-butyl acrylate) and a photoreactive species (anthraquinone).
Upon activation of the reactive group in the prepolymer, a C,H insertion reaction initiates crosslinking into neighboring chains as well as covalent attachment to the surface (see **Figure 1**).
This technique, known as two-photon crosslinking, results in the formation of stable surface-attached microstructures.[5,6,7]

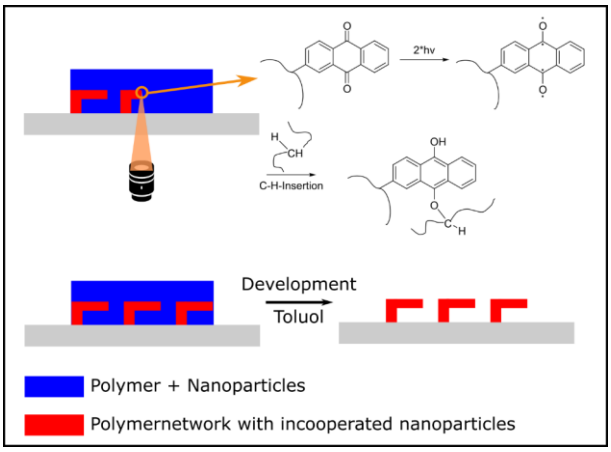

Figure 1 Scheme for direct writing and development of micro actuators using two-photon crosslinking starting from a polymer nanoparticle composite to a crosslinked structure.

3 3D magnetical microstructures

By using prepolymers in conjunction with superparamagnetic nanoparticles, it becomes possible to fabricate micro actuators in a single-step process using a polymer-nanoparticle composite.[8]
Figure 1 shows a schematic representation of this process. A simple development procedure, where unreacted polymer is washed out, yields the final micro actuators. Figure 2 shows the high resolution achieved in the structures, which are in the low micrometre range. Importantly, these structures show the ability to be manipulated in an external magnetic field. This highlights the potential for direct writing of high-resolution magnetic micro actuators via two-photon crosslinking.
In **Figure 3** a 1 cm big field of micro actuators is shown. The distance between this micro actuators is very small (6 µm) and on top because of different architecture only half of them is able to move.

A primary goal is to use this toolkit to fabricate and study micro actuators characterised by complex and versatile shapes (such as spheres and overhanging elements) with tunable properties, enabling tailored applications such as cell stimulation.

Figure 2 Schematic and light microscope images of moving micro actuators under a rotating magnetic field.

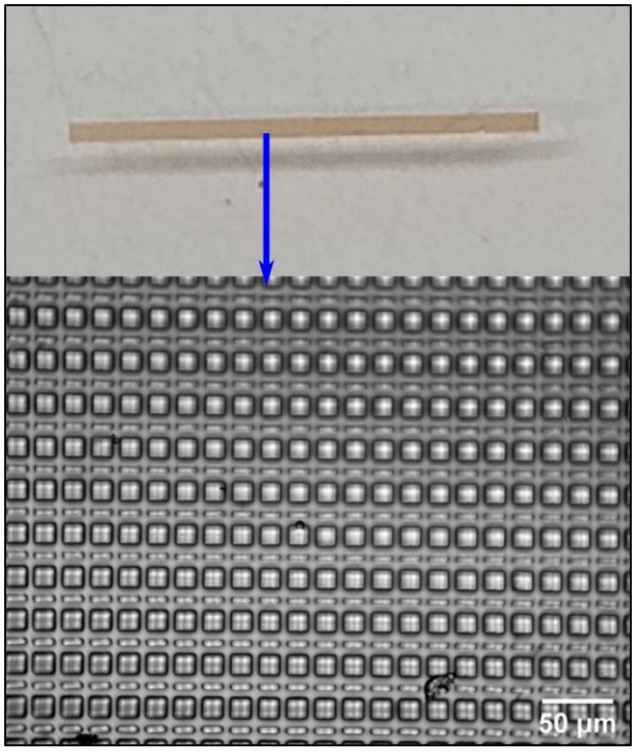

Figure 3 Photographical and light microscope images of a 1 cm big field of non-moving and moving magnetic micro actuators.

4 Materials and Methods

The copolymer was prepared by free-radical polymerisation using 92.5 mol% nBA and 7.5 mol% 2-amino-3-hydroxyanthraquinone (AAHAQ) at a temperature of 30 °C using V70 initiator. The reaction lasted for 24 hours and a yield of 70% was obtained. The AAHAQ content was determined to be 7.4% by NMR spectroscopy, based on the integration of signals from aromatic protons (7.6-7.9 ppm). According to GPC data, the molecular weight of the copolymer is M_n = 93,000 g/mol and M_w = 241,000 g/mol, suggesting an average of about 70 AAHAQ repeat units per polymer chain.

The magnetic resin was prepared by mixing 25 µL of commercial Fe_3O_4 superparamagnetic ferrofluid (EMG 905, containing oleic acid as a stabiliser, from Ferrotec, NH, Bedford, USA) with a solution of 100 mg of photocurable copolymer P(nBA-7.5%AAHAQ) in 0.975 mL of toluene, resulting in a uniform dispersion.

To form a polymer nanoparticle layer of 80 to 100 µm thickness, 50 to 100 µL of the above dispersion was deposited on a silanized glass slide. The toluene was allowed to evaporate gradually. After solidification of the layer, a glassy polymer composite layer containing about 10% by weight of nanoparticles was obtained. The 2-photon writing process was performed using a NanoOne setup (UpNano GmbH, Vienna, Austria) equipped with a 20× magnification lens with 0.7 NA. Printing was performed in bottom-up mode with the lens immersed in water. Slicing was set at 0.5 µm and hatching at 0.15 µm, with a laser power of 15-18 mW and a scan speed of 100 mm/s. Upon completion of the 2-PC process, the substrates were immersed in n-butanol and allowed to develop for at least 2 hours to effectively rinse out any unreacted polymer.

5 Literature

[1] Ranzoni, A.; Janssen, X. J. A.; Ovsyanko, M.; van Ijzendoorn, L. J.; Prins, M. W. J. Lab on a chip 2010, 10, 179–188.

[2] J. Hussong; N. Schorr; J. Belardi; O. Prucker; J. Rühe, Westerweel, Lab Chip 2011, 11, 2017–2022.

[3] den Toonder, J. M. J.; Onck, P. R. Trends in biotechnology 2013, *31*, 85–91.

[4] Dong, X.; Lum, G. Z.; Hu, W.; Zhang, R.; Ren, Z.; Onck, P. R.; Sitti, M. Science advances 2020, *6*.

[5] D. Schwärzle; X. Hou; O. Prucker; J. Rühe, Advanced materials (Deerfield Beach, Fla.) 2017, 29.

[6] O. Prucker; T. Brandstetter; J. Rühe, Biointerphases 2017, 13, 10801.

[7] Song, D.; Husari, A.; Kotz-Helmer, F.; Tomakidi, P.; Rapp, B. E.; Rühe, J. Small (Weinheim an der Bergstrasse, Germany) 2024, 20, e2306682.

[8] N. Geid; J. U. Leutner; O. Prucker, J. Rühe Actuators 2023, 12(3), 124.

Development of microbubble shock wave reflection needle-free injection

Yibo Ma[1], Wenjing Huang[2], Naotomo Tottori[1], Yoko Yamanishi[1]
[1]Bio-medical Fluid Engineering Laboratory, Mechanical engineering, Kyushu University, Fukuoka, Japan
[2]Kindai University Technical College, Mie, Japan
ma.yibo.190@s.kyushu-u.ac.jp

Abstract

We developed a novel needle-free injection system through electrically induced microbubble. This system generated microbubbles and applied repetitive mechanical stimulation to perforate on tissue and introduce the reagent. In this research, we proposed improving reagent introduction depth through reflecting the shock wave from microbubble. Our result showed that the developed shock wave reflection method improving the reagent introduction ability of microbubble needle-free injection.

1 Background

Metal needles are often used for drug injections and vaccinations. The metal needles have advantages of easy skin perforation and controllable drug injection volume. However, incorrect metal needle use and reuse of needles often leads to infections. Also, some patient has a needle phobia and a fear of needle sticking. These has been a worldwide problem for a long time.[1] To solve the problems of metal needle, the needle-free injection system was developed.[2] The needle-free injection system generated the high velocity jet at the injector tip, perforate on human skin and inject the drug into tissue. Also, the needle-free injection systems have been developed for many years, there are still problem with these systems, the reduced flexibility, an uncontrolled fluid stream, and the cross-contamination. In our lab, a device maned electrically induced microbubble generator has been developed. The micro size bubbles are generated at the device tip via applying high voltage pulse. We have achieved the metal deposition[3] and cell transfection[4] by microbubble generator. We are developing a novel needle-free injections system via microbubble injector.

In this research, to improve the perforation performance of microbubble needle-free injection system, we proposed focusing the shock wave from microbubble collapse. Our results showed that comparing to perforation depth by original microbubble needle-free injection system, the perforation depth was improved via shock wave focusing.

2 Mechanism and concept

We developed a device named electrically induced microbubble generator where the micro size bubbles could be generated via applying the high voltage pulse. When the high-voltage electric field is concentrated at the tip of the injector, the ions near the tip move at high speed and collide with each other. The collision of ions causes the molecules to disperse, which eventually leads to the production of tiny bubble.[5][6][7] The temperature in the tiny bubbles rises rapidly and the pressure of the bubble is not released in the process which lead the microbubble expansion.[8][9][10][11] The microbubble starts to collapse after reaches its maximum volume. The jet and shock wave would be generated from microbubble collapse.

In figure 1 (a) showed the concept of microbubble needle-free tissue injection. When microbubble collapse, the microjet and shock wave are generated. The Microjet causes damage to the tissue and thus open hole that allows the drug to enter the tissue. Although tissue damage from a single microjet is minimal, by our system, 600 microbubbles were generated in 18 ms. Multiple impacts over a short period of time were sufficient to damage the tissue surface and perforate to inject the drug. The 600 microjets in 18 ms contribute to the tissue perforation. The shock wave from the collapse point of the bubble transmits in all directions in a spherical shape. Only the shock wave transmitting towards the tissue contributes to the perforation.

To focus the shock wave and enhance the perforation performance, we proposed a semi-ellipsoid shock wave focusing device. There are two focal point in an ellipsoid. Based on the geometric properties of the ellipsoid, the shock wave generated from one of the focal points will be reflected and focused on the other focal point. Thus, the shock wave from microbubble will be focused on the second point if the shock wave was generated from focal point. The design of the shock wave focusing device was showed in Figure 1 (b). The concept of microbubble needle-free injection becomes both the microjet and focused shock contributing to the tissue perforation. The concept was showed in Figure 1 (c).

3 Experiments

The experimental setup was showed in Figure 2 (a). Using a PC and a control circuit to control a high frequency power source, Hyfrecator® 2000 (CONMED Co., Ltd, U.S.). The Hyfrecator® 2000 was connected to a resistance and the microbubble generator. The Hyfrecator® 2000 supplies 600 pulse in 18 ms. We set the output to 600 pulses every 4 seconds for 30 times. The injection experiment was performed at power of 20, 25, 30, and 35 W and with no injection as the control. The solution was fluorescent beads

(Fluoro-Max, Thermo Scientific Co. Ltd, U.S.) with a diameter of 2.1 µm in 0.9% saline. The injection object was chicken muscle meat. After injection, clean the tissue by saline and observe the cross section of the injected object. Binarize the fluorescence at the wound and get the depth by measuring the depth of the fluorescence from the beads inside the tissue. The experiment was done with/without the shock wave focusing device. The Figure 2 (b) showed a microbubble generation. The tungsten wire (Φ 100 µm) is inside a glass tube (Φ 300 µm).

4 Result and discussion

Figure 3 (a) shows the cross section of tissue injected with 1.1-µm diameter fluorescence beads suffering 25 W microbubbles. The left image is the sample suffering microbubbles, and the right image is the sample suffering microbubbles and shock wave focusing. The pictures are fluorescence from tissue injected with beads (up), and the binarized images to obtain the injection depth (down). The white dotted line is used to indicate the location of the tissue surface. The mean injection depths were 20, 220, 250, 380, and 600 µm at power of 0 (control), 20, 25, 30, and 35 W suffering microbubble. The mean injection depths were 20, 350, 570, 690, and 830 µm at power of 0 (control), 20, 25, 30, and 35 W suffering microbubble and shock wave focusing. Figure 3 (b) showed the injection depth at each power with/without the shock wave focusing.

At the result of injection without shock wave focusing, from power 20 W to 35 W, the injection depth increased with the power increasing. When the power is higher, the generated microbubble diameter would become larger, so the mechanical energy of microjet and shock wave would be stronger, which would make perforation deeper. When power is higher than 35 W, the depth of injection will continue to rise, but the heat generated by the discharge will burn the tissue. There is error of injection depth at each power. The reason for the error is that the group used for the experiment is not a homogeneous material and its density varies at different locations. At the result of injection with shock wave focusing, from power 20 W to 35 W, the injection depth increased with the power increasing, and the injection depth at each power was deeper than the samples of same power without the shock wave focusing. The injection depth was improved 230 µm. By imaging the shock wave and focused shock wave, we found that the shock wave was not fully reflected. There are two reason we thought may cause this, the unevenness of the surface of the reflector and the shift of the centre point of the microbubbles during microbubble generation.

5 Conclusion

In this work, we proposed the injection depth improvement by microbubble needle-free injection through focusing the shock wave from microbubble collapse. Our result showed that the injection depth increased with power creasing. The developed shock wave focusing device improved the injection depth comparing to injection without shock wave focusing. The maximum injection was 830 µm. In the future, we will improve the shock wave focusing device to achieve a higher injection depth by electrically induced microbubble needle-free injection.

6 Acknowledgements

This work was supported by JSPS KAKENHI Grant Number (JP22K18783, JP22H00198), JST Moonshot R&D (JPMJMS2217-3-1), and JST SPRING, Grant Number JPMJSP2136.

7 Literature

[1] Ali Khan, Anokhi, et al. "Examining unsafe injection practices associated with auto-disable (AD) syringes: a systematic review." Human vaccines & immunotherapeutics 17.9 (2021): 3247-3258.

[2] Barolet, Daniel, and Antranik Benohanian. "Current trends in needle-free jet injection: an update." Clinical, cosmetic and in```vestigational dermatology (2018): 231-238.

[3] Yamashita, Yu, Shinya Sakuma, and Yoko Yamanishi. "On-Demand Metallization System Using Micro-Plasma Bubbles." Micromachines 13.8 (2022): 1312.

[4] Huang, Wenjing, et al. "Viscosity-aided electromechanical poration of cells for transfecting molecules." Lab on a Chip 22.22 (2022): 4276-4291.

[5] K. Ichikawa, S. Maeda and Y. Yamanishi : “Evaluation of invasiveness by collapsing of electrically induced bubbles for a needle-free injector”, Journal of Microelectromechanical systems, Vol.27, No.2, pp.305-311 (2018)

[6] O. Lesaint et al., “A comparison of negative and positive,” J. Phys. D. Appl. Phys., vol. J. Phys. D (2001)

[7] J. F. Kolb, R. P. Joshi, S. Xiao, and K. H. Schoenbach, “Streamers in water and other dielectric liquids,” J. Phys. D. Appl. Phys., vol. 41, no. 23 (2008)

[8] G. Paltauf and H. Schmidt-Kloiber, “Photoacoustic cavitation in spherical and cylindrical absorbers,” Appl. Phys. A Mater. Sci. Process., vol. 68, no. 5, pp. 525–532 (1999)

[9] G. Paltauf and P. E. Dyer, “Photomechanical processes and effects in ablation,” Chem. Rev., vol. 103, no. 2, pp. 487–518 (2003)

[10] A. Vogel and V. Venugopalan, “Mechanisms of pulsed laser ablation of biological tissues,” Chem. Rev., vol. 103, no. 2, pp. 577–644 (2003)

[11] A. Vogel, J. Noack et al., : “Mechanisms of femtosecond laser nanosurgery of cell and tissues”, Applied physics B, Vol.81, pp.1015-1047 (2005)

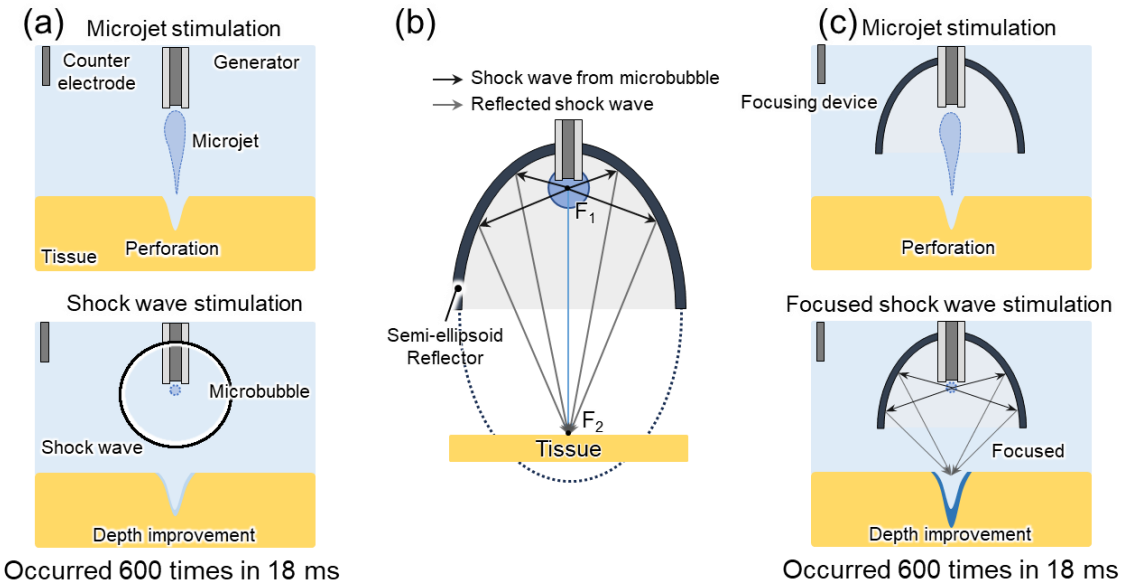

Figure 1 Concept of (a) microbubble tissue perforation, (b) Semi-ellipsoid shock wave focusing reflector and (c) Perforation performance improvement via focusing shock wave from microbubble collapse

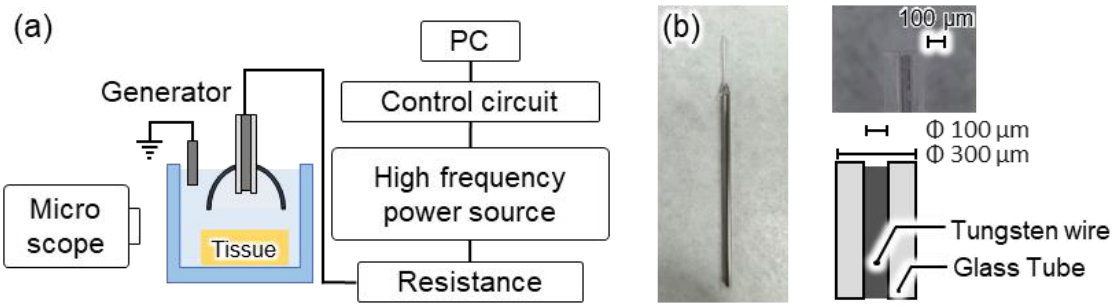

Figure 2 (a) Experimental setup of microbubble tissue injection; (b) Electrically induced microbubble generator

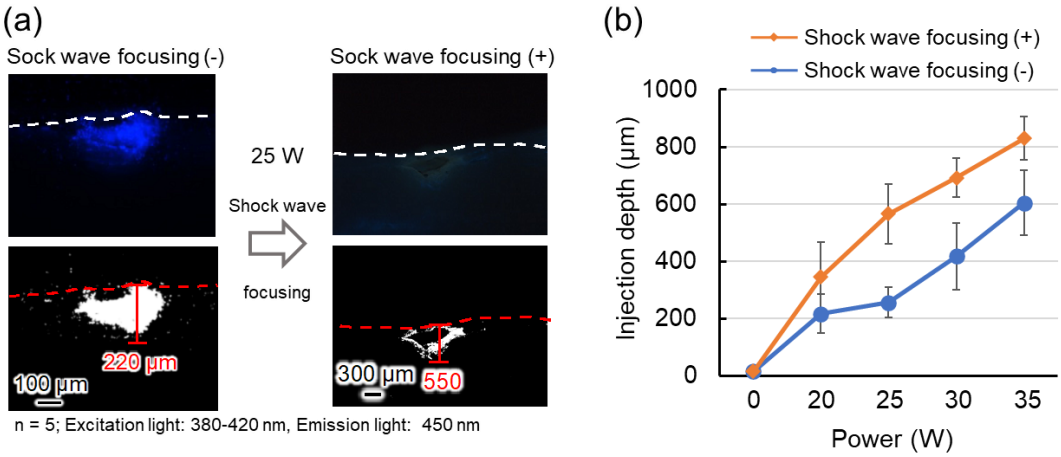

Figure 3 (a) Images of fluorescence from tissue injected with beads (up), and the binarization of fluorescence (down) at power of 25 W; (b) Injection depth at each power with/without shock wave focusing

Computational Study of Fluid Flow in Multi-Stage Pinch Mode MR Valves

Janusz Gołdasz[a], Bogdan Sapinski[b], and Michal Kubik[c]
[a]Cracow University of Technology, Krakow, Poland
[b]AGH University of Krakow, Krakow, Poland
[c]Brno University of Technology, Brno, Czech Republic

Abstract

Magnetorheological (MR) fluids are well-known representatives of smart materials. While in the presence of magnetic field the material develops a yield stress. The technology has been used in the automotive industry in semi-active vehicle suspension applications using MR fluid-based controlled dampers. The vehicle dampers utilize MR valves operating in one of the four fundamental modes, i.e., the flow mode. In the essence, the (existing) conventional flow-mode valves energize the MR fluid by magnetic flux perpendicular to the fluid flow path. In the study the authors explore opportunities for extending the dynamic range of controlled MR valves operating in pinch mode. By convention, a pinch mode valve would feature a single constant cross-section area flow channel with magnetic poles located in it over which non-uniform magnetic field is induced. The single pole-gap pair is a so-called valve stage assembly. Here, the authors examine ways of extending the dynamic range of pinch mode valves by employing a number of valve stages in series in the channel. The authors examine various scenarios based on variations of the number of stages in the channel and the number of solenoids in the valve assembly. To accomplish this, the authors propose a magnetostatic model of the MR pinch mode valve that is one-way coupled with a CFD (computational fluid dynamics) model of the flow channel, and then execute a parametric study to estimate the pinch valve output changes with respect to the number of stages and the solenoids in the valve. The results are then presented in the form of plots of averaged pressure drop vs volumetric flow rate, respectively, at various levels of ampere turns (or coil current). To summarize, the obtained results reveal improvements in the pinch mode valve dynamic range, however, challenges in reducing the magnetic flux leakage between the neighbouring poles are evident at the same time.

1 Introduction

Since the invention by J. Rabinov [1], magnetorheological (MR) fluids have been researched and utilized in several application areas, to name only vibration reduction or optical finishing [2]. The materials when subjected to magnetic fields develop a yield stress of sufficient magnitude to be exploited in in the above mentioned applications. The fluids can be operated in one of the the four fundamental modes: flow (valve) mode, shear (rotary) mode, squeeze mode and (the least explored) gradient pinch mode [2, 6, 4, 3]. Contrary to the other operating modes, in pinch mode the magnetic field distribution is designed to be nonhomogenous in the flow channel, i.e. the flux density is configured to be the highest in the zone adjacent to the wall and (ideally) zero in the center of the channel. Moreover, it is orientated in parallel to the direction of the fluid flow. The result is what has been often described as the Venturi type controlled semi-orifice achieved solely by material property modifications. The effect was first demonstrated by Goncalves and Carlson [4, 5] who claimed to have developed a method of varying the effective diameter of the flow channel filled with MR fluid upon the application of non-uniform magnetic fields. That was followed by several (mostly experimental) research studies and analyses, to name only [8]. Modeling studies are still rare [8, 9]. They are complicated by the non-stationary nature of the phenomenon and perhaps the need to model the behaviour of individual particles incl. collisions. It is likely that in the presence of magnetic fields the iron particle concentration within the pinch zones varies not only spatially but also with time as the particles are attracted to the pinch zones. Most of the existing works utilize the single-stage pinch valve concept [10]. In addition to that, the authors have carried out an experimental study of a multi-stage MR pinch valve [11]. The outcome of this research allows to conclude on the valve's output increase with the larger number of stages in the flow channel, however, at a cost of significant magnetic flux leakage.

Given the above challenges, the purpose of the present study is to develop a simple one-way CFD-FE (CFD – Computational Fluid Dynamics, FE – Finite Element) model for sizing a multi-stage pinch mode MR valve and provide some estimates of the pressure drop vs flow rate valve's characteristics. To accomplishe the goal, the authors describe the two-stage pinch valve concept. That is followed by the results of a magnetostatic analysis, and the application of the previously developed one way weakly coupled CFD-FE model to estimate the valve's performance. Conclusions are also provided as to the future goals and computing challenges.

2 Valve

This research was based on the concept described in [7, 10], and the reader should refer to prior art for a detailed description of the test rig and the single-stage valve assembly. Briefly, the two-stage valve illustrated in Fig. 1 reveals the thru-hole, the solenoid assembly (1) incl. the coil (2) of $N = 300$ copper wire turns and a magnetic core. The fluid in the channel (4) is subjected to the magnetic field generated by the coil's current up to $I = 4$ A (or 1200 ampere turns). The diameter of the flow channel is 3 mm, and its length 30 mm. The neighbouring poles are separated by non-magnetic spacers (pinch gaps) (3) (not shown in the illustration); the distance between the poles is 1 mm. Moreover, the assumed fluid's properties are as follows: fluid – 22 % Fe vol. MR fluid, viscosity – 103 cP, density – 2.6 g/cc, solenoid material – low carbon steel alloy SAE1018. The MR material fundamental characteristics (yield stress vs flux density, magnetisation) were acquired using the Anton Paar MCR 302 magnetocell and Lake Shore 707 VSM (Vibrating Sample Magnetometer) measurements, respectively.

3 Magnetostatic analysis

The magnetostatic analysis was conducted using the geometry highlighted in Fig. 1. The calculations were performed within the input current range from 0.5 A to 4 A in 0.5 A steps. Selected results are presented in Figs. 2 to 5.

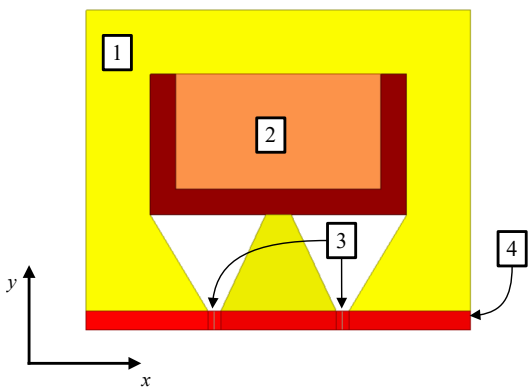

Figure 1 Magnetostatic model overview, 1 – core, 2 – coil assembly, 3 – pinch gap(s), 4 – flow channel

In particular, Figs. 2 and 3 reveal the magnetic flux density B maps in the solenoid and the flow channel computed at the current levels $I = 1$ A and $I = 4$ A, respectively. Furthermore, Figs. 4 and 5 highlight the flux density variation in the axial direction (computed along the main axis) and the direction perpendicular to the fluid flow at both pinch gap locations. The results illustrate that the highest magnetic flux density can be located in the regions above the pinch gaps. Moreover, as the current increases the difference between the flux density in the zone adjacent to the wall and the flux density level at the center of the flow channel increases. The results in the form of spatial B maps provide a valuable input information for the subsequent CFD analysis.

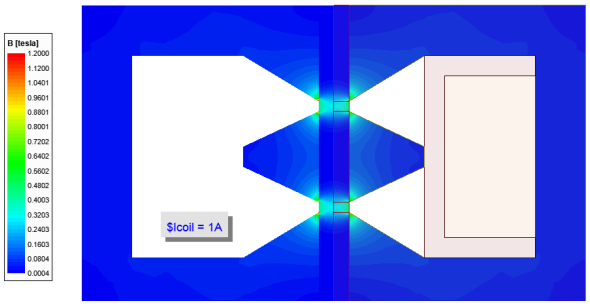

Figure 2 Flux density map, $I = 1$ A (300 ampere turns)

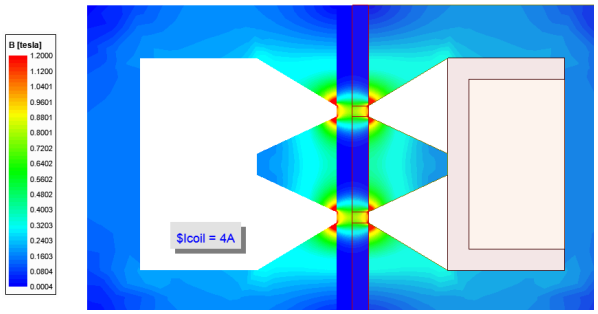

Figure 3 Flux density map, $I = 4$ A (1200 ampere turns)

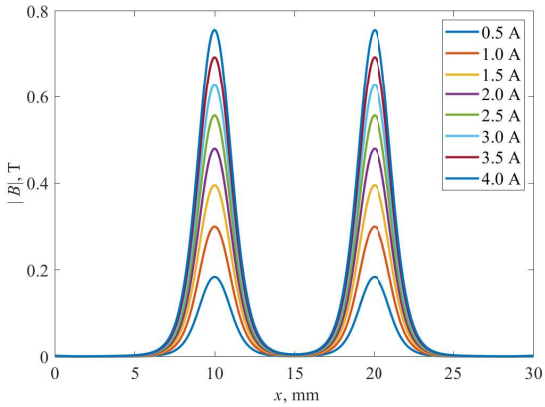

Figure 4 Flux density variation along the flow channel's main axis at various coil current levels

4 Fluid flow model

As already stated, this type of analysis could not be performed using only magnetostatic field calculations. Given the nonhomogenous nature of the phenomenon the coupled approach is required [9]. As such, the magnetostatic analysis is carried out to yield static magnetic flux density distributions corresponding to specific coil current inputs, and then the CFD model is developed based on the geom-

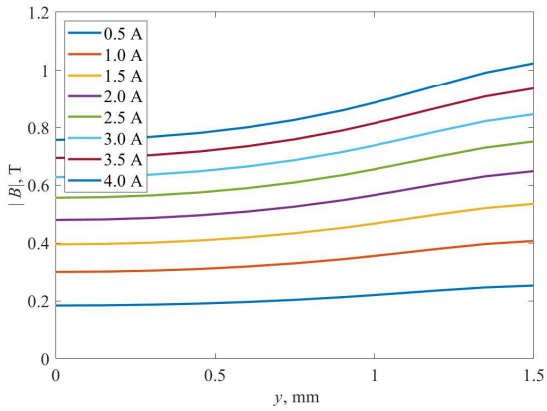

Figure 5 Flux density variation at pinch gap locations in the direction perpendicular to the fluid flow at various coil current levels

etry seen in Fig. 1 and the computed flux density maps in the flow channel. This is to allow for calculating the yield stress distributions in the fluid. The analysis was then performed within the above mentioned current range and the fluid's mean gap velocity V up to appr. 1.1 m/s. The obtained results can be observed, e.g. in Figs. 6 to 8.

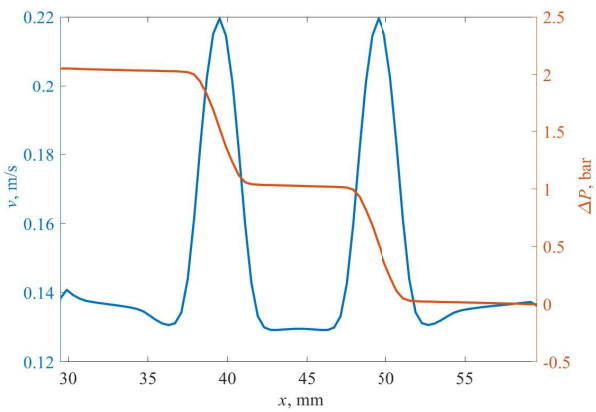

Figure 6 Velocity and pressure distribution in the flow channel in the axial direction, $I = 4$ A, $V = 0.1$ m/s

Specifically, Fig. 6 shows the pressure drop change in the axial direction (i.e. along the length of the flow channel), and the accompanying fluid velocity change calculated at the center of the thru-hole. The illustration shows the fluid accelerates at the pinch gap locations. Moreover, the pinch gaps regions most contribute to the observed pressure drop changes. This statement is reinforced by the observations of the ęxemplary flow velocity contour maps in Fig. 7. Next, Fig. 8 illustrates the obtained pressure drop vs gap velocity (or flow rate) relationship. The results show the increase in the pressure drop when compared the single-stage valve as in [11], however, the change in the $\Delta P - V$ curve slope was not captured with this approach. It is likely that the model underestimates the shear stress levels in the near-the-wall areas, and, hence, the problems in predicting

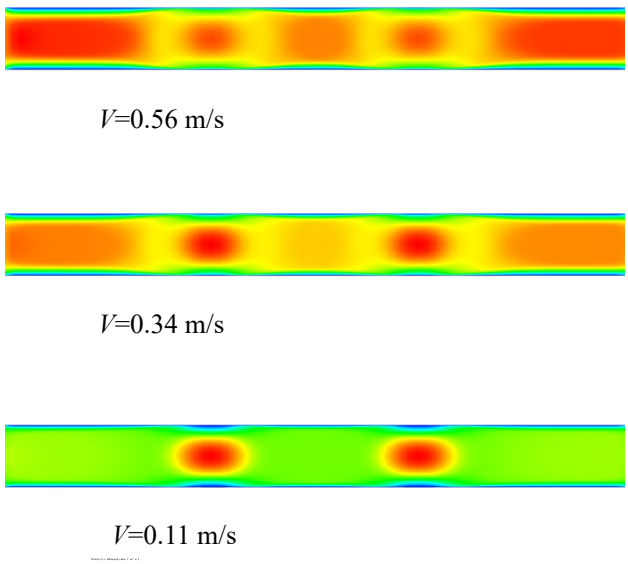

Figure 7 Velocity map in the flow channel, $I = 4$ A (1200 ampere turns)

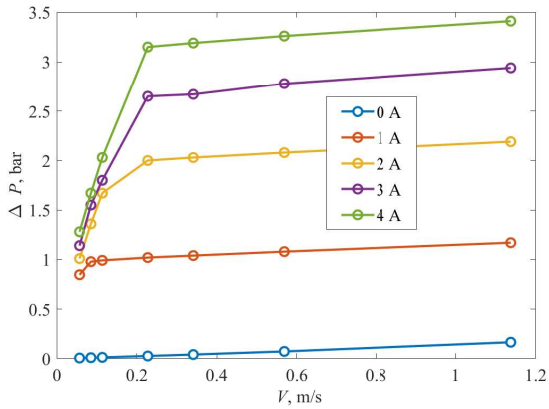

Figure 8 Pressure drop vs gap velocity

the curve slope variation at the higher fluid flow velocities.

5 Summary

The study reveals the results of a preliminary CFD analysis targeted at estimating the output of a multi-stage pinch mode MR valve. The data reveal the increase in the pressure drop vs the previously analyzed single-stage pinch mode valve configurations [10], however, the change in the $\Delta P - Q$ or $\Delta P - V$ curve slope could not be captured with this one-way coupled model. It is likely that the inefficiency of the model is due to its inability to handle the local accumulation of the particles in the high flux concentration zones between the neighbouring poles [12] and the problems in estimating the resulting shear stress levels. It is, therefore, planned to employ more sophisticated computing schemes to model the behaviour of the suspension on the micro scale for tracking the individual particle tra-

jectories and their collisions.

Acknowledgment

The authors wish to acknowledge the support of the Czech Science Foundation (GACR) and the National Science Center (NCN, Poland) – grant IDs: GACR 21-45236L (CZ) & 2020/39/I/ST8/02916 (PL)

6 Literature

[1] Carlson, J. D., Schwartz, M.: Magnetorheological fluids. Smart Materials, CRC Press, New York, 2008.

[2] Jolly, M., Bender, J.W., Carlson, J.D.: Properties and applications of commercial magnetorheological fludis. Journal of Intelligent Material Systems and Structures. Vol. 10, 1997, pp. 1–5

[3] Farjoud, A., Cavey, R., Ahmadian, M.: Magnetorheological fluid behaviour in squeeze mode. Smart Materials and Structures. Vol. 18, No. 9, 2009, 095001

[4] Carlson, J.D., Goncalves, F.D., Catanzarite, D., Dobbs, D.: Controllable magnetorheological fluid valve, devices and methods. US Patent App. No. 11/844, 2007

[5] Goncalves, F., Carlson, J.D.: An alternate operation mode for MR fluids – magnetic gradient pinch. Journal of Physics: Conference Series. Vol. 149, 2009, 012050

[6] Wereley, N., Cho, J., Choi, Y.-T., Choi, S.B..: Magnetorheological dampers in shear mode. Smart Materials and Structures. Vol. 17, 2007, 015022

[7] Goldasz, J., Sapinski, B.: Magnetostatic analysis of a pinch mode magnetorheological valve. Acta Mechanica et Automatica. Vol. 17, No. 3, 2017, pp. 229–232

[8] Lee, T.H., Kang, B.H., Choi, S.B.: A quasi-static model for the pinch mode analysis of a magnetorheological fluid flow with an experimental analysis. Mechanical Systems and Signal Processing. Vol. 134, 2019, 106308

[9] Gołdasz J, Sapiński B, Kubik M, Machacek O, Bańkosz W.: Pinch mode magnetorheological flow bench: fluid flow analysis. In: Saravanos D, Benjeddou A, Chrysochoidis N, Theodosiou T, eds. SMART2023 : 10th ECCOMAS Thematic Conference on Smart Structures and Materials, 3-5 July 2023, Patras, Greece. Mechanical Engineering & Aeronautics Department. University of Patras; 2023, pp. 1373–1380

[10] Kubík, M., Gołdasz, J., Macháček, O., Strecker, Z., Sapiński, B.: Magnetorheological fluids subjected to non-uniform magnetic fields: experimental characterization. Smart Materials & Structures. Vol. 32, 2023, 1–13

[11] Žáček, J., Goldasz, J., Sapiński, B., Sedlačík, M., Strecker, Z., Kubík, M.: Assessment of the dynamic range of magnetorheological gradient pinch-mode prototype valves. Actuators. Vol. 2023, 2023, pp. 1–14.

[12] Kubík, M., Žáček, J., Gołdasz, J., et al. Grasping the behavior of magnetorheological fluids in gradient pinch mode via microscopic imaging. Physics of Fluids. Vol. 36, 2024, pp. 1–10

Rheological properties of abrasive magnetorheological fluids for immersed tumbling processes

Fabian Sordon[a], Christian Lahoda[b], Eckart Uhlmann[b,c] and Jürgen Maas[a]
[a]Mechatronic Systems Lab EMK, Technische Universität Berlin, Berlin, Germany
[b]Technische Universität Berlin, Institute for Machine Tools and Factory Management, Berlin, Germany
[c]Fraunhofer Institute for Production Systems and Design Technology, Berlin, Germany

Abstract

Micro-milling tools face challenges related to wear and edge homogeneity, which are addressed through various post-processing methods including grinding with magnetorheological fluids (MRF). This paper explores the rheological properties of abrasive MRF, crucial for optimizing performance of recently investigated MRF immersed tumbling processes. A full factorial design of experiments investigates the effects of carbonyl iron particle (CIP) and abrasive particle (AP) volume fractions and AP diameter on yield point and dynamic viscosity. Using a specially developed rheometer test bench 27 different MRF compositions are evaluated. Results show that increasing CIP and AP volume fractions heighten shear stresses, while smaller AP diameters enhance shear stresses due to their solid-state chain embedding.

1 Introduction

To mitigate cutting edge wear in micro-milling tools and ensure uniform edge radii, various cutting-edge preparation methods such as brushing, blasting, electrochemical machining, laser ablation, magnetic finishing, and immersed tumbling are employed for post-processing [1], [2]. Presently, grinding processes involving magnetorheological fluids (MRF) are emerging as crucial technologies [3]. We previously investigated an innovative immersed tumbling process utilizing MRF for directed processing under an applied magnetic field and explored the material removal rate for different MRF compositions [4]. In the process shown in **Figure 1**, abrasive MRF is magnetically excited to form solid-state chains. Samples made of high-speed steel are then moved relative to the MRF, resulting in an abrasive effect. Promising outcomes were attained, as the process combines straightforward plant engineering with high material removal rates due to the adjustable flow resistance of the MRF [4]. **Figure 2** illustrates the edges of a workpiece made of high-speed steel before and after the immersed tumbling process for an abrasive MRF composition featuring the highest material removal rate [4].

In this study, our aim is to examine the influence of fluid composition on the rheological properties of abrasive MRF, which significantly impact process performance. A common approach to model MRF behavior is the Bingham model $\tau(B,\dot{\gamma}) = \tau_0(B) + \eta \cdot \dot{\gamma}$, where $\tau(B,\dot{\gamma})$ is the shear stress, $\tau_0(B)$ the yield point and η the dynamic viscosity. This investigation addresses several questions: How does the volume fraction of abrasive particles (AP) or carbonyl iron particles (CIP) affect the yield point $\tau_0(B)$ and the dynamic viscosity η in the MRF? Does the diameter of the abrasives have any effect on the rheological properties? To achieve this, a full factorial design of experiment is conducted, varying the CIP volume fraction φ_{CIP}, AP volume fraction φ_{AP} and AP diameter d_{AP}. The corresponding yield point and dynamic viscosity are measured using a modified rheometer based on the test bench outlined in [5]. Based on these measurements, the composition variables are correlated with the maximum yield point. This research provides a fundamental understanding of the rheological properties of abrasive MRF and facilitates a criteria-based selection of MRF composition.

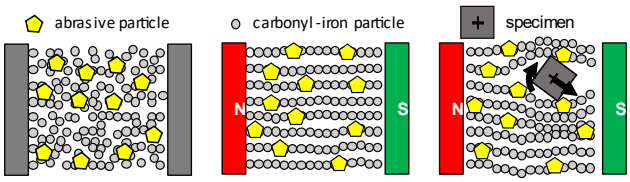

Figure 1 Schematic diagram of the novel immersed tumbling process using MRF. Grinding effect by means of relative movement of a workpiece within magnetically excited abrasive MRF.

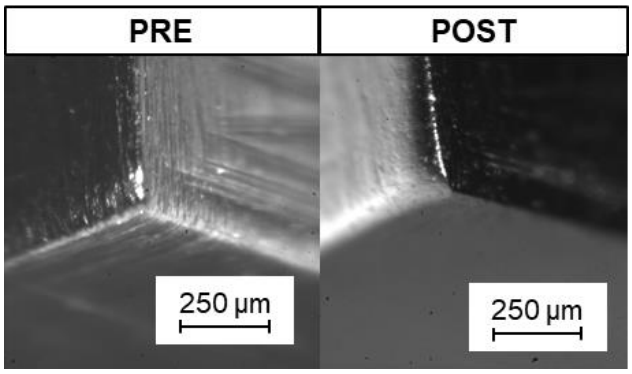

Figure 2 Workpiece edges before and after the MRF immersed tumbling process for the abrasive MRF composition $d_{\mathrm{AP}} = 297$ µm, $\varphi_{\mathrm{CIP}} = 45$ % and $\varphi_{\mathrm{AP}} = 15$ % causing maximum material removal rate as presented in [4].

2 Materials and methods

2.1 MRF test bench

In order to ascertain the rheological characteristics, specifically the yield point $\tau_0(B)$ and the dynamic viscosity η, a

rheometer, previously employed in a study [4], was utilized. Given the rheometer's high sensitivity to the quantity of MRF introduced into its container, modifications were made to its rotor geometry for this investigation. Instead of employing a purely cylindrical configuration, a cylindrical shaft groove was incorporated to enhance magnetic properties and impede the flow of MRF towards the upper portion of the rheometer. The structure and finite element (FE) simulation of the modified rheometer for a coil current of 5 A are depicted in **Figure 3**. It comprises a stator housing a coil encased by 11SMn30 steel and an externally bearing-mounted rotor. Together, they establish an axial shear gap where the MRF is situated. The design target was selected to achieve approximate homogeneity in the magnetic flux density within the shear gap. An overview of the rheometer test bench is provided in **Figure 4**, illustrating the test bench setup for a typical experiment both during and after the test. The rheometer stator is fixed to a linear guidance system to facilitate the straightforward handling of the MRF filling and cleaning procedures. The rotor's bearing is externally positioned and aligned with respect to the rheometer stator. Torque measurement is conducted utilizing a torque sensor, namely the DATAFLEX 16/10 model manufactured by KTR SYSTEMS GMBH, Rheine, Germany, while magnetic flux density monitoring is achieved through Hall-sensors, calibrated with the TESLAMETER FM302 instrument from PROJEKT ELEKTRONIK MESS- UND REGELUNGSTECHNIK GMBH, Berlin, Germany. The rheometer was evaluated using an MRF containing 47 vol.% CIP. As shown in **Figure 5**, the obtained results were compared with the datasheet of a 47 vol.% BASONETIC ® 5030 MRF from BASF SE, Ludwigshafen, Germany, which exhibits very similar shear stress curve characteristics as our reference MRF.

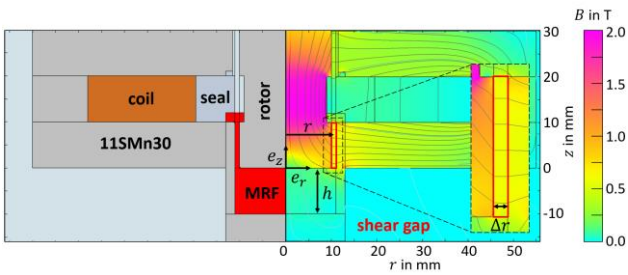

Figure 3 FE-simulation of the rheometer for abrasive MRF.

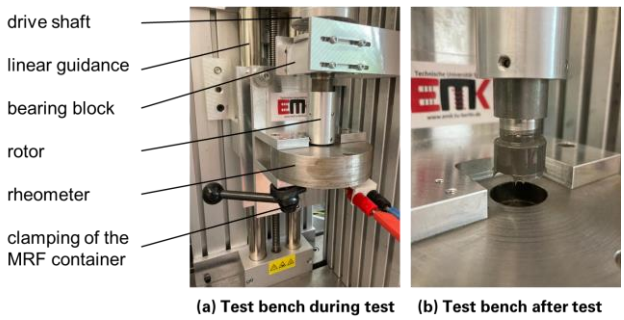

Figure 4 Rheometer test bench for abrasive MRF.

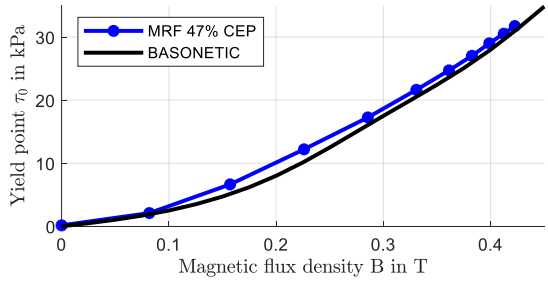

Figure 5 Yield point $\tau_0(B)$ for a reference 47 vol.% reference compared to BASONETIC® 5030 MRF.

2.2 Preparation of MRF

In the rheological investigation undertaken in this study, various MRF compositions were synthetized. We follow the MRF compositions outlined in our prior study, which examined material removal rates, wherein CIP volume fraction φ_{CIP}, AP volume fraction φ_{AP} and AP diameter d_{AP} were varied across three distinct factor levels [4]. **Table 1** presents the corresponding numerical values for each factor level. Three different types of diamond particles with varying diameters (SYM 8-16, FRD-A D107 and FRD-A D252) from VAN MOPPES & SONS SA, Carouge, Switzerland, were chosen as abrasive particles, as depicted in **Figure 6**. Additionally, CIP with a diameter of $d_{\mathrm{CIP}} = 6\ \mu\mathrm{m}$ were utilized, and polyalphaolefin oil served as the carrier fluid. The components were homogenized using the T 25 EASY CONTROL dispersing instrument from IKA, Staufen, Germany.

Input	Factor levels		
	-1	0	1
CIP volume fraction φ_{CIP} in %	20.00	32.50	45.00
AP volume fraction φ_{AP} in %	3.00	9.00	15.00
AP diameter d_{AP} in µm	12.30	148.60	296.70

Table 1 Factor levels of the MRF composition parameters.

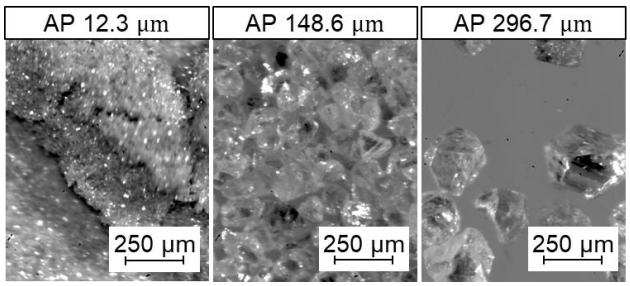

Figure 6 Abrasive particles $d_{\mathrm{AP}} = 12.3\ \mu\mathrm{m}$, $d_{\mathrm{AP}} = 148.6\ \mu\mathrm{m}$ and $d_{\mathrm{AP}} = 296.7\ \mu\mathrm{m}$ from VAN MOPPES & SONS SA.

2.3 Design of experiment

In this investigation, we employ a full-factorial design of experiments involving three input variables with three factor levels $[-1,0,-1]$ resulting in $3^3 = 27$ MRF distinct

compositions and corresponding experiments. In each experiment, we determine the yield point $\tau_0(B)$ and dynamic viscosity $\eta(\dot{\gamma})$ by measuring the torque M_m while varying the rotational speed ω or the magnetic flux density B. The effective torque, accounting for MRF viscous properties, is represented by $M = M_\mathrm{m} - M_\mathrm{f}$, where M_f denotes the friction torque. Following [7] and [8] while assuming a homogeneous flux density B and neglectable small shear rate $\dot{\gamma}$, the yield point $\tau_0(B)$ can be directly derived from $M(B)$ using

$$\tau_0(B) = \frac{M(B)}{2\pi\, l\, r^2}, \tag{1}$$

where r represents the averaged shear gap diameter and l is the shear gap length, determined by the rheometer's geometries depicted in **Figure 3**. However, for $\eta(\dot{\gamma})$, both the active axial shear gap and the radial shear gap must be considered, as the MRF is located both in cylindrical and disc arrangements. Given that $\tau = \eta \cdot \dot{\gamma}$ holds for $B = 0\,T$ according to the Bingham model and $\dot{\gamma} = r/\,\Delta r \cdot \omega$, the equation

$$M(\eta, \omega) = 2\,\pi \left(\frac{l\, r^3}{\Delta r} + \frac{r^4}{4h} \right) \cdot \omega \cdot \eta, \tag{2}$$

is derived for the effective torque, where Δr represents the shear gap width and h is the radial shear gap width. Thus, $\eta(\dot{\gamma})$ can be derived from $M(\eta, \omega)$ using

$$\eta = \left(2\,\pi \left(\frac{l\, r^3}{\Delta r} + \frac{r^4}{4h} \right) \omega \right)^{-1} \cdot M. \tag{3}$$

Through the obtained characteristic curves $\tau_0(B)$ and $\eta(\dot{\gamma})$ for the 27 MRF compositions under investigation, a qualitative analysis of rheological characteristics is feasible. Nonetheless, we aim to deduce a general function from the comprehensive experimental dataset that maps the input parameters φ_CIP, φ_AP and d_AP to a target value. To achieve this, we designate the maximum yield point τ_max as the most influential value on overall process performance, determined by evaluating the yield point $\tau_0(B)$ at $B = 0.4$ T. To derive general expressions for τ_max, we presume a trivariate polynomial of second order

$$\begin{aligned} \tau_\mathrm{max} = g(x_1, x_2, x_3) \\ &= \alpha_0 + \alpha_1 x_1 + \alpha_2 x_2 \\ &+ \alpha_3 x_3 + \alpha_4 x_1 x_2 \\ &+ \alpha_5 x_1 x_3 + \alpha_6 x_2 x_3 \\ &+ \alpha_7 {x_1}^2 + \alpha_8 {x_2}^2 + \alpha_9 {x_3}^2, \end{aligned} \tag{4}$$

where $\{x_1, x_2, x_3\}$ represent the normalized corresponding variables for $\{\varphi_\mathrm{CIP}, \varphi_\mathrm{AP}, d_\mathrm{AP}\}$. The coefficients $[\alpha_0, \ldots, \alpha_9]$ of the polynomial can then be estimated via a regression algorithm based on the measurements. Subsequently, the parameterized estimation model $g(x_1, x_2, x_3)$ can be maximized to derive the parameters leading to the largest τ_max.

3 Results

The MRF components were homogenized using a dispersing instrument according to the specified MRF composition parameters detailed in **Table 1**. Following the full-factorial DOE, a total of 27 distinct MRF compositions were synthetized. Subsequently, experiments were conducted to determine the yield point $\tau_0(B)$, maximum yield point τ_max and dynamic viscosity $\eta(\dot{\gamma})$. To achieve this, the respective MRF was filled into the rheometer of the developed test bench. The dynamic viscosity η was determined across shear rates ranging from 0 to $2250/s$, while the yield point τ_0 was identified for magnetic flux densities B spanning 0 to $0.42\,T$ at a shear rate $\dot{\gamma} = 66/\mathrm{s}$. During the mixing process, it was found that no homogeneous MRF could be produced from one composition $\varphi_\mathrm{CIP} = 45\%$, $\varphi_\mathrm{AP} = 15\%$ and $d_\mathrm{AP} = 12.3$ µm. Instead, the experiment was repeated with the MRF composition of $\varphi_\mathrm{CIP} = 45\%$, $\varphi_\mathrm{AP} = 9\%$ and $d_\mathrm{AP} = 12.3$ µm.

The coefficients $[\alpha_0, \ldots, \alpha_9]$, depicted in **Figure 7**, were subsequently estimated forming the trivariate model $\tau_\mathrm{max} = g(x_1, x_2, x_3)$. By maximizing the model quantity, the target normalized variables $\boldsymbol{x}_\mathrm{t} = [1.0,\ 0.906, -1.0]$ were determined, corresponding to the composition parameters $\varphi_\mathrm{CIP} = 45\%$, $\varphi_\mathrm{AP} = 14.76\%$ and $d_\mathrm{AP} = 12.3$ µm. According to the model, an increase in CIP and AP volume fractions (φ_CIP, φ_AP) in the MRF leads to a larger maximum yield point τ_max, while an increase in AP diameter d_AP results in a smaller magnitude of τ_max.

This correlation is also qualitatively observed in the yield point curves $\tau_0(B)$. The upper diagrams in **Figure 8** illustrate the averaged yield point curves across all factor levels $[-1{,}0, -1]$ of the input parameters φ_CIP, φ_AP and d_AP. Within the upper left diagram, the influence of φ_CIP is illustrated, where $\tau_0(B)$ exhibits a notably greater magnitude for $\varphi_\mathrm{AP} = 45\%$ compared to other factor levels. Conversely, the upper middle diagram demonstrates that the magnitude of $\tau_0(B)$ diminishes for lower AP volume fractions ($\varphi_\mathrm{AP} = 3\%$), yet displays no significant difference for larger values ($\varphi_\mathrm{AP} = 9\%$ and $\varphi_\mathrm{AP} = 15\%$). Furthermore, the upper right diagram reveals that a relatively elevated magnitude of $\tau_0(B)$ is observed for lower AP diameters ($d_\mathrm{AP} = 12$ µm). This observation aligns with findings presented in [6], where it was established that greater deviations between CIP and AP diameter result in diminished yield stress.

Furthermore, insightful correlations between MRF composition and dynamic viscosity are evidenced in the lower diagrams of **Figure 8**. An observed increase in dynamic viscosity $\eta(\dot{\gamma})$ for larger CIP and AP volume fractions (φ_CIP, φ_AP) aligns with expectations, indicating a significant increase in MRF viscosity. Additionally, smaller AP diameters $d_\mathrm{AP} = 12$ µm result in a larger dynamic viscosity $\eta(\dot{\gamma})$.

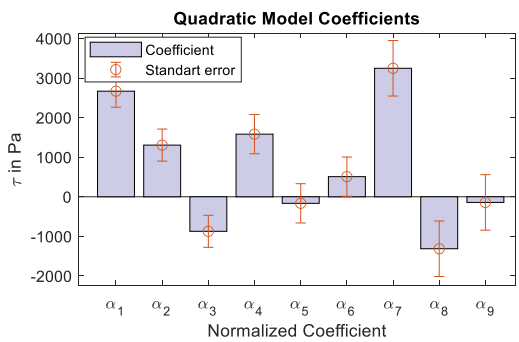

Figure 7 Estimated model parameters and estimation error.

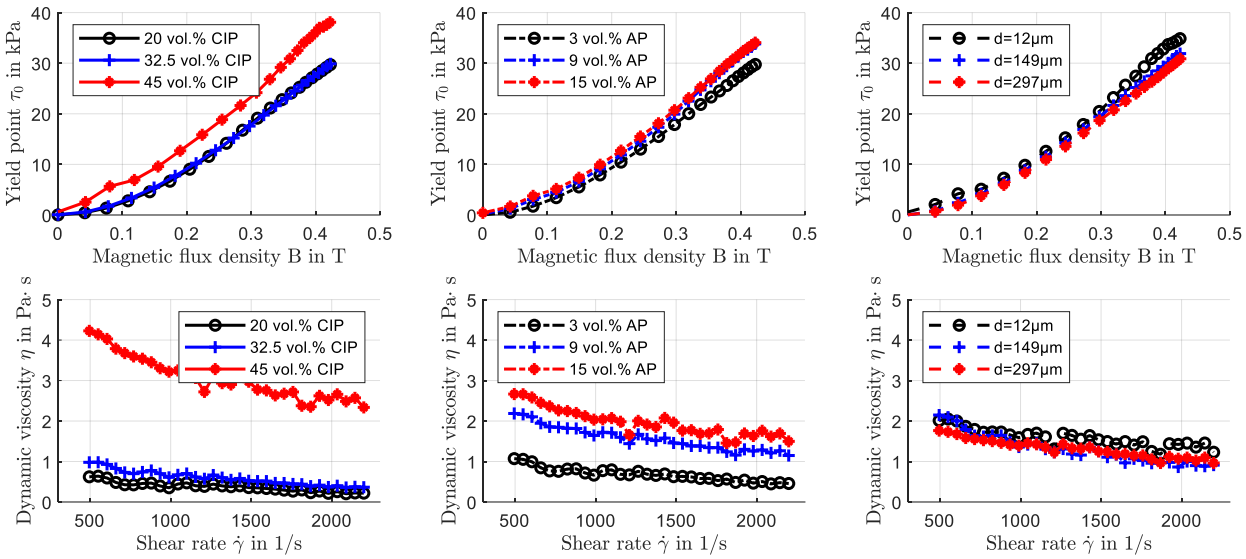

Figure 8 Averaged courses of yield point curves $\tau_0(B)$ and dynamic viscosity curves $\eta(\dot{\gamma})$ for varying CIP volume fraction φ_{CIP}, AP volume fraction φ_{AP} and AP diameter d_{AP}.

4 Conclusion and outlook

In this study, extensive rheological investigations were conducted to characterize MRF intended for use in innovative MRF immersed tumbling processes. Diverse MRF compositions were synthetized, varying the CIP volume fraction, AP volume fraction and AP diameter. Subsequently, 27 rheological tests were performed using a modified abrasive rheometer developed for this purpose. The following findings were observed:

- A significant rise in shear stresses was noted with an increase in the volume fraction of CIP (45%).
- Similarly, heightened shear stresses were observed with an increase in the volume fraction of AP (14.8 %), attributed to the reduced volume fraction of the carrier fluid.
- AP with a diameter (12.3 µm) comparable to that of CIP exhibited higher shear stresses compared to larger AP diameters, facilitated by their embedding in solid-state chains [6].

In future work, our object is to merge the employed model with models that encompass relevant target variables such as material removal rate and surface roughness.

5 Acknowledgements

The authors thank the German research foundation DFG for funding this project (project number 503335130). Special thanks go to the student assistants in this project, Niklas Buhl and Noureddine Jarmouni, for their excellent support.

6 Literature

[1] Uhlmann, E., Oberschmidt, D., Kuche, Y. and Löwenstein, A.: Cutting edge preparation of micro milling tools. Procedia CIRP (2014), p. 349 – 354.

[2] Uhlmann E., Oberschmidt D., Kuche Y., Löwenstein A. and Winker I.: Effects of different cutting edge preparation methods on micro milling performance. Procedia CIRP (2016), p. 352-355.

[3] Denkena, B., Köhler, J. and Schindler, A.: Behavior of the magnetic abrasive tool for cutting edge preparation of cemented carbide end mills. Prod. Eng. Res. Devel. 8 (2014), 5, p. 627 – 633.

[4] Sordon, F., Ludwig, J., Hocke, T., Uhlmann, E. and Maas, J.: Abrasive properties of magnetorheological fluids for immersed tumbling processes. ASPE Proceedings (2023), Volume 81, p. 304-309.

[5] Sordon, F., Schreiner, V. and Maas, J.: Rheometer design to investigate abrasive magnetorheological fluids. ERMR Chongqing (2023).

[6] Nagdeve, L., Sidpara, A., Jain, V. K. and Ramkumar, J.: On the effect of relative size of magnetic particles and abrasive particles in MR fluid-based finishing process. Machining Science and Technology (2018), 22 (3), p. 493-506.

[7] Wiehe A. and Maas J.: Magnetorheological actuators with currentless bias torque for automotive applications. Journal of intelligent material systems and structures. JIMSS 21 (2010), 15, p. 1575-85.

[8] Güth, D. and Maas, J.: Characterization and modeling of the behavior of magnetorheological fluids at high shear rates in rotational systems. JIMSS 27 (2016), 5, p. 689 – 704.

Utilization of Sedimentation in Magnetorheological Fluids for Online Rotor Balancing

Valentin Schreiner and Jürgen Maas
Technische Universität Berlin, Fachgebiet Elektromechanische Konstruktionen, 10623 Berlin
Valentin.Schreiner@tu-berlin.de

Abstract

This contribution presents a system for balancing rotating machines during operation. For this purpose, the usually undesirable tendency of magnetorheological fluid to separate due to the difference in density between carbonyl iron particles and the carrier fluid is utilized. Therefore, three chambers on the rotor are filled with magnetorheological fluid. The magnetorheological fluid is stabilized by permanent magnets integrated in the chambers. By selectively influencing the magnetic field of individual chambers with a fixed electromagnet, the separation can now be controlled and thus the mass distribution can be balanced. Following the explanation of the functional principle, the sedimentation behavior of different magnetorheological fluids will be discussed and the functionality of the system is demonstrated using an exemplary balancing process. Finally, an additional application of the system for the experimental investigation of the sedimentation behavior of magnetorheological fluid by measuring the unbalance is presented.

1 Introduction

If the center of mass in a rotating system is not aligned with the axis of rotation defined by the bearing, a speed-dependent excitation occurs. Apart from a few exceptions, this excitation, known as unbalance, is undesirable and can lead to increased wear, acoustic disturbance and transmission of vibrations to the entire system. Therefore, rotating machinery is usually balanced during the manufacturing process. This is done by either removing material on the side of the unbalance or adding material on the opposite side until the excitation is within an application-specific tolerance [1]. However, adding and removing material without additional equipment is only possible when the system is at standstill, so an unbalance that changes during rotation cannot be easily corrected. Online balancing systems fill this gap. These systems allow the unbalance condition to be detected and corrected during rotation. This is made possible by a variety of systems rotating on the rotor. In addition to passive systems such as ball balancers [2] or fluid filled rings [3], where the excitation itself is used to displace balancing elements, there are various approaches to actively influence the mass distribution. Examples include motorized displacement of balancing rings [4] or the injection of liquids during rotation [5]. While passive systems are limited to supercritical speed ranges, active systems require the transport of energy or material to the rotating part of the system. Such systems require slip rings or rotary seals, resulting in relatively complex designs.

One possibility for a simple approach to active online balancing is the utilization of Magnetorheological fluids (MRF). MRF are a suspension of small ferromagnetic carbonyl iron particles (CIP) dispersed in a carrier fluid. When a magnetic field is applied, the normally homogeneous distributed particles form bridges and allow the transmission of a shear stress τ based on magnetic forces. Several articles have presented MRF-based balancing systems, however, they suffer from some of the disadvantages mentioned above and require a complex design [6, 7]. The system proposed in this work is based on the previously presented and relatively simple approaches of the authors [8, 9], but follows a fundamentally different method by using the local particle volume concentration within the MRF for mass balancing.

To provide an overview of the underlying principle, Section 2 focuses on sedimentation in MRF. Section 3 subsequently describes how the system is set up on the rotor to magnetically control this sedimentation and use it for balancing, before the results of a balancing run are presented in section 4. Finally, Section 5 introduces a further application of the system for the optimization of stable MRFs.

2 Sedimentation in MRF and preventive measures

The magnetorheological fluids used in this work are based on a polyalphaolefin oil (PAO) as a carrier fluid with a specific mass of $\rho_{\mathrm{PAO}} = 0.8$ g/ml and CIP with a specific mass of $\rho_{\mathrm{CIP}} = 7.8$ g/ml. Due to the large difference in mass density, a slow separation between the two main components occurs even under the effect of gravitational acceleration. This separation process is called sedimentation. When MRF is filled into a test tube as shown in Figure 1, zones of different particle volume concentration φ can be identified during the sedimentation process [10].

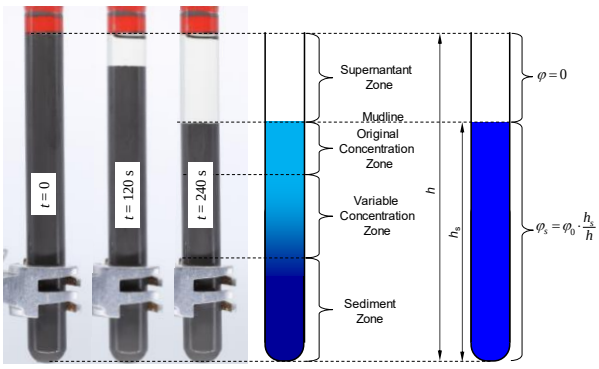

Figure 1 Left: Sedimentation of MRF at different times. Middle: Classifying sedimentation state into different zones after [10]. Right: Simplified approach calculating the average particle concentration below the mudline.

Initially, the MRF has a constant particle concentration over the entire height of the test tube, over time, a clear zone of PAO, the "supernant zone", is formed, in which no particles are contained. Below this, separated by the mudline, is a zone maintaining the original concentration, lying next to a zone where the concentration increases downward. Finally, at the bottom of the test tube is the sediment zone where sedimentation is complete. With increasing duration, the transition zones disappear until the sedimentation process is complete and the mudline forms a separation between the carrier fluid and the sediment. While various measurement methods can distinguish between the different zones, the optical method can only identify the position of the mudline. To simplify matters, as shown on the right in Figure 1 only a distinction between pure carrier fluid and remaining MRF is made, taking the particle concentration as constant for both zones.

As the formation of the shear stress τ is strongly dependent on the particle volume concentration, commercially available products try to prevent sedimentation by using additives in order to maintain the controllability of the MRF. Furthermore, a turbulent flow within the MRF and thus redispersion can be achieved in certain operating states through careful actuator design [11]. Finally, separation can also be prevented by the magnetorheological effect itself. In this approach, which is used for this contribution, the MRF is subjected to a magnetic field, leading to chain formation and consequently the development of a shear stress that counteracts sedimentation and slows it down or even prevents it completely [12, 13].

The MRF used in this work is based on BASF Basonetic 5030 [14], but to increase the sedimentation tendency, no sedimentation inhibitors were added during production, an average particle size of $d_{50} = 100$ µm and a particle volume concentration of $\varphi_0 = 28\%$ were selected.

3 Principle of Operating and magnetic circuit

The system presented takes advantage of the tendency of the MRF to segregate, thus forming areas of different density. To exploit this property, three chambers completely filled with MRF are placed evenly around the circumference of the rotor, as shown in Figure 2. Rotating at the speed ω, the MRF is subjected to a centripetal acceleration that is dominant over the acceleration from the Earth's gravitational field, even at low speeds. This forces the CIP outward, as shown for chamber a in Figure 2. Considering the two components of the MRF, CIP and carrier fluid, separately, the mean center of gravity of all CIPs shifts outward. The mean center of gravity of the carrier fluid shifts slightly in the opposite direction to the axis of rotation. Due to the significantly higher density of the carbonyl iron particles, this results in a shift of the center of mass for the continuum and thus in direction of chamber a of the rotor. However, without magnetic control of the MRF, the same conditions would result in all three chambers, making selective mass balancing impossible. Thus, as shown in Figure 3, two permanent magnets with opposite polarization are positioned in each of the three chambers to provide a homogeneous magnetic field distribution within the chambers and prevent separation. When one of the chambers moves through the cut out of the energized electromagnet, the magnetic field inside the chamber can be displaced by the electromagnet. This results in the condition described above and a shift in the center of mass.

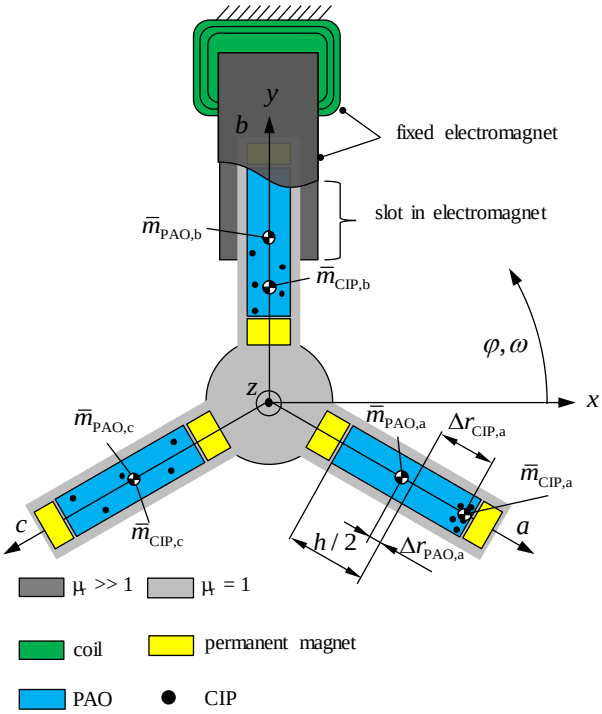

Figure 2 Balancing head with three MRF chambers of different mass distribution. Chamber a: center of gravity in outermost position, chamber b: center of gravity in innermost position, chamber c: center of gravity in neutral position.

Figure 3 shows on the right-side different operating states of the electromagnet and their effect on the magnetic field inside the chamber. For $I_{EM} = 0$ the chamber is shown passing through the electromagnet in off-state. Due to the permanent magnets, the magnetic flux density inside the chamber is approximately B = 250 mT (left part of right figure). The same case is shown for the energized electromagnet $I_{EM} = 5.2$ A at the right part of right figure. As illustrated, this results in a deflection of the magnetic field, causing the magnetic flux density inside the chamber to drop to almost zero allowing the particles to move outwards. This motion causes the shift in particle concentration shown in Figure 2. And, under the simplifying assumption of constant particle concentration in both zones shown in Figure 1, the change in mass imbalance ΔU_i can be calculated according to Equations 1, 2 and 3.

$$\Delta U_i = \Delta r_{CIP,i} \cdot \bar{m}_{CIP,i} - \Delta r_{PAO,i} \cdot \bar{m}_{PAO,i} \tag{1}$$

$$\frac{\varphi_0}{h} = \frac{\varphi_s}{h_s},\ h = h_s + 2\Delta r \tag{2}$$

$$\Delta r_{CIP} = \left(\frac{\varphi_0}{\varphi_s} - 1\right) \cdot \frac{h_s}{2} \text{ and } \Delta r_{PAO} = \frac{\varphi_s}{2} \cdot \frac{h_s \cdot h - h_s^2}{h - h_s \cdot \varphi_s}. \tag{3}$$

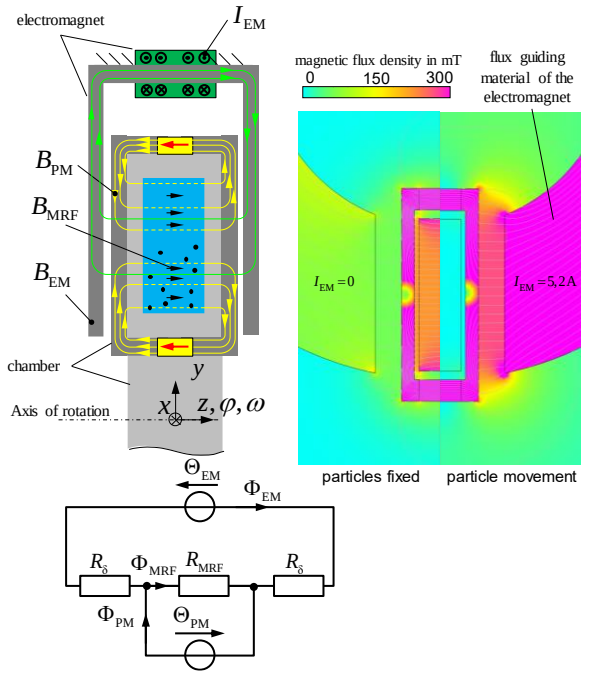

Figure 3 Left: Design of the magnetic circuit. Right: Simulation of the magnetic flux density for different excitations of the electromagnet. Bottom: Equivalent magnetic circuit diagram of the assembly.

4 Experimental validation of the proposed system

To verify the functionality of the presented system, the vibration-based test bench described in [9] is used, as shown in Figure 4. An arbitrary unbalance state is set on the rotor by attaching several additional weights. After accelerating the rotor to an angular velocity of $\omega = 50\ \mathrm{s}^{-1}$, the balancing process is initiated. An algorithm, using sensor signals [8], identifies the chamber in which a CIP displacement will contribute the most to equalize the current unbalance.

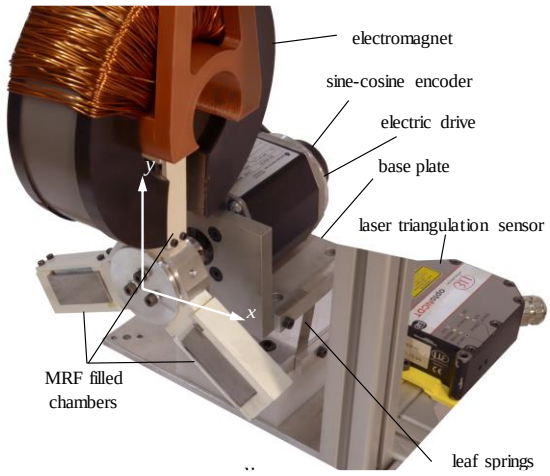

Figure 4 Vibration-based test rig for experimental investigation of the system [9].

The electromagnet is then energized in such a way that the magnetic field in the previously identified chamber is compensated as it passes through the electromagnet. This process is repeated until the unbalance falls below a predetermined threshold.

Figure 5 illustrates the result of such a balancing process. The effect of each chamber can be clearly seen. The initial unbalance condition requires in the first phase correction mainly by chamber a, after an angular position of the unbalance of about 220° is reached, the correction is alternated between chambers a and b. Chamber c does not need to be corrected in this process due to its position relative to the unbalance.

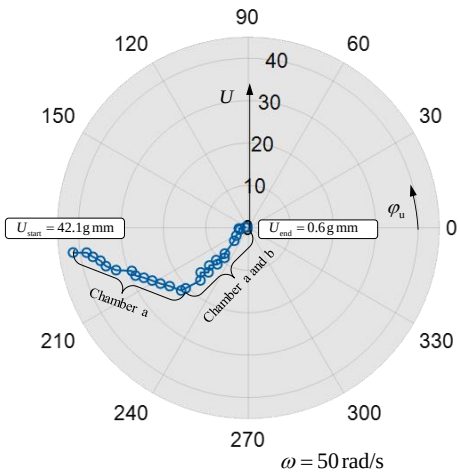

Figure 5 Evaluation steps of the executed balancing process using a discrete algorithm.

Figure 6 shows the result of the balancing process based on the recorded amplitude spectrum. The drop at the first harmonic resulting from the reduced mass imbalance can be clearly identified. Higher harmonic components, which presumably result from interaction between the deactivated electromagnet and the chambers, are slightly damped.

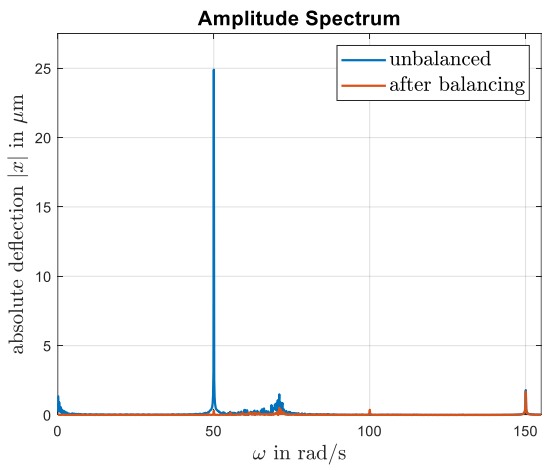

Figure 6 Resulting amplitude spectrum of the executed balancing run.

5 Characterization of the sedimentation behavior of MRF by the proposed balancing system

Apart from using the system for balancing, the setup offers another interesting possibility that can be used in the development of stable MRFs. Centrifuges are often used to investigate the sedimentation behavior of MRF within a short period of time. The sedimentation process can be speed up due to the high radial acceleration. However, to record the sedimentation state, the experiment must be stopped and the sample removed. In contrast, the system presented offers the possibility of continuously recording the current sedimentation state by measuring the unbalance. Such an experiment is shown in Figure 7. For this test, the magnetic excitation system in the chamber and the electromagnet are removed. The chamber is filled with MRF and then mounted on the rotor. Additional weights are used to create a balanced initial state. Figure 7 shows the course of the unbalance measurement and the optical states at the beginning and end of the test. A transparent cover was placed over the chamber for this purpose.

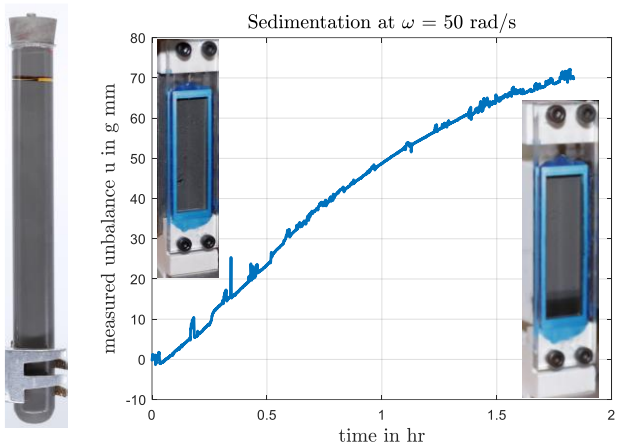

Figure 7 Sedimentation results shown for Basonetic 5030 after 105 minutes. Compared with a fixed test tube after 24 hours under the influence of the earth's gravitational field.

6 Summary

This contribution introduced a system for automatic balancing during operation. The key element of the system is the magnetically controlled sedimentation of MRF inside three chambers placed on the rotor. The use of a hybrid magnetic circuit consisting of permanent magnets mounted on the rotor and a stationary electromagnet enables the construction of a system that is easy to implement. In addition to a balancing run in which an unbalance could be successfully reduced by more than 98.5%, a further field of application, the efficient investigation of the sedimentation behavior of MRF, was presented and successfully validated using the BASF Basonetic 5030. The measuring principle enabled continuous monitoring of the sedimentation state while the process is accelerated by radial acceleration.

7 Literature

[1] ISO 21940-1, Mechanical vibration — Rotor balancing — Part 1: Introduction, International Organization for Standardization, Geneva, First edition 2019.

[2] Rodrigues, D. et al.: Experimental investigation of a single-plane automatic balancing mechanism for a rigid rotor. Journal of Sound and Vibration. Vol. 330. 2011.

[3] Bae, S., et al.: Dynamic analysis of an automatic washing machine with a hydraulic balancer. Journal of Sound and Vibration Vol. 257, pp. 3–18, 2002.

[4] Li-Fang, C., Xi, C. and Jin-Ji, G.: A study on electromagnetic driven bi-disc compensator for rotor autobalancing and its movement control. WSEAS Transactions on Systems and Control Vol. 5, 2010.

[5] Zhang, X., Liu, X. and Zhao, H.: New Active Online Balancing Method for Grinding Wheel Using Liquid Injection and Free Dripping. Journal of Vibration and Acoustics, 2018.

[6] Nakamoto, K., Adachi, K. and Shirase K.: Proposal of Real-Time Balancing mechanism Using Magnetic Fluid for Machine Tool Spindle. Manufacturing Systems and Technologies for the New Frontier: The 41st CIRP, 2008.

[7] Zhang, X et al.: An Online Active Balancing Method Using Magnetorheological Effect of Magnetic Fluid. Journal of Vibration and Acoustics Vol. 141, 2019.

[8] Schreiner, V.; Hegger, C.; Maas, J.: Automatic active balancing of rotating systems using real-time controlled magnetorheological fluids, Smart Materials and Structures, Vol. 31(10), 2022.

[9] Schreiner, V., Maas, J.: Online rotor balancing by weight spheres controlled by magnetorheological fluids. ACTUATOR 2022.

[10] Mingfu Wen et al.: Monitoring sedimentation of magnetorheological fluids using a vertical axis monitoring system with a low aspect ratio sensor coil. Smart Materials and Structures, Volume 28, 2019.

[11] Güth, D.; Maas, J.: Characterization and Modeling of the Behavior of Magnetorheological Fluids at High Shear Rates in Rotational Systems. Journal of Intelligent Material Systems and Structures, Volume 27, 2016.

[12] Vicente J., et al.: Stability of cobalt ferrite colloidal particles: effect of pH and applied magnetic fields. Langmuir Volume 16, 2000.

[13] Hegger, C. and Maas, J.: Smart Sealing for MR-Fluid Actuators. Journal of Intelligent Material Systems and Structures, Volume 30 Issue 5, 2018.

[14] BASF SE, 2009 Magnetorheological Fluid Basonetic® 5030 - Optimum Torque Transmission for Clutch-Type Applications BASF SE.

Innovative Fin Ray gripper with integrated SMA actuator wires

Shivaani Anitha Sivakumar 1,2, Yannik Goergen 1, Tom Gorges 1, Gianluca Rizzello 2, Paul Motzki 1,2
1 ZeMA – Center for Mechatronics and Automation Technology, Depart. Smart Material Systems, Saarbruecken, Germany
2 Saarland University, Depart. Systems Engineering, Saarbruecken, Germany

Abstract

In the growing field of Shape Memory Alloys (SMA), there is a wide scope for innovative actuator designs, modelling approaches as well as control algorithms using the self-sensing capability of SMAs. Lightweight and compact gripping systems based on SMAs have been of increased interest over the past years, pursuing the optimization of the gripper design while supporting or even improving the functionality. Mostly, current research work is not investigating the enhancement of the overall system, but rather deploying well-known traditional rigid-link gripper designs. In contrast, this work focuses on the system optimization by combining SMAs with an optimized gripper geometry exploiting the Fin Ray® Effect (FRE). FRE-based grippers feature a soft structure, a low weight and a high adaptability to different shapes and sizes of objects. There is a considerable amount of research work done on using FRE-based grippers in modelling, simulations, and experimental results but there is still room for work specifically in building a smart FRE gripper actuated by self-sensing SMA wires, resulting in a highly integrated and smart actuator-sensor system. SMA actuators provide the advantage of not needing a bulky pneumatic periphery or motor drive or an external sensor for adapting to fragile objects. This motivation directs investigating the placement, sensitivity, and calibration of SMA wires on the FRE structure in such a gripper system. A major part of the work focuses on optimizing the SMA-FRE integration and a first investigation is done on exploring self-sensing behavior to detect the contact with an object gripped by the gripper system.
The study's key finding demonstrates that it is possible to detect object contact with the proposed gripper system. This discovery opens avenues for enhancing FRE-based grippers by utilizing the self-sensing property of SMA further for also accurately measuring applied force on gripped objects, enabling fragile object manipulation without needing additional weight or installation space.

1 Introduction

In the era of advances in soft robotics, material science and stretchable electronics, adaptive grippers have become the need of the hour. Soft grasping of different shaped objects in changing environments is getting more focus in research in soft robotics. Many adaptive grippers have been developed for various industrial purposes and one major sector is the handling of fragile objects or objects prone to damage easily, especially in the food industry. Modern soft robotic grippers like the entanglement grasping tentacles developed by Becker et al. [1], vacuum based soft grippers like Piab piSOFTGRIP [2] and soft compliant electro adhesion-based grippers [3] are some of the latest progresses that have laid the course for more innovative approaches in soft grasping by integrating soft and smart materials.

1.1 Motivation

The primary limitation of existing grippers for handling fragile objects is their reliance on exerting gripping force at specific contact points, which can increase the risk of damage. An adaptive gripper, however, offers a more promising solution by conforming around the object, increasing the contact surface area, and distributing gripping force more evenly. The flexible FRE structure, known for its conformability, is particularly advantageous in this regard, utilizing frictional force for gripping and reducing the gripping force required, as demonstrated by Y. Yang et al [4], making it ideal for delicate objects. (See **Figure 1**)

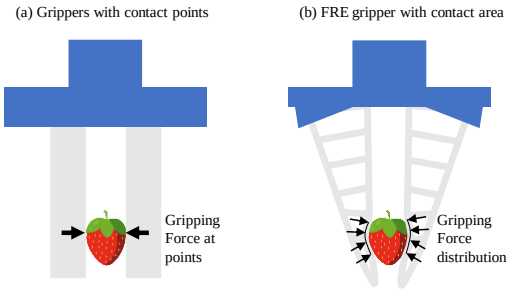

Figure 1 Gripping force acting on the fragile object gripped with other conventional grippers and FRE gripper

Existing grippers for fragile objects suffer from various drawbacks, including bulky components, high space requirements, noise, dependence on external sensors, limited contact area, and hardcoded force control algorithms. These challenges indicate the need for a compact and smarter gripper system. The proposed solution combines the flexible FRE structure with SMA wire actuation and sensing. SMA wire, with its actuation capabilities and self-sensing behavior through resistance changes, offers a promising path for enhancing gripper performance by detecting object contact, position the FRE structure, and potentially controlling the exerted force. [5, 6]
Given the non-linear behavior of the elastic FRE structure, understanding how attaching SMA wires affects its intrinsic behavior is crucial. This paper's focus lies in determining the optimal attachment points to analyze the combined behavior of FRE and SMA, aiming to enhance the FRE's

inherent capabilities in handling fragile objects. This research not only addresses current limitations but also paves the way for more efficient and adaptable gripper systems, crucial in meeting diverse industrial needs and ensuring compatibility with Industry 4.0 standards.

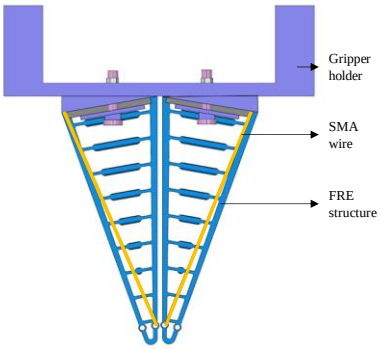

Figure 2 Gripper Design – Integrating Fin Ray gripper and SMA wire

2 Assessment criterion

Understanding the optimal placement of SMA wire on the FRE structure involves assessing the gripper system's behavior. The proposed system operates in four steps (**Figure 3**): (1) home position, (2) opening using bi-stable or antagonistic SMA systems, (3) wrapping around the object, and (4) actuating SMA wires to enhance grip. Step (4) is the focus in this paper, aiming to analyse the impact of SMA wires combined with the FRE structure, optimizing grip for heavier but fragile objects.

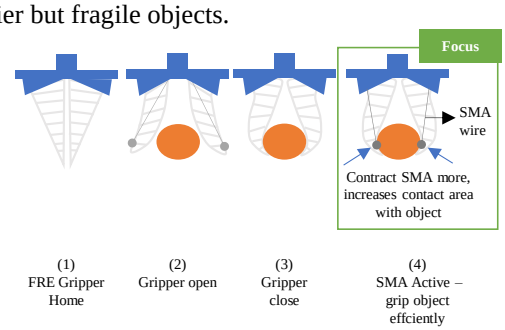

Figure 3 Gripper function explained in steps specifying the function under focus

Several criteria have been used to compare different FRE structure designs [7,8] but there is none to find the best placement of the actuator wire on the same structure. In this case, the comparison is between the several points of attachment in the same structure. In absence of an object, the displacement of the FRE structure is an arc which can be segmented by each beam. Curvature measures the displacement of the FRE structure across all the beams for every placement position. As seen in step (4), the curvature of the tip of the FRE structure (consists of at least the last two beams and the pointed tip in case of a regular FRE structure) plays a major role in holding and eventually exerting more force on the object to optimize the gripping. The resulting criterion thereby is the maximum curvature at the tip, while actuating with SMA.

3 Investigations

The proposed gripper's development utilizes the widely used FESTO DHAS gripper structure [9], aiming to explore the optimization of soft gripping by integrating SMA. The flexible material FORMLABS Elastic Resin (50A) is chosen based on its high flexibility and durability, aligning with the behavior of the FRE structure.

The research methodology begins with non-linear simulations to assess whether the optimal displacement of the FRE structure occurs at the farthest attachment points of the SMA wire, considering the recommended maximum 4% stroke based on lifetime studies for SMA-based actuators [10,11]. The identified attachment points are further validated using non-elastic steel wires as substitutes for SMA wires to simplify the examination of different placements. Subsequently, the most favorable placement is used for further investigation with SMA wires. The developmental adaptations include studying the optimized SMA wire placement on a single FRE structure (without an object) to analyze its behavior and displacement capacity and investigating self-sensing behavior by integrating SMA wires on one FRE structure with an object to wrap around.

3.1 Non-linear simulation – Fin Ray Effect structure behavior analysis

The simulation aims to identify the attachment point that maximizes tip curvature and confirm the assumption that farther attachment points yield greater displacement. As the displacement of the structure is ideally in two dimensions, the simulation is simplified to 2D with a fixed flat end. The tracked sensor points are at the beam joints as in **Figure 4** (b). Along with the beam joints that are physically feasible to monitor, the tip (F1) is also marked to get the most accurate curvature at the tip of the structure.

The visual results of the simulation verify that the longer the distance between the attachment points, the higher the actuation displacement of the FRE structure (see **Figure 5**). This validates choosing R10 on the right side as the attachment point. It is noticeable that configurations 1 and 2 have greater displacement than the rest.

With the distance between the consecutive sensor points and the rotation data collected from the coordinates from the simulation, the curvature of the structure after displacement is calculated as in **Figure 8**.

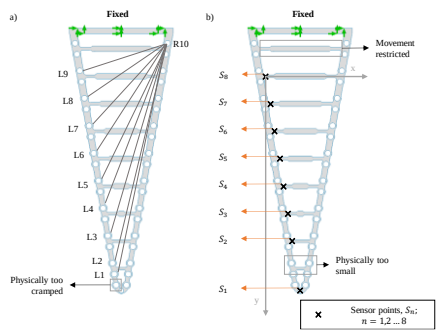

Figure 4 Simulation set up explained, 2D simplified view with a) attachment points (Left - L, Right - R), b) chosen sensor points

The curvature after the displacement is calculate as follows:

$$\boldsymbol{Curvature} = \frac{d\theta}{ds} = \frac{\varphi_{n+1} - \varphi_n}{\sqrt{(X_{n+1} - X_n)^2 + (Y_{n+1} - Y_n)^2}}$$

Where ds represents the distance between consecutive sensor points in home position (X, Y) and $d\theta$ is the difference in Euler angle about Z axis of consecutive sensor points (φ), $n = 1,2 \ldots 7$.

Studying the curvature at the tip for each configuration shows clearly how configuration 1 has the highest curvature at the tip and hence, is the best placement for the SMA wire on the FRE structure. (See **Figure 6**) The deviation in the trend at configuration 4 is attributed to the stiffness behavior of the structure.

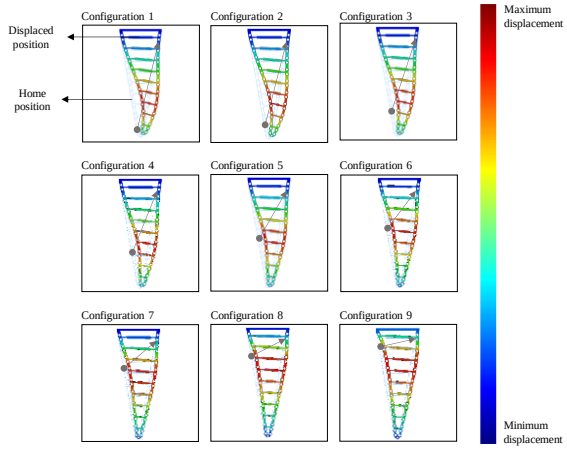

Figure 5 Visual results of every simulation with independent color scale showing the displacement

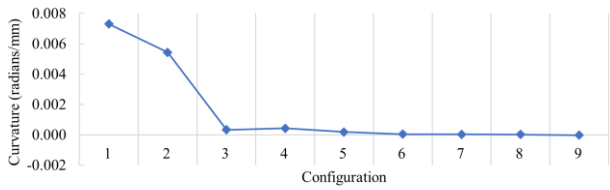

Figure 6 Curvature of the tip (sensor points: S7 and S8) for each configuration

3.2 Experimental study with steel-wire

The same procedure is repeated with an experimental setup using a non-elastic steel wire (Flexonit 0.36 mm, fishing line) to emulate the SMA actuator wire by controlled displacement using a micro linear motor (ZABER T-NA08A50). Checkerboards are attached to the structure in the same positions as the sensor points from simulation. The images of the resulting motion of the FRE structure are recorded continuously during each experiment and each checkerboard is chosen as a region of interest (ROI). From the chosen ROIs, three strong edges are detected (see **Figure 7** (b)), and their positions are tracked from the home position to the displaced position. A load cell (KD24s 10 N) is attached between the linear motor and the FRE structure to measure the force required to displace the FRE structure. To ensure that the structure moves with the pulled wire for each configuration, the non-elastic wire is pulled up until the wire is completely straightened (noticeable increase in rate of change of measured force) and the structure is ready to move. The FRE structure is rotated for every experiment aligning the attachment points maintaining collinearity of the wire to avoid additional frictional forces in the measurement (see **Figure 7**(a)). The steel wire is inserted into the 'U' shaped tube (U-tube) that is inserted at the bottom attachment point as seen in **Figure 7** (b).

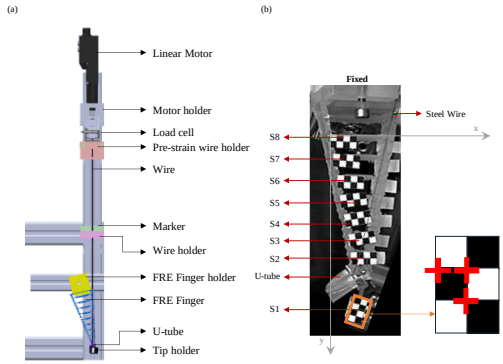

Figure 7 a) Experiment set-up, b) Focused on FRE finger displaying the checker boards marked as Sensor points (S1, S2...S8)

From the tracked coordinate information, the curvature of the structure for each configuration is calculated and verified. The chosen best placement configuration 1 has the highest curvature and is plotted in comparison to the curvature from the simulation in **Figure 8**. The required force to pull the structure in configuration 1 is 0.6 N.

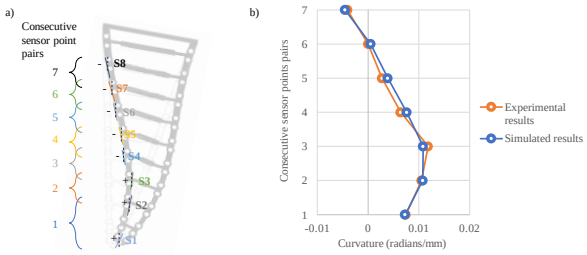

Figure 8 a) Reference for Euler angles measured, b) Curvature of Configuration 1 from simulation and experiment with non-elastic steel wire

3.3 Experimental study with SMA wire

The experimental set up is the same as the one in the previous experiment as in **Figure 7** (a) except for this experiment is not an emulation and uses SMA wires directly. The Nickel-Titanium (FLEXINOL) wire of diameter 76 μm is used because of its actuation load capacity of up to 0.8 N. After training with a constant load of 1.5 N (350 MPa) more than the required load of 1.2 N (A single wire is pulled through the U-tube and is attached on each side of the FRE structure contributing to $2 * 0.6\ N$), at a constant current of 150 mA, heating 10 s and cooling 5 s for 50 cycles, a range of current controlled SMA wire actuation ($150mA\ to\ 200mA$) is tested based on the manufacturer recommended current for actuation. Due to the stable active sensor active region during the heating period (see resistance behavior in **Figure 9** (1)) constant current of 150 mA is chosen for further analysis. (See **Figure 9** (b)) The target object chosen is a cylindrical segment of an 80 mm diameter cylinder, which is the maximum gripping size of the movable part of the FRE structure when fixed at

the top like in the experiment. The target object set up is designed as in **Figure 9** (a). The target object is made to contact the FRE structure at the focus points (4,3) where the maximum curvature is attained in the previous investigations in configuration 1.

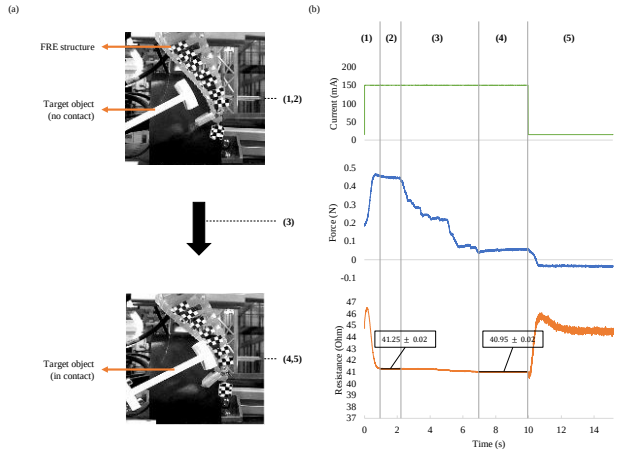

Figure 9 a) Setup with the target object, b) Current across the SMA wire, Force acting on the SMA wire and Resistance of the SMA wire plotted for configuration 1 with SMA wire with distinguished sections: No contact with object – (1) thermal activation of SMA wire, (2) constant current controlled stable resistance; (3) object in contact and pushed against the FRE structure; object in contact fixed – (4) constant current controlled stable resistance, (5) thermal deactivation of SMA [12]

From **Figure 9** (b), after the thermal activation of the SMA wire (1), the resistance reaches a constant of 41.25 ± 0.02 Ohm in the absence of a target object (2). The force acting on the SMA wire drops with the force distributed on the target object by the FRE structure. This drop in mechanical stress leads to decreases the resistance of the SMA wire. (3) The target object is fixed when it is completely in contact with the FRE structure, the resistance is constant again at 40.95 ± 0.02. (4) As soon as the power supplied is cut off, the SMA cools down after the influence of the temperature drop and contraction as seen in the resistance. This experiment shows how the contact with an object can be detected by measuring the resistance of the SMA wire attached to the FRE structure.

4 Conclusion

This research innovatively utilizes the curvature of the FRE structure and integrates SMA wires to enhance performance. Simulation effectively narrowed down potential SMA placements, guiding further experimental investigations. Experiments with a non-elastic steel wire confirm simulation accuracy and provide crucial physical dimensions for SMA wire integration. The study proves the possibility of contact detection with SMA and FRE combination utilizing the SMA self-sensing property.
Future work includes calibrating contact detection and developing a systematic relationship between the exerted force and the resistance change in the SMA, which builds a basis for potential force control in the gripper system.

Literature

[1] K. Becker, C. Teeple, N. Charles, Y. Jung, D. Baum, J.C. Weaver, L. Mahadevan, and R. Wood. 2022. “Active Entanglement Enables Stochastic, Topological Grasping.” Proceedings of the National Academy of Sciences 119 (42). https://doi.org/10.1073/pnas.2209819119.

[2] piSOFTGRIP by Piab, https://www.piab.com/suction-cups-and-soft-grippers/soft-grippers/pisoftgrip-vacuum-driven-soft-gripper-/pisoftgrip-/

[3] V. Cacucciolo, J. Shintake and H. Shea, "Delicate yet strong: Characterizing the electro-adhesion lifting force with a soft gripper," 2019 2nd IEEE International Conference on Soft Robotics (RoboSoft), Seoul, Korea (South), 2019, pp. 108-113, doi: 10.1109/ROBOSOFT.2019.8722706.

[4] Y. Yang et al., “A 3D-printed Fin Ray Effect Inspired Soft Robotic Gripper with force feedback,” Micromachines, vol. 12, no. 10, p. 1141, Sep. 2021. doi:10.3390/mi12101141

[5] K. Ikuta, "Micro/miniature shape memory alloy actuator," Proceedings., IEEE International Conference on Robotics and Automation, 1990, pp. 2156-2161 vol.3, doi: 10.1109/ROBOT.1990.126323.

[6] J. Selvarani Ruth D. and K. Dhanalakshmi, "Shape Memory Alloy Wire for Force Sensing," in IEEE Sensors Journal, vol. 17, no. 4, pp. 967-975, 15 Feb.15, 2017, doi: 10.1109/JSEN.2016.2642299.

[7] W. Crooks, S. Rozen-Levy, B. Trimmer, C. Rogers, W. Messner. “Passive gripper inspired by Manduca sexta and the Fin Ray® Effect,” International Journal of Advanced Robotic Systems. 2017;14(4). doi:10.1177/1729881417721155

[8] J. Suder, Z. Bobovský, J. Mlotek, M. Vocetka, P. Oščádal, Z. Zeman. “Structural Optimization Method of a FinRay Finger for the Best Wrapping of Object,” Applied Sciences. 2021; 11(9):3858. https://doi.org/10.3390/app11093858.

[9] FESTO FRE structure, https://www.festo.com/media/pim/048/D15000100122048.PDF

[10] P. Motzki and S. Seelecke, “Industrial Applications for Shape Memory Alloys,” in Reference Module in Materials Science and Materials Engineering, Elsevier, 2019.

[11] Technical characteristics of FLEXINOL actuator wires, Dynalloy, https://www.dynalloy.com/pdfs/TCF1140.pdf

[12] F. Schiedeck, “Entwicklung eines Modells für Formgedächtnisaktoren im geregelten dynamischen Betrieb,” Gottfried Wilhelm-Leibniz-Universität Hannover, 2009.

Development of an integrated foil-based sensor for position sensing of magnetic shape memory alloy actuators

Patrick Fleischmann[1], René Schnetzler[2], Prof. Dr.-Ing. Bernd Gundelsweiler[1]
Corresponding author: E-Mail: patrick.fleischmann@ikff.uni-stuttgart.de
[1] *Institute of Design and Production in Precision Engineering, University of Stuttgart, Pfaffenwaldring 9, 70569 Stuttgart*
[2] *ETO GRUPPE TECHNOLOGIES GmbH, Hardtring 8, 78333 Stockach*

Abstract

The growing demand for energy efficient and highly integrated drives has led to an increasing interest in innovative actuator concepts. By utilizing the smart capabilities of magnetic shape memory alloys, it is possible to meet these requirements. Passive magnetic shape memory alloys with internal friction can transform conventional drives into self-locking actuators, addressing the need for energy efficient miniature valves [1,2]. In addition, integration density can be increased by using the stroke-dependent permeability of the alloy to determine the position of the valve actuator [3]. The combination of these features enables the development of self-locking valves with integrated position monitoring. This paper aims to develop an integrated sensor system on a low-cost flexible printed circuit board to measure the stroke and thus the position of actuators with passive magnetic shape memory elements.

1 Introduction

The objective of this work is to demonstrate a sensor concept based on previous studies [4] in the context of energy efficiency and integration density requirements in miniature valve technology. The proposed sensor is intended to detect and provide the armature position in a valve with a passive magnetic shape memory alloy (MSM). The material properties of the MSM element are utilized to replace the integration of an external sensor system, such as a permanent magnet with a Hall element, into the valve system. Furthermore, the sensor concept is designed to be space-optimized and simplistic. With this in consideration, two inductive sensor pads are designed to convert the variable magnetic permeability of the MSM alloy into a technically usable output signal. In addition to the measurements and characterization, a corresponding circuit concept is proposed. The process is concluded with the evaluation of the sensor characteristics.

2 Magnetic shape memory alloys

The magnetic shape memory material used in this work is a monocrystalline Ni-Mn-Ga alloy, which is available as a quboidal material sample of several millimeters edge length (MSM element). In MSM-based actuators, the magnetically anisotropic material reorients itself in an applied magnetic field (MIR), which leads to twin boundary motion and thus to macroscopic deformation (MFIS) of the Ni-Mn-Ga material up to the double-digit percentage range [4,5]. The material can change its shape not only due to an applied magnetic field, but also due to an external mechanical load. So-called passive applications, that are actuated by an external load, are also known from publications on valves, dampers and harvesters [1,2]. In the sensor application considered here, the MSM element is used in passive mode in a self-locking miniature valve. In order to deform the material (twin boundary motion), a force is required to overcome the induced internal friction.

The force, called twinning stress, is shown schematically in **Figure 1**. It shows both the compression force and the extension force at a stroke of 750 µm of the sample used in this work.

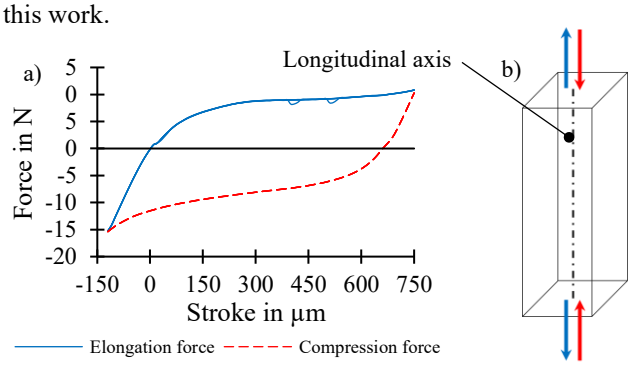

Figure 1 Passive pseudoelastic force-stroke characteristic in a) of the Ni-Mn-Ga MSM specimen selected b). The tensile and compressive load is applied 5 times by the test rig shown in [4].

If such a MSM element is deformed solely mechanically in a passive application, the magnetic anisotropy also causes the element to have a high magnetic permeability ($\mu = 50$) along the longitudinal axis in the fully compressed state (stroke = 0 µm), while a magnetic permeability of about ($\mu = 2$) is present along the longitudinal axis in the stretched state [5]. This characteristic enables the development of a sensor system that detects the deformation state and thus the valve position based on the material properties of the MSM element.

3 Experimental exploitation of sensing properties

A sensor concept is presented in this section that converts the change in permeability of the MSM element into an

electrical position signal. Therefore, two foil-based designs of inductive sensor pads for the transformation of permeability change into inductance change are designed and experimentally evaluated. An inductive sensor pad is a linked structure of copper traces on a 100 µm thick polyimide foil substrate. **Figure 2** illustrates the layout of the two inductive sensor pads and their typical arrangement around the MSM element.

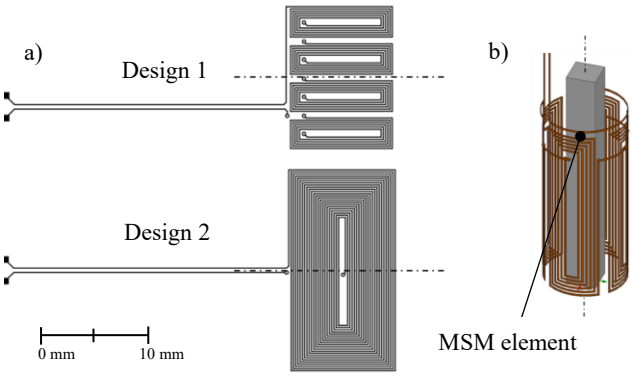

Figure 2 a) Layout of the two inductive pads. b) Exemplary arrangement of the bent pad of Design 1 around the MSM element

For application as a position sensor in a miniature valve, the pad is bent around the MSM element and aligned so that the longitudinal axes of the pad and the MSM element coincide. Pad Design 1 is characterized by having the majority of the conductor length aligned with the longitudinal axis of the MSM element, while pad Design 2 has the majority of the conductor length aligned perpendicularly to the longitudinal axis. The key design parameters are summarized in **Table 1**.

Table 1: Summary of the pad design parameters

Inductive pad parameter	Design 1	Design 2
Dimension in mm	9.5 x 18.7	9.5 x 12.7
Polyimide foil thickness	100	
Copper trace width in µm	100	
Copper trace spacing in µm	100	
Copper trace thickness in µm	12	
Copper resistance in Ω	6.82	13.24

Each pad forms a specific self-inductance, whose magnitude depends on its environment. Considering this property, the following section shows the inductance of the two designs as a function of the MSM element stroke.

3.1 Experimental Characterization of the inductive sensor pads

The pad inductance measurements shown here relate to the extreme states defined as fully compressed (stroke = 0 µm) and fully stretched (stroke = 750 µm). This definition is done to measure the amount of change in inductance between these two states. For measurement, the foil-based sensor pads are wrapped around a polymer winding body with an outer diameter of 3 mm. The MSM element is located inside the winding body and thus forms the stroke-dependent permeability core of the bent pad. The inductance and the AC resistance of the respective design are measured in a frequency band analysis using an impedance analyzer (Wayne Kerr, PRECISION IMPEDANCE ANALYZER 6500B). **Figure 3** shows the measurement results for both pads.

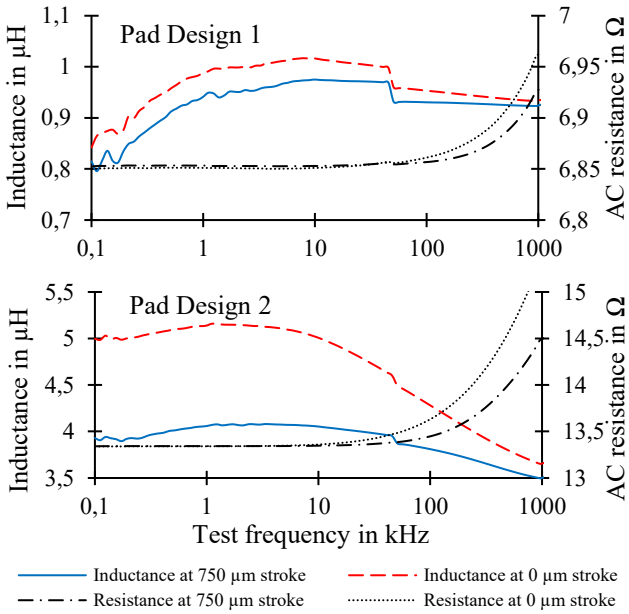

Figure 3 Measurement of the pad inductance and the AC resistance of both designs at a test frequency sweep

The measurements make it evident that both pad designs exhibit a dependence of the pad inductance on the stroke of the MSM element. In particular, it can be observed that Design 1 has an inductance change of approximately 5% and Design 2 has an inductance change of 26.6% at a test frequency of 1 kHz. Furthermore, the AC resistance shows a dependence on the measurement frequency. This phenomenon is explained by eddy current effects in both, the pad and the MSM element. Design 2 exhibits a generally higher sensitivity to deformation than Design 1. An explanation can be derived from the orientation of the magnetic permeability in the MSM element and the flux direction in the bent pad. The main flux direction of the bent pad in Design 2 is aligned with the direction of the magnetic permeability in the longitudinal axis, which has a more significant influence on the inductance change. Design 2 is selected for further investigations in this work. A circuit concept is presented that converts the measured inductance change into an electrical signal that is processed by a microcontroller.

4 Embedded measurement system

In the context of the development of a sensor for a miniature valve, an electrical circuit concept is presented that captures and processes the stroke-dependent change in inductance in a compact and economical design. In the first step, an oscillator system for measuring the change in inductance is proposed. Secondly, a design for the sensor electronics integrated on a foil PCB is provided.

4.1 Oscillator circuit for inductance sensing

To detect the change in inductance, a Colpitts oscillator circuit is designed, which oscillates at its characteristic resonant frequency. The resonant frequency of the circuit is largely determined by an LC tank. As shown in [6], this circuit is suitable for measuring inductance changes in coil-based sensing probes. The schematic diagram of the oscillator designed in this work is shown in **Figure 4**.

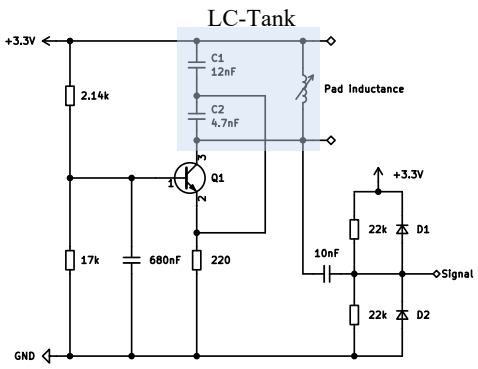

Figure 4 Schematic diagram of the Colpitts oscillator for measuring the inductance change

The resonant frequency of the circuit results from the series connection of capacitors C1 = 12 nF and C2 = 4.7 nF in combination with the variable inductance of the sensor pad. For the selection of the capacitors, a resonant frequency of approximately 1.2 MHz was chosen. However, this choice is based on the method used to obtain the resonant frequency. The method is based on a microcontroller that samples periods of the oscillator signal over a defined time interval. A high base frequency is required so that a sufficient number of periods can be sampled, even in a short measurement interval. To validate the circuit, the signal for both extreme stroke states is recorded by an oscilloscope (Keysight, INFINIVISION DSO-X-3024T) and plotted in **Figure 5**.

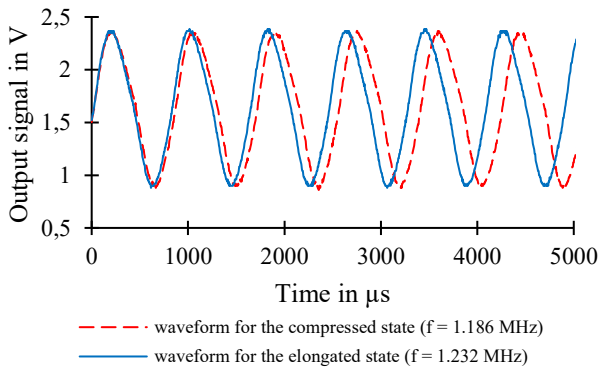

Figure 5 Measured sinusoidal output signal from the Colpitts oscillator for the compressed (stroke = 0 µm) and elongated (stroke = 750 µm) state

The **Figure 5** shows that there is a resonant frequency difference of several kilohertz for the selected sensor pad, meaning that a 750 µm stroke is mapped to approximately 46,000 Hz. Depending on the accuracy of the frequency measurement, the resolution of the sensor can be estimated in further work. A microcontroller (STMicroelectronics, STM32G071EB) is added to the oscillator circuit to measure, process and provide a signal via the built-in digital analog converter (DAC). The 12-bit DAC is able to provide an analog output signal between 0 V and 3.3 V. The entire circuit is fabricated on a flexible polyimide PCB. This design allows the sensor pad and measurement electronics to be manufactured in one single process. **Figure 6** shows the entire PCB structure with the unbent sensor pad.

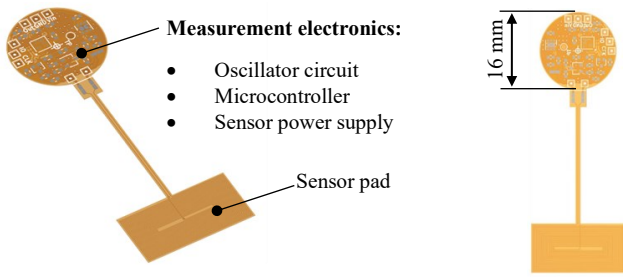

Figure 6 Measurement electronics and sensor pad integrated on 100 µm thick polyimide foil PCB design

The area required for the measurement electronics on the PCB is approximately 200 mm², which corresponds to a diameter of 16 mm in the actual design. The sensor pad connections can be flexibly adapted to the spatial requirement of the valve actuator during the development process. The solution provides design flexibility, ease of integration and cost reduction compared to a dedicated sensor coil with external signal processing.

5 Characteristics of the sensor

After the electronics have been developed, the sensor characteristic is measured for a stroke cycle of 750 µm in this section. Here, the MSM element is elongated through the test rig presented in previous work. **Figure 7** shows the analog sensor output from the microcontroller in combination with the simultaneously logged force characteristic for five stroke cycles.

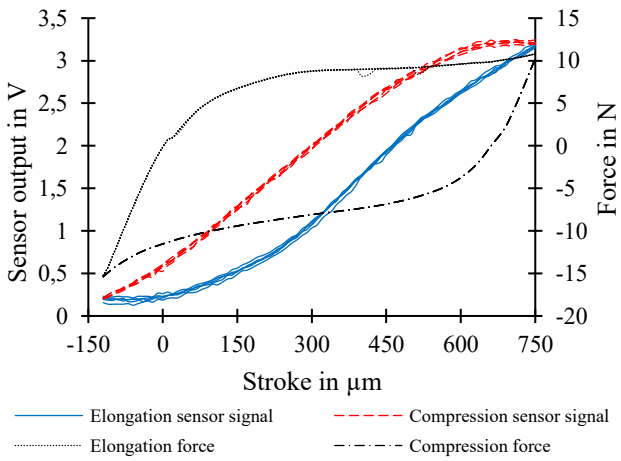

Figure 7 Sensor and force characteristics for five 750 µm stroke cycles

It is evident that the output signal from the sensor represents the elongation curve and can be used to indicate the valve position. It can also be observed that the characteristic curve of the sensor exhibits a hysteresis with a maximum horizontal deviation of approximately 200 µm. By averaging the pull and push sensor curves, the deviation can be adjusted to approximately ± 100 µm of the mean. For simple armature motion detection or monitoring in safety-critical valve applications, this resolution might be sufficient. Other ways of increasing the accuracy of the sensor and further optimisation potential are discussed below.

6 Conclusion and Discussion

This paper demonstrates the development process based on previous work for an optimized sensor concept for detecting the armature position of miniature valves with passive MSM elements. The stroke-dependent magnetic permeability of MSM elements was utilized in the first step of the process, which involved the design of two inductive sensor pads. The inductance of both pads was subsequently measured, thereby demonstrating the sensor effect and enabling the selection of a preferred pad design. An oscillator circuit was then designed to convert the change in inductance into a change in the frequency of an electrical signal. The oscillating signal is obtained, processed and provided as an analog signal by a dedicated electronic system. All the circuit components are integrated on a low-cost foil-based PCB. The characterisation of the sensor properties shows a direct dependence on the stroke of the MSM element and can be used to determine the valve position.

However, it can be seen that the sensor characteristic has a pronounced hysteresis and must be compensated depending on the application. In addition to simply averaging the hysteresis, another compensation option would be to feed the direction of movement as a digital signal to the sensor to adjust the output signal as a function of the direction of movement. Due to the low variance between the individual paths of the sensor hysteresis curve, it can be assumed that the sensor resolution can be reduced to the double-digit micrometer range. With such improved resolution, it is conceivable that precise valve position control can be realized. This aspect will be investigated in future work. Other issues, such as temperature and aging dependence, small motion cycles, and comprehensive characterization of sensor properties, are still open and offer potential for further studies.

7 Literature

[1] J. Happel, R. Schnetzler and M. Laufenberg, “Multistable valve technology with magnetic shape memory alloy as passive element activated by a bidirectional solenoid actuator” in *12th International Fluid Power Conference (IFK)*, vol.3, pp. 315-320, October 12-14, 2020, Dresden, Germany.

[2] J. Happel, E. Pagounis, R. Schnetzler, J. Heider and M. Laufenberg, “Multistable proportional valve: An energy efficient approach for high temperature passive magnetic shape memory applications" *ACTUATOR; International Conference and Exhibition on New Actuator Systems and Applications 2021*, Online, 2021, pp. 1-3.

[3] I. Suorsa, E. Pagounis and K. Ullakko, “Position dependent inductance based on magnetic shape memory materials“ in *Sensors and Actuators A: Physical,* vol.121, pp. 136-141, May 31, 2005.

[4] P. Fleischmann, J. Happel, and B. Gundelsweiler, “Analysis and development of a sensor concept for multistable actuators with passive magnetic shape memory alloy,” *Tm - Techisches Messen*, vol. 0, no. 0, Mar. 2024, doi: 10.1515/teme-2023-0158.

[5] E. Pagounis, R. Chulist, T. Lippmann, M. Laufenberg, W. Skrotzki, “Structural modification and twinning stress reduction in a high-temperature Ni-Mn-Ga magnetic shape memory alloy” in *Applied Physics Letters,* vol.103 (11), September 2013

[6] P. S. Sever and B. Vlad, "LC Oscillator Design Used in Sensor Measurement Based on Embedded Technology," *2021 IEEE 27th International Symposium for Design and Technology in Electronic Packaging (SIITME)*, Timisoara, Romania, 2021, pp. 125-128, doi: 10.1109/SIITME53254.2021.9663673.

Flux control in magnetic circuits using variable reluctance of magnetic shape memory alloys

Marco Hutter, Institute of Design and Production in Precision Engineering, University of Stuttgart, Stuttgart, Germany
Prof. Dr.-Ing. Bernd Gundelsweiler, Institute of Design and Production in Precision Engineering, University of Stuttgart, Stuttgart, Germany

Abstract

Control of flux in magnetic circuits, especially in those with permanent magnets, can be an option to achieve magnetic actuators without the constant generation of power loss as for example in solenoids. To this end, the variable reluctance of magnetic shape memory alloys (MSM) is considered here. The impact of design parameters of the stick and its immediate surroundings alongside an idealized limit are examined using lumped-model and FEA simulation approaches. The air gap in which the MSM-stick is set and the shape of the stick that deviates from conventional geometry are found to be of particular interest, while the low magnetic saturation of the alloy is found to be a limiting factor. Concluding, a brief assessment on the application of this concept in systems is given.

1 Introduction

Magnetic shape memory alloys (MSM) are counted among the smart materials, as they exhibit a number of properties fit for use in actuation and sensing. Actuator concepts often times employ deformation caused by magnetic fields directly to create motion [1, 2]. However, the magneto-mechanical coupling provides other uses, of which the control of magnetic flux via variable reluctance is discussed here.
The ability to control flux in a magnetic circuit by having a variable reluctance can be achieved by an air gap in a magnetic circuit into which ferromagnetic material is inserted. Using the magneto-mechanical properties of MSM-alloys instead may be advantageous in terms of actuator volume and abrasion free operation. A demonstrator employing this concept has already been presented [3]. This study aims to take a more general perspective on the potential of this type of actuator by different approaches to simulation of an MSM-sticks reluctance within an air gap. In particular, theoretical limits and influencing parameters of this approach are to be investigated.

2 Material properties

MSM alloys possess a martensitic microstructure, featuring martensite variants, that can be distinguished by their spatial orientation. The lattice structure exhibits magnetic anisotropy, with a difference in magnetisation energy between the axes [4]. This is depicted in **Figure 1** for the magnetically soft and hard axes of a NiMnGa-alloy.
Given sufficient mobility of the microstructure, external magnetic fields lead to magnetically induced reorientation (MIR) of the martensite variants. During MIR the axis with the lowest magnetization energy will align with the direction of the external magnetic field. On a macroscopic scale this leads to a magnetic field induced strain (MFIS), due to the different lengths of the axes. The resulting strain is pseudoplastic in nature, as internal resistance towards deformation, characterized by the so-called twinning stress, will maintain the strain even without the external field [5].

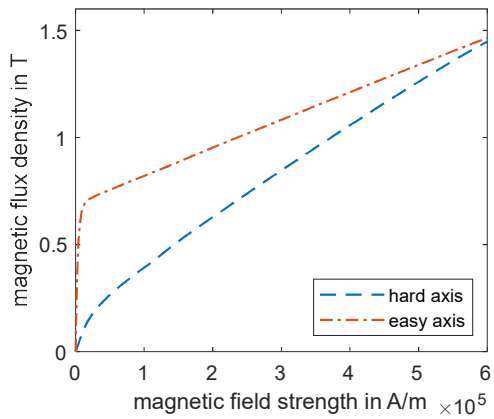

Figure 1 Magnetic anisotropy of NiMnGa-MSM-alloy, shown by the magnetization of the lattice axes.

For macroscopic samples of MSM-alloys, which in the context of this work are widely used single crystal cuboids with edge lengths in the mm-range, the magnetic anisotropy presents as a change in reluctance upon deformation. This reluctance change can be used to influence the flux in a magnetic circuit. Volume consistency dictates lateral deformation of the MSM-stick, due to which the MSM-stick has to be examined within an air gap, that is also necessary for a plausible modelling approach of technical applications.

3 Lumped-element modelling

Applying a lumped-element modelling approach first, an air gap containing an MSM-stick is considered. The air gap constitutes the volume between two pole pieces of magnetic flux guidance and is just as wide in parallel to the flux as the MSM-stick is in compression and just as long as the elongated MSM-stick perpendicular to the flux. Subsequently, in both configurations, as depicted in the top half of **Figure 2**, there is still air volume within the air gap. The third dimension is considered to be constant, as for the alloys examined here no significant deformation occurs in this axis.

Representing each of the described sections as a reluctance, two networks for the two respective air gap configurations can be obtained. These are shown in the lower half of **Figure 2**.

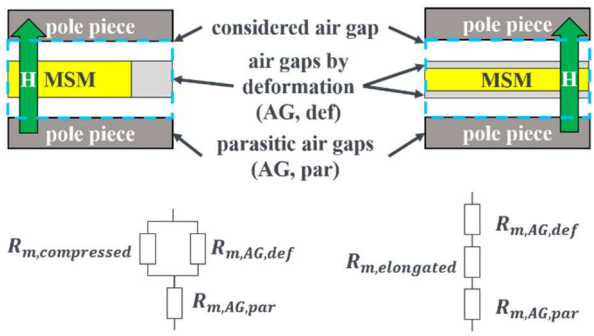

Figure 2 Schematic (top) and simplified reluctance network (bottom) depiction of the considered air gap containing the compressed (left) and elongated (right) MSM-stick, distribution of air within the remaining volume and parasitic air gaps.

Presuming homogenous material properties within each of the sections, their individual reluctance can be calculated using (1). Reluctance in this representation is dependent only on the section's geometry, explicitly its length l and cross-section A, and the permeability μ of the respective material.

$$R_m = \frac{l}{\mu \cdot A} \tag{1}$$

Applying this to the reluctance networks shown above excludes stray fields, saturation and is used here only for the MSM-stick in its fully compressed or fully elongated state. The relation between these states is described by the strain ϵ and the permeabilities μ_h for the hard and μ_e for the easy axis.

Determining the ratio of the two configurations respective overall reluctances yields (2).

$$\frac{R_{m,compressed}}{R_{m,elongated}} = \frac{\mu_e \cdot \epsilon^2}{(\mu_h + (\epsilon - 1))(1 + \mu_e(\epsilon - 1))} \tag{2}$$

Remarkable about this representation is that by using the maximum strain ϵ to describe the geometric relation between the compressed and elongated stick the equation is independent from the specific geometry. Instead, material properties have influence on the reluctance ratio. Therefore, a theoretical maximum, specific to the used alloy, can be calculated. Commonly employed NiMnGa-alloys with show a maximum strain of 6 %, and a simplified permeability range of 2 … 50 [6]. As an exemplary case the theoretical maximum can be calculated to be 6.82 for these alloys.

For real systems, additional volume between the MSM-stick and these poles has to be accounted for due to manufacturing tolerances, handling of the MSM-stick and bending that can occur during deformation [7]. In the model this can be represented by additional air gap volume in series with the networks shown in **Figure 2**, referred to here as parasitic air gap.

The reluctance ratio of this setup cannot be simplified to a result comparable with the representation in (2). However, to visualize the influence of the added parasitic air gap the network model is implemented in Matlab and the dimension of the parasitic air gap is varied. This is done first for the dimensions of a typical MSM-stick with nominal dimensions of 2 x 3 x 15 mm³ and also for a cube shaped stick with dimensions of 10 x 10 x 10 mm³. The results are displayed in **Figure 3**.

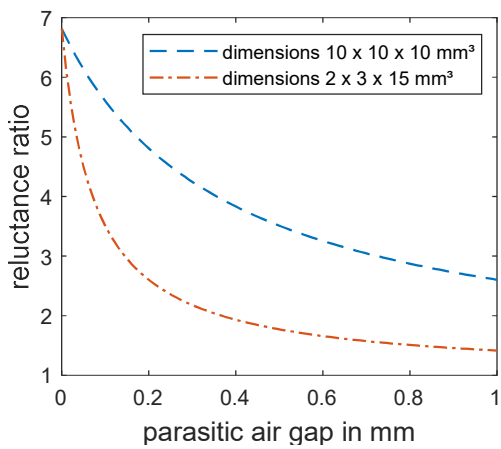

Figure 3 Influence of the length of the parasitic air gap in parallel to the magnetic flux on the reluctance ratio for two geometries of MSM-stick

As can be seen, the reluctance ratio reduces exponentially with the size of the parasitic air gap. This can be explained, as there is no change in the reluctance of the parasitic air gap during MSM-deformation. With a rising proportion of the air gap not exhibiting a change, the overall effect is reduced.

It is also apparent, that while the maximum for both sticks is the same and is equal to the result obtained from (2), the

cube-shaped stick achieves higher ratios for all other dimensions of the parasitic air gap. This demonstrates, that the presence of a parasitic air gap, geometry of the MSM-stick has to be considered. At this stage of modelling this geometry can be simplified into the cross-section perpendicular to the flux and the length in parallel with it. Importantly, these are not identical with the dimensions responsible for determining stroke and force generation in most actuator concepts, such as push-actuators.

4 FEA simulations

The modelling in the previous section has been done omitting magnetic stray fields and saturation effects. To assess their influence, a model for FEA simulation is set up. This is done using Ansys Electronics Desktop 2022 R1. A basic electromagnetic circuit, consisting of a coil for magnetic excitation and flux guidance is set up. In the flux guidance an air gap is included, containing the MSM-stick. This is shown for the compressed MSM-stick in **Figure 4** The setup is duplicated with the MSM-stick compressed in one of them and elongated in the other one. A third setup with no air gap is used as a reference for calculations of the results.

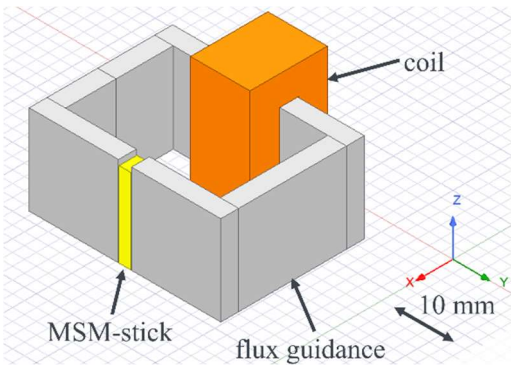

Figure 4 FEA model setup for the compressed MSM-stick (depicted with dimensions of 2 x 3 x 15 mm²).

For both setups the MSM-alloy is modelled using anisotropic and nonlinear permeability, ascribing the magnetic characteristic of the hard or easy lattice axis as shown in **Figure 1** to the respective axis in the model.

The flux guidance is modelled using nonlinear isotropic magnetic characteristic of machining steel 1.0715. The whole model is parametrized, so that the length, height and width of the MSM-stick, magnetic excitation from the coil and the length of the parasitic air gap can be varied. The flux guidance is parametrized to have the same cross-section as the MSM-stick. Because its permeability and saturation are higher than that of MSM, saturation within the flux guidance is not expected to impact results in a significant way.

To obtain the reluctance in this simulation, the relation between magnetic excitation and magnetic flux is used. The magnetic flux is calculated by integrating the flux density over a section of the flux guidance, while the excitation is one of the input parameters. Their ratio yields the reluctance of the entire circuit. To obtain the reluctance change in the air gap, results from the reference setup are subtracted from the other two configurations, before the reluctance ratio is calculated.

To get started the 2 x 3 x 15 mm³ stick is examined again. The parasitic air gap in this instance is varied in a range of $l_{AG,par} = 0 \ldots 0.3\ mm$. Different from the previous results the excitation given by the current in the coil is another input parameter here, with a range of $I_{ex} = 150 \ldots 450\ A$. the results for the air gaps' reluctance ratio over these two inputs is given by the plots in **Figure 5**.

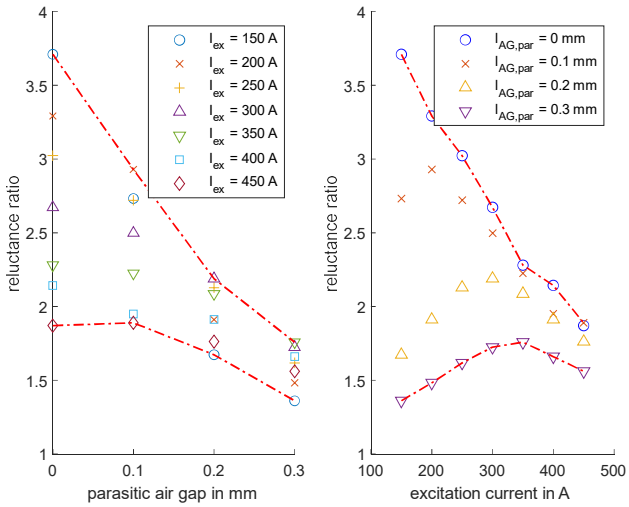

Figure 5 Influence of parasitic air gap length $l_{AG,par}$ and excitation current I_{ex} on the reluctance ratio for an MSM-stick with dimension of 2 x 3 x 15 mm³

The results again show the decrease in reluctance ratio for larger parasitic air gaps. However, it also shows smaller overall ratios compared to the previous model. The depiction of reluctance ratio over excitation current clearly shows different peaks for the different air gaps. Both effects are attributed to the limited saturation flux density of the MSM-alloy at around 0.7 T (see **Figure 1**). Stray fields may also play a limited role here. Therefore, optimal excitation is to be considered and generally rises with the size of parasitic air gaps, as can be expected.

The indication of the lumped model results in the previous section towards an influence of MSM-stick geometry on the reluctance change warrant further investigation. This is done here by a parametric study with the FEA model. As it is meant to give a broad overview and to limit simulation complexity all spatial dimensions of the MSM-stick are varied in three steps in a range of $2 \ldots 10\ mm$. The parasitic air gap and excitation current are again considered from $0.1 \ldots 0.3\ mm$ and $100 \ldots 500\ A$ respectively.

For the results displayed in **Figure 6**, the geometric properties are displayed as the length of the MSM-stick in parallel to the flux and the cross-section perpendicular to it. To give a more detailed picture of the influence of the specific geometry, the aspect ratio of the cross-section is given.

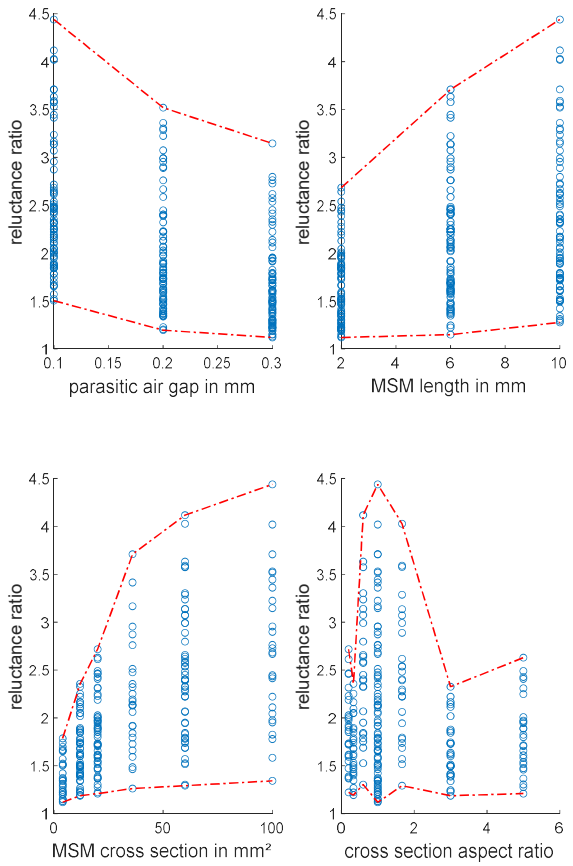

Figure 6 Influence of design parameters on the reluctance ratio between compressed and elongated MSM-stick.

Despite the widely spread distribution of the results, trends are clearly visible by the upper and lower limits. The negative impact of the parasitic air gap is again clearly visible, even though the spread at each evaluated size also emphasizes the importance of the other parameters. The length of the MSM-stick in parallel to the magnetic flux generally shows a positive impact on reluctance ratio, which can be explained the same way as the influence of the parasitic air gap. Each of these being larger makes their contribution to the overall characteristic more dominant.

The positive influence of the MSM cross section (perpendicular to the flux) can instead be attributed to the fact, that the cross section of the elongated stick is larger than for the compressed which supports the change in permeability and has a larger impact for a larger cross-section. The positive influence however decreases for larger cross-sections and might trend to a fixed value or even decrease. An interesting addition here is the prominent peak of the reluctance ratio for a quadratic cross-section. This is a significant deviation of desirable MSM-stick geometries from those typically used in actuators employing motion directly.

5 Conclusion

In this paper, variable reluctance of MSM-sticks has been discussed for use in system design. Therefore, an MSM-stick has always been considered within an air gap as part of a magnetic circuit. By a lumped model approach a theoretical maximum of the change in reluctance, that is only dependent on material properties, has been found. From this the use of alloys with larger maximum strains promises more influence on the reluctance, which however has not been examined here.

By means of FEA simulation the reluctance change has been investigated in more depth. By using a nonlinear, anisotropic modelling approach for the MSM-alloy, the influence of saturation has been considered. Its impact needs to be accounted for in the design of circuits with variable reluctance, as it limits effective maximum flux. From the FEA simulations, trends for the impact of MSM-geometry have also been identified, which suggest a deviation from the more typical shape of MSM-sticks.

While moving highly permeable steel into and out of air gaps can yield greater changes in reluctance, MSM-based solutions may prove viable for miniaturized systems, especially if integration of additional properties of MSM can be achieved.

6 Literature

[1] J.-Y. Gauthier, A. Hubert, J. Abadie, N. Chailet, and C. Lexcellent, Eds., Magnetic Shape Memory Alloy and Actuator Design, 2006.

[2] T. Schiepp, E. Pagounis, and M. Laufenberg, Eds., Magnetic Shape Memory Actuators for Fluidic Applications, 2014.

[3] M. Hutter, A. Kazi and B. Gundelsweiler, "Experimental Investigation of an MSM controlled Reluctance Actuator," *ACTUATOR; International Conference and Exhibition on New Actuator Systems and Applications 2021*, Online, 2021, pp. 1-4.

[4] L. Riccardi, “Position Control with Magnetic Shape Memory Actuators,” Dissertation, 2014.

[5] J. M. Stephan, K. Retan, P. Ruther and O. Paul, "On the influence of thermal treatment on strain sensors based on the ferromagnetic shape memory alloy NiMnGa," *SENSORS, 2011 IEEE*, Limerick, Ireland, 2011, pp. 85-88, doi: 10.1109.

[6] ETO Magnetic, Magnetoshape. [Online]. Available: http://etogroup.com/MAGNETOSHAPE.html

[7] E. Pagounis and P. Müllner, Eds., Recent developments in magnetic shape memory actuation, 2014.

Investigation of the influencing factors in the production of Shape Memory alloy wire bending actuators for integration in micro-electro-mechanical systems

Andreas Erben[1], Kenny Pagel[1], Daniel Hoffmann[2], Andrea Böhm[1], Welf-Guntram Drossel[1]
[1] Fraunhofer Institute for Machine Tools and Forming Technology IWU, Dresden, Germany
[2] Hahn-Schickard Gesellschaft, Villingen-Schwenningen, Germany
Andreas.Erben@iwu.fraunhofer.de

Abstract

The combination of shape memory alloys and micro-electro-mechanical systems possesses to rethink and downscale the size of actuator systems to MEMS level. Thus, the heterogeneous integration of shape memory alloy actuators is a focus of current research to enable the use of standardized semi-finished products such as wires and to exploit their good actuator properties. To integrate the actuator into the mechanical structure, it must first be deformed to fit into the intended installation space and to realize a form-fit connection after the first activation. This pre-deformation has a significant influence on the actuator performance. In this paper, the influence of preforming on the resulting actuator behaviour will be investigated. For this purpose, the change in the transformation temperatures and the resulting stroke are investigated. The experiments carried out were based on experimental plans that were created by means of design of experiments.

1 Introduction

Actuator systems based on shape memory alloys (SMA) are well known in the field of valve technology [1]. The large volume-specific working capacity makes it possible to design cost-effective actuators in a small installation space. These advantages, combined with the good availability of standardized semi-finished wire products < 76 µm, make the integration of wires in MEMS systems interesting [2,3].
The focus of the research is on the reproducible production of heterogeneously integrable SMA actuators and forms the basis for the development of novel sensor and actuator systems. One approach to integrating the actuators is research into form-fit embedding in the silicon actuators using preformed actuators. The knowledge to be acquired is of great importance for further system approaches in the field of MEMS. The type and degree of cold forming during the manufacturing of SMA actuators has a significant influence on the characteristics (stroke and force) of the actuator and is the focus of this publication.

2 Experimental Results and Discussion

2.1 Production of the preformed actuators

To investigate the influencing variables of preforming with a three-point bending on the resulting actuator behaviour a variable deformation tool was developed. A push-pull module from Kammrath und Weiss [4] was used as drive unit. Tool inserts have been developed for this purpose, which can be set up in different geometries. Geometrical parameters such as the diameter of the bearing points, the distance between the bearing points and the angle of the bend are varied to investigate their influence on the actuation performance (**Figure 1**).

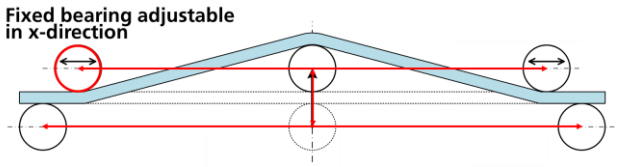

Figure 1: Schematic representation of the variable forming parameters.

Once the parameters to be varied are determined, the design of experiments (DOE) is used in order to obtain the maximum information with the minimum amount of testing. The Cornerstone program is used to carry out the design of experiments.

Based on the sample plan of the DOE, the forming tools are manufactured using stereolithography 3D printing. According to the small forces occurring below 1N, this manufacturing process enables the structures to be produced quickly with good quality. Dispenser cannulas were used as guide pins, as these are available in different diameter sizes < 1 mm **(Figure 2)**.

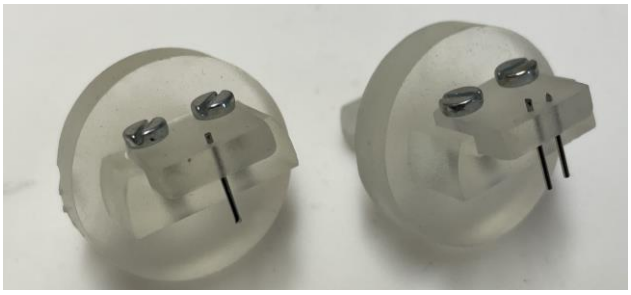

Figure 2: Forming inserts for the tension and compression module from Kammrath and Weiss

2.2 Determination of the transformation temperatures and actuating strokes

The Linkham THMS 3000 temperature chamber [5] is used to examine the actuators under thermal load **(Figure 3)**. This chamber can be controlled via an RS232 interface and can control temperatures with an accuracy of 0.1 K. A glass window allows the actuators to be monitored and measured using a microscope during the thermal tests. Accordingly, the manufactured actuator elements are subsequently activated on a heating plate to determine the transformation temperatures and the degree of shape reset. Further measurements are carried out in the actuator system. For this purpose, test structures in MEMS with different offsets and restoring stiffnesses were manufactured (**Figure 4**) and investigated experimentally. Here, the resulting transformation temperature and the actuating strokes are determined.

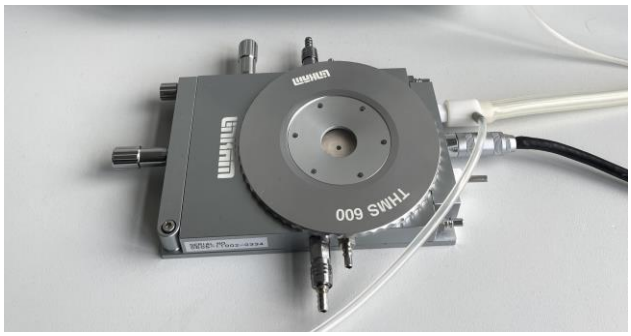

Figure 3: Linkham temperature chamber

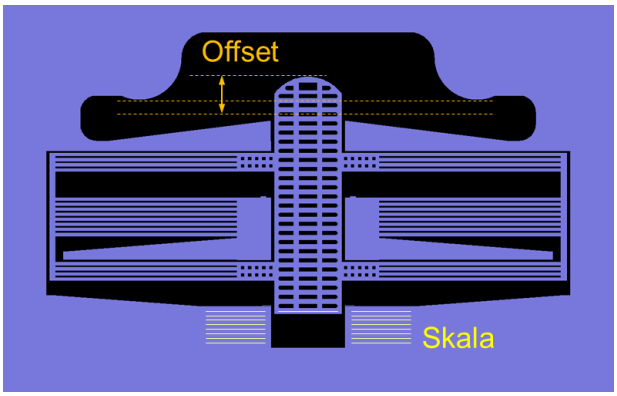

Figure 4: MEMS test structure

Figure 5 shows the temperature-displacement characteristic of a 76 µm SmartFlex actuator which is integrated into the MEMS actuator shown in Figure 6. A more detailed consideration of the influences on the transformation temperatures will be presented in the lecture.

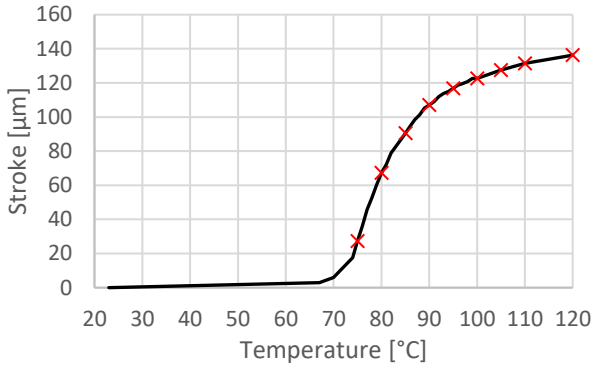

Figure 5: Resulting Stroke depending on the Offset of the manufactured MEMS Structure

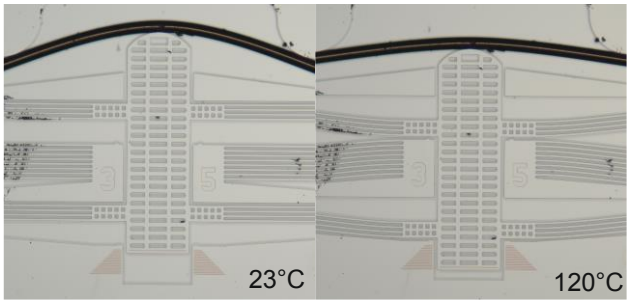

Figure 6: Comparison of the displacement at 23°C and 120°C with 76 µm SmartFlex wire

Acknowledgement

The described results were discovered in the project 23003 BG "Prozesstechnologien für die heterogene Integration von Formgedächtnislegierungen am Beispiel eines autonomen Sterilisationszyklenzählers (ProAuSter) " of the Hahn-Schickard-Gesellschaft für angewandte Forschung e.V. supported via the German Federation of Industrial Research Associations (AiF) within the program for promoting the Industrial Collective Research (IGF) of the German Federal Ministry of Economic Affairs and Energy (BMWi) based on a resolution of the German Parliament.

3 Literature

[1] https://www.actuatorsolutions.de/products/pneumatics-and-fluidics/3-3-module-as8p/ (14.02.2024)

[2] Daniel Hoffmann et al., Hybrid Integration of A Shape Memory Alloy Actuator For Micro Thermal Mechanical Systems, https://doi.org/10.1109/MEMS51670.2022.9699649

[3] K. Pagel; Daniel Hoffmann et al., "Development of a shape memory alloy actuator for a micromechanical sterilization cycle counter", SMASIS2020. http://dx.doi.org/10.1115/SMASIS2020-2242

[4] https://www.kammrath-weiss.com/de/zug-druck-module/ (14.02.2024)

[5] https://www.linkam.co.uk/temperature-controlled-stages (14.02.2024)

Analysis of the controller and damping behavior of an electrodynamic actuator system for an 11 kW two-pole induction motor on an elastic steel frame foundation

Raimund Wachter, ELSYS - Institute for Power Electronic Systems, Nuremberg Institute of Technology, Keßlerplatz 12, 90489 Nuremberg, Germany, raimund.wachter@th-nuernberg.de;
Ulrich Werner, Faculty EFI, Nuremberg Institute of Technology, Keßlerplatz 12, 90489 Nuremberg, Germany, ulrich.werner@th-nuernberg.de;
Hans-Georg Herzog, Professorship of Energy Conversion Technology, Technical University of Munich (TUM), Hans-Piloty-Straße 1, 85748 Garching, Germany, hg.herzog@tum.de;
Christian Bauer, IN HVM HVM, Innomotics GmbH, Vogelweiherstraße 1-15, 90441 Nuremberg, Germany, bauer-christian@innomotics.com;

Abstract

This paper describes the open loop configuration of the simulation and measurement of a controller hardware and a voice coil actuator for vibration control of a 11 kW motor on steel frame foundation. The paper discusses the phase response regarding damping behavior of the actuator force and identifies approaches for improvements. Further, the paper offers a comparison of measurements as a result of the run up of the motor in open loop and closed loop operation with rubber elements and with steel springs. It is shown that all vibration modes with vertical movement at the motor feet can be reduced. Finally, the paper discusses the change in the system's natural frequencies due to the replacement of the rubber elements by steel springs.

1 Introduction

Vibrations can be problematic in a large variety of applications. For this reason motors are sometimes installed on passive or in special cases on active mounts. Depending on the elasticity of the mechanical assembly, the required stroke and the force of the actuator, different actuators types, e.g. voice coil actuators, can be used. An overview of active mounts is given in [1]. Large induction motors (> 1 MW) are designed for massive foundations as regards international motor standards, e.g., IEC 60034-14 . In practice, induction motors are often mounted on elastic steel frame foundations, influencing the system's natural frequencies – motor with foundation. Therefore, the entire operating speed range may not be used any-more, due to resonance problems. The consequence is that off-limit speed ranges must be defined, where steady-state operation is not allowed. To challenge this issue with focus to open speed range restrictions, in [2], a test bench (**Figure 1.1**), which consists mainly of a two-pole induction motor, a steal frame foundation and a specially developed actuator system (**Figure 1.2**), was investigated. The focus was on the setup of the actuator system, including passive damping elements (rubber elements) and the vibration behavior of the entire system. Afterwards, in [3], a mathematical model of the test bench with 1-DOF was used for fundamental investigations. For damping the system efficiently in closed loop, it is important that the actuator force has mainly a damping characteristic. The comparison between the measurement and the simulation is to show that the actuator force has mainly a damping characteristic and to show the quality of the simulation model. The voice coil actuator have no mechanical guidance. For this reason, initially damping elements were used for adjusting the actuators and damp one special mode. It must be considered whether there are advantages when using steel springs instead of damping elements.

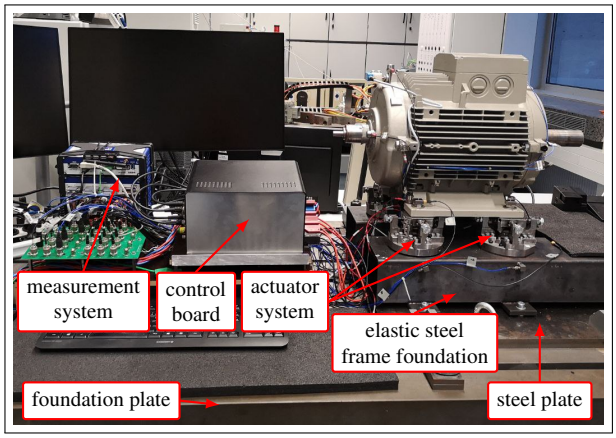

Figure 1.1: Test bench with foundation plate, steel plate, elastic steel frame foundation, actuator systems, motor and electrical equipment for measurement and control

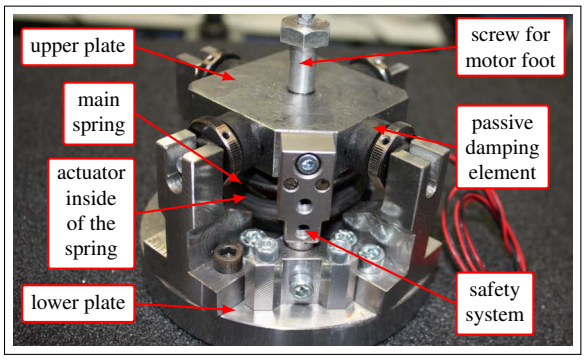

Figure 1.2: Single actuator system with main parts such as the voice coil actuator, main spring and the passive damping elements (rubber elements) – steel springs for replace the rubber elements not shown

2 Control loop design

In **Figure 2.1**, the closed control loop is shown, with the entry point 1, the output point 2 and the path break (X) for simulation and measurement in the open loop configuration. Measurements of the signal conditioning module confirms

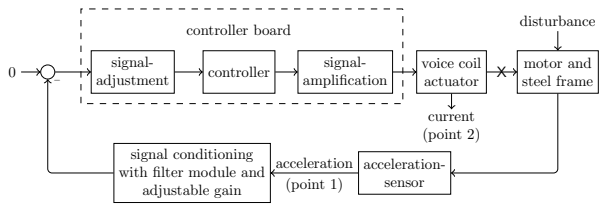

Figure 2.1: Closed control loop with the additions of the entry point 1 (acceleration signal), the measurement point 2 (current signal) and the path break symbol (X) for the open loop investigation

that its transfer function $G_{\text{cond}}(s)$ in Laplace domain can be written as fourth order low pass Butterworth filter with a cutoff frequency of 3 kHz. The signal adjustment and the signal amplification consist of different operational amplifiers. In the low frequency band, they only influence the amplitude of the signal. The phase shift of the amplification of the signal is very small and can be neglected. For simulation, they get the constant amplification parameters K_{OPin} for the signal adjustment and K_{OPout} for the signal amplification. To filter the noise of the signal on the controller board, a first order analogue low pass filter $G_{\text{LP}}(s)$ with a cutoff frequency of 3 kHz is used. As result of the investigation of different control algorithms in previous studies [3–5], the control algorithm from Equation (1), described in the Laplace domain, is used:

$$G_{\text{c}}(s) = \frac{K_{\text{I}}}{s} \cdot \frac{s}{s+\omega_{\text{c1}}} \cdot \frac{s}{s+\omega_{\text{c2}}} \tag{1}$$

The first term in Equation (1) integrates the acceleration signal and amplifies it by K_{I}. The first term in combination with the second term represent a low pass controller ([6]) which suppresses high frequency signals with the cutoff frequency ω_{c1}. As third term, for suppressing low frequency signals, a first order high pass with the cutoff frequency ω_{c2} is used. Each voice coil actuator always operates in its midstroke position with small displacements caused by the vertical vibration of the motor feet. The basic equation that describes the relationship between the actuator voltage $u_a(t, z_{\text{rel}})$, the actuator current $i_a(t)$ and the relative velocity between the coil and the stator of the actuator $\mathrm{d}z_{\text{rel}}(t)/\mathrm{d}t$, can be written as:

$$u_a(t, z_{\text{rel}}) = R \cdot i_a(t) + K_{\text{back}} \cdot \frac{\mathrm{d}z_{\text{rel}}(t)}{\mathrm{d}t} + L \cdot \frac{\mathrm{d}i_a(t)}{\mathrm{d}t} \tag{2}$$

The constant parameters of the voice coil actuator in Equation (2) are the resistance R for the coil and the inductance L. In general, the Back-EMF constant K_{back} and the force constant K_{ED} changes over the stroke of the actuator coil. It is assumed that the back EMF constant and the force constant do not change in this mechanical setting (Figure 1.1 and 1.2).

With small displacements of the actuator the relationship between the current of the actuator coil $i_a(t)$ and the actuator force $f_{\text{a}}(i)$ can be written as

$$f_{\text{a}}(t) = K_{\text{ED}} \cdot i_a(t). \tag{3}$$

The assumption of $\mathrm{d}z_{\text{rel}}(t)/\mathrm{d}t \approx 0$ can be made because the actuator is blocked by a rigid frame (see section 3). Therefore, the second term of electromagnetic force from Equation (2) can be neglected. The transfer function in Laplace domain for the blocked voice coil can be described as

$$G_{\text{a}}(s) = \frac{F_{\text{a}}(s)}{U_{\text{a}}(s)} = K_{\text{ED}} \cdot \frac{1}{R + L \cdot s}. \tag{4}$$

The transfer function for the simulation of the actuator voltage (with the actuator voltage as output and the acceleration as input, neglecting the negative feedback) in open loop can be written as

$$G_{\text{OL,u}}(s) = G_{\text{cond}}(s) \cdot K_{\text{OPin}} \cdot G_{\text{LP}}(s) \cdot G_{\text{c}}(s) \cdot K_{\text{OPout}}, \tag{5}$$

and the transfer function for simulating the actuator current (with the actuator current as output and the acceleration as input)

$$G_{\text{OL,i}}(s) = G_{\text{OL,u}}(s) \cdot \frac{1}{R + L \cdot s}. \tag{6}$$

As will be described in section 4, it is better to compare the currents instead forces.

3 Measurement setup

As a result of development of the steel frame foundation and the actuator system (Figure 1.1 and 1.2), the stiffness of the actuator system in vertical direction is very low. When investigating the damping characteristics of the actuator force, it is undesirable that the frame of the actuator system influences the measurement. For this reason, a separate frame (**Figure 3.1**) was designed to observe the damping characteristic of the actuator force. The first natural frequency of this frame is far beyond the interested frequency range. An aluminium block is used for fixing the actutator in its midstroke position.

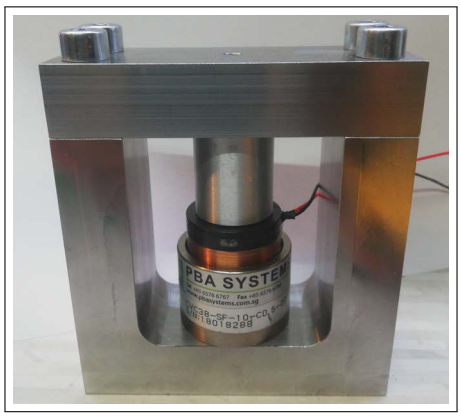

Figure 3.1: Steel frame and aluminium block for fixing the actuator in its midstroke position

4 Results

This section is divided in tree parts. The first part deals with the comparison of the results of the simulation and the measurement of the frequency response function of the signal conditioning with the controller board and the blocked voice coil actuator. The second part presents the results of the measurements of run up of the motor in open and closed loop operation with damping elements and in open loop operation with spring elements. The third part shows the change in resonance frequencies as a result of replacing the damping elements by steel springs in the actuator system.

4.1 Force characteristic

In order to verify the correctness and to improve the simulation model, the calculations of the analytical transfer function from the open control loop (Equation (5) and (6)), will be compared with the results of the measured frequency response function. The focus when designing the controller was on the damping characteristic of the actuator force. Therefore, the information especially about the phase of the actuator force is relevant. For the dynamic measurement of low forces with sufficiently high resolution the frequency behavior of the force sensor together the load must be considered. The stiffness of the sensor together with its modal mass and the mass of the actuator coil represent a single-mass oscillator. For this reason, a force sensor is not used, and the phase shift is compared on the basis of the currents between the simulation and the measurement. For determining the frequency response function a constant acceleration amplitude of 0.125 g was chosen. The chosen acceleration amplitude results in a voltage amplitude of 0.0125 V when using an IEPE acceleration sensor with a sensitivity of 100 $^{\mathrm{mV}}/_{\mathrm{g}}$. As a result of the measurement and the simulation, **Figure 4.1** show a bode plot for the interesting frequency range. The comparison of the results of the phase response only show a marginal shift between the simulated and the measured actuator voltage. In contrast, the phase shift between the simulated and the measured current is

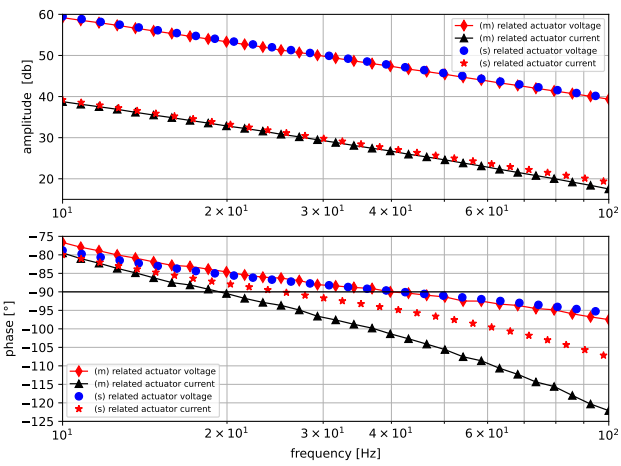

Figure 4.1: Bode plot with the measurement (m) and the simulation (s) with the acceleration as input and the voltage and the current of the voice coil actuator as output

significantly higher. At the maximum rotational frequency of the rotor (60 Hz), the measured phase response shows a phase shift of about −20° to the ideal −90°. For this reason, the actuator force can be assumed to be a force with mainly damping characteristic.

4.2 Vibration analysis during motor run up

This section presents the results of vibration measurements taken during the run up of the motor with two mechanical settings. First, **Figure 4.2 a)** and **b)** shows the amplitudes of vibration velocity over the rotation frequency of the rotor as a result of measurement during the run up of the motor in open loop (passive) and in closed loop operation (active). Secondly, **Figure 4.2 c)** show the results of measurement of the run up of the motor in open loop operation when steel springs are used. The mode shapes are described in detail in [2], so that only the modes that are relevant for the comparison are discussed here. Initially, the using of damping elements was planned for damping the vibration modes, which can not be influenced by the actuator system, because of missing vertical movements of the motor feet. In Figure 4.2 a), at about 44 Hz, the curve in horizontal

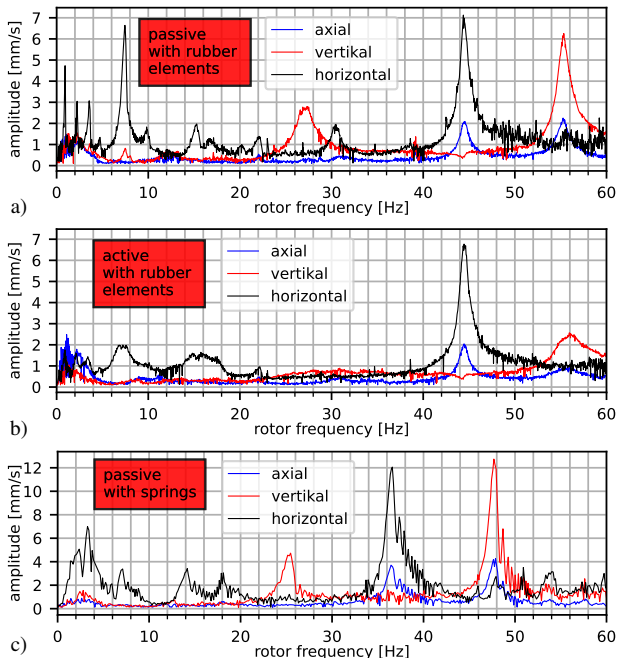

Figure 4.2: Measured amplitudes of vibration velocities of the three spatial directions over the rotor frequency: a) in open loop operation, b) in closed loop operation – both with damping elements and c) in open loop operation with steel springs in the actuator system

direction shows a vibration peak of 7 $^{\mathrm{mm}}/_{\mathrm{s}}$, a lower peak in axial direction 2 $^{\mathrm{mm}}/_{\mathrm{s}}$ and no peak in vibrations in vertical direction. This vibration mode presents a rotation at the vertikal axis without vertical movements of the motor feet. Therefore, it can not be influenced by the active vibration control system. As a result of measurement of the run up of the motor with steel springs the curves in Figure 4.2 c) show significant lower resonance frequencies, especially

in the upper rotor frequencies. The vibration mode with the resonance frequency at 44 Hz decreases to 36 Hz with an increase in amplitude from 7 mm/s to 12 mm/s. On the one hand, this comparison show that the damping elements reduce the amplitudes in that resonance significantly. On the other hand the reduction of amplitudes is not effective enough for running the motor in steady state operation at the frequency of 44 Hz.

4.3 Frequency change

For the comparison of the mechanical settings, **Table 4.1** show the resonance frequencies of different measurements. The second and the third column in Table 4.1 show the natural frequencies as a result from experimental modal analysis (EMA) and the resonance frequencies from the run up of the motor with the damping elements (initial mechanical setting). It can be seen that the results of these two measurements deviates more from each other with increasing frequency. The deviation is attributed to the influence of the damping elements. One mode was not excited or and one mode was out of the speed range of the motor. The fourth and the fifth column in Table 4.1 show the resonance frequencies as a result from EMA and from the run up of the motor with steel springs instead of the damping elements. The results of the measurements with steel springs hardly deviates from each other. During the run up of the motor with steel springs only one mode is not excited. Overall, the measured values of the EMA and those of the run up with steel springs are significantly closer together than the results of the measurements with damping elements.

Table 4.1: Comparison of the frequencies of the rigid body modes with damping elements and with steel springs: Column two and four show the natural frequencies as a result of experimental modal analysis (EMA); Column three and five show the resonance frequencies as a result of the run up of the motor

	rubber elements		**steel springs**		
Mode	**EMA**	**Run-up**	**EMA**	**Run-up**	
1	12.1	-	11,3	-	Hz
2	14.6	15	13,5	14	Hz
3	25.0	27	24,9	25	Hz
4	41.2	44	35,9	36	Hz
5	52.9	56	47,2	47	Hz
6	59.6	-	53,5	54	Hz

5 Discussion and conclusion

The results of the observed phase response show that the force of the voice coil actuator has mainly damping characteristic in the frequency range of the motor. In order to improve the phase behaviour in the higher frequency range, it could be beneficial to compensate the actuator behaviour by transfer function by e.g. a lead compensator. The comparison with the simulation results suggest investigating the behaviour of the actuator in more detail and to improve the simulation model. The passive damping elements, which were initially planned for damping vibration modes without vertical movements (at the motor feet), were not able to reduce the amplitudes for a steady state operation of the motor. Another way to damp all vibration modes actively is to couple the modes by mechanical change of only one actuator system as suggested in [7] ("vibration mode coupling by asymmetry"). Therefore, one actuator system is changed in its horizontal and axial stiffness. The result of this change is that the rigid body modes are more coupled and have a vertical movement at each motor foot. The advantages of active damping for all vibration modes compensate the disadvantage of higher vibration amplitudes when steel springs are used. Another major benefit is that the finite-element model can be kept simple and the stiffness and damping of the damping elements does not have to be adapted to ageing, temperature, preload, etc. [8]. With the stiffening of one actuator system and the reduction of the passive damping, the vibration behavior in the closed control loop at higher frequencies must also be investigated.

Literature

1. Zhang, H., Shi, W., Ke, J., Feng, G., Qu, J. & Chen, Z. A Review on Model and Control of Electromagnetic Active Engine Mounts. *Shock and Vibration* (2020).
2. Wachter, R., Werner, U., Herzog, H.-G. & Bauer, C. *Vibration behaviour of a 11 kW two-pole induction motor mounted on elastic steel frame foundation with actuator system* in *12th International Conference on Vibrations in Rotating Machinery* (2020).
3. Wachter, R., Werner, U., Herzog, H.-G. & Bauer, C. *1D-Simulation and experimental validation of active vibration damping of an induction motor mounted on an elastic steel frame foundation using modified integral controllers* in *Proceedings of ISMA2022 - International Conference on Noise and Vibration Engineering* (2022).
4. Werner, U. Active Vibration Control of Rotating Machines with Active Machine Foot Mounts on Soft Foundations Based on a 3D-Model. *Journal of Applied Mathematics and Physics* (2021).
5. Werner, U. Active Vibration Control of a Rotating Machine with Voltage-Driven Electrodynamic Actuators Between Machine Feet and Steel Frame Foundation Under Multiple Base Excitations. *Journal of Vibration Engineering & Technologies* (2023).
6. Janschek, K. & Richmond, K. *Mechatronic systems design: methods, models, concepts* (Heidelberg, 2012).
7. Werner, U. 3D Model for Active Vibration Control of Rotating Machines Mounted on Active Machine Foot Mounts Using Vibration Mode Coupling by Asymmetry. *Journal of Vibration Engineering & Technologies* (2020).
8. Kari, L. Dynamic stiffness of chemically and physically ageing rubber vibration isolators in the audible frequency range: Part 2—waveguide solution. *Continuum Mechanics and Thermodynamics* (2017).

Design of a range of attachable Lorentz force actuators adapted to different active damping applications

Alexander Pena-Sevillano [1]*, Iker Mancisidor [1], Rafa Barcena [2], Inaki Laka [1], Jokin Munoa [1]
[1] Dynamics & Control, Ideko, 20870 Elgoibar, Basque Country, Spain
[2] Mechanical Engineering Department, University of Basque Country (UPV-EHU), 48013 Bilbao, Basque Country, Spain
* Corresponding author: apenasevillano@ideko.es

Abstract

Vibrations are among the greatest enemies of productivity in machining processes. Milling of thin walls and lightweight structures is often limited by chatter vibrations of those parts. For this application active damping devices have been proposed as they offer high adaptability and power density, however, there is no unique device design which can be used for every kind of workpiece. The present article deals with the design of a range of electromagnetic attachable dampers, which can be applied in a wide array of applications. The design starts from a baseline actuator designed for large, welded steel structures as target workpieces, while in this paper two other actuators are designed with scaled down proportions adapted to smaller steel and composite fibre structures. The design methodology covers both electromagnetic and mechanical aspects, considering different magnetization configurations. In the paper several validation tests are presented for the force capacity and thermal behaviour of the prototypes. Lastly, experimental cutting tests are performed in a multitasking milling machine to demonstrate the efficacy of the actuators.

1 Introduction

The productivity of machining processes is often limited by the vibration of the workpieces, especially in thin-walled parts and lightweight structures [1]. That kind of workpieces usually have lowly damped vibration modes which are prone to unstable chatter vibrations and, at the same time, are not well suited for many of the lower cost chatter elimination techniques such as changes in cutting conditions or special tools [2]. In fact, the most common solution is to use customized fixtures for each workpiece reference ([3],[4]), which is only cost-effective for medium and large batches, while it can also create dimensional problems if an excessive force is applied to the flexible workpiece. Alternatively, the use of attached active dampers has been proposed for these vibration problems, but it is not yet a common industrial practice [5].

One of the simplest realizations of attached active dampers is through inertial actuators, which generate force by accelerating a suspended mass connected to the main structure. Although many technologies are available for this purpose, electromagnetism is most commonly used because it offers a fast response, good force density and is easy to control [6]. These actuators must be rigidly fixed to the workpiece in order to ensure good force transmission.

The selection of the correct actuator for each application is crucial. Enough force to obtain a stable process is required, but an oversized actuator could cause static bending or collision problems. Additionally, the bandwidth of the actuator, heavily influenced by the moving mass suspension mode and available stroke, must cover that of the targeted range of workpieces' frequency, but also be as wide as possible to adapt to new parts.

In this work, the design and validation of two new electromagnetic actuators is presented, based on a previously designed prototype [5], and creating an intercompatible range of actuators. First, the required characteristics to adapt to different kinds of workpieces are established. Then, the electromagnetic and mechanical design process is presented, including attachment method. Finally, experimental validation is performed in two steps: first each actuators' characteristics are tested at laboratory level and, later, cutting tests are performed for chatter suppression demonstration.

2 Actuator requirements

As mentioned above, the two new actuators are based on a previously designed prototype which was designed for medium to large steel structures, which usually have critical modes of tens to hundreds of kilograms of modal mass. For that purpose, it offers a 250 N nominal force on a 50 to 400 Hz frequency range and weights 8 kg. The new actuators aim to cover other applications, such as lightweight metal and composite fibre structures, for which smaller actuators are needed. Indeed, the use of the same connectors and power and control electronics systems is a requirement to ensure their intercompatibility.

2.1 Lightweight metal structures

Medium to small sized metal structures are common in automation, robotic and aerospace industries. In these cases, especially those of aluminium alloys, problematic modes present modal masses of less than 100 kg so the size of the actuator must be reduced, and the frequency range should cover slightly higher frequencies. Considering as reference the improvement carried out by passive tuned mass dampers (TMDs) with a 10% mass ratio, a nominal force of 100 N should be required for the new actuator, while its total mass should be reduced to the half of the reference prototype with an increased focus on reducing the actuator length. Considering the targeted workpieces, the required working frequency range will be set to from 60 to 500 Hz.

2.2 Composite fibre structures

Composite fibre workpieces are much lighter than steel ones while also being much stiffer than equivalent metal

structures. This results in modal masses for critical vibration modes an order of magnitude lower than metal structures, ranging from several hundred grams to a few kilograms. For that purpose, a maximum total weight of 1 kg is established as a requirement for the new actuator. It makes the actuator ten times smaller than the base so a force of 20N is expected. Finally, a reference plane wing machining project expects modes from 80 to 300 Hz, which sets the actuator working range.

3 Design

Among electromagnetic devices, Lorentz force actuators are widely employed because of their linear relationship between force and current allows for precise control applications. All the actuators proposed in this article work under the Lorentz force principle, where a charged particle moving through a magnetic field experiences a force orthogonal to the field direction. Voice coil actuators, originated from loudspeaker design, are one of the most common actuators based on the Lorentz's principle. These actuators consist of a coil suspended in a flexible manner within a magnetic field, usually generated by a permanent magnet. Among many possible physical implementations, the moving magnet configuration is chosen for the present work (**Figure 1**). There, the coil is fixed to the actuator core and the permanent magnets become the moving element, consequently the force per stroke unit is maximized thanks to the higher density of neodymium magnets and steel cores compared to copper wires wound on non-ferromagnetic aluminium bodies.

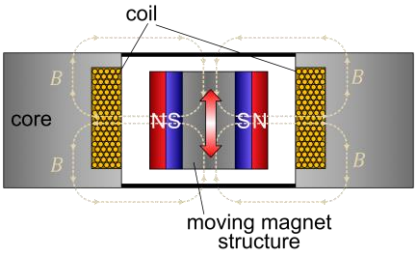

Figure 1 Simplified moving magnet voice coil.

In order to introduce a damping force into a structure the actuators must be attached in a way that the actuator core can be considered fixed. In this case the acceleration of the actuator moving mass is transferred as a force into the structure through the suspension springs. It makes the inertial actuators to possess a suspension mode at low frequencies from which the actuator starts behaving as a linear force generator. Hence, the suspension spring must be designed to obtain a lower frequency than the lowest critical mode. However, springs do not behave linearly with excessive stroke and a compromise must be met.

3.1 Electromagnetic design

Initially, a radial symmetry electromagnetic design is chosen for the new actuators in the same manner as the reference actuator. In this configuration, the coil is surrounded by a U-shaped magnetic core where magnets are embedded.

The key to ensure actuator force requirements is a correct sizing of magnets and coils. As shown by Laplace force equation ($d\boldsymbol{F} = i \cdot d\boldsymbol{l} \times \boldsymbol{B}$), three parameters must be tuned. Magnetic field $\boldsymbol{B}$ depends on the magnet size and disposition, and on the ferrous core saturation. Coil length $\boldsymbol{l}$ is given by the number of turns and coil diameter. Electric current i is limited by thermal considerations.

As all those considerations must be taken into account simultaneously, electromagnetic design has been carried out by means of FLUX electromagnetic finite element modelling (FEM) software. This way, all the design parameters can be considered at the same time, force linearity with respect to the stroke can be ensured and different magnet dispositions can be tested.

In order to use the same power electronics in all actuators, the coil wire properties have been set to be the same for every actuator, that is 0.5 mm diameter copper wire. As a result of the simulation, each of the new actuators uses a different magnet disposition and coil number.

3.1.1 Lightweight metal structures actuator

The actuator for lightweight metal structures follows the same radial configuration as the reference actuator. Here, several magnets of radial polarity are stacked vertically at each side of the coils, with smaller axially magnetized magnets in between forming a Halbach configuration to maximize the magnetic field intensity. Two coils have been included, because it allows for bigger magnets compared to three coil configuration, therefore yielding more force for the same size. **Figure 2** shows the magnetic field isolines and core saturation for the final design.

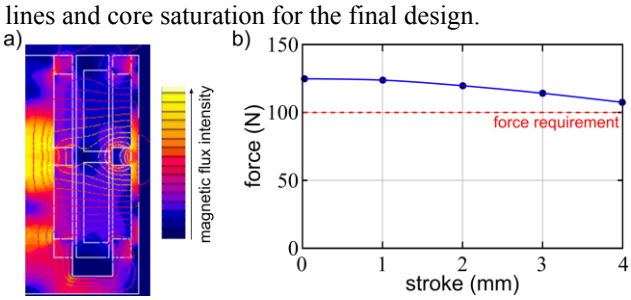

Figure 2 a) Electromagnetic FEM of light metal structures actuator with isolines; b) force linearity results.

Based on electromagnetic FEM results, the force requirement of 100 N is surpassed, while the total volume of the actuator electromagnetic core is reduced by 50%. Furthermore, this force requirement is met over the complete stroke of 4 mm.

3.1.2 Composite fibre structures actuator

Although radial configuration was initially defined, scaling the reference prototype design to ten times less volume for meeting composite fibre structures actuators' requirements is impractical, as proportionally reduced magnets become too thin to create an intense enough field.

Because of that, a single magnet design has been selected where the field is directed by the steel core to cross trough the coil section. The magnet is located at the base of the central axis of the core and has axial direction of polarity. Sizing both sides of the steel core becomes critical as maximum Lorentz force is achieved when there is no saturation and field isolines are orthogonal to the coil.

With a magnet radius of 13.5 mm, simulation results give a maximum electromagnetic force of 23N, hence meeting the requirements. The moving mass of this actuator is estimated at 270 g which means a 84% volume reduction.

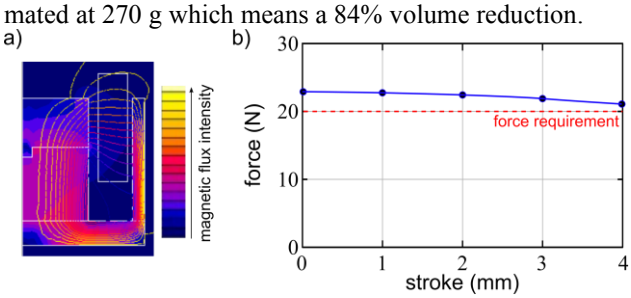

Figure 3 a) Electromagnetic FEM of composite structures actuator with isolines; b) force linearity results.

3.2 Mechanical design

The mechanical design of the actuators is focused in delivering the inertial force of the moving mass to the workpiece to apply damping. For this purpose, the design has two main aspects: suspension springs and actuator's attachment method.

Firstly, the suspension of the magnetic core, which is the inertial mass of the actuator, is designed. These springs are required to show high radial stiffness and a relatively low axial stiffness. Indeed, actuator natural frequency is determined by axial stiffness and inertial mass. The springs are designed to withstand the maximum electromagnetic force possible at the lowest frequency within the actuator's bandwidth. A topological optimization has been performed by FEM simulations to design spring geometries (**Figure 4-a**). FEM simulations resulted in 0.7 mm thickness 1.4031Mo stainless steel spring for the lightweight metal structures actuator, which results in a theoretical natural frequency of 40 Hz; and a 0.5 mm thickness spring for the composite fibre structures actuator, obtaining a natural frequency of 78 Hz. In this way, both natural frequencies remain below their respective actuator's frequency ranges.

Secondly, each of the new actuators' attachment to the workpieces has been addressed. As previously explained, the actuators' stator must be securely attached to the workpiece to effectively apply the damping force. However, any modifications to the workpieces such as the use of screws or drilling holes are strictly prohibited. Additionally, the attachment method must allow for easy removal, generate a high force when locked, and be adapted to work close to the machining process.

Although the lightweight metal actuator is designed to work with both ferromagnetic and non-ferromagnetic parts, in this work, only the magnetic attachment device has been designed for this actuator. The new magnetic clamping is switched mechanically by turning a cylindrical magnet of radial magnetization surrounded by two iron pieces. Depending on the rotation of the magnet, the variation in thickness of the surrounding iron causes the magnetic flux to either escape the clamping and pass through the workpieces or be retained withing the clamping device resulting in minimal force exerted on the part (**Figure 4-b**). The simulation results in a magnetic force of 2500 N in fixing position at 0.1 mm of a continuous steel surface and just 300 N in open position.

The actuator designed for composite structures will only be used for damping of non-ferromagnetic workpieces, so the vacuum clamping concept has been selected as the attachment method. To ensure a high stiffness fixturing to transmit the inertial force into the part, a custom vacuum solution has been designed (**Figure 4-c**). The vacuum clamping consists of a soft sucker, which allows for adapting to irregular surfaces, along with three screwed contacts in the outside spread at 120º to avoid force orientation changes due to sucker deformations.

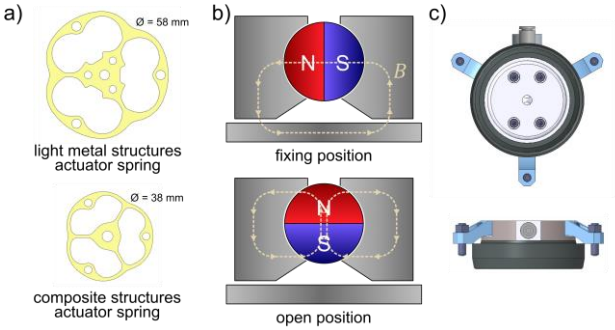

Figure 4 a) suspension springs' topology; b) magnetic clamping design concept; c) vacuum clamping 3D model.

4 Experimental validation

The validation of the new actuators is performed in two steps. First, open loop characteristics of the actuator are tested in the laboratory level to ensure the fulfilment of design requirements. After that, active damping and cutting tests are performed in a milling process of an aluminium workpiece attached to a steel flexure.

4.1 Validation of the actuators in open loop

The first validation tests of the actuators consist of obtaining their current to force relation curve. Since the relation between coil current and commanded voltage is linear in the actuator bandwidth thanks to used current amplifiers, the force curve is measured in newtons per commanded volts (N/V). **Figure 5** shows the force curves of each actuator.

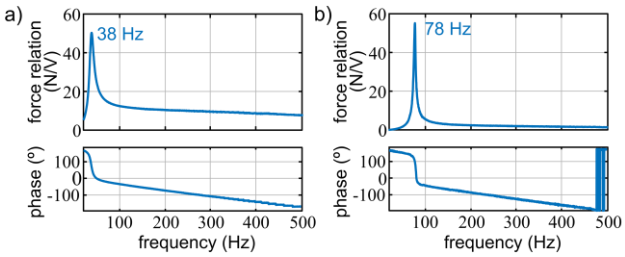

Figure 5 N/V relation for both actuators: a) light structures actuator; b) composite structures actuator.

From the N/V curves each actuator's natural frequency is also obtained, being of 38 Hz for the 100N actuator and of 78 Hz for the 20N actuator, hence, below of the respective frequency ranges.

Next, the actuators' maximum force in the working range is obtained. The maximum force is limited by two factors:

below and around the natural frequency, spring fatigue limits the stroke, and above this frequencies, maximum current limits the achievable electromagnetic force.

Results shown in **Figure 6** demonstrate that the actuators exceed their nominal force for most of their working range, not going below 10% of that in any case. In fact, when applying damping force, filtering the command signal for avoiding spring fatigue will be necessary.

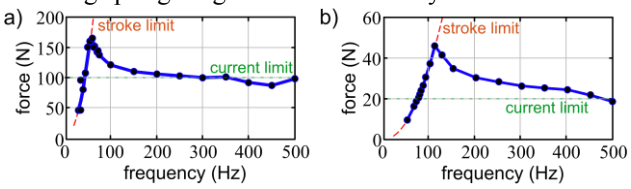

Figure 6 Maximum force for a) light metal structures actuator; b) composite structures actuator.

Finally, thermal behaviour of the actuators has been analysed. Results show that both actuators can overcome the safety 90 ºC body temperature, which is set not to overheat the coils and cause an electric failure of the actuators. This limit is reached after 25 minutes with a maximum current 150 Hz sine excitation for the lightweight metal actuator and after 40 minutes for the fibre actuator. Therefore, a temperature control algorithm is introduced on the controller to limit the current when this temperature is reached.

4.2 Active damping and cutting tests

Finally, milling tests over an aluminium workpiece attached to a lightweight flexure are performed for testing the actuators operation behaviour. The steel flexure permits the attachment of both actuators, and its dynamics consist of a main mode of 157.8 Hz, 23.9 kg modal mass and 0.014 damping coefficient, which is slightly modified when any of the actuators is attached because of the added mass. Cutting conditions are selected for emulating real cutting conditions of an aluminium structure, by using a 14 mm diameter three-fluted milling tool with 2 mm of radial engagement and a spindle speed of 5000 rpm.

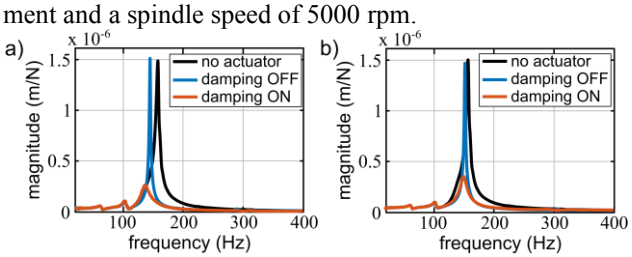

Figure 7 Frequency response function of the flexture, without any actuator, and with each of them with damping OFF and ON.

As shown in **Figure 7**, the dynamic stiffness is improved 82.5% and 77.2% with respect to the original flexure dynamics, by respectively the lightweight metal and composite fibre actuators.

Regarding the cutting tests, a maximum axial depth of cut of 5 mm is permitted for stable cutting when active damping solution is not applied. However, this stability can be increased by 140% (12 mm depth of cut) when composite fibre actuator is used, while the lightweight metal actuator permits to cut up to the maximum depth of cut allowed by the tool, which is 30 mm, more than 500% of the original cutting capacity (see **Figure 8**).

5 Conclusions

The present work presents the design and validation of two Lorentz actuators for the damping of critical workpieces' vibrations, hence, completing a range of intercompatible actuators to cover multiple applications of flexible workpieces by means of a single system. With careful FEM based electromagnetic and mechanical design the requirements of different industrial sectors where chatter is a productivity limiting factor are met. Then, both actuators have been validated in cutting tests increasing the stable cutting limit 2.4 and 6 times respectively. Further work will be centred in the design on a low-natural frequency actuator for damping of whole-body modes of large workpieces.

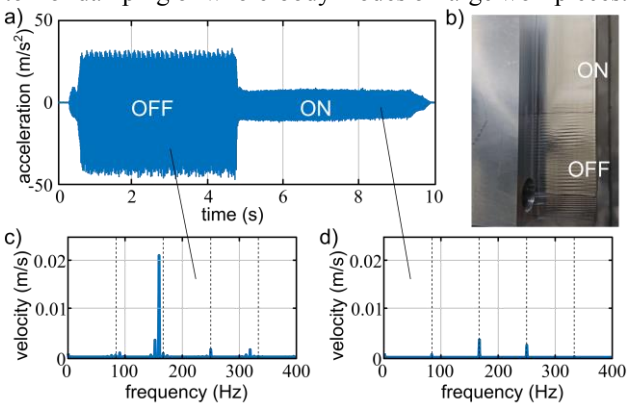

Figure 8 Cutting test with the actuator designed for lightweight metal structures (27 mm of depth of cut): a) Accelerometer time signal; b) Surface finishing on the workpiece; c) Frequency spectrum with actuator disabled; d) Frequency spectrum with actuator enabled.

6 Literature

[1] Munoa J, Beudaert X, Dombovari Z, Altintas Y, Budak E, Brecher C, Stepan G (2016) Chatter suppression techniques in metal cutting. CIRP Annals 65(2):785–808.

[2] Dombovari Z, Altintas Y, Stepan G (2010) The effect of serration on mechanics & stability of milling cutters. International Journal of Machine Tools & Manufacture 50(6): 511–520.

[3] Zeng S, Wan X, Li W, Yin Z, Xiong Y (2012) A novel approach to fixture design on suppressing machining vibration of flexible workpiece. Int. J. Mach. Tools & Manuf., 58: 29-43.

[4] Matsubara A, Taniyama Y, Wang J, Kono D (2017) Design of a support system with a pivot mechanism for suppressing vibrations in thin-wall milling. CIRP Annals, 66(1), 381-384.

[5] Beudaert X, Erkorkmaz K, Munoa J (2019) Portable damping system for chatter suppression on flexible workpieces. CIRP Annals, 68(1), 423-426.

[6] Mancisidor I, Beudaert X, Aguirre G, Barcena R, Munoa J (2018) Development of an active damping system for structural chatter suppression in machining centers. Int. J. Autom. Tech., 12(5), 642-649.

Development of a compact jumping lunar rover driven by shape memory alloy actuators

Yuki Oka, Hironari Taniguchi, Taichi Izumi, Koki Yura
Graduate School of Robotics and Design, Osaka Institute of Technology
1-45, Chayamachi, Kitaku, Osaka, Japan

Abstract

In this study, we developed a compact rover for hopping on low-gravity planets like the moon, exploring the use of Shape Memory Alloy (SMA) actuators to lighten propulsion. Previous designs attached SMA actuators directly to toggle mechanism vertices, consuming energy. To enhance force, we devised a horizontal slider mechanism to drive SMA actuators and the toggle mechanism independently. Validation experiments included correcting initial positions using additional SMA actuators to ensure the proper functioning horizontal slider mechanism. Evaluation experiments showed a 3.6-fold increase in hopping force compared to the previous design. These results establish the feasibility of combining SMA actuators and toggle mechanisms for hopping rovers.

1 Introduction

Humanity's interest in the moon spans resource utilization and understanding Earth's origins. In recent years, intensified exploration efforts have been spurred by the discovery of water on the moon, leading to the consideration of various mobility methods on planetary surfaces [1]. These methods range from wheeled vehicles to those capable of hopping movement. While wheeled vehicles offer stability in movement, they face challenges on solid planets due to fine regolith, like lunar soil, which poses a risk of getting stuck. For instance, NASA's Mars Exploration Rovers (MER) achieved remarkable distances but encountered issues, such as MER-A getting stuck in sand [2][3]. Various solutions have been attempted, such as increasing wheel diameter or altering wheel shape, but they run counter to the prevailing trend of downsizing exploration vehicles. On the other hand, hopping exploration vehicles offer high mobility in low-gravity planets compared to Earth, making it easier to detach from regolith. Hopping methods include using reaction wheels and springs. For example, the German Aerospace Center's MASCOT, deployed on the JAXA's asteroid exploration mission HAYABUSA-2, demonstrated hopping capabilities of up to 200 meters on an asteroid [4]. However, due to ultralow gravity challenges, implementing these methods on bodies like the moon or Mars is difficult. Thus, JAXA spearheaded the development of LEV-1, the inaugural lunar surface hopping exploration rover [5]. Other rovers, like SphereX and a wheel-and-hop robot, combine rolling and hopping movements [6][7]. Numerous proposals have been put forth for compact exploration vehicles employing spring-based hopping mechanisms, but most depend on motor-driven actuators, which can increase complexity, power requirements, and weight. The notion of deploying multiple small exploration vehicles for swarm-based exploration is gaining momentum [8]. Therefore, this study investigates the use of shape memory alloy (SMA) actuators for lightweight hopping mechanisms [9][10]. SMA actuators utilize alloys with shape memory properties that return to a predefined shape upon reaching a certain temperature, offering high energy efficiency and widely used in various applications [11]. Additionally, these actuators generate greater force with larger shape memory-induced strains. Coil-shaped linear actuators with stored shape memory are employed in this study, combined with a toggle mechanism for force amplification. This paper presents findings from validation testing performed on a proof-of-concept model of the horizontal sliding mechanism designed to independently drive the toggle mechanism and SMA actuators.

2 Working Principle

Figure 1 provides an overview of the prototype with the horizontal slider mechanism. The prototype stood 150 mm tall with a disk diameter of 130 mm, weighing 256.2 g. The toggle mechanism comprised two 55 mm-long links and compressed two springs from their natural length of 92 mm to 42 mm, achieving a total spring constant of 1.14 N/mm. Eight SMA actuators were utilized for toggle operation, four for retraction, and one for triggering hopping. These SMA actuators were constructed from Ni-Ti-Cu alloy, featuring a wire diameter of 0.6 mm and a coil outer diameter of 3.2 mm. Figure 2 shows an overhead view of the prototype, highlighting eight SMA actuators (yellow) arranged in two sets of four parallel actuators for toggle. For retraction, blue-highlighted areas indicate SMA actuators arranged in pairs and connected electrically in series. This setup facilitated evaluation experiments.

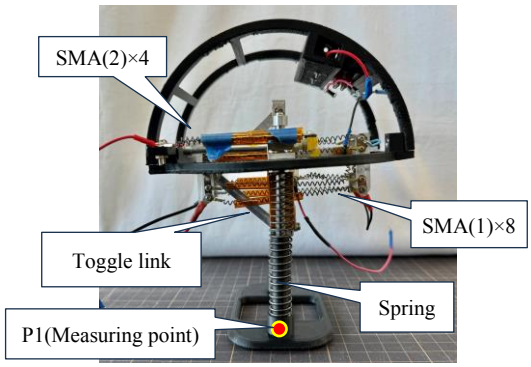

Figure 1 Overview of the prototype

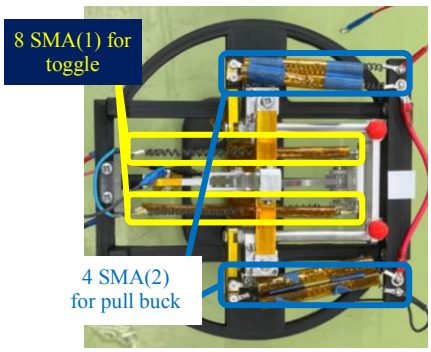

Figure 2 Arrangement of SMA actuators on prototype viewed from above

Figure 3 illustrates the spring actuation by SMA directly attached to the toggle mechanism. The actuation force of SMA (1) is transmitted through the toggle mechanism, which amplifies the force and transfers it to the spring, inducing spring compression. However, there was an issue where the SMA actuator, being directly attached to the link vertex of the toggle mechanism, interfered with the contracted SMA actuator during the energy release of the spring, resulting in loss of jump energy. Therefore, a horizontal slider mechanism as shown in Figure 4 was incorporated into the device. The horizontal slider mechanism is equipped with two different SMAs. By operating SMA (1), pressure is applied to the link vertex of the toggle mechanism, activating the spring. Following this motion, SMA (2) is actuated to retract SMA (1). This action was achieved by a new SMA actuator, de-signed to ensure that the SMA does not hinder the hopping. Subsequently, validation testing of the prototype constructed based on this configuration was conducted.

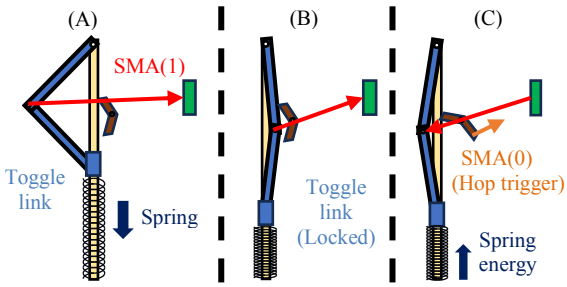

Figure 3 Spring actuation by SMA directly attached to the toggle mechanism

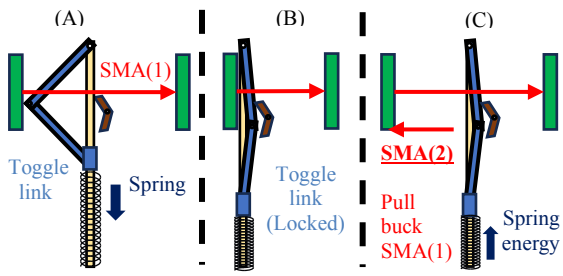

Figure 4 Spring actuation by horizontal slide mechanism

3 Experiments and Results

3.1 Operation Verification Test

The purpose of this test is to assess the feasibility of the expected operations of the horizontal sliding mechanism and to compare the speed and temperature of the SMA actuators during operation to elucidate their operational characteristics. The experimental setup diagram is presented in Figure 5.

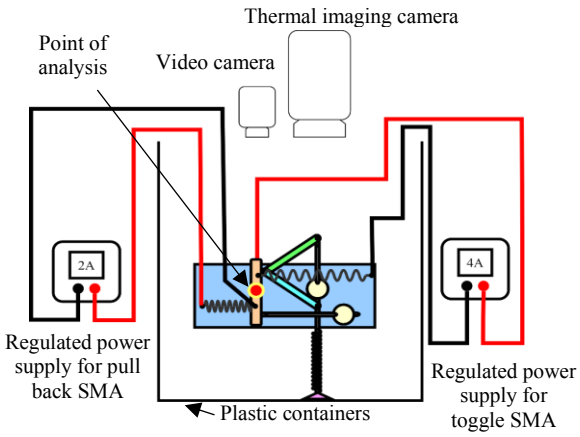

Figure 5 Experimental setup of the operation verification test

The SMA actuators for the toggle mechanism are under constant tension from the retraction SMA actuators. Consequently, it is expected that the SMA actuators for the toggle mechanism will maintain their elongated state even after contraction due to cooling. The same principle applies to the retraction SMA actuators. Additionally, to mitigate the impact of convection on the cooling of SMA actuators, the experimental setup is enclosed in a plastic container. This enclosure prevents convection induced by human movement in the experimental environment from affecting the experimental apparatus. An overview of the experimental procedure is provided below.

1. Set up the testing machine inside the plastic case according to Figure 5.
2. Position a thermal imaging camera (testo885, testo K.K.) and a video camera (HC-VX985M, Panasonic) on tripods to capture images from above, ensuring a distance of 206mm from the analysis point
3. Apply a constant current of 4A to the SMA actuator for the toggle mechanism and operate the toggle mechanism. The voltage ranged from 5.5V to 6.0V.
4. After operating the toggle mechanism, wait for the SMA actuator for the toggle to cool down.
5. Apply a constant current of 2A to the SMA actuator for retraction and retract the sliding component. The voltage ranged from 2.7V to 3.0V.
6. Wait for the retraction SMA actuator to cool down.
7. Repeat steps 3 to 6 ten times.

During the experiment, the room temperature was 23°C with 33% humidity. Figure 6 summarizes the displacement of analysis points over time. While the cooling time of the

toggle SMA actuator was extended in the sixth trial, there was no significant variation in displacement observed across all trials. The average operation time of the toggle mechanism was 17.97 seconds, with an average displacement of 30.17mm and an average velocity of 1.68mm/s. However, during cooling, the points were pulled back by the retraction SMA actuator's contraction, and this phenomenon persisted even after the retraction SMA actuator's operation. Therefore, it is recommended to supply current to the trigger SMA actuator for jumping immediately after the retraction SMA actuator's current supply ends. This experiment revealed the operational characteristics of the prototype and confirmed its functionality.

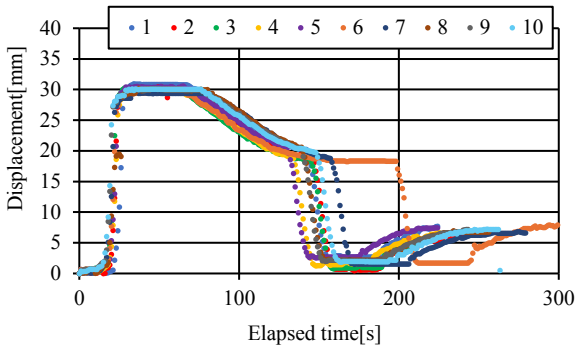

Figure 6 Displacement of points for analysis

3.2 Jumping Test

To evaluate the impact of the horizontal sliding mechanism on jumping force, experiments were conducted using a prototype. The focus was on vertical jumping force, comparing two conditions: one with the sliding mechanism activated and no load on the SMA actuator for retraction, and the other with the sliding mechanism deactivated, resulting in contact between the toggle mechanism's link and the sliding component. This contact loaded the spring to retract the SMA actuator. Jumping height was determined by measuring the vertical distance between the leg and the ground. Infrared reflectors were attached at point P1 (as shown in Figure 1) for tracking using 3D motion analysis software (DIPP-Motion, DITECT). The procedure is outlined below.

1. Attach infrared reflective material to the testing machine, install an infrared high-speed camera (HAS-L1, DITECT), and calibrate using a cube with infrared reflective material on its corners.
2. Apply current to the SMA actuator for the toggle under the same conditions as the operational test, compressing the spring to lock the toggle mechanism.
3. Sufficiently cool the SMA actuator for the toggle.
4. If the horizontal sliding mechanism is not operated, skip this Step 4 and proceed directly from Step 3 to Step 5. Otherwise, apply current to the SMA actuator for retraction to retract the sliding component, following the operational test conditions.
5. Apply a current of 1.2V and 2A from a AAA rechargeable battery (eneloop pro, Panasonic) to the trigger SMA actuator and make it jump.
6. Record the jumping process with the infrared high-speed camera.
7. Perform steps 2 to 6 for each of the two types of operation of the horizontal sliding mechanism ten times.

Figure 8 shows experiments with the horizontal sliding mechanism activated (A) and deactivated (B). Figure 9 illustrates the maximum vertical leap under each condition. When the horizontal sliding mechanism is activated, the maximum vertical leap increases to approximately 259.9mm, compared to approximately 72.0mm when it is not activated. However, the standard deviations are 10.7 and 3.6 respectively, indicating increased variability due to the mechanism's operation. Nevertheless, considering the leap increase ratio of approximately 360% and the standard deviation increase ratio of about 300%, it can be argued that the variability has relatively decreased.

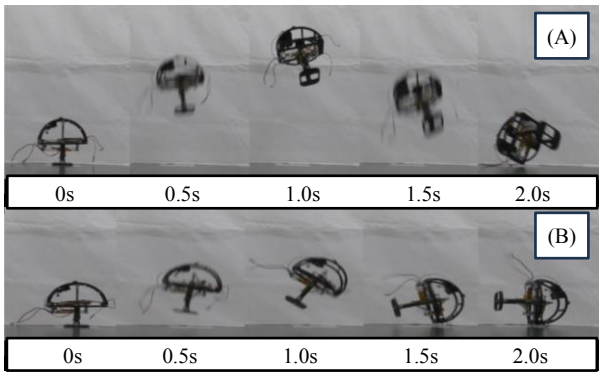

Figure 8 Jumping motion experiments with the horizontal sliding mechanism activated (A) and deactivated (B)

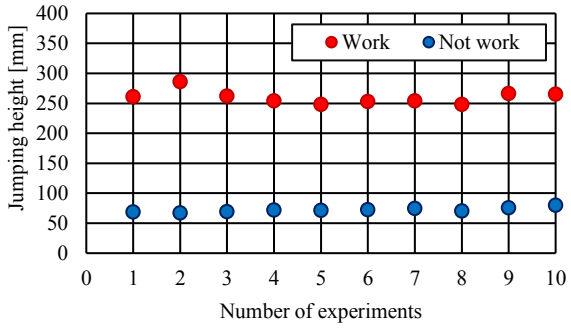

Figure 9 Comparison of maximum vertical leap of jumping

4 Conclusions

This study reported on the development of a jumping mobile small rover incorporating SMA actuators as the driving source and a toggle mechanism as a method for exploring the lunar surface. Previous devices had examined methods of amplifying the varying actuation force of SMA actuators with a toggle mechanism to drive the jumping spring, but faced the issue of the contracted SMA actuators becoming a load during the jump. To address this issue, a horizontal slider mechanism was proposed to drive the SMA actuators separately from the

toggle mechanism. In the investigation of operational characteristics in the prototype, the operation of eight SMA actuators for toggle mechanism action and four retracting SMA actuators to return them to their initial state was examined in terms of temperature, time, and distance traveled. As a result, it was confirmed that the introduced retracting SMA actuators functioned properly. Additionally, insights were gained that the retracting SMA actuators should be activated immediately after completing the jump to drive the trigger SMA actuators. In vertical jump evaluation tests based on the presence or absence of the horizontal slider mechanism, the average of 10 jumps with the horizontal slide mechanism activated was approximately 259mm, while without activation it was about 72mm. This result indicated an approximately 3.6-fold increase in jumping force, demonstrating a significant improvement in jumping force by introducing the horizontal slider mechanism.

Through this study, the operation of a jumping exploration vehicle combining SMA actuators and toggle mechanisms was established, providing insights for the fabrication of future demonstration models. Since the prototype in this study only performs vertical jumps, further development is expected to address leg design, optimal SMA actuators, and spring selection to conduct actual mobility exploration.

5 Acknowledgments

We would like to express our sincere gratitude to the Space Oriented Higashiosaka Leading Association (SOHLA) for their generous support and cooperation in advancing this research. Additionally, we extend our heartfelt thanks to FURUKAWA TECHNO MATERIAL Co., Ltd. for providing the Ni-Ti-Cu alloy actuators used in this study.

6 Literature

[1] M.D. Gray, A. Baudry, A.M.S. Richards, E.M.L. Humphreys, A.M. Sobolev, J.A. Yates, “The physics of water masers observable with ALMA and SOFIA: model predictions for evolved stars“, Monthly Notices of the Royal Astronomical Society, Volume: 456, Issue: 1, 2015.

[2] Joy A. Crisp, Mark Adler, Jacob R. Matijevic, Steven W. Squyres, Raymond E. Arvidson, David M. Kass : Mars Exploration Rover mission, Journal of Geophysical Research: Planets, Volume 108, Issue E12, 2003.

[3] R. E. Arvidson, et. al., “Spirit Mars Rover Mission: Overview and selected resultsfrom the northern Home Plate Winter Haven to the sideof Scamander crater“, Journal of Geophysical Research E: Planets, Volume 115, Issue E7, 2010.

[4] J. Reill, H.-J. Sedlmayr, P. Neugebauer, M. Maier, E. Krämer, and R. Lichtenheldt : MASCOT - Asteroid Lander with innovative Mobility Mechanism, Conference: 11th Low-cost Planetary Mission Conference, Abstract und Poster, Berlin, 2015.

[5] JAXA, “Result and Achievements of the Lunar Excursion Vehicle (LEV-1) on board Smart Lander for Investigating Moon (SLIM) “, https://global.jaxa.jp/press/2024/01/20240125-2_e.html, View 2024.03.08.

[6] Himangshu Kalita, Troy M. Jameson, George Stancu, Jekan Thangavelautham, “Design and Analysis of a Mechanical Hopping Mechanism Suited for Exploring Low-gravity Environments“, 2020 IEEE Aerospace Conference, pp1-10, 2020.

[7] Y. Zhang, L. Zhang, W. Wang, Y. Li and Q. Zhang, "Design and Implementation of a Two-Wheel and Hopping Robot With a Linkage Mechanism," in IEEE Access, vol. 6, pp. 42422-42430, 2018.

[8] Logan Yliniemi, Adrian K. Agogino, Kagan Tumer, “Multirobot Coordination for Space Exploration“, AI MagazineVolume 35, Issue 4, p.61-74, 2014.

[9] Tomoki Hirota, Hironari Taniguchi and Masato Tanaka,“Development of a lightweight jumping unit using SMA actuators for a small lunar rover” , Proceedings of The 8th International Conference on Manufacturing, Machine Design and Tribology,2019.

[10] T. Hirota and H. Taniguchi,“Jumping Mechanism Using Shape Memory Alloy Actuators for a Lunar Rover“, 2020 IEEE/SICE International Symposium on System Integration (SII), pp. 1335-1339, 2020.

[11] Arias Guadalupe J., Copaci, D., Serrano del Cerro D.,

[12] Moreno L., Blanco D., “Efficiency Analysis of SMA-Based Actuators:Possibilities of Configuration According to the Application.“, Actuators 2021, 10, 63, 2020.

Performance Optimization of an SMA-Actuated Camera Gimbal

Alexander Schwegler M. Sc., Aalen University of Applied Sciences, Aalen, Germany
Dennis Niklas B. Eng., Aalen University of Applied Sciences, Aalen, Germany
Dipl.-Ing. Tobias Schumm, Actuator Solutions GmbH, Gunzenhausen, Germany
Prof. Dr.-Ing. Arif Kazi, Aalen University of Applied Sciences, Aalen, Germany

Abstract

Camera drones use a gimbal to orient the camera in the desired direction and to compensate aircraft movement in flight. The gimbal contributes a significant amount to the weight of the drone. As EU regulations impose limits on the weight of drones, there is a need for novel ways to reduce aircraft weight.
Previous work proposed a novel concept for a lightweight SMA-actuated camera gimbal. This study investigates the performance of a first gimbal prototype and ways to improve its shortcomings. The prototype gimbal successfully demonstrated that the requirements regarding angular range and velocity can be met. The weight of the prototype (including camera dummy) was only 2.25 g. However, the stress in the SMA wires was significantly higher than expected, and the 3D printed flexures exhibited issues with high damping, longevity, and buckling. The SMA actuator unit was redesigned by incorporating steel flexures in a pull arrangement. A scaled functional prototype of the actuator unit verified that the above issues are solved, paving the way for a new gimbal prototype at the target size.

1 Introduction

Camera drones have seamlessly integrated themselves into the content creation industry. Large professional drones require training, a license, and a permit to fly. On the other hand, smaller drones of the <250 g class are almost free to use for everyone within the EU [1]. This weight cap, however, raises the need for innovative approaches to save weight.
The camera gimbal is a complex system that contributes a significant amount to the weight of a drone. The excellent power-to-weight ratio of SMA actuators makes them an attractive choice for actuating camera gimbals. [2] solved constraints in SMA actuator stroke by a novel design of a rotatory actuator based on an inverted pendulum. [3] combined these actuators with parallel kinematics derived from the “Agile Eye” kinematics [4] and showed possible actuator arrangement as well as the manufacturing techniques and test benches.
This paper presents the findings and issues of the first prototype, as well as the optimization process and the resulting improvements. Section 2 starts off by revisiting the requirements set for the camera gimbal. Section 3 presents a first prototype of the gimbal in target size. Section 4 discusses the performance of this prototype and issues with the first design. Approaches on how to solve these issues are shown in Section 5, together with a redesign of the actuator. Section 6 illustrates how the actuator redesign solves the issues of the first gimbal prototype. Finally, Section 7 provides an outlook on what an improved version of the camera gimbal could look like.

2 Gimbal Requirements Revisited

[3] proposed a set of requirements that were based on the performance claims of major drone manufacturers. To verify these claims, a test flight with a DJI Mini 2 drone was performed to capture the flight data through its integrated flight data recorder. The test flight included multiple flight scenarios and maneuvers in different flight modes to cover a broad spectrum of use cases.
The recorded data showed that the aircraft motion range of ±40° cannot always be stabilized as specified by the drone manufacturers. ±30° could be stabilized in all axes and scenarios. Therefore, the requirement for the dynamic image stabilization range of the gimbal is set to ±30°. The requirement for a static gimbal stroke of ±45° [3] remains unchanged.
The angular velocity for the Mini 2 is rated at 130°/s. In flight, the drone reached angular velocities of 50°/s, only exceeding the specification during hard braking maneuvers. This means that an angular velocity of 50°/s is sufficient for all flight scenarios except emergency braking maneuvers, which do not need to be perfectly stabilized for content creation.

3 Camera Gimbal Prototype

The concept for an SMA Camera Gimbal proposed in [3] was implemented in a first prototype. This prototype is shown in **Figure 1**.

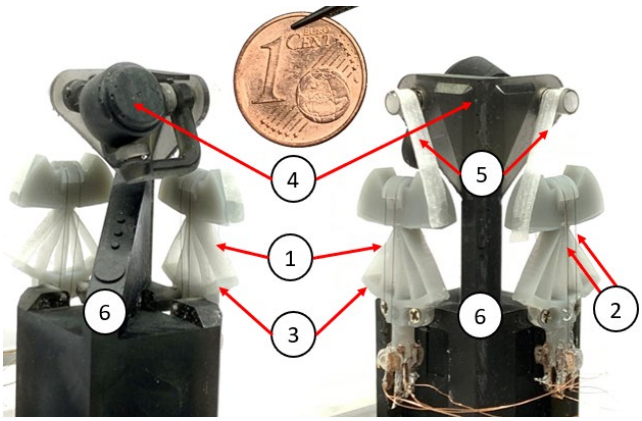

Figure 1 SMA Camera Gimbal Prototype

The SMA actuator units ① in the gimbal prototype comprise a pair of antagonistic 50 µm SmartFlex® Clean Melt SMA wires ② from SAES Getters. The actuator units use 3D printed flexures ③ to guide and stabilize the 'inverted pendulum' kinematics. They are designed to provide an angular stroke of ±15°. The 300 µm thin flexures were 3D printed using an ELEGOO Mars 4 Digital Light Processing (DLP) printer. The parallel kinematics ④ enables image stabilization in two degrees of freedom. Its links are also DLP printed. The joints are realized with miniature ball bearings (Ø3x1 mm). A belt transmission ⑤ with a gear ratio of 4.6 transmits and amplifies the actuator stroke. The weight of the system shown in Figure 1 – excluding the base ⑥ – is only 2.25 g. This includes the camera dummy of 0.72 g.

4 Prototype Performance

During testing, the prototype SMA actuator achieved a maximal angular stroke of up to +15°/-24°, which resulted in an angular range of almost ±90° on the gimbal axes. Angular velocities up to 70°/s and dynamic strokes of ±42° were recorded on the gimbal's axis. However, the actuator motion suffered from a high amount of damping, as shown in **Figure 2**.

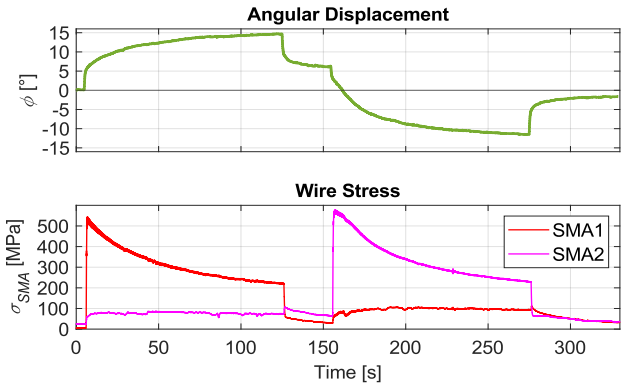

Figure 2 Step response of a prototype actuator unit

The plot illustrates the actuator motion, as well as the recorded wire stress, after a step change in heating power to the first SMA wire. The actuator reached its full stroke after 120 s. The SMA wire stress was initially at 550 MPa and reached its designed value only after the actuator motion had come to a standstill. After the heating power was turned off, an angular offset remained until the second SMA wire was heated. As the flexures were made from a photopolymer, it was assumed that this behavior was caused by the viscoelastic damping of the material.

Apart from these issues with the dynamic behavior, the lifetime of the 3D printed flexures was limited to a few hours of operation. Prototypes usually failed through buckling due to fatigue in the flexures. In addition, the inverted pendulum actuator kinematics requires a finely tuned flexure stiffness, which proved difficult to achieve with a photopolymer and may change over time. In conclusion, 3D printed flexures may be a sensible approach to prove the feasibility of an actuator design, but will not be the preferred choice for prototypes to undergo rigorous testing.

5 Redesign and Optimization

The issues described above led to the decision to go back to conventional metal flexures. Spring steel 1.1274 was chosen as the flexure material, as it has favorable mechanical properties with a high permittable stress of 1440 MPa and a Young's modulus of 210 GPa. To avoid buckling problems, the resulting SMA wire force on the flexure was inverted from a pushing force to a pulling force as shown in **Figure 3**.

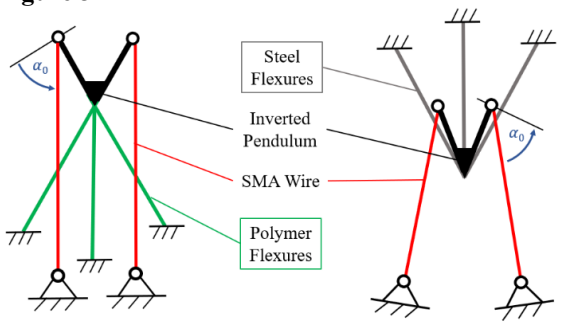

Figure 3 Original actuator unit geometry (left) compared to the redesigned geometry (right)

In the redesigned geometry, the SMA wires are arranged at an angle to allow them to fit in between the bending beams of the flexure. This geometry results in a slightly larger actuator. This was deemed acceptable, as for a camera gimbal, a highly miniaturized size will be less important than a small weight. From a kinematic point of view, both geometries are equivalent.

For testing the redesigned actuator unit with steel flexures, a functional prototype was designed at a 3:1 scale. The diameter of the SMA wire was increased to 150 µm, and the required flexure stiffness calculated accordingly [2]. For the design of the flexure, a two-step approach was taken. The first design step identified suitable geometric flexure parameters from analytical calculations. **Figure 4** shows possible flexure geometries for the required stiffness and different numbers of bending beams. The red area designates flexure geometries that exceed the allowable stress.

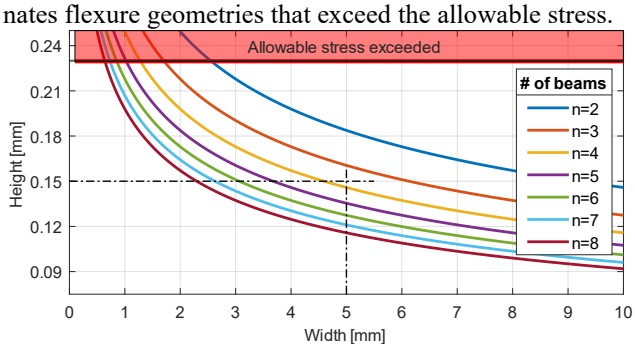

Figure 4 Analytical computation of flexure geometries for a given stiffness

In the redesigned actuator geometry, an even number of bending beams makes the arrangement of the SMA wires easier. As a higher number of bending beams will lead to an increased complexity in terms of assembly, a configuration with four bending beams (each 0.15 mm thick and 5 mm wide) was selected. The beams were to be glued into the 3D printed structure.

The second design step used Finite Element Analysis (FEA) to verify the selected flexure geometry for large deflections, and also to reflect the properties of the adhesive. Four different adhesives were compared for both their static and dynamic strength, as well as for creep. The Uhu® Plus Endfest 2-K adhesive emerged as the preferred candidate. However, modeling the glue contacts proved to be quite challenging. Comparison of FEA results with experimental results from a test flexure showed that only contacts under the influence of friction were able to replicate the real behavior.

The FEA of the functional prototype flexure showed stress levels in the bending beams had a sufficient safety margin (>2.1). FEA was also used to calculate the angular deflection of the flexure for different combinations of SMA wire forces. The deflection calculated by FEA was then fitted by a 3rd order polynomial function of both SMA wire forces. The polynomial function was integrated into a MATLAB® simulation model of the entire actuator unit, which also included the SMA model described in [5, 6]. The antagonistic SMA wires were used in a "U" shaped configuration, with each free leg having a length of 62 mm. **Figure 5** illustrates the simulation results.

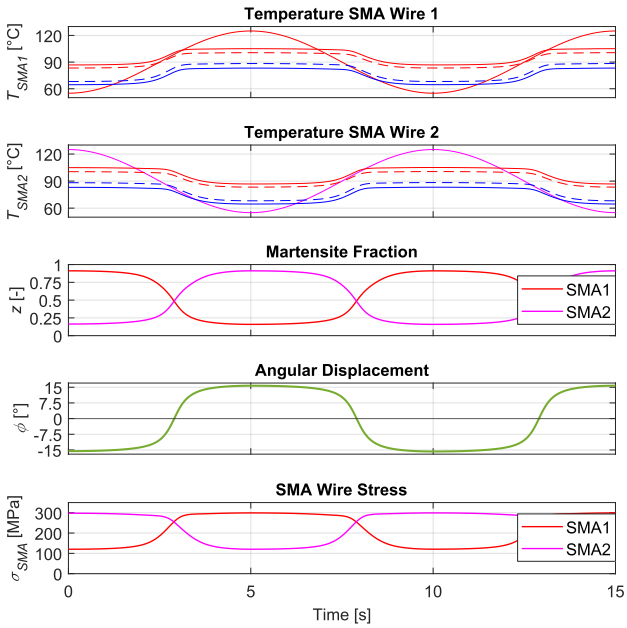

Figure 5 Simulation of the functional prototype

The simulation predicted angular deflections of ±15.7° at SMA wire stress levels below 300 MPa. The differential strain in the SMA wires was calculated to 2.3 %, which was also considered a good value for an actuator design.

6 Experimental Results

The testing of the scaled redesigned actuator unit used the assembly and testing setup described in [3]. Figure 6 illustrates the redesigned SMA actuator unit ① with steel flexures ② in the test setup.

The setup comprises two force sensors (ME Messsysteme KD40s ③) for measuring SMA wire ④ forces and manual positioning tables ⑤ for adjusting SMA wire pre-strain. The angular displacement is measured using a video tracking system.

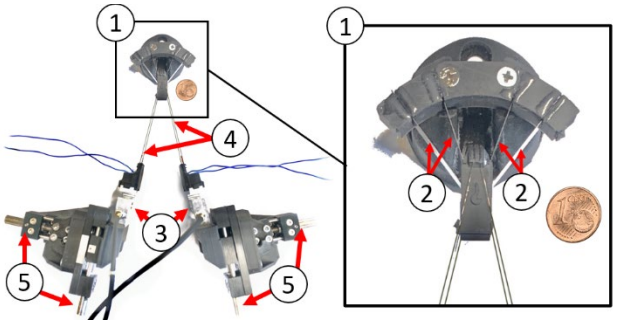

Figure 6 Functional prototype of the actuator unit in the test setup

Performance evaluation started with a comparison of the functional model to the simulation in **Figure 5.** Experimental results are shown in **Figure 7**.

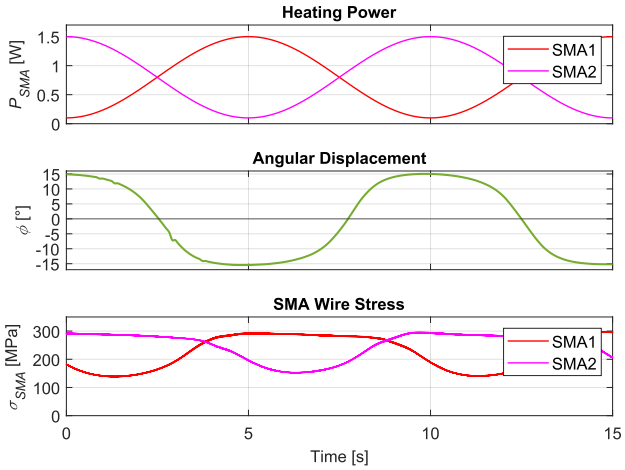

Figure 7 Experimental results of the functional prototype.

The performance of the functional prototype matched the simulation well. The angular displacement reached ±15.2° with a small offset of the middle position. SMA wire stress did not exceed 290 MPa. Subsequently, the response to a step increase in heating power was recorded in the same manner as in **Figure 1**. **Figure 8** shows the results.

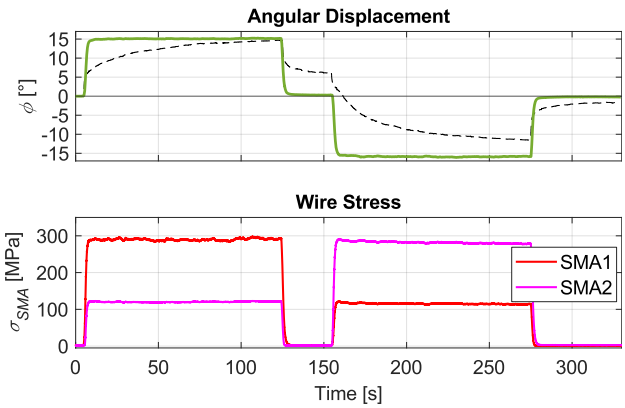

Figure 8 Step response of the functional prototype

The redesigned actuator unit showed significantly lower damping than the first prototype (displacement is shown as a grey dotted line). The actuator unit reached its maximum angular displacement without delays or offsets. The wire

stress remained within an acceptable range, ranging from 140 to 300 MPa. The dynamic behavior of an actuator unit in target size will improve significantly due to the increased surface-to-volume ratio of the SMA wires.

7 Outlook: SMA Camera Gimbal 2

Further research will discuss the development of a second Gimbal prototype. A first concept for the rearranged system is depicted in **Figure 9.**

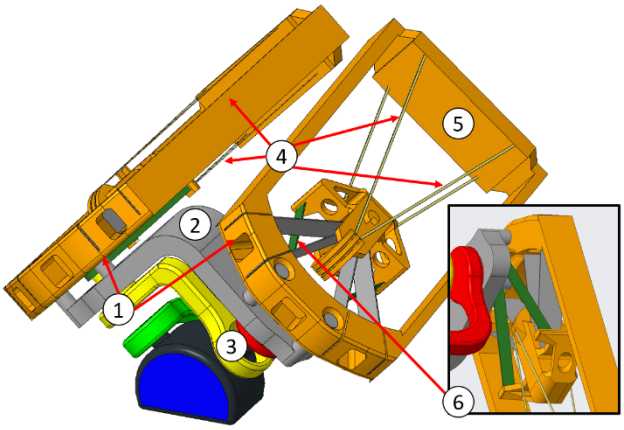

Figure 9 CAD design of the SMA Camera Gimbal 2

The redesigned actuator units ① are attached to the chassis ② around a 45° tilted kinematics ③. The SMA wires ④ will be attached the new actuator frame ⑤. The updated packaging demonstrates improved compatibility with the redesigned flexure geometry and the consequent realignment of the actuator driveshaft. The motion of the actuator will be transmitted similarly to the first prototype via a belt drive ⑥.

Upon scaling down the prototype back to its initial size, the weight is calculated to be smaller than 2.5 g. The switch to metal flexures increases the system weight by only 0.18 g which is deemed acceptable.

Future research aims to reduce this number even further through a higher degree of integration. Additionally, the second iteration of the gimbal will integrate position sensing and closed-loop control.

8 Summary and Conclusions

This paper evaluates the prototype performance of a lightweight miniaturized SMA-actuated camera gimbal with two rotational degrees of freedom. At the start, the requirements are revisited and updated with actual flight data from a state-of-the-art drone. Consequently, the requirements for the dynamic stroke of the gimbal are set to ±30° and the angular speed to 50°/s.

The camera gimbal prototype reached angular strokes of almost ±90° and dynamic strokes of ±42° at an angular velocity of up to 70°/s. The weight of the prototype was only 2.25 g. Therefore, the feasibility of the concept presented in [3] could be proven.

However, the actuator units of this prototype faced longevity and damping issues that increased SMA wire stress to critical levels. A redesign of the actuator unit replaced the 3D-printed prototype flexures with spring-steel flexures and inverted the SMA wire geometry so that only pulling forces are exerted on the flexures. The new flexures were designed in a two-step approach, comprising an initial geometrical design based on analytical calculations followed by FEA optimization.

A 3:1 scale functional prototype was realized to verify the predicted performance. The experimental results compared well with the simulation, showing a dynamic angular actuator stroke of ±15.2° at stress levels below 300 MPa. Damping in the flexures was significantly reduced, paving the way for a performant and durable new version of the SMA camera gimbal.

Future work will focus on bringing the actuator unit down to target size and implementing actuator position sensing and closed-loop control.

9 Acknowledgements

The authors thank the German Ministry of Education and Research (BMBF) for funding this work within the context of the projects *miniSMArt* (grant no. 13FH040PX8) and *SMArtMed* (grant no. 13FH080KX1).

10 References

[1] European Commission, Commission Implementing Regulation (EU) 2019/947 of 24 May 2019 on the rules and procedures for the operation of unmanned aircraft: (EU) 2019/947, consolidated version from April 1 2022

[2] A. Kazi, T. Ehrmann, M. Bäuml, M. Köpfer; Inverted Pendulum-Type SMA Actuator. 18th International Conference on New Actuator Systems and Applications (Actuator 2022), Mannheim, 2022

[3] A. Schwegler, T. Schumm, M. Köpfer, A. Kazi; Concept for an SMA-Actuated Camera Gimbal, 18th International Conference on New Actuator Systems and Applications (Actuator 2022), Mannheim, 2022

[4] G. Palmieri, M. Callegari, L. Carbonari, and M. C. Palpacelli; "Design and testing of a spherical parallel mini manipulator," in 2014 IEEE/ASME 10th International Conference on Mechatronic and Embedded Systems and Applications (MESA), Senigallia, 2014

[5] A. Kazi, P. Frenzel, N. Bobic; Modelling the Stress-dependent Hysteresis of Shape Memory Alloys, 17th International Conference on New Actuators (Actuator 2021), Online Conference, 2021

[6] A. Kazi; M. Hauber; M. Honold: Thermomechanical Characterization of Phase Transformation Surfaces for Thin SMA Wires, Journal of Intelligent Material System and Structures (Vol 34(19)), 2023

Magnetic Fast Steering Mirror for Inter-satellites and Feeder Link Optical Communication

Etienne Betsch, Augustin Bedek, Nicolas Bourgeot, Arnaud Barnique, Patrick Meneroud, Hugo Grardel, Pierre Personnat, Théo Simon, Marc Fournier, Sylvain Chardon, Gérald Aigouy, Xavier De Lepine, Frank Claeyssen
CEDRAT TECHNOLOGIES, 38240 Meylan, FRANCE, gerald.aigouy@cedrat-tec.com.

Abstract

In order to cope with performances of Fine Pointing, and Fast Steering mirror requirements for Space Optical Communication, CEDRAT TECHNOLOGIES (CTEC) is developing magnetic Fast Steering Mirror's (M-FSM) family, based on proprietary MICA™ flexure bearing magnetic actuators mechanism (Moving Iron Controllable Actuator), with embedded eddy current sensors (ECS).
FSM design expected for Optical Inter-Satellite Link (OISL) in large-scale New Space constellations, is highly driven by mandatory cost-efficiency for high quantities recurrent production, while FSM design expected for Feeder-Link communication is driven instead by high power Laser requirements together with high level of redundancy.
In this publication CTEC is presenting both the M-FSM45 and M-FSM-HPL designs, and test results, respectively for inter-satellites and feeder link optical communications.

1 Introduction

Starting from M-FSM62 former design heritage, CTEC has designed first the M-FSM45 dedicated to Giant constellations based on inter-satellites Communication, focusing on mandatory cost efficiency, with high repeatability of performances and reliability, while targeting no defect at customer integration over quantities beyond several thousands of units delivered in very short production time series.
After successful achievement of M-FSM45 Engineering Models design and testing, CTEC is proposing alternate M-FSM-HPL (High Power Laser) design dedicated to Feeder-link applications. The proposed design has been optimized for continuous laser power under vacuum, ranging from 40W to 80W, leading to SiC mirror design with very high reflectivity, and high conductivity. Together with the mirror heat conduction design optimization, a drastic improvement of the FSM heat sinking has been achieved, in order to maintain low equilibrium temperature on mirror surface, together with low thermal gradient, in order to cope with stringent wave front error (WFE) requirement. The FSM size has been increased in order to implement two redundant coils assemblies, each connectable to two separate drive electronics (redundant and nominal).

1.1 M-FSM45 design and tests

The angular stroke amplitude has been increased from +/- 1,5° on M-FSM45 to +/- 2,5° on M-FSM-HPL, together a new concept of eddy currents position sensors, allowing redundancy. Additional end-stops devices have been implemented for the launch vibrations and shock loads, successfully tested to 1,5g²/Hz random vibration level at actuation resonance frequency, and to 1000g SRS shock, avoiding any electrical launch locking device.

Starting from the very first former PYSCHE PAM30 flight project heritage for Deep Space Optical Communication (DSOC), CTEC is developing FSM SiC mirror technology, for both cost-efficient large-scale constellations focusing on mirror cost optimization versus performance, and for Feeder-link high power Laser, focusing on very high reflectivity, and high thermal conductivity.
The environmental tests campaign for Space qualification have been passed, which includes launch vibrations and shock tests, thermal vacuum tests, high frequency accelerated lifetime fatigue tests, and closed loop position control tests, based on advanced control achieved with LQG state feedback controller, in order to reach highest bandwidth possible at high stroke amplitude.

1.1.1 M-FSM45 design description

The M-FSM45 is a magnetic mechanism driving two tilt axes on a large angle requirement. This FSM, which derives from M-FSM62 [4,5] is composed of the following parts:

- A Magnetic circuit in Soft Magnetic Composite material with 4 magnets and a moving part.
- 4 Coils optimized to provide the best induction in the short volume, with potting to dissipate the generated heat.
- An Eddy Current Sensor device with aluminium targets embedded on the moving parts, and 4 sensing heads on a single PCB below.
- A moving part suspended on a flexure bearing ensuring high lifetime performances.
- A mirror fixed on a flexible baseplate limiting the integration deformations.

The magnetic design relies on forces due to tangential variable magnetic reluctance, which offers higher forces than Lorentz forces [6] and more linear forces than normal variable magnetic reluctance [7].
To ensure the FSM performances, magnetic calculations by FEA have been performed. The magnetic saturation, available torque and parasitic forces were verified.

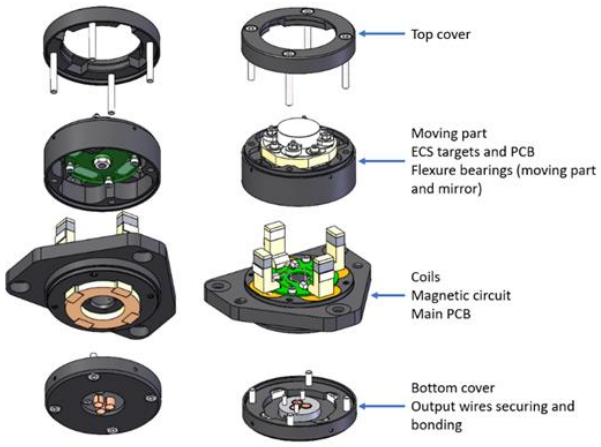

Figure 1: M-FSM cost efficient design concept

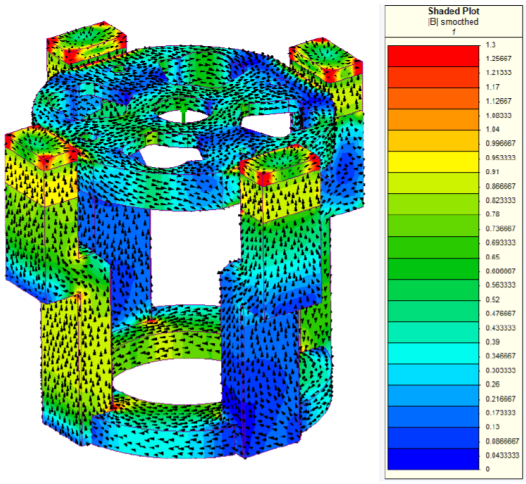

Figure 2: Magnetic circuit finite element modelling

1.1.2 Eddy current position sensors (ECS)

To measure the mirror position and perform closed loop control, an eddy current sensor assembly is embedded in the mechanism. The sensor assembly is eased thanks to the design of a single PCB including the 4 sensing coils, taking advantage of space qualification of PCB-ECS sensors [8]. This solution makes the M-FSM more compact, with an efficient one step assembly. The sensitivity has been optimized for the FSM stroke, making the sensor non-linearity acceptable for the application.

1.1.3 M-FSM45 Manufacturing and Assembly

The mechanism design has been optimized with the objective of reducing the assembly complexity and time, in order to achieve high cost efficiency for very large quantities production. Specific tooling was designed for critical steps such as mirror integration, coils' potting, or moving part assembly into the magnetic circuit.
The magnetic parts were manufactured by industrial molding processes, dedicated to composite magnetic material featuring very low eddy currents. The geometrical tolerances were considered by design to sustain the worst-case air gaps in the torque calculation.

Figure 3: Moving part and coils' assembly

Figure 4: M-FSM45 Engineering Model

The mirrors were manufactured for the engineering models and optical verifications were performed.
The following pictures show the mirrors RWE (reflected wave front error measured with Zygo interferometer at CTEC laboratory).

Figure 5: Free state mirror (left) and Mirrors RWE test after integration (right).

After the mechanism assembly, the mirror surface flatness was controlled. The optical verification indicates that the

mirrors are compliant with important margins in both free state and after integration.

	M-FSM45
Mirror RWE before integration (nm rms)	10
Mirror RWE after integration (nm rms)	12.7

Table 1: mirror optical control results (specification: RWE < 40nm rms)

1.1.4 M-FSM45 tests main results

The M-FSM performances have been measured in open-loop to validate the available stroke, frequency and coils values.
As expected, the first resonance frequency is located around 100Hz. The calculated coils parameters are validated trough the impedance and inductance measurements.

The stroke measured shows that the M-FSM is allowing a maximal stroke slightly lower than +/-1.5° (+/-25.8mrad) for a +/-1A current input. The measurements have been performed thanks to a large angle autocollimator allowing a single angle low frequency acquisition.

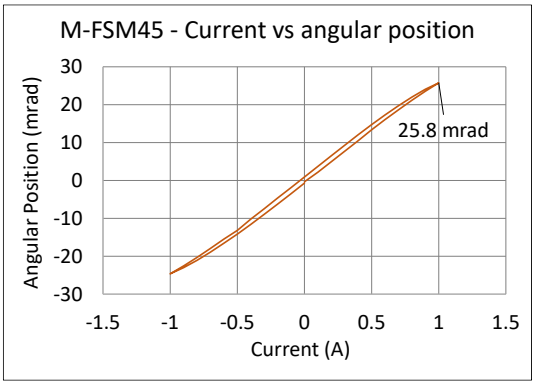

Figure 6: M-FSM45 stroke amplitude test

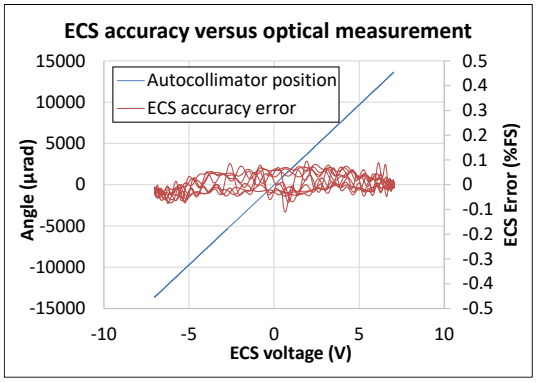

Figure 7: M-FSM45 ECS accuracy test

After complete assembly of the M-FSM45 the ECS position sensors accuracy was measured compared to the optical measure of mirror position with an autocollimator facility. The accuracy error of ECS position sensors was in the range of +/- 0,08% of the +/- 15mrad measurement full scale.

The frequency bandwidth test was achieved at +/-500µrad position amplitude and has shown a -3dB frequency bandwidth up to 320Hz on M-FSM45, which is considered a very good result.

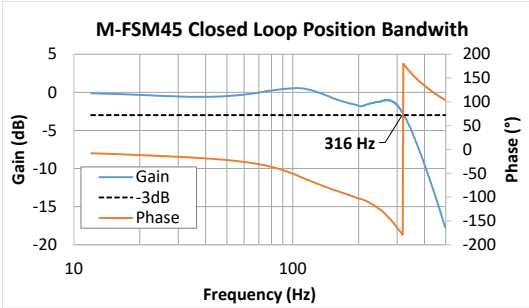

Figure 8: M-FSM45 Closed control bandwidth test

1.2 M-FSM45-HPL design evolution

The M-FSM45-HPL is then derived from the M-FSM45 with some key points added to makes it suitable for High Power Lasers applications.
The functioning principle stays the same with the magnetic circuit in Soft Magnetic composite material to remove the eddy current perturbations, 4 Coils (+ redundant channel) to generate the moving magnetic field, the Eddy current sensor system with a new detection system, a moving part with optimized flexures bearings, and a mirror. As described in Figure 10, the coils will create a magnetic field that will couple with the permanent magnet effect in order to generate a torque on the moving iron.

As for the MFSM45, to hold the mirror on the moving part, a specific flexible element is designed to limit the impact of the screws tightening on the reflected wavefront error, while keeping the mechanism resonances as high as possible.

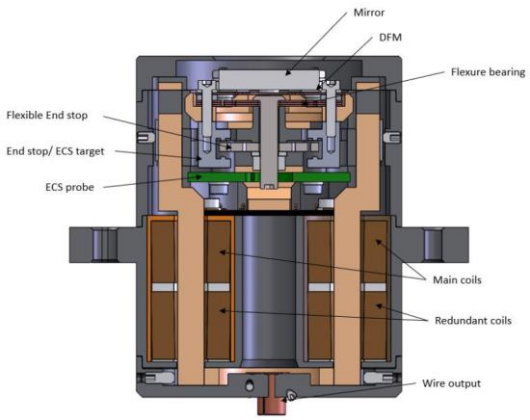

Figure 9: M-FSM45-HPL detailed view

The -3dB bandwidth expected to be reached by the mechanism is higher than 500Hz.

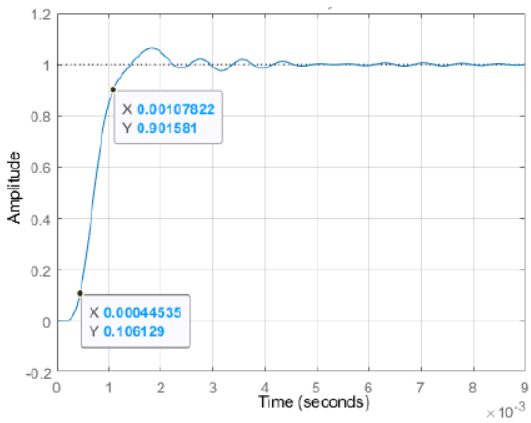

Figure 10: Step and Stay simulation

The mechanism has been reworked in order to optimize the available space inside the 45mm diameter. Thanks to a magnetic redesign, the overall torque is increased, allowing an angle of +/-2.5° while keeping the main resonance frequency higher than 80Hz.

1.2.1 Angle increase

The mechanism has been reworked in order to optimize the available space inside the 45mm diameter. Thanks to a magnetic redesign, the overall torque is increased, allowing an angle of +/-2.5° while keeping the main resonance frequency higher than 80Hz.

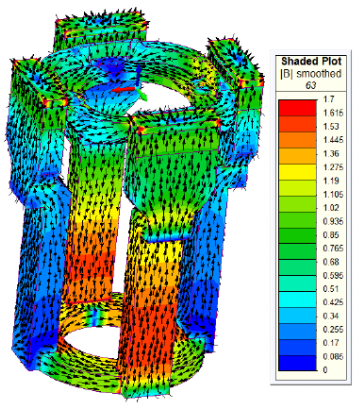

Figure 11: Magnetic field optimisation

These magnetic performances improvements are also visible on the foreseen dissipated power. While the M-FSM45 reaches +/-1.5° for a 4W RMS power at low frequency, the M-FSM45-HPL performs a +/-2.5° angle for a power lower than 0.7W on the redundant channel worst case.

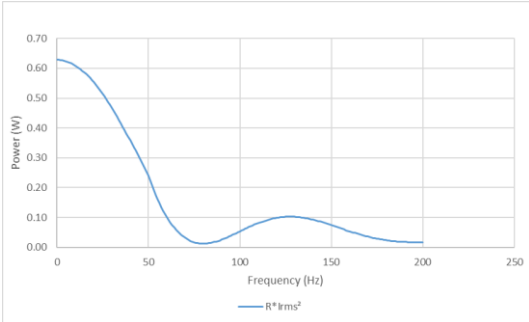

Figure 12: Calculated electrical performances

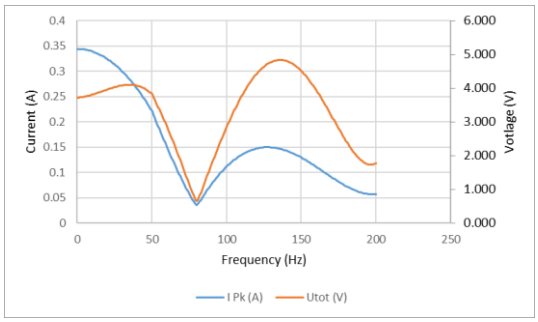

Figure 13: Calculated electrical performances

1.2.2 Thermal optimisation

One of the key performances of the mechanism is to be able to sustain a high power laser up to 80W. The mirror reflectivity is required to be higher than 99.5% to minimize the absorbed power by the mirror. The SiC mirror high thermal conductivity will allow an homogenous thermal distribution inside the mirror in order to reduce the laser effect on the reflected wavefront error. The flexure bearings are designed to dissipate as much heat as possible. Their material is chosen because of its good combination of high thermal conductivity and high yield strength. A stack of a few bearings is preferred instead of a single thicker one to adjust the global tilting stiffness and increase the heat exchange surface.

This design choices allows the mirror to stay under 80°C, which is foreseen to be the maximal temperature for the chosen mirror coating.

1.2.3 Coil redundancy design

The redundancy management for this mechanism is mandatory as it needs to fulfill space flight requirements. The redundant coils system is then added below the main coils channel inside the main coil casing, increasing the length of the mechanism. A cold redundancy solution is chosen here.

1.2.4 Eddy Current Sensor redundancy design

The ECS system is also reworked to include the redundancy functionality. To improve the mechanism linearity performance a differential mode on a full axis is performed by software after the linearization of each probe individually. As each eddy current probe is independent with a single frequency detection strategy, the redundancy is ensured in case of a failure detection.
The same mechanical design is used, with the probes on a single PCB to ease the integration.

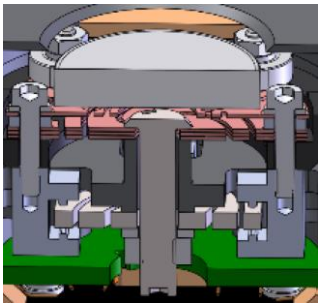

Figure 14: Eddy current sensors integration (PCB in green) implemented on end stops

1.2.5 End stops design

The M-FSM45-HPL is a mechanism with a moving part suspended on its flexure bearings. The high vibration level required for space launch environment is a difficult part of the design. Without additional elements, several notches would be required on the specified levels. The end-stop system designed for the mechanism (Figure 14) allows to sustain the full level of 1,5g²/Hz random vibration at actuation resonance frequency, and up to 1000g SRS shock.
A test campaign has been conducted on a mechanical breadboard with a representative moving part (Figure 15).

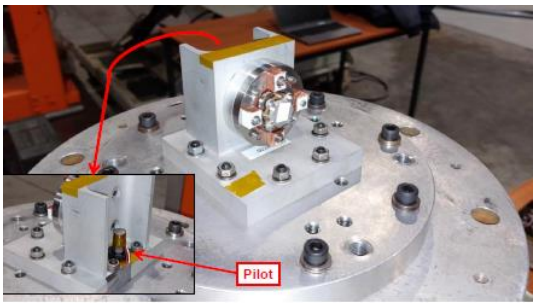

Figure 15: Random vibration test set up

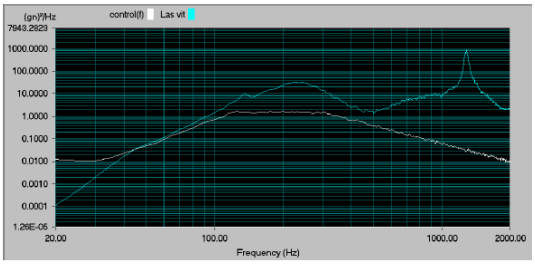

Figure 16: Random vibration PSD test results

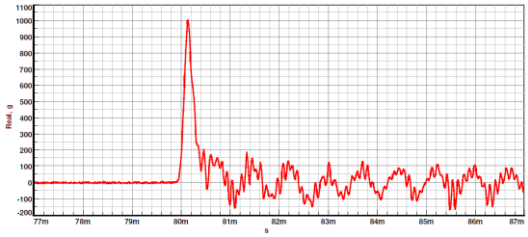

Figure 17: Shock test results

The health of the system is checked before and after the test campaign to validate the good behaviour of the moving part and the flexure bearings. A particle pollution tests has been conducted under the CNES funded COOP program, leading to the conclusion that there is no risk of contamination for the mirror embedded in the mechanism.

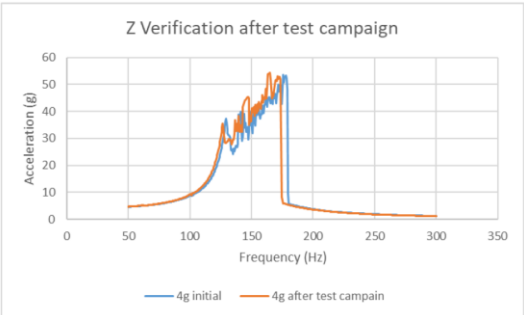

Figure 18: Health check sweeps

1.2.6 M-FSM45-HPL Manufacturing and Assembly

The M-FSM45-HPL tooling have also been reworked to ease the global integration. Specific parts has been designed to allow a mobile part positioning with a high precision and good repeatability. The coils potting is also performed with a specific housing in order to avoid any leakage on critical parts.

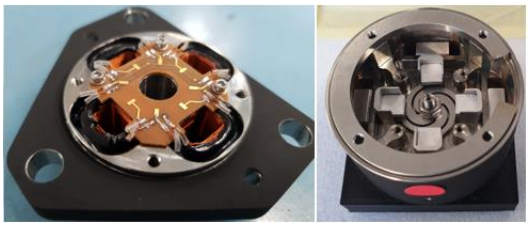

Figure 19: Assembly pictures

At the time of publication only preliminary tests have been achieved, and complete test campaign results are foreseen by end of 2024. The following pictures shows the tested actuation transfer function versus frequency (fig.20), highlighting the actuation resonance at 80Hz as expected by design, and the +/-45mrad maximum stroke amplitude versus current (fig.21). One can see in fig. 21 the maximum angular range tested up to +/- 47mrad with +/- 0,37A current, measured on autocollimator (fig.22), which illustrates the hysteresis of large stroke magnetic mechanisms. This hysteresis is suppressed by the embedded Eddy Current Sensors when used in position feedback closed loop control.

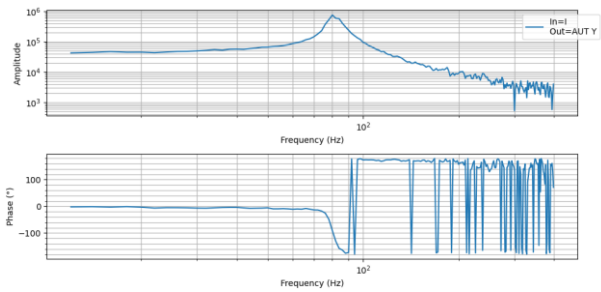

Figure 20: Current to stroke amplitude transfer function

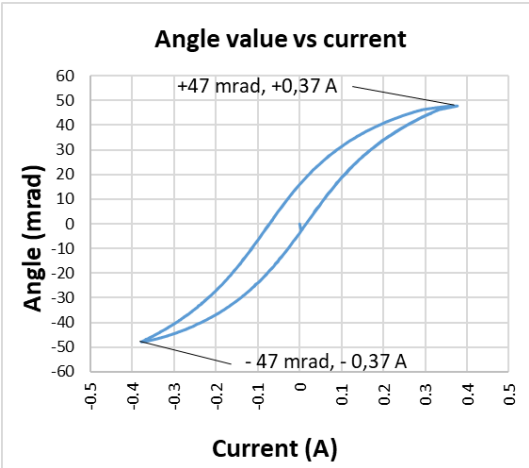

Figure 21: Angular position versus current (open loop)

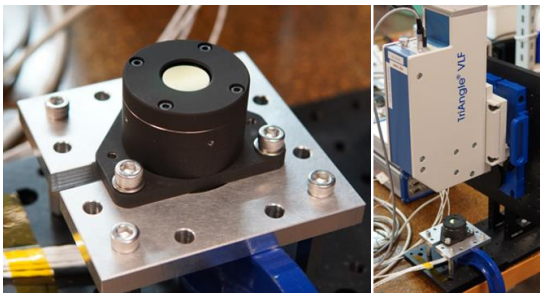

Figure 22: M-FSM45-HPL on autocollimator bench

1.3 Performances summary

As a relevant summary the following table presents the difference of performance of both M-FSM versions.

	Tested on M-FSM45	Expected on M-FSM45-HPL
Mirror aperture	15mm	16.2mm
Housing Diamer	45mm	45mm
Height	35mm	58mm
Mass	195g	370g
Stroke amplitude	+/- 15mrad	+/- 45mrad
Resonance freq.	100Hz	80Hz
Rated voltage	12V	<7V
Rated current	0,5A	<0,4A

Table 2: Performances summary table

1.4 Acknowledgement and conclusion

These performances will be validated through a qualification test campaign that will be performed during 2024. All the key parameters will be checked through functional, environmental (thermal, vacuum) and lifetime tests. All this work was made possible through CO-OP funding via France Relance, with Airbus Defence & Space leading the project in collaboration with CNES.

2 Literature

[1] G. Aigouy, A. Guignabert, E. Betsch, H. Grardel, P. Personnat, J.M Nwesaty, X. De-Lepine, A. Bedek, A. Baillus, N. Bourgeot, F. Claeyssen, ICSO 2022 – « Piezoelectric and Magnetic Fast Steering Mirrors for Space Optical Communication ».

[2] G. Aigouy, E. Betsch, A. Bedek, N. Bourgeot, A. Baillus, H. Grardel, P. Personnat, J.-M. Nwesaty, X. De Lepine, T. Maillard, F. Claeyssen, AMS 2022 – « From PYSCHE PAM30 to Large Scale Free-Space Optical Communication ».

[3] A. Guignabert, T. Maillard, F. Barillot, O. Sosnicki, F. Claeyssen, AMS 2020 – « Point Ahead Mechanism for Deep Space Optical Communication, Development of a New Piezo-Based Fine Steering Mirror ».

[4] F. Claeyssen, Large-stroke Fast Steering Mirror for space Free-Space Optical communication, OPTRO 2020, n°0062, 28-30 Jan 2020

[5] A. Guignabert, E. Betsch, G. Aigouy, Large stroke Fast Steering Mirror, Proc. ICSO, February 2021

[6] W. Coppoolse, Dual-axis single-mirror mechanism for beam steering and stabilisation in optical inter satellite links, Proc ESMATS conf, 2003

[7] Y. Long, Design of a Moving-magnet Electro magnetic Actuator for Fast Steering Mirror, J. of Magnetics, Vol. 19 (3), 2014

[8] JC Barriere, Qualification of euclid-near infrared spectro-photometer cryomechanism, Proc. ESMATS 2017

Self-sensing in spring-loaded SMA actuators using artificial neural networks

Krunal Koshiya* [1], Vladimir Naumov[1], Tom Gorges[1], Gianluca Rizzello[2], Paul Motzki[1,2]

1 ZeMA – Center for Mechatronics and Automation Technology, Depart. Smart Material Systems, Saarbrücken, Germany
2 Saarland University, Depart. Systems Engineering, Saarbrücken, Germany

* krunal.koshiya@imsl.uni-saarland.de

Abstract

When shape memory alloy (SMA) wires are heated above their austenite finish transformation temperature, their length reduces because of a phase transformation from martensite to austenite. Consequently, the electrical resistance of the SMA changes depending on the wire length, its cross-section area, as well as the material temperature and austenite/martensite phase composition. Based on this fact, changes in SMA resistance can be correlated to the wire strain, opening up the possibility of self-sensing in SMA-actuated systems.

To effectively achieve self-sensing, it is important to model the correlation between the actuator electrical resistance and the corresponding mechanical strain. Such a correlation, however, is affected by various factors like biasing mechanism, amplitude of force acting against the wire, actuation frequency, and electrical activation strategy for heating the SMA wire. Moreover, the resistance-strain curve may exhibit a non-monotonic and hysteretic behavior, which makes its inversion practically hard to achieve. In this paper, we present an artificial neural network-based approach to model the electro-mechanical characteristics of a spring-loaded SMA wire actuator. Data is collected via a custom-developed experimental test rig. Different types of neural network architectures are implemented on a microcontroller, capable of predicting the displacement achieved by an SMA actuator based on electrical signals measurements. The self-sensing predictions are finally validated against a displacement laser sensor, to assess the accuracy of the proposed approach.

1 Introduction

Thermal Shape Memory Alloy (SMA) actuators operate based on contraction of the material by a temperature-induced phase transformation. When an SMA wire transforms from martensite to austenite phase, its length reduces thus resulting in an actuation. SMA actuators are used in variety of applications, like robotics [1], nanoscale devices [2], biorobotic systems [3], medical instruments [4], Industrial systems[5], [6], aerospace industry [7] and transportation technologies [8], [9].

One of the major advantages of SMA actuators is their self-sensing capability, which means it can sense its own mechanical state based on given electrical input. Self-sensing based SMA-actuated closed loop control systems can be lighter, low-priced and compact in size. For self-sensing, it is crucial to identify correlation between electrical input and mechanical output of the SMA-actuated system, which can be complicated depending upon various factors, like, biasing mechanism, additional external loads, actuation frequency, as well as the electrical activation strategy for heating SMA wires.

When the SMA wire is not fully contracted in an actuator application, its input-output response results in a hysteresis with complex inner loops, which turn out to be highly challenging to model. In recent years, several works have shown that artificial intelligence (AI) represents a promising approach solution for modelling the complex SMA response [10], [11].

In this paper, we present an artificial neural network (ANN)-based approach for self-sensing in a spring-loaded SMA actuator system when a power signal of random amplitude and frequencies is used as an input. The goal is to use a neural network to approximate the highly nonlinear relationship between the material displacement and electrical quantities (power, resistance) measured during actuation. In this way, the material mechanical state can be estimated during actuation without additional electro-mechanical sensors. An experimental setup has been developed to perform different experiments on a spring-loaded SMA actuator. Based on experimental results, input-output characterization data is collected, and is used for training different neural network models. The calibrated neural networks are used to predict a displacement of an SMA actuator when electrical power of random amplitude and frequency is applied to the SMA wire by using an ST32H743ZI2 microcontroller, and the accuracy of the prediction is reported. Comparison of performance of different neural networks is made based on its meta-parameters as well as type of neurons. We conclude the paper with a discussion on the trade-off between neural network computational burden and the resulting accuracy, when employed in real-time applications.

2 Background

When shape memory alloy wires are heated above their austenite finish transformation temperature, the length of the wire reduces because of a phase transformation from martensite to austenite phase. This is due to the fact that martensite phase is stable at low temperature, while austenite phase is stable at high temperature. Therefore, temperature-induced transformation of an SMA wire can be used in actuator applications when the wire is connected to a biasing mechanism, because the reduction in wire length exerts pulling forces on a biasing mechanism. For this work, we have used a simple mechanism where an SMA wire is acting against a linear spring. An experimental setup of a spring-loaded SMA actuator is presented in section 2.1.

2.1 Experimental Setup

An experimental setup has been developed to collect characterisation data of an SMA actuated system where an SMA wire is connected to a linear spring in series via air bearings [11], as shown in **Figure 1**.

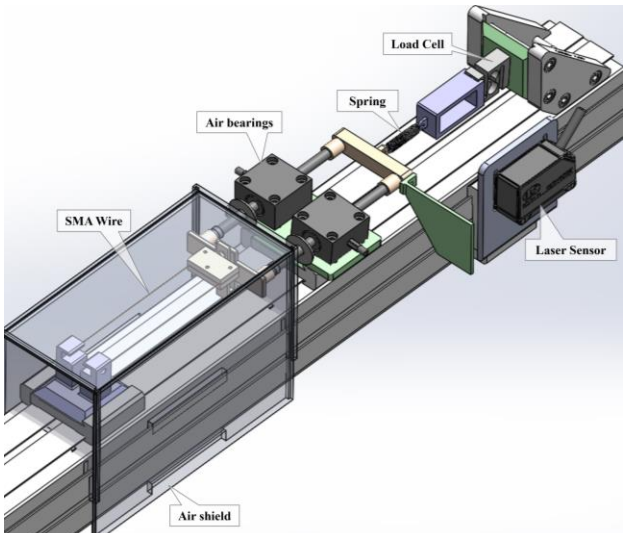

Figure 1 Experimental setup of a linear spring-biased SMA wire actuator

In this experimental setup, a current source is used to apply electrical current to a 50 µm diameter wire provided by Dynalloy [12], which is connected to a linear spring having a 0.05N/mm stiffness, and resulting displacement is measured using a laser sensor - optoNCDT 1607 micro-epsilon [13]. Laser sensor readings, applied current, and voltage across the wire are measured using a microcontroller [14]. Applied electrical power and electrical resistance are calculated from measured current and voltage using

$$\text{Power} = \text{Voltage} * \text{Current} \quad (1)$$

$$\text{Resistance} = \text{Voltage} / \text{Current} \quad (2)$$

For the collection of training data, an experiment is performed in which an electrical input power of random amplitude between 0-0.7 W and random frequency between 20-200 mHz is applied to the SMA wire of 200 mm austenite length. As shown in **Figure 2**, applied electrical power, resistance across the wire, and displacement are collected at 1 kHz sampling frequency during the experiment to prepare the input-output dataset for training and validation of different neural network architectures. **Figure 3** demonstrates the hysteretic correlations between power and displacement as well as resistance and displacement. It can be seen that when the SMA wire is not fully transformed to austenite phase, inner loops are formed in hysteretic correlations, which makes it hard to model the interdependencies.

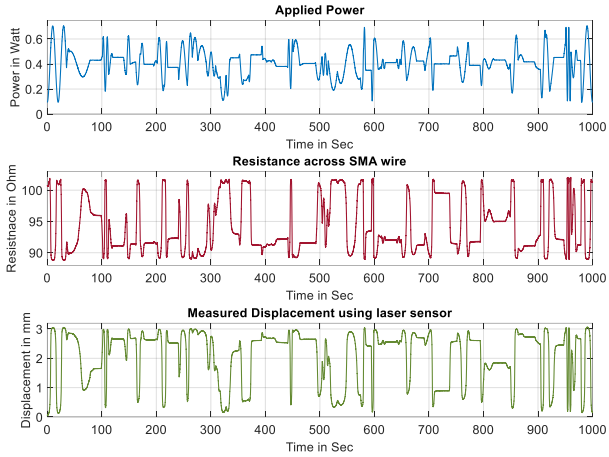

Figure 2 Characterization data for training of neural networks.

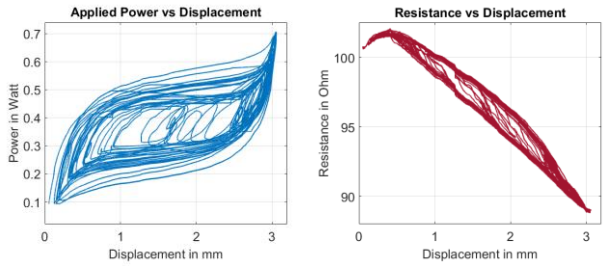

(a) (b)

Figure 3 Hysteretic correlations, (a) power-displacement, (b) resistance-displacement.

2.2 Artificial Neurons

ANNs are simplified models of the human brain. Like in the human brain, interconnected neurons as shown in **Figure 4**, are the basic computational units of an ANN. Basically, each neuron multiplies the inputs with its weights and performs summation of those weights. Output of the neuron is the functional value of that sum. This function is called activation function, here denoted by f.

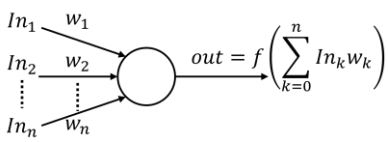

Figure 4: Schematic diagram of a simple neuron

In this work, we use recurrent neurons [15] in which a simple neuron is extended over time as depicted in **Figure 5**. Here, a neuron takes one input element from the sequence of inputs at each timestamp, and outputs its last state at the end of the sequence. As shown in **Figure 5**, each layer has

previous state and current input to process, and weights w_{rec} and w_{in} are shared for a sequence of input. Therefore, it is required to give inputs in a form of sequence in a time series to use recurrent neurons.

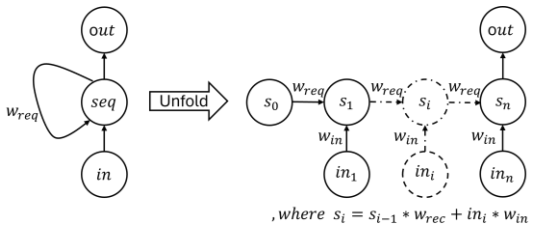

Figure 5: Schematic diagram of a recurrent neuron

Recurrent neurons outperform simple neurons when time series data is available for prediction, because it takes previous values of the input into consideration for the estimation of the current output. By interconnecting these neurons, the ANN is formed as shown in **Figure 6**. With increasing number of neurons and number of layers, the performance of the network improves, but required computation power also increases because of the complexity of the networks.

3 Neural Network Architectures

In this work, we have analyzed different ANN architectures to find the optimum solution for self-sensing in SMA actuator systems. **Figure 6** represents a generalized structure of a neural network with 2 hidden layers to predict the displacement as an output by using available inputs, e.g., resistance, power, difference in resistance and difference in power. Difference in resistance and power at time instance i, are calculated by subtracting $(i\text{-}7)^{th}$ timestamp value from i^{th} timestamp value which means it is subtracted from the value that is collected 7 milliseconds prior, to reduce signal-to-noise ratio.

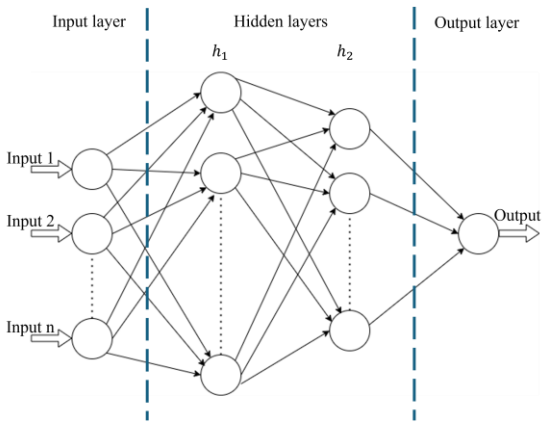

Figure 6 Generalized neural network structure

3.1 Training And Validation

All ANNs in this work are trained using the TensorFlow open-source library, with ADAM [16] as an Optimizer and Mean Squared Error as a loss function. The characterization data that is shown in **Figure 2**, is used for training all ANNs by 100 epochs when batch size is kept 10000, 1000 and 100, successively. The trained networks are validated on a separate data set, as shown in **Figure 7**. After training and validation of the networks, percentage fit is calculated using **Equation 3**, where D is vector of displacement measured by laser sensor and $estD$ is displacement estimated using neural network.

$$fit(\%) = 100 * \left(1 - \frac{\|D - estD\|}{\|D - mean(D)\|}\right) \quad (3)$$

Higher number of neurons in hidden layers gives comparatively better prediction of displacement at a cost of computational power. To find an optimum number of neurons in hidden layers when resistance, power, and difference in resistance and power are used as inputs, we have trained 3 NNs as shown in **Table 1**. In the 1st network, h1 hidden layer has 2(1S, 1L) neurons, which means 1 neuron with Sigmoid activation and 1 neuron with Linear activation, and h2 hidden layer has 1(1L) neuron with linear activation. Likewise, in the 2nd network, h1 hidden layer has 8 (7S,1L) neurons and h2 hidden layer has 4 (3S,1L) neurons. In the 3rd network, h1 hidden layer has 16 (15S,1L) neurons and h2 hidden layer has 8 (7S,1L) neurons. $fit(\%)$ of these networks are shown in **Table 1**. Based on validation fit (%), Network 2 shows 13.68% improvement over Network 1, and Network 3 performs only 0.6% better than Network 2. Therefore, Network 2 is chosen as an optimal solution among the three networks and improved further.

Network	h1 Neurons	h2 Neurons	Training Fit (%)	Validation Fit (%)
1	2 (1S, 1L)	1(1L)	87.02	81.03
2	8 (7S, 1L)	4(3S,1L)	96.15	94.71
3	16 (15S,1L)	8(7S,1L)	96.51	95.31

Table 1 Neural networks using simple neurons only

To improve the performance of Network 2, we replace the simple neurons in h1 layer by recurrent neurons and call it a Network 4, as shown in **Table 2**. For recurrent neurons sequence length is 8 consecutive samples. Network 4 has recurrent neurons in h1 layer that takes temporal aspect of data in consideration, because of which it further improves the estimation of displacement. The result of Network 4 for training as well as for validation data is shown in **Figure 7**.

Network	Inputs	Training Fit (%)	Validation Fit (%)
4	R, ΔR, P, ΔP	97.22	96.29
5	R, ΔR	89.96	84.17

Table 2 Neural networks with recurrent hidden layer 1

For self-sensing in SMA actuated system, it is ideal to use only resistance values for prediction of the displacement. Therefore, in Network 5 we have removed the power and difference in power from the set of inputs to check the performance of only resistance dependent neural network. As shown in **Table 2**, using only resistance values in the ANN is not enough to model hysteretic non-linearities in resistance-displacement correlations of SMA actuators. If power is also included in the set of inputs to the neural network, as in Network 4, the displacement can be estimated reliably as shown in **Figure 7.**

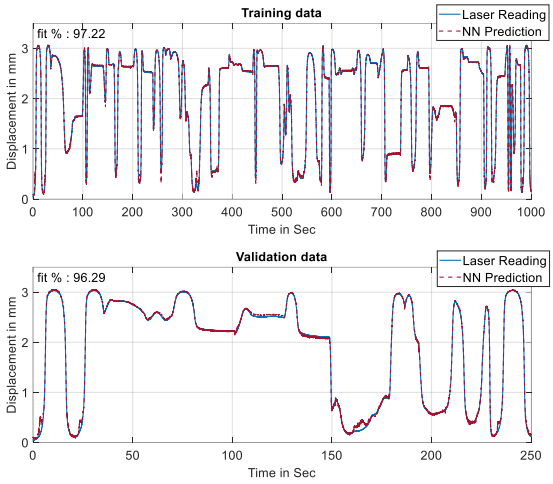

Figure 7 Comparison of estimated displacement of Network 4 with laser sensor reading

4 Conclusion

For self-sensing in SMA actuated systems, it is required to identify the correlation between electrical inputs and mechanical output of the system. In this paper, we have presented a neural network-based approach for modelling hysteretic input-output correlations of an SMA actuated systems. The accuracy of a neural network in the estimation of the wire displacement, using applied power and resistance values as inputs, depends on the complexity of the neural network. As presented in this paper, Network 4 with 1 hidden layer of 8 recurrent neurons followed by 1 hidden layer of 4 simple neurons, is sufficient to predict the displacement of the SMA actuator using resistance and power with 96.29% accuracy. In future works, neural networks will be optimised further for the development of a self-sensing based closed-loop position controlled SMA actuated system.

5 Literature

[1] D. J. S. Ruth, J. W. Sohn, K. Dhanalakshmi, and S. B. Choi, "Control Aspects of Shape Memory Alloys in Robotics Applications: A Review over the Last Decade," *Sensors*, vol. 22, no. 13. MDPI, Jul. 01, 2022. doi: 10.3390/s22134860.

[2] A. P. Orlov *et al.*, "Shape memory effect nanotools for nano-creation: Examples of nanowire-based devices with charge density waves," *Nanotechnology*, vol. 32, no. 49, Dec. 2021, doi: 10.1088/1361-6528/ac2190.

[3] J. W. Phillips, A. Prominski, and B. Tian, "Recent advances in materials and applications for bioelectronic and biorobotic systems," *VIEW*, vol. 3, no. 3. John Wiley and Sons Inc, May 01, 2022. doi: 10.1002/VIW.20200157.

[4] H. Holman, M. N. Kavarana, and T. K. Rajab, "Smart materials in cardiovascular implants: Shape memory alloys and shape memory polymers," *Artificial Organs*, vol. 45, no. 5. John Wiley and Sons Inc, pp. 454–463, May 01, 2021. doi: 10.1111/aor.13851.

[5] D. Scholtes, S. Seelecke, G. Rizzello, and P. Motzki, "Design of A compliant industrial gripper driven by A bistable shape memory alloy actuator," in *Conference on Smart Materials, Adaptive Structures and Intelligent Systems, SMASIS 2020*, American Society of Mechanical Engineers (ASME), 2020. doi: 10.1115/SMASIS2020-2204.

[6] F. Welsch, M. Schmidt, S. M. Kirsch, S. Seelecke, and P. Motzki, "Vacuum gripper system based on bistable SMA actuation," in *ASME 2018 Conference on Smart Materials, Adaptive Structures and Intelligent Systems, SMASIS 2018*, American Society of Mechanical Engineers (ASME), 2018. doi: 10.1115/SMASIS2018-7980.

[7] P. N. Shah, E. L. Blades, M. R. Nucci, N. D. Reveles, T. L. Turner, and D. P. Lockard, "Fully Coupled Aeroelastic Stability Analysis of Adaptive Shape Memory Alloy Structural Technologies for Airframe Noise Reduction." [Online]. Available: http://www.sti.nasa.gov

[8] E. Ferede, F. Gandhi Redfern Professor, M. Director, and D. Lagoudas Professor, "Numerical Investigation of Autonomous Camber Morphing of a Helicopter Rotor Blade using Shape Memory Alloys."

[9] M. Balasubramanian, R. Srimath, L. Vignesh, and S. Rajesh, "Application of shape memory alloys in engineering - A review," in *Journal of Physics: Conference Series*, IOP Publishing Ltd, Oct. 2021. doi: 10.1088/1742-6596/2054/1/012078.

[10] R. Hmede, F. Chapelle, and Y. Lapusta, "Review of Neural Network Modeling of Shape Memory Alloys," *Sensors*, vol. 22, no. 15. MDPI, Aug. 01, 2022. doi: 10.3390/s22155610.

[11] Krunal Koshiya, Gianluca Rizzello, and Paul Motzki, "An Embedded System for Data-Based Self-Sensing in Shape Memory Alloy Wire Actuators," in *Proceedings of the ASME 2023 Conference on Smart Materials, Adaptive Structures and Intelligent Systems SMASIS*, 2023. [Online]. Available: https://doi.org/10.1115/SMASIS2023-110385

[12] Dynalloy, "NICKEL-TITANIUM ALLOY PHYSICAL PROPERTIES." Accessed: Mar. 15, 2024. [Online]. Available: https://www.dynalloy.com/pdfs/TCF1140.pdf

[13] Datasheet, "Non-Contact Laser-Optical Displacement Measurement Compact PSD sensor opto 1607 NCDT." Accessed: Mar. 11, 2024. [Online]. Available: http://www.micro-epsilon.pl/download/Datasheet_-_optoNCDT_1607_-_en.pdf

[14] Datasheet, "STM32H743xI/G microcontrollers." Accessed: Mar. 13, 2024. [Online]. Available: https://www.st.com/resource/en/datasheet/stm32h743vi.pdf

[15] D. E. Rumelhart, G. E. Hinton, and R. 1 Williams, "Learning Internal Representations by Error Propagation."

[16] D. P. Kingma and J. Ba, "Adam: A Method for Stochastic Optimization," Dec. 2014, [Online]. Available: http://arxiv.org/abs/1412.6980

The Effects of Training on Electro-Thermo-Mechanical Actuation and Sensing Characteristics of NiTi Actuator Wires

Joshua Mayer [1], Dominik Scholtes [1,2], Tom Gorges [1], Gianluca Rizzello [2], Paul Motzki [1,2]
[1] Smart Material Systems, Center for Mechatronics and Automation Technology - ZeMA gGmbH, Saarbruecken, Germany
[2] Saarland University, Department of Systems Engineering, Saarbruecken, Germany

Abstract

Commercially available shape memory alloy (SMA) wires are usually trained during the manufacturing process for a stable behavior for mechanical stresses up to 200 MPa. It is of interest in actuator design to increase this stress to gain a higher force output, increase transformation temperature and reduce installation space. Characterization of SMA wires is usually done thermo-mechanically, however in technical applications they are activated electrically. This work presents methods for a thorough and systematic characterization of SMA wires under joule heating, as well as investigating the effectiveness of purely mechanical training and thermal training compared to an untreated wire. Both training methods aim to achieve a stable behavior for SMA wires above 200 MPa as well as improved sensor properties. Having actuation and sensing in a single SMA element allows for different control strategies, reduces weight, complexity, and cost. For this purpose, a custom-built test bench, is used to perform electro-thermo-mechanical characterization and training of SMA wire specimen directly from the spool.

1 Introduction

This paper presents results from three previous publications aiming to improve SMA wire characteristics especially for actuator applications. The first discusses the development of the test rig used to conduct the experiments [1]. The second one goes into detail about the effect of training on sensor and actuator characteristics at room temperature [2]. The last one builds upon the second, by exploring the change in characteristics at increasing environmental temperatures [3].

The goal of training is a stable behavior at up to 400 MPa and a linear resistance-strain relationship. With these characteristics small, lightweight, efficient actuator systems can be realized, by improving the force output per wire and enabling self-sensing for better control of the actuator system. To achieve this a multi-purpose test bench is used for training and characterization. Nickel Titanium (NiTi) wires can be trained using purely mechanical training, utilizing conventional tensile testing. This method is compared to thermo-mechanical testing, where the wire is heated due to joule heating, inducing a phase transformation from martensite to austenite in the wire. This phase transformation allows SMA wires to be used in actuator applications [4]. Afterwards, the SMAs are characterized at room temperature using the same setup. The performance is rated based on the stress-strain, resistance-strain and power-strain relationships. Real applications experience varying environmental temperatures. Therefore, the last set of tests are performed at increasing environmental temperatures of up to 100 °C.

2 Experimental Study

To explore the influence of different training methods on actuator and sensing properties as well as basic characteristics of NiTi wires, a ready-to-use 72 µm "Dynalloy FlexinolHT" wire [5] is selected. Commercially available wires such as this show stable properties up to stresses of 200 MPa. The goal of the experiments is to achieve a stable behavior at up to 400 MPa of stress using additional training. This is desirable in high frequency applications with cycle times below one second, which can only be performed repeatedly using bundled thin wires at high stresses [6]. Generally, a stable behavior at higher stresses allows for the construction of more efficient systems by requiring less and or thinner wires.

After this training, the wires are characterized using tensile testing and actuator testing. During tensile testing the wire is pulled to a certain strain and relaxed again at a fixed strain rate while heated by a constant current or constant power source. In this case, the wires are heated to austenite phase and pulled into martensite by the external load applied with the linear actuator. In actuator testing the wire experiences a constant force or spring load while undergoing a phase transformation due to cyclic joule heating. The constant load or spring load is simulated by the linear actuator through an implemented "hardware-in-the-loop" strategy, using the load cell and the displacement sensor to apply various load profiles with a PID controller. The tensile tests give basic material properties to allow a first comparison of the different training methods, the actuator test gives a more detailed result regarding actuator and sensing properties as well as functional stability. Finally, tests at increasing environmental temperature up to 100 °C are performed.

To set a baseline for reference, an untreated wire undergoes the same characterization steps directly from the spool without any kind of training.

All experiments are performed using a multi-purpose test rig (**Figure 1**) rigorously described by Scholtes et al. [1]. The setup consists of two clamps, in which the wire is fixed. The wire is clamped inside an isolating chamber to eliminate ambient air flow. One clamp is connected through an air bearing to a load cell, the other to a linear actuator. Two main programs are available. The first runs the linear actuator in a position control mode, for tensile testing. While the other uses a closed-loop force-controlled

mode. It allows mapping of arbitrary loads to the wire. Generally, Joule Heating is used to heat the wire, with power provided by a controllable constant current source. To increase the environmental temperature the isolating chamber can be heated up to 100 °C using heating elements on the inside walls. Another linear actuator is used to set up a new wire specimen in a stress-controlled manner to achieve repeatable results. Strain is measured by the encoder of the linear axis, force by the loadcell, current by the current source, voltage directly across the clamps and the environmental temperature using PT 100 temperature sensors inside the chamber.

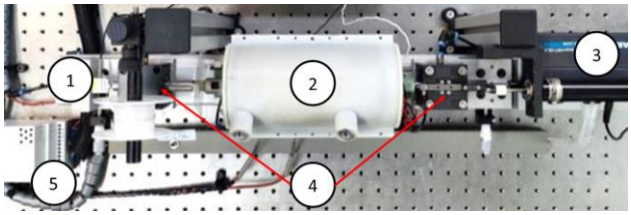

Figure 1 Photo of the multi-purpose test rig, showing the load cell (1), isolating chamber (2), linear actuator (3), air bearings (4) and constant current source (5).

2.1 Mechanical Training

Mechanical training is performed using tensile testing for 100 cycles at a constant electrical power of 0.35W up to a strain of 5.5%. The temperature in the wire can be assumed as constant because of the constant heating power and the low strain rate of 0.05 s^{-1}.

Looking at (**Figure 2**) the evolution of the Stress-Strain relationship over the 100 training cycles can be observed. The overall shape remains the same, while the hysteresis tightens. The upper plateau stress decreases from 455 MPa to 383 MPa at 3% strain. The upper plateau stress increases from 190 MPa to 205 MPa at 3% strain. The stress at 5.5% strain increases from 450 MPa to 468 MPa.

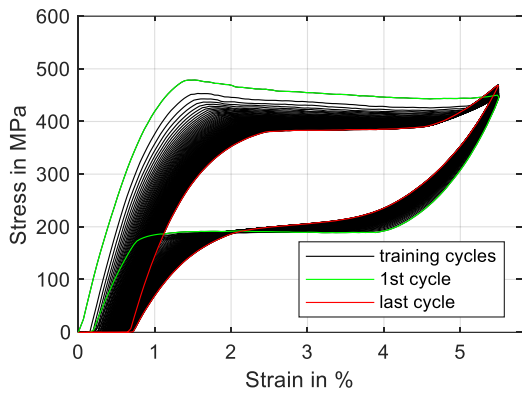

Figure 2 Stress-strain diagram for 100 cycles of mechanical training **[2]**.

The resistance-strain diagram over the 100 training cycles shows little change (**Figure 3**). The measurements show a linear behavior for the first and last cycle. The minimum resistance increases from 19.5 Ω to 19.9 Ω. The maximum value drops to 25.1 Ω from 25.4 Ω.

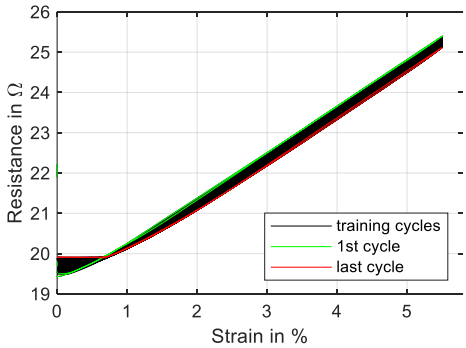

Figure 3 Resistance-Strain Diagram for 100 cycles of mechanical training **[2]**.

2.2 Thermal Training

For thermal training the wire is pulled to a constant stress of 400 MPa. It is heated using a triangular signal with an amplitude of 180 mA and a cycle time of 40 s. To measure the resistance consistently the current never falls below 10 mA. The working range of the wire changes from 1.08% to 6.93% for the first cycle and from 3.26% to 7.65% for the last cycle. The hysteresis changes from a wide almost rectangular shape to a narrow-slanted shape (**Figure 4**).

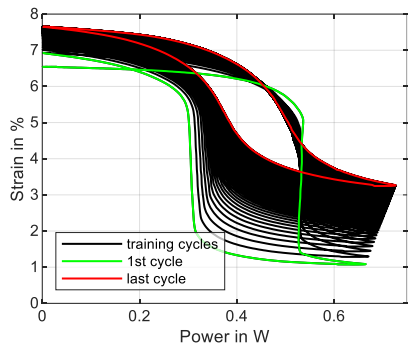

Figure 4 Strain-power diagram for 100 cycles of thermal training **[2]**.

The resistance behavior is different to the mechanical training because of the phase transformation and temperature changing during thermal training **(Figure 5)**. This is more representative of the resistance observed in a real system. Because of the increased minimum length of the wire the minimum resistance increases from 20.5 Ω to 22.5 Ω after 100 cycles. The hysteresis narrows down to an almost linear state between 4% and 6% strain.

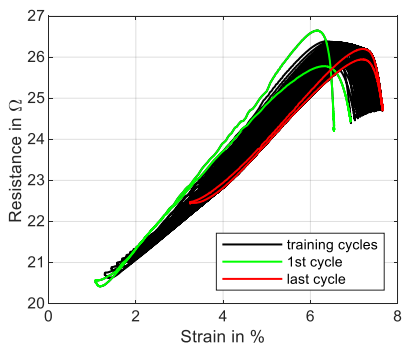

Figure 5 Resistance-strain diagram for 100 cycles of thermal training **[2]**.

2.3 Basic Characterization

The tensile testing consists of five tests up to a certain strain at increasing heating powers. The maximum strain for the untreated and mechanical trained wire is set to 5.5%. For the thermally trained wire it is increased to 6.5% because of the changed working range due to remnant strain [7]. The first two tests are performed with a current of 10 mA to measure the resistance without heating the wire significantly.

By comparing the untreated wire to the mechanically trained wire a reduction of the area inside the hysteresis is observed, which is further reduced for the thermally trained wire **(Figure 6)**. With training the peak stress occurs at the maximum strain instead of at about 1.5% strain for the untreated wire.

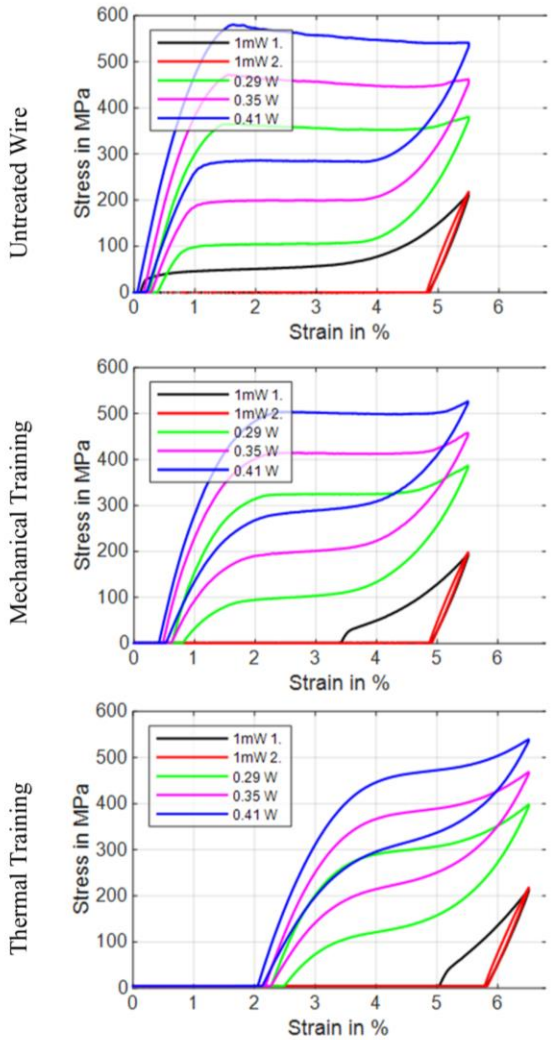

Figure 6 Basic characterization for an untreated wire, a mechanically trained wire, and a thermally trained wire [2].

2.4 Actuator Characterization

Four different actuator tests are carried out with each specimen. Test one and two are done with a constant force of 200 and 400 MPa respectively, while test three and four are performed with spring loads from 100-200 MPa and 200-400 MPa respectively. Shown here is only the last test cycle. Training narrowed the hysteresis in the resistance-stress relationship for the mechanical training compared to the untreated one **(Figure 7)**. At the cost of a decrease in stroke of about 0.5% the hysteresis is narrowed further with thermal training.

Looking at the strain over power diagrams (**Figure 8**) the required energy to achieve the maximum load reduces with training compared to the untreated wire, which is shown by the area inside the hysteresis getting smaller.

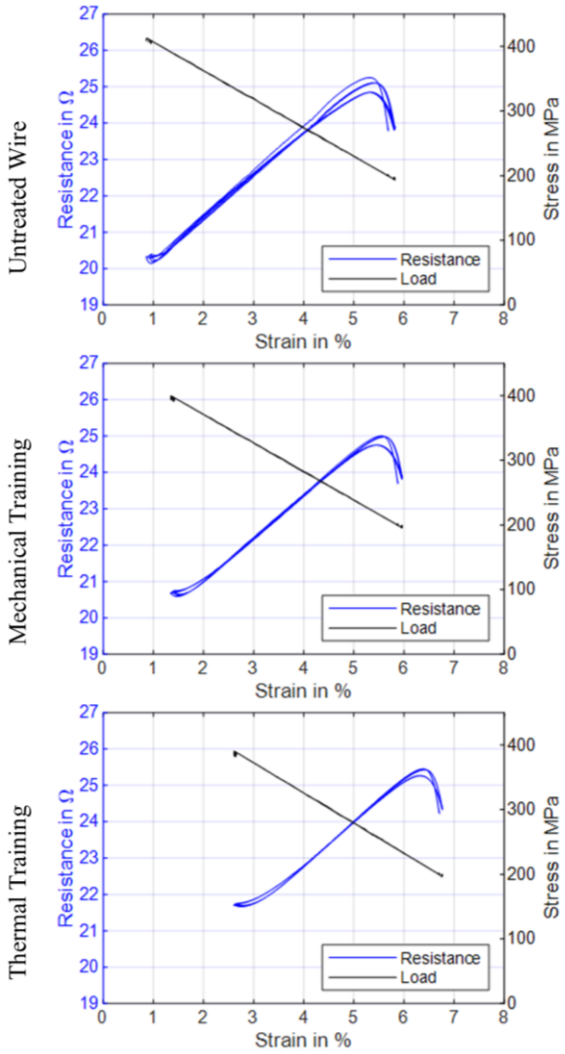

Figure 7 Resistance and stress over strain for an untreated, a mechanically trained, and a thermally trained wire against a spring load **[2]**.

2.5 Environmental Temperature Tests

The actuator characterization experiments from the section before are repeated at increasing temperatures up to 100 °C for a thermally trained wire and an untreated wire.

Shown is the exemplary result for the test against a spring load from 100-200 MPa **(Figure 9)**. The stroke performance for the trained wire is worse at low ambient temperatures as discussed in the previous section. The remnant strain reduces overall stroke but stabilizes the wire behavior. However, the trained wire achieves more stroke at temperatures above 50 °C.

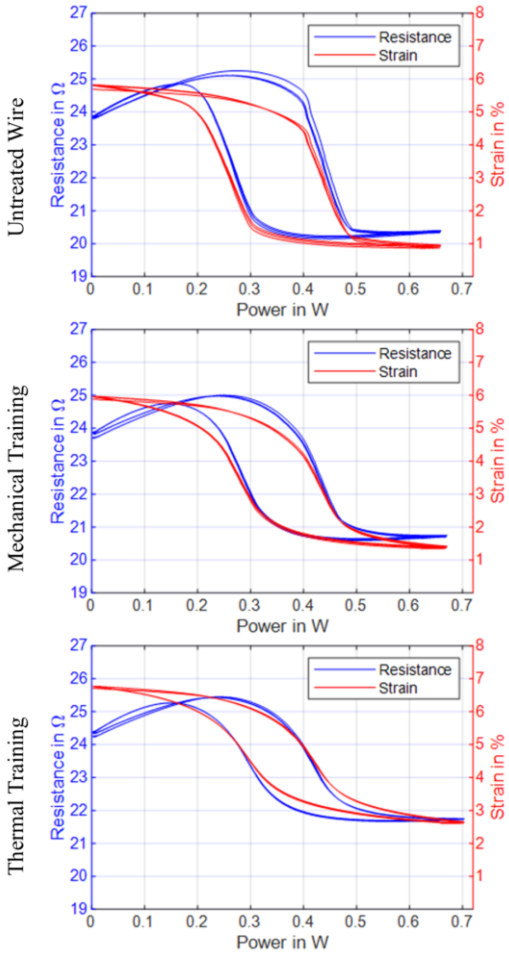

Figure 8 Resistance and strain over power for an untreated, a mechanically, and a thermally trained wire against a spring load **[2]**.

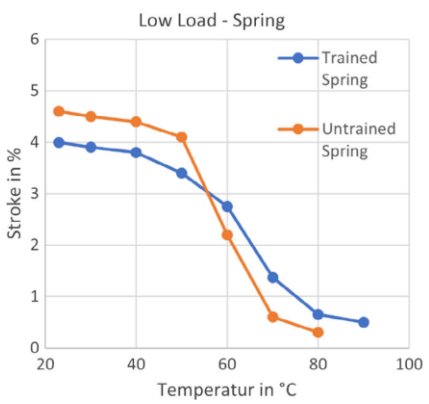

Figure 9 Achieved stroke over temperature for a thermally trained wire and an untreated wire against a spring load from 100-200 MPa **[3]**.

3 Conclusion and Outlook

In this work, methods to train SMA wires mechanically and thermally to achieve a stable behavior at up to 400 MPa of stress have been developed. To compare the training methods to an untreated specimen a characterization procedure was laid out. The results show that training improves the basic characteristics as well as the actuator and sensor properties of SMA wires at room temperature as well as at higher ambient temperatures. In high force applications these wires allow for a reduction in size, cycle time and power consumption by requiring less and or thinner wires for the same performance, compared to untreated wires. The improvement in the resistance-strain relationship eliminates the need for additional sensors in systems using trained wires by improving self-sensing capabilities. Together, those improvements make SMA driven actuator systems lighter, faster, more efficient and easier to control [8]. The next step is to explore the influence of training on other parameters such as lifespan [9] [10].

4 Literature

[1] D. Scholtes, M. Schmidt, P. Linnebach, P. Motzki and S. Seelecke, “A Multifunctional Characterization Test Bench for Shape Memory Alloy Micro-Wires—Design, Implementation and Validation,” *Materials, Volume 16, Issue 13,* 2023.

[2] D. Scholtes, P. Motzki and S. Seelecke, “Electro-thermo-mechanical characterization of shape memory alloy wires for actuator and sensor applications—Part 1: The effects of training,” *Engineering Reports,* 2024.

[3] D. Scholtes, P. Motzki and S. Seelecke, “Electro–Thermo–Mechanical Characterization of Shape Memory Alloy Wires for Actuator and Sensor Applications, Part 2: High-Ambient-Temperature Behavior,” *Advanced Engineering Materials,* 2024.

[4] D. Lagoudas, Shape Memory Alloys, New York: Springer, 2008.

[5] “dynalloy,” [Online]. Available: https://www.dynalloy.com/pdfs/TCF1140.pdf. [Accessed 30 04 2024].

[6] D. Scholtes, G. Rizzello and P. Motzki, “Design of a Compliant Industrial Gripper Driven by a Bistable Shape Memory Alloy Actuator,” *SMASIS,* 2020.

[7] F. Auricchio, A. Constantinescu, C. Menna and G. Scalet, “A shakedown analysis of high cycle fatigue of shape memory alloys,” *International Journal of Fatigue,* vol. 87, pp. 112-123, 2016.

[8] S. Seelecke and S. Furst, “Modeling and experimental characterization of the stress, strain, and resistance of shape memory alloy actuator wires with controlled power input,” *Journal of Intelligent Material Systems and Structures,* vol. 11, no. 23, pp. 1233-1247, 2012.

[9] L. Fumagalli, F. Butera and A. Coda, “Smartflex NiTi Wires for Shape Memory Actuators,” *Journal of Materials Engineering and Performance,* vol. 18, no. 5, pp. 691-695, 2008.

[10] J. Mayer, P. Molitor, Y. Goergen and P. Motzki, “Design of a Modular Lifespan Test Bench for Shape Memory Alloy Wires,” *SMASIS,* 2022.

Precision Atmospheric Pressure Driven Actuator controlled by Self-Sensing Electro-Magnetic Valve

Yahui Zhang and Bintang Yang* State Key Laboratory of Mechanical System and Vibration, School of Mechanical Engineering, Shanghai Jiao Tong University, 200240 Shanghai, China
E-mail address: btyang@sjtu.edu.cn.

Abstract

This paper presents an innovative Atmospheric Pressure Driven Actuator (APDA) that achieves precise control by utilizing a Self-Sensing Electro-Magnetic Valve (SEMV). SEMV detects the magnitude of the magnetic field change through the magnetoelectric effect of the magnetostrictive/piezoelectric composite material, which results in the corresponding valve opening. The actuator operates via fluid transmission and requires offline charging. A constant and stable energy supply is available throughout the actuation process, resulting in quasi-static characteristics. Precise trajectory tracking can be achieved by local closed-loop control of the control element SEMV merely. According to Pascal's principle, the diameter of the APDA is adjusted to change the transmission ratio, which can be adapted to a variety of working environments with different load and precision requirements. To ensure precise flow control and efficient fluid transmission, system dynamics were modeled to complete the prototype design. In addition, Simulation results show that nanometer displacement resolution and submicron trajectory tracking accuracy are obtained under global open-loop conditions. This technology enables high-precision with infinitely expandable travel ranges, and is particularly suitable for applications with high stability requirements.

1 Introduction

High-precision, long-stroke actuators have found extensive application across various domains characterized by multi-scale workspace requirements, including cell injection [1], precision alignment [2], scanning probe microscopy [3], and numerous other fields. In these applications, the stability of the output, whether it be displacement or force, plays a pivotal role in determining the actuators' output accuracy. Current methodologies employed to achieve precision actuation over extended distances often rely on the accumulation of single-step displacements for the conversion or application of mechanical or other forms of energy [4]-[7] (such as electric, optical, magnetic, or thermal) to the actuated object. This practice, as time progresses, inevitably results in fluctuations in the driving force, particularly at high or ultra-high frequencies. These fluctuations introduce undesired noise into the actuator's output.

Ideally, the driving force should remain independent of displacement and spatial position, i.e., have a zero-force gradient characteristic, and ultimately act on the actuator as a steady state form of energy. When subjected to a constant driving force, precise control over the singular variable governing the system's output (whether it is time or a time-stabilized relational quantity) facilitates the realization of targeted ultra-precise and long-stroke actuation outputs.

The aim of this paper is to propose a novel actuation method that achieves high accuracy over a long stroke and minimizes actuation noise. This approach combines fluid drive transmission with the precise control capability of SEMV to achieve accurate and stable actuator motion. In this paper，Firstly, a stabilized energy input drive method based on atmospheric pressure is proposed and the system dynamics is modeled, Secondly, utilizes a self-sensing electro-magnetic valve to provide continuous and precise control of the output flow/velocity, allowing the generation of arbitrary motion trajectories. Finally, a prototype was designed, a model for the system's fluid dynamics was established, and the performance of the drive system was assessed through simulation.

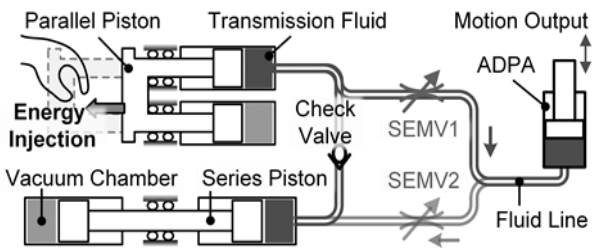

Figure 1 Precision atmospheric pressure driven actuator with self-sensing electro-magnetic valve.

2 Working Principle

2.1 Driving Mechanism

The large-stroke, ultra-precision driving mechanism (see **Figure 1**), is powered by atmospheric pressure potential energy and comprises four main components: a constant-force drive system, precision flow control unit, fluid transmission pipelines, and a terminal actuator. This system reduces transient energy fluctuations by implementing offline energy injection and steady-state energy input, enhancing output stability.

The system uses a combination of series and parallel structured negative pressure and fluid chambers to maintain consistent driving force. Constraint restrictions on the non-moving directions of the piston connecting shaft prevent unbalanced torques, stabilizing the driving force.

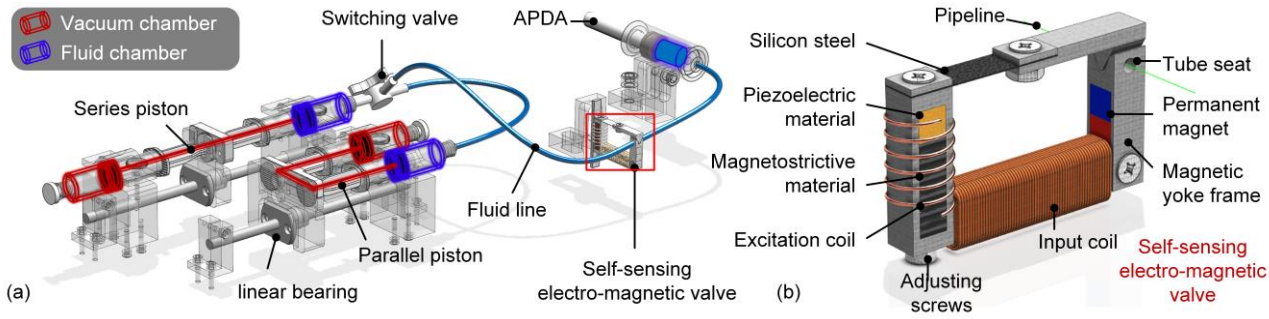

Figure 2 Design and implementation of actuation system: (a) overall structure, (b) components of SEMV.

Additionally, the negative pressure chambers facilitate both forward and backward displacements of the actuator. Fluid transmission connects the terminal actuator to the drive system's fluid chamber through two pipelines, with one-way valves directing fluid flow during charging. By adjusting the flow valve unit, fluid channel area can be precisely controlled, enabling fine-tuning of the terminal actuator's speed. The quasi-static nature of the driving process means valve precision directly influences output accuracy, allowing for high-precision outputs along any trajectory, unaffected by the system's stroke.

2.2 Prototype Design

2.2.1 Drive System and Actuator

Based on the driving mechanism described in the previous section, structural designs were completed for the drive system, flow control unit, fluid transmission pipelines, and terminal actuator, as shown in **Figure 2(a)**. Within the drive system, the actuator piston shaft is connected using a series and parallel structure through rigid components, forming the system's energy input component. Flexible silicone tubes are used for the fluid transmission pipelines, with switching valves arranged between channels for easy fluid channel switching and the removal of air bubbles. Water is chosen as the working fluid due to its low dynamic viscosity, minimal transmission pressure loss, and incompressibility, which provides high rigidity to the hydrostatic transmission and reduces force and motion delay between the master and slave actuators.

2.2.2 Self-Sensing Electro-Magnetic Valve

Undoubtedly, the flow control components play a crucial role in enhancing output performance. The specific structure of the SEMV is shown in **Figure 2(b)**. The valve's overall structure is exquisitely simple and compact, with dimensions of only 50×10×50 mm. The valve body uses Permalloy (1J50) as the material for the magnetic yoke frame, and silicon steel can deform to control the displacement at the end of the valve body, thereby adjusting the cross-sectional area of the pipeline opening. The permanent magnet inside the valve provides the initial squeezing force to the valve body, ensuring that the valve remains closed in its initial position. Magnetostrictive (Terfenol-D) and piezoelectric (PZT-5) composite materials are embedded in the magnetic circuit of the yoke. When the excitation coil is powered, the piezoelectric material enters a resonant state. Moreover, when the drive coil is energized, a magnetic field is generated within the closed magnetic circuit to counteract the magnetic field of the permanent magnet, thereby increasing the cross-sectional area of the valve opening and opening the valve. Simultaneously, as the magnetic field of the magneto-electric material changes, the piezoelectric material produces a voltage change according to the magneto-electric effect, thereby precisely controlling the size of the output flow.

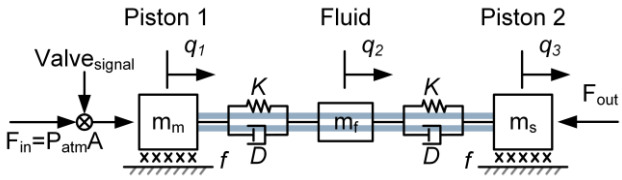

Figure 3 Hydrostatic transmission dynamics model.

3 Dynamic model

3.1 Hydrostatic Transmission

Dynamics model of hydraulic transmission under flow valve signal, describing the relationship between input force F_{in} from the drive system and the output of the end actuator. This model presents the dynamics of a hydraulic transmission influenced by a flow valve signal, linking the input force F_{in} from the drive system to the output at the end actuator. **Figure 3** illustrates a spring-mass-damper system that reveals the interaction between the piston and the hydraulic fluid. The model incorporates the flexibility of the transmission fluid pipelines and the compressibility of the fluid, represented by a spring component with stiffness K. The friction between the piston and the hydraulic cylinder walls, as well as the friction during fluid transmission, can be represented by the friction force f and damping coefficients D.

Firstly, consider applying an input force F_{in} on Piston 1 with the valve closed and derive the deformation characteristics of the pipeline. The volume change in the pipeline within a closed system should equal the fluid volume change in the input hydraulic cylinder, considering the axial stress and radial stress on the internal pipe wall under applied pressure. Assuming the pressure results from the input force $F_{in} = p\,(\pi D_{in}^2/4)$, derive the pipeline's equivalent stiffness K_p

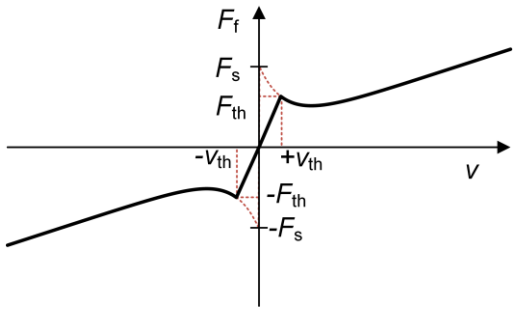

Figure 4 Friction between the piston and hydraulic cylinder wall is represented by Stribeck friction.

$$K_p = \frac{F_{in}}{\Delta x_{in}} = \pi \frac{\pi E D_{in}^4}{8 D_{pi}^2 L}\left[\frac{D_{pi}^2 + D_{po}^2 + \nu D_{po}^2 - \nu D_{pi}^2}{D_{po}^2 - D_{pi}^2}\right] \quad (1)$$

Δx_{in} is the displacement of the input piston, and L is the length of the pipeline. D_{in} is the diameter of the input cylinder(Piston 1), D_{pi} is the pipe diameter, E is elastic modulus, ν is Poisson's ratio, D_{pi} and D_{po} denote the outer and inner diameters of the pipeline.

The fluid's compressibility is modeled with a stiffness $K_f = \beta_e \cdot A_{in}^2 / V$, where A_{in} is the cross-sectional area of the Piston1, V is the total volume of the fluid, and β_e is the volumetric modulus of the fluid. The equivalent transfer stiffness K of the hydraulic pipeline is calculated as $K = K_p K_f / (K_p + K_f)$ the equivalent damping coefficient D is determined by.

$$D = \frac{F_{in}}{v_{in}} = 8\pi\mu L\left(\frac{D_{in}}{D_{pi}}\right)^4 \quad (2)$$

Friction between the piston and hydraulic cylinder wall is represented by Stribeck friction[8] as shown **Figure 4**.

Regarding fluid inertia, we consider the equivalent fluid mass at the piston, determined through energy calculations. The equivalent mass m_f, including the fluid mass in the cylinder m_{cyl} and in the pipeline m_{pi}, is computed.

$$m_f = m_{cyl} + m_{pi}(D_{in} / D_{pi})^4 \quad (3)$$

The dynamics of the hydraulic transmission are described by a linear differential equation, and the friction introduced by the piston is treated equivalently, leading to the system's state-space expression.

$$\mathbf{Kq} + \mathbf{C}\dot{\mathbf{q}} + \mathbf{M}\ddot{\mathbf{q}} = \mathbf{F} \quad (4)$$

$$\begin{cases} \mathbf{K} = \begin{bmatrix} 2K & -2K & 0 \\ -2K & 4K & -2K \\ 0 & -2K & 2K \end{bmatrix} \\ \mathbf{C} = diag(0, D, 0) \\ \mathbf{M} = diag(m_p, m_f, m_p) \\ \mathbf{F} = [F_{in} - f_m, 0, -F_{out} + f_s]^T \end{cases} \quad (5)$$

The system's state-space expression can be obtained:

$$\begin{bmatrix} \dot{\mathbf{q}} \\ \ddot{\mathbf{q}} \end{bmatrix} = \begin{bmatrix} \mathbf{0} & \mathbf{I} \\ -\mathbf{M}^{-1}\mathbf{K} & -\mathbf{M}^{-1}\mathbf{C} \end{bmatrix}\begin{bmatrix} \mathbf{q} \\ \dot{\mathbf{q}} \end{bmatrix} + \begin{bmatrix} \mathbf{0} \\ -\mathbf{M}^{-1}\mathbf{F} \end{bmatrix} \quad (6)$$

3.2 Valve Opening and Flow Sensing

Under laminar flow conditions, the output flow rate is controlled and fluid leakage is prevented by adjusting the flow channel area through a non-contact method. This is achieved by compressing the flexible fluid tube, which effectively modifies the valve opening area.

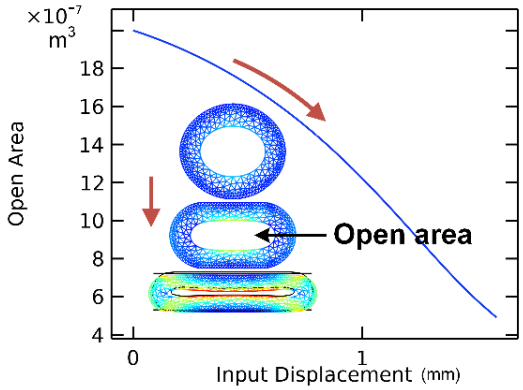

Figure 5 Relationship between valve cross-sectional area and input displacement.

$$Q = k_q x_v \sqrt{\Delta p},\ \Delta p = \begin{cases} p_s - p & x_v > 0 \\ p - p_r & x_v < 0 \end{cases} \quad (7)$$

Where:k_q, x_v, p_s, p_r are flow gain coefficient, valve opening area, fluid supply pressure, reference pressure.

Valve opening is directly related to the control input, but due to system nonlinearity, the relationship does not satisfy an ideal linear static mapping. To determine the relationship between the squeeze displacement and valve opening, this paper uses a flow-solid coupled finite element method under constant pressure input conditions. It simulates the deformation of the internally fluid-filled flexible tube after compression and the fluid flow conditions. This analysis (**Figure 5**)allows us to derive the mapping relationship between the input displacement and the valve cross-sectional area.

The direct magnetoelectric (ME) effect describes the phenomenon where a magnetic field H induces an electric field E. A very useful metric for evaluating the performance of ME sensors is the ME voltage coefficient, denoted as α This coefficient quantifies the sensor's sensitivity by measuring the electric field produced per unit of magnetic field. It is expressed as [9]:

$$^{l}\alpha_{33}^{E} = \frac{^{p}E_3}{^{m}H_3} = \frac{\eta\, ^{p}d_{33}\, ^{m}d_{33}}{^{p}\varepsilon_{33}\left(^{p}s_{33}^{E} + \eta\, ^{m}s_{33}^{E}\right) - {}^{p}d_{33}^2} \quad (8)$$

where E is the induced electric field and H is the applied magnetic field. In this context, $\eta = l_m / l_p$ represents the length ratio of the Terfenol-D rod to the PZT (lead zirconate titanate) disc. The superscript l on the left indicates sensitivity under low-frequency (static/quasi-static) conditions, while the superscript E on the right denotes that the piezoelectric output is measured in terms of electric field strength. The subscript 33 indicates that the magnetic field is applied along the magnetostrictive axis 3, and the polarization electric field is detected along the piezoelectric axis 3. For the specific Terfenol-D/PZT-5 composite magnetoelectric material, other related material parameters can be found in [9].The relationship between the magnetic field H and the output flow rate is determined through experimental calibration. Due to the high accuracy of magnetoelectric sensors in detecting magnetic fields, it is possible to obtain relatively precise flow rate measurements. This accuracy is critical in applications where precise control of fluid dynamics is necessary.

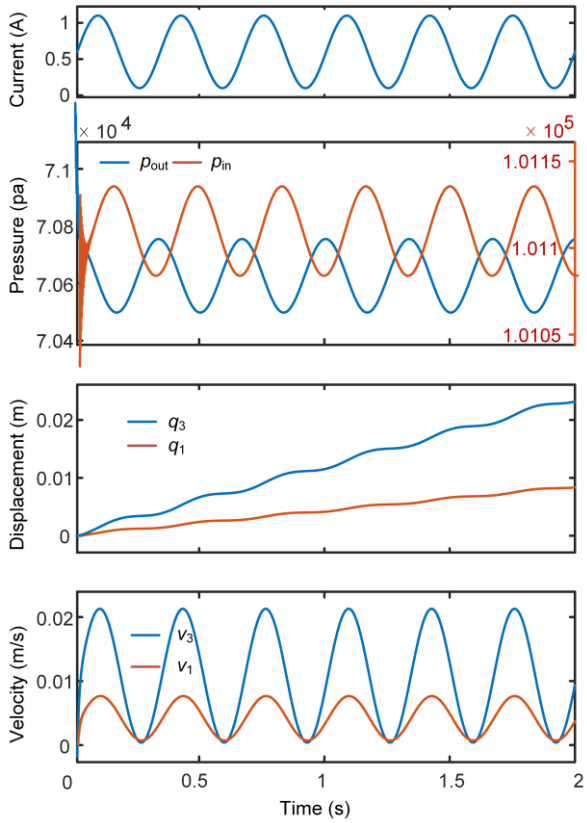

Figure 6 Simulation results of system output based on the dynamic model.

3.3 Simulation and result

The valve is simplified and modeled as a first-order system. Pipeline length: 30mm; Diameters of APDA and driving system are 6mm and 10mm. Input signals included an amplitude of 1A, a frequency of 2Hz, and a continuous sine signal at 3Hz. The critical velocity threshold v_{th} was set at 300μm/s for control purposes. The results are depicted graphically in **Figure 6**. The velocity and pressure curves display oscillations due to fluid elasticity, particularly noticeable when the flow rate approaches zero. At this point, non-linear friction terms contribute non-linearity to the system's output characteristics, leading to more pronounced oscillations near the zero point in the control mode.

4 Conclusion

Our investigation into this novel driving method, informed by comparative test results, demonstrates that it achieves higher precision in output during uniform motion than traditional methods like microfluidic pumps and motor-driven actuators. This advantage stems from our approach of utilizing offline energy injection, which decouples the energy supply from the control process, reducing pulsations commonly observed with real-time energy conversion. This stabilization of the energy input significantly lowers the external control energy requirements, enhancing the overall precision of the fluid drive system. Notably, our method leverages stable atmospheric potential energy and includes a local closed-loop control at the valve to ensure high precision in valve operation. This setup avoids the complexities associated with vacuum pumps and negative pressure systems, offering a simpler and potentially more efficient solution.

5 Acknowledgements

This project was funded by Specific Project of Shanghai Jiao Tong University for "Invigorating Inner Mongolia through Science and Technology"(2022XYJG0001-01-04).

6 Literature

[1] Kim J, Ladjal H, Folio D, et al. Evaluation of Kim J, Ladjal H, Folio D, et al. Evaluation of telerobotic shared control strategy for efficient single-cell manipulation[J]. IEEE transactions on automation science and engineering, 2011, 9(2): 402-406.

[2] Kim H, Kim J, Ahn D, et al. Development of a nanoprecision 3-DOF vertical positioning system with a flexure hinge[J]. IEEE Transactions on Nanotechnology, 2013, 12(2): 234-245.

[3] Habibullah H, Pota H R, Petersen I R. A novel control approach for high-precision positioning of a piezoelectric tube scanner[J]. IEEE Transactions on Automation Science and Engineering, 2016, 14(1): 325-336.

[4] Yan X, Zhou Q, Vincent M, et al. Multifunctional biohybrid magnetite microrobots for imaging-guided therapy[J]. Science robotics, 2017, 2(12): eaaq1155.

[5] Li X, Liu C, Chen S, et al. In vivo manipulation of single biological cells with an optical tweezers-based manipulator and a disturbance compensation controller[J]. IEEE Transactions on Robotics, 2017, 33(5): 1200-1212.

[6] Guo F, Mao Z, Chen Y, et al. Three-dimensional manipulation of single cells using surface acoustic waves[J]. Proceedings of the National Academy of Sciences, 2016, 113(6): 1522-1527.

[7] Urbano R L, Clyne A M. An inverted dielectrophoretic device for analysis of attached single cell mechanics[J]. Lab on a Chip, 2016, 16(3): 561-573.

[8] R.Stribeck,“Die wesentlichen eigenschaften der gleit- und rollenlager [the key qualities of sliding and roller bearings],” Z. Vereines Seutscher Ing., vol. 46, pp. 1432–1437, 1902.

[9] BICHURIN.M, PETROV V. Modeling of Magnetoelectric Effects in Composites[M]. Springer Netherlands, 2014.

MULTISTABLE MAGNETIC LIFT ACTUATION UNDER VARIABLE LOADS

Pascal M. Weber[1], Yannik T. Rüde[1], Ulrike Wallrabe[1]*
[1] Laboratory for Microactuators, IMTEK – Department of Microsystems Engineering, University Freiburg, Germany
* Correspondence: wallrabe@imtek.uni-feiburg.de

Abstract

This paper investigates the load-dependent behavior of a multistable out-of-plane actuator. By combining an electromechanical solenoid and a reluctance-based holding system, our actuator achieves stable positioning at three distinct positions without continuous energy consumption. We measured response times as low as 5.5 ms and out-of-plane displacements exceeding 3.5 mm, with a stable intermediate position at around 1.8 mm. Furthermore, it successfully lifts additional loads of up to 70 mg while maintaining functionality of all three stable positions.

1 Introduction

Most MEMS applications frequently rely on cantilever-based actuation mechanisms, valued for their simplicity but burdened with some drawbacks. These include an increasing restoring force hindering large displacements, or the continuous power consumption even for static actuation. Thereby, the displacement is defined by the equilibrium of actuation and restoring forces.

To address these limitations, researchers have explored various cantilever-free and often multistable approaches, achieving displacements up to centimeters in scale [1]. These systems utilize a wide range of actuation principles, ranging from Piezo-driven stick-slip actuators [1] over micro valve arrays [2] moving samples horizontally on a cushion of air to magnetic actuators. The latter have been proven for linear microdrives [3], magnetic linear guides [4, 5] and eddy currents based levitation devices [6]. Notably, vertical multistability was achieved in [7] using several magnet rings and a magnetic plunger.

In [8] we presented a multistable, cantilever-free lifting actuator, combining a simple magnetic plunger with a small coil. This actuator not only overcame the limitations of traditional cantilever-based systems but also enabled lifting its plunger to three distinct multistable positions, where it remains without continuous energy consumption. In this paper, we will explore the maximum load capacity of this actuator, when traversing between the stable states and investigate its behavior under varying load conditions.

First, we will provide a brief overview of the actuator's design. Then, we will examine its dynamic behavior under different load conditions and how the intermediate stable position shifts with increasing load. Eventually, we will investigate the tilting behavior of the actuator across its various stable positions.

2 Actuator Setup

With our actuator we combine the function of an electromechanical solenoid and a reluctance-based holding system to create a multistable lifting actuator for out-of-plane displacement. This actuator is capable of lifting a movable plunger higher than 3.5 mm and holding it at multiple stable and well-defined positions.

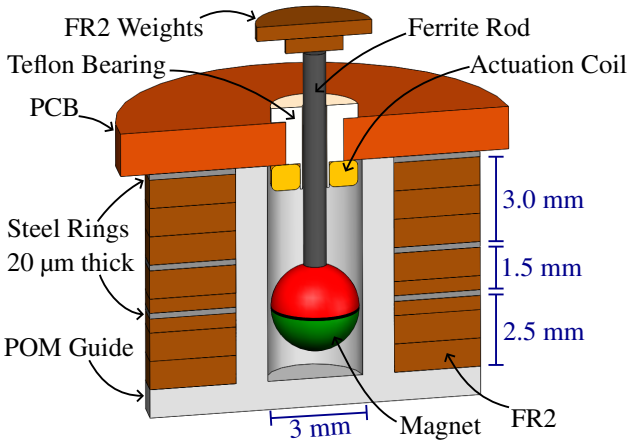

Figure 1 Sectional view of the device. The actuation coil is bonded to the PCB above. A Teflon bearing allows the ferrite rod to slide freely up and down. FR2 spacers are used to adjust the height of the steel rings. For better visibility we increased the steel ring's thickness.

In Figure 1, we see a sectional view of the actuator. At the top, we have a stationary coil with a diameter of 3 mm for actuation, glued to the PCB. The movable plunger, weighing 126 mg, consists of a soft magnetic ferrite rod glued to a 3 mm permanent magnetic NdFeB sphere. The plunger sits within the POM guide and the Teflon bearing, guiding the ferrite rod through the center of the actuation coil. We chose ferrite material for the rod to alter the magnetic field and increase the efficiency of actuation [8]. To ensure multistability we use three 20 µm thick steel foils, placed along the plunger's travel path at different heights.

These rings provide stable positions by balancing gravitational, magnetic, and frictional forces. For details, we refer to [8]. The vertical position of each steel ring can be adjusted thanks to the stack of phenolic paper (FR2), allowing flexibility in fine-tuning the actuator's stable positions. To test the load-dependent behavior, we used small discs, with diameters of 2 and 4 mm, cut from 300 µm hard paper sheets. These weights were glued to the tip of the ferrite rod and then incrementally stacked for each measurement taken.

3 Characterisation

For measuring the dynamic behavior of the actuator, we used a confocal distance sensor pointing at the top of the ferrite rod. To prevent the coil from overheating, short current pulses with a maximum amplitude of 700 mA were used for actuation.

Figure 2 displays a typical actuation, showing the three stable positions of our new prototype when no load is applied. This prototype achieved a response time of 5.5 ms but showed increased ringing for the center position compared to the previous proof of concept [8], as we were able to reduce the friction on the plunger. Interestingly, all measured transitions from the top to the intermediate position showed a downward spike. Here, the plunger most likely bounced off from the bottom substrate, before coming to a rest in the intermediate position. But, due to the limited measurement frequency (1 kHz), this interaction was not fully captured.

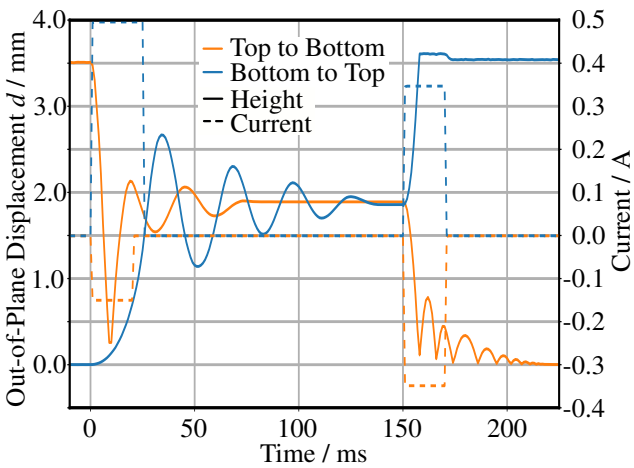

Figure 2 Actuation of the plunger without applied load. The measured out-of-plane displacement d of the plunger includes a pause at the stable intermediate point within the movement range. Corresponding actuation currents are marked by matching colors as dashed lines.

In Figure 3, we see the transition from the bottom to the stable intermediate position for different loads added to the plunger. We adjusted the actuation current to minimize the likelihood of overshooting or undershooting the intermediate position. For loads exceeding 24.1 mg, the risk of overshooting increased significantly.

However, it was still feasible to lift the plunger from the bottom to the top position. Therefore, we continued increasing the actuation current stepwise, to determine the maximum liftable load. But as the current was adjusted for the weight, the resulting trajectories barely changed. The maximum weight it could reliably lift was up to 70 mg with a 700 mA current pulse (Fig. 3, brown), resembling more than half of the weight of the plunger itself. Surprisingly, the current pulse designed to return the plunger to the bottom position between measurements sometimes resulted in the plunger getting caught in the intermediate stable position. This finding demonstrates that the intermediate position could still be utilized for loads as high as 70 mg.

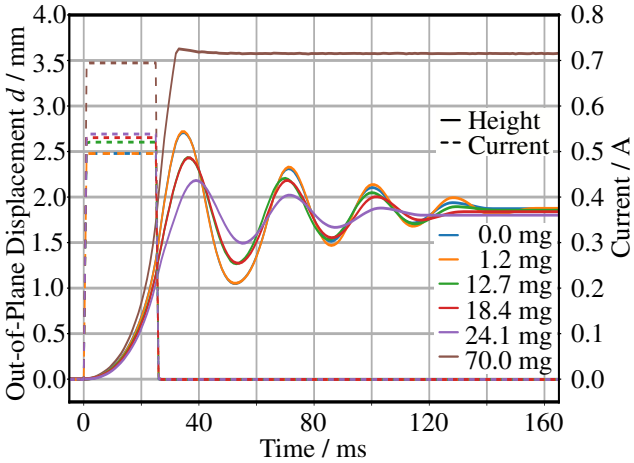

Figure 3 Measured transition from the bottom to the intermediate position under varying loads. The actuation currents (dashed lines) were selected to minimize the likelihood of over- or undershooting for each load condition. Marked in brown is the trajectory of the maximum load, traversing from the bottom to the top position. Note: The total weight is comprised by the mass of the plunger (126 mg) plus the added loads mentioned here.

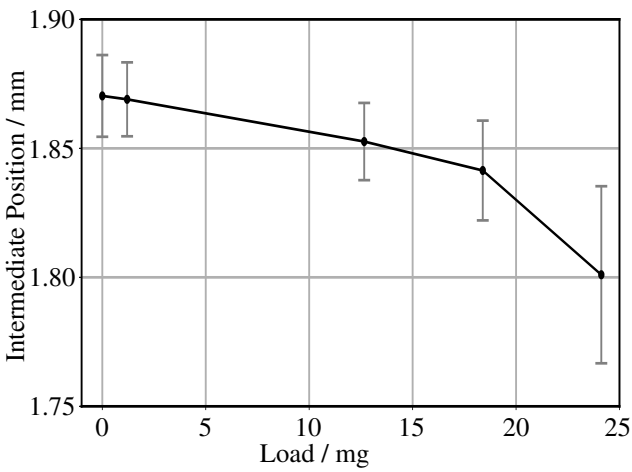

Figure 4 Stable intermediate position of the plunger after the actuation of Fig. 3. The shown position represents the average of all measured actuations that remained in the middle, with error bars indicating the standard deviation.

Figure 4 illustrates the load-dependent resting point of the intermediate position. The shown position is formed by the average of around 40 actuation measurements that stayed in the middle. It is evident that the stable point shifts downward as the load increases, i.e., the force equilibrium is shifted accordingly. As one would expect, the relationship between position and load is non-linear, as the magnetic force is non-linear. For details, we again refer to [8]. Additionally, the standard deviation of the position increases with the load which could be attributed to the plunger becoming increasingly top-heavy, resulting in higher friction as it leans to one side. This effect is also hinted at in Figure 3, where a higher damping is observed for a load of 24.1 mg.

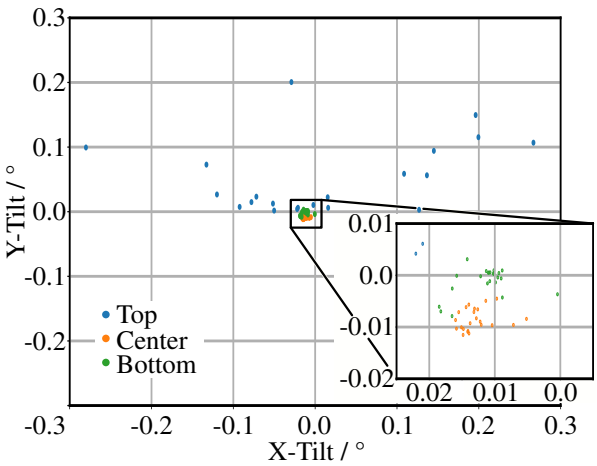

Figure 5 Measured tilts of the plunger in the three stable positions after actuation starting from the bottom. The 'bottom' data represent a short lift and return to the bottom position. The repeated measurements show only a small deviation for the bottom and center positions, but a significantly larger one for the top position.

Given that the plunger isn't supported by cantilevers, it could potentially tilt within the guidance structure. Therefore, we measured the tilt of the platform in all three stable positions, following an actuation initiated from the bottom. In Figure 5, the x and y tilt for 25 measurements are illustrated. We note that the tilt for the bottom and center positions align nicely within a range of $\pm$ 0.02° (inset). However, the tilt of the top position is noticeably larger in magnitude. This behaviour can be attributed to a less favorable guidance situation in this position, as the Teflon bearing is now located at the bottom of the ferrite rod, reducing the influence of the POM guide.

4 Conclusion

We examined the load-dependent behavior of our multistable lifting actuator. By using a combination of an electromechanical solenoid and a reluctance-based holding system, the actuator enables stable positioning at three distinct positions without continuous energy consumption. The experimental results demonstrate the actuator's capability to achieve a response time as low as 5.5 ms and a out-of-plane displacement of more than 3.5 mm. We showed that the actuator was able to lift additional loads of up to 70 mg, corresponding to a total load of almost 200 mg, while maintaining the functionality of the three stable positions. However, as the intermediate position is defined by gravitational and magnetic forces, we observed how the resting position shifts downward with increasing load.

Since the actuator does not rely on cantilevers but on a guidance structure rather acting as a slide bearing for the freely moving plunger, we investigated the tilting behavior of the plunger across the three stable positions. Our examination revealed minimal scattering for the bottom and intermediate positions of $\pm 0.02°$, but a magnitude larger scattering for the top position. In our future work we will try to reduce ringing and to avoid overshooting, particularly during transitions to the intermediate stable position. This improvement could be achieved through the implementation of a model-based input sequence [9] or by adopting a closed-loop control approach using self-sensing, as demonstrated in [10].

5 Literature

[1] Jean-Marc Breguet, Ricardo Pérez Suárez, A. Bergander, Camille Schmitt, R. Clavel, and Hannes Bleuler. Piezoactuators for motion control from centimeter to nanometer. In *IEEE International Conference on Intelligent Robots and Systems 2000*, volume 1, pages 492 – 497 vol.1, Takamatsu, Japan, 02 2000. doi: 10.1109/IROS.2000.894652.

[2] Guillaume J. Laurent, Anne Delettre, Rabah Zeggari, Reda Yahiaoui, Jean-François Manceau, and Nadine Le Fort-Piat. Micropositioning and fast transport using a contactless micro-conveyor. *Micromachines*, 5(1):66–80, 2014. doi: 10.3390/mi5010066.

[3] Yixuan Zhang, Qiwei Xu, Yun Yang, Longjiang Gao, and Yizhou Zhao. High-integrated micro permanent magnet linear actuator positioning system. *Energy Reports*, 9:990–1002, 2023. doi: 10.1016/j.egyr.2023.05.180.

[4] Christine Ruffert, Ralf Gehrking, Bernd Ponick, and Hans Gatzen. Magnetic levitation assisted guide for a linear micro-actuator. *IEEE Transactions on Magnetics*, 42:3785 – 3787, 12 2006. doi: 10.1109/TMAG.2006.879160.

[5] Christine Ruffert, Jixiang Li, Berend Denkena, and Hans H. Gatzen. Development and evaluation of an active magnetic guide for microsystems with an integrated air gap measurement system. *IEEE Transactions on Magnetics*, 43(6):2716–2718, 2007. doi: 10.1109/TMAG.2007.893779.

[6] Kirill Poletkin, Zhiqiu Lu, Ulrike Wallrabe, Jan Korvink, and Vlad Badilita. Stable dynamics of micromachined inductive contactless suspensions. *International Journal of Mechanical Sciences*, 131-132:753–766, 2017. doi: 10.1016/j.ijmecsci.2017.08.016.

[7] Michael Olbrich, Arwed Schütz, Tamara Bechtold, and Christoph Ament. Design and optimal control of a multistable, cooperative microactuator. *Actuators*, 10(8), 2021. doi: 10.3390/act10080183.

[8] Pascal M. Weber and Ulrike Wallrabe. Cantilever Free Magnetic Actuation for Multistable Vertical Displacement. In *MikroSystemTechnik Kongress 2023*, pages 839–843, Dresden, Germany, 2023. VDE Verlag.

[9] Michael Olbrich, Pascal M. Weber, Ulrike Wallrabe, and Christoph Ament. Optimized Feedforward Control of a Multistable Magnetic Actuator. In *Actuator 2024 - 19th International Conference on New Actuator Systems and Applications (Actuator 2024)*, Wiesbaden, Germany, jun 2024.

[10] Pascal M. Weber, Ulrike Wallrabe, and Matthias C. Wapler. Self-sensing of a magnetically actuated prism. *Sensors*, 23(12), 2023. doi: 10.3390/s23125493.

Model Order Reduction Augmented by a Neural Network for a Nonlinear Electrostatic Microactuator

Arwed Schütz[1], Lars Nolle[1,2], Tamara Bechtold[1]*
[1] Jade University of Applied Sciences, Wilhelmshaven, Germany
[2] German Research Centre for Artificial Intelligence, Oldenburg, Germany
* Correspondence: tamara.bechtold[at]jade-hs.de

Abstract

Projection-based model order reduction is a well-established technique to generate highly efficient yet accurate models of microsystems based on, i.e., finite element models. However, the methodology is unsuited for nonlinear effects, which are commonly found in microsystems. Approaches to overcome this gap are referred to as hyperreduction. They typically require access to the mathematical formulation of nonlinear terms. These data are hardly accessible in commercial software. A recent alternative based on easily accessible data are artificial neural networks (ANNs) to efficiently approximate the nonlinear terms. This method operates directly at the reduced level and is therefore associated with significant computational efficiency. Furthermore, its automatic differentiation provides inexpensive access to the nonlinear terms' Jacobian matrix, which is commonly required for nonlinear solvers. This contribution demonstrates hyperreduction by an ANN for an electrostatic microactuator modeled in commercial finite element software. In addition, a modified snapshot-based scheme to compute the reduced basis using not only snapshots of states but also of forces is proposed.

1 Introduction

A key component for microsystems is accurate and efficient modeling, with applications ranging from design optimization to closed-loop control. The commonly deployed finite element method (FEM) provides reliable insights, but at high computational costs. A technique to drastically reduce computational costs while hardly sacrificing accuracy is projection-based model order reduction (MOR). Based on FEM models, MOR constructs significantly more efficient yet highly accurate surrogate models [1]. However, this framework cannot reduce nonlinear effects. This limitation affects microsystems in particular as these commonly feature nonlinear effects like geometrical nonlinearities, electromechanical coupling, or mechanical contact. A designated methodology referred to as hyperreduction closes this gap by efficiently approximating nonlinear terms. Although prominent hyperreduction methods such as the discrete empirical interpolation method (DEIM) [2] achieve great results, they require comprehensive mathematical descriptions of the nonlinear terms. Hence, these methods' intrusive nature is hardly compatible with commercial FEM software. A recent alternative method for hyperreduction using easily accessible data are artificial neural networks (ANNs) [3, 4, 5]. As training data are reduced by MOR, small architectures associated with significantly lower training times are sufficient. In addition, ANNs allow for efficient evaluations of their Jacobian matrix via automatic differentiation. This is particularly useful since nonlinear solvers such as Newton-Raphson are based on iterative linearizations and incremental solution updates.

This work investigates hyperreduction by an ANN for a reduced model of an electrostatic beam actuator described in Section 2. Section 3 presents the modeling process, including the FEM model for reference, the methods of MOR by proper orthogonal decomposition (POD), and hyperreduction via an ANN. Section 4 evaluates the ANN's numerical performance, which is subsequently discussed in Section 5.

2 Case Study: Beam Actuator

This work's case study is part of an innovative micromirror for quasi-static rotation with large angles [6, 7]. The idea is to incrementally rotate a spherical cap according to the operating principle in Figure 1. An actuation cycle starts with the spherical cap resting on four electrostatic beam actuators. Applying voltages to the beam actuators launches the mirror into a flight phase with a controllable spin. An active catch completes the cycle. The design's novelty lies in omitting all structural links and minimizing friction as opposed to well-established stick-slip actuation. Furthermore, a large range of continuous mirror orientations is stable by design and does not require energy once reached. Figure 2 provides microscope pictures in top view of both the system and a single beam actuator.

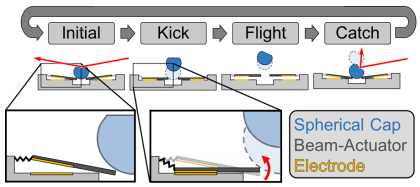

Figure 1 The microsystem's [6, 7] basic motion sequence: initially, the spherical cap rests on the four electrostatic beam actuators. These are actuated into pull-in, launching and spinning the spherical cap. An active catch ends the sequence, which can be repeated for large deflections.

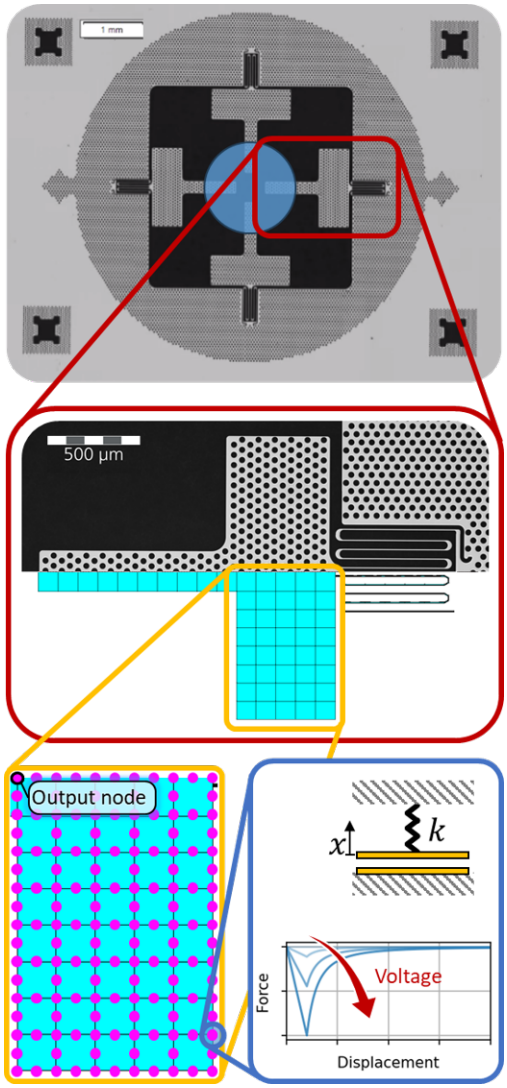

Figure 2 Modeling workflow starting with a microscope picture of the microsystem in top view, of which a single beam actuator is modeled in FEM. Its perforation is represented by effective material data [8, 9]. Each FEM node of the electrode framed in yellow is connected to a one-dimensional transducer element. Each transducer generates a nonlinear force according to Equation (3), introducing electrostatic attraction and mechanical contact. The force at the output node is chosen for model evaluations.

3 Modeling

The modeling stage includes three steps: firstly, a FEM model described in Section 3.1 establishes the reference solution. In Section 3.2, two variants of MOR approximate the underlying mathematical model and data, significantly reducing their dimension. Finally, an ANN approximates the reduced nonlinearities in Section 3.3 to achieve efficient hyperreduction.

All FEM studies are carried out in *Ansys® Academic Research Mechanical, Release 2022 R2*. All subsequent steps are implemented in Python, relying on NumPy, scikit-learn, and TensorFlow.

3.1 Finite Element Model

A single beam actuator is modeled using shell elements in general and beam elements for the meander spring. All elements deploy quadratic shape functions. In addition, one-dimensional transducer elements are attached to the electrode to incorporate electrostatic attraction and mechanical contact upon pull-in. These elements' electrostatic attraction assumes parallel plate capacitors. The beam's perforation is converted to effective material parameters [8], affecting elasticity, density, and area for the transducer elements. Specific values are given in [9]. This model is analyzed with a linearly ramped voltage up to 40 V in 1,000 increments to study electrostatic pull-in.

Mathematically, the FEM model corresponds to a large-scale system of nonlinear algebraic equations:

$$\Sigma = \begin{cases} \boldsymbol{f}(\boldsymbol{x}, U) = \boldsymbol{B}\boldsymbol{u} \\ \boldsymbol{y} = \boldsymbol{C}\boldsymbol{x} \end{cases}, \tag{1}$$

where each row of the first line corresponds to a nodal force balance. The state vector $\boldsymbol{x} \in \mathbb{R}^n$ contains $n = 3102$ degrees of freedom. The input matrix $\boldsymbol{B} \in \mathbb{R}^{n \times p}$ distributes the inputs $\boldsymbol{u} \in \mathbb{R}^p$ and the output matrix $\boldsymbol{C} \in \mathbb{R}^{q \times n}$ assembles the user-defined outputs $\boldsymbol{y} \in \mathbb{R}^q$. The nonlinear restoring forces are denoted by $\boldsymbol{f}(\boldsymbol{x}, U) \in \mathbb{R}^n$ for a voltage U. For the model considered here, the nonlinear restoring forces are composed of a linear stiffness $\boldsymbol{K}$ and nonlinear forces $\boldsymbol{f}_{TD}$ due to the transducer elements:

$$\boldsymbol{f}(\boldsymbol{x}, U) = \boldsymbol{K}\boldsymbol{x} + \boldsymbol{f}_{TD}(\boldsymbol{x}, U) \tag{2}$$

This nonlinear force vector has $n_{TD} = 285$ nonzero elements, each corresponding to a lumped transducer force at a single node i as indicated in bottom left of Figure 2:

$$f_{TD,i}(x_{z,i}, U) = \begin{cases} \frac{\varepsilon A_i}{2} \frac{1}{(x_{z,i}+g_0)^2} U^2 & \text{if } (x_{z,i}+g_0) \geq 0 \\ k_n(U)\,(x_{z,i}+g_0) & \text{else,} \end{cases} \tag{3}$$

where ε is the vacuum permittivity, A_i the area associated with node i for capacitance computation, $x_{z,i}$ the vertical displacement of node i, g_0 the initial gap, and $k_n(U)$ a voltage-dependent contact stiffness.

Note that the results for the state x and the forces f of all 1,000 steps provide the data used in Sections 3.2 and 3.3.

3.2 Model Order Reduction

Projection-based MOR is a methodology to generate low-dimensional surrogate models while hardly compromising on accuracy. In addition, the same methodology can also be applied for dimensionality reduction in data analysis. The key idea is to identify and exploit dominant patterns in the original model's solution. Mathematically, the original state is approximated by a combination of dominant patterns:

$$\boldsymbol{x} \approx \boldsymbol{W}\boldsymbol{x}_{\boldsymbol{r}}, \tag{4}$$

where $\boldsymbol{W} \in \mathbb{R}^{n \times r}$ is the reduced basis comprising r patterns as column vectors and $\boldsymbol{x}_{\boldsymbol{r}} \in \mathbb{R}^r$ is the reduced state vector containing their respective weights. A well-established

method to construct a reduced basis is the POD. After collecting N_S solution vectors of the original model into a snapshot matrix $\boldsymbol{S_x} \in \mathbb{R}^{n \times N_S}$, a singular value decomposition identifies the most relevant patterns:

$$\boldsymbol{S_x} = \begin{bmatrix} \boldsymbol{x}_1 & \cdots & \boldsymbol{x}_{N_S} \end{bmatrix} = \boldsymbol{U}\boldsymbol{\Sigma}\boldsymbol{V}^T. \tag{5}$$

The descending singular values in $\boldsymbol{\Sigma}$ indicate the relevance of corresponding left singular vectors in $\boldsymbol{U}$. All r vectors with a normalized singular value above a threshold of 1×10^{-6} form the reduced basis $\boldsymbol{W}$. This work extends this approach by not only considering snapshots of the state vector but also of the nonlinear forces. Hence, the above procedure identifies two reduced bases which are finally merged and orthonormalized. This augmentation ensures a reduced basis that accurately captures both displacements and forces. Inserting this approximation into the original system in Equation (1) and projecting the equation onto the subspace spanned by $\boldsymbol{W}$ leads to the reduced system:

$$\Sigma_r = \begin{cases} \overbrace{\boldsymbol{W}^T \boldsymbol{K} \boldsymbol{W}}^{\boldsymbol{K}_r} \boldsymbol{x}_r + \boldsymbol{W}^T \boldsymbol{f}_{TD}(\boldsymbol{W}\boldsymbol{x_r}, U) = \overbrace{\boldsymbol{W}^T \boldsymbol{B}}^{\boldsymbol{B}_r} \boldsymbol{u} \\ \boldsymbol{y} = \underbrace{\boldsymbol{C}\boldsymbol{W}}_{\boldsymbol{C}_r} \boldsymbol{x_r} \end{cases} \tag{6}$$

All components except for the input and output are reduced versions of their counterparts, i.e., they are of dimension $r = 23 \ll n$. However, the reduction only affects linear components. In contrast, the nonlinear forces become more computationally expansive than the original model as they require expanding $\boldsymbol{x_r}$, evaluating the full set of nonlinarities, and then reducing them.Techniques to remedy this bottleneck are termed hyperreduction. The basic idea is to efficiently approximate the nonlinear relation between the reduced forces $\boldsymbol{f}_{TD,r}$ and the reduced state $\boldsymbol{x}_r$:

$$\boldsymbol{W}^T \boldsymbol{f}_{TD}(\boldsymbol{W}\boldsymbol{x_r}, U) \approx \boldsymbol{f}_{TD,r}(\boldsymbol{x}_r, U). \tag{7}$$

It is worth noting that nonlinearities are commonly evaluated by iterative linearizations, i.e., by the well-established Newton-Raphson solver. Hence, not only the nonlinear function but also its Jacobian are of matrix interest.

3.3 Hyperreduction via a Neural Network

A recent approach for hyperreduction is regression via ANNs to infer relations between the reduced state x_r and the reduced forces f_r [3, 4]. In contrast to conventional hyperreduction methods [2], the only data required are also the most accessible in commercial FEM software. As sampled states and forces are reduced to a drastically smaller dimension, only small network architectures are required. Furthermore, an ANN's Jacobian matrix is conveniently available by automatic differentiation, increasing compatibility to established solvers.

This work deploys a fully-connected, feed-forward neural network architecture, featuring one input layer, two hidden layers as recommended for hyperreduction [4], and one output layer. Each hidden layer comprises 15 neurons as determined by a grid search with 30 models per architecture. The ANN uses the swish activation function due to its performance [10]. Furthermore, it is continuously differentiable which might lead to more robust Jacobian matrices when deployed within a nonlinear solver. The output layer uses linear activations to enable unbounded outputs for regression. All weights are initialized with He initialization [11] according to the swish function's original work [10]. The training uses a root mean squared error for loss and mini-batches of 25, which is well within the recommended range of 32 or smaller [12]. The gradient-based optimization utilizes ADAM due to its robustness [13] and its previous successful application to hyperreduction-related work [4]. Its default learning rate of 1×10^{-3} is slightly lowered to 0.75×10^{-3} as recommended for swish activation functions [10]. A maximum training duration of 5,000 epochs is combined with early stopping after no improvement within 250 epochs. The raw data for regression are 1,000 sampled results obtained by the FEM as specified in Section 3.1. Left-multiplying these snapshots matrices with $\boldsymbol{W}^T$ reduces their dimension to $r = 23$, creating the initial raw data. After shuffling, the data is divided into three sets for training (70 %), validation (15 %), and testing (15 %). Based on the training set, all data are standardized. Note that results for the reduced force can be expanded to the original dimension by Equation (4).

4 Numerical Results

Figure 3 shows the decay of singular values for snapshots of the states and forces, respectively. Two reduced bases of the same dimension are built: one exclusively from states and one additionally considering forces. To assess their performance, both are used to approximate the snapshotted forces at the output node. As Figure 4 illustrates, the reduced basis built solely from states fails to represent the forces. Therefore, the hybrid reduced basis is used to prepare data for the ANN. The final ANN's prediction is expanded to the original model and also shown in Figure 4.

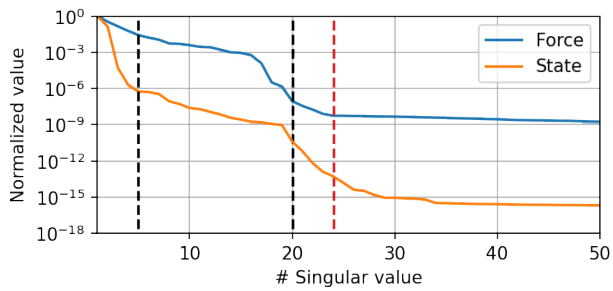

Figure 3 The first 50 normalized singular values of the snapshot matrices for displacement and forces in descending order, respectively. The black dashed lines indicate the truncation threshold of 1×10^{-6}, resulting in a total reduced dimension of $r = 4 + 19 = 23$. The red dashed line indicates conventional POD-made reduced basis of the same dimension exclusively comprising state snapshots.

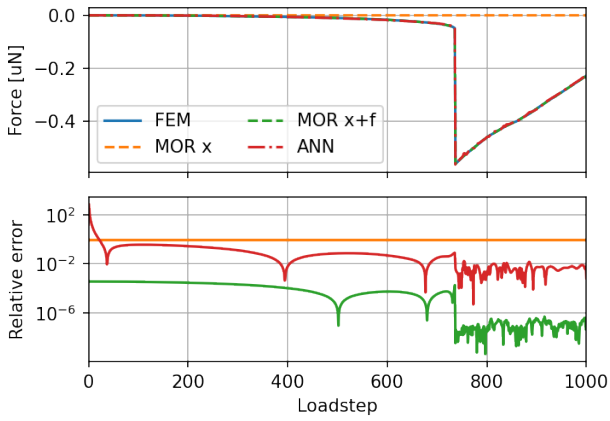

Figure 4 Transducer force at the output node computed by the FEM, reduced POD of states $\boldsymbol{x}$, reduced by POD augmented by force $\boldsymbol{f}$, and the latter approximated by an ANN. Absolute relative errors indicate approximation quality.

5 Conclusions and Outlook

This work has successfully demonstrated ANN-based hyperreduction for an electrostatic beam actuator. The ANN accurately approximates the relation between the reduced state and the reduced forces. A modified POD that additionally considers force snapshots has been introduced and shown superior accuracy.

Future work will additionally evaluate the whole reduced model with hyperreduction via an ANN. Furthermore, the ANN's prediction quality regarding the Jacobian matrix will be studied. To improve accuracy, we plan to augment the ANN's training data and loss function by FEM-based Jacobian matrices to improve accuracy [14, 15].

6 Acknowledgements

This research is part of the project *ADOPT - Adaptive Optics for THz* within the priority program *KOMMMA - Cooperative Multistage Multistable Microactuator Systems* and was funded by Deutsche Forschungsgemeinschaft (German Research Foundation) grant number 424616052.

Mario Farny from Microsystems Technology at the Ruhr-University Bochum designed the microsystem considered in this work under supervision of Prof. Dr. Martin Hoffmann. Further, Mario Farny took and supplied the microscope images used in Figure 2.

7 Literature

[1] Athanasios C. Antoulas. *Approximation of large-scale dynamical systems*. Advances in design and control. Society for Industrial and Applied Mathematics, Philadelphia, 2005. ISBN 0898715296.

[2] Saifon Chaturantabut and Danny C. Sorensen. Nonlinear Model Reduction via Discrete Empirical Interpolation. *SIAM Journal on Scientific Computing*, 32 (5):2737–2764, 2010.

[3] J. S. Hesthaven and S. Ubbiali. Non-intrusive reduced order modeling of nonlinear problems using neural networks. *Journal of Computational Physics*, 363(9): 55–78, 2018.

[4] Han Gao, Jian-Xun Wang, and Matthew J. Zahr. Non-intrusive model reduction of large-scale, nonlinear dynamical systems using deep learning. *Physica D: Nonlinear Phenomena*, 412:132614, 2020.

[5] Ludovica Cicci, Stefania Fresca, and Andrea Manzoni. Deep-HyROMnet: A deep learning-based operator approximation for hyper-reduction of nonlinear parametrized PDEs, 2022.

[6] Mario Farny and Martin Hoffmann. Kick & Catch: elektrostatisches Rotieren einer Kugel. In *MikroSystemTechnik Kongress*, pages 274–277. VDE Verlag GmbH, Stuttgart-Ludwigsburg, 2021. ISBN 978-3-8007-5656-8.

[7] Mario Farny, Michael Olbrich, Christoph Ament, and Martin Hoffmann. Kick & Catch: Coaction of an electrostatic kick and magnetic catch system for the rotation of a sphere. In *ACTUATOR 2022*, GMM-Fachbericht. VDE VERLAG, Berlin and Offenbach, 2022. ISBN 978-3-8007-5894-4.

[8] D. C. Webb, K. Kormi, and S.T.S. Al-Hassani. Use of FEM in performance assessment of perforated plates subject to general loading conditions. *International Journal of Pressure Vessels and Piping*, 64(2):137–152, 1995.

[9] Arwed Schütz, Sönke Maeter, and Tamara Bechtold. Nonlinear Model Order Reduction of a MEMS Actuator by a Trajectory Piecewise-Linear Approximation. In *MikroSystemTechnik Kongress 2023*, pages 551–554. VDE VERLAG, Berlin, 2024. ISBN 978-3-8007-6203-3.

[10] Prajit Ramachandran, Barret Zoph, and Quoc V. Le. Searching for Activation Functions, 2017.

[11] Kaiming He, Xiangyu Zhang, Shaoqing Ren, and Jian Sun. Delving Deep into Rectifiers: Surpassing Human-Level Performance on ImageNet Classification. In *2015 IEEE International Conference on Computer Vision (ICCV)*, pages 1026–1034. IEEE, 12/7/2015 - 12/13/2015. ISBN 978-1-4673-8391-2.

[12] Dominic Masters and Carlo Luschi. Revisiting Small Batch Training for Deep Neural Networks, 2018.

[13] Diederik P. Kingma and Jimmy Ba. Adam: A Method for Stochastic Optimization, 2014.

[14] Arjpolson Pukrittayakamee, Martin Hagan, Lionel Raff, Satish T. S. Bukkapatnam, and Ranga Komanduri. Practical training framework for fitting a function and its derivatives. *IEEE transactions on neural networks*, 22(6):936–947, 2011.

[15] V. I. Avrutskiy. Enhancing Function Approximation Abilities of Neural Networks by Training Derivatives. *IEEE transactions on neural networks and learning systems*, 2020.

Optimized Feedforward Control of a Multistable Magnetic Actuator

Michael Olbrich[1]*, Pascal Weber[2], Ulrike Wallrabe[2], Christoph Ament[1]
[1] University of Augsburg, Chair of Control Engineering, Germany
[2] University of Freiburg, Department of Microsystems Engineering (IMTEK), Germany
* Correspondence: michael.olbrich@uni-a.de

Abstract

Multistable actuators have a great potential to open up new areas or extend the function of existing applications for microactuators. Their advantage lies in the ability to remain in different resting positions without further energy consumption. A challenge lies in finding suitable inputs to guarantee stable transitions between these positions, especially for actuators with more than two resting positions. This is the case because the area between the resting positions is unstable and may be sensitive to disturbances and input variations. In particular, poorly designed inputs or large disturbances may lead to transitions to undesired positions. In this work, we therefore propose a sampling-based optimization approach to obtain feedforward control inputs, which are robust against such stochastic influences. The inputs generated with our algorithm are applied to a magnetic actuator with three resting positions. We show that the number of successful transitions is increased, while the variance of the outcome is lower compared to manually tuned input signals.

1 Introduction

Magnetic mechanisms are widely used in microsystems technology due to their broad range of applications. Microactuators in particular benefit from this operating principle since forces can be applied without mechanical connections. This has led to a variety of microactuators for applications including micromirrors [1], micropumps [2], and micro positioning [3]. An advantage of using magnetism is the contactless force transmission and the existence of permanent magnets. This enables the replacement of mechanical restoring forces and the design of multistable actuators by exploiting their nonlinearity. The latter allows objects to be kept in different resting positions without energy consumption.

Within the research project ADOPT [4], such a multistable, magnetic actuator for large displacements has been designed and its functionality has been demonstrated [5]. The actuator's objective is to vertically move a permanent magnetic plunger between three predefined resting positions generated by thin steel rings. This is achieved by a current controlled solenoid. Due to the unstable transition between the stable states and large, stochastic disturbances, a challenge lies in the targeted change to a specific resting position. Model-based control approaches can be used to stabilize the motion. Since closed-loop control is not always an option, the investigation of robust open-loop approaches is required.

Different strategies have been investigated in literature with the goal to achieve a predefined final state. In [6], a linear system with polytopic parameter uncertainty is considered. The optimal control signal is found by minimizing the worst case tracking error within the uncertainty space. For nonlinear systems with uncertain system parameters, Plooij et al. [7] obtain feedforward control inputs by minimizing the sensitivity of the final state with respect to the parameters. A method that considers stochastic disturbance influences is presented in [8]. Under the assumption of a Gaussian process, the stochastic control problem is transformed into a deterministic one that only depends on the evolution of the mean and covariance of the process. The respective differential equations are obtained by statistical linearization. The open-loop control problem can be solved using advanced numerical tools.

While these works have in common, that optimization is used to compute suitable inputs, they differ in the way the disturbances and uncertainties are handled. In this work, we propose an alternative, optimization-based, robust feedforward control approach for the magnetic actuator, which combines parameter uncertainty and disturbances. The goal is to increase the probability of successful transitions from one resting position to another.

To this end, we set up a model of the actuator and the combination of time-varying disturbances and model uncertainties. This is used for a sampling-based optimization approach comparable to methods in [9]: First, we generate a number of random disturbance trajectories. Then, model-based simulations estimate the actuator motion for these disturbance scenarios. Finally, the robust input is found by minimizing a cost function for all simulated scenarios. In a hardware experiment, we demonstrate the ability of this approach to significantly improve the robustness of the transition in comparison to manually tuned inputs.

2 Multistable Actuator Setup

To motivate the control approach presented in this work, we briefly introduce the investigated actuator system, which was first published in [5]. The basic concept is to vertically move a magnetic plunger, consisting of a ferrite rod attached to a spherical neodymium magnet with a diameter of 3 mm. The actuator setup is illustrated in Fig. 1 and will be explained in the following.

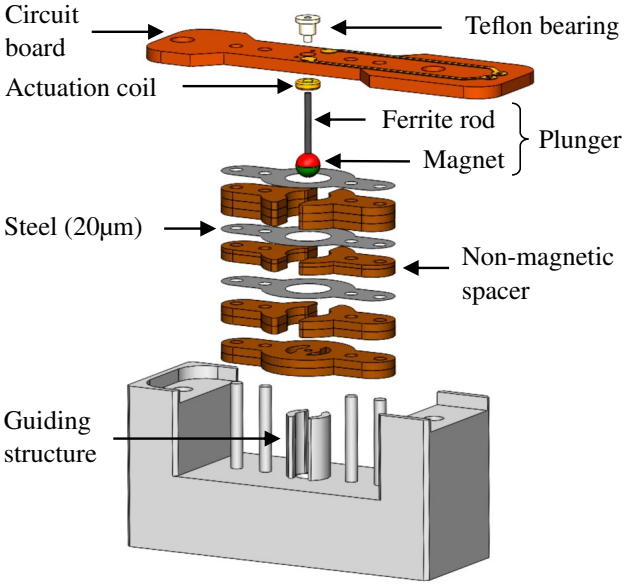

Figure 1 Exploded view of the multistable, magnetic actuator setup [5].

The plunger is restricted to a vertical motion by a guiding structure and tilting is suppressed by guiding the ferrite rod through a teflon bearing located at the top. The plunger is actuated by applying an electrical current to a coil attached around this bearing. The objective is to move the plunger between different resting positions, $z_{\text{low}} = 0\,\text{mm}$, $z_{\text{middle}} \approx 1.7\,\text{mm}$, and $z_{\text{up}} = 3\,\text{mm}$. The middle and upper position are achieved by incorporating thin steel rings around the guiding structure. The lower resting position, where the plunger is in contact with the base structure, results from the balance between gravity and contact force. To adjust the resting positions, stacks of phenolic paper are used as spacers between each steel ring. The vertical displacement is limited to 3 mm by the upper contact with the bearing.
Currently, rectangular current pulses are used to move the plunger. Suitable amplitudes and signal lengths have to be determined experimentally. However, the observed motion can strongly vary, even when identical inputs are applied. This effect is particularly reflected in the motion from the lower to the middle position, as can be seen in Fig. 2.

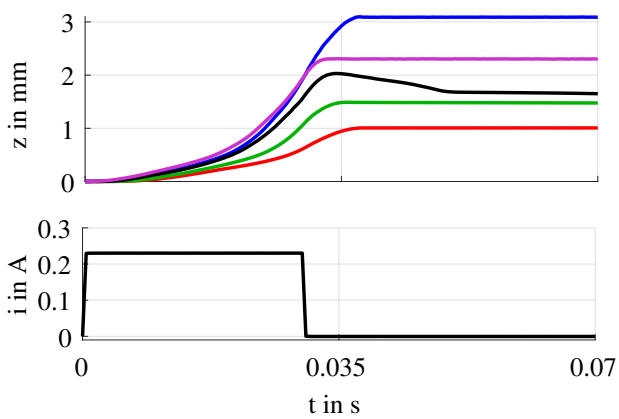

Figure 2 Different motions when applying identical input currents due to high, stochastic friction effects.

The main reason for this stochastic behavior is the variable friction force, e.g., due to small random tilts of the plunger. As a result, the transition to the middle position is challenging and the plunger may get stuck at positions that deviate from the theoretical equilibrium position at around 1.7 mm. To improve the probability of reaching the vicinity of the desired middle position, a robust feedforward control approach will be derived.

3 Actuator and Disturbance Model

A model-based approach will be used to compute suitable inputs that lead to the desired resting position. To this end, we present a physical model of the actuator including a representation of the stochastic, time-varying disturbances. The vertical motion $z(t)$ of the plunger is described by

$$m\ddot{z} = F_{\text{pm}}(z) + i(t) f_{\text{em}}(z) + F_{\text{c}}(z,\dot{z}) + F_{\text{fr}}(\dot{z},t) \qquad (1)$$

with its mass m, the z-dependent permanent magnetic force F_{pm}, electromagnetic force characteristic f_{em}, input current $i(t)$, contact forces F_{c}, and friction force F_{fr}. Note, that we omitted the time and state dependency, where it is clear from the context. For the magnetic forces, we use single layer radial basis function neural networks. The contact and static friction force models correspond to slight adaptations of that in [10]. All parameters and neural networks have been determined in such a way that the measurement data is well represented.
We assume that the dominant part of the disturbances is caused by time-varying friction forces. To model this behavior, we split the friction force F_{fr} into a deterministic characteristic f_{fr} and a multiplicative disturbance input $v(t)$, i.e.,

$$F_{\text{fr}} = f_{\text{fr}}\, v(t)\,. \qquad (2)$$

The disturbance input can then be interpreted as simplified normal force: The larger $v(t)$ is, the higher the friction force will be. While the nominal case corresponds to $v(t) = 1$, the extreme cases are $v(t) = 0$, where no friction occurs, and $v(t) \to \infty$, which corresponds to a complete blockage of the plunger. From this follows that $v(t) \geq 0$.
It is important to mention, that, although this disturbance description is physically motivated in terms of varying friction, it can also represent other disturbances and parameter uncertainties to some extend. A more general approach would be to define the disturbance as additive force. The advantage of our formulation is that a zero velocity also corresponds to a zero disturbance force, which has shown to be useful in our case.
This model enables simulations under any disturbance influence. This will later be necessary for the input optimization. It remains to model the time-varying behavior of $v(t)$. Since the disturbance is assumed to proceed in a continuous way, we used piecewise linear functions with random amplitudes. In this work, it was found sufficiently accurate to use constant time steps T between each interpolation point, resulting in

$$v(t) = \sum_{k=1}^{K} v_k(t)\,, \tag{3}$$
$$v_k(t) = \begin{cases} a_k + \dfrac{a_{k+1} - a_k}{T}(t - kT), & kT \le t \le (k+1)T \\ 0, & \text{otherwise}\,. \end{cases}$$

While we experimentally determined $T = 3\,\text{ms}$ as a good choice, we can identify the stochastic amplitudes a_k using a simulative control approach: We consider $v(t)$ as control input and minimize the deviation between simulation and a reference motion, in this case the measurement data. Here, we used an optimization-based approach called model predictive control. The details of this method are out of scope of this work, but the interested reader is referred, e.g., to [11] for a general idea of this method.

The obtained amplitudes of the disturbance sequences can be analyzed in terms of a probability density function. Since it will later be necessary to draw samples from this random distribution, an approximation as normal distribution is used. The normalized, relative frequency and its approximation are visualized in Fig. 3. Note, that in this case, the critical amplitudes ($v(t) \neq 1$) will mostly be overestimated by the normal distribution. The exact effects need to be investigated further, but in general, this leads to more robust but less efficient behavior.

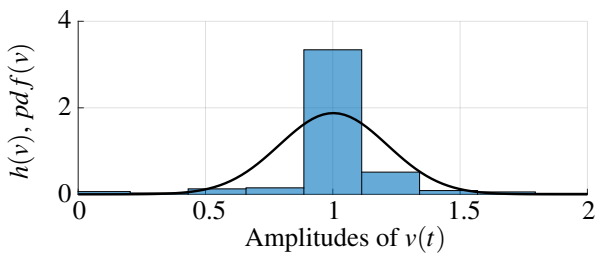

Figure 3 Relative frequency of the disturbance amplitudes of $v(t)$ as histogram $h(v)$ and its probability density function $pdf(v)$ roughly approximated by a normal distribution.

4 Optimal Feedforward Control

The disturbance model and its probabilistic amplitude distribution can now be used to compute robust input sequences, moving the plunger to the desired position. The idea is to generate a number of N artificial disturbance scenarios and find inputs that achieve the desired goal for a maximum number of these simulation scenarios. Such sampling-based strategies are common for stochastic optimal control, and a large number of variations exists [9]. In this work, we aim to minimize a cost function

$$J = \sum_{n=1}^{N} \left(\int_0^{T_\text{f}} w_\text{z}\,(z_n(t) - z_\text{ref})^2 + w_\text{i}\, i(t)^2 \,\text{d}t \right. \tag{4}$$
$$\left. + w_\text{f}\,(z_n(T_\text{f}) - z_\text{ref})^2 \right)$$

over the input current $i(t)$. In contrast to typically applied probabilistic constraints on the minimum success probability, we here simplify the optimization by using an appropriately large terminal state weighting w_f. Here, w_i and w_z are weighting factors for the input current and the deviation from the desired reference position z_ref. The trajectory $z_n(t)$ corresponds to the motion with input current $i(t)$ under the influence of the n-th artificial disturbance scenario with simulation time T_f. The integral in (4) is computed by a rectangular approximation. For the following results, we used $N = 20$ random scenarios and a simulation time of $T_\text{f} = 0.15\,\text{s}$. The cost function allows us to trade-off accuracy against input energy. To demonstrate this effect, we used two different input weighting factors $w_{\text{i},1} = 3 \times 10^{-2}$, $w_{\text{i},2} = 4 \times 10^{-2}$, while $w_\text{z} = 1.5 \times 10^{-4}$, $w_\text{f} = 6.4 \times 10^{-3}$ were kept constant. The input current was parameterized as piecewise constant function with a maximum length of 30 ms. It is given by

$$i(t) = \sum_{k=1}^{K} i_k(t)\,, \tag{5}$$
$$i_k(t) = \begin{cases} c_k, & kT_\text{s} \le t \le (k+1)T_\text{s} \le 30\,\text{ms} \\ 0, & \text{otherwise}\,. \end{cases}$$

with optimization parameters c_k. Each constant piece of the current sequence has a length $T_\text{s} = 5\,\text{ms}$, resulting in six current amplitudes to be optimized. It is important to mention, that inbetween each current amplitude, we use a linear transition of length 1 ms.

5 Experimental Results

The effectiveness of our approach is demonstrated in the experimental setup. As mentioned before, we generated two optimal input sequences by using different penalties w_i for the input currents. Similarly, we manually tuned rectangular input signals with different lengths. The amplitudes were tuned to achieve a high transition success rate. As successful transition, we define a motion whose final position lies within the middle range $1\,\text{mm} \le z \le 2\,\text{mm}$. All inputs were applied 100 times starting at the lower resting position $z = 0\,\text{mm}$. The plunger motion was captured by a profilometer. The results are shown in Fig. 4.

In case of the manually tuned inputs, signals with short duration and increased amplitude (see Fig. 4 a) achieve good results in terms of the success rate. Here, 95% of the trajectories successfully reached the target region. In contrast, a smaller amplitude with longer duration as in Fig. 4 b only needs 89% of the energy, but reduces the success rate to 70%. In both cases, however, the variance of the final position is high and there are significant outliers.

In comparison, the optimized inputs show both, smaller final state variance, and higher probability of success with comparable energy consumption. Weighting the input within the cost function with the smaller factor $w_{\text{i},1}$ achieves a 100%-success rate, see Fig. 4 c. The energy consumption amounts less than 1% more than the rectangular signal a). It is possible reduce the input current by using

a larger input penalty $w_{i,2}$ within the optimization. This results in the motions depicted in Fig. 4 d. The energy consumption is then only 83% of that in the nominal case a), but has a larger success probability, which is 98%.

Although the optimized trajectories show better results, it is worth to mention that, in contrast to the reference case a), the reached position tends to settle in the lower part of the allowed region. A more desirable behavior would be a shift of the final position in the direction of the center. This may be due to unexpectedly large model uncertainties, since some actuator parts have been replaced by similar components between the identification process and the measurements presented in this work. However, this demonstrates the robustness and suitability of this approach for multistable systems under the influence of disturbances and uncertain model parameters.

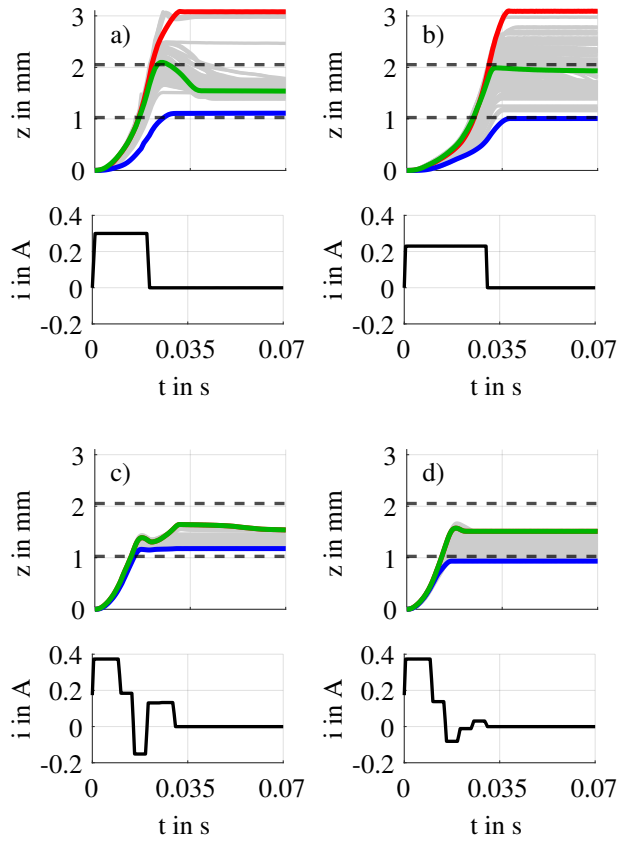

Figure 4 Measured motions corresponding to different manually tuned, rectangular input signals (top) and optimized input currents (bottom). The target area lies between the dashed lines. All outcomes are plotted in gray, the trajectories leading to the largest deviations are marked in red and blue. In green, the motion with the minimum costs according to (4) is visualized.

6 Conclusions and Outlook

In this work, we derived a method that computes optimal feedforward control inputs for multistable actuators with high disturbance influence. Based on artificially generated disturbance scenarios, a sampling-based optimization approach was used to find robust input sequences for the transition between different resting positions. The approach was applied to a magnetic actuator and the results were compared to manually tuned inputs. We could show that our approach has advantages in terms of increased probability of successful transitions and a lower variance in the resulting motion. Although this takes into account parameter uncertainty to some extend, the model quality has an influence on the resulting motion. In future work, an improved parameter identification will therefore be used. Moreover, the feedforward approach will be extended to closed-loop control to improve the transient behavior.

Acknowledgements

This research was funded by the German Research Foundation (DFG) within the priority program SPP2206 “KOMMMA”, project “ADOPT - Adaptive Optics for THz”, grant number 424616052.

7 Literature

[1] S.Y. Kang et al. Design optimization of a 6.4 mm-diameter electromagnetic 2D scanning micromirror. *Opt. Express*, 28(21):31272–31286, 2020.

[2] M.Q.A. Rusli et al. Electromagnetic actuation dual-chamber bidirectional flow micropump. *Sens. Actuators A: Phys.*, 282:17–27, 2018.

[3] Y. Zhang et al. High-integrated micro permanent magnetic linear actuator positioning system. In *3rd ICPEE*, pages 990–1002, 2022.

[4] German Research Foundation (DFG). ADOPT - Adaptive Optics for THz. URL `https://gepris.dfg.de/gepris/projekt/424616052`. [Available online; accessed 03-April-2024].

[5] P.M. Weber and U. Wallrabe. Cantilever Free Magnetic Actuation for Multistable Vertical Displacement. In *MST Kongress*, pages 839–843. VDE Verlag, 2023.

[6] A.A. Khalate et al. A waveform design method for a piezo inkjet printhead based on robust feedforward control. *JMEMS*, 21(6):1365–1374, 2012.

[7] M. Plooij et al. Robust feedforward control of robotic arms with friction model uncertainty. *Robot. Auton. Syst.*, 70:83–91, 2015.

[8] B. Berret and F. Jean. Efficient computation of optimal open-loop controls for stochastic systems. *Automatica*, 115:2–9, 2020.

[9] T. Homem-de Mello and G Bayraksan. Monte carlo sampling-based methods for stochastic optimization. *Surv. Oper. Res. Manag. Sci.*, 19(1):56–85, 2014.

[10] T. Specker et al. Dynamical modeling of constraints with friction in mechanical systems. In *8th MATHMOD*, pages 514–519, 2015.

[11] L. Grüne and J. Pannek. Nonlinear model predictive control. Springer International Publishing, 2017.

Natural Rubber Foil-Based Elastocaloric Cooling

Carina Ludwig[1], Jan Leutner[2], Oswald Prucker[2], Jürgen Rühe[2], and Manfred Kohl[1*]
[1]Institute of Microstructure Technology (IMT), Karlsruhe Institute of Technology (KIT), Postfach 3640, 76021 Karlsruhe, Germany
[2]Department of Microsystems Engineering (IMTEK), University of Freiburg, Georges-Köhler-Allee 103, 79110 Freiburg, Germany

Abstract

We present the design and characterization of solid-state elastocaloric cooling devices based on a natural rubber (NR) foil. Two different loading mechanisms are explored using either two linear actuators or a bistable actuation mechanism using a rotating lever arm, which allows for reduced loading forces by a factor of three. The thicknesses of the investigated NR foil refrigerants are 290 and 650 µm in initial undeformed state while their lateral size is 9 x 26.5 mm^2. Owing to the small thickness, heat transfer is accomplished by solid-solid contact between the NR foil and planar heat sink and source elements. The optimal operation frequency depends on the NR foil thickness increasing from 140 to 540 mHz for a thickness of 650 and 290 µm, respectively. The maximum temperature span ΔT_{Device} is 4.1 K while the coefficient of performance COP_{Device} reaches values up to 4.7. A maximum cooling power of 144 mW is achieved for bistable actuation, which is enhanced by 17% compared to linear actuation. The specific cooling power increases with decreasing foil thickness reaching 1.2 Wg^{-1} at 290 µm for bistable actuation.

1 Introduction

Nowadays, around 17 % of the global electricity consumption is caused by cooling applications, which predominantly comprise vapor-compression based devices with a high global warming potential (GWP) [1]. Elastocaloric (eC) cooling has recently been identified as a promising alternative to environmentally harmful vapor compression and energy inefficient thermoelectrics [2]. Superelastic shape memory alloys (SMAs) show an extraordinary eC effect due to their first order phase transformation [3]–[5]. For miniature scale cooling, like temperature control of lab-on-chips and local cooling of electronics, refrigerants of films and foils are of special interest due to their large surface to volume ratio. Recently, SMA film-based eC devices with a specific cooling power of 19 Wg^{-1} and temperature span of 27.3 K have been reported [6,7]. However, major obstacles in utilizing shape memory alloys as refrigerants are the large stress range of 600-800 MPa that is necessary for cycling as well as material availability and costs. Elastomers like NR may offer a promising cost-efficient and environmentally friendly alternative [8]. Moreover, low loading forces combined with an excellent fatigue resistance under dynamic conditions as well as a large adiabatic temperature change of around 20 K associated with NR films are of special interest for cooing applications.

To date, a few studies have been conducted on the development of rubber-based eC devices [9–11]. An inflated NR membrane has been presented showing a bistable snap-through motion, while heat transfer is enabled by mechanical contact [10]. In this case, a cooling power of 0.87 W and maximum specific cooling power of 20.9 Wg^{-1} have been reported, while a low coefficient of performance of about 1 and a limited cyclic lifetime <10^3 were achieved. NR tubes have been investigated using water as a heat transfer liquid [11]. By implementing the concept of regeneration, a maximum temperature change of 9 K, a cooling power of 1.5 W and a specific cooling power of 0.14 Wg^{-1} have been demonstrated [9]. However, major challenges remain including issues of efficiency and cyclic lifetime. In the following, we introduce alternative device concepts aiming at miniature-scale eC cooling by NR foil refrigerants.

2 Material Characteristics and Device Design

The thicknesses of the investigated NR foil refrigerants are 290 and 650 µm in initial undeformed state while their lateral size is 9 x 26.5 mm^2. The temperature change due to the eC effect is monitored by infrared thermography. A typical tensile test of a NR foil specimen is shown in Fig. 1 revealing a high temperature change of +9 K upon loading to a maximum strain of 700 % and -10 K upon unloading under adiabatic conditions at a strain-rate of 9.3 s^{-1}.

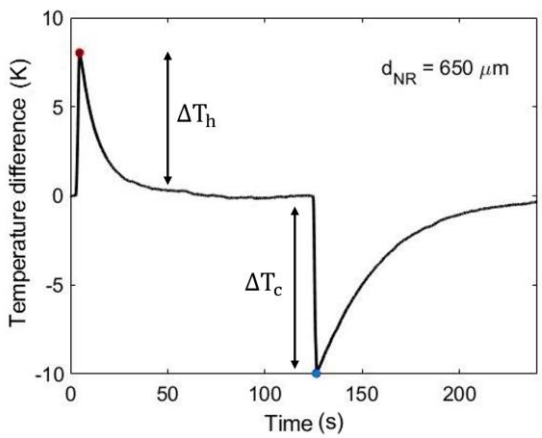

Figure 1: Temperature difference versus time of a NR foil of 650 µm thickness (d_{NR}) after loading (ΔT_h) by 700% and subsequent unloading (ΔT_c).

The influence of different maximum strains, pre-strains and strain-rates on the temperature output are evaluated. Most of the temperature change occurs within the strain range of 300 to 700 %, which is therefore chosen as the strain regime for device operation. The required strain-rate to obtain quasi-adiabatic conditions strongly depends on the NR foil thickness. For example, a foil of 290 µm thickness requires a strain-rate of 9.3 s^{-1}, while 4.7 s^{-1} is sufficient for a foil thickness of 650 µm. Further information on the material characterization can be found in [12].

The eC cooling cycle based on the use of two linear actuators is illustrated in Fig. 2. The operation principle consists of four steps. At first, the NR foil is mechanically loaded and heat is generated due to strain-induced crystallization and entropy elasticity (I). Afterwards the heat is absorbed by a heat sink (II). Subsequently, quasi-adiabatic unloading causes a reverse transformation (III). In the final step, cooling of the source is achieved (IV). The device architecture comprises parallel sink/source elements. Two linear actuators are applied to independently control the tensile loading and the mechanical contact with the sink and source elements for heat transfer.

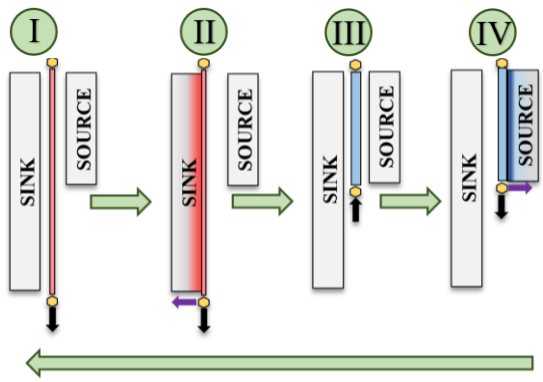

Figure 2: Schematic of the eC cooling cycle based on the use of two linear actuators for loading (black arrows) and for enabling mechanical contact for sold-solid heat transfer (purple arrows).

The eC cooling cycle based on bistable actuation is illustrated in Fig. 3. In this case, sink and source elements are arranged perpendicular with respect to each other. Only one actuator is required to mechanically load the NR foil and to enable mechanical contact to the sink and source elements via a rotating lever arm. The strain is cycled in the range of 300 to 700 %. Fig. 4 depicts a section of the heat source module including a copper plate that is in contact with the NR foil in the pre-elongated state. The assembly of the sink and source includes 3D-printed flexible spring-like structures to counteract misalignment with the NR foil. Typical force versus angle characteristics of the bistable actuation mechanism are shown in Fig. 5. Only the tangential force component (green) needs to be provided by the actuator, while the normal force component in the direction of the lever arm (orange) is picked-up by the bearing. On the other hand, the displacement is 1.6 times larger and,

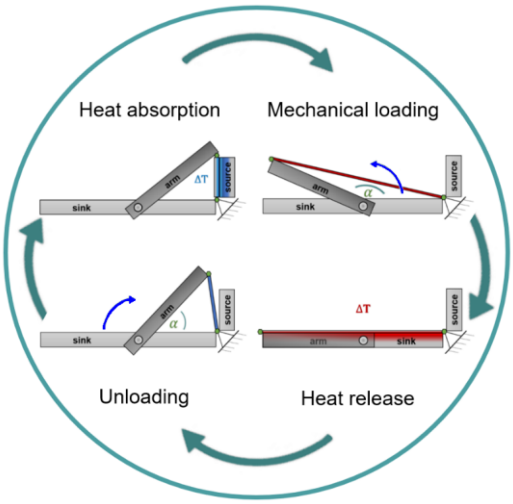

Figure 3: Schematic of the eC cooling cycle based on bistable actuation using a rotating lever arm. Blue arrows indicate the loading and unloading directions of the bistable system.

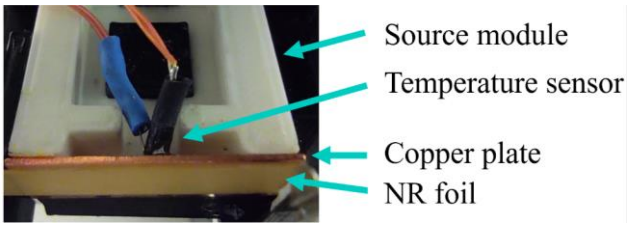

Figure 4: Heat source module including a copper plate and temperature sensor on the back side. The copper plate is in mechanical contact with the NR foil to enable solid-solid heat transfer.

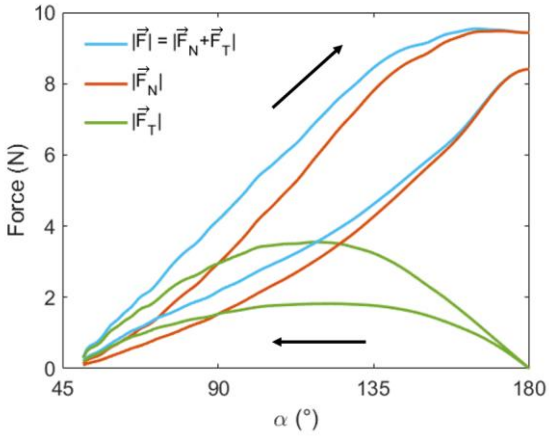

Figure 5: Force - angle characteristics of the bistable device for a NR foil of 650 µm thickness. The directions of loading and unloading are indicated by arrows.

Legend: $|\overrightarrow{F_N}|$ - absolute value of the force along the lever arm (orange), $|\overrightarrow{F_T}|$ – absolute value of the tangential loading force (green) with respect to the loading trajectory. Only the tangential force needs to be applied for actuation.

thus, the same work is required as for the linear actuation mechanism. For the of 650 µm thick NR foil, the maximum required force for loading is reduced by a factor of 2.8.

3 Device characterization

The time durations of loading, unloading and the holding time at solid-solid contact to enable heat transfer to heat sink or source are illustrated in Fig. 6. The strain is cycled in the range of 300 to 700 % at a strain-rate of 9.3 s^{-1}, thus, the loading and unloading times are about 430 ms. The resulting actuation frequency is given by the holding time and an additional delay time in the case of linear actuation.

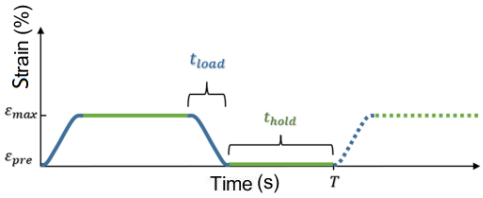

Figure 6: The frequency is defined by the time durations of loading and unloading t_{load}, and the holding times t_{hold} to enable heat transfer to sink and source. Legend: ε_{pre}– pre-strain, ε_{max}– maximum strain.

The temperature evolution of the heat sink and heat source of the bistable device µm is shown in Fig. 7 for operation frequencies between 110 and 540 mHz. In this case, the thickness of the NR foil refrigerant is 650 µm. The strain rate is 9.3 s^{-1}, at which the loading and unloading times are 430 ms. The thermal mass of the heat sink it about two times larger compared to the heat source and, therefore, it exhibits a lower maximum sink temperature.

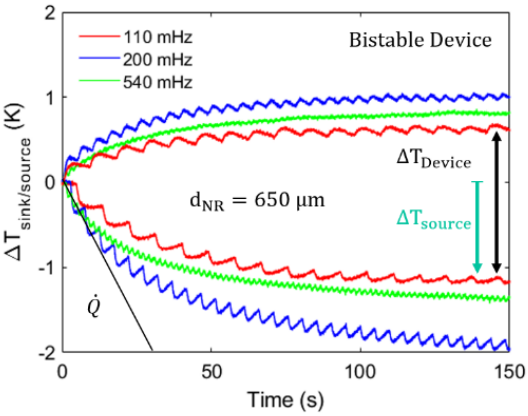

Figure 7: The temperature evolution of the heat sink and the heat source with respect to room temperature of the eC bistable cooling device with a NR foil thickness d_{NR} of 650 µm. The operation frequency is adjusted between 110 and 540 mHz, while the strain-rate is 9.3 s^{-1}. The slope of the black line is used to evaluate the cooling power $\dot{Q}$.

In the initial stage of load cycling, the largest temperature changes occur and, thus, the temperature difference between sink and source increases most. The device cooling power is evaluated from the initial slope of the cooling curve (black line). Parasitic heat flow causes the observed temperature oscillations in each cycle. The maximum device temperature span ΔT_{Device} is determined after reaching stationary equilibrium conditions. ΔT_{Device} reaches its maximum of 3 K at the frequency of about 200 mHz, indicating an optimal balance between heat transfer and heat losses. Fig. 8 summarizes the results on the temperature span of the heat source ΔT_{source} versus frequency. For the eC cooling device with linear actuation and a thickness of NR refrigerant of 650 µm, optimal conditions are reached at a frequency of about 150 mHz revealing a source temperature span ΔT_{souce} of 2.1 K. The corresponding coefficient of performance COP_{Device} is determined to be 4.7. At lower frequencies, parasitic heat flow becomes dominant, while at higher frequencies heat transfer becomes incomplete. The optimal frequency shifts towards a higher value of 300 mHz for decreasing foil thickness to 290 µm due to faster heat transfer. The temperature span ΔT_{source} of the bistable eC cooling device is less temperature-dependent. It exhibits a broad maximum at 200 mHz for the 650 µm thick NR refrigerant, while maximum values are above 300 mHz in the investigated frequency range at 290 µm thickness.

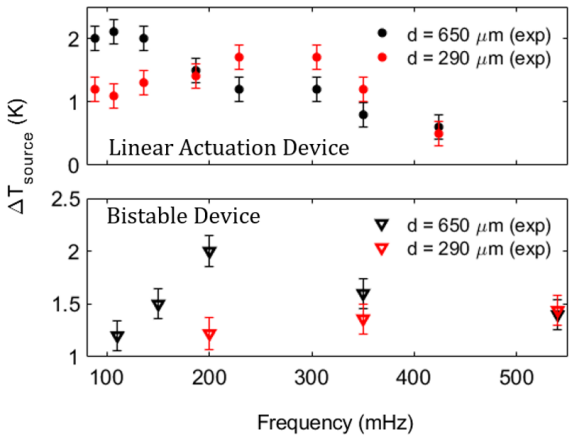

Figure 8: The temperature span of the heat source ΔT_{source} versus frequency of the investigated eC cooling devices for NR foil refrigerants of 650 and 290 µm thicknesses. The error bars are determined by the measurement accuracy of the temperature sensors.

The corresponding results on cooling power versus frequency are given in Fig. 9. This performance correlates with the frequency-dependent variation of ΔT_{source} in Fig.8. For a decreasing foil thickness of 290 µm, the optimum frequency shifts to a higher frequency, which indicates that heat transfer occurs more rapidly allowing for more cooling cycles in a given time period. These results are complemented by lumped-element model (LEM) simulations as described in [12]. For the investigated single stage device, we obtain consistent results on the maximum cooling power and maximum ΔT_{Device}. For the foil thickness of 650 µm and a frequency of 136 mHz an optimum cooling power of 123 mW is reached. The corresponding specific cooling power is 954 mWg^{-1}, which refers to the mass of the NR foil. For the 290 µm thick foil, a maximum cooling power of 78 mW is attained at 230 mHz. Moreover, the specific cooling power increases with decreasing foil thickness reaching 1.1 Wg^{-1}. The corresponding coefficient of

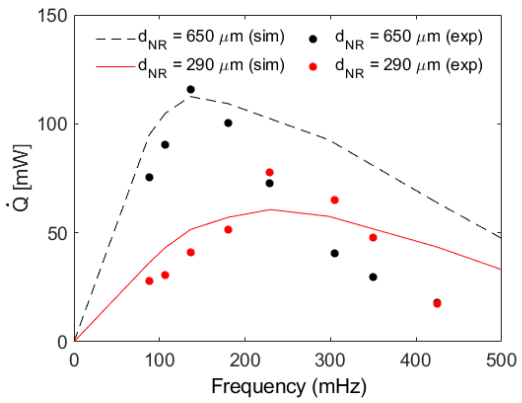

Figure 9: Cooling power, $\dot{Q}$ versus frequency of the eC cooling device with linear actuation for the foil thicknesses of 290 and 650 µm. Measurements (dots) are compared with LEM simulation results (lines).

performance COP_{Device} is determined to be 4.0. For bistable actuation, a maximum cooling power of 144 mW is achieved at 650 µm foil thickness, which is enhanced by 17% compared to linear actuation. The specific cooling power increases with decreasing foil thickness reaching 1.2 Wg^{-1} at 290 µm, while COP_{Device} decreases by 75% caused by the additional mechanical power input at the maximum frequency of 540 mHz.

4 CONCLUSION

In this paper, we have presented two different kinds of solid-state single stage elastocaloric cooling devices based on NR foils. The thicknesses of the investigated NR foil refrigerants are 290 and 650 µm in initial undeformed state, which enables efficient heat transfer by solid-solid contact and avoids the use of a heat transfer fluid. Two different loading mechanisms are explored using either two linear actuators or a bistable actuation mechanism. The bistable mechanism requires only one actuator and the maximum required loading force is significantly reduced. The performance, quantified by the cooling power and the COP_{Device} reveals a significant dependence on foil thickness. The optimal operation frequency increases from 140 mHz / 200 mHz to 300 mHz / 350 mHz for decreasing thickness from 650 µm to 290 µm in case of linear / bistable actuation. The specific cooling power increases with decreasing foil thickness reaching 1.2 Wg^{-1} at 290 µm for bistable actuation.
Further reduction of foil thickness will lead to enhanced heat transfer and, thus, will further improve the specific cooling power. Moreover, the addition of conductive fillers is expected to enhance the cooling performance. The device temperature span can be improved by cascading as has been demonstrated for SMA film-based eC cooling. Depending on the cooling application, upscaling of the eC device through parallelization will be needed to meet the cooling power needs of specific applications.

Acknowledgements

This work was funded by the German Science Foundation (DFG).

5 Literature

[1] U.S. Energy Information Administration, „International Energy Outlook 2019 with projections to 2050“, Sep. 2019. Zugegriffen: 29. Dezember 2023. [Online]. Verfügbar unter: https://www.eia.gov/outlooks/ieo/pdf/ieo2019.pdf

[2] „Energy Savings Potential and RD&D Opportunities for Non-Vapor-Compression HVAC Technologies“, EERE Publication and Product Library, Washington, D.C. (United States), DOE/EE-1021, März 2014. doi: 10.2172/1220817.

[3] E. A. Pieczyska, S. P. Gadaj, W. K. Nowacki, und H. Tobushi, „Phase-Transformation Fronts Evolution for Stress- and Strain-Controlled Tension Tests in TiNi Shape Memory Alloy“, *Exp. Mech.*, Bd. 46, Nr. 4, S. 531–542, Aug. 2006, doi: 10.1007/s11340-006-8351-y.

[4] H. Ossmer, F. Lambrecht, M. Gültig, C. Chluba, E. Quandt, und M. Kohl, „Evolution of temperature profiles in TiNi films for elastocaloric cooling“, *Acta Mater.*, Bd. 81, S. 9–20, Dez. 2014, doi: 10.1016/j.actamat.2014.08.006.

[5] D. Cong *u. a.*, „Colossal Elastocaloric Effect in Ferroelastic Ni-Mn-Ti Alloys“, *Phys. Rev. Lett.*, Bd. 122, Nr. 25, S. 255703, Juni 2019, doi: 10.1103/PhysRevLett.122.255703.

[6] F. Bruederlin, L. Bumke, C. Chluba, H. Ossmer, E. Quandt, und M. Kohl, „Elastocaloric Cooling on the Miniature Scale: A Review on Materials and Device Engineering“, *Energy Technol.*, Bd. 6, Nr. 8, S. 1588–1604, 2018, doi: 10.1002/ente.201800137.

[7] F. Brüderlin, „Advanced Elastocaloric Cooling Devices Based on Shape Memory Alloy Films“, 2022. doi: 10.5445/KSP/1000125495.

[8] Z. Xie, G. Sebald, und D. Guyomar, „Elastocaloric effect dependence on pre-elongation in natural rubber“, *Appl. Phys. Lett.*, Bd. 107, Nr. 8, S. 081905, Aug. 2015, doi: 10.1063/1.4929395.

[9] G. Sebald, A. Komiya, J. Jay, G. Coativy, und L. Lebrun, „Regenerative cooling using elastocaloric rubber: Analytical model and experiments“, *J. Appl. Phys.*, Bd. 127, Nr. 9, S. 094903, März 2020, doi: 10.1063/1.5132361.

[10] F. Greibich *u. a.*, „Elastocaloric heat pump with specific cooling power of 20.9 W g–1 exploiting snap-through instability and strain-induced crystallization“, *Nat. Energy*, Bd. 6, Nr. 3, Art. Nr. 3, März 2021, doi: 10.1038/s41560-020-00770-w.

[11] G. Sebald, G. Lombardi, G. Coativy, J. Jay, L. Lebrun, und A. Komiya, „High-performance polymer-based regenerative elastocaloric cooler“, *Appl. Therm. Eng.*, Bd. 223, S. 120016, März 2023, doi: 10.1016/j.applthermaleng.2023.120016.

[12] C. Ludwig, J. Leutner, O. Prucker, J. Rühe, und M. Kohl, „Miniature-scale elastocaloric cooling by rubber-based foils“, *J. Phys. Energy.*, Vol. 6, Num.1, Nov 2023, doi: 10.1088/2515-7655/ad0cff

A Dielectric Elastomer based Miniaturized Soft Planar Microactuator

Simon Holzer*, Bhawnath Tiwari*, Stefania Konstantinidi, Yoan Civet and Yves Perriard,

Integrated Actuators Laboratory (LAI), Ecole polytechnique fédérale de Lausanne (EPFL), Rue de la Maladière 71b, Neuchâtel CH-2000, Switzerland

E-Mail: simon.holzer@epfl.ch

*Authors contributed equally

Abstract

Precise and robust positioning features are vital need in modern-day industries, particularly in the context of industrial automation within the micro/meso domain. In this work, we present a novel miniaturized planar microactuator with a total size of 40 mm in diameter, allowing maximum planar stroke of 220 µm in 100 ms. The actuator exhibits fine positioning with an accuracy of 4.5 µm. This paper discusses the system design, fabrication and experimental validation of the device performance.

1 Introduction

Automation is playing a crucial role in this fast-changing world, where industries are undergoing significant transformations to enhance their production efficiency [1]. One key element in such automated production processes is the actuation system. In different tasks such as micro-assembly [2], the precision and the stroke play significant role in defining overall quality of the product [3]. Therefore, the choice of the actuation system becomes more demanding. For a given application, where higher order of flexibility is needed, soft actuators may do a better job compared to their rigid counterparts [4]. There are varieties of soft actuators available to address the need of fine positioning, but the planar soft actuators capable of micro positioning (resolution < 5 µm) over a long range (> 200 µm) with low weight (4.25 g) and high speed (> 10 Hz) is lacking. Dielectric elastomer actuators (DEAs) are a promising alternative which have the capability to fulfill the aforementioned requirements due to their high strains, fast actuation and high energy density [5]. Depending on their design, DEAs can enable uniaxial, biaxial or equiaxial strain patterns. These strain patterns can be realized by different strategies. One approach is based on a convenient pre-stretch, which optimizes besides the strain pattern also the maximum strain [6], the second strategy employs additional components to enhance displacements in specific directions like out-of-plane displacement by biasing mechanisms [7] and a third method is based on the use of fibers to reinforce DEAs and to impede displacements only along certain directions [8].

In this paper, the design conception, fabrication and characterization of a microactuator based on a DEA are given. Therefore, the design and functionality are introduced followed by the device fabrication and packaging. After the explanation about the experimental setup, the results are given. At the end, the results are discussed, related works are compared with the proposed design and the paper is concluded with an outlook for future possibilities.

2 System Design and Conception

2.1 System Design

Figure 1 provides a schematic illustration of the investigated design and its working principle. The device consists of four electrodes positioned on each side of the dielectric elastomer (two powered and two unpowered electrodes). The electrodes are quarter rings with a distance of 2 mm between each electrode and have an unstretched radial length of 5 mm with an outer diameter of 20 mm (unstretched). The electrodes are based on carbon black composite, have a thickness of around 20 µm and are oriented perpendicular to each other. Actuation of electrode 1 will lead to the displacement along x-axis and the actuation of electrode 2 to the displacement along y-axis. Symmetrical electrodes (unpowered) are added to ensure uniformity in mass and stress distribution and to decouple the deformation along the two axes during actuation. The chosen design shows enhanced displacement (improvement of 20 – 30 %) and decreased coupling between the two-axis compared to a design with squared electrodes with dimensions of 5 x 6 mm. The dielectric membrane has a thickness of 50 µm and is equibiaxial pre-stretched (1.5 times) to enhance the DEA performance and increase its maximum deformation capacity [9]. The thickness of 50 µm is chosen because of the lower actuation voltages which allows more precise electrode designs without electrical breakdown. A rigid platform measuring 10 x 10 mm is mounted at the center of the stretchable membrane. Feeding the DEA with the appropriate supply voltage allows precise control over the platform's position within plane.

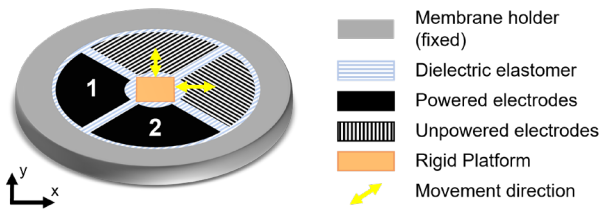

Figure 1 Schematic illustration of the device design.

2.2 Functionality and Model

The operational physics of DEAs are based on electrostatics. Applying a high voltage across the electrodes induces an electric field between them, resulting in a Maxwell stress. This reduces the thickness between the actuated electrodes, increasing the surface of the electrode and leading to displacement of the rigid platform. The behaviour of the DEA can be explained using electromechanical models. In general, a DEA can be defined as a deformable capacitor. The Maxwell stress σ_M induced by the electric field E is described by equation (1).

$$\sigma_M = -\varepsilon_0 \varepsilon_r E^2 \qquad (1)$$

where ε_0 is the vacuum permittivity and ε_r the relative permittivity of the dielectric material. The stress-strain behaviour of the elastomer is non-linear and viscoelastic.

3 Device Fabrication and Packaging

The fabrication of the device includes the stencil printing of the powered carbon electrodes, the printing of unpowered carbon electrodes for mechanical equilibrium and the attachment of the rigid plate to the membrane surface. The dielectric elastomer (DE) used as the membrane is Elastosil 2030 from Wacker Chemie AG, with a thickness of 50 µm (± 5 %) and a dielectric constant of 2.8. The electrodes used for the DEAs are carbon composite electrodes [9]. Next, a thin Elastosil layer of around 20 µm is applied to the surface to cover the electrodes and insulate them form the environment. Then, the process is repeated for the other side. After the electrodes are applied, an equibiaxial pre-stretch of 1.5 is applied to the DEA and a round acrylic frame with an inner diameter of 30 mm holds the pre-stretch in place. Subsequently, a rigid acrylic plate is mounted in the middle of the DE membrane. The electrodes are connected to the power supply with copper tape and copper wires.

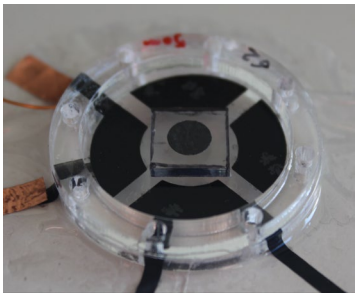

Figure 2 Fabricated microactuator.

4 Experimental Setup

The experimental setup consists of a computer, a data acquisition device (DAQ), two high voltage sources and a camera. The actuation signal is generated with the help of NI LabVIEW and is then transmitted to the DAQ (NI DAQPad-6259 Pinout). The DAQ passes the signal in the form of a voltage signal (0 – 10 V) to the respective high voltage sources. The two high voltage sources (Stanford Research Systems Inc. Model PS 375 and Keithley Model 248) are used to actuate the DEAs. To perform so, they multiply the received input signal by a factor 2000 for the x-axis (Stanford Research Systems Inc. Model PS 375) and factor 500 for the y-axis (Keithley Model 248). The high voltage sources have a limited charging and discharging time which are strongly influencing the DEA behaviour in these measurements. The camera (Canon EOS 650D) is used to determine the displacement of the center of the rigid platform. A video of the actuation is recorded and with which the displacement of the platform is determined using image processing (MATLAB R2022b). Thus, the displacement of the center of the rigid platform can be computed.

5 Methodology and Results

The device design and the signal attribution should be in the way that a repeatable and decoupled actuation can be achieved. The device design comprises of necessary symmetry to decouple the two actuation axes when subject to electrical stimuli.

Figure 3 shows the displacements along the two axes. Figure 3a presents the displacements along the x- and y-axis generated by the actuation of electrode 1. Figure 3b shows the corresponding displacements for electrode 2. For the actuation with 500 V, a minimal deformation of 4.5 µm is achieved. Further increasing of the actuation voltage leads to higher displacements. This is in accordance with equation (1) which describes the quadratic relation between the actuation voltage and Maxwell stress. The displacement for an actuation voltage of 3000 V is in the range of about 220 µm and 210 µm respectively for x- and y-axis.

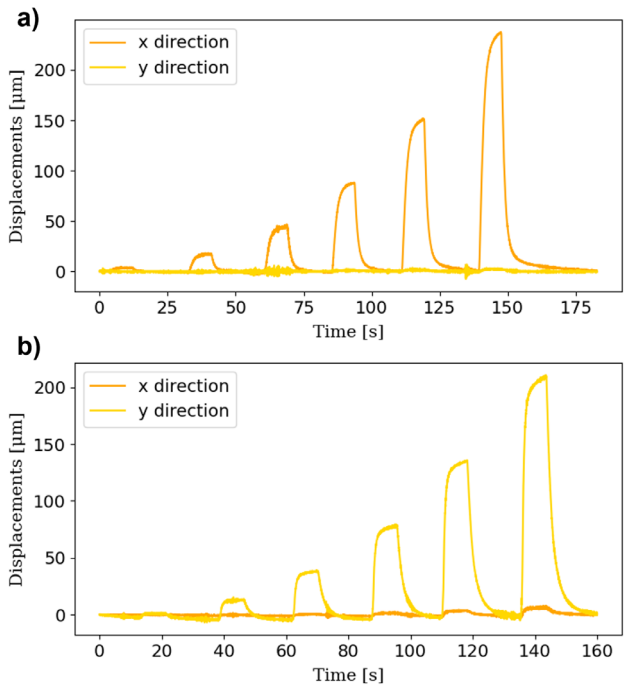

Figure 3 a) Actuation along x-axis (electrode 1 powered) and b) y-axis (electrode 2 powered) with a stepwise input voltage from 500 V to 3 kV.

In **Figure 4**, both electrodes are actuated simultaneously with a stepwise input voltage of 500 V to 2.5 kV represented by different colours. Figure 4 is presenting the maximum displacement for a given voltage in x- and y-direction. Because the charging and discharging time are different between the two high voltage power supplies, a hysteresis is emerging between the charging and discharging trajectory.

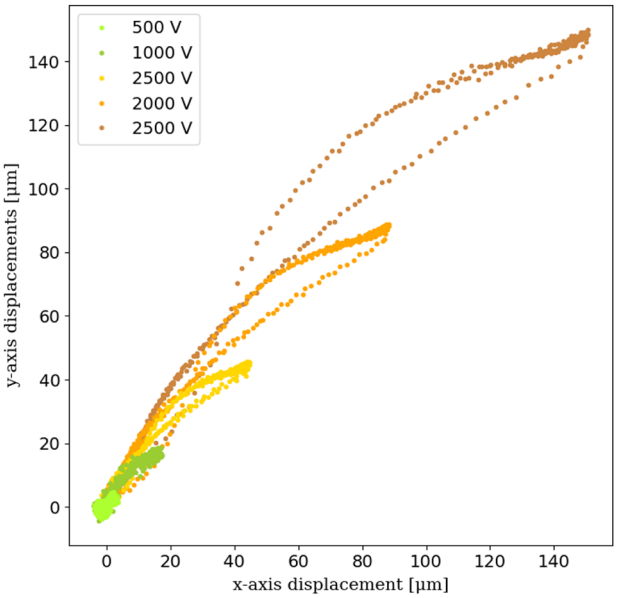

Figure 4 Planar displacement achieved by simultaneous actuation of both electrodes (1 and 2) with stepwise voltage of 500 V to 2.5 kV.

6 Discussion

A first interesting parameter of the device is the full displacement of the actuator. To determine it, the electrodes are actuated separately up to 3 kV. The electric field at these voltages is equivalent to 60 V/µm which is below the breakdown field of the dielectric material (80 – 100 V/µm) and thus, the DEA is actuated without reaching its electrical limitations. The determined full displacement for an actuation of 3 kV along the x-axis is 220 µm and along the y-axis 210 µm, respectively. The small displacement differences between the two axes of around 5 % can be attributed to various reasons. First, it is possible that the pre-stretch is not completely homogeneous along both axes. Second, the device may not be concentrically aligned in the frame during pre-stretch. Third, the DEA are actuated with different high voltage sources, which may lack in their accuracies. Fourth, the alignment and the shape of the electrodes is influenced by misalignments during the electrode's fabrication process. The full displacement can be doubled by exchanging the unpowered electrodes with powered ones (-200 to 200 µm). However, the hardware required for actuation and control must be adapted so that four electrodes can perform displacements at the same time.

A further parameter needed to characterize the device is the interaction between the actuation of the electrode along one axis and the achieved displacement along the perpendicular axis. From the measurements presented in Figure 3, the displacement along the y-axis during actuation along the x-axis is 1 % of the total displacement (220 µm in x-axis and 2 µm in y-axis) and 2.7 % for the opposite actuation (210 µm in y-axis and 6 µm in x-axis). These values show that the displacement along one axis depends mainly on the actuation of the associate electrode and the displacement along the perpendicular axis can be neglected. The origin of the displacement on the perpendicular axis can be explained by similar reason as the difference in the maximum displacement by the electrodes. These are possible inhomogeneous pre-stretch, non-concentrical alignment of the DEA in the frame, differences between the two high voltage sources and inexactness during fabrication of the electrodes.

In Figure 4, a hysteresis between the charging and discharging cycle is visible. The hysteresis occurs due to the different charging and discharging behaviour of the two sources used for the measurements. In future, to decrease the difference between the full displacement, to reduce the inhomogeneous displacement along the perpendicular axis compared to the actuation axis and to avoid the hysteresis, improvements on the fabrication as well as the use of similar high voltage sources can be better controlled.

The displacement step of the microactuator is about 4.5 µm for an actuation voltage of 500 V. This is the minimum detectable displacement step of the proposed microactuator and the corresponding experimental setup. In theory, the minimum displacement at every displacement of a DEA can be nearly zero as the actuation can be adjusted continuous. In reality, there are different parameters which complexify a continuous displacement. First, the actuation is limited by the voltage output generated by the high voltage source. Second, the accuracy of the positioning is limited by image capturing and processing. The limitation with the bigger influence in our case is the accuracy of the image capturing and processing. Thus, we can improve the minimum detectable displacement step by adapting the image processing algorithm or by changing the measurement system. Alternative systems can consist of a camera with improved resolution or a laser system. A third challenge are the visco-elastic material properties of the DE. These lead to viscous behaviour which need to be integrated into a control strategy.

The time to reach a certain position is at the moment limited by the charging and discharging time of the high voltage sources. The charging time to reach the voltage output is about 2 s. The sources also do not contain an active discharging, which is also limiting the discharging time at 15 s for the proposed design. An improved charging/discharging time can be achieved by changing the current high voltage sources by a more adapted high voltage sources capable to generate faster switching like the Trek 10/10b HS. Thus, normally displacements in the time of faster than 100 ms are possible.

7 Related Work

Different devices for micro-assembly and positioning are existing on the market. These devices often rely on DC or stepper motors in combination with screws [10] or piezoe-

lectric actuators [11] [12]. In literature, an ionic electroactive polymer based micro-stage for displacements on the z-axis is presented in Mutlu et al. [13].
In comparison with conventional technologies, the DEA based microactuator introduced in this work has different advantageous and challenges. The DEA based microactuator enables a quasi-continuous positioning and different sensing methods like optical readout or self-sensing. Furthermore, by applying suitable fabrication methods, the miniaturization of DEAs is possible. In addition, DEA based microactuators allow a high and fast displacement combined with an accurate positioning. Drawbacks of DEA based micropositioners are the high driving voltage and the viscoelastic behaviour of the DE which introduces non-linearities into the system.
In comparison with the micro-stage introduced in Mutlu et al. [13], the proposed device differs in its functionality and the required high voltages. Our device is used for positioning of a platform on the xy-plane and is based on a DEA (up to 3 kV) compared to the micro-stage in [13] which is used for displacement in z-direction and is based on an ionic electroactive polymer (0.25 – 1.00 V).

8 Conclusion

In this study, a novel miniaturised fast planar microactuator is presented, which can precisely cover planar actuation in a workspace of 220 x 210 µm with a single axis resolution of 4.5 µm. The platform offers a suitable alternative for soft actuators used in industry for precise positioning. As a future work, different control strategies for precise trajectory generation will be tested especially in the context of micro-assembly.

Acknowledgement

This project is graciously supported by the Werner Siemens-Stiftung.

References

[1] H. Lasi, P. Fettke , H.-G. Kemper, T. Feld and M. Hoffmann, “Industry 4.0,” *Business & Information Systems Engineering,* pp. 239-242, 2014.

[2] B. Tiwari, C. Clévy and P. Lutz, “High-Precision Gluing Tasks Based on Thick Films of Glue and a Microrobotics Approach,” *IEEE Robotics and Automation Letters,* vol. 4, no. 4, pp. 4370 - 4377, 2019.

[3] J. Cecil , M. B. Bharathi Rai Kumar, Y. Lu and V. Basallali, “A review of micro-devices assembly techniques and technology,” *The International Journal of Advanced Manufacturing Technology,* vol. 83, pp. 1569 - 1581, 2015.

[4] M. Li, A. Pal, A. Aghankhani, A. Pena-Francesch and M. Sitti, “Soft actuators for real-world applications,” *Nature Review Materials,* pp. 235-249, 2022.

[5] E. Hajiesmaili and D. R. Clarke, “Dielectric elastomer actuators,” *Journal of Applied Physics,* p. 151102, 2021.

[6] A. Poulin, C. S. Demir, S. Rosset, T. V. Petrova and H. Shea, “Dielectric elastomer actuator for mechanical loading of 2D cell cultures,” *Lab on a Chip,* pp. 3788 - 3794, 2016.

[7] P. Loew , G. Rizzello and S. Seelecke, “A novel biasing mechanism for circular out-of-plane dielectric actuators based on permanent magnets,” *Mechatronics,* pp. 48 - 57, 2018.

[8] S. Konstantinidi, T. Martinez, B. Tandon, Y. Civet and Y. Perriard, “Uni-axial reinforced dielectric elastomer actuators with embedded 3D printed fibers,” *Smart Materials and Structures,* p. 125011, 2023.

[9] S. Holzer, F. Hartmann, F. Öz, T. Martinez, Y. Civet and Y. Perriard, “Study of Potential Factors and their Interaction in Dielectric Elastomer based Cell Stretcher,” in *2023 26th International Conference on Electrical Machines and Systems (ICEMS)*, Zhuhai, China, 2023.

[10] Physik Instrumente (PI) GmbH & Co. KG, “Physikinstrumente.de,” 23 04 2024. [Online]. Available: https://www.physikinstrumente.de/de/produkte/lineartische/tische-mit-dc-buerstenlosen-dc-bldc-schrittmotoren/m-110-m-111-m-112-kompakter-lineartisch-412418433.

[11] Xeryon, “xeryon.com,” 23 04 2024. [Online]. Available: https://xeryon.com/products/mini-linear-actuators/?utm_source=adwords&utm_campaign=Actuators&utm_medium=ppc&utm_term=micro%20linear%20actuator&gad_source=1.

[12] B. Tiwari, M. Billot, C. Clévy, J. Agnus, E. Piat and P. Lutz, “A Two-Axis Piezoresisitive Force Sensing Tool for Microgripping,” *MDPI sensors,* p. 6059, 2021.

[13] R. Mutlu, G. Alici, X. Xiang and W. Li, “An active-compliant micro-stage based on EAP artificial muscles,” in *IEEE / ASME International Conference on Advanced Intelligent Mechatronics (AIM)*, 2014.

Investigation of the influence of fiber reinforcement onto electro-active strain and force in uniaxial DEAs

Stefania Konstantinidi[a,*], Markus Koenigsdorff[b,*], Simon Holzer[a], Johannes Mersch[c], Thomas Martinez[a], Yoan Civet[a], Gerald Gerlach[b], Yves Perriard[a]

[a]Integrated Actuators Laboratory (LAI), Ecole polytechnique fédérale de Lausanne (EPFL), Neuchâtel, Switzerland
[b]Institute of Solid-State Electronics, Faculty of Electrical and Computer Engineering, Dresden University of Technology (TUD), Dresden, Germany
[c]Institute of Measurement Technology, Faculty of Mechatronics, Johannes Kepler University Linz, Linz, Austria
[*] These authors contributed equally to this work.

Abstract

Dielectric elastomer actuators (DEAs) are electro-active polymers that show high potential for soft robotic applications. This study focuses on the influence of fiber reinforcement onto the electro-active force. By fabricating actuators with various aspect ratios, width-dependent effects are investigated. Results indicate that fiber-reinforced DEAs exhibit higher initial active forces, with aspect ratios influencing force profiles. Comparisons with isotropic DEAs show increased forces for fiber-reinforced DEAs.

1 Introduction

Dielectric elastomer actuators (DEAs¥) are electroactive materials consisting of a thin elastomeric membrane sandwiched between compliant electrodes. When an electric field is applied, it induces an electrostatic pressure between the electrodes, leading to mechanical deformation. DEAs are known for their versatility and are employed in various applications, ranging from soft robotics to haptic feedback systems [1, 2]. DEAs exhibit many attractive properties, for instance, a high strain and strain rate, self-sensing capabilities, and a powerless halting state [3]. The strains achievable with these actuators, however, are highly dependent on the geometry and external loading conditions [4, 5]. To favor large uniaxial deformations, DEAs can be constrained in the other direction. This can be achieved by reinforcing the actuators with unidirectional fibers. Even though applying fiber reinforcement to DEAs introduces mechanical anisotropy and leads to an overall stiffening of the actuator, it has been shown to improve the uniaxial strain under dead loads [6]. Hence, the electro-active force of the DEA increased by the introduction of fibers.

This improvement in performance can be attributed to the mechanical anisotropy introduced by the fibers, which leads to a favorable deformation state of the dielectric membrane as illustrated in Figure 1.

As ideal fibers will prevent any deformation in fiber direction, the width of the actuator stays constant when strained, which in turn will lead to an increased reduction in thickness. Therefore, the resulting true electric field is

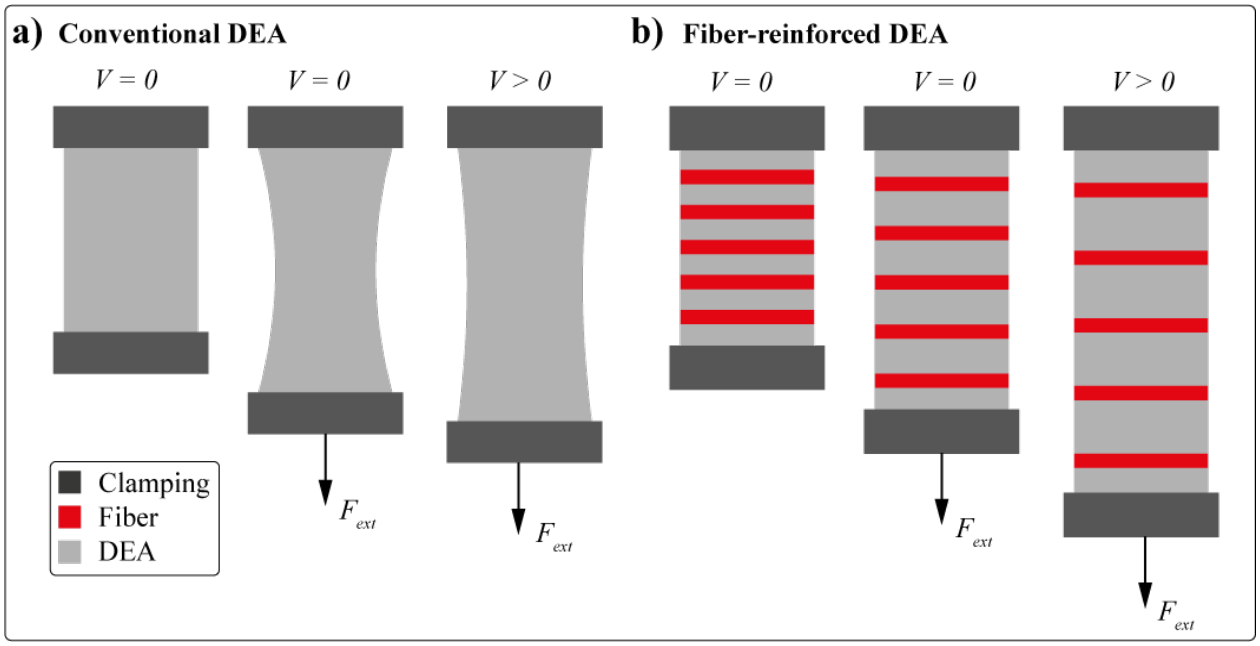

Figure 1 Uniaxial DEAs: a) Conventional DEA without fiber reinforcement and b) Fiber-reinforced DEA experiencing improved electro-active strain.

higher in fiber-reinforced DEAs than in conventional DEAs in the strained state [7].
Another effect influencing the performance of the DEAs is that the fibers prevent the deformation of the DE below them also perpendicular to the fiber direction. Therefore, if a higher percentage of the dielectric material is covered by fibers, the overall actuator stiffness significantly increases, because the material between the fibers undergoes correspondingly increased strains. Hence, each segment of actuator between two fibers can be viewed to be in a stretch state of pure shear [8]. The optimal coverage ratio to achieve maximal strain for specific actuator structures has been investigated in previous works [6].
The objective of this work is to investigate the influence of fiber reinforcement onto the electro-active force. Additionally, the aspect ratio, meaning the ratio between length and width of the actuators is varied, to evaluate width-dependent effects of the fiber reinforcement on the electro-active force.

2 Methods

2.1 Manufacturing

The actuators are composed of silicone films (Elastosil 2030 from Wacker Chemie AG, München, Germany) and of carbon electrodes stencil-printed onto them. The fabrication process involves stencil-printing a carbon electrode onto 100 µm silicone films, curing it at 80°C for 4 hours, and applying carbon-silicone glue on it while protecting a corner for electrical contact. A 20 µm silicone layer is then deposited as encapsulation and the actuators are cured at 80°C for 2 hours to bond with the first electrode. The final actuators consist of stacks of 2 active layers of 100 µm each.
PET fibers, laser-cut from PET sheets and primed for enhanced adhesion to silicone, are incorporated into the actuators. A PET frame maintains fiber alignment and support the fiber placement during fabrication. Silicone glue (LSR 4305 from Elkem, Oslo, Norway) is applied onto the fabricated actuators before depositing the fibers. Fiber spacing of 1 mm is considered, and the fibers cover the whole length of the actuators. The fabrication process is conducted in a grey room to prevent contamination. Finally, the fibers and glue cure for 2 hours at 80°C.

2.2 Electro-mechanical characterization

The electro-mechanical characterization assesses the impact of fiber reinforcement instabilities on the actuators' mechanical and electrical performance. Actuators of in plane aspect ratios (1:2, 1:1, 2:1), with and without fiber reinforcement, undergo testing. Actuators are clamped opposite to the fibers, and electrical connections are established with copper cables. A high voltage power supply (Trek 20/20C-HS Series, Advanced Energy, Fort Collins, Colorado, USA) is operated using MATLAB/Simulink and the data is acquired through a NIDAQ.
Force measurements are conducted using a tensile testing machine (IMADA force recorder, Japan) with 10 cycles of stretching from 1.0 to 1.25 in the direction opposite to the fibers at a speed of 100 mm/min. Each cyclic test involves applying a voltage of 0, 1, 2, 3, 4 or 5 kV, totaling 60 cycles per actuator.

3 Results

Figure 2 shows the measured force-displacement curves for a fiber-reinforced actuator at 0 and 5 kV respectively. Applying a voltage to the actuator leads to an extension

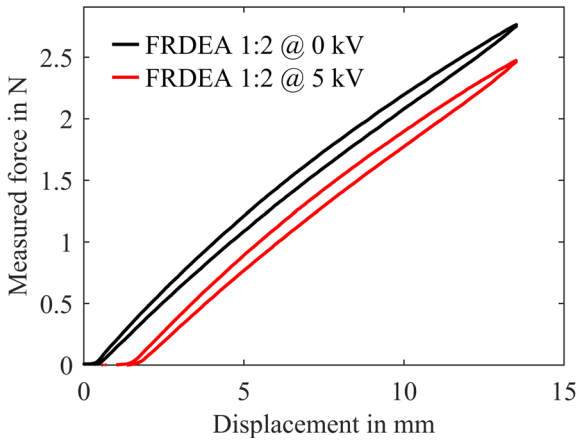

Figure 2 Measured force-displacement curves of a fiber-reinforced DEA at 0 V and 5 kV voltage.

perpendicular to the fiber-direction, which in turn will lead to lower measured forces for constant displacements. The applied displacement during the tensile test equates to a maximal strain of 25 %. Figure **3** shows the results of the same measurement regimen but for an actuator with an no fiber-reinforcement. Compared to the measurements pre-

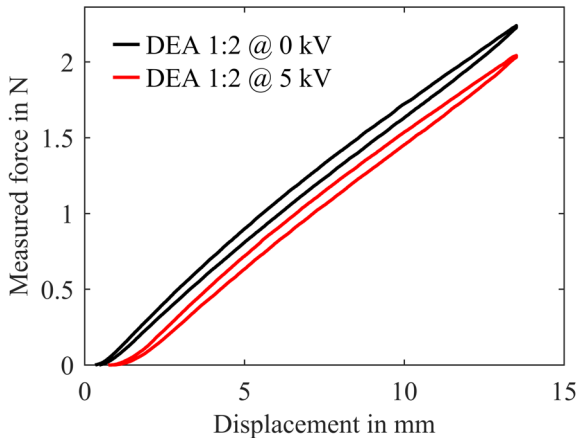

Figure 3 Measured force-displacement curves of a conventional DEA at 0 V and 5 kV voltage.

sented in Figure **3**, a lower maximum recorded force can be noticed, which is explained by the stiffening effect of the fiber-reinforcement. To investigate the influence of the fiber-reinforcement onto the electro-active force, the difference between the recorded force at 0 and at 5 kV is calculated in dependence of the applied displacement. Figure **2** illustrates the electro-active force of 3 aspect ratio

variations of FRDEAs. Interestingly, the initial active force is the highest for the longest FRDEA (aspect ratio of 1:2), while it's the lowest for the shortest version (aspect ratio

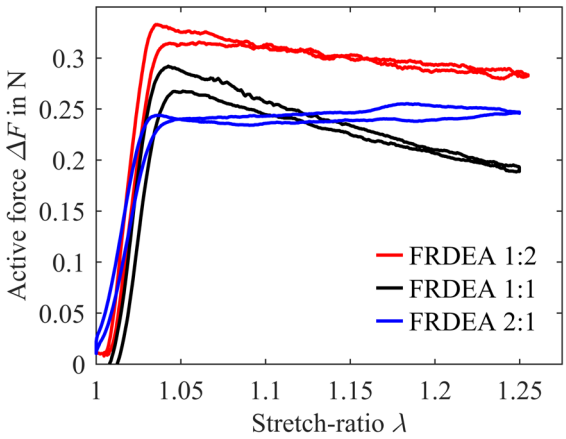

Figure 2 Calculated active force for variations of aspect ratios in FRDEAs at 5 kV activation voltage.

2:1). With more applied stretch however, both the 1:2 and 1:1 variant decrease in active force, while the force of the 2:1 actuator even slightly increases. Intuitively, one would suspect that all DEAs would behave similarly, as the bonded fibers prevent the width of the DEA from changing. The measured difference in electro-active behavior, however, could be caused by weaknesses in the fiber-silicone bond. As a shorter actuator results in the fibers experiencing more support against out-of-plane buckling, this could lead to a more stable active-force profile.

In Figure 3 the results of the repeated measurements of actuators without fiber reinforcement are shown. Due to manufacturing errors, the actuator with the aspect ratio of 1:1 suffered an early electrical breakdown; hence it is excluded in the figure. Comparing the force of the isotropic DEAs

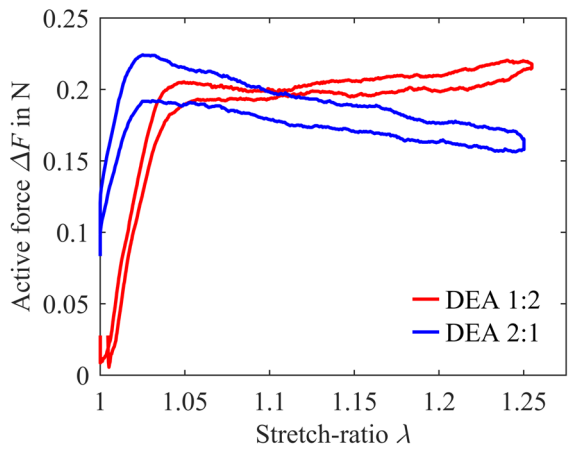

Figure 3 Calculated active force for two variations of aspect ratios in DEAs at 5 kV activation voltage.

with the results of the FRDEAs, the isotropic DEAs show a slightly lower initial active force. This can be attributed to the combined effect of the fibers fixing the width of the film and the increased strain due to the fiber surface coverage. This will lead to a lower thickness of the DE between the fibers than in the isotropic sample, hence increasing the true electric field and therefore the induced Maxwell stress. Interestingly the trend of longer actuators leading to a negative slope in the active force does not persist for isotropic samples. These results do not correspond to the expectation, that a shorter actuator should provide higher electro-active forces and a better coupling of this force to the strain because it is closer to a stretch-state of pure shear.

4 Conclusions

Within this work DEAs with varying aspect-ratios were manufactured and the influence of the fiber-reinforcement onto the electro-active force was investigated. It was shown that actuators with fiber-reinforcement provide higher electro-active forces than isotropic actuators. The influence of the aspect-ratio onto the actuators' performance still is not fully clarified. To gain a better understanding, more samples and larger variations of the aspect ratio are needed. Additionally, DIC measurements would be beneficial to investigate the influence of the fibers on the strain state of the DE.

5 Acknowledgements

The authors gratefully acknowledge the funding by the Werner Siemens-Stiftung and the Deutsche Forschungsgemeinschaft (DFG, German Research Foundation), research project 380321452/GRK2430 (Interactive Fiber Rubber Composites). Johannes Mersch is the recipient of an APART-MINT Fellowship from the Austrian Academy of Sciences at the Institute of Measurement Technology of the Johannes Kepler University Linz.

6 Literature

[1] H. Zhao *et al.,* "A Wearable Soft Haptic Communicator Based on Dielectric Elastomer Actuators," *Soft robotics*, vol. 7, no. 4, pp. 451–461, 2020, doi: 10.1089/soro.2019.0113.

[2] E.-F. M. Henke, K. E. Wilson, and I. A. Anderson, "Entirely soft dielectric elastomer robots," in *Electroactive Polymer Actuators and Devices (EAPAD) 2017*, Portland, Oregon, United States, 2017, 101631N.

[3] I. A. Anderson, T. A. Gisby, T. G. McKay, B. M. O'Brien, and E. P. Calius, "Multi-functional dielectric elastomer artificial muscles for soft and smart machines," *Journal of Applied Physics*, vol. 112, no. 4, 2012, doi: 10.1063/1.4740023.

[4] M. Koenigsdorff, H. Liebscher, P. Osipov, J. Mersch, and G. Gerlach, "Influence of Active-to-Passive Ratio on the Deformation in Circular Dielectric Elastomer Actuators," *Micromachines*, vol. 15, no. 1, 2024, doi: 10.3390/mi15010125.

[5] T. Lu *et al.,* "Dielectric elastomer actuators under equal-biaxial forces, uniaxial forces, and uniaxial constraint of stiff fibers," *Soft Matter*, vol. 8, no. 22, p. 6167, 2012, doi: 10.1039/c2sm25692d.

[6] S. Konstantinidi, T. Martinez, B. Tandon, Y. Civet, and Y. Perriard, "Uni-axial reinforced dielectric elastomer actuators with embedded 3D printed fibers," *Smart Mater. Struct.*, 2023, doi: 10.1088/1361-665X/ad0447.

[7] M. Koenigsdorff, J. Mersch, S. Pfeil, and G. Gerlach, "Anisotropic Carbon Fibre Electrodes for Dielectric Elastomer Actuators," in *ACTUATOR 2022; International Conference and Exhibition on New Actuator Systems and Applications*, 2022, pp. 1–4.

[8] T. Lu, Z. Shi, Q. Shi, and T. J. Wang, "Bioinspired bicipital muscle with fiber-constrained dielectric elastomer actuator," *Extreme Mechanics Letters*, vol. 6, pp. 75–81, 2016, doi: 10.1016/j.eml.2015.12.008.

Tubular Dielectric Elastomer Transducer with Hydrostatic Force Transmission

Tim Krüger[a] and Jürgen Maas[a]
[a]Mechatronic Systems Lab, Technische Universität Berlin, Hardenbergstr. 36, 10623 Berlin, Germany

Abstract

In this contribution a design for an actuator based on multilayer dielectric elastomer (DE) laminates is presented, which combines a DE-tube made of a rolled DE multilayer laminate with an oil based hydrostatic force transmission to control force-stroke characteristic. Based on a fundamental design concept, an exemplary actuator design is proposed and realized. An FE-simulation validates the functional principle of transmitting force and stroke via hydrostatic pressure and estimates resulting force-stroke characteristic of the actuator. Moreover, a realized prototype experimentally confirms the actuator's functionality, whereby a maximum stroke of $\Delta z \approx 0.5\,\mathrm{mm}$ at an electric field strength $E > 60\,\mathrm{V\,\mu m^{-1}}$ was measured. The present work validates the proposed actuator concept, but also indicates some remaining shortcomings, which have to be improved in the future.

1 Introduction

Dielectric elastomers (DE) can be used to create space-saving, lightweight and energy-efficient actuators for various applications [1, 2]. Among others, a possible actuator design is based on rolled, respectively tubular DEs. Hoffstadt et al. investigated a polymer core roll-actuator, considering various design parameters on the force-stretch behavior and presented a realized prototype of the polymer core roll-actuator [3]. Although an elastic core can be advantageous to generate pre-stretch, it can also reduce actuator performance or limit actuation bandwidth due to additional stiffening. In this respect, core-less roll actuators are considered advantageous. Carpi and Rossi have modeled and experimentally validated a cylindrical actuator that achieves an axial elongation of 4.5 % at an electric field strength of $100\,\mathrm{V\,\mu m^{-1}}$ [4]. An analytical model was deduced to adequately describe the deformation of a thin, free-standing DE tube. Based on this work, Cameron et al. investigated miniaturized tubular linear actuators using coextrusion method to enable an inexpensive production [5]. Thin tubes were made from extruded polyurethane and conductive carbon grease. In contrast to full material DE actuators, hollow DE cylinders can start to buckle when exposed to critical pressure or voltage, which was intensively investigated by Su et al. [6]. Sarban et al. reviewed the fabrication, characterization and active vibration isolation performance of a core-free rolled tubular DE actuator. Using corrugated silver electrodes, push actuators with an initial DE lengths of 60 mm achieved strokes over 1 mm for an electric voltage in the range of 2.5 kV [7]. Zhao et al. designed and fabricated a core-less roll actuator made from a multilayer DE laminate which was equipped with flat caps glued to the ends [8]. Actuators with an active height of 12 mm generated a maximum axial displacement of about 0.95 mm and a blocking force of around 0.45 N. In order to transmit tensile force and reduce the detrimental influence of rigid mechanical connections on the actuation performance, the concept of hydrostatic force transmission has been applied to the mechanical interface of multilayer DE stack-transducers [9].

In this work, the hydrostatic force transmission is combined with a multilayer DE-tube in order to transform axial and tangential deformation into a linear displacement and to control the actuator's force-stroke characteristic. First, a fundamental actuator concept combining a DE-tube with hydraulic fluid is proposed. Second, an exemplary actuator design is presented and investigated using an FE-simulation. Finally, an experiment is carried out on a realized prototype to measure voltage dependent stroke and compare it with simulation results.

2 Actuator concept and design

A schematic of the actuator design is illustrated in Figure 1. The tubular DE, a rigid base, cap, and the compliant sealing form a closed system containing a fluid of volume V_0 inside. In unactuated state (a), fluid pressure corresponds to ambient pressure p_0. Essential design parameters are inner radius of the the DE r_i, outer radius r_a and the height h_DE of the active DE material. The piston, where F_act acts, is connected to the external load. The piston radius r_p can be varied to determine the actuator's force-displacement characteristic. For better clarity the DE, depicted in Figure 1, contains one outer and one inner electrode, which are electrically connected via cap and base. To reduce actuation voltage v_p, multilayer DE stripes with small dielectric thicknesses t_p are rolled to form a tubular DE. The volume of the actuator's inner fluid $V_0 = V_\mathrm{p} + V_\mathrm{DE}$ is composed of the piston volume V_p and the DE-tube volume V_DE.

When a voltage v_p is applied, an electric field strength E induces Maxwell pressure σ_el to the DE-tube, causing stretch $\lambda_\mathrm{r} < 1$ in r-direction. Due to the assumed incompressibility of the material, stretch in tangential direction $\lambda_\phi > 1$ and in

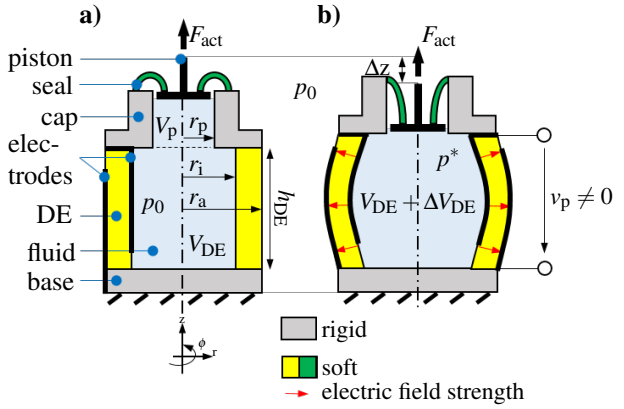

Figure 1 Schematic of the DE-tube actutor supported by hydrostatic force transmission illustrating a) the unactuated and b) the actuated state.

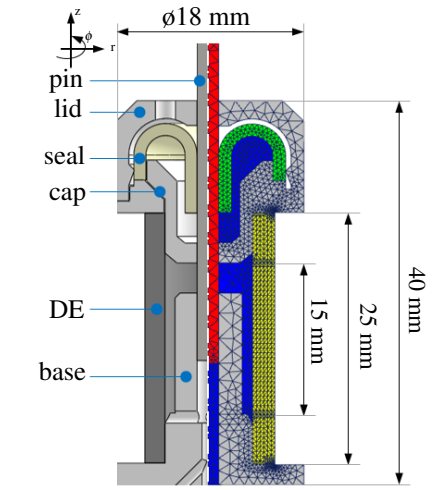

Figure 2 Combined depiction of actuator design and corresponding FE-model for numeric investigation using COMSOL Multiphysics®.

axial direction $\lambda_z > 1$ result, which increases V_{DE} by ΔV_{DE}. Assuming $V_0 = \text{const.}$ and a round piston geometry, for the corresponding piston stroke relative to the cap it holds

$$|\Delta z| \approx \frac{\Delta V_{DE}}{\pi r_p^2}. \tag{1}$$

The change in inner fluid pressure $\mathrm{d}p^*$ is related to the change in volume $\mathrm{d}V$ by

$$\kappa = -\frac{\mathrm{d}V}{V\,\mathrm{d}p^*}, \tag{2}$$

where κ represents the compressibility of a fluid. Integrating and simplifying eq. (2), p^* can be approximated by

$$p^* - p_0 \approx -\frac{\Delta V}{\kappa \cdot V_0}. \tag{3}$$

Pressure p^* acts on the piston surface, and yields the actuation force

$$F_{act} = \pi r_p^2 \cdot (p^* - p_0). \tag{4}$$

2.1 Constructive design and FE modeling

In Figure 2 the sectional view of the actuator design (left) and the corresponding FE-model (right) is illustrated. A cylindrical steel pin, which can be connected to the mechanical system to be actuated, is merged with the elastomer sealing and can freely move in z-direction. It is linearly guided through the lid, cap and base. The lid protects the dome-shaped seal and contains air holes for pressure equalization. Through-holes are provided in cap, and base, so fluid can freely move inside the actuator. The liquid is injected through an opening in the base, which is then sealed. For the DE-tube, a 200 mm long and 25 mm wide DE-stripe is manufactured using thin film-based sheet-to-sheet manufacturing process [10]. The laminated stripe comprises $N = 6$ layers of Wacker ELASTOSIL® 2030 [16] film with polymer thickness $t_p = 50\,\mu\text{m}$ and $N = 6$ electrode layers. The electrode layer thickness is $t_e \approx 8\,\mu\text{m}$ [13]. As depicted on the right half of Figure 2, the active electrode area height is 15 mm. A five millimeter wide edge on each side is provided for electrical contacting and mechanical connection. To calculate the number of turns, an archimedean spiral [14] is assumed. By specifying $r_i = 4.25\,\text{mm}$, a number of $M \approx 6$ turns and an outer radius $r_a \approx 6.3\,\text{mm}$ is calculated. The actuator design is implemented as an FE-model in COMSOL Multiphysics®. Electrostatic physics are applied to the yellow colored DE-tube region, calculating Maxwell pressure σ_{el} and forwarding it to solid mechanics domain. All blue areas are specified as deforming mesh, representing the incompressible fluid. The inner pressure is calculated from volume change ΔV of the mesh using eq. (3) and applied to the inner fluid boundaries, where $\kappa \approx 1.2$ [15] is used to represent the compressibility of an exemplary hydraulic oil. Gray and red colored areas are modeled as rigid domains, where cap, lid, and pin are not constrained in z-direction. The red pin is connected to the green elastomer seal. First, unconstrained displacement $\Delta z_{max}(v_p)$ is determined, increasing v_p up to $v_{max} = 3\,\text{kV}$. In a second simulation step, $v_{max} \in [3, 2.5, 2]$ kV is applied and F_{act} is specified to determine force-stroke characteristic.

2.2 FEM results

Selected FE results are illustrated in Figure 3. The actual inner pressure p^* is dedicated to the fluid domains, represented by the moving mesh. The actual electric field strength E is evaluated in the active DE area. The colors of all rigid domains represent the free deflection Δz.

The simulation results confirm the expected actuator behavior. By increasing v_p, the piston is pulled further into the actuator, reaching a maximum stroke $\Delta z_{max} \approx -1.5\,\text{mm}$ for $v_p = 3\,\text{kV}$. Although inner pressure drops when increasing v_p, no significant buckling of the dome-shaped seal appears. However, at $v_p = 3\,\text{kV}$, the DE-tube slightly tend to start buckling, which would not have an effect on the actuation due to the hydrostatic coupling. Besides the DE-tube expansion in radial direction, a small negative deflection of

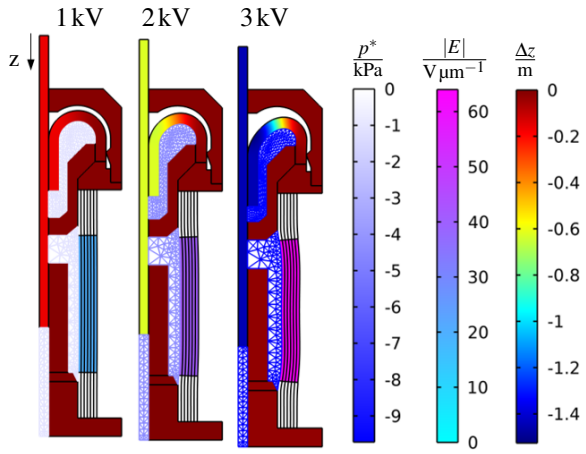

Figure 3 FE-simulation results of free stroke Δz for three different actuation voltages v_p.

the base part can be stated.

In Figure 4 the simulated force-stroke characteristic for three different initial electric field strengths E_0 are plotted. For $E_0 = v_{p,max}/t_p = 60\,\mathrm{V\,\mu m^{-1}}$ a blocking force $F_B \approx 2.3\,\mathrm{N}$ is calculated, which decreases continuously with the stroke Δz. As expected, a reduction in E_0 reduces both the maximum blocking force and the free stroke to lower values.

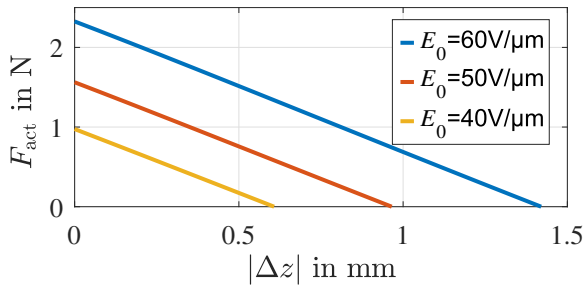

Figure 4 Simulated force-stroke characteristics of the DE actuator for three constant electric field strengths E_0.

3 Experimental investigation

Figure 5 provides an overview of the sample preparation. First, multilayer DE stripes were manufactured (a) to create DE-tubes (b). Rigid components were realized using *Ultimaker S5* PLA-printer and a mold was created to cast the yellow seal element using RTV-2 silicone rubber (c). Moreover, thin copper rings were added to cap and base to enhance electric contacting. Finally, three assembled samples (d) were filled with an hydraulic oil through a hole in the actuator base, which was sealed afterwards. For the experimental investigation, the samples were fixed in a sample holder in order to measure the stroke of the pin with a *Micro-Epsilon optoNCDT-ILD2220-20* laser triangulation sensor positioned above the sample while applying a trapezoidal voltage profile with maximum voltage $v_{p,max} = 3\,\mathrm{kV}$ (e).

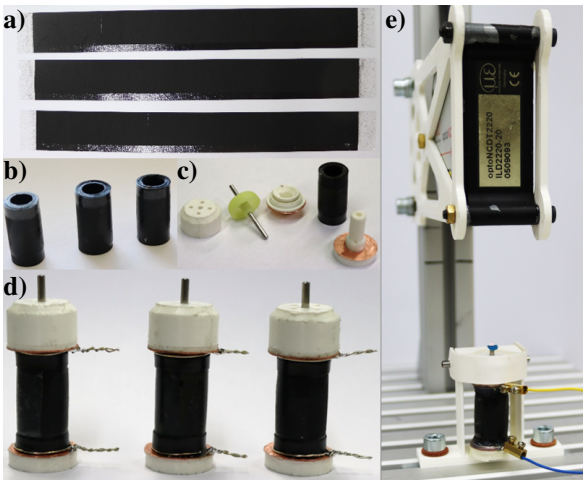

Figure 5 Actuator manufacturing and measuring setup. a) Multilayer DE-stripes, b) rolled DE-tubes, c) actuator components, d) tube-actuators and e) clamped sample and laser triangulation sensor for stroke measurement.

3.1 Experimental results

Due to electrical defects and inadequacies in sample preparation, only one prepared sample was suitable for obtaining reproducible measurement data. In Figure 6 applied voltage and measured stroke are plotted against measuring time. The data reflect the quadratic dependence of DE deformation on the electric voltage. Both, the slightly delayed rise and the remained stroke, after voltage has been deactivated, indicate hysteresis effects in the system, e.g. due to friction losses. Moreover, creep during hold time can be observed, which may be caused by the electrode material. In-depth investigations, considering creeping and visco-elastic material behavior, were carried out by Mertens et al.[12].

In Figure 7 simulated and measured free stroke are plotted against actuation voltage. A maximum stroke of $\Delta z_{exp,max} \approx 0.5\,\mathrm{mm}$ at $v_p = 3\,\mathrm{kV}$ was measured, which is approximately one third of the stroke predicted by FE results. This could indicate, that inadequacies of electrically contacting the six electrode layers have caused passive electrodes, which on the one hand do not contribute to force generation and on the other hand represent additional passive material reducing maximum actuation stroke

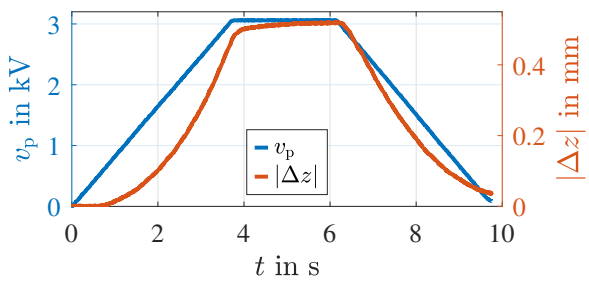

Figure 6 Experimental results of voltage and stroke against measuring time.

[11]. In addition, a thin film of RTV-2 silicone was applied to the stripe during the production of the DE-tubes to bond it, which was not taken into account in the simulation. When voltage v_p is reduced after holding $v_{p,max}$ for about three seconds, Δz_{exp} stays almost constant until voltage has fallen below $v_p \approx 2.8\,kV$. Stick-slip between the cylindrical pin and the guide elements made of PLA (base, cap, lid) could be the reason for this.

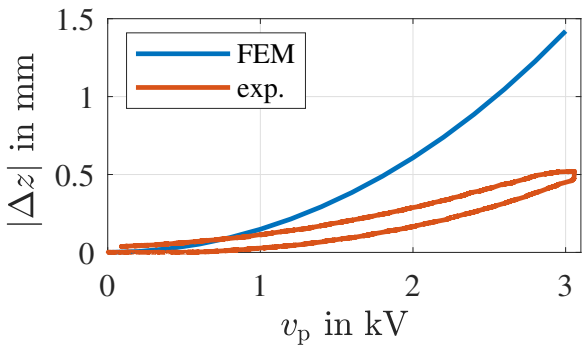

Figure 7 Simulated and measured free actuation stroke $|\Delta z|$ against actuation voltage v_p.

4 Conclusion

In this work an alternative concept for a DE-based actuator that combines DE-tubes with hydrostatic force transmission and piston-supported force-stroke scaling was presented. One exemplary actuator design was carried out and an FE simulation was performed proving functionality and estimating maximum stroke and force. One successfully realized actuator prototype also experimentally proved the functionality of the actuator concept and additionally also demonstrated the ability of manufactured DE multilayer laminates to stand actual field strengths above $60\,V\,\mu m^{-1}$. However, the measured stroke $z_{exp,max} \approx 0.5\,mm$ was only about one third of the maximum simulated stroke $z_{sim,max} \approx 1.5\,mm$, which is expected to be caused by inadequacies of sample production. Furthermore, actuation force was not experimentally investigated at this point of time, but needs to be conducted in the future. Moreover, a more detailed analytic modeling can be useful for designing actuators with specifically adjusted force-stroke characteristics. However, considering hystrostatic force transmission in DE actuator design can offer a great advantageous, as it can be efficiently taken advantage of the DE volume change on the one hand and on the other hand an independent mechanism to adjust force and stroke can be provided.

5 Literature

[1] O'Halloran, A. et al.: "A review on dielectric elastomer actuators, technology, applications, and challenges". J. Appl. Phys. 1 October 2008; 104 (7): 071101.

[2] Mirfakhrai, T., Madden,J. D. W., Baughman, R.H.: "Polymer artificial muscles", Materials Today, Volume 10, Issue 4, 2007, Pages 30-38.

[3] Hoffstadt, T., Graf, C., Maas,J.:"Modeling of roll-actuators based on electroactive polymers", Proc. SPIE 8687, EAPAD, 2013, 86871F, 9 April 2013.

[4] Carpi,F., De Rossi, D.:"Dielectric elastomer cylindrical actuators: electromechanical modelling and experimental evaluation", Materials Science and Engineering: C, Volume 24, Issue 4, 2004, Pages 555-562.

[5] Cameron, C.G., et al.:"Linear actuation in coextruded dielectric elastomer tubes", Sensors and Actuators A: Physical, Volume 147, Issue 1, 2008, Pages 286-291.

[6] Yipin Su et al.:"On buckling of a soft incompressible electroactive hollow cylinder", International Journal of Solids and Structures, Volumes 97–98, 2016, Pages 400-416.

[7] R. Sarban et al.:"A tubular dielectric elastomer actuator: Fabrication, characterization and active vibration isolation", Mechanical Systems and Signal Processing, Volume 25, Issue 8, 2011, Pages 2879-2891.

[8] H. Zhao et al.: "Compact Dielectric Elastomer Linear Actuators", Adv. Funct. Mater. 2018, 28, 1804328.

[9] Krüger, T., Maas, J.:"Optimized mechanical interface design for multilayer DE stack-transducers", Proc. SPIE 12042, EAPAD XXIV, 120420E, 20 April 2022.

[10] Krüger, T.,Çabuk, O., Maas, J.: "Manufacturing Process for Multilayer Dielectric Elastomer Transducers Based on Sheet-to-Sheet Lamination and Contactless Electrode Application", Actuators 2023, 12, 95.

[11] Krüger, T., Maas, J.: "Impact of uncertainties on the actuation of DE multilayer transducers", Proc. SPIE 11375, EAPAD XXII, 1137516, 3 June 2020.

[12] Mertens, J., Cabuk, O., Maas, J.:" Modeling and experimentally parameterizing approach of the viscoelastic material behavior of DE-based transducer materials", Proc. SPIE 12042, EAPAD XXIV, 1204214, 20 April 2022.

[13] Cabuk,O., Maas, J.: "Investigation of a deposition method for the application of electrode layers for dielectric elastomer transducers," Proc. SPIE 11587, EAPAD, XXIII, 115871Q 22 March 2021.

[14] Dietmar, H.: "Die antike Mathematik. Eine Geschichte der griechischen Mathematik, ihrer Probleme und Lösungen. Berlin, 2014, Heidelberg: Springer Spektrum (SpringerLink Bücher).

[15] Nollau, R., Herschel, D.: "Hydraulik. Grundlagen, Komponenten, Schaltungen", 5. Aufl. 2011. Berlin, Heidelberg: Springer Berlin Heidelberg.

[16] Wacker Chemie AG: "ELASTOSIL® FILM 2030 BLATT 250/50", https://www.wacker.com/h/de-de/c/elastosil-film-2030-blatt-25050/p/000005177, (Accessed: 30 March 2024).

Design and Fabrication of a Five-Fingered Soft Robotic Hand with Embedded SMA Actuator and Piezoresistive Flexible Sensor

Racha Benarrait, Institut fûr Mikrotechnik, Technische Universitât Braunschweig, Alte Salzdahlumer Str. 203, 38124 Braunschweig, Deutschland, r.benarrait@tu-braunschweig.de
Monika Leester-Schädel, Institut fûr Mikrotechnik, Technische Universitât Braunschweig, Alte Salzdahlumer Str. 203, 38124 Braunschweig, Deutschland, m.leester@tu-braunschweig.de
Frederic Lamarque, Université de Technologie de Compiègne, CNRS FRE 2012, Roberval, (Mechanics energy and electricity), Centre de recherche Royallieu – CS 60 319 – 60203 Compiègne Cedex , frederic.lamarque@utc.fr
Andreas Dietzel, Institut fûr Mikrotechnik, Technische Universitât Braunschweig, Alte Salzdahlumer Str. 203, 38124 Braunschweig, Deutschland, a.dietzel@tu-braunschweig.de

Abstract

This abstract focuses on the innovative performance and potential applications of a shape memory alloy as a material that can ideally actuate piezoresistive strain sensors. These sensors are made up of four gold strain gauges that are arranged in a Wheatstone bridge configuration on a flexible polyimide substrate. The SMA actuator was embedded in Polydimethylsiloxane (PDMS) along with the strain sensor to ensure better adhesion and stability. The sensor can detect the curvature and bending of the SMA and provide a voltage output. The experiment results reveal the displacement from the actuator as provided by the piezoresistive sensor.

1 Introduction

Robotic grippers are flexible and can handle small, soft, and irregularly shaped objects that rigid grippers cannot, mimicking the dexterity of human hands [1]. To enhance performance, sensors must provide specific information about their movements. Flexible and wearable electronics integrated with sensors allow for precise measurements of joint curvature, directly affecting the type and shape of an object being grasped [2]. Piezoresistive sensors have great potential in enhancing robotic grasping, with applications in industrial automation, healthcare, and assistive robotics [3]. Creating soft robots presents a hard challenge in the manufacturing and fabrication process [4]. A critical aspect of the soft robot design process is the pivotal task of crafting the actuator. The Shape Memory Alloys (SMAs) offer promising potential for developing advanced and cost-effective actuators [5]. SMA is frequently employed in actuator applications where mechanical motion or force is required in response to an external stimulus, such as a change in temperature. The actuation process is achieved by utilizing the shape memory effect, leading to a change in shape of the SMA and the production of mechanical work. This paper describes the design and fabrication of a fully integrated soft robotic hand with five fingers that incorporate an embedded shape memory alloy (SMA) actuator and a piezoresistive flexible sensor.

2 The SMA actuator design

SMAs are intelligent materials capable of withstanding significant inelastic strains, which are affected by their prior loading experiences and can be restored through heating or unloading. Ni-Ti-based SMAs are the most commonly used among all types and are particularly preferred by engineers due to their remarkable mechanical properties. The characteristic is typically described by the austenite start (As), austenite finish (Af), martensite start (Ms), and martensite finish (Mf) temperatures.

Figure 1: Connected Sensors to the Finger-Finger PCB: (a) Bended sensors, (b) Sensors flat after temperature exposure

A Ni-Ti SMA strip is cut into a rectangular shape. Its performance and specifications were measured with experiments. SMA strips were prepared, integrated into flexible host material, and used to create robotic fingers as could in future be used to develop prosthetic hands where the amount of bending can be controlled by adjusting the electrical current flowing through the SMA. A NiTi sheet from Memetis GmbH with 100 µm thickness (+/- 15 µm) was used for the study. After deformation the SMA strips return to their original flat shape upon exposure to a modest temperature from the hotplate of 100 degrees Celsius. The bending of the smart fingers is sensed using piezoresistive sensor (see Fig. 1). In this way, it can be used to develop prosthetics hands or robotic manipulators to replicate the natural bending motion of human fingers.

2.1 Fabrication procedure of the smart fingers

Incorporating SMA into host materials including composites has so far been a challenge to the poor bonding characteristics of SMA. To enable self-fixation and ensure the stability of the sensor, the SMA strip is integrated within a two-layer PDMS encapsulation.

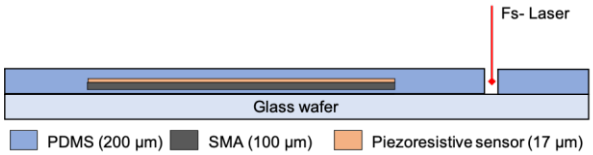

Figure 2: Schematic cross-section of the sensor strip embedded in PDMS & SMA

The SMA strip possesses the unique property of bending into various shapes depending to the memorized form and maintaining its form, providing a stable measurement state of the sensor. The process involves placing the SMA under the sensor strip, which is then encapsulated with 200 µm PDMS during assembly. After the PDMS is cured, the assembly is cut and released from the glass wafer using a Fs-laser (see Fig. 2).

3 Smart Finger shape feedback sensor

In this project, we use a flexible piezoresistive sensor array with four nodes. Each node comprises four resistors arranged in a Wheatstone bridge configuration. Two resistors are placed diagonally on the top surface, and the other two are placed diagonally at the bottom. This arrangement allows strain gauges on both sides of the neutral axis, providing higher sensitivity. The strain gauges on the top experience tensile strain, while those on the bottom experience compressive strain. This study employed five piezoresistive sensors, each bent to emulate various grasping postures (see Fig. 3).

Figure 3: Grasping experiment of the assembled hand

After this, data was gathered, revealing a notably elevated output voltage in the star-shaped matrix. The bending of the sensors explains the noticeable rise in the output voltage within the star-shaped matrix. This shift in output voltage corresponds to the deformation of the SMA and its capacity to discern distinct grasping postures of the simulated object (see Fig. 4). The flexible sensor feeds back the smart finger shape for precise control and we demonstrated its capability of grasping various kinds of regular or irregular objects.

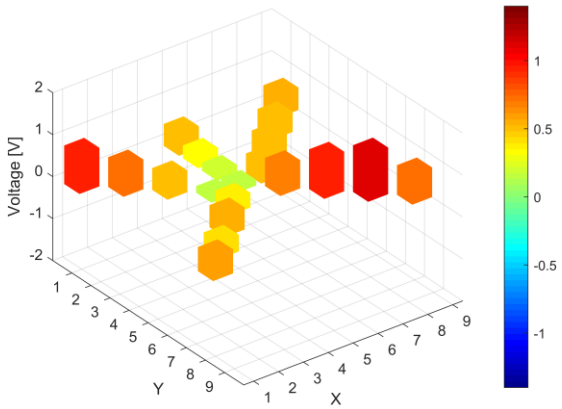

Figure 4: Raw sensor signals of the grasped object

4 Conclusion and outlook

This paper outlines the design and fabrication procedures for an integrated soft robotic hand. The finger design incorporates actuators composed of shape memory alloy (SMA) strips for actuation and shape recovery and flexure sensors for shape feedback. The outcome is a lightweight, sturdy, and fully integrated robotic hand capable of providing a surface reconstruction of the grasped object.
Despite incorporating feedback sensors, attaining precise control over output force and configuration for soft robots still needs to be discovered. This complexity arises primarily from the infinite degrees of freedom inherent in soft robots, which rely on material deformation to control their position.

5 Literature

[1] Y.-G. Kim, J.-H. Song, S. Hong, et S.-H. Ahn, « Piezoelectric strain sensor with high sensitivity and high stretchability based on kirigami design cutting », *Npj Flex. Electron.*, vol. 6, nº 1, Art. nº 1, juin 2022, doi: 10.1038/s41528-022-00186-4.

[2] S. Xu *et al.*, « Recent Advances in Flexible Piezoresistive Arrays: Materials, Design, and Applications », *Polymers*, vol. 15, nº 12, p. 2699, juin 2023, doi: 10.3390/polym15122699.

[3] J. Li, L. Fang, B. Sun, X. Li, et S. H. Kang, « Review—Recent Progress in Flexible and Stretchable Piezoresistive Sensors and Their Applications », *J. Electrochem. Soc.*, vol. 167, nº 3, p. 037561, janv. 2020, doi: 10.1149/1945-7111/ab6828.

[4] F. Schmitt, O. Piccin, L. Barbé, et B. Bayle, « Soft Robots Manufacturing: A Review », *Front. Robot. AI*, vol. 5, 2018

[5] K. Hu, K. Rabenorosoa, et M. Ouisse, « A Review of SMA-Based Actuators for Bidirectional Rotational Motion: Application to Origami Robots », *Front. Robot. AI*, vol. 8, 2021, https://www.frontiersin.org/articles/10.3389/frobt.2021.678486

Fabrication of pneumatic soft fingers taking into account material/process/design interaction

Baptiste Kraehn[1], Thibault Delrieu[2], Laurence Meylheuc[1], Pascal Seguin[2], Jean-Pierre Gazeau[2], Olivier Piccin[1]
[1] ICube, INSA Strasbourg, France - baptiste.kraehn@insa-strasbourg.fr
[2] Pprime Institute, Poitiers University, France

Abstract

Soft robots derive their remarkable properties and performance from the characteristics of their constituent materials, silicones being widely represented in this field. Besides its very high stretch capacity, silicone has a complex behavior linked to solicitation speed and loading history. This paper presents a study of pneumatic finger behavior produced by a silicone injection molding and analysed through a comparative experimental and simulation analysis. The design of the finger is based on the particularities of the injection process, so that it can be produced in a reduced number of steps.

1 Introduction

Silicone is a material widely used in soft robotics due to its ability to withstand large deformations. Silicone-based soft actuators are well suited for manipulating objects due to their high degree of compliance. This makes them particularly relevant for handling fragile or unshapely objects [1]. The resulting performance of soft actuators depends on a complex interaction between material properties, process and design [2]. Silicone exhibits hyper-elastic properties that is coupled with a dependence on deformation history, making material characterization and finger control more complex. A repeatable manufacturing process is then required to identify these intrinsic material properties. As traditional molding methods are multi-step and poorly consistent [3], variations in behavior can occur between multiple manufactured actuators, resulting in poor repeatability [4] and increased complexity of actuator control.
In this work, we propose a specific manufacturing method for Room Temperature Vulcanization (RTV) silicone fingers dedicated to multi-fingered manipulation tasks. Mechanical properties are first studied on silicone specimens in order to define its mechanical behavior law. A pneumatic soft finger design is then proposed for single-step injection molding. The finger behavior is studied by pressurizing cavities. Finite Element Method (FEM) simulation, performed with the material law determined on the silicone, is finally used to analyze the finger's response.

2 Low-pressure silicone injection

Molding is a widely used manufacturing process for polymeric materials. Commonly used in soft robotics, gravity molding involves pouring liquid silicone into a partially open mold. Filling is often followed by a vacuum stage to remove any bubbles that may have been trapped in the liquid silicone. As the flow of silicone relies solely on gravity and its viscosity is high (around 50 Pa.s compared to water's 0.001 Pa.s), molding thin walls (in the millimeter range) can be relatively complex. This limitation can be overcome with silicone injection molding [3]. Unlike the industrial injection technique, RTV silicones can be processed at room temperature using low pressure injection. The most commonly used RTVs are two-component and therefore require mixing and degassing prior to injection. The mixing of the two silicone components must be conditioned in a device with a piston for injection, such as a syringe [5]. Filling the syringe can be relatively complex, as the silicone in the syringe needs to be degassed. By dispensing each part of the silicone into a degassed container with a plunger, injection with a mixing nozzle can be achieved [6]. Our approach is to use a device that allows silicone to be mixed under vacuum. The container in which the mixing takes place has a piston which, once released and under the action of the vacuum, collects the silicone. The collected container is then mounted on a manual injection gun. The device used, is a specific mixing system originally designed to inject a plastic orthopaedic cement for medical applications (Palamix, Heraeus). It has the advantage of performing the mixing and injection stages under constant vacuum, which improves the quality of the material after vulcanization.

3 Silicone mechanical behavior characterization

Silicone is an elastomeric material that undergoes large deformations with a highly non-linear behavior: hyperelasticity. In order to identify a hyperelastic behavior law, characterization tests must be carried out to determine the strain-stress curve. Uniaxial tensile testing is a commonly used characterization method due to its ease of processing. However, silicone also exhibits viscoelastic behavior, resulting in a strain rate dependence. Experimental tests carried out at different strain rates therefore allow us to define a complete mechanical behavior model for silicone: hyperelastic - viscoelastic. Silicones also show a dependence on deformation history due to the Mullins effect [7]. To reduce the number of analysed parameters, this dependency is not studied in this section. The different specimens are used only once, so that each test is carried out on a specimen with no loading history. In this case, the characterization carried out focuses solely on the behavior of the silicone in a pristine state. The silicone processed in this study is the Rhodorsil RTV 3428.

3.1 Uniaxial tensile strength testing

Characterization tests are carried out on Type-1 ISO 527 specimens fabricated using the low-pressure injection procedure described in section 2. Deformation is measured using an extensometer with an initial measurement length of 75 mm. Six specimens are tested at a strain rate of 500 mm.min^{-1} to determine if the manufacturing procedure is repeatable. Note that the tensile speed is deliberately chosen to be high, il line with the conditions encountered for applying pressure in the experimental finger.

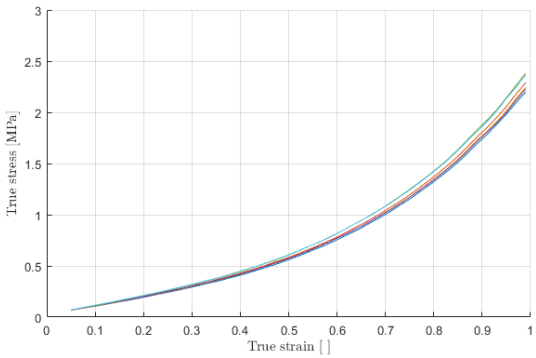

Figure 1 True uniaxial tensile stress-strain for 6 silicone specimens

The true stress-strain curves shown in **Figure 1** present very similar tensile behavior for the six specimens. The relative standard deviation calculated on the true stress is less than 4 % over the observed range, with a maximum standard deviation of 0.08 MPa. The tensile behavior of the test specimens is therefore considered repeatable. Two other deformation rates are investigated to highlight the influence of the viscoelasticity of the material on the stress-strain curve. Three specimens are tested at 250 mm.min^{-1} and three others at 50 mm.min^{-1}, the usual speed for a tensile test on polymers. The mean curves for each testing speed are shown in **Figure 2**.

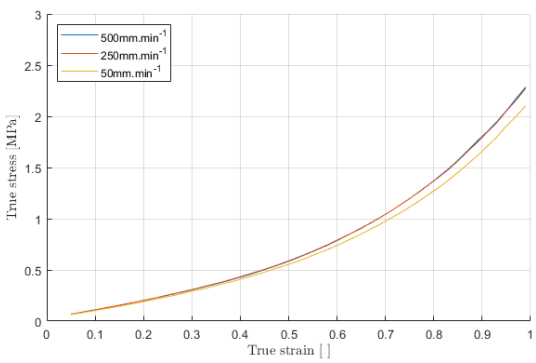

Figure 2 True uniaxial tensile mean stress-strain for 3 different testing speed

Tensile tests show that below a 50% strain there is virtually no effect of speed, but above 50% strain the material hardens at high test speeds. Increasing the testing speed limits the creep of the material, which is inherent in viscoelasticity. For the selected silicone, the stress-strain curve is invariant for test speeds above 250 mm min^{-1}.

3.2 Identification of mechanical behavior laws

From the mean stress-strain curve for each test speed, an identification is made to determine a hyperelastic law and parameters that best fit each experimental result for use in the Ansys-Mechanical FEM software. Identification is performed via the MCalibration software. For each tensile speed, Ansys-ArrudaBoyce law has the lowest Normalized Mean Absolute Difference (NMAD) error. For each identification, the silicone is considered incompressible (incompressibility parameter $d = 0\ MPa^{-1}$). The parameters of the behavior law for each speed are given in **Table 1**. A hyperelastic-viscoelastic law is identified from all three curves. The Ansys-ArrudaBoyce-PronySpectrum law, named HypVisc, gave the best result with the parameters given in **Table 2**.

Table 1 Parameters for the Ansys-ArrudaBoyce law according to the test speed

Name	Test speed [mm/min]	μ [MPa]	λ_L [ ]	NMAD [ ]
Hyp500	500	0.24	2.58	1.06
Hyp250	250	0.2414	2.61	0.924
Hyp50	50	0.227	2.67	0.745

Table 2 Parameters for the Ansys-ArrudaBoyce-PronySpectrum law, named HypVisc

μ [MPa]	λ_l [ ]	t_m [s]	t_s [s]	B [ ]	Np [ ]	Σg [ ]	Σk [ ]	NMDA [ ]
0.3	2.49	2.26	15	0.6	10	0.484	0	1.37

The experiments carried out highlighted the viscoelastic and hyperelastic properties of the silicone and lead to the definition of behavior laws to study these phenomena on a pneumatic finger geometry using simulation.

4 Finger design

The studied finger, similar in size with a human finger, is composed of four cylindrical cavities enabling flexion, extension and both lateral movements. Each cavity is independent and connected to a pneumatic inlet screwed after injection. The injection process enables the overmolding of elements previously inserted into the mold. The finger's design was therefore focused on a solution where the full finger is manufactured in a single injection step with the overmolding of a rigid base, referred to as the hub (see **Figure 3.a**). The hub enables the finger assembly to be fixed to an experimental platform and provides the link between the cavities and the pneumatic inlets. To achieve single-injection fabrication, the cavities are molded by cores positioned in the hub. As the sealing quality is a prominent feature the hub is designed with a lattice volume into which

the silicone can flow during injection. Upon curing completion, the lattice structure filled with silicone results in a strong interface between the hub and the soft finger. A protrusion (referred to as sealing protrusion in **Figure 3.b**) with an internal shoulder is added to each cavity to increase the strength of the seal. Vents are designed in the hub to allow air to escape during injection. Once the silicone cured, the soft finger with its overmolded hub is demolded and caps are inserted into the hub to seal the cavities.

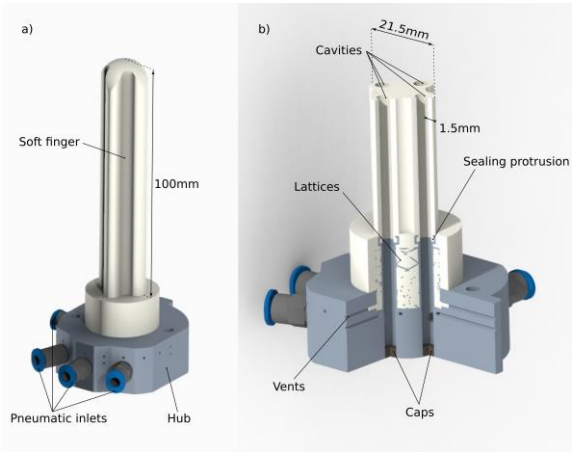

Figure 3 Finger assembly representation. Full view of the pneumatic finger in a) and partial view in b).

5 Finger behavior

Finger behavior is studied in the case of inflation of a single cavity at a time, with the resulting movement being bending. The evolution of the cavity pressure required for the fingertip to reach a given point is tracked, in order to demonstrate the influence of material viscoelasticity and Mullins softening.

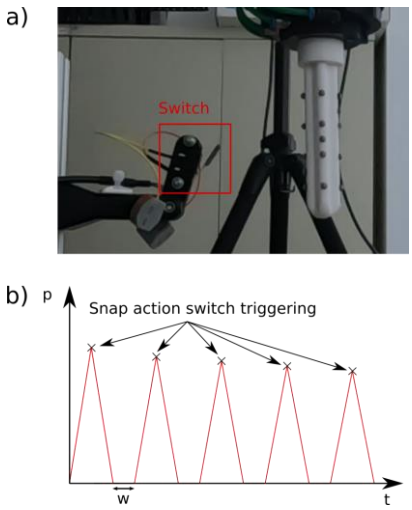

Figure 4 a) Experimental setup with finger at rest position and b) pressure profile in function of time.

The experimental setup is designed with a snap action switch positioned in the flexion plane of the finger at a point defined as the maximum fingertip position (see **Figure 4.a**). The experimental protocol consists of a series of five triangle pressure waves or cycles applied to the cavity as depicted in figure 4.b, at a pressure rate of 10kPa/s. Cavity deflation is triggered by activation of the switch with a waiting time of w=5s between consecutive waves. The maximum pressure has been set to 180kPa. If the pressure reaches 180kPa, but the switch has not been triggered at this point, this maximum pressure is maintained until the finger activates the switch as a result of creep.

5.1 Experimentation results

The experimental protocol is applied to one cavity for three fingers manufactured using the injection method presented previously. For each pressure wave, the mean pressure at contact is calculated over the three fingers. If the maximum pressure of 180kPa is reached during a pressure cycle, the creep time is specified (see **Table 3**).

Table 3 Evolution of the mean contact pressure for three fingers

Cycle number	**1**	**2**	**3**	**4**	**5**
Mean pressure at contact [kPa]	179.8	179.3	175.6	172.2	169.5
Creep time [s]	18	0.5	/	/	/

The maximum pressure of 180kPa is reached for the two first cycles. Creep time is almost 20s for the first cycle, and becomes quasi null for the second. From the third cycle onwards, the pressure required for contact is less than 180kPa, with an evolution of -2% per cycle. The finger's behavior therefore depends on the stress history, with a combination of creep due to the viscoelastic effect and softening of the material due to the Mullins effect. These two characteristics have a particularly significant impact on the evolution of the finger's deformation state.

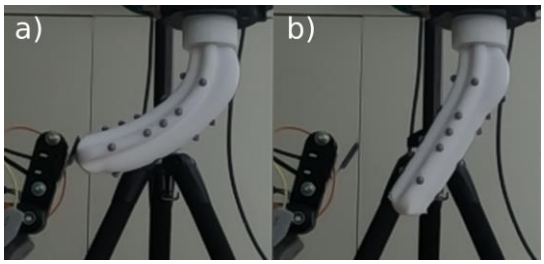

Figure 5 Finger deformation. Deformation at contact in the first cycle in a) and during loading in the fifth cycle in b).

During the first cycle, the deformation is not homogeneous along the pressurized cavity: a hernia appears at the base of the finger as shown in **Figure 5.a**. The Mullins effect induces a softening of the material as the number of cycles increases, resulting in an enlargement of the hernia and thus a modification of the geometry of the finger. In subsequent cycles, it is the hernia area that is deformed to the greatest extent, generating the flexion (see **Figure 5.b**). This hernia around the base of the finger occurs in all the finger cavities produced when inflated. The defect being

reproducible, this characteristic can be assumed to be induced by the geometry and the impact of material properties on it. Using the previously defined material laws, an FEM simulation is then set up to study the finger deformation and hernia formation.

5.2 FEM simulation

FEM steady-state simulations are performed on the finger using the hyperelastic laws shown in **Table 1**. Another (unsteady) simulation with the hyperelastic-viscoelastic law shown in **Table 2** is also carried out with pressure loading applied via a ramp of 10kPa/s. For each run, a maximum pressure of 130kPa is applied in a cavity, with the effect of gravity in a similar direction to the experiment.

Table 4 Bending computed according to the material law

Material law	Hyp500	Hyp250	Hyp50	HypVisc
Bending angle [°]	34.1		70.1	54.93

For each simulation, the bending determined from the orientation of the fingertip is computed (see **Table 4**). A 9% difference in behavior on a uniaxial tensile curve generates a 100% difference in bending in the case of finger inflation, illustrating the major impact of viscoelasticity on finger behavior. The results obtained for the HypVisc material show an intermediate finger behavior compared with previous results. The deformation speed performed in the experimentation of the finger therefore does not allow accurate simulation based on a hyperelastic law obtained for the three speeds tested. However, all the simulations carried out show the finger behaving more softly than in reality: a pressure of 180kPa (which is not sufficient to reach the switch in the first cycle) generates a bending of more than 180° in simulation. This variation may be due to the hernia and its location.

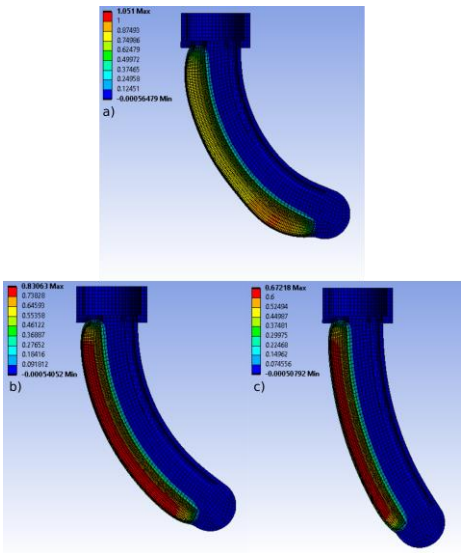

Figure 6 FEM results for Hyp50 in a), HypVisc in b) and Hyp250 in c).

Results for the Hyp500, Hyp250 and ViscoHyp laws show homogeneous deformation along the length of the cavity as shown in **Figure 6.b** and **6.c**. The Hyp50 simulation, with a higher bending, shows hernia formation at the tip of the finger and a second, less pronounced, towards the base of the finger (see **Figure 6.a**). In simulation, the defined material behavior coupled with the finger geometry do not replicate exactly the same hernia location as the experimentally one. The location of the hernia at the base of the finger could then be related to the handling of the finger during the manufacturing phase. As the cores molding the cavities adhere to the silicone, removal of the cores causes slight deformation of the cavities at the base of the finger. This slight deformation history can then generate localized softening of the material due to the Mullins effect, resulting in the formation of a hernia at the next inflation as well as a modification of finger behavior for a given pressure

6 Conclusion

The viscoelastic property of silicone has a major influence on the behavior of a pneumatic finger through a dependence on solicitation speed. Because of the Mullins effect, non-homogeneous deformation along the cavity induces softening concentration and hernia formation, leading to a change in the finger's trajectory as a function of cycles. FEM simulation can therefore be used to optimize finger geometry to avoid hernia formation and improve the control of soft finger for manipulation tasks. Attention must be paid to handling of the finger, such as during the demolding phase, which can generate a deformation history.

References

[1] D. Rus and M. T. Tolley, “Design, fabrication and control of soft robots,” Nature, vol. 521, no. 7553, pp. 467–475, May 2015.

[2] F. Tauber, M. Desmulliez, O. Piccin, and A. A. Stokes, “Perspective for soft robotics: the field’s past and future,” Bioinspir. Biomim., vol. 18, no. 3, p. 035001, Mar. 2023.

[3] K. C. Galloway et al., “Soft Robotic Grippers for Biological Sampling on Deep Reefs,” Soft Robotics, vol. 3, no. 1, pp. 23–33, Mar. 2016.

[4] J. H. Chandler, M. Chauhan, N. Garbin, K. L. Obstein, and P. Valdastri, “Parallel Helix Actuators for Soft Robotic Applications,” Frontiers in Robotics and AI, vol. 7, 2020.

[5] M. A. Bell, K. P. Becker, and R. J. Wood, “Injection Molding of Soft Robots,” Advanced Materials Technologies, vol. 7, no. 1, p. 2100605, 2022.

[6] M. Chauhan, J. H. Chandler, A. Jha, V. Subramaniam, K. L. Obstein, and P. Valdastri, “An Origami-Based Soft Robotic Actuator for Upper Gastrointestinal Endoscopic Applications,” Front. Robot. AI, vol. 8, May 2021.

[7] S. Krpovic, K. Dam-Johansen, and A. L. Skov, “Importance of Mullins effect in commercial silicone elastomer formulations for soft robotics,” Journal of Applied Polymer Science, vol. 138, no. 19, p. 50380, 2021.

Soft aquatic robot using shape memory actuators based on an octopus jellyfish to improve water quality in aquariums

Yoshiaki Fujiwara, Hironari Taniguchi, and Teppei Ueda,
Graduate School of Robotics and Design, Osaka Institute of Technology,
1-45 Chayamachi, Kitaku, Osaka, Japan

Abstract

In this study, an octopus jellyfish-shaped robot is being developed to solve problems in aquarium water filtration. The robot collects suspended solids in the aquarium and supports the filtration process. It consists of a bell and a control box, and utilizes a shape memory alloy actuator to drive the bell. The robot mimics the ecology of an octopus jellyfish, and the filter is mounted under the bell. The filter utilizes the water flow generated when the bell closes to capture suspended solids and help improve the quality of the water in the tank. Previous robots have been able to operate in water, but have not been able to collect suspended solids. The bell part of the robot has been improved, and its ability to collect suspended solids has been verified. The results suggest that the robot can collect suspended solids in the aquarium and has a high potential to improve the water quality of the aquarium.

1 Introduction

In aquariums, suspended solids and particulate matter are collected by filtration equipment to maintain water quality and control water temperature [1-3]. Suspended solids are particles suspended in water that do not dissolve. Additionally, suspended solids pose a problem as they adhere to the body hairs of aquatic organisms and form mud balls in the filtration tanks. Research has been conducted on filters within filtration units to maintain aquarium water quality [4-6]. Moreover, Lasse Lange Jensen et al. reported that an increase in turbidity in the aquarium slowed down the feeding activity of captive organisms [7]. Methods for monitoring water quality in aquariums have also been investigated [8]. Therefore, filtering the water in the aquarium is crucial. During the filtration process, water from the tank is pumped into the filtration unit, but if a large amount of waste is sent to the filtration tank, the tank becomes clogged, and filtration cannot be carried out.

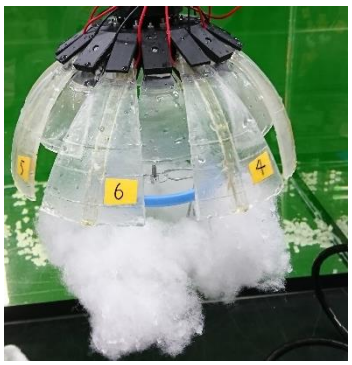

Figure 1 Moon jellyfish robot

The research group has developed a jellyfish-shaped soft robot [9]. **Figure 1** shows a soft robot to collect microplastics in the sea. In this study, an octopod jellyfish soft robot was considered for collecting suspended solids in aquariums. Sabine Holst et al. reported that octopus jellyfish have a characteristic of collecting food such as micro-organisms with their mouth-arms under the bell [10]. We hypothesized that the robot could collect suspended solids by mimicking the way it forages with its mouth-arms. Previous robots have been able to generate water flow, but the water flow has not been able to reach the filter due to the weak water flow, and thus have not been able to collect suspended solids. This paper reports on the structure of the soft robot, the investigation of the bell, and the confirmation of the operation of the octopus jellyfish soft robot.

2 Octopus Jellyfish-shaped Robot

2.1 Structure

Figures 2 and **Figure 3** show the appearance of the octopus jellyfish soft robot. The main body is 422 mm in width, 242 mm in height, and weighs 1,716 g. A total of eight bells are utilized for the robot, which were fabricated using silicone rubber. An SMA actuator, attached to the surface of the bells, facilitates their opening and closing. This reduces the possibility of injury to horizontal organisms in contact with the bells.

The actuator used for the soft robot was fabricated using shape memory alloy wire (Toki Corporation, BMF150) and silicone rubber (ShinEtsu, KE-1603-A/B). The shape memory alloy wire has a diameter of Φ0.15 mm. The actuator consists of two shape memory alloy wires, each with dimensions of 7 mm in width, 150 mm in length, and 1.5 mm in thickness. While shape memory alloy wires typically exhibit flexible movement, they harden and contract when heated by electricity. Upon cooling, they regain their original flexibility. Leveraging this contracting property, the actuator attached to the jellyfish's bell contracts when heated by electricity, causing the bell to close. When the electric current is discontinued, the actuator cools, allowing the bell to open. This cycle repeats to facilitate the opening and closing of the bell.

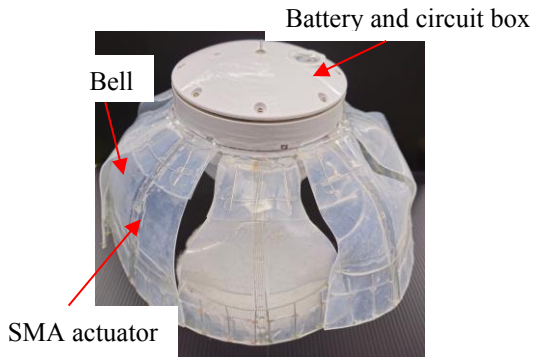

Figure 2 Overall view of the robot

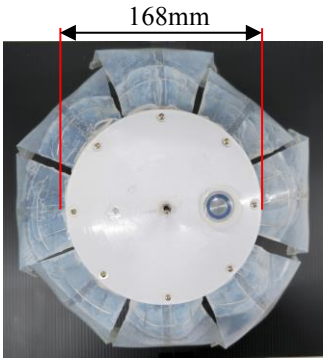

Figure 3 Top view of the robot

2.2 Design of octopus jellyfish robot bell

Drawing from the trajectory investigation experiments of the bell, we envisioned that suspended solids could be effectively collected by designing the bell to close from a wide-open state, allowing the generated water flow to directly enter the filter. We explain the design of the bell for this expanded state as follows: the thickness of the bell was doubled in the section from the base to 70 mm to minimize drooping (see **Figure 4**). The bell measures 170 mm in length, 150 mm in width, and is fan-shaped. At the tip of the 1 mm thick silicone sheet depicted in yellow (refer to **Figure 5**), a 1 mm thick acrylic plate shown in blue was affixed. The combined thickness of the silicone sheet and actuator is 2.5 mm. At the base of the bell, a 1 mm thick silicone sheet (depicted in red) was attached. Additionally, to widen the bell, Φ1 mm stainless steel wires (shown in grey) were inserted between the silicone sheets at the base and the tip of the bell. The inclusion of these stainless steel wires (Φ1 mm) allows for adjustments to the bell's shape. With this design, the bell operates under the conditions of a 2.5-second energization time and a 1.2 A current. The bell's shape was achieved by bending a wire near the base, resulting in dimensions of 65 mm in width and 32 mm in height (see **Figure 6**).

The movement of the bell as shown in **Figure 7** involves the tip moving from 127 mm to 49 mm laterally and from -78 mm to -112 mm in depth, covering a linear distance of 86 mm, and closes within an operating time of 1.7 seconds.

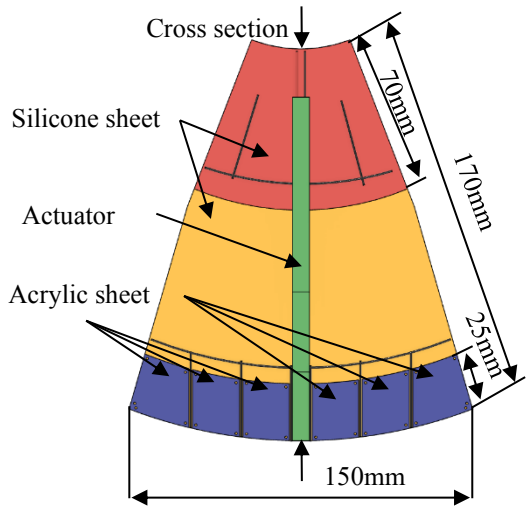

Figure 4 Top view of the bell

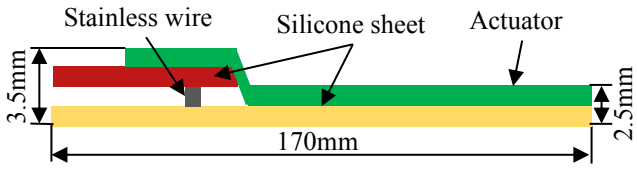

Figure 5 Cross section view of the bell

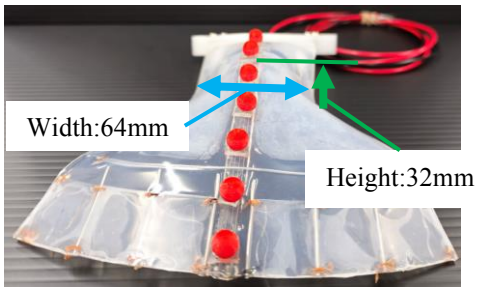

Figure 6 Bell shape

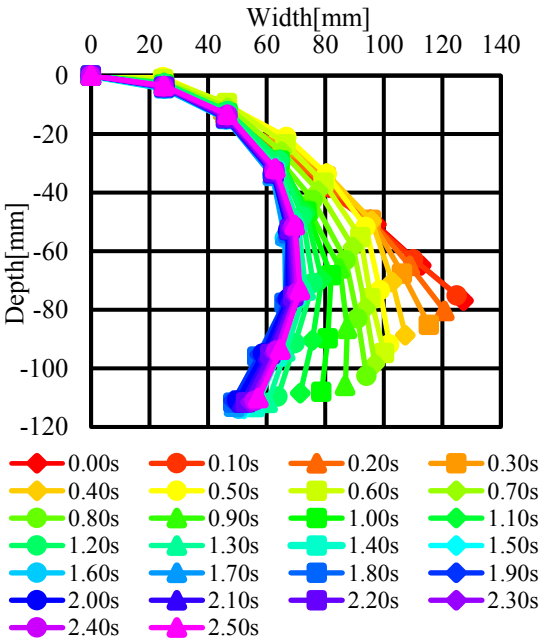

Figure 7 Bell motion

3 Experiment and Results

This section describes the operation of the octopus jellyfish robot through the movement of its bell and an experiment to investigate water currents. The robot was secured in a tank and set to a water temperature of 24°C, a voltage of 22.0 V, and a current of 19.2 A. The experiment was conducted with a power-on time of 2.5 seconds and a power-off time of 10.0 seconds. Although wireless drive with batteries is envisioned for practical use, a stabilized power supply was utilized in this experiment for operation confirmation via wired connection. The filter installed at the bottom of the robot utilized thin, high-density matting, cut to achieve a diameter of 190 mm. To simulate debris and assess water flow, 10.0 g of small fish food was employed. The experiment involved repetitive robot operations without a specified number of bell openings and closings. After 50 minutes of operation, the experiment was concluded when the fish food, used as simulated debris, ceased sinking and began floating on the water's surface. The flow of debris during the experiment is illustrated in **Figures 8-10**. It was observed that the bell's opening and closing induced water flow towards the filter. This suggests that the robot's movements can gather suspended matter towards the filter, indicating a high likelihood of successful collection. Additionally, in the area depicted in **Figure 9**, debris appeared to flow in a whirlpool-like motion, suggesting that installing the filter at whirlpool-generating points could be effective. Moreover, despite the generated water flow being directed towards the filter, it tends to roll up on the filter's surface, resulting in areas where debris bounces back and remains uncollected, indicating the need to modify the filter's shape. Furthermore, some water flow did not reach the filter but hit the tank's bottom, stirring up deposited debris that eventually reached the filter, necessitating experiments in larger tanks.

Next, a magnified photograph of the filter after the experiment is shown in **Figure 11**, confirming that the debris is entangled in the filter. These results indicate that the motion of the bell's opening and closing can generate a water flow towards the filter, suggesting the potential for collecting suspended matter. However, since many pseudo-dust particles were not trapped by the filter and flowed away, it is necessary to reconsider the shape and installation of the filter. Additionally, although this experiment was conducted using a stabilized power supply, it is essential to verify whether similar collection efficiency can be achieved using a battery.

As a result, it became evident that the debris, assumed to be pseudo-litter, was flowing in the direction of the filter, indicating a high likelihood of rubbish collection. However, it is necessary to reconsider the position and shape of the filter, as some debris that flowed onto the filter may have been rolled up and swept away again by the water flow caused by the bell.

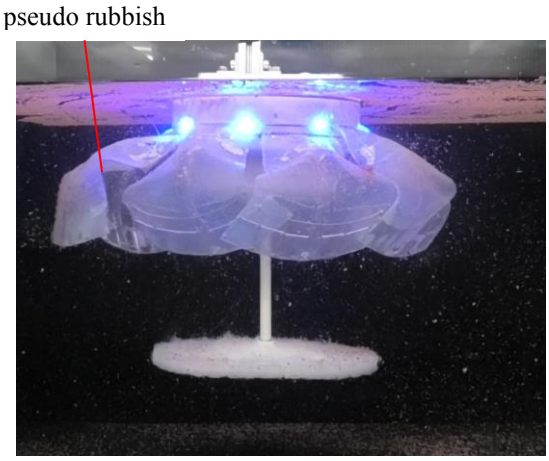

Figure 8 Bells begin to move

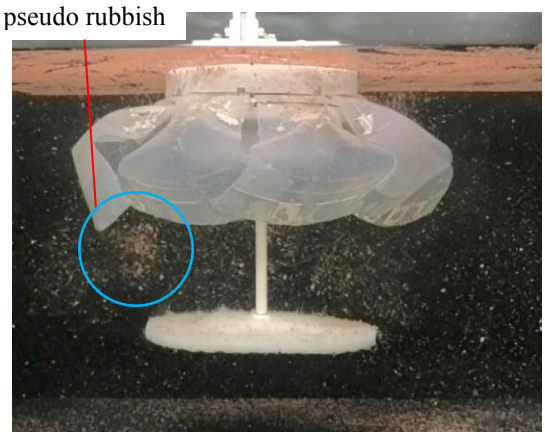

Figure 9 Bells after bending

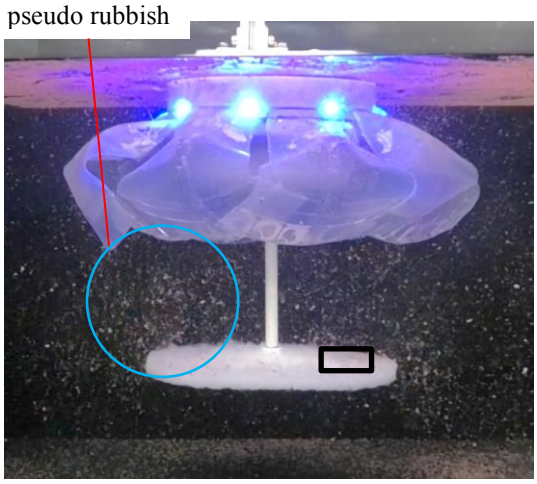

Figure 10 Post-flexion flow

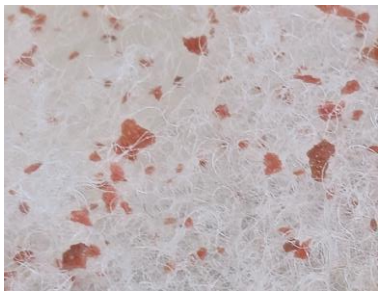

Figure 11 Larger view of the filter after recovery

4 Conclusions

In this paper, we proposed a robot that addresses issues in aquariums while preserving the landscape and assists in improving water quality. The operation of the robot suggested the potential for collecting suspended solids with a filter installed at the bottom of the jellyfish robot. However, debris flowing onto the filter rolled up on its surface, preventing effective collection. Additionally, due to the lower installation position of the filter, pseudo-dust could not be collected at the vertexing part. Therefore, it was noted that there is a possibility of improving suspended solids collection by adjusting the installation position of the filter.
In the future, we plan to confirm whether the same effect can be achieved using a battery and to study the installation position and shape of the filter.

5 Literature

[1] Dorota Stachowiak, Pawel Hemmerling, : Development of an Automatic Water Exchange System for Smart Freshwater Aquarium. Electronics 2022, Vol. 11, No. 17, 2705, Aug. 2022.

[2] Muhammad Hazim Hisyamuddin Said, S. Siti Hafshar, : CONTROLLING AND MONITORING WATER QUALITY IN SALTWATER AQUARIUM. Malaysian Journal of Industrial Technology, Vol. 5, No.2, 2021.

[3] Aranya Ponpornpisit, Malinee Jongjaroenjai, Naowarat Suthamnatpong, Sanit Piyapattanakorn and Surachet Burut-Archana, : Single-tank sequencing batch bioreactor with a cellulose substrate for simultaneous nitrification and denitrification of an aquarium. Ponpornpisit A. et al. / Thai J Vet Med. 2023. Vol. 53, No.1, Aug. 2023, pp. 83-96.

[4] Sarah Al-Ajeel, Emilie Spasov, Laura A. Sauder, Michelle M. McKnight, Josh D. Neufeld, : Ammonia-oxidizing archaea and complete ammonia-oxidizing Nitrospira in water treatment systems. Water Research X, Vol, 15, May. 2022.

[5] Laura A. Sauder, Katja Engel, Jennifer C. Stearns, Andre P. Masella, Richard Pawliszyn, Josh D. Neufeld, : Aquarium Nitrification Revisited: Thaumarchaeota Are the Dominant Ammonia Oxidizers in Freshwater Aquarium Biofilters. PLoS ONE, Vol. 6, No. 8, Aug. 2011.

[6] Monika R. Snowdon, Robert F. L. Liang, Avneet Kaur, Erika A. Burton, Shasvat Rathod, Wenkai Fang, Hadi A. Dhiyebi, Leslie M. Bragg, Norman Y. Zhou, Mark R. Servo and Marina Freire-Gormaly, : Effects of Substituting Activated Carbon with Titanium-Dioxide-Coated Cenospheres in Conventional Aquarium Filters. Environments 2023, Vol. 10, No. 11, 188, Oct. 2023.

[7] Lasse Lange Jensen, Thomas Bjørn, Andreas Hein Korsgaard, Cino Pertoldi and Niels Madsen, : Influence of Turbidity on Foraging Behaviour in Three-Spined Sticklebacks (Gasterosteus aculeatus). Fishes 2023, Vol. 8, No. 12, 609, Dec. 2023.

[8] Chiara Scapuzzi, Barbara Benedetti, Marina Di Carro, Elvira Chiesa, Nicola Pussini, and Emanuele Magi,: Passive Sampling of Organic Contaminants as a Novel Approach to Monitor Seawater Quality in Aquarium Ocean Tanks. Applied Sciences, Vol. 12, No. 6, 2951, Mar. 2022.

[9] Hironari Taniguchi, Tatsuki Ohno, Yusuke Inoue, Kazunori Hosotani, : Development of a jellyfish soft robot to collect rubbish floating in the water. Proceedings of The 8th International Conference on Manufacturing, Machine Design and Tribology, TH-PO-44, 2019.

[10] Sabine Holst, Ilka So¨tje, Henry Tiemann, Gerhard Jarms, : Life cycle of the rhizostome jellyfish Rhizostoma octopus (L.) (Scyphozoa, Rhizostomeae), with studies on cnidocysts and statoliths. Marine Biology, Vol. 151, Feb. 2007, pp. 1695-1710.

Development of a soft avatar robot using soft pneumatic actuators for an exhibition hall

Yuki Hirano[1], Hironari Taniguchi[1], Hideaki Kokubu[1], Ryo Kawabata[1], Yuki Tanaka[1], Shinji Miura[2]
[1]Department of Robotics, Faculty of Robotics and Design, Osaka Institute of Technology
[2]Department of Design and Architecture, Faculty of Robotics and Design, Osaka Institute of Technology

Abstract

Telepresence avatar robots are used to facilitate communication between people in remote locations. In this study, we have developed a soft avatar robot suitable for exhibitions. Specifically, the robot is installed in an exhibition booth to facilitate communication between exhibition visitors and individuals in remote locations. The soft avatar robot is equipped with a monitor for video chatting and an arm with bellows-type pneumatic soft actuators. The functioning arm allows for skin-to-skin conversations. The exterior of the robot is made of soft urethane foam. We conducted the communication tests with two types of soft avatar robots with different exteriors and examined the effects of the robots.

1 Introduction

As a means of remote communication, robotic avatars are utilized. They are remotely operable robot devices that can represent humans who are not physically present. For example, Oussama Khatib and others are studying robotic avatars for exploring the ocean, where access by skilled humans is required [1]. These robotic avatars focus on use in places where humans cannot enter. On the other hand, Kazuaki Takeuchi and others proposed 'Avatar Work,' a telework system that allows people with disabilities to engage in physical tasks such as customer service. They confirmed that by controlling robotic avatars with mouse or gaze input tailored to their disabilities, remote engagement in physical tasks is possible, allowing for adaptive workload design [2]. Such robotic avatars are used in welfare and caregiving. Therefore, it can be seen that many institutions are developing robotic avatars for use in various locations.

This study focuses on exhibition venues where human congestion is expected. As an example of a robotic avatar used in exhibition venues, Beem is equipped with a monitor, microphone, and speaker to facilitate communication for the operator, and it is capable of moving on wheels. Carman Neustaedter and others investigated the effectiveness of using Beem for remote participation in meetings [3]. They concluded that it outperforms other telepresence tools like video conferencing. Safety is crucial for robots used in such situations; therefore, we focused on soft actuators. James Walker have stated that soft robots using soft actuators create a safer environment and provide flexibility and adaptability to workspaces, especially when humans and robots are integrated [4]. Hence, the primary objective of our research group is to develop a robotic avatar for exhibition venues utilizing pneumatic soft actuators, capable of mitigating malfunctions and collisions with individuals in the blind spots of the robotic avatar. Furthermore, we regard the impression of robots on humans as a crucial aspect of exhibition venue robotic avatars. Yutaka Hiroi proposed a method for improving the robot's familiarity with elderly people, including gestures and impressions of the robot's appearance [5]. As a result, they stated that the proposed method for improving robot familiarity is effective not only for young people but also for elderly people. Thus, it is necessary to tailor the appearance of the robot appropriately depending on the usage context. This paper reports on the communication test results of two types of telepresence avatar robots, 1st version and 2nd version, that we have developed.

2 Design and Fabrication

2.1 Soft Avatar Robot 1st Version

The robot shown in Figure 1 is a version of the telepresence avatar robot. It consists of a body, shoulder, arm, and hand, with dimensions of 1450mm in height, 750mm in width, and 1200mm in depth. The robot is capable of wheel drive movement, and various pneumatic devices and control equipment are installed as the driving mechanism for the arm. Additionally, a monitor, microphone, and speaker are installed on the top of the robot for video calls. Commands to open and close electromagnetic valves are sent from the control PC to the robot. According to these commands, regulated air pressure is sent to each actuator, driving the shoulder, arm, and hand. Soft actuators, specifically bellows-type actuators [6][7], are used for driving the shoulder and arm of the telepresence avatar robot. These actuators elongate axially when positive pressure is applied and contract axially when negative pressure is applied. Moreover, these actuators possess the characteristic of flexible deformation under external forces. The exterior is made considering contact with humans, using soft materials such as urethane sponge in areas where contact with humans is likely.

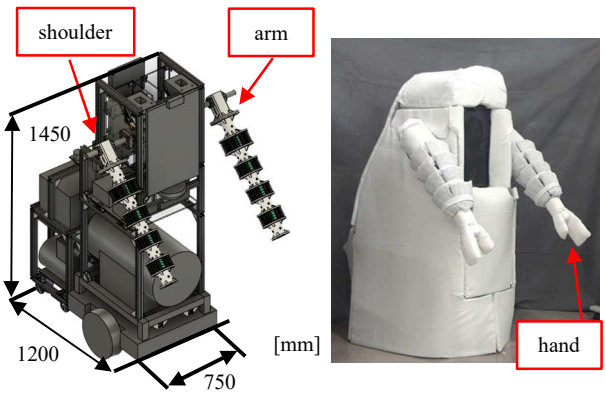

(a) No exterior (b) Exterior available

Figure 1 Soft avatar robot 1st version

2.2 Soft Avatar Robot 2nd Version

Based on the issues identified in the user test of the robot Ver.1, we prototype a new telepresence avatar robot Ver.2 (Figure 2) to resemble the appearance of humans more closely. It measures 1600mm in height, 710mm in width, and 730mm in depth. The operating principle remains the same as that of soft avatar robot Ver.1. The monitor and webcam have been relocated to the top of the robot, and the robot's height has been adjusted to the average of 165.5cm, calculated from the average heights of Japanese men (172cm) and women (159cm) [8]. Furthermore, changes in the robot's structure have resulted in modifications to the exterior of both the robot body and arms.

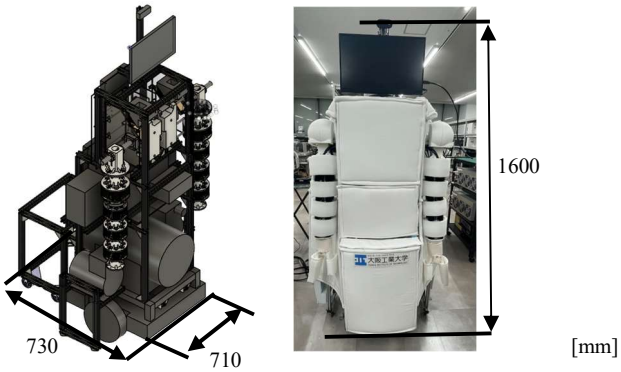

(a) No exterior (b) Exterior available

Figure 2 New Soft Robotic Avatar

3 Communication Evaluation Test

3.1 Soft Avatar Robot 1st Version

The user test was conducted on 20 healthy men and women in their 20s. The purpose of this test was to assess the effectiveness of Robotic Avatar Ver.1 in engaging in communication involving physical contact with individuals in remote locations. The test procedure involved briefing the subjects on the purpose and functions of the Robotic Avatar beforehand, followed by conducting the test. The test method involved the operator sending commands to control the Robotic Avatar from nearby, followed by engaging in communication with the subjects using video calls. During communication, handshake gestures were used at the beginning of the conversation via video calls between the operator of the Telepresence Avatar Robot and the subjects, while hug gestures were used at the farewell. This test was conducted with the approval of the Ethics Committee for Life Sciences Experiments at Osaka Institute of Technology (2022-46).

We conducted a survey among the participants who participated in the user testing. The aim of this survey was to identify issues with Robotic Avatar Ver.1 by calculating the average and standard deviation of each question. The survey questions are listed in Table 1. The survey was conducted using the Likert scale [9], where 'yes' was scored as 5 points, 'somewhat yes' as 4 points, 'neutral' as 3 points, 'somewhat no' as 2 points, and 'no' as 1 point. Furthermore, for questions 1 and 4, which were negatively worded, 'yes' was assigned a score of 1 point and 'no' a score of 5 points. A free-text section was provided on the survey sheet. The survey results as shown in Figure 3 revealed that participants found it difficult to perceive the other party as human. One contributing factor was the delay in operation caused by the command-based control of the Robotic Avatar used in this study. Additionally, other factors included the position of the monitor at chest level, the significant deviation of the robot's exterior from human shape, and the wide variation in responses to the question 'Did you feel soft when you saw the robot?' indicating that the robot's exterior may give participants a rigid impression, leading to a negative impression. Furthermore, another identified issue was discomfort in performing high fives.

Table 1 Questionnaire content

Question Number	Questions
1	Did you feel scared when you saw the robot?
2	Did you find the robot approachable?
3	Did you feel soft when you saw the robot?
4	Did you feel pain when you saw the robot?
5	Did you like the feel of the robot?
6	Did you feel familiar with the robot when you touched it?
7	Did you feel comfortable shaking hands with the robot?
8	Did you feel comfortable hugging the robot?
9	Did you feel comfortable high-fiving the robot?
10	Did you feel you were able to communicate more in-depth than on a video call?
11	Did you get a sense of being in touch with the other person, rather than with the robot?
12	Would you like to use this robot for communicating with people in remote areas?

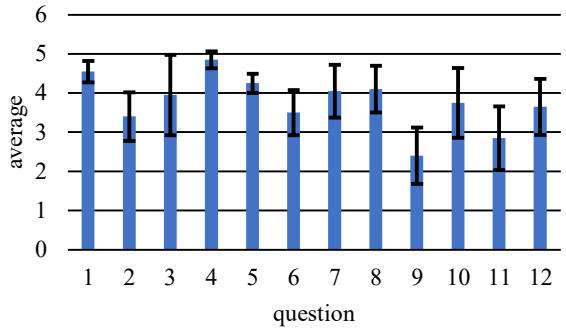

Figure 3 Results of the 1st version survey

3.2 Soft Avatar Robot 2nd Version

We conducted an impression survey on the current robot using Robotic Avatar ver.2. The purpose of this test is to make a comparison with Robotic Avatar ver.2. The subjects of the survey were healthy visitors aged from their teens to their seventies, totaling 25 individuals. The test procedure, scenario, and questionnaire were the same as those used in the user test mentioned earlier. This test was conducted with the approval of the Ethics Committee for Life Sciences Experiments at Osaka Institute of Technology (2023-4).

As for the survey results as shown in Figure 4, Questions 1 to 3 pertained to the appearance of the Robotic Avatar. As a result, it was found that this robot was perceived as less approachable. Next, Questions 4 to 9 were about impressions when interacting with the Robotic Avatar. The results suggested that the arm of the robot is suitable for human interaction. Additionally, Questions 7 and 8 showed large standard deviations. Finally, Questions 10 to 12 were about the communication system of the Robotic Avatar. The decrease in the average values from Questions 10 to 12 was attributed to operational delays. Furthermore, we obtained feedback and opinions on communication through free-form responses. Additionally, we will provide detailed comparisons of the average values and standard deviations from the questionnaire survey of the previous Robotic Avatar in the next chapter.

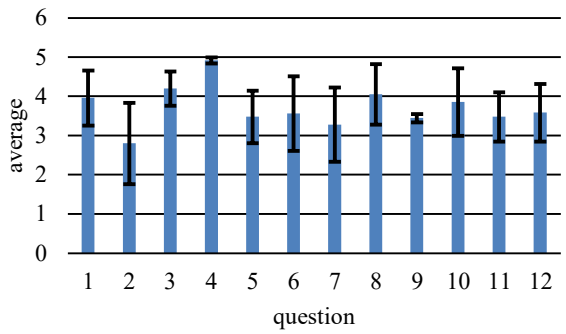

Figure 4 Results of the new Robotic Avatar survey.

4 Comparison of survey results

Table 2 shows the average and standard deviation of both survey results. Firstly, questions 1 to 3 were about the appearance of the Robotic Avatar. It was found that compared to Robotic Avatar Ver.1, questions 1 and questions 2 for the new Telepresence Robot had lower average values and larger standard deviations. As one of the changes from Robotic Avatar Ver.1 mentioned in Section 3.1, raising the monitor to eye level with a person resulted in a higher height compared to Robotic Avatar Ver.1. Therefore, it was inferred that the height of the Robotic Avatar was causing a worse appearance compared to Robotic Avatar Ver.1, suggesting the need to miniaturize the Robotic Avatar to make it more acceptable to people. Secondly, questions 4 to 8 were about the impressions of interacting with the Robotic Avatar. In the survey results for Robotic Avatar Ver.2, 24 out of 25 people answered "No" to question 4, "Did you feel pain when interacting with the robot?". However, for question 8, "Was it comfortable to hug the robot?", the average was 4.05 with a standard deviation of 1.55, which was worse than the survey results for Robotic Avatar Ver.1. Additionally, comments in the free-text section included opinions such as "The hug was forceful" and "The hug was scary". This indicated that while the robot did not cause pain to the participants, the force of the arm made them feel scared. Therefore, it was concluded that it is necessary to slow down the speed of the arm and reduce the force when making contact with people. Finally, questions 10 to 12 were about the communication of the Robotic Avatar. Regarding question 11, "Did you feel like you were interacting with a person rather than a robot?", the average was 3.48 with a standard deviation of 1.26, which was higher compared to the results for Robotic Avatar Ver.1. As mentioned in Section 2.2.2, one of the challenges of Robotic Avatar Ver.1 was the delay in executing commands and the difficulty in perceiving the robot as human-like due to its significant deviation from the human form. Therefore, we consider that the robotic avatar used in this study was designed to resemble a human form, resulting in an improvement in this issue.

Table 2 Means and standard deviations of the results of both questionnaires

	average		standarddeviation	
No.	Ver.1	Ver.2	Ver.1	Ver.2
1	4.55	3.96	0.55	1.40
2	3.4	2.80	1.24	2.08
3	3.95	4.2	2.05	0.88
4	4.85	4.92	0.43	0.15
5	4.25	3.48	0.49	1.34
6	3.5	3.56	1.15	1.90
7	4.05	3.28	1.35	1.89
8	4.1	4.05	1.19	1.55
10	3.75	3.86	1.79	1.72
11	2.85	3.48	1.63	1.26
12	3.65	3.58	1.43	1.46

5 Conclusions

An impression survey was conducted using a questionnaire for soft avatar robot Ver.1. As a result, it became clear that motion delays and the robot's distant appearance make it difficult for individuals to perceive the other party as human. Based on the issues identified through user testing, a soft avatar robot Ver.2 was developed. Subsequently, the results of the user testing for both versions were compared. The comparison revealed that, although participants perceived Ver.2 as soft upon seeing the robot, its appearance was intimidating, making it difficult for them to approach. Additionally, Ver.2's taller height compared to Ver.1 negatively impacted the appearance of the telepresence avatar robot, and the movement of the arms induced fear in the participants.

6 Acknowledgement

The authors gratefully acknowledge funding by Tokyo metoropolitan industrial technology research institute through Project to promote 5G, IoT, and Robotics among SMEs.

7 Literature

[1] Oussama Khatib, Xiyang Yeh, Gerald Brantner, Brian Soe, Boyeon Kim, Shameek Ganguly, Hannah Stuart, Shiquan Wang, Mark Cutkosky, Aaron Edsinger, Phillip Mullins, Mitchell Barham, Christian R. Voolstra, Khaled Nabil Salama, MichelL ’Hour, and Vincent Creuze:Ocean One:A Robotic Avatar for Oceanic Discovery: IEEE Robotics & Automation Magazine, Vol.23,No.4, Nov.2016, pp.20-29.

[2] Kazuaki Takeuchi, Yoichi Yamazaki, Kentaro Yoshifuji : Avatar Work: Telework for Disabled People Unable to Go Outside by Using Avatar Robots "OriHime-D" and Its Verification: Tje 15th annual ACM/IEEE International Conference on Huma-Robot Interaction.

[3] Carman Neustaedter, Gina Venolia, Jason Procyk, Daniel Hawkins: To Beam or Not to Beam: A Study of Remote Telepresence Attendance at an Academic Conference: the 19th ACM Conference, pp.418-431.

[4] Xianzhi Tang, Huaqiang Li, Teng Ma, Yang Yang, Ji Luo, Haidan Wang, Pei Jiang: A Review of Soft Actuator Motion: Actuation, Design, Manufacturing and Applications, Actuators 11, 331.

[5] Yutaka HIROI, Akinori ITO, Eiji NAKANO: EVALUATON OF ROBOT-AVATAR-BASED USER-FAMILIARITY IMPROVEMENT FOR ELDERLY PEOPLE: Kansai Engineering International, Vol.8, pp.59-66.

[6] Wyatt Felt, Matthew A. Robertson, Jamie Paik: Modeling Vacuum Bellows Soft Pneumatic Actuators with Optimal Mechanical Performance, 2018 IEEE International Conference on Foft Robotics.

[7] Gabriel Dämmer, Hartmut Bauer, Michael Lackner, Rüdiger Neumann, Alexander Hildebrandt, Zoltán Major: Design and Additive Manufacturing of a Continuous Servo Pneumatic Actuator, Micromachines , Vol.14, Iss.8.

[8] Masaharu Kagawa, Colin W. Binns, Andrew P. Hills: Body composition and anthropometry in Japanese and Australian Caucasian males and Japanese females ,Asia Pac J Clin Nutr 2007,16pp.31-36.

[9] Dane Bertram: Likert Scales, CPSC 681—Topic Report. Poincare, 1-11.

Integrated Force Sensing Technology for Twisted String Actuation Using Conductive Yarns

Giuliano A. Giacoppo, Sina Öztürk, Peter P. Pott,
Institute of Medical Device Technology, University of Stuttgart
giuliano.giacoppo@imt.uni-stuttgart.de

Abstract

Twisted String Actuators (TSA) are compact, lightweight, and low-cost mechanical devices. They can be used in robotics to convert rotary motion into linear tensile force. It is often necessary to measure the tensile force of TSAs. However, these measurements are currently performed using external force sensors in TSA systems, which are bulky and expensive. We propose to use conductive yarns as integrated force sensors to eliminate the need for external sensors, thus saving space and cost. Our approach calculates the applied force from the change in resistance of the conductive yarns, which changes with the angle of rotation and the applied force. To verify this approach, a mathematical model is developed and experiments are carried out on a TSA test rig using silver-coated conductive yarns as strings. The results show that the resistance decreases with increasing angle of rotation and force. However, for reliable and robust measurements, issues such as wear, standard deviation of resistance measurements, and yarn properties need to be addressed. Despite these challenges, the use of conductive yarns for TSA force sensors is promising, provided that improvements in yarn properties and contact friction are achieved.

1 Introduction

Twisted String Actuators (TSA) are compact, strong, lightweight, and low-cost mechanical devices that convert rotational motion into linear tensile forces. These actuators have a wide range of applications in different robotic devices since they have a very good tensile force to torque ratio. In most setups, two TSAs are required to work in antagonistic opposition because a single TSA provides only unidirectional tensile force. To maintain pre-tension in a system, it is often necessary to apply a controlled antagonistic force. However, today's methods for measuring and applying external force sensors in TSA systems are bulky and expensive, reducing the benefits of space-saving and low-cost technology. Currently, the tensile force applied to the TSA is measured using expensive strain-gauge-based force sensors [1] or spring systems with optical readout [2].

Our aim is to use conductive yarns as integrated force sensors to eliminate the need for an external force sensing principle, saving both space and cost. The force applied to the TSA is calculated from the strain-dependent resistance of these conductive yarns. The change in resistance results from changes in the cross-sectional shape of the helix as it rotates (Figure 1), depending on both the applied force and the rotation angle. The research question is whether changes in the cross-sectional shape can be used to develop a force sensor that detects the tensile force on a TSA as a function of the measured rotation angle and the change in resistance.

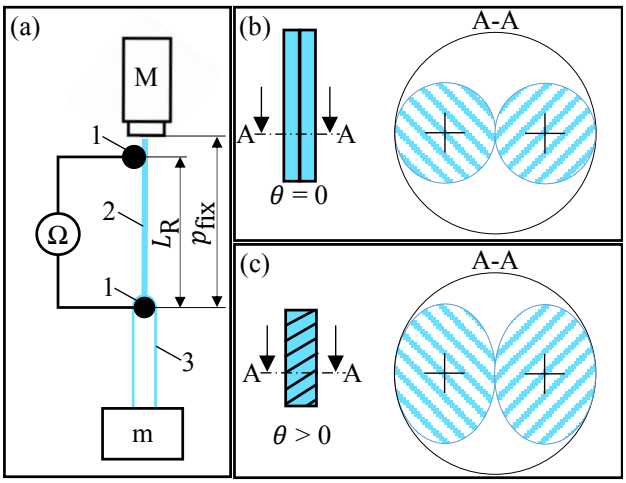

Figure 1 Schematic illustration of the experimental setup (a) with the copper pin contacts (1) and the twisted (2) and un-twisted (3) yarns of the fixed-twist zone lifting a load. At a twist angle theta of zero, the yarns are adjacent and have a circular cross-section (b). As the twist angle increases, the cross-sectional area increases (c).

2 Material and Methods

A TSA is constituted by two or more strings twisted along their common longitudinal axis. When an electric motor twists the string bundle, it forms a helix, which reduces its initial length [3]. A pin is used to create a counter-torque and separate the individual strings, allowing twisting to take place in a pre-defined zone [4]. Another pin, located near the motor, acts as a contact to the helix. The two pins that are in constant contact with the helix and at a fixed distance L_R from each other are used to determine the resistance (Figure 1a). The following section presents a mathematical model of the change in resistance of a helix, as it occurs in a TSA, as a function of the angle of rotation and tensile force.

2.1 Mathematical Model

It is assumed that the electrical resistance of the helix is a function of the angle of rotation θ and the applied tensile force F: $R = f(\theta, F)$.

The electrical resistance

$$R = \rho \cdot \frac{L_R}{A} \tag{1}$$

of the helix formed when strings are twisted is considered to be a nearly ideal conductor and is therefore dependent on its specific electrical resistivity ρ, length L_R and cross sectional area A. It can be observed that for strings with an ideally circular cross section, the cross sectional area

$$A = n \cdot \pi \cdot r_H \cdot r_e \tag{2}$$

of the helix consists of two ellipses for $n = 2$ strings used, as shown in Figure 1b and 1c. It is assumed that the small half-axis of the ellipse is constant and corresponds to the radius $r = r_H$ of the string used. The large half-axis

$$r_e = \frac{r_H}{\cos(\alpha)} = \frac{r_H \cdot L_0}{\sqrt{L_0{}^2 - (\theta \cdot r_H)^2}} \tag{3}$$

of the ellipse, on the other hand, varies with the helix angle α (Figure 2) and therefore with the angle of rotation θ. This can be deduced from the trigonometric analysis of the right-angled triangle formed by unrolling the helix on a plane (Figure 2). The hypotenuse is the arc length L_0 of the helix. The horizontal cathetus is a multiple of the angle of rotation θ and the helix radius r_H, which is the string radius r for a two string helix. In a fixed twisting zone, where rotation is stopped by the position p_{fix} of a pin, the length

$$L_0 = \sqrt{(\theta \cdot r_H)^2 + p_{fix}{}^2} \tag{4}$$

of the arc can be determined using Pythagoras' theorem. Combining equations 2 to 4 with $n = 2$ gives the cross-sectional area

$$A = \frac{2 \cdot \pi \cdot r_H{}^2 \cdot \sqrt{(\theta \cdot r_H)^2 + p_{fix}{}^2}}{p_{fix}} \tag{5}$$

as a function of the angle of rotation θ.

The length and diameter of the string changes when tensile force is applied, resulting in a corresponding change in the radius of the helix $r_H = f(F)$. Under the effect of the tensile force F, longitudinal deformation occurs, with the axial strain

$$\varepsilon_a = \frac{F}{S} \tag{6}$$

depending on the strain stiffness S. Simultaneously, a transverse contraction

$$\varepsilon_t = \frac{\Delta r}{r_0} = \frac{r_H - r_0}{r_0} \tag{7}$$

is apparent. Poisson's ratio

$$\mu = -\frac{\varepsilon_t}{\varepsilon_a} \tag{8}$$

of the strings can be used to calculate the resulting helix radius

$$r_H = r_0 \left(1 - \frac{\mu}{S} F\right) \tag{9}$$

as a function of tensile force F and with the initial helix radius r_0 by $F = 0$ N.

Equations 1 to 5, taking into account the helix radius r_H according to equation 9, give the helix resistance

$$R = \frac{\rho \cdot L_R \cdot p_{fix}}{2 \cdot \pi \cdot r_H{}^2 \cdot \sqrt{(\theta \cdot r_H)^2 + p_{fix}{}^2}} \tag{10}$$

as a function of the angle of rotation θ and the tensile force F. The tensile force

$$F = \frac{S}{\mu}\left(1 - \frac{r_H}{r_0}\right) \tag{11}$$

for a known angle of rotation θ and resistance R can be calculated from equations 9 and 10. The helix radius r_H is determined from the resistance R.

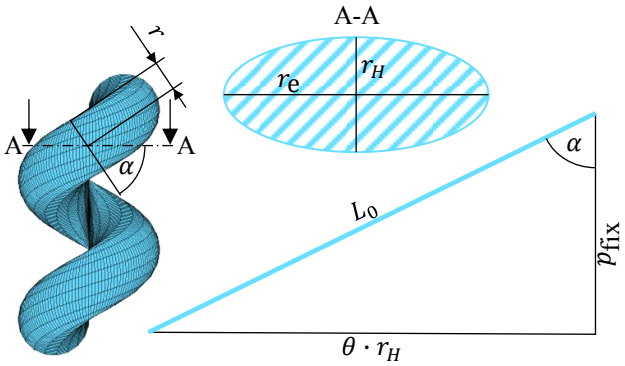

Figure 2 When the helix untwists on a plane within the fixed twist zone, it forms a right-angled triangle with the hypotenuse as the arc length L_0. The horizontal cathetus is a multiple of the angle of rotation θ and the helix radius r_H, which corresponds to the string radius $r = r_H$ for n = 2 strings. The height of the helix corresponds to the position of the fixed counter-moment p_{fix}. The cross section shows an ellipse with the small half-axis r_H and the large half-axis r_e.

2.2 Experimental Setup

To validate the model, conductive yarns (Shieldex® 235/36 HC+B, Statex Produktions- und Vertriebs GmbH, Bremen, DE) were placed as strings in a TSA test rig [5]. The yarns are made of silver-coated fibres (polyamide/nylon 6.6) with a resistance of < 600 Ω/m according to the manufacturer's data sheet. The TSA is driven by a DC motor (2657W024CR (51 mNm nominal torque at 5060 rpm), Faulhaber, Schönaich, DE with IE3-1024 incremental encoder) mounted vertically on a frame. Constant loads (5 N, 7 N, 10 N) were lifted n = 10 times. The absolute value of the resistance over the angle of rotation is determined over rotation angle increments. In order to measure the resistance, measuring contacts made of copper pins are attached to the helix (Figure 3). The copper pins were also coated with a copper-pigmented contact paste (ÄRONIX GmbH, Walldorf, DE) to reduce friction and improve electrical conductivity between the pins and the TSA. The resistance is determined via a Wheatstone bridge circuit. The measured resistance is compared with the calculated resistance from the mathematical model represented by eq-

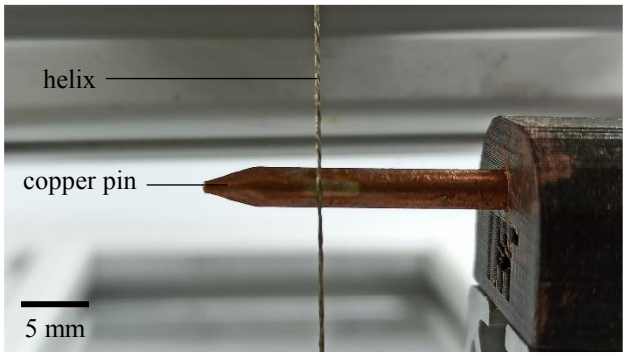

Figure 3 The helix, which is composed of two conductive yarns, is in contact with the copper pin.

uation 10. Apart from the geometric parameters, the parameters required for the calculation must be assumed. The values are given in Table 1. Measuring the resistance R and taking into account the known rotation angle θ allows the estimation of the tensile force acting on the TSA. To determine the unknown helix radius r_H from the resistance R, for which there is no explicit solution to equation 9, a numerical solution is used. The *fzero* function in Matlab (The MathWorks, Inc., Natrick, MA, USA) is used to determine the helix radius from the resistance. This makes it possible to determine the force for a known angle of rotation using equation 11.

3 Results

The results of the measurement indicate that for a constant load, the resistance decreases with increasing angle of rotation, which is consistent with the mathematical model (Figure 4). This has to be considered when calculating the force. Furthermore, the higher the load, the higher the resistance value and standard deviation.
The average resistance values at the respective angle of rotation were used to calculate the applied force (Figure 5). The root mean square error RMSE is less than 1 N compared to the reference value. In relation to the reference value, the relative error is 6.6 % at 5 N, 12.7 % at 7 N, and 9.5 % at 10 N.

Table 1: Calculation parameters and values

Symbol	Description	Value	Unit
α	helix angle	calculated	°
ε_a	axial strain	calculated	-
ε_t	transverse contraction	calculated	-
μ	poisson's ratio	0.5	-
θ	angle of rotation	measured	rad
ρ	specific electrical resistance	4.5e-4	Ωm
A	cross sectional area of the helix	calculated	m²
F	force	calculated	N
L_0	arc length of the helix	calculated	m
L_R	resistance measurement length	117e-3	m
p_{fix}	Position of the bolt for the TSA	137e-3	m
R	Resistance	calculated	Ω
r_0	initial helix radius	0.55e-3	m
r_e	large half-axis	calculated	m
r_H	helix radius	calculated	m
S	strain stiffness	16.7	N

4 Discussion

The use of conductive yarns for resistance measurement in a TSA has been demonstrated to be basically functional. However, a limitation of this approach is that the resistance measurement exhibits a notable degree of variability. It is postulated that this may be attributed to the electrical contact.
Furthermore, friction on the copper pins affects the behaviour of the TSA and leads to a reduction in the yarns' lifetime. The conductive yarns are subject to wear and tear as the silver coating on the yarns wears off and deposits on the pin. It is also necessary to consider the low breaking force of the yarns themselves. In order to design an actuator system capable of withstanding higher loads, it is necessary to identify conductive yarns that can withstand such loads. Additionally, it can be observed that the yarns exhibit variability in their properties, including resistance and diameter, over the entire length. This may also contribute to the high standard deviation. The large relative error is likely a

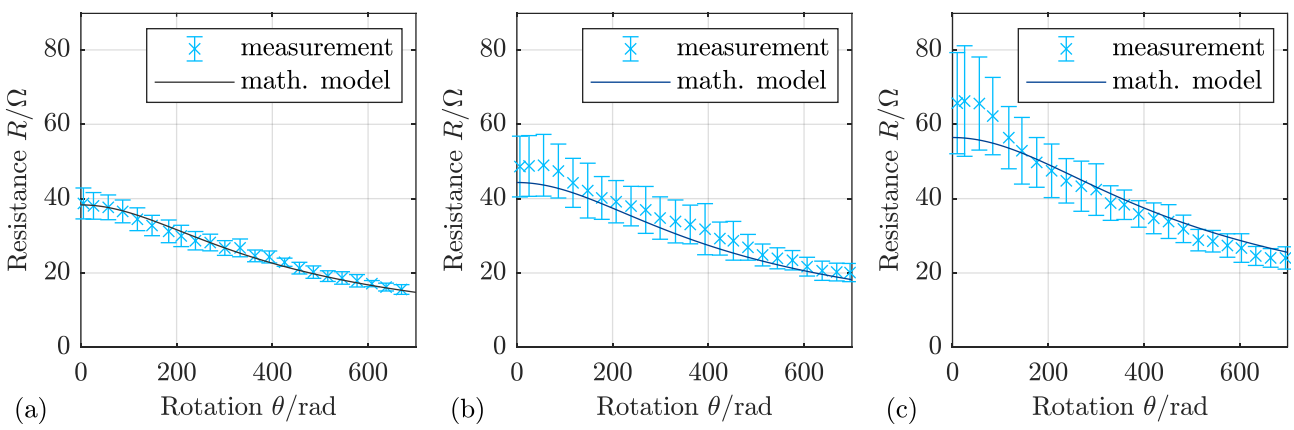

Figure 4 Results of the resistance measurements over the rotational angle theta at loads of 5 N (a), 7 N (b), and 10 N (c). For each load condition, the rotational angle increments were approached ten times.

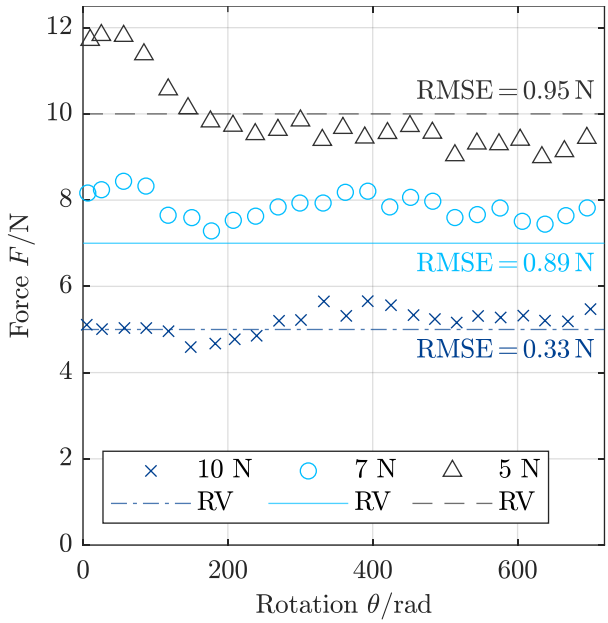

Figure 5 Results of calculating the force F applied to the TSA depending on the angle of rotation θ compared to the reference value RV. The average resistance values R measured were used to calculate the force.

consequence of this variability. To ensure reliable and robust measurement, it is essential to maintain consistent properties across the length of the yarn.
Verification of the parameters used is essential to ensure accuracy and reliability. Currently, the results of the mathematical model are based on assumed parameters that may not reflect the actual properties. An example of this is the specific electrical resistance of the yarns, which has not yet been accurately determined. This ambiguity can lead to distortions, especially if the specific electrical resistance is not constant over the angle of rotation. The formation of a helical structure introduces an anisotropy that must be taken into account.
It is also important to note that the contact resistance is not currently included in the mathematical description. Furthermore, the current mathematical description is incomplete because it fails to account for the fact that the tensile force F acting on the helix in the longitudinal direction is not equal to the internal axial tensile force of the yarns. The internal axial tensile force depends on the helix angle α and is currently underestimated. As the helix angle increases, the inner axial tensile force acting on the yarns will increase, as will the axial strain ε_a.

In conclusion, the utilisation of conductive yarns as integrated force sensors for TSA is is feasible. Nevertheless, it is apparent that further research and development are required to overcome the challenges that have been identified.

Author Statement
Research funding: The author state no funding involved.
Conflict of interest: Authors state no conflict of interest.

5 Literature

[1] Weymann, S. et al. "Development of an EMG-based Elbow- Exoskeleton with Twisted String Actuation" Current Directions in Biomedical Engineering, vol. 8, no. 2, 2022, pp. 552-555.

[2] Scarcia, U. et al. "Design of a twisted-string actuator for haptic force rendering." IFAC-PapersOnLine 51.22 (2018): 479-485.

[3] G. Palli, C. Natale, C. May, C. Melchiorri and T. Wurtz, "Modeling and Control of the Twisted String Actuation System," in IEEE/ASME Transactions on Mechatronics, vol. 18, no. 2, 2013, pp. 664-673.

[4] G. A. Giacoppo et al., "Influence of a fixed twisting zone on Twisted String Actuation," ACTUATOR 2022; International Conference and Exhibition on New Actuator Systems and Applications, Mannheim, Germany, 2022, pp. 1-4.

[5] G. A. Giacoppo, M. B. Schaefer and P. P. Pott, "Endurance Test Rig for Twisted String Actuators," IKMT 2022; 13. GMM/ETG-Symposium, Linz, Austria, 2022, pp. 1-4.

Direct writing of multilayer multistimuli micro-actuators

Eleonora Galli[1], Nicolas Geid[1,2] , and Jürgen Rühe[1,2],
[1]Labor für Chemie und Physik von Grenzflächen, Institut für Mikrosystemtechnik (IMTEK), Universität Freiburg, Georges-Kohler-Allee 103, 79110 Freiburg
[2]Freiburger Zentrum für interaktive Werkstoffe und bioinspirierte Technologien (FIT), Universität Freiburg, Georges-Kohler-Allee 105, 79110 Freiburg
eleonora.galli@students.uni-freiburg.de

1 Introduction

The rising demand for magnetic micro-actuators in microfluidics, particularly for tasks such as microliter-scale liquid pumping in lab-on-a-chip applications and precise mechanical manipulation of cells, has driven the need for advanced fabrication techniques. While previous approaches, predominantly mask-based or template-based methods, have played a pivotal role in the fabrication of these actuators, they encounter limitations when applications demand the individualized design of complex structures or varied chemical properties along each structure.
The conventional methods' limitations are effectively addressed by this study, which introduces an innovative one-step direct writing technique for multilayer micro-actuators using two-photon lithography (2PL). Actuation controlled by magnetic field variations can be achieved by including superparamagnetic nanoparticles [1] in the top-layer polymer (**Figure 1**).

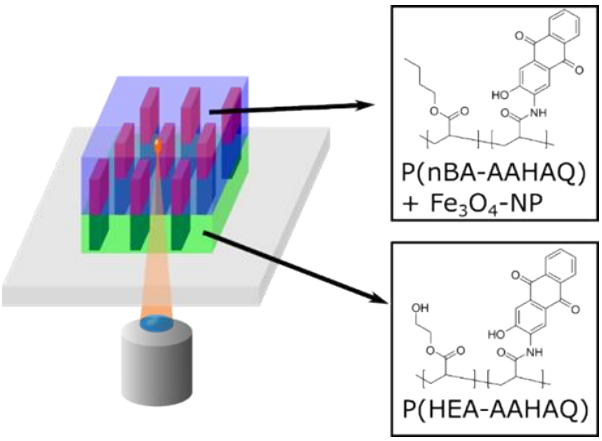

Figure 1 Scheme of direct writing process of microstructures into double polymer layer via two-photon lithography.

2 Materials and writing technique

Our cutting-edge approach employs a photochemical C,H insertion cross-linking (CHic) reaction [2] within solid polymers, specifically a copolymer containing n-butyl acrylate and 2-hydroxyethylacrylate. Activated by a femtosecond laser, the reaction enables precise direct writing in all three spatial directions, facilitating voxel-by-voxel assembly [2]. At the core of our innovative approach is the utilization of a copolymers with primary functional group and a photoreactive species (anthraquinone). The resulting C,H insertion reaction initiates two-photon cross-linking, independently of chain nature, promoting the joining of different solid polymer layers into a cohesive network. This unique feature results in the creation of stable surface-attached microstructures [3], seamlessly integrating different solid polymer layers into a cohesive and stable structure [4] (**Figure 2**).

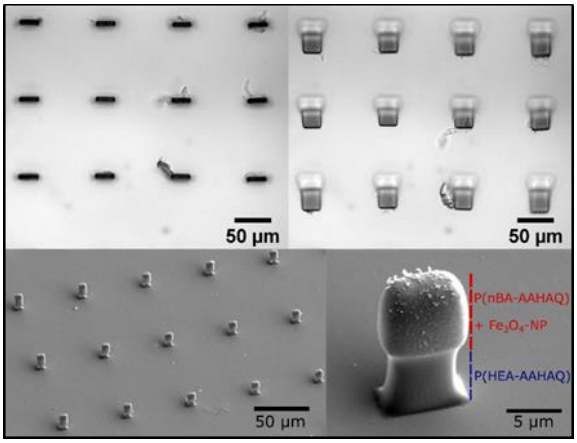

Figure 2 Top pictures: light microscope images of multilayered micro actuators deflected under an external magnetic field. Bottom pictures: SEM images of the microstructures showing the two layers.

The advantage of this technique lies in the possibility to combine the properties of different polymers in one structure. For instance, a softer hydrophilic bottom layer can increase the deflection range and stability of structures in aqueous medium, which is required by most biological applications. A schematic representation of a double-layer system is shown in **Figure 3**.

In addition, this technique can lead to great technological advancement, such as micro-actuators cotrolled by multiple stimuli. Multistimuli actuation can be achieved by combining layers of polymers, each responsive to a specific kind of stimulation. In particular, we design and prototype three-dimensional micro-structures made of a magneto-responsive top layer and a thermo-responsive bottom layer. The top layer is a hydrophobic polymer network which incapsulates superparamagnetic nano particles.

Therefore a force *F* is applied to the micro-structures when immersed in a magnetic field.

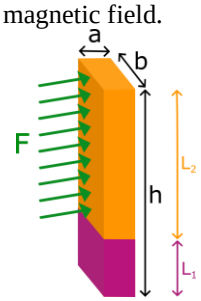

Figure 3 Scheme of the structure of a multistimuli actuator. The different materials are represented by the two colors. The parameters relevant to the actuation range are specified.

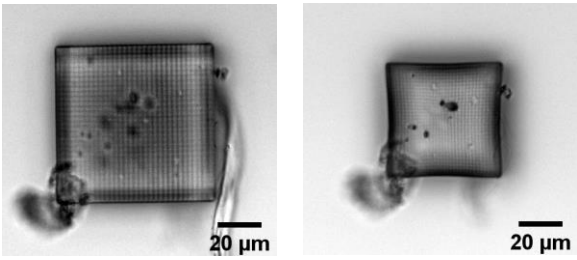

Figure 4 Swelling of te same cubic structure in water at different temperatures. On the left, T < T*; on the right, T > T*.

The bottom layer is charaterized by a temperature dependent stiffness. This property is due to the behavior of one of the copolymers, the N-Isopropylacrylamid (NIPAM), in water [5]. At lower temperatures (of order of 0 °C), the polymer network significantly swells in water (**Figure 4**), making the structure softer, hence prone to actuation even when a small force *F* is applied. Conversely, an increase in temperature determines an increase in Young's modulus: there must be a temperature *T** at which the force *F* is insufficient to produce appreciable actuation, thus at *T** a lock mechanism is switched on. This thermally driven lock-unlock mechanism overlaps the actuation driven by magnetic field variation. Crucial parameters for the multistimuli controlled actuation are the aspect ratio of the structures, the ratio of top and bottom layer Young's modulus and the relative thickness of the two layers.
The geometry related parameters can be freely tuned to achieve a great variety of actuation range.
For intance, a variation of the volume distribution and structure's thickness along its height can produce actuators with a various deflection ranges and with specific surface properties to adapt them to peculiar applications.

3 Conclusion

Our technique's versatility opens up a wide range of diverse applications. The ability to precisely differentiate the chemical properties of different layers during the one-step printing process allows the creation of magnetic micro-actuators with tailored functionalities. For example, our approach enables the design of micro-actuators with cell adhesion properties on the top layer, while a cell-repellent behavior characterizes the bottom layer of the structures and of the surface they are attached to. This unique capability is particularly promising for applications in mechanical cell stimulation, where controlled interaction with cell surfaces is critical. In addition, our method offers the possibility of designing bistable and multi-stimulus responsive systems, thereby increasing the adaptability and functionality of the micro-actuators, making them suitable for a range of applications where reversible and switchable behavior is desired.

4 Literature

[1] N. Geid; J. U. Leutner; O. Prucker; J. Rühe. "Maskless Writing of Surface-Attached Micro-Magnets by Two-Photon Crosslinking". In: Actuators 12 (2023).

[2] A.J.Straub, F.D.Scherag, H.I.Kim, M.Steiner, T.Brandstetter; J. Rühe. . "'CHicable' and 'Clickable' Copolymers for Network Formation and Surface Modification". In: Langmuir 37 (2021).

[3] D. Schwärzle; X. Hou; O. Prucker; J. Rühe. "Polymer Microstructures through Two-Photon Crosslinking." In: Advanced materials 29 (2017).

[4] O. Prucker; T. Brandstetter; J. Rühe. "Surface-attached hydrogel coatings via C,H-insertion crosslinking for biomedical and bioanalytical applications (Review)". In: Biointerphases 13 (2017).

[5] D.Song, F.Kotz-Helmer, B.Rapp, J. Rühe. . "Substrate-Independent Maskless Writing of Functionalized Microstructures Using Chic Chemistry and Digital Light Processing". In: ACS Applied Materials & Interfaces 14 (2022).

[6] K.Jain, R.Vedarajan, M.Watanabe, M.Ishikiriyama, N.Matsumi. "Tunable LCST behavior of poly(N-isopropylacrylamide/ionic liquid) copolymers". In: Polym. Chem. 6 (2015).

Rate Dependent Prandtl-Ishlinskii (RDPI) Model based motion compensation of Mitraclip® Delivery System

Syed Zain Mehdi[a], Mouloud Ourak[a], and Emmanuel Vander Poorten[a]
[a]Department of Mechanical Engineering, KU Leuven, Celestijnenlaan 300B, 3001 Leuven,Belgium

Abstract

Mitral Valve regurgitation is a heart condition where the mitral valve doesn't close properly, causing backward blood flow. Transcatheter Edge to Edge Repair (TEER) with Mitraclip® is used for treating this condition. Efforts are underway to robotize this process however, the Mitraclip® cable-driven actuation of the instrument causes friction-related deadband and hysteresis during bending and translation. These complexities are compounded by the beating heart. This paper focuses on investigating and addressing hysteresis that arises during Clip Delivery System (CDS) translation inside a Steerable Sleeve Catheter (SSC) of the Mitraclip instrument. Rate-dependent Prandtl-Ishlinskii (RDPI) model has been used for modeling and compensating for these non linearities. The performance of the model in combination with a feed-forward controller against varying signals and different bending configurations is reported, showing better tracking performance and reduced error.

1 Introduction

Mitral Regurgitation (MR) is the most common valvular heart disease [1]. Clinical guidelines recommend mitral valve surgery in patients with severe MR; however, a large number of such patients have high surgical risk due to advanced left ventricle systolic dysfunction. Transcatheter Edge to Edge Repair (TEER) using Mitraclip® implantation is used to treat such conditions as an alternative for open heart surgery [2]. The procedure involves a transeptal puncture, followed by advancing a Clip Delivery System (CDS) via a Steerable Guide Catheter (SGC) into the left atrium, grasping the leaflets, and finally, the clip release. The instrument with multiple control knobs and different steps poses a unique challenge for new clinicians in their learning curve for optimizing clinical outputs [1]. The actuation of the sheath is cable-driven causing friction which introduces deadband and hysteresis during bending. The same applies to the translation of CDS inside a Steerable Sleeve Catheter (SSC) as showin in Figure 1. The beating heart also needs to be considered while the clip delivery system is deploying the clip. These non-linearities contribute to the operational difficulty of the instrument. ARTERY project funded by the EU aims to robotize this process by developing a robotic steerable guide catheter and accompanying control schemes. This study aims to investigate and address the hysteresis that arises during the translation of the CDS inside SSC as it is pushed proximally through the vessel crossing the septum and towards the heart. Additionally, motion compensation using the developed hysteresis model is also implemented. The following sections describe in further detail the experimental setup and methodology for achieving the above-mentioned results.

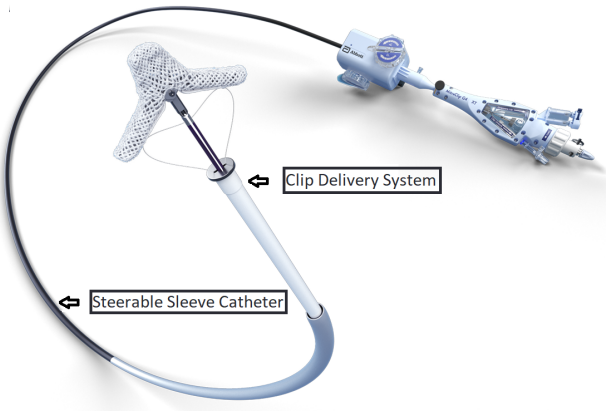

Figure 1 Clip Delivery System for Mitraclip® (Abbott Laboratories, Menlo Park, California, USA)

2 Motion Compensation of the Tip

As was observed experimentally, a rate-dependent hysteresis exists between the Clip Delivery System and the Steerable Sleeve Catheter. Aside from hysteresis, a dead band also exists both of which are dependent on input frequency and the bending angle. To compensate for this hysteresis nonlinearity effect, different methods can be used. Classical methods include Bouc-Wen [3], Prandtl-Ishlinskii [5], Preisach [8], and Maxwell-slip [9]. Recently deep learning based methods [6] have also been deployed to model and compensate for nonlinear hysteresis effects. We selected the Rate Dependent Prandtl-Ishlinskii model [5] for this study as it can effectively characterize hysteresis nonlinearities in various systems, and the inverse can be easily used in feed-forward compensation to eliminate hysteresis effects.

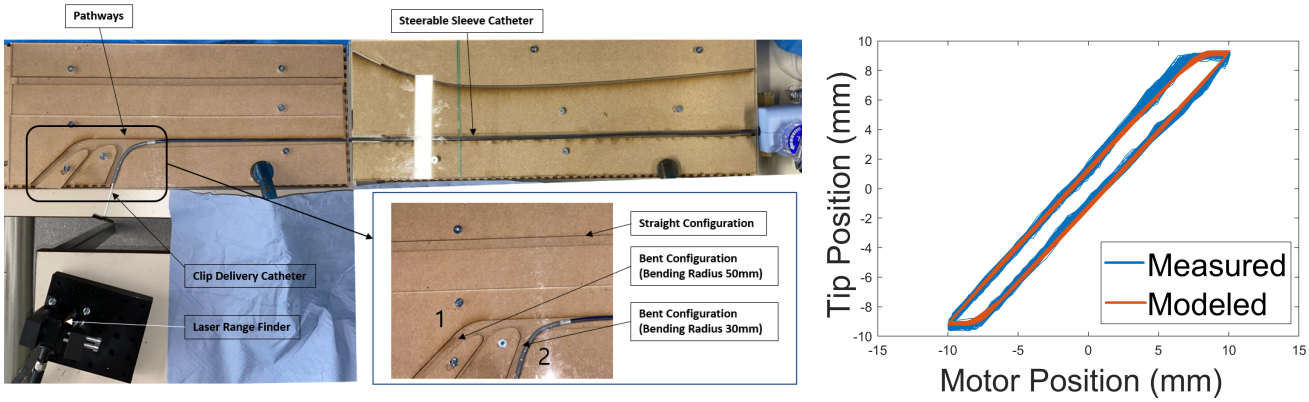

(a) (b)

Figure 2 (a) Setup used for data acquisition. A laser range finder was used for measuring tip displacement for two different configurations. (b) Hysteresis Loop between motor and tip position and its RDPI Model

2.0.1 Rate-Dependent Prandtl-Ishlinkii (RDPI) Model

The Rate dependent Prandtl-Ishlinksii(RDPI) model integrates play operators with different thresholds to characterize hysteresis. The output of the RDPI model can be expressed as

$$\psi(u(t)) = a_0 u(t) + \sum_{i=1}^{n} a_i \phi_{r_i(u'(t))}[u, x_i](t) \tag{1}$$

where: n represents the number of time-dependent play operators, a_0 and a_i are positive weights, $x_i \in [-r_i, r_i]$ are given initial conditions, $r_i(u'(t))$ are dynamic thresholds, ϕ is the time-dependent play operator, which is a function of input u and the initial conditions x_i.
The dynamic threshold $r_i(\dot{u}(t))$ can be expressed as

$$r_i(\dot{u}(t)) = \alpha_i + g(\dot{u}(t)) \tag{2}$$

where $\alpha_i = \delta_i$ for $i = 1, 2, \ldots, n$ and δ is a positive constant. The function $g(\dot{u}(t))$ is chosen as

$$g(\dot{u}(t)) = \beta |\dot{u}(t)| \tag{3}$$

where β is a positive constant.
If the input u is monotone in an interval $t \in [t_0, t_i]$, then the output of the play operator $\zeta(t) = \phi_{r_i(\dot{u}(t))}$ can be written as

$$\zeta(t) = P(u(t), r, \zeta_0(t)) \quad \text{for} \quad t \in [t_0, t_1] \tag{4}$$

where the function $P(U, R, Z)$ is defined as

$$P(U, R, Z) = \max(U - R, \min(U + R, Z)) \tag{5}$$

2.0.2 Inverse Rate-Dependent Prandtl-Ishlinkii (IRDPI) Model

The inverse of the RDPI can be expressed as

$$\psi^{-1}[u](t) = b_0 u(t) + \sum_{i=1}^{n} b_i \phi_{s_i(u'(t))}[u, y_i](t) \tag{6}$$

where: $\phi_{s_i(u'(t))}[u, y_i](t)$ is the output of the rate-dependent play operator of the inverse model. The thresholds of the inverse model are

$$s_1(\dot{u}(t)) = a_0 r_1(\dot{u}(t)) \tag{7}$$

$$s_{i+1}(\dot{u}(t)) = s_i(\dot{u}(t)) + \left(\sum_{j=0}^{i} a_j \right) (r_{i+1}(\dot{u}(t)) - r_i(\dot{u}(t))) \tag{8}$$

The weights of the inverse model $b_0, b_1, \ldots, b_n$ are

$$b_0 = \frac{1}{a_0}, \quad b_i = \frac{1}{\sum_{j=0}^{i} a_j} - \frac{1}{\sum_{j=0}^{i-1} a_j} \tag{9}$$

The initial conditions of the inverse model $y_1, y_2, \ldots, y_n$ are

$$y_1 = a_1 x_1 \tag{10}$$

$$y_{i+1} = y_i + \left(\sum_{j=0}^{i} a_j (x_{i+1} - x_i) \right) \tag{11}$$

Readers are directed towards [5] for a detailed tutorial on the model.

2.1 Experimental Setup

To identify the rate-dependent hysteresis for the CDS the setup shown in Figure 2 (a) was used where two different arrangements were utilized to capture a wide operational range:

1. Configuration with a bending radius of 50 mm
2. Configuration with a bending radius of 30 mm

The translation of the catheter was achieved using Faulhaber Linear Motors (LM-2070). The displacement of the tip was measured using a laser range finder (Baumer 8501). The data was acquired using the Compact-Rio data acquisition module.

2.2 Parameter Identification

To acquire data for identifying the parameters of the RDPI model, an input displacement signal $x_{\text{in}}(t)$ with varying sinusoidal frequency was used:

$$x_{\text{in}}(t) = A \sin\left(2\pi \int_0^t \left(f_s + \frac{f_f - f_s}{t_{\text{tot}}} \right) dt \right) \tag{12}$$

where $A = 10\,\text{mm}$ is the sine amplitude, $f_s = 0.1\,\text{Hz}$ and $f_f = 3\,\text{Hz}$ are the starting and final frequencies, $t_{\text{tot}} = 80\,\text{s}$ is the total time. The function was evaluated over each

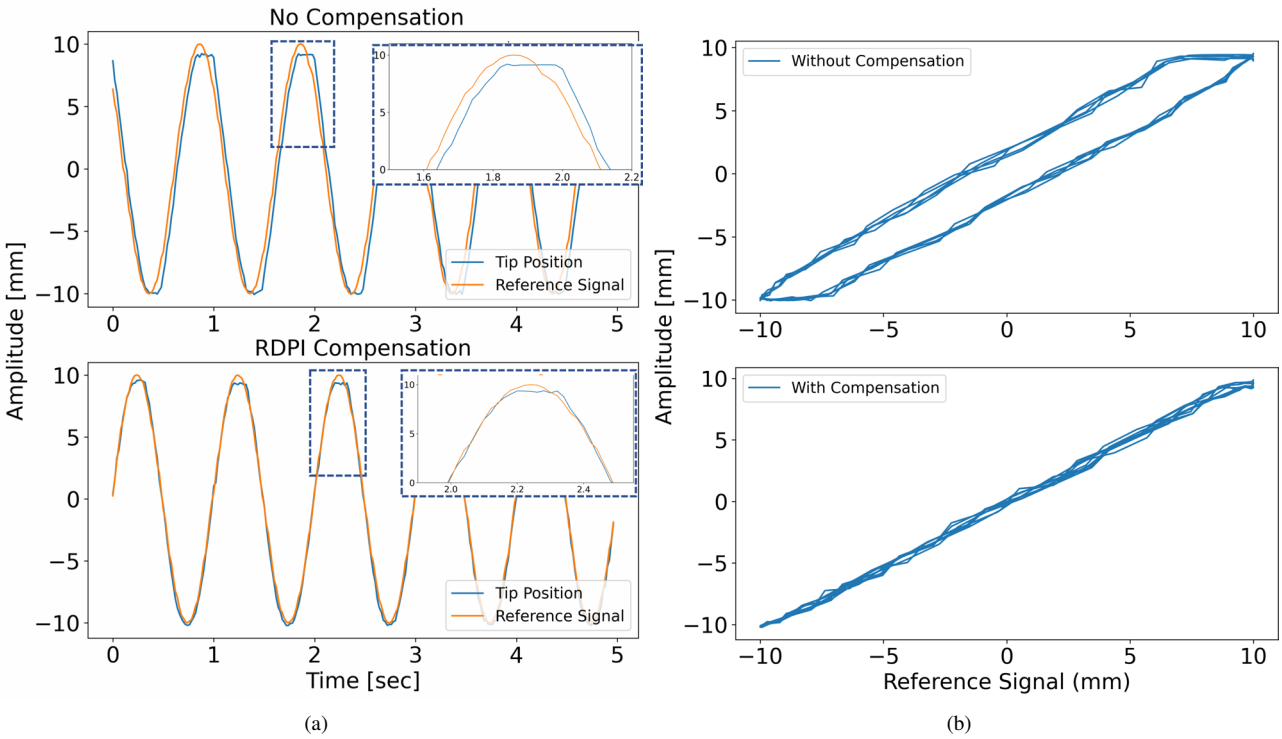

Figure 3 (a) Top: Input signal without Compensation, Bottom: Input signal with Compensation (b) Top: Resulting hysteresis without Compensation, Bottom: Resulting hysteresis with Compensation

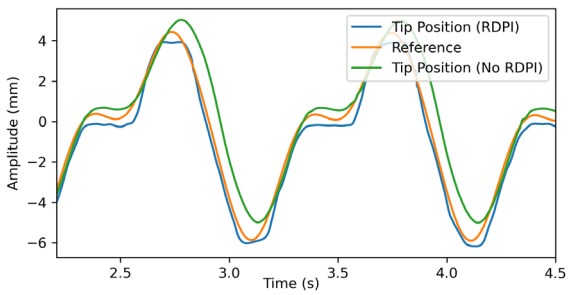

Figure 4 Tracking performance of the model against heart motion profile input signal

interval $\Delta t = 0.025\,s$. Configuration 1, with a bending radius of 50mm, was used to acquire data. The tip was made to protrude slightly out of the pathway to ensure one-dimensional translation at the tip, allowing us to measure the displacement easily. The acquired data was used to identify parameters for the model. Only 5 Play operators were used to model the hysteresis. The resulting hysteresis loop and the hysteresis model are shown in Figure 2 (b). FMINCON from the MATLAB Optimization Toolbox was used for the optimization. The identified parameters were $a_0 = 0.0053$, $a_1 = 0.3138$, $a_2 = 0.0066$, $a_3 = 0.3656$, $a_4 = 0.1536$, $a_5 = 0.1802$, $\zeta_1 = 0.8403$, $\zeta_2 = 0.6736$, $\zeta_3 = 1.0956$, $\zeta_4 = 0.8234$, $\zeta_5 = 1.1194$, and $\beta = 0.0024$, where $a_{0..5}$ are the weights, $\zeta_{1..5}$ are the constants for the dynamic threshold operator, and β is a positive constant.

2.3 Experimental Validation

To test the performance of the model, the two configurations mentioned in section 1.2 were considered. A sinusoidal input displacement signal $A\sin(2\pi f \Delta t)$ with an amplitude A=10 mm and f=1,2,3 Hz was used as input, and the tip position was monitored against the input signal. The result for f = 1Hz for configuration 1 is shown in Figure 3. RMSE for the experiments using both configurations are reported in Table 1. To validate the model in a more realistic scenario, a heart motion profile signal was generated with major frequency components around 1.3 Hz, 2.6 Hz, and 5.2 Hz according to the following equation [7].

$$x(t) = c + \sum_{i=1}^{m} r_i \sin(i\omega t + \theta_i) \tag{13}$$

where $x_h(t)$, where c is the motion offset, m is the total number of sinusoid harmonics, r_i is the amplitude of the i-th sinusoid, ω is the fundamental angular frequency (2π rad/s in this case), θ_i is the angular phase shift of the i-th sinusoid harmonic, and t is the time. The simulation was carried out with $c = 0.0\,mm$, $r_{i=1...8} = [4.0, 2.0, 0.4, 0.1, 0.005, 0.001, 0.0005]\,mm$, $\omega = 2\pi\,rad/s$, and $\theta_{i=1...8} = [0.0, 2.8, 2.8, 0.0, 3.7, 1.2, 5.6, 7.3]\,rad$. The scenario is similar to the situation that arises just before deploying the clip, where the heart's beating motion needs to be taken into account. Configuration 2 was selected for this test because it resembled the actual arrangement of CDS in the left atrium just before deploying the clip. The model was effectively able to compensate for hysteresis with an RMSE of 0.47 mm with the RDPI model against 1.32 mm without the RDPI model, as shown in Figure 4 and the resulting hysteresis loops can be seen in Figure 5

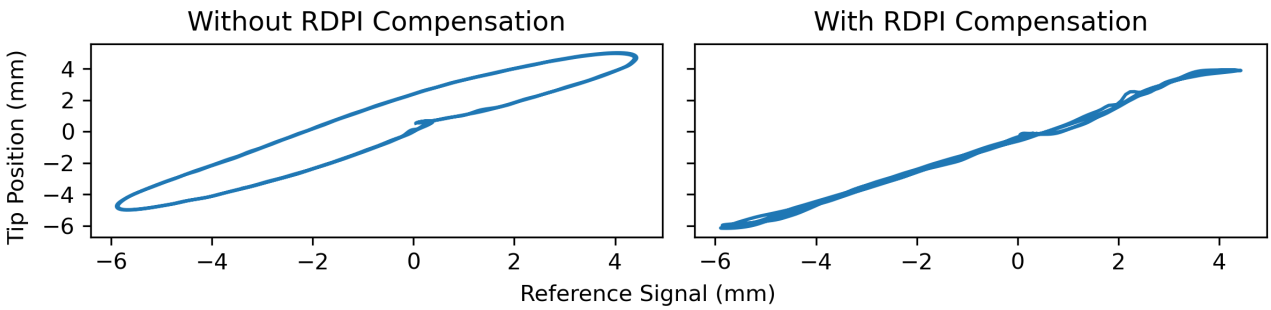

Figure 5 Resulting Hysteresis loop for heart motion profile signal. [Left] Without RDPI Compensation [Right] With RDPI Compensation

Table 1 RMSE for the experiments (Error in mm, Frequency in Hz)

Frequency	Configuration 1		Configuration 2	
	No RDPI	RDPI	No RDPI	RDPI
1	1.49	0.4	1.48	0.67
2	2.2	0.9	1.9	1.26
3	2.93	1.67	2.45	1.48
Heart Signal			1.32	0.47

3 Conclusion and Results

The RDPI model was successfully able to model hysteresis associated with the translation of the catheter and, in conjunction with a feedforward controller reduced the tracking error. Moreover, the experiments with the heart motion profile tracking showed the adequacy of the RDPI model in improving motion compensation performance. The error, however, increases as the frequency goes up. Future work will focus on force tracking in addition to motion compensation for increased robustness.

4 Acknowledgments

This work received funding from the European Union's Horizon 2020 research and innovation programme under grant agreement No.101017140, the ARTERY project and CURE, a KU Leuven internal project (3E210658). The authors would like to thank Mohammad Al Saaideh, Mohammad Al Janaideh, Yao Zhang, and Di Wu for their valuable help and suggestions.

5 References

[1] Sherif MA, Paranskaya L, Yuecel S, Kische S, Thiele O, D'Ancona G, Neuhausen-Abramkina A, Ortak J, Ince H, Öner A. "MitraClip step by step; how to simplify the procedure". Neth Heart J. 2017 Feb;25(2):125-130.

[2] Vuyisile T Nkomo, Julius M Gardin, Thomas N Skelton, John S Gottdiener, Christopher G Scott, Maurice Enriquez-Sarano, "Burden of valvular heart diseases: a population-based study", The Lancet, Volume 368, Issue 9540,2006, Pages 1005-1011.

[3] F. Ikhouane, M. Victor, and J. Rodellarab, "Dynamic properties of the hysteretic Bouc-Wen model," Syst. Control Lett., vol. 56, no. 3, pp. 197–205, Mar. 2007, doi: 10.1016/j.sysconle.2006.09.001.

[4] I. D. Mayergoyz, "Mathematical Models of Hysteresis and Their Applications". New York, NY, USA: Elsevier, 2003.

[5] M. Al Janaideh and P. Krejčí, "Inverse Rate-Dependent Prandtl–Ishlinskii Model for Feedforward Compensation of Hysteresis in a Piezomicropositioning Actuator," in IEEE/ASME Transactions on Mechatronics, vol. 18, no. 5, pp. 1498-1507, Oct. 2013, doi: 10.1109/TMECH.2012.2205265.

[6] D. Wu et al., "Hysteresis modeling of robotic catheters based on long short-term memory network for improved environment reconstruction," IEEE Robotics and Automation Letters, vol. 6, no. 2, pp.2106–2113, 2021

[7] S. G. Yuen, et al., "Robotic motion compensation for beating heart intracardiac surgery," International Journal of Robotics Research, vol. 28, no. 10, pp. 1355–1372, 2009

[8] I. Mayergoyz, "Mathematical models of hysteresis," IEEE Transactions on Magnetics, vol. 22, no. 5, pp. 603-608, September 1986, doi: 10.1109/TMAG.1986.1064347.

[9] Y. Liu, H. Liu, H. Wu, and D. Zou, "Modelling and compensation of hysteresis in piezoelectric actuators based on Maxwell approach," Electron. Lett., vol. 52, no. 3, pp. 188–190, Feb. 2016, doi: 10.1049/el.2015.3138

Light-controlled mechanisms based on photomobile polymers for seamless integration in demanding environments

Mathieu Thomachot, Jolan Gauthier, Patrick Meneroud, Sylvain Duc, Frank Claeyssen, Guillaume Mansuy Cedrat Technologies, Meylan, France
mathieu.thomachot@cedrat-tec.com

Abstract

Photomobile polymers (PMP) are active materials that convert light into mechanical movement. They can be used in energy harvesters, light-controlled actuators, or mechanisms. Because they are controlled by light and work without electricity, they offer unique opportunities for designing devices that can be integrated seamlessly and that require virtually no maintenance. This finds interest in fields like nuclear energy, medical implants, biology, space, or Internet of Things (IoT). Cedrat Technologies have designed, built, and tested 3 proof of concept prototypes: a mechanical switch, a mechanical valve, and an optical deflector. The present paper will present these 3 concepts and the tests results in detail.

1 Photomobile polymers

Photomobile polymers are made by the polymerization of Azo-LC-PMPs monomers which are azobenzene based liquid crystals. At molecular dimensions, the use of adapted light frequency changes the energy state and then modifies the shape of the polymer. The trans form (thermodynamically stable) can be converted to the cis form (metastable) using a UV wavelength of 300-400 nm. Visible illumination at >400 nm converts the molecule back to the trans form. Alternately, the molecule thermally relaxes to the stable trans form. At macroscopic dimensions the local deformation extends to the whole polymer film part and make it bend.

The interest of PMP is to get a high stroke actuation driven with light. The energy used is low and is supplied remotely. The counterpart of such characteristics is the generation of a slow movement with low forces.

2 Benefits of light-driven mechanisms

Light-driven mechanisms are controlled remotely, without wires or mechanical transmissions. This makes their integration very easy in environments that must be separated from the control area: vacuum, nuclear reactors, sterile chamber, human body. In such environment, a solution based on wires would require complex and expensive systems, such as feedthrough connectors or bellows, and would increase the risk of contamination.

3 Light-driven mechanisms prototypes

In the frame of the PULSE-COM, H2020-FETOPEN-2018-2020, 863227 project, 3 proof-of-concept mechanisms were designed, built and tested.

3.1 Opto-switch

3 different opto switch topologies were designed, manufactured, and tested: a normally closed switch, a normally open switch, and a selector switch. The prototype showing the most promising result is the normally closed switch, that was able to open and close a circuit with a current flowing through.

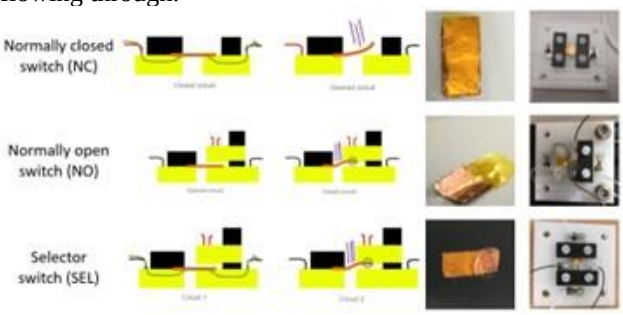

Figure 1 Opto-switch prototypes

3.2 Opto-valve

3 different kinds of opto-valves were designed and tested. The best results were obtained with prototype C, that showed a significant difference of flow between its open and close states.

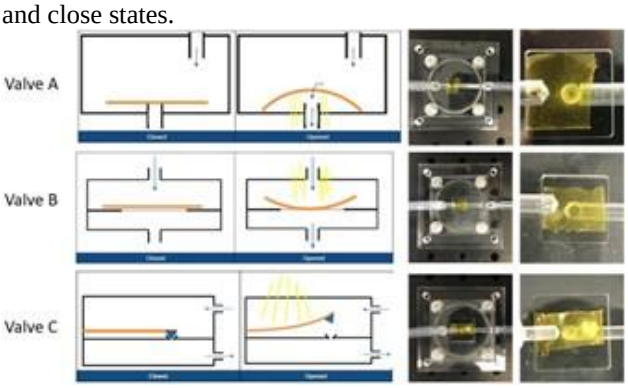

Figure 2 Opto-valves prototypes

3.3 Optical deflector

An optical deflector was made by fixing a mirror on a PMP device. The deflector showed its capability to change the orientation of a laser beam on one axis, in closed loop configuration.

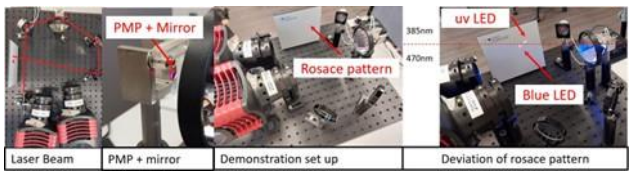

Figure 3 Deviation of a laser beam with a mirror mounted on a PMP device

4 Conclusion

The tested proofs of concept demonstrated the possibility of using PMP for designing light-driven mechanisms, opening new opportunities for innovative applications in demanding environments.

5 Literature

[1] Oscurato, S. L., Salvatore, M., Maddalena, P., Ambrosio, A., "From nanoscopic to macroscopic photo-driven motion in azobenzene-containing materials,", Nanophotonics, vol. 7, p. 40, (2018).

[2] Castagna, R., Rippa, M., Simoni, F. , Villani, F. , Nenna, G., Petti, L., "Plasmonic Photomobile Polymer Films," Crystals, vol. 10, p. 660, (2020).

[3] Castagna, R., et al., "An Unconventional Approach to Photomobile Composite Polymer Films,", Adv. Mater. Deerfield Beach Fla, vol. 29, no 13, (2017).

[4] Chen, M., et al., "Photodeformable CLCP material: study on photo-activated microvalve applications," Appl. Phys. Mater. Sci. Process., vol. 102, p. 667 672, (2011).

[5] Chen, M., et al., "Photodeformable polymer material: towards light-driven micropump applications," Appl. Phys. A, vol. 100, no 1, p. 39 43, (2010).

[6] Sagnelli, D., Rippa, M., D'Avino, A. Vestri, A., Marchesano, V., Petti, L. "Development of LCEs with 100% Azobenzene Moieties: Thermo-Mechanical Phenomena and Behaviors," Micromachines,13, x, pg#1-12 (2022).

[7] Jalabert, T., Pusty, M., Mouis, M., Ardila, G., "Investigation of the diameter-dependent piezoelectric response of semiconducting ZnO nanowires by Piezoresponse Force Microscopy and FEM simulations,", Nanotechnology, V34, N11, pg# 5402, (2023)

[8] Garcia, A.J.L., Mouis, M., Cresti, A., Tao, R., Ardila, G., "Influence of slow or fast surface traps on the amplitude and symmetry of the piezoelectric response of semiconducting-nanowires-based transducers," Journal of physics D: Applied physics, V55, N40, 405502, (2022).

[9] Wlazlo, M., Haras, M., Kolodziej, G., Szawcow, O., Ostapko, J., Andrysiewicz, W., Skotnicki, T., "Piezoelectric response and substrate effect of ZnO nanowires for mechanical energy harvesting in internet of things applications," Materials,1,0, pg#1-14 (2022).

[10] Peireira, P.V.D., Hundwarsden, M.T., Cahoy, K., "Characterization of laser thermal loading on micro-mechanical system-based fast steering mirror in vacuum," Opt. Eng. 59(5), pg#056109_1-056109_16 (2020).

Miniaturized Arbitrary Waveform Generator for Micropumps with Piezoelectric Actuators

Oliver Zett, Carlos Arteaga, Agnes Bußmann, Sebastian Kibler
Fraunhofer Institute for Electronic Microsystems and Solid State Technologies (EMFT), Munich, Germany
E-mail address oliver.zett@emft.fraunhofer.de

Abstract

Microdosing systems with micropumps have multiple applications in the biomedical field, e.g., drug delivery or implants. Many of these applications pose challenging restrictions in terms of system size, which is why micropumps are attractive. However, not only the microfluidic actuator itself, but also its driving unit needs to be miniaturized whilst preserving optimal performance. In the case of piezoelectric micro diaphragm pumps the performance strongly depends on the piezoelectric actuator and its driving signal in terms of signal form, frequency, and voltage amplitudes. We introduce a pump driver with custom signal generation to meet the requirements of the micropump while remaining small with an outline of 22x11.5 mm². This driver features a combined boost and boost-buck converter where the necessary Pulse-Width Modulation (PWM) is controlled by a microcontroller. The chip receives feedback from the high and low voltage generation to calculate the necessary PWM outputs and reach its target wave points. Frequency, waveform, as well as positive and negative peak voltages can be changed by user input. In this work, the signal generation from five Printed Circuit Boards (PCB) were measured, to demonstrate the capability of the system. Measurements with two wave forms include negative peak voltages from -10 V to -60 V and positive peak voltages from 50 V to 110 V with frequencies of up to 600 Hz. The miniaturized circuitry design enables flexibility for applications that require miniaturization. The flexible wave form generation enables to minimize the mechanical stress on the bending actuator and allows to optimize dosing precision and pressure generation.

1 Introduction

The application of micropumps for medical treatment and diagnostics has become more popular over the last decades [1]. The piezoelectric silicon micropumps developed by Fraunhofer-EMFT, are fabricated with precise semiconductor technology. A glued on piezoelectric disc actuator bends the pump's diaphragm upwards or downwards. The resulting compression and expansion of the pump chamber transports fluid from the inlet to the outlet (**Figure 1**). Both suction and ejection stroke are possible thanks to a flying inductor circuit which is controlled via Pulse-Width Modulated signals (PWM).

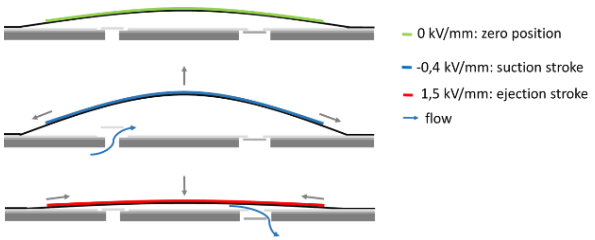

Figure 2 Micropump working principle. Figure adapted from [2].

The biomedical applications involving micropumps such as implants [3] or drug delivery systems [4], demand miniaturized devices with optimal functional features. The designed Printed Circuit Board (PCB) that drives the silicon pump, abides this idea, and can deliver high voltages in both positive and negative range regarding to ground potential without sacrificing functionalities. The PWM signals are generated by a microcontroller. The voltage output levels of the PCB presented in this article range from -60V to +110 V and are reached by employing the working principle of two circuits: Buck-boost converter and Boost converter, which we call flying inductor circuit [5].

1.1 Principles of high voltage generation

The flying inductor circuit merges the principle of the Buck-boost and Boost converter to generate both positive and negative voltages, respectively. The resulting voltages have a much higher magnitude than its primary voltage source Vcc. The circuit schematic is shown in (**Figure 3**). Furthermore, this configuration allows a compact PCB design. The boost converter is an electrical circuit that benefits from the electrical properties of the inductor to generate a higher voltage than its main voltage source. This can be achieved by controlling an attached P-MOSFET transistor through a PWM signal. All transistors will act as a digital switch, enabling the possibility to control the current flow. The working principle is described as follows:
In a polarized case, when the P-MOS is switched on, the current flows through the inductor L1 generating an increase of its magnetic field. At this stage, the diode D1 and BJT-PNP are in a non-conducting state. When the P-MOSFET is no longer polarized, a fast-decaying voltage peak is generated and stored in a capacitor or an equivalent element such as a piezoelectric actuator. Here both the BJT-NPN and D1 are in a conducting state and the total voltage delivered to the piezoelectric actuator is the sum of the voltage source plus the inductor's generated voltage peaks. The generated voltage is proportional to the duty cycle of the PWM applied to the gate of the P-MOSFET. The higher the duty cycle of the PWM signal, the higher the achieved voltage at the output.

Regarding the negative voltage generation (Buck-boost converter), the polarity of the diode D2 is inverted, a complementary transistor is implemented (N-MOSFET) and the BJT has a PNP character.

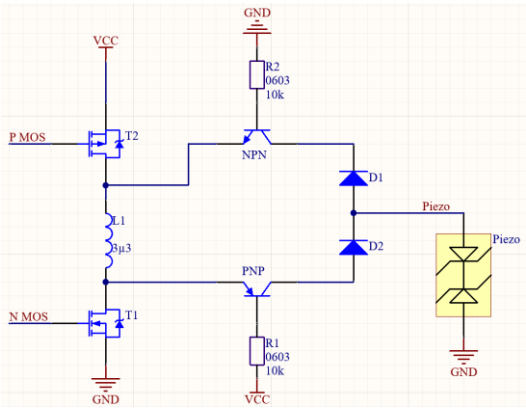

Figure 4 Flying inductor circuit for high voltage generation.

The performance regarding flow rate, suction pressure, and back pressure of the micropump relies on the applied output signal form in terms of voltage levels, frequencies and signal slope steepness [6].

2 Pump driver hardware and software features

Both, hardware and software of the pump driver are optimized to enhance pump performance and flexible use.

2.1 Pump Driver Hardware

The developed pump driver for piezoelectric micropumps is depicted in (**Figure 5**). The PCB dimensions are 22 x 11.5 x 1 mm^3. The top side (depicted in the left) consists of a USB-C connector, an STM32G941KEU6 microcontroller and a feedback circuit.

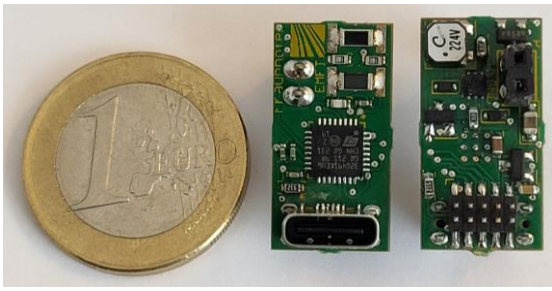

Figure 6 Two pump driver PCBs showing the top (left) and bottom side (right).

The electronic components of the feedback circuit depicted in (**Figure 7**) were chosen to have a tolerance smaller than 0.1% to reduce the impact of errors in the resulting signal generation. The Analog to Digital Converter (ADC) from the STM32G941KEU6 has 12-bit resolution and a range from 0 V to a reference voltage close to Vcc. The voltage applied to the piezoelectric actuator must be reduced to be read by the microcontroller. This can be achieved with two voltage dividers where 110V corresponds to approximately Vcc, meanwhile –60V is near to ground. An additional capacitor is included to filter possible noise on the ADC input. The PCB's bottom side (**Figure 8**, on the right) features a programming header to flash the program to the microcontroller, a female 2-pin header to connect the micropump, a Low-Dropout Regulator (LDO) to reduce the 5 V USB power to 3.3 V (Vcc) for the microcontroller and the flying inductor circuit explained in Section 1.1.

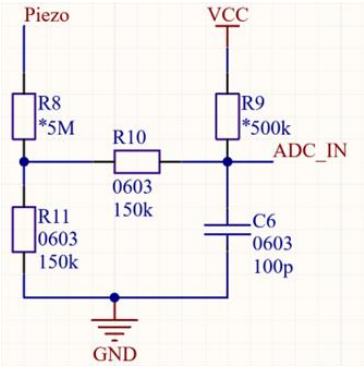

Figure 9 Feedback circuit for closed loop control.

2.2 Pump Driver Software

The software running on the microcontroller must accomplish multiple tasks: closed loop PWM duty cycle control, communication and storing settings on the internal flash memory.

2.2.1 Closed Loop Control

The main task of the software is to follow a given set of target voltages by controlling the PWM duty cycle for the flying inductor circuit according to the input of the feedback circuit.

The frequency of the PWM is set to 40 kHz as a compromise between time resolution and maximum voltage boost per period. At the end of each period, an internal interrupt in the software is triggered, after which the internal ADC reads the voltage level of the feedback circuit. This value is then compared with the stored target value and depending on the output fed into either of two Proportional-Derivative-Integral (PID) controllers. Both PID controllers are needed to account for the asymmetric system behavior of boosting or bucking the absolute voltage. The PID output then sets the duty cycle for the period until the period elapsed and the next interrupt repeats the process.

Target values for each period are calculated beforehand when the output is switched on or when a parameter, e.g., the frequency, is changed by user input (see Section 2.2.2). The calculated values are stored in an array with a length of 4000 words and the time elapsed between two values of the array is 25 µs. The array is parsed repetitively. Therefore, the array needs to be filled completely for a 10 Hz signal but only to a quarter for 40 Hz. It becomes apparent that, with this array, periodic signals with frequencies under 10 Hz cannot be generated. Therefore, an if statement

checks for that case and increases the time between two values accordingly.

2.2.2 Settings and Communication

The microcontroller allows communication via serial port monitor COM port (Hercules from HW-Group) to send commands (**Table 1**) to the microcontroller. For each command ending with colons, a parameter of type and range specified in the last two columns is sent together with the command. With these commands frequency and other parameters can be customized and stored non-volatile, without the need to flash a new program.

Table 1 Available commands for pump driver

Command	Function	Type	Range
setV+:	Sets pos. peak voltage	int	-60 to 110
setV-:	Sets neg. peak voltage	int	110 to -60
setF:	Sets frequency	int	1 to 600
setWFM:	Set waveform: 1 rectangular, 2 sinusoidal, 3 rectangular with sinusoidal flanks	int	1 to 3
setStatus:	Turns output on or off	Bool	1 or 0
setBurst:	Starts a number of bursts with the current settings.	uint	1 to 4.29×10^9
getAll	Returns all current settings	-	-
saveSettings	Stores all current settings into the internal flash	-	-

3 Results and Discussion

The same micropump was attached for each measurement while the signal output to the micropump was measured with a digital oscilloscope (Analog Discovery 3 from Digilent). The first measurement is depicted in (**Figure 10**). The measurement shows a combined sinusoidal and square wave parts with a ratio of 10% to 90%. The combination of these signals reduces the mechanical stress of the pump's diaphragm compared to a pure square wave signal. A frequency of 100 Hz and voltage peaks of 70 V and -20 V were set to 5 different drivers to investigate deviations between their output signals. The mean value of the tested pump drivers is shown in red while their standard deviation is shown in blue in the plot, as well as in the plot below. The resistor tolerances of 0.1% in the feedback circuit keeps the deviation between individual drivers small. As expected, signal parts with steep slopes have a higher standard deviation due to the tolerances in the parts of the flying inductor circuit resulting in slightly different dynamic behaviors.

While the frequency is accurate, the peak voltages differ from the set peak voltages. The differences between the set peak voltage and actual peak voltage comes from the internal linear function, mapping the ADC values to the corresponding voltages, by assuming an ideal linear relationship, and additionally form the PID parameters.

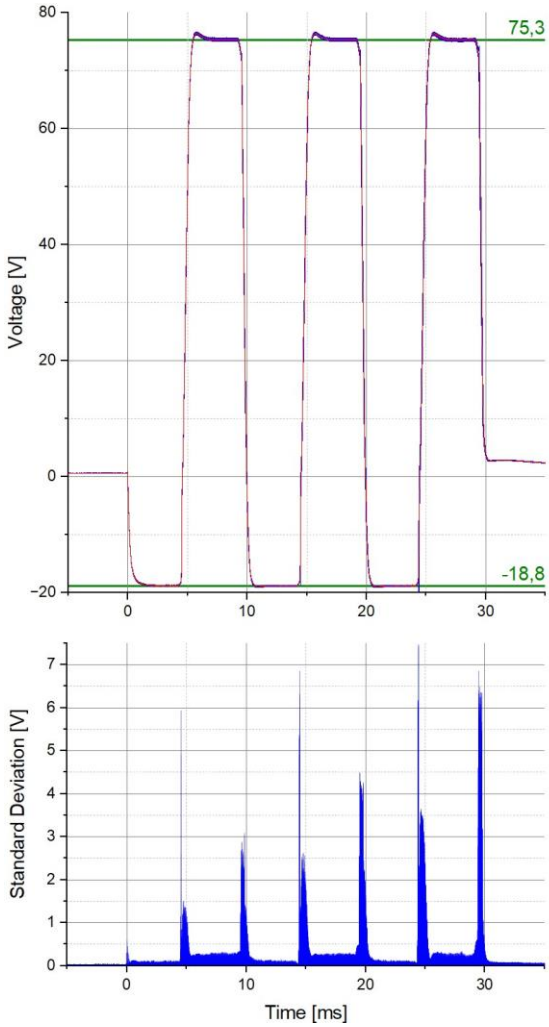

Figure 11 Mean signal output of 5 pump drivers (red) and their standard deviation (blue). For more clarity, the standard deviation is displayed additionally in the lower plot. A square wave with sinusoidal flanks, a frequency of 100 Hz and peak voltages of –20 V and 70 V were set.

Figure 12 and Figure 13 illustrate various peak voltage combinations for two signal forms. The ADC range covers -60 V to 110 V, thanks to the design of the feedback circuit mentioned in the previous section.

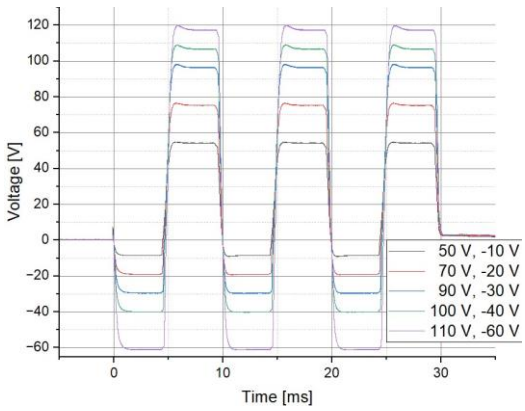

Figure 14 Different peak voltages according to the legend were set for the combined signal of sinusoidal and square wave parts at 100 Hz.

The Frequency of 100 Hz is kept in both figures but **Figure 15** shows a sinusoidal waveform. The sinusoidal signal is distorted. This shift is caused by the initial calculation of the array values: At first, a sine is generated with the correct peak to peak voltage then it is shifted to match the positive and negative peak voltages, causing a shift in the duty cycle.

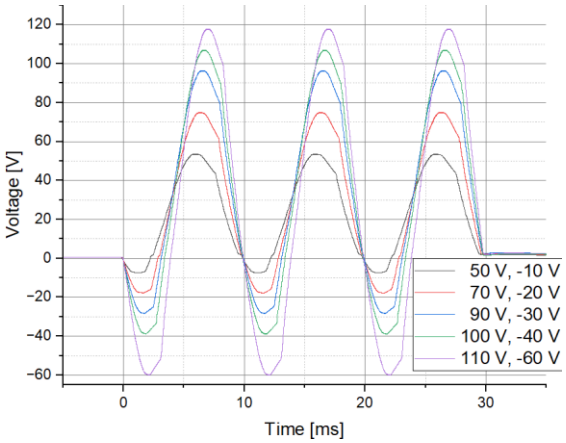

Figure 16 Different peak voltages according to the legend were set. The signal was set to 100 Hz and a sinusoidal waveform.

For the rectangular signal with sinusoidal flanks the effect is less pronounced due to the steep flanks.
The presented voltage control is sufficient to operate micropumps with an accuracy for the sinusoidal measurement of 93% ±0.2% in the positive voltage generation and a varying accuracy between 99.9% to 74,4% for the negative voltage generation. The accuracy for the negative voltage generation is lowest at -10 V (74.4%) and rises with higher absolute target voltages showing 99.9% at -60 V. The precision is high and in the mV regime.

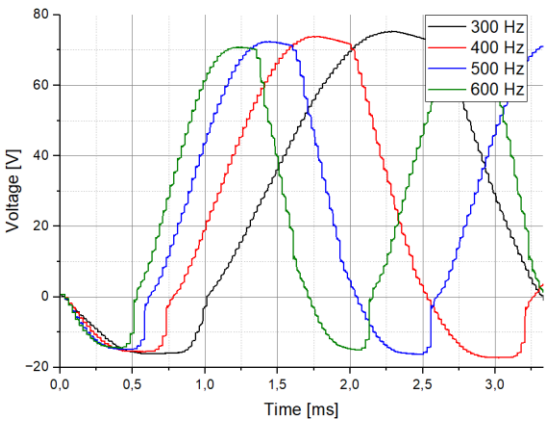

Figure 17 Signal for higher frequencies from 400 Hz up to 600 Hz are depicted. The signal form was set to sinusoidal and peak voltages were set to -20 V and 70 V.

Higher frequencies for sinusoidal waveforms are shown in **Figure 18**. The signal quality can be observed when zooming into the time scale showing the individual boost and buck-boost steps. Moreover, for higher frequencies, a lower amount of target values is used to form the signal. Although even higher frequencies of over 1 kHz were tested it is advisable to stay below this working frequency because of the limited time resolution caused by the fixed 40 kHz PWM signal.

4 Conclusion

We were able to generate accurate customized signals with frequencies up to 600 Hz with the presented functional PID control that responds dynamically to adjust the output voltage. The peak voltages can be set from -60 V up to 110 V and one of the preinstalled waveforms can be used. Also, a new custom waveform can be implemented by simply adding an array or a function which generates an array of target values to be followed by the pump driver. In addition to the very flexible functionality, the formfactor of the PCB is very advantageous, as it remains small with only 22 mm x 11.5 mm x 1 mm.
Signal quality is sufficient to operate piezoelectrically driven micropumps from Fraunhofer EMFT although improvements on the closed loop control are beneficial when it comes to voltage accuracy as well as signal form: The signal form can be optimized when assuring a 50% duty cycle during the calculation of the target values. Furthermore, the closed loop control can be improved by enhancing the current function which is mapping the ADC values to the voltage levels. Additionally, another two sets of PID parameters can improve the signal form by distinguishing between the boost and boost-buck converter and their underlying different transistors and with that switching characteristics.

5 Literature

[1] S. Mohith, et al, “Recent trends in mechanical micropumps and their applications: A review”. Elsevier, Vol. 60,2019, P. 34-55.

[2] A. Bußmann, et al. "Piezoelectric titanium based microfluidic pump and valves for implantable medical applications." Sensors and Actuators A: Physical 323 (2021): 112649.

[3] G. Biancuzzi, et al, “An efficient Low-voltage micropump for an implantable sphincter system”, Springer: 4th European Conference of the international federation for medical and biological engineering, 2009.

[4] D. Plano, et al, “Silicon-Based Piezo Micropumps Enable Fully Flexible Drug Delivery Patterns” Elsevier: Journal of Pharmaceutical Sciences,2024.

[5] D. Rossi and K. Tanaka. "Boost converter for driving a capacitive load." U.S. Patent No. 5,668,703. 16 Sep. 1997.

[6] H. Leistner, et al, "Robust Silicon Micropump of Chip Size 5x5x0.6 mm3 with 4 ml/min Air and 0.5 ml/min Water Flow Rate for Medical and Consumer Applications," Actuator 2021,online, pp. 1-4.

An inchworm using piezoelectric actuators and electromagnets with MR fluid

Takeshi Inoue, Hayata Takashima, Akihiro Torii, Suguru Mototani, Kae Doki
Aichi Institute of Technology, 1247 Yachigusa, Yakusa, Toyota 470-0392 Japan,
V23701VV@aitech.ac.jp

Abstract

This paper describes an inchworm using piezoelectric actuators and electromagnets with a magneto-rheological (MR) fluid. The inchworm is operated by controlling the timing of the electromagnetic force of the electromagnet and the expansion of the piezoelectric actuators. The MR fluid increases the attractive force of the electromagnets, which improves the motion of the inchworm. The viscosity of MR fluid changes depending on the electromagnetic field. The increased viscosity of the MR fluid increases the force holding the electromagnet in position. The increased attractive force of the electromagnet improves the motion of the inchworm.

1 Introduction

Miniaturization and improvement of various products are progressing. Small components used in these products are highly integrated. Developing small-scale production systems offers significant advantages. Inchworm-type mechanisms are suitable for the small-scale production systems. We have developed inchworm actuators for applications in positioning and motion devices [1]. A lot of research groups have developed various types of inchworms [2]. A feature of the inchworms we developed is the absence of guide mechanisms. The inchworm incorporates electromagnets for clamping and piezoelectric actuators (piezos) for moving. However, the inchworms have the disadvantage that the electromagnets are not strong enough to hold their position. The desired displacement cannot be obtained due to this drawback. In this paper, we propose an inchworm using piezos, electromagnets, and magneto-rheological (MR) fluid [3]. The MR fluid is known for increasing its apparent viscosity in a magnetic field, which enhances the clamping force of the inchworm.

2 Inchworm

Figure 1 shows an inchworm-type actuator we developed. This actuator has a delta-shaped structure with three piezos (AE0505D16, Tokin, Japan) on each side and three electromagnets (400 turns) at the apex of the triangle. The position of the actuator is defined from the positions of the electromagnets, which are measured by laser displacement sensors.

Figure 2 shows the principle of movement of the actuator. First, (1) Electromagnets B and C are excited and adhere to magnetic materials, and then (2) piezos b and c extend by the voltage applied. This excitation causes electromagnet A in the non-excited state to move in the y-direction. Subsequently, (3) with electromagnet A in the excited state

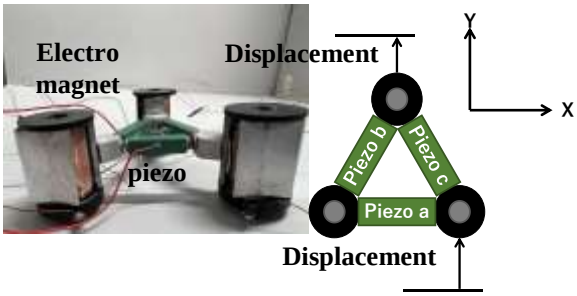

Figure 1 Inchworms with three piezos and three electromagnets

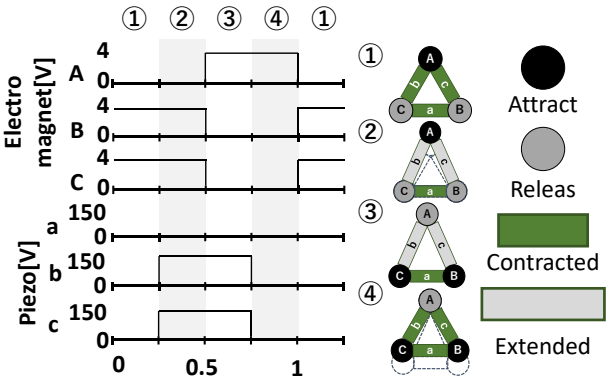

Figure 2 Operating principle of inchworm

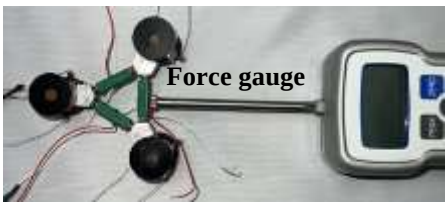

Figure 3 Resistance force measurement by force gauge

Table 1 Resistance force with/without MR fluid

	voltage applied to electromagnet		
	0 V	3 V	4 V
with MR fluid	0.000 N	5.378 N	over
w/o MR fluid	0.734 N	2.744 N	6.461 N

and adhered to the magnetic floor, and electromagnets B and C in the non-excited state, then (4) piezos b and c contract, allowing electromagnets B and C to move. This sequence is repeated, propelling the inchworm actuator.

A resistance force is measured by a force gauge as shown in **Figure 3**. The resistance force is defined as a horizontal force which starts the inchworm to move by the force applied by the force gauge. An MR fluid of type E-600M (oil-based) produced by Sigma Hi-Chemical, Japan, is used. A drop of the MR fluid, less than 0.1 ml, is applied between the bottom of the electromagnet core and the magnetic floor. An electromagnet field is applied to the MR fluid by the electromagnets. MR fluid generates a resistance force in the direction opposite to the motion, expected to enlarge the attractive force of the electromagnet. Three electromagnets are excited by 0 V, 3 V and 4 V. Results are summarized in **Table 1**. The resistance force of the inchworm with an oil-based MR fluid is zero when the voltage applied to the electromagnet is zero. In contrast, the resistance force without the MR fluid is 0.7 N. The resistance force with the MR fluid is 5.4 N at 3 V, which is larger than that without the MR fluid. These results show that the MR fluid increases the resistance force of the electromagnet with an applied voltage and decreases the resistance force of the non-excited electromagnets.

3 Experiment and results

The electromagnets are control by the signals shown in **Figure 2**. The piezos are not operated. The position change of the electromagnets is measured and compared with and without an MR fluid. **Figure 4** shows the position change of electromagnets. Although the voltage is not applied to the piezos, the electromagnets without the MR fluid moves by on and off of the electromagnets. In contrast, they do not move while the MR fluid is used. This result indicates that the MR fluid applied at the bottom of the electromagnet core increases the attractive force of the electromagnet and holds the position of the electromagnets.

Next, electromagnet B and C are continuously excited, electromagnet A is not excited, and piezo b and c are extended and contracted with one second interval. The position of electromagnet A and B are measured. **Figure 5** shows the result. While electromagnet A shows the reciprocal motion with and without an MR fluid, the position of electromagnet A without the MR fluid shifts in the negative direction as shown in **Figure 5**(a). The excited electromagnet B is designed not to move. However, electromagnet B moves as shown in **Figure 5**(b). The position change of electromagnet B without MR fluid is slightly larger than that with MR fluid. This indicates that the MR fluid increases the attractive force of the electromagnet.

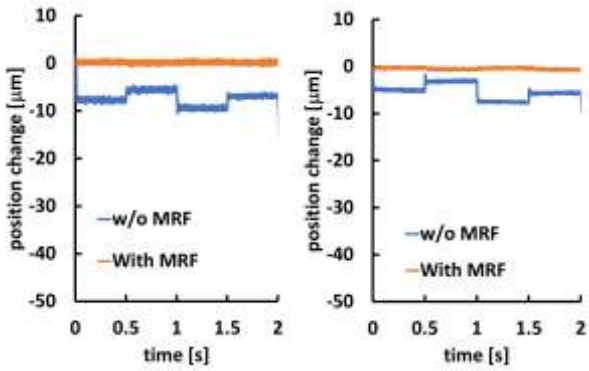

(a) Magnet A (b) Magnet B

Figure 4 Position change of electromagnets while all electromagnets are operated and piezos are not operated

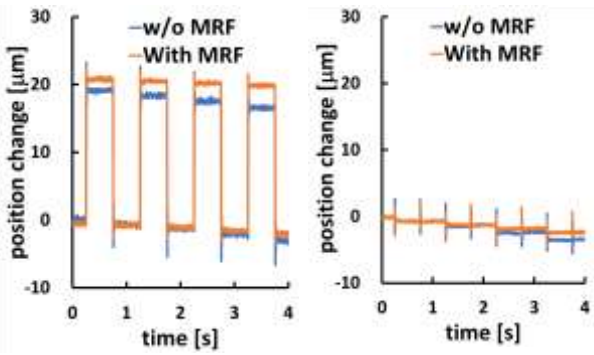

(a) Magnet A (b) Magnet B

Figure 5 Position change of electromagnets while electromagnets B and C

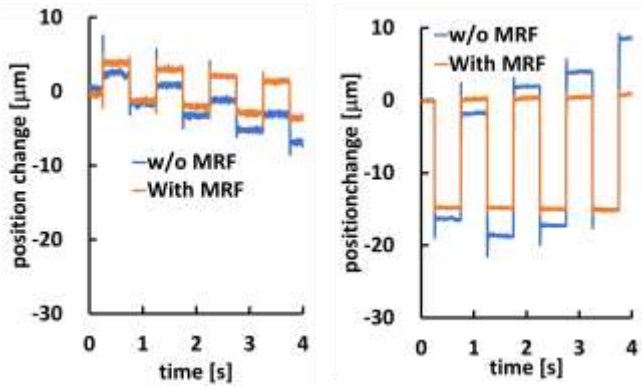

(a) Magnet A (a) Magnet B

Figure 6 Position change of electromagnets while electromagnets A

Then, While electromagnet A shows the reciprocal motion with and without an MR fluid, the position of electromagnet A with and without the MR fluid shifts in the negative direction as shown in **Figure 6**(a). While electromagnet B shows the reciprocal motion with and without an MR fluid according to the piezo deformation, the position of electro-

magnet B without the MR fluid fluctuates as shown in **Figure 6**(b). The position change of electromagnet A and B without MR fluid is slightly larger than that with MR fluid. This indicates that the MR fluid increases the attractive force of the electromagnet.
The inchworm is operated by the signals shown in **Figure 2**. The y-position of electromagnet A is measured. **Figure 7** shows the displacement of the inchworm. The displacement of the inchworm using the MR fluid is approximately 5 μm, although that without the MR fluid is approximately 1 μm in one control cycle. The step displacement of the inchworm caused by the deformation of the piezo is approximately 17 μm. The control period, 1.0 s, is divided by four intervals. The displacement obtained by the inchworm with an MR fluid indicates the backward motion of the interval of 0.5 s. However, the displacement without an MR fluid indicates additional decrease of 0.25 s interval, which is caused by insufficient attractive force of the electromagnet. In conclusion, an MR fluid applied to the electromagnets improves the motion of the inchworm.

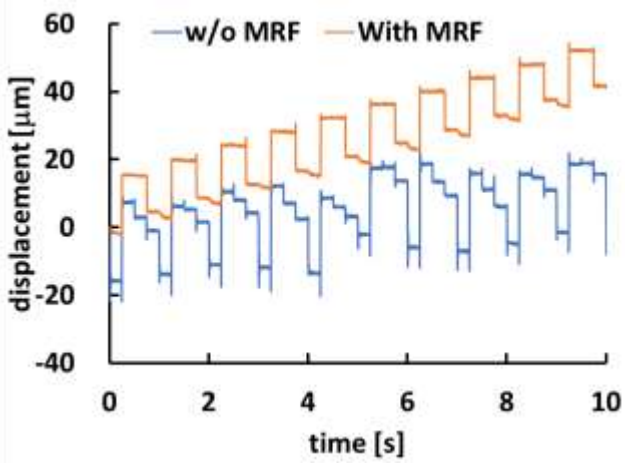

Figure 7 Displacement of the inchworm with/without MR fluid

4 Literature

[1] Torii A, Mitsuyoshi Y, Mototani S, and Doki K: Int. J. of Automotion Technology, Vol. 12, No. 5, 2018, pp. 784-790

[2] Li J, Huang H, Morita T: Sensors and Actuators A: Physical,Vol. 292, pp. 39-51, 2019

[3] S A Mazlan, N B Ekreem and A G Olabi: The performance of magnetorheological fluid in squeeze mode, Smart Mater Struct, Vol.16, pp1678-1682, 2007

A Flow Control Valve using Piezoelectric Vibrator for Hydraulic Soft Actuators

Takefumi Kanda[1], Kou Hashimoto[1], Yuma Mizokuchi[1], Yusuke Ota[1], Shuichi Wakimoto[1], Daisuke Yamaguchi[1], Koichi Suzumori[2], Hiroyuki Nabae[2]
[1] Okayama University, 3-1-1 Tsushima-naka, Kita-ku, Okayama, 700-8530, Japan
[2] Tokyo Institute of Technology, 2-12-1 Ookayama, Meguro-ku, Tokyo, 152-8552, Japan

Abstract

In this study, we have fabricated and evaluated a flow control valve for oil-hydraulic soft actuators. To install oil-hydraulic actuators on a robot to realize actuation with high-power, there is a demand for compact and lightweight control valve. Based on particle excitation type valve driven by piezoelectric vibrators, we have designed a fluidic control valve for hydraulic actuators. In this valve, the particle excitation type valve is used as a pilot valve to control the spool of main valve. The fabricated valve has been evaluated for a control of the supplied fluid at a pressure of 5 MPa. As a result, we have succeeded in controlling a hydraulic artificial muscle.

1 Background and motivation

Recently, hydraulic actuators have attracted attentions as actuating of robots from the viewpoint of output power. However, such a robot with many degrees of freedom requires many large and heavy fluid control components, especially for oil-hydraulic actuators. Thus, there is a need to miniaturize the control valve. We proposed particle excitation type flow control valves using a piezoelectric vibrator to reduce the volume and weight of the control valve in previous research [1-4]. In this study, we focused on a two-stage control valve structure [5] that can control high pressurized working fluid with high flow rate by using fluid force in order to increase the pressure of the conventional particle excitation type control valve. The proposed valve has been fabricated and evaluated to control the working fluid. We have also applied the fabricated valve to control the motion of an oil-hydraulic soft actuator.

2 Structure and principle

The basic working principle of the valve using the particle excitation is illustrated in Fig.1. In this valve, the flow rate of the fluid is controlled by the vibration of piezoelectric vibrator. In this study, the particle excitation type control valve is used as the pilot valve. As shown in Fig. 2, the two-stage control valve consists of a pilot valve and a main valve. The pilot valve controls the main valve as shown in Figs. 3 to 4. The main fluid is controlled by the fluid force acting on the spool.

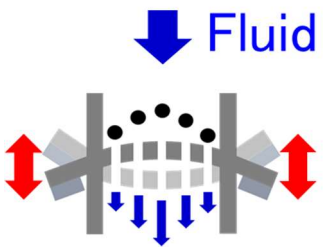

Figure 1 Working principle of a valve using particle excitation

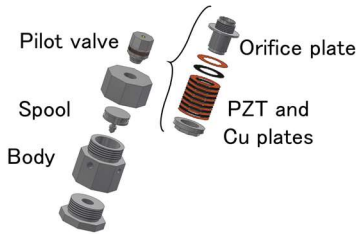

Figure 2 Structure of the proposed two-stage valve

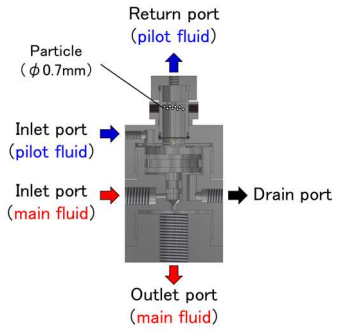

Figure 3 Cross-sectional view of the proposed valve

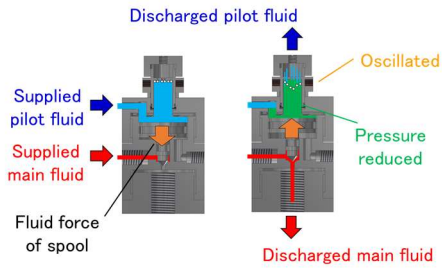

Figure 4 Working principle of the proposed valve: closed state (left) and opened state (right)

3 Experimental

3.1 Evaluation of valve

The fluid flow rate controlled by the piezoelectric vibrator was evaluated about the fabricated valve. A mineral oil with a viscosity of 32 cSt (mm^2/s) was used as the main fluid, and the supply pressure was 1 to 5 MPa. Figure 5

shows the relationship between duty ratio of PWM applied on the piezoelectric vibrator and pilot fluid flow rate. The flow control of the main fluid which is 10 times as high pressure as the pilot fluid supply pressure was realized by the duty change with PWM control.

3.2 Control of actuator

The fabricated valve was mounted on a hydraulic artificial muscle (HAM) and controllability was evaluated. The HAM has high power weight ratio and flexibility [6]. The experimental setup for the driving of HAM by using the valve is show in Fig.6. The length of the HAM is 300 mm. The pressure of the main fluid was 5 MPa, which is the maximum working pressure of HAM, and the pilot fluid pressure was 0.5 MPa. The driving frequency was 117 kHz, and the carrier period was 200 ms. Figures 7 and 8 show the dynamic characteristics of the main fluid flow rate and the contraction characteristics of HAM when the particulate excitation control valve is driven at 100% duty. From Fig. 7, the main fluid flow rate was generated to follow the PWM signal of 100% duty. From Fig. 8, the contraction rate of HAM reached a maximum of 31.8% after about 3 s. At 100% duty, continuous contraction moving of HAM was obtained.

4 Conclusion

In this study, a flow control valve which has two-stage structure has been proposed for a control of hydraulic soft actuators based on particle excitation type valve driven by piezoelectric vibrators. The valve has been evaluated for a control of the supplied fluid at a pressure of 5 MPa. In addition, the oil-hydraulic actuator has been successfully controlled by using the valve mounted on the actuator.

5 Literature

[1] D. Hirooka, K. Suzumori, T. Kanda, Flow Control Valve for Pneumatic Actuators using Particle Excitation by PZT Vibrator, Sensors and Actuators A: Physical, Vol. 155, pp. 285-289, 2009.

[2] T. Ukida, K. Suzumori, H. Nabae, T. Kanda, Fabrication and Evaluation of Hydraulic Particle Excitation Valve Vibrated Perpendicularly to Direction of Flow Path", JFPS International Journal of Fluid Power System, Vol. 49, No. 1, pp. 9-17, 2018.

[3] H. Osaki, T. Kanda, S. Ofuji, N. Seno, K. Suzumori, T. Ukida, H. Nabae, A Small Three-way Valve using Particle Excitation with Piezoelectric for Hydraulic Actuators, Advanced Robotics, Vol.32, No.9, pp.500-510, 2018.

[4] H. Yamamoto, T. Kanda, S. Wakimoto, Y. Ota, H. Takami, K. Suzumori, T. Ukida, H. Nabae, A Small Three-way Valve using Particle Excitation Driven by a Single Piezoelectric Transducer for Hydraulic Actuator, Sensors and Actuators A: Physical, Vol.316, 112363, 2020.

[5] T. Kanda, K. Hashimoto, H. Yamamoto, S. Wakimoto, K. Suzumori, T. Ukida, H. Nabae, Particle Excitation by Using a Piezoelectric Vibrator for a Hydraulic Valve, IEEE International Ultrasonics Symposium, 2413, 2020.

[6] R. Morita, H. Nabae, G. Endo, K. Suzumori, A Proposal of a New Rotational-compliant Joint with Oil-hydraulic McKibben Artificial Muscles, Advanced Robotics, Vol. 32 No. 9, pp. 511–523, 2018.

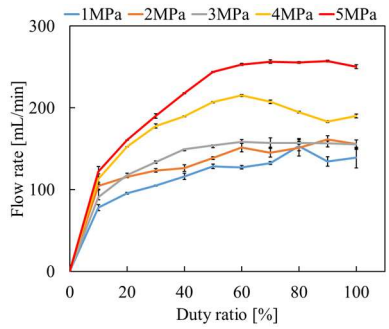

Figure 5 Relationship between pilot fluid flow rate at outlet port and duty of the applied voltage.

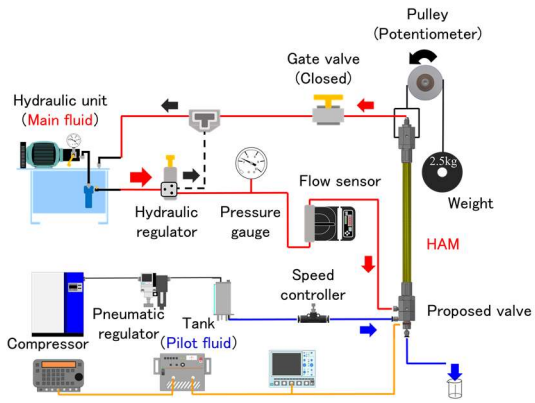

Figure 6 Experimental setup for the measurement of HAM motion

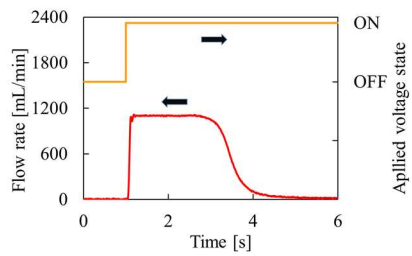

Figure 7 Main fluid flow rate at outlet port under the applied voltage in duty of 100%

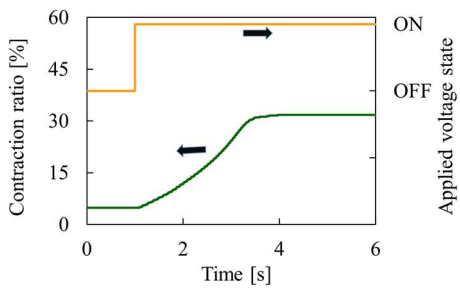

Figure 8 Contraction motion of HAM under the applied voltage in duty of 100%

Conference Focus: *Piezoelectric actuators /Bone Conduction Devices*
Application: *Poster*

The Application of Piezoelectric-Driven Actuators in Bone Conduction Devices

Julia Lieber[a] and Alexander Reininger[b]
[a]MED-EL, Innsbruck, Austria
[b]Linz Center of Mechatronics, Linz, Austria

Abstract

Bone conduction devices use an actuator that converts electrical signals into mechanical vibrations to transfer sound through skull bone to the cochlea. The design of this core element has a great impact on the overall device size and complexity. Piezo-based actuators offer a major benefit in size, slim shape and mass compared to conventional electromagnetic actuators [1]. For this rationale, an elaborated piezoelectric transducer was tested for integration in the field of bone conduction.
The actuator's impedance and response to audio signals was measured under mimicking the conditions for sound transmission through bone. In addition, the output force level (OFL) was measured when the transducer was attached to bone conduction device (BCD) electronics. For evaluation of proper signal conversion, the total harmonic distortion (THD) was measured.
The piezo transducer has a capacitive behavior and resonates at 1030 Hz. It properly converts electrical audio signals at frequencies that are sensitive to speech with a THD below 1% between 600 and 4000 Hz. BCD electronics, modified for the capacitive transducer was found to be compatible for frequencies between 800 and 4000 Hz with a THD below 3%. With a measured and simulated pure tone average at the frequencies 500, 1000 and 2000 Hz (PTA3) OFL of 75 dBμN, the output is still too low for the purpose of rehabilitation, compared to existing devices. With ongoing optimizations, aiming to increase OFL and reduce distortion at low frequencies, the potential of using piezoelectric actuators in bone conduction rehabilitation devices is rising.

1 Introduction

Piezo- based actuators exploit the inverse piezoelectric effect by translating electrical signals into mechanical motion [2]. Piezoelectric actuators consist of materials with an asymmetrical arrangement of atoms in their crystal lattice due to its lack of a symmetric center [2]. To induce an alternating deformation in the actuator, an AC voltage is applied to the electrodes covering the piezoelectric layer. Between these electrodes, an alternating electric field builds up which exerts a force on the material's randomly orientated dipoles, causing them to align in the same direction. This dipole reorientation results in a deformation of the piezo layer. The direction of deformation depends on the signal's polarity. Thus, an alternating electric field causes the actuator to expand and contract. At certain high frequencies, this alternating deformation results into vibration [3]. This motion generation can be utilized in bone conduction hearing systems. The piezoelectric actuator serves as a vibrating element that transmits the sound through skull bone to the cochlea, completely bypassing outer and middle ear [4]. This transfer of sound, called bone conduction can be used in head- or earphones (see figure 1) providing the benefit of an open ear canal and hence, allowing ambient sounds to be heard.

Figure 1 Skin-drive bone conduction earphones SWYM (OPN SOUND)[5]

Bone conduction technology can also be exploited in hearing rehabilitation devices, regaining the hearing of patients with conductive or mixed hearing loss [6].
Bone conduction ear- and headphones as well as some hearing rehabilitation devices such as the ADHEAR (MED-EL), shown in figure 2 feature an externally-worn transducer that stimulates the bone indirectly through the skin. Partially implantable rehabilitation devices incorporate a hermetically housed actuator which enables direct stimulation of the bone, thereby minimizing skin-induced signal attenuation [7].

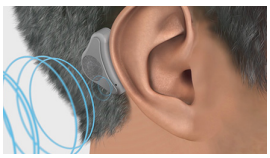

Figure 2 Skin-drive bone conduction rehabilitation device ADHEAR (MED-EL) [8]

2 Piezoelectric Actuators for Bone Conduction Technology

The piezo transducer investigated in this work consists of springs, rigid bodies and piezo elements, covered with electrodes. The given structure of the transducer comprises a cylindrical shape, a maximum height of 5 mm and diameter of 20 mm. This work examines whether a piezo transducer with these requirements is suitable for integration into bone conduction technology.

a Impedance of a Piezoelectric Actuator

To characterize the behavior of the actuator, its impedance was measured. The transducer was connected to a skull impedance simulator (SIS) which enables a realistic setting by mimicking sound transmission through skull bone [9]. Figure 3 shows the measured impedance magnitude along the frequencies relevant for hearing. The actuator behaves capacitively, as it exhibits a high impedance at low frequencies and a low impedance at high frequencies. The downward pointing peak indicates the resonance, occurring at 1030 Hz. The resonance and the curve gradient are dependent on the structure and design of the actuator, including the quantity, arrangement and dimensions of the piezoelectric material, springs and moving masses. In this work, the primary focus is speech recognition, hence, a resonance peak in the frequency range that is most sensitive to speech (500 to 4000 Hz) was intended to take advantage of the high output levels.

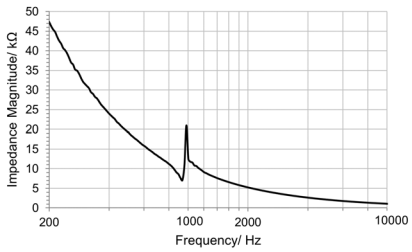

Figure 3 Impedance magnitude of the piezo transducer over frequency. The downward pointing peak indicates the resonance at 1030 Hz, the upward pointing peak the antiresonance.

b Response of a Piezoelectric Actuator to Audio Signals

The actuator was connected to the SIS and exposed to direct stimulation of audio signals, generated by the *Audio Precision APx515b*. Input properties were set in the according software *APx500*, such as the driving voltage of 0 dBV which is usually generated by a conventional low-voltage battery. The mechanical output u was sensed by an accelerometer and analyzed in the software. The output force level (OFL) was calculated by equation 1, accounting for the accelerometer's sensitivity s and moving mass of the SIS m_{SIS}.

$$OFL = \frac{u}{s} \cdot m_{SIS} \tag{1}$$

Usually, the OFL is given in dB relative to 1μN. This unit conversion is performed with equation 2.

$$OFL_{dB} = 20 \cdot log\left(\frac{OFL}{1\mu N}\right) \tag{2}$$

The setup is illustrated in figure 4. Furthermore, the actuator was modelled for simulations in the electronic circuit simulator software *LTspice*. Figure 5 shows the simulated and measured OFL of the piezo transducer along frequency at a driving voltage of 0 dBV. The resonance is recognizable on the high peak. Simulation and measurement differ in output and resonance due to uncertainties in the production of the individual prototype parts and final assembly of the transducer. After the resonance peak has subsided, both, measurement and simulation show a relatively constant OFL in the range from 2000 to 8000 Hz. The measurement results in a pure tone average for the frequencies 500, 1000 and 2000 Hz (PTA3) of 88 dBμN and a peak OFL of 118 dBμN. The simulation reaches a PTA3 of 85 dBμN and a peak OFL of 112 dBμN.

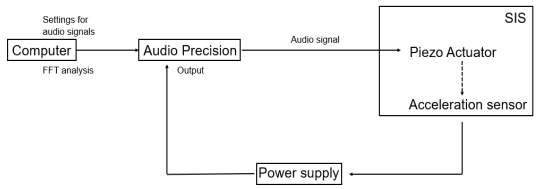

Figure 4 Setup for the measurement of the actuator response to audio stimulation.

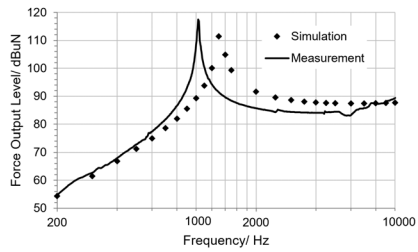

Figure 5 Measured and simulated OFL of the piezo actuator over frequency in response to direct stimulation at 0 dBV.

Figure 6 shows the measured total harmonic distortion (THD) at 0 dBV. The THD is a figure of merit that quantifies the unwanted harmonic components in the spectrum compared to the respective fundamental frequency [10]. High THD values indicate a high distortion level. The curve is shown over the speech recognition frequency range from 500 to 4000 Hz. The THD is 2.3% at 500 Hz and remains below 1% above 600 Hz. Figure 7 shows the simulated voltage waveform of the piezo transducer over time at 1500, 2500 and 3500 Hz. The former exhibits a significantly higher amplitude compared to the other two frequencies, caused by the nearby resonance peak at 1030 Hz. All three signals are clear sine curves as expected due to the low THD.

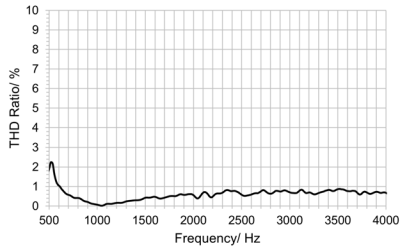

Figure 6 THD ratio of the piezo transducer over frequencies relevant for speech recognition at 0 dBV.

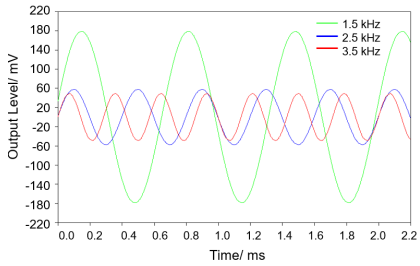

Figure 7 Output of the piezoelectric actuator at an input voltage of 0 dBV along the time for the frequencies 1500, 2500 and 3500 Hz.

c Piezoelectric Actuator integrated in a Bone Conduction Device

The piezo transducer was integrated in a bone conduction device (BCD) which was initially designed for an inductive actuator. The electronics was adapted to be compatible with the capacitive behavior of the piezo actuator. The transducer was connected to the SIS and BCD electronics according to figure 8. For this setup, an additional layer, incorporated in the SIS was used to account for the thickness of the skin, and with that, the signal loss through it. Figure 9 shows the simulated and measured OFL of the piezo-driven transducer over frequency at 0 dBV. Compared to the OFL, resulted by direct stimulation (see figure 5), the OFL in figure 9 is lower, caused by the voltage drop across the BCD electronics and the additional "skin-mimicking" layer. Additionally, the deviation between measurement and simulation increased due to the summed uncertainty of the individual electronic components used in the measurement. Both, measurement and simulation, result in a PTA3 of 75 dBμN and a peak OFL of 104 dBμN and 102 dBμN, respectively.

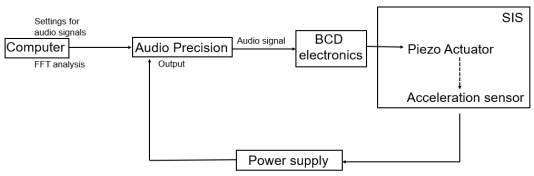

Figure 8 Setup for the measurement of the actuator response to audio stimulation when connected to BCD electronics.

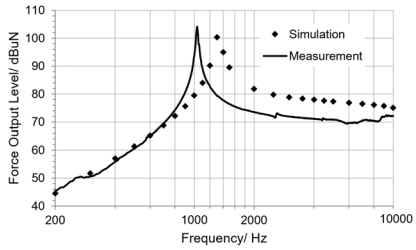

Figure 9 Measured and simulated OFL of the piezo-driven BCD over frequency in response to stimulation at 0 dBV.

Figure 10 shows the measured THD profile of the piezo-driven BCD. For low frequencies around 500 Hz, the BCD reaches THD values up to 80 %. The steep peak declines rapidly, resulting in a THD below 3 % above 800 Hz. Figure 11 shows the appearance of those harmonics at 500 Hz in the simulated voltage waveform, confirming the conclusion from figure 10. Figure 12 shows the simulated voltage waveforms, generated with the piezo-driven BCD at 1500, 2500 and 3500 Hz at 0 dBV. In comparison to figure 11, clear sinusoidal signals can be seen with no harmonics, confirming the low THD at these frequencies. Compared to the waveforms in figure 7, the piezo-driven BCD exhibits lower outputs and more noise in the signal due to the attached BCD electronics.

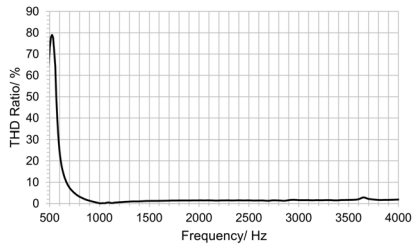

Figure 10 THD ratio of the piezo-driven BCD over frequencies, relevant for speech recognition at 0 dBV.

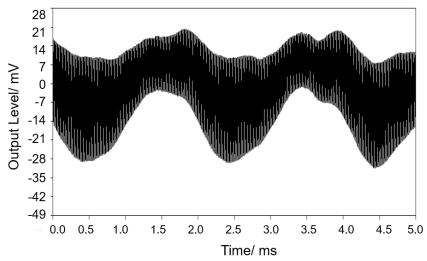

Figure 11 500 Hz voltage waveform with harmonic distortion and noise, generated with the piezo-driven BCD at 0 dBV.

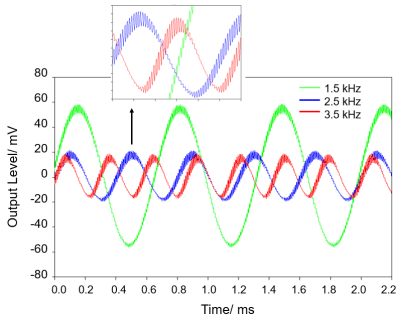

Figure 12 Voltage waveforms of the piezo-driven BCD at 0 dBV over time at 1500, 2500 and 3500 Hz.

3 Conclusion

The response of a piezoelectric transducer with a given structure (see chapter 2) to audio signals was studied. The actuator was directly stimulated by a 0 dBV signal. Additionally, the actuator was connected to the BCD electronics to test for its integration.

a OFL and Resonance

The OFL was determined for the hearing spectrum from 200 Hz to 10 kHz. Due to uncertainties in the prototype setup, measurement and simulation deviate from each other. For rehabilitation, the requirements of the OFL and resonance depend on the type and grade of hearing loss, see [11]. BCDs on the market have the OFL specifications, listed in table 1 at a sound pressure level of 90 dBSPL. Compared to these rehabilitation devices, the OFL of the piezo-driven BCD, used in this work has a significantly lower PTA3 with 75 dBμN. For the purpose of rehabilitation, the OFL must be increased by further optimizations of the actuator and BCD electronics. The peak OFL is only slightly lower to that of existing BCDs. The resonance of the used piezo transducer is with 1030 Hz above that of the referred rehabilitation devices. However, a resonance around 1000 Hz is beneficial for maximizing the higher frequencies.

BCD, Company, Source	PTA3 OFL	Peak OFL	Resonance
OSIA 2, Cochlear, [12]	~114 dBμN	115 dBμN	~650 Hz
SAMBA 2 BB, MED-EL, [13]	~100 dBμN	110 dBμN	~900 Hz
Ponto 5 Mini, Oticon Medical, [14]	~112 dBμN	124 dBμN	~900 Hz
BAHA Connect, Cochlear, [15]	~115 dBμN	121 dBμ	600 - 700 Hz
BAHA Attract, Cochlear, [15]	~116 dBμN	121 dBμN	500 - 600 Hz
ADHEAR, MED-EL, [8]	~111 dBμN	124 dBμN	800 - 900 Hz

Table 1 Resonance, PTA3 OFL and peak OFL specifications. The latter is directly obtained from the datasheets while the resonance and PTA3 OFL values are read from the frequency response curves.

b THD

The piezo-driven BCD produces a high THD around 500 Hz. Above 800 Hz, the THD is below 3%. In comparison, the OSIA2 (Cochlear) and the ADHEAR (MED-EL) feature a THD below 5% above 600 Hz. Hence, with the piezo-driven BCD, electrical signals are properly converted between 800 and 4000 Hz. With ongoing optimizations, aiming to reduce the THD at low frequencies and to increase the OFL, the potential of piezo-driven actuators rises in the field of bone conduction, benefiting in size and complexity [1].

4 Acknoledgement

This work has been supported by the COMET-K2 Center of the Linz Center of Mechatronics (LCM) funded by the Austrian federal government and the federal state of Upper Austria.

5 Literature

[1] X. Gao, J. Yang, J. Wu, X. Xin, Z. Li, X. Yuan, and Dong S. Shen, X.: *Piezoelectric actuators and motors: Materials, designs, and applications.* 5(1):22–31, 2019.

[2] Jing Feng Li: *Fundamentals of Piezoelectricity, Chapter 1*, pages 1–18. 2021, ISBN 9783527817047.

[3] K. Hwang, H. Woo, H. Chang, L. Geon, C. Gangho, R. Jaechan, and J. Wook: *5 - piezoelectrics*. pages 157–206, 2020.

[4] S. Solowsky: *Mechanisms of bone conduction: A review of the literature (doctoral dissertation)*. 2021.

[5] OPN SOUND: *Swym waterproof headphones*. `https://opnsound.com/products/swym`.

[6] C. Dun, T. Faber, M. de Wolf, C. Cremers, and M. Hol: *An overview of different systems: the bone-anchored hearing aid.* 71:22–31, 2011.

[7] G. Casazza and B. Kesser: *Modern advances in bone conduction–hearing devices*. Current Otorhinolaryngology Reports, 10:370–376, 2022.

[8] MED-EL: *Adhear factsheet*. `https://www.medel.pro/products/adhear`, date accessed: 04.2024.

[9] B. Håkansson, P. Carlsson, and A. Ringdahl: *Force threshold for hearing by direct bone conduction*. J. Acoust. Soc. Am., 97:1124–1129, 1995.

[10] D. Shmilovitz: *On the definition of total harmonic distortion and its effect on measurement interpretation*. Power Delivery, IEEE Transactions on, pages 526 – 528, 2005.

[11] T. Rahne and S. Plontke: *Apparative therapie bei kombiniertem hörverlust*. HNO, 64:91–100, 2015.

[12] Cochlear: *Osia 2 system*. `https://assets.cochlear.com/api/public/content/OSI086-Osia-System-Datasheet.pdf`, date accessed: 04.2024.

[13] MED-EL: *Bonebridge bci 602 active bone conduction implant - technical data*. `https://www.medel.pro/products/bci602`, date accessed: 04.2024.

[14] Oticon Medical: *Ponto 5 mini pi*. `https://www.oticonmedical.com/us/downloads/`, date accessed: 04.2024.

[15] Cochlear: *Datasheet - cochlear baha 6 max sound processor*. `https://mss-p-007-delivery.stylelabs.cloud/api/public/content/BUN871-Baha-6-Max-DataSheet.pdf`, date accessed: 04.2024.

Piezoelectric Spindle Drives

Alexej Wischnewski, Physik Instrumente (PI) GmbH & Co KG, Auf der Römerstraße 1, 76228 Karlsruhe, Germany, a.wischnewski@pi.de

Abstract

This paper presents two types of piezoelectric motors in which the friction contact takes the form of a threaded connection. The driven element of the motor is a threaded shaft or spindle. The piezoceramic stator of the drive also contains a threaded contact element, which is in operative contact with the spindle. The stator is piezoelectrically excited to oscillate. The mechanical energy of the stator is transmitted to the spindle through the contact element, causing rotary and linear movement of the spindle. Drives with inertial and ultrasonic operating principles are shown and compared with each other. The vibration behavior of their motors is illustrated with FEM simulations.

1 Introduction

Lasers are used in many areas of technology, including metrology, medical technology, and metalworking. The laser beams in such industries are usually precisely directed, or guided, via tip/tilt mirrors. The necessary precision in the guidance of the laser beam is achieved via micrometer screws. They are often manually operated [1]. However, there are numerous use cases in which it is impossible or undesirable to position the tip/tilt mirror manually, such as on a tachymeter or inside a vacuum chamber or lithography machine. Piezoelectric friction contact drives are commonly used for automatic positioning of the tip/tilt mirror [2]. Here, an element to be driven, i.e., the rotor or runner, is connected to or coupled with the piezoelectric actuator via a friction contact, whereby a targeted deformation, or movement, of the actuator effected by an electrical control signal is transmitted to the element to be driven via the friction contact. Such drives can be based on two functional principles: the inertia operating principle and the ultrasonic operating principle.

In a piezoelectric drive based on the inertia operating principle, a piezoelectric actuator is first slowly expanded. This causes the element to be driven, which is pressed against the actuator, to move along with the actuator. In the second step of the process, the actuator contracts quickly. Due to its inertia, the element to be driven is no longer able to follow this fast movement and maintains its position. The movement cycle repeats continuously. The first inertia drive designs in which the part to be moved is a screw is known from [3]. This is screwed into a threaded nut and remains in frictional contact with it. The threaded nut is in turn connected directly or indirectly to a piezo actuator, which moves the screw based on the inertia principle.

In a piezoelectric drive based on the ultrasonic operating principle, acoustic waves are excited in the resonator. This causes the points in frictional contact with the element to be driven to oscillate along elliptical paths, setting the element to be driven into rotary or linear motion. A spindle drive based on the ultrasonic operating principle with two-phase excitation in a piezoceramic ring resonator of a continuous bending vibration wave is known from [4].

Physik Instrumente (PI) has researched piezoelectric drives for decades. Various spindle drive designs based on the inertia or ultrasonic operating principles were developed [5] – [7] and tested and are on the market. This article describes two drive variants of piezoelectric spindle drives.

2 Spindle Drives

2.1 Inertia Principle

Figure 1 shows a piezoelectrically driven spindle drive developed by Physik Instrumente (PI) that functions based on the inertia operating principle [6]. The spindle drive comprises a drive element (stator), two piezoelectric multilayer actuators, and a threaded element to be driven in the form of a threaded rod or spindle. The drive element contains two contact elements with threads on their inner surfaces. The two contact elements grip, or contact, the element to be driven symmetrically on two sides. The contact elements engage the element to be driven via friction between the sets of threads. A two-phase electrical excitation device controls the drive.

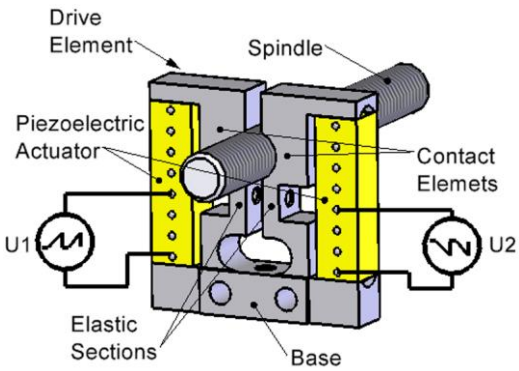

Fig. 1 CAD model of a spindle drive based on the inertia operating principle

A base element supports one side of each piezoelectric actuator. The other, opposite side of a given piezoelectric actuator is connected to the respective contact element of the drive element. Each contact element has two elastic sections, which act on the contact elements in a spring-like

manner. The piezoelectric actuators are bonded to the respective base element and are preloaded through elastic elements with a screw (see Fig. 4).
A two-phase electrical excitation device controls the drive. The electrical excitation device generates two sawtooth-like voltages U1, U2 with identically timed processes, the same magnitude of voltage, and different polarity (see Fig. 2). The time curve of the voltages U1, U2 has two areas t1, t3 with different slopes. The first area, t1, has a small slope. In this area, the magnitudes of the voltages U1, U2 slowly increase to their final value, U1max, U2max. In the second area with the large slope t3, the magnitude of the voltages U1, U2 decreases very quickly. The differential is one to two orders of magnitude. Furthermore, the time curve of the voltages U1, U2 can have two additional areas t2, t4 where the magnitudes of the voltages U1, U2 remain unchanged.

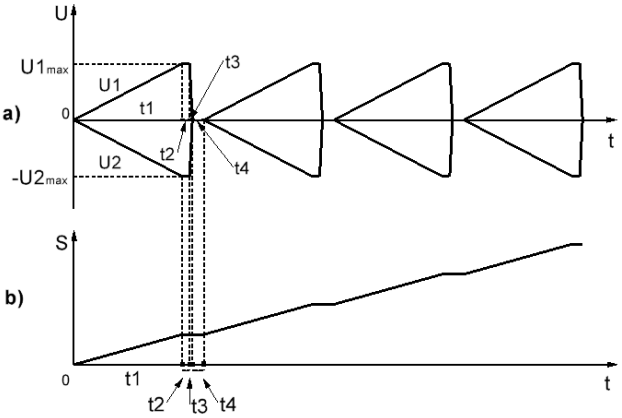

Fig. 2 Voltage curve a) and trajectory b)

To excite the piezoelectric inertia drive, the voltages U1, U2 are applied to each piezoelectric actuator at time t = 0 (see Fig. 2b). Subsequently, the actuator to which the positive voltage U1 is applied slowly expands, while the actuator to which the negative voltage U2 is applied contracts. The expansion or contraction of the actuators causes the drive element of the drive element connected to them to experience the deformation depicted in Figure 3.
The inner surfaces of the drive elements engaged with the element to be driven cause the element to be driven to rotate due to the prevailing static friction force between the surfaces. The direction of rotation depends on the polarity of the voltages U1, U2, or the direction of deformation of the actuators.

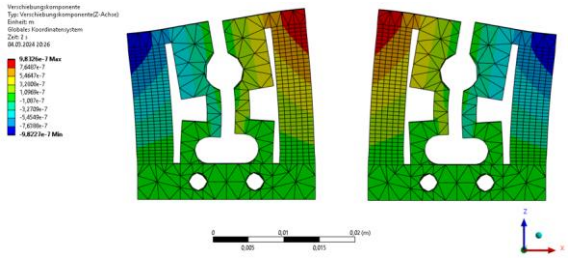

Fig. 3 Deformation of the stator upon clockwise and counterclockwise rotation of the spindle

After the phase of the small slope t1, phase t2 can occur, during which the actuator voltages remain unchanged and the element to be driven comes to a stop. In the subsequent phase of the large slope t3, the magnitudes of the voltages U1, U2 decrease very quickly. The actuators follow the voltages and simultaneously change their direction of deformation. I.e., the previously expanded actuator contracts and the contracted actuator expands. Because the element to be driven has mass, inertia prevents it from following the actuator movement, or the movement of the drive elements, and it remains in position. Due to the forces in the friction contact, the static friction transitions into a sliding friction. The surfaces of the friction contact between the drive element and the element to be driven slide against one another. Phase t4 then occurs, in which the voltages U1, U2 are zero and the element to be driven stops. The movement sequence repeats periodically at a maximum frequency of a few kHz. The element to be driven is set directly into rotating motion and indirectly into linear motion. Voltages U1, U2 are swapped to reverse the direction of motion of the element to be driven.
To increase the maximum force of the drive, drives are installed parallel to one another on one spindle. Figure 4 shows one version of an inertia drive with two drive elements and a common spindle to be driven.

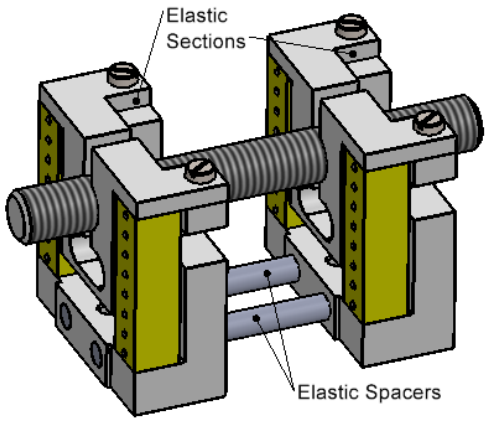

Fig. 4 CAD model with two drives on one spindle

The drive elements are kept apart from each other via elastic spacers or leaf springs. It is possible to use three or more drive elements instead of the two shown here.
The drives use PICMA® multilayer actuators with the dimensions 3x3x3 mm^3, 5x5x9 mm^3, and 5x5x18 mm^3 from PI Ceramic GmbH in Lederhose, Germany. The actuators enable a control voltage of 100 V_{dc}.
The inertia drive with two actuators with the dimensions 3x3x3 mm^3 develops a maximum force of 20 N and reaches a maximum rotational velocity of 2 rpm. The inertia drives with the two larger actuators have a maximum force of up to 40 N and a travel velocity of the spindle of 3 rpm.
Figure 5 shows prototypes of the inertia drives developed.

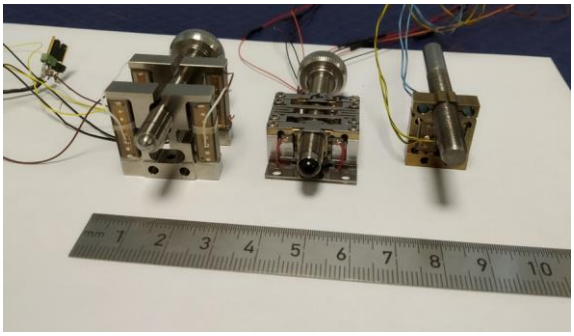

Fig. 5 Prototypes of PI spindle drives, which function based on the inertia operating principle, driven by PICMA® multilayer actuators with the dimensions 5x5x18 mm3, 3x3x3 mm^3 and 5x5x9 mm^3

2.2 Ultrasonic Principle

A further realization of spindle drives is based on the ultrasonic operating principle [7], wherein a continuous longitudinal wave is generated in the actuator of the drive. Longitudinal waves have a high effective coupling factor K_{eff}, enabling the efficient realization of an ultrasonic drive. Figure 6 shows the structure of the drive.

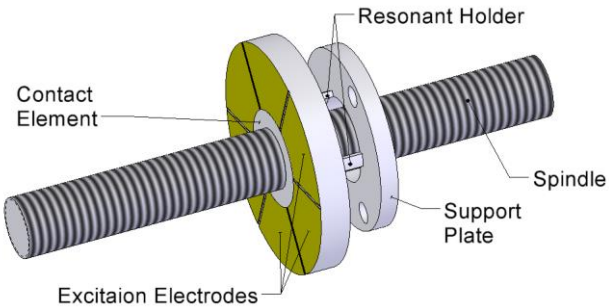

Fig. 6 CAD model of a spindle drive with an ultrasonic actuator

The drive comprises a piezoelectric actuator, a metal or ceramic spindle, and a support plate. The actuator is a resonator in the form of a round, thickness polarized piezoceramic disk with a hole in the center. There is a thin-walled contact element in the hole. The contact element is an internally threaded ring made of metal or ceramic. The contact element is connected to a support plate via resonant supports and forms a single part with it. The contact element is bonded inside the resonator with an organic adhesive (e.g., epoxy resin). The drive is fixed to a housing or a system part via the support plate. The resonant supports prevent the transmission of ultrasound waves from the resonator to the support plate or other system parts.
Excitation of a travelling wave in the resonator occurs via superposition of standing waves. The standing waves can be excited via at least three standing wave generators (SWG). For a travelling wave to form in the resonator, the SWGs must have a distance of λ/n and an electrical phase shift φ of $2\pi/n$, where n is the number of SWGs.
The actuator of the spindle drive developed is excited through three phases. One large side of the resonator has six identical excitation electrodes for this purpose. The electrodes across from each other are electrically connected. The electrodes, together with the piezoceramic between them, form three SWGs. The SWGs are connected to an electrical excitation source, which generates three sinusoidal voltages. The other large side of the resonator is fully metallized and forms the common electrode. The common electrode can remain electrically free, or it can be connected to the common ground of the excitation sources.

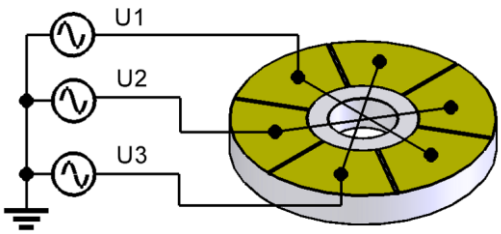

Fig. 7 Electrode circuit of an ultrasonic actuator

When the actuator is energized, each of the voltages U1, U2, U3 on the circumference of the resonator excites the fourth longitudinal mode, or a standing longitudinal wave. I.e., there are two wavelengths λ on the circumference of the resonator, wherein $\lambda = \pi$. Because the SWGs are spaced $\lambda/3$ apart and the phase angle φ between each of the three phases is 120°, the standing waves generated superimpose into a traveling wave. In this process, there are always two crests, or two oscillation velocity maxima, along the resonator circumference. The resonator deforms the contact element in the center of the resonator in the radial, or tangential, direction. The contact element always contacts, or drives, the spindle on two opposite sides. The spindle is set in rotation and concurrently executes a linear movement. A change in the direction of rotation of the traveling wave, or the spindle, occurs by swapping two phases.
Figure 8 shows a snapshot of the piezoceramic resonator upon excitation of the fourth longitudinal mode as the output of a harmonic analysis in the FEM program ANSYS.

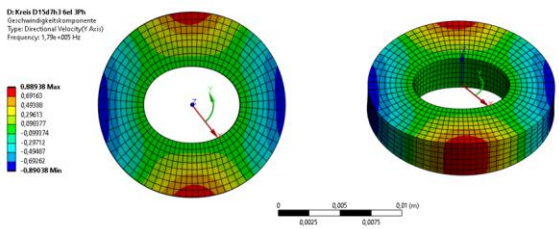

Fig. 8 Distribution of oscillation velocity amplitudes in the y direction in a piezoceramic resonator with the dimensions OD:ID:H 15:7:3 mm^3 upon excitation on the circumference of the fourth longitudinal mode as the output of a harmonic analysis in the FEM program ANSYS

The deformation of the resonator on its inner circumference is elliptical. The oscillation velocity maxima are on the outer circumference. This is not optimal. However, the

oscillation amplitudes on the contact element are large enough to drive the spindle.
Figure 9 shows two tested functional models of ultrasound spindle drives with resonators of different sizes.

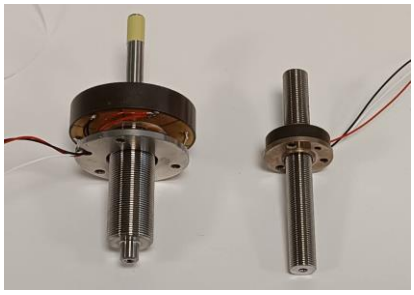

Fig. 9 Functional models of ultrasound spindle drives with the resonator dimensions OD:ID:H 15:7:3 mm^3 and 28:12:6 mm^3

The resonators of the functional models are made of piezoceramic PIC181 from PI Ceramic GmbH. Their dimensions are OD:ID:H 15:7:3 mm^3 and 28:12:6 mm^3. The threads of the spindles are M6x0.5 mm and 10x0.5 mm. The operating resonant frequencies of the drives are 178 kHz and 95 kHz. At a voltage of 80 Vrms, the smaller drive develops a force of 6 N at 240 rpm or 2 mm/s. The electrical power is 2.2 W.

3 Conclusion

The main disadvantage of the inertia drive is the relatively low velocity of the part to be moved or the screw. This is due to the inertia-based drive principle of the motor. In this design, the piezo actuator cannot drive the screw faster than some 10 kHz, as the static friction between the actuator and screw transitions into a sliding friction above a specific frequency. When this occurs, there is relative motion or sliding between the actuator and the screw without the screw being driven, and the screw simply stops.
Inertia drives emit sound waves because their operating frequency is in the audible range. As such, inertia drives are rather loud during operation. An advantage of spindle drives that function based on the inertia operating principle is their relatively high force.
The disadvantages of inertia spindle drives can be precluded by driving the spindle with an ultrasonic actuator. Spindle drives that function based on the ultrasonic operating principle are faster than inertia drives. No unpleasant noise is generated during operation because the drives operate in the ultrasonic range. They are fast and quiet. The rotor reaches a rotational velocity of up to 300 rpm.
It is also possible to design ultrasound spindle drives with other longitudinal oscillation modes. For example, the sixth longitudinal mode can be used for the function of the drive. In such a design, the circumference of the resonator has three wavelengths λ, or three oscillation velocity maxima, such that the spindle is contacted, or driven, at three points. This proves advantageous but requires more electrodes (nine, in fact). They are connected to form sets of three electrodes each.
Furthermore, it is possible to use the first longitudinal mode with a two-phase excitation. For this design, four SWGs are electrically connected to two phases. The distance between the SWGs is then $\lambda/4$ and $\varphi = 90°$. In this case, the spindle is driven on one side and asymmetrically from the contact element because it has only one oscillation velocity maximum on the circumference, which is not optimal.

4 Literature

[1] Luecke et. Al., Optical Mounting Apparatus, New Focus Inc., US Patent No: 5,140, 470 Aug. 18, 1992

[2] https://pdf.directindustry.de/pdf-en/physik-instrumente/piezo-mike-linear-actuators/13949-523819.html

[3] Luecke et. Al., Piezoelectric Actuator for Optical Alignment Screws, New Focus Inc., US Patent No: 4,734, 610 Apr. 25, 1995

[4] Okumura et. al., Vibration Wave Motor, Canon Kabushiki Kaisha, US Patent No.: 4,734,610, Mar. 29, 1988

[5] Reinhard Huebner, Harry Marth, Piezoelectric Rotary Drive for a Shaft, Physik Instrumente (PI) GmbH, US Patent No: 9,106, 158 B2 Aug. 11, 2015

[6] A. Wischnewski, Piezoelektrischer Trägheitsantrieb, Physik Instrumente (PI) GmbH, DE Patent DE10 2022 113 382 B3, 19.10.23

[7] W. Wischnewskiy, A. Wischnewski, Ultraschallmotor, Physik Instrumente (PI) GmbH, DE Patent 10 2010 022 812 B4, 18. 01. 2018

A wideband vibration energy harvester with integrated energy management designed for harsh environment.

Timotéo Payre, Nabil Bencheikh, Clément-Joseph Galteau, Alexandre Pagès, Guillaume Mansuy, Boris Laluc
Cedrat Technologies SA, Meylan, France. alexandre.pages@cedrat-tec.com

Abstract

Bistable energy harvesters (BEH) are well adapted devices to deal with the variation of the vibration source frequency spectrum. Indeed, the non-linear motion of this kind of harvester allow to reach a harvesting bandwidth up to 50% of the resonant frequency [2] compared to 1-2% of the resonant frequency typically for conventional linear energy harvesters. CEDRAT TECHNOLOGIES proposes a design using buckled beam and Amplified Piezoelectric Actuator (APA®) technology based on an architecture patented by the USMB. The nonlinear behavior of such a kind of energy harvester has already been studied in the literature and has demonstrated promising results [1].
Due to the use of buckled beam, the bistable energy harvester is very sensitive to the thermal expansion resulting from the harsh environment. In this paper, it is proposed an improved design to manage the thermal expansion and ensure harvesting capabilities on a wide temperature range from -40°C to +80°C.
Furthermore, an electronic extraction circuit has been implemented to deliver a regulated output voltage to power an IoT. Moreover, this electronic circuit can deal with spontaneous excess of energy by storing it into a supercapacitor or a battery and sink this energy to still powering the IoT when the vibration level decrease. The BEH with the electronic extraction circuit can generate a power of 8mW (see Figure 6).
The combination of an athermalized Bistable Energy Harvester with an electronic extraction circuit increases the technological readiness level to be integrated in system subjected to harsh environment like railway application for instance.

1 Wideband Bistable energy harvester

The following figure illustrates the prototype of a wideband bistable harvester based on buckled beam and using an APA® Electromechanical transducer. This prototype was design to survive to harsh environments but also to be versatile by allowing buckling level tuning.

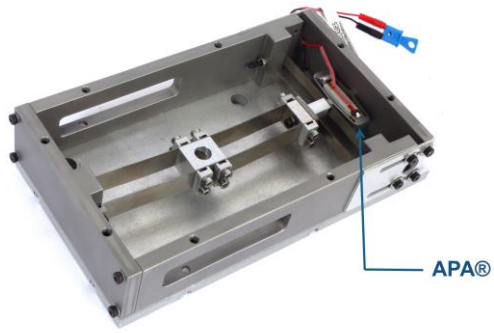

Figure 1 Bistable energy harvester

1.1 Modelling

The bistable energy harvester based on buckled beam can be modelized according to the following figure.

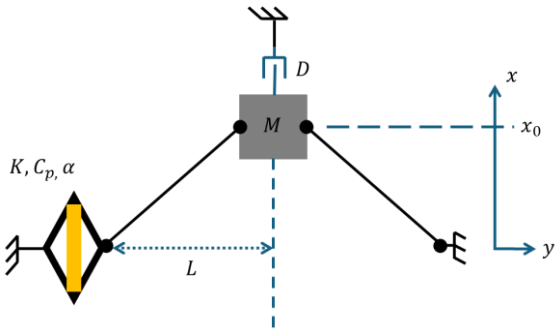

Figure 2 Bistable schematic

The governing equation of this system has already been studied in the literature [1] [2]

$$\begin{cases} M\gamma = M\ddot{x} - 2K\frac{x_0^2}{L^2}x + \frac{2Kx^3}{L^2} + D\dot{x} + \frac{2\alpha x v}{L} \\ \frac{v}{R} = \frac{2\alpha x \dot{x}}{L} - Cp\dot{v} \end{cases} \quad (1)$$

The buckling level allows to tune the potential well which is a determinant parameter for the dimensioning of bistable harvester. This parameter is set after manufacturing and must be maintained during the harvester's life for optimum performance. The monitoring of the buckling level can be done with low level admittance measurement. Indeed, at low level of excitation the moving mass oscillate around one equilibrium position and the equation 1 can be approximated in case of small displacement i.e. $x \ll x_0$.

$$\begin{cases} M\ddot{x} + \frac{4Kx_0{}^2x}{L^2} + \frac{4\alpha V x_0}{L} + D\dot{x} = M\gamma \\ I = \frac{2\alpha x_0 \dot{x}}{L} - 2C_p\dot{V} \end{cases} \quad (2)$$

In this set of equation is it possible to identify the resonant frequency:

$$f_0 = \frac{1}{2\pi}\frac{x_0}{L}\sqrt{\frac{4K}{M}} \quad (3)$$

By measuring the resonant frequency f_0 from the admittance it is possible to estimate the buckling level x_0 :

$$x_0 = L.2\pi f_0\sqrt{\frac{M}{4K}} \quad (4)$$

2 Thermal expansion management

The bistable harvester is based on buckled beam to get the bistability. The drawback of this architecture is the sensitivity of the harvester to the thermal differential expansion. Indeed, the piezoelectric element has a coefficient of thermal expansion almost 5 times lower than the stainless steel of the APA® shell. To limit the impact of this phenomenon on the harvester performance Cedrat has design a new APA®400M athermalized with an aluminium wedge to equilibrate the coefficient of thermal expansion along the piezoelectric element axis (see Figure 3).
The bistable harvester has been tested in climatic chamber to measure the impact of the temperature on the buckling level.

Figure 3 Athermalized APA®400M

The buckling level can be indirectly measured thanks to the bistable harvester resonant frequency:
See equation number (4)

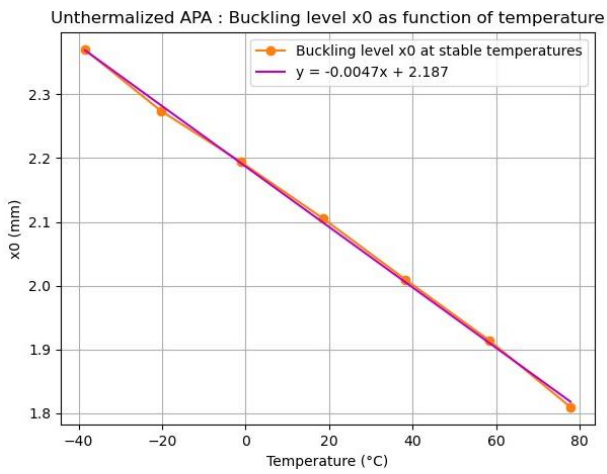

Figure 4 Buckling level as function of the temperature

The buckling level was set at approximately 2.1mm at 20°C, the test results show that the buckling level remains between 1.8mm and 2.4mm which correspond to a variation a less than ±15% over a temperature range from -40°C to +80°C which allows to use such harvester in harsh environment.

3 Electronic extraction circuit

This harvester was tested with COTS electronic extraction circuit AEM00330 from E-PEAS to demonstrate the capabilities of the harvester to power an IoT.

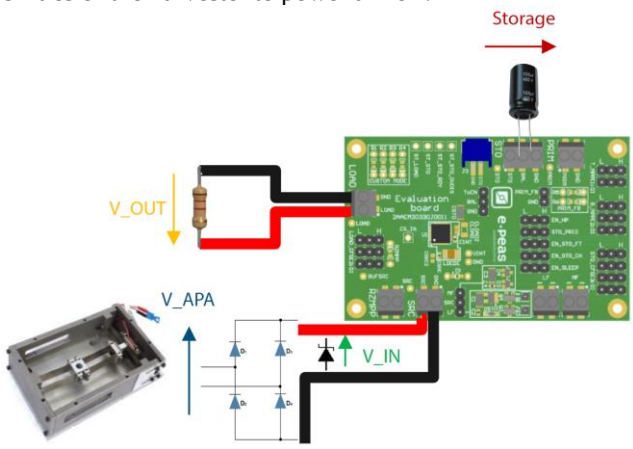

Figure 5 BEH and electronic extraction circuit

The blue curve corresponds to the voltage generated by the bistable harvester, the green curve is the rectified voltage at the end of the electronic extraction circuit whereas the orange curve is the voltage on restive load and the red curve is the voltage on a storage capacitor. This electronic circuit can deal with spontaneous excess of energy by storing it into a supercapacitor or a battery and sink this energy to still powering the IoT when the vibration level decrease. The BEH with the electronic extraction circuit can generate a power of 8mW (combination of the regulated voltage of 1.8V on a resistive load and speed of charging a 10mF capacitor).

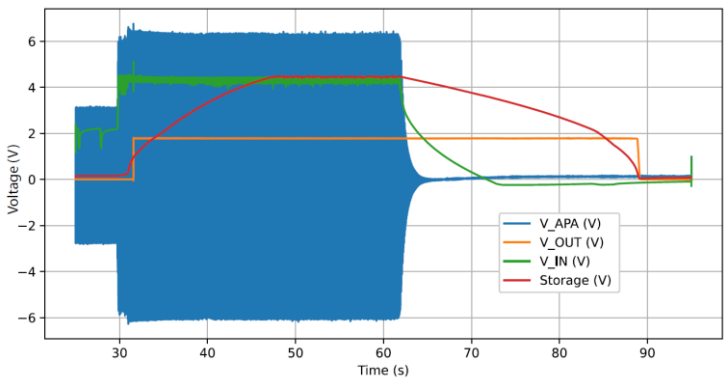

Figure 6 BEH voltage curves

4 Automated test bench

An automated test bench was designed to increase the tests capabilities of bistable harvester. This bench allows to study the generated power as function of the frequency and the resistive load which is a crucial parameter for the setting of the electronic extraction circuit.

This automated test bench is composed of:
A computer: to control the shaker and interact with the acquisition board.
An acquisition board: to acquire the power generated by the bistable harvester and the displacement of the moving mass.
A CTEC controllable decade box: this electronic is control by the computer with USB protocol to increment the resistive load value between each test.
The Bistable harvester is excited by the shaker with a swept sine signal 1.2g from 20 to 120Hz. Then, the generated power is measured on a resistive load. This load is increased between each test to obtain the mapping of the Figure 6.

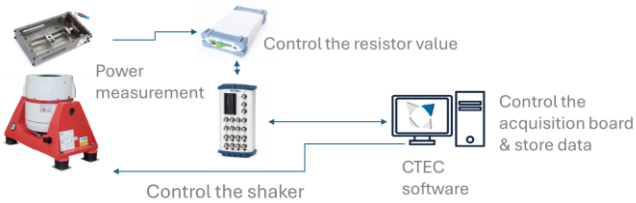

Figure 7 Automated test bench

Thanks to the high amount of data generated by the automated bench allows to adjust the model parameters on each version of bistable harvester to progress on the dimensioning for dedicated use case.

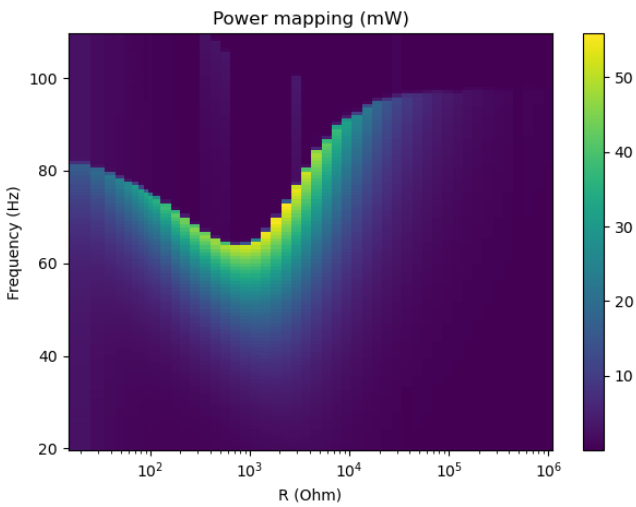

Figure 8 BEH power mapping

5 Conclusion

The bistable harvester equipped with this electronic suit for monitoring application by delivering a regulated voltage of 1.8V with a power of 8mW and capabilities to deal with an external storage element.
Moreover, the differential thermal expansion has been equilibrated to ensure a working temperature from -40 to 80°C.
The automated test bench allows to study the wideband behaviour of the bistable harvester in function of the resistive load value.

6 Acknowledgment

CTEC has received funding from EU thanks to the H2020 FAST-SMART project. Grant Agreement number: 862289.

7 Literature

[1] T. Huguet, A. Badel, et M. Lallart, « Parametric analysis for optimized piezoelectric bistable vibration energy harvesters », Smart Mater. Struct. Struct., vol. 28, no 11, Art. no 11, oct. 2019, doi: 10.1088/1361665X/ab45c6

[2] N. Bencheikh, T. Payre, A. Pagès, A. Benhamou, A. Badel, « A wideband piezoelectric vibration energy harvester », JNRSE 2022

Material Properties of Hard and Soft Piezoelectric Ceramics at Cryogenic Temperatures

Burhanettin Koc, Physik Instrumente (PI) GmbH & Co. KG, Karlsruhe, Germany (b.koc@pi.de)
Jan Homberg, Physik Instrumente (PI) GmbH & Co. KG, Karlsruhe, Germany (j.homberg@pi.de)
and
Sebastian Schlack, PI Ceramic GmbH, Lederhose, Germany (s.schlack@piceramic.de)

Abstract

It is well known that piezoelectric ceramic materials behave differently at cryogenic temperatures compared to ambient temperature. Temperature dependency of material properties such as dielectric and piezoelectric coefficients are characterized in the literature. In this study, we present complete sets of material properties at different temperatures for two types of piezoelectric ceramics, namely hard PZT (PIC 181) and soft PZT (PIC 255), respectively. For each material, a complete set of mechanical, piezoelectric, and dielectric coefficients was obtained by resonance characteristics of differently shaped piezoelectric samples. Transverse, longitudinal, thickness, shear and planar resonance modes were measured at temperatures from 300 K down to about 80 K. From these measurements, the material parameters were calculated for each temperature following DIN EN 50324 [1]. Using GID-ATILA finite-element-analysis (FEA) software, their corresponding impedance spectra were calculated and compared with the measured data.

1 Introduction

Piezoelectric actuators find applications in various fields, e.g., in ultrasonics or nanopositioning [3-4]. Since the piezoelectric charge coefficients (d_{31}, d_{33}, d_{15}) for soft piezoelectric ceramics are larger compared to the hard piezoelectric ceramics, it is not surprising to see that for positioning applications, primarily multilayer piezoelectric actuators made from soft piezoelectric ceramics are used.

However, the properties of the piezoelectric actuators differ significantly at cryogenic temperatures. Various piezoelectric multilayer actuators available on the market have been considered for application in cryogenic environments. The literature reports about their deviant behaviour at low temperatures compared to ambient conditions [4-9]. In these studies, mostly two important characteristics were observed: the displacement behaviour and the capacitance change.

To fully understand the different behaviour at different temperatures, one must consider the full positioning system – including, e.g., mechanical and electrical interfaces. The identification of the individual contributions of the system components however remains challenging.

If the behaviour of specific parts in a positioning system is known, the positioning system can be simulated and optimized for the intended conditions in advance, and the behaviour can be tuned accordingly.

Our aim in this study is to characterize the complete small signal material properties of hard and soft type piezoelectric ceramics at cryogenic temperatures and to obtain a complete set of mechanical, piezoelectric, and dielectric coefficients, as well as the behaviour of these parameters with decreasing temperature.

2 Characterizing Piezoelectric Ceramics with Resonance Method

Four different geometries from both soft and hard piezoelectric ceramics were used to determine the set of material properties (Figure 1). The capacitances of two test samples, and the resonance and antiresonance frequencies of the primary resonance modes - transverse, radial, longitudinal, shear, and thickness - were measured to calculate relative permittivity, elastic compliances, and piezoelectric charge constants [1-2]. In addition, the loss factor $\tan\delta$ was measured and the mechanical quality factor Q_m determined from resonance curves.

Figure 1 Soft (top) and hard (bottom) piezoelectric ceramic test samples used for small signal characterization.

The test samples, held with spring forced pins, were placed in the cryo-chamber, which has two layers of internal thermal radiation shielding (Figure 2). In addition to the four sample holders, a fifth identical setup with a Pt100 temper-

ature sensor held with spring forced pins was used to monitor the temperature of the test samples. Capacitances, loss factor, corresponding resonance and anti-resonance frequencies, and the temperature (Pt100 resistance) were measured with an impedance analyser (E-4990A, Keysight) during cooldown and warmup of the cryo-chamber from room temperature down to about 80 K. The collected data were then analysed to calculate mechanical, electrical, and electromechanical properties following DIN EN 50324 [1]. Furthermore, the full parameter sets were optimized via a repeated matrix optimization routine [13].

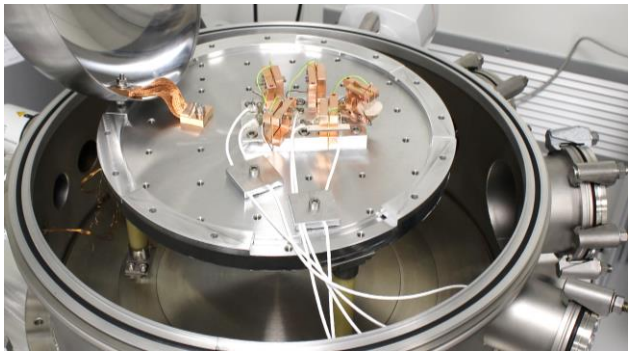

Figure 2 Test samples were held with spring force sample holders in the cryo-chamber.

The material properties for the soft (PIC255) and the hard (PIC181) PZT piezoelectric ceramics are summarized in Table 1 for both room temperature (RT) and 80 K.
At a first glance, one can see that the piezoelectric charge coefficients (d_{31}, d_{33}, d_{15}) for PIC181 are larger than for PIC255. The decrease of thickness mode piezoelectric charge coefficients (d_{33}) for PIC255 is about 65 %. Only 35 % of the displacement can be generated by a multilayer actuator if it is exposed to a temperature of 80 K. Whereas in the case of hard piezoelectric ceramic the decrease of thickness mode piezoelectric charge coefficients (d_{33}) is only at about 20 %. 80 % of the displacement can be generated by a hard PZT multilayer actuator if it is exposed to the temperature of 80 K. Similar tendencies are also true for the relative permittivity ($\varepsilon_{11}^T/\varepsilon_0$, $\varepsilon_{33}^T/\varepsilon_0$).

Table 1 Piezoelectric material parameters at room temperature (RT) and at 80 K for PIC255 and PIC181.

Parameters	PIC 255		PIC 181	
	at RT	at 80 K	at RT	at 80 K
σ (kg/m^3)	7800		7850	
S_{11}^E (10^{-12} m^2/N)	16.2	11.6	11.63	11.36
S_{12}^E	-5.4	-2.91	-3.9	-3.6
S_{13}^E	-6.85	-4.4	-4.33	-4.23
S_{33}^E	17.4	12.7	12.81	12.63
S_{44}^E	42.2	30.5	29.41	28.40
d_{33} (10^{-12} m/V)	341	120	186	144
d_{31}	-171	-63	-96	-77.5
d_{15}	515	226	289.2	229
$\varepsilon_{11}^T/\varepsilon_0$	1734	600	1204	806
$\varepsilon_{33}^T/\varepsilon_0$	1660	500	1051	734
Q_m	105	196	2450	121
tan δ (10^{-3})	15.3	24	3.5	32

2.1 Behaviour of the Soft Piezoelectric ceramic

The tendency of relative permittivity change to temperature is linear for PIC255. Relative permittivity in thickness direction ($\varepsilon_{33}^T/\varepsilon_0$) decreased from 1660 to 500 (-70%) as the temperature decreased from RT to 80 K (Figure 3). Similarly, the decrease of relative permittivity in transverse direction ($\varepsilon_{11}^T/\varepsilon_0$) is from 1734 to 600 (-65%) (Figure 3).

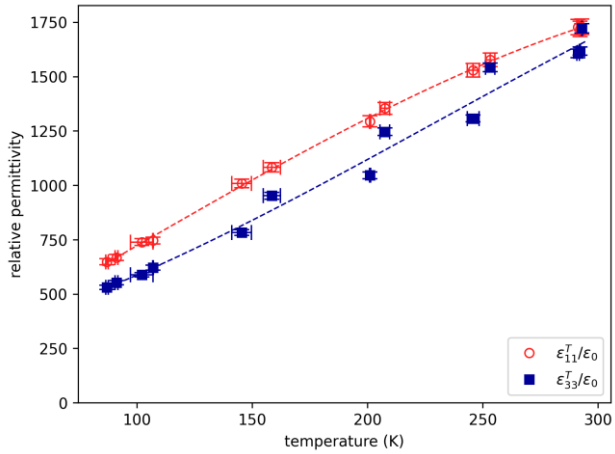

Figure 3 Relative permittivity changes with temperature for PIC255.

Figure 4 shows the piezoelectric charge coefficients (d_{31}, d_{33}, d_{15}) for soft piezoelectric ceramic (PIC255), which decrease steadily as temperature is decreased from RT to about 80 K. The relative decrease of d_{33} is largest in this temperature range (-65%).

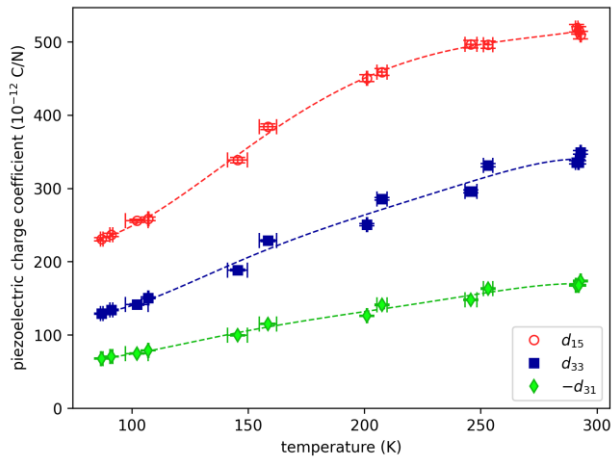

Figure 4 Change of piezoelectric coupling coefficients (d_{31}, d_{33} and d_{15}) with temperature for PIC255.

To verify the material parameters, we simulated the resonance characteristics of respective ceramic samples using

the obtained material coefficients with the GID-ATILA finite-element-analysis (FEA) software and compared the resulting curves to the measured data. To improve the result for 80 K, we slightly tuned the parameters s_{11}^E (11.9 10^{-12} m^2/N) and s_{12}^E (-3.61 10^{-12} m^2/N). This procedure was stimulated by sensitivity analyses shown in reference [12]. Figures 5 and 6 show the measured and calculated impedance curves at both RT and 80 K for the transverse and radial mode of PIC255, respectively.

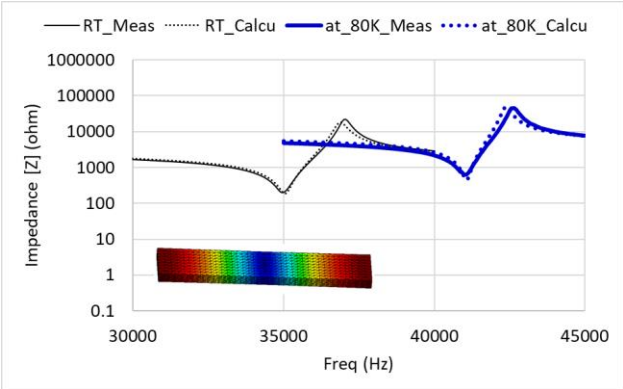

Figure 5 Measured and calculated impedance for the first longitudinal mode in the transverse direction of the PIC255 plate (40x8x2 mm^3) at RT and at 80 K.

After optimizing s_{11}^E using the measured impedance spectra around the first radial mode of the disc at 80 K, s_{12}^E was adjusted to the spectra of the transversal mode.
Figures 5 and 6 also confirm the shift of the frequencies from room temperature to about 80 K. The impedance data show that not only the piezoelectric charge coefficients (d_{31}, d_{33}, d_{15}) and the relative permittivity values ($\varepsilon_{11}^T/\varepsilon_0$, $\varepsilon_{33}^T/\varepsilon_0$), but also the elastic compliance constants change significantly (see also Table 1).

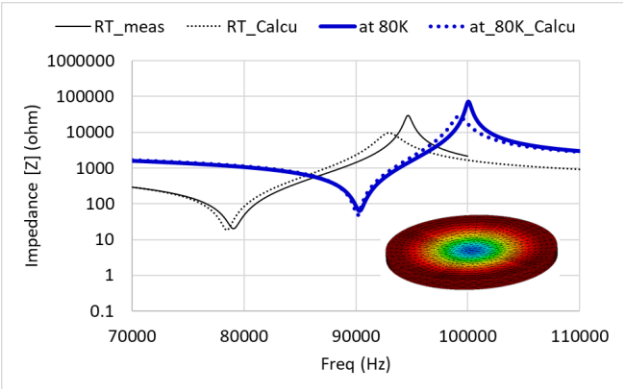

Figure 6 Measured and calculated impedance for the first radial mode of the PIC255 disc at RT and at 80 K.

2.2 Behaviour of the Hard Piezoelectric ceramic

Figure 7 shows the relative permittivity ($\varepsilon_{33}^T/\varepsilon_0$, $\varepsilon_{11}^T/\varepsilon_0$) for PIC181. A decrease of about 30% is observed at 80 K, much less than for PIC255.

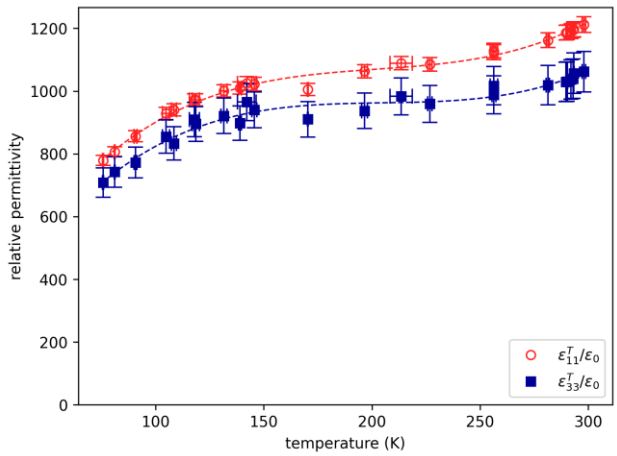

Figure 7 Relative permittivity changes with temperature for PIC181.

Figure 8 shows the piezoelectric charge coefficients (d_{31}, d_{33}, d_{15}) for PIC181. Compared to PIC255, the rate of change is much smaller. Notably, at 80 K, the piezoelectric charge coefficients of PIC181 are even higher than for PIC255. An actuator system at 80 K would therefore generate a larger displacement, if built with hard instead of soft piezo ceramic.

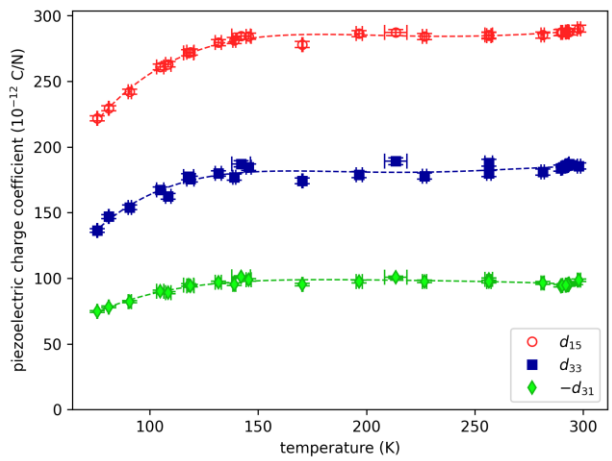

Figure 8 Change of piezoelectric coupling coefficients (d_{31}, d_{33}, and d_{15}) from RT down to 80 K for PIC181.

As in the case of soft PIC255, measured impedance spectra were compared with calculated impedance spectra. Here, however, no further fine tuning of the parameters was applied.
Figure 9 shows the measured and the calculated impedance at RT as well as at 80 K. In comparison to PIC255 (Figure 5), the frequency shift of the transversal mode is much smaller. However, the impedance magnitude at the resonance point increase significantly at 80 K compared to the resistance value at RT. This corresponds to the significant decrease of the quality factor (see Table 1).

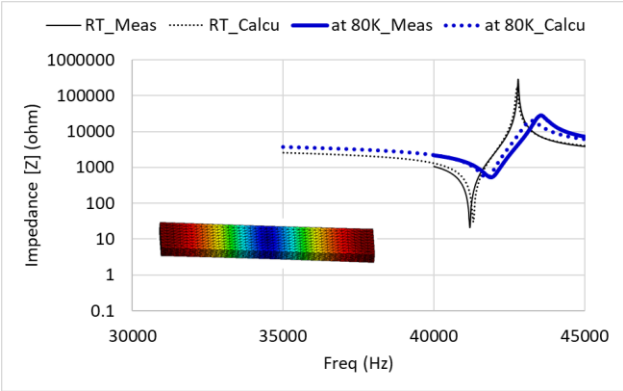

Figure 9 Measured and calculated impedance for the first longitudinal mode in the transverse direction of the PIC181 plate (40x8x2 mm3) at RT and at 80 K.

Figures 10 shows impedance spectra of the first radial mode of the PIC181 disc. The resonance frequency changed barely with temperature. However, there is a significant increase of the impedance magnitude at the resonance point.

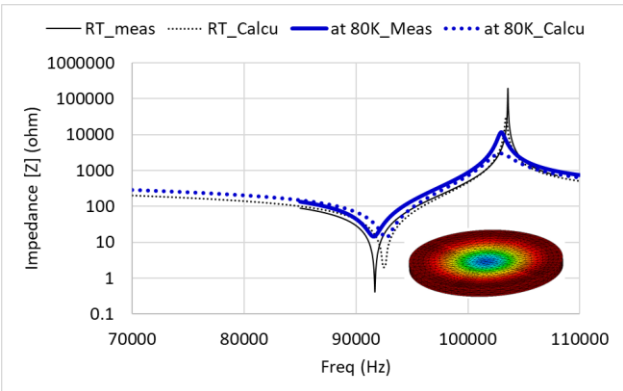

Figure 10 Measured and calculated impedance for the first radial mode of the PIC181 disc at RT and at 80 K.

2.3 Remarks on Simulated Spectra

Using the measured material properties, impedance spectra of all the test samples were calculated with the GIDATILA program. While the spectra shown above match the measured curves very well, not quite as good matches could be achieved for the shear and thickness modes. This is understandable because shear and thickness modes are at higher frequencies and overlap with various higher modes. A detailed sensitivity analysis might help to optimize the parameters even further [12].

3 Conclusion

We present temperature dependency of complete material properties for hard (PIC 181) and soft (PIC 255) piezoelectric PZT ceramics from room temperature down to 80 K. Our measurements reveal that the reduction of piezoelectric coupling coefficients and dielectric constants are lower for the hard piezoelectric ceramic than for the soft one. At 80 K, the piezoelectric charge coefficients of PIC181 even surpass those of PIC255. This observation suggests that the use of hard PZT ceramics could be beneficial for cryogenic actuator applications.

On the other hand, our data shows that the mechanical quality factor of PIC181 drops dramatically at low temperatures, while for PIC255 an increase was observed. This finding is highly relevant for ultrasonic applications at cryogenic temperatures.

While the reliability of the presented data is limited due to the small sample number, the obtained parameters already enable us to accurately simulate the behavior of piezoelectric actuators at low temperatures, which will greatly benefit research and development in this area. It is planned to verify and improve the data sets with further experiments.

4 Literature

[1] DIN EN 50324: Piezoelektrische Eigenschaften von keramischen Werkstoffen und Komponenten, 2002

[2] IEEE Standard on Piezoelectricity 1987 IEEE/ANSI Standard 176-1987

[3] Uchino, K. Piezoelectric Actuators and Ultrasonic Motors; Kluwer: Boston, MA, USA, 1997

[4] P. Pertsch, "Piezoelectric Actuator Applications - Status 2018," ACTUATOR 2018; 16th International Conference on New Actuators, Bremen, Germany, 2018, pp. 1-7.

[5] Halverson, P.G., Parker, T.J., & Levine, M.B., Cryogenic performance of piezo-electric actuators for opto-mechanical applications, SPIE Optical Engineering + Applications (2007).

[6] Martinet, Guillaume & Blivet, S. & Chatelet, F. & Fouaidy, Mohammed & Hammoudi, Nazek & Olivier, A. & Saugnac, H., Low temperature prop-erties of piezoelectric actuators used in SRF cavities cold tuning systems. EPAC 2006

[7] Halverson, P.G., Parker, T.J., & Levine, M.B., Cryogenic performance of piezo-electric actuators for opto-mechanical applications, SPIE Optical Engineering + Applications (2007).

[8] Fouaidy et al., "Full Characterization at Low Temperature of Piezoelectric Actuators Used for SRF Cavities Active Tuning," Proceedings of the 2005 Particle Accelerator Conference, Knoxville, TN, USA, 2005, pp. 728-730, doi: 10.1109/PAC.2005.1590542.

[9] Pischalnikov, Y.: Contreras-Martinez, C.: Review of the application piezoelectric actuators for SRF cavity tuners, euspen's 23rd, International Conference & Exhibition, Copenhagen, DK, 2023

[10] Oliveira, A. N. e. al.: Review of Scintific Instrument 88, 063104, 2017

[11] Nakazono, M. et. al.: Jpn. J. Appl. Phys. 54. 07HE15, 2015

[12] Kar, B.: Basaeri, H.: Roundy, S.: Wallrabe, U.: Smart Mater. Struct. (2023) 32 085012

[13] Scholehwar, T.: Charakterisierung der Struktur- Gefüge- Eigenschaftsbeziehungen von piezokeramischen Werkstoffen des Systems PZT/SKN, Dissertation, Technische Universität Dresden, 2010

HASEL-Actuated Pneumatic Valve for Image Guided Robotic Systems

Fabian Sadi and Jan Holthausen
Mannheim Institute for Intelligent Systems in Medicine (MIISM), Mannheim, Germany
Fabian.sadi@medma.uni-heidelberg.de

Abstract

Robotic systems for image-guided interventions need to be smaller, more compact, and more flexible in their applicability to gain clinical acceptance. Actuators need to be compatible with medical imaging modalities and at the same time compact enough to be integrated into small robots. HASEL (Hydraulic-Amplified-Self-Healing-Electrostatic) actuators demonstrate significant potential for this application, given their high energy density and straightforward mechanical design, which surpass common mechanical principles. Conventional pneumatic valves are unsuitable for use in Magnetic resonance imaging (MRI), which is why pneumatic actuators are equipped with long supply lines into the MRI control room. This results in long response times, complicating the control of the actuators. The aim of this work is to examine the possibility of a HASEL-actuated pneumatic valve. A valve design has been developed and tested that can be actuated by HASEL actuators. Experiments showed that the valve, under electric signal control, can handle differential pressures exceeding 10 kPa. There is potential for design improvements, particularly in eliminating leaks to increase the valve switching pressure. Final tests of a HASEL actuator in the MRI scanner field confirmed its fundamental MRI compatibility.

1 Introduction

The expeditious diagnosis of cancer enables swifter therapeutic interventions, thereby substantially enhancing treatment outcomes. Image-guided interventions play a pivotal role in early diagnosis and therapy, as exemplified by procedures such as biopsies and ablation [1]. The development of appropriate robotic biopsy systems is crucial for facilitating fast, resource-efficient, and precise biopsy procedures. Therefore, robotic systems must be smaller, easier to handle, better integrated into the clinical environment, and compatible with a wider range of imaging systems [2]. Currently available robotic systems, both in the market and in research, do not meet these requirements. This paper introduces an initial concept for the implementation of a HASEL-actuated valve, which is capable of being operated directly within the scanning area of an MRI or Computer tomography (CT). This makes the system more compact by avoiding a bulky bundle of hoses extending into the shielded MRI control room, as only a single supply line is required. Individually supplying each actuator from the control room results in extended response times and more complex control processes, which are avoided through an integrated valve architecture. Through the integrated solution in close proximity to the patient, a vacuum valve concept was designed to enhance sterility.

1.1 HASEL-Actuators

HASEL actuators are soft electrohydraulic actuators and were first presented in 2018 [3]. They consist of a thermoplastic shell containing a dielectric liquid. On either side of the shell, flexible electrodes are affixed, as illustrated in **Figure 1** on the left. Applying an electrical voltage causes a Maxwell stress on the shell [4]. Thereby the electrodes approach each other and push the dielectric liquid into the free ends of the thermoplastic shell (**Figure 1**, right) [5].

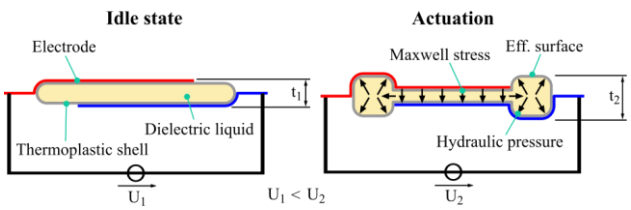

Figure 1 Schematic representation of the operation of an expansion HASEL actuator

Depending on the geometric arrangement of the electrodes, either contraction or expansion can be achieved. The hydraulic amplification of these actuators results in a very high force density, which is why it is very suitable for miniaturization. Simultaneously, the use of electrostatic forces enables a very fast and efficient activation. From a physical standpoint, the HASEL actuator consists of a system of capacitances connected in series [6]. By incorporating Coulomb's law, the electrostatic force F_{ele} of a HASEL actuator is derived according to:

$$F_{ele} = \frac{A\varepsilon_0 V^2}{2} \frac{\left(\frac{2}{\varepsilon_{rf}} + \frac{1}{2\varepsilon_{rl}}\right)}{\left(\frac{2d_f}{\varepsilon_{rf}} + \frac{d_l}{\varepsilon_{rl}}\right)^2} \quad (1)$$

Here, A represents the electrode area and V the electrical voltage. The parameter ε_0 denotes the vacuum permittivity, where ε_{rf} and ε_{rl} are the relative permittivities of the film and the liquid, respectively. Similarly, d_f and d_l represent the material thicknesses of the film and the liquid. The displacement of the liquid during the actuation of the HASEL actuator results in a continuous decrease in d_l. The determination of d_l is thus governed by the relationship with solid mechanics [6]:

$$d_l = d_{max} - 2d_f - 2\frac{d_w}{d_x} \quad (2)$$

In this context, d_{max} represents the total thickness of the actuator, including the thermoplastic film, while the last term describes the slope of the thermoplastic film as it deflects by w. Alternatively, the actuation force can also be derived using the free energy [7]. To enhance the electrostatic force F_{ele} as per **Eq.(1)**, a high voltage, large electrode areas, and high material-dependent permittivities are pursued, while minimizing the electrode spacing. If F_{ele} is referenced to the electrode area A , this describes the Maxwell stress, which is directly coupled to the hydraulic pressure of the actuator. According to this relationship the actuation force of a HASEL actuator can be controlled similarly to a hydraulic cylinder, through the effective surface area (**Figure 1**, right). A smaller electrode area results in lower strain and higher actuator force, whereas a larger electrode area leads to greater strain but reduced actuator force [3].

2 Materials and Methods

2.1 Film Materials for HASEL Actuators

Prior to the development of the valve concept, a thorough examination of the manufacturing process of HASEL actuators was conducted. In previous publications [8, 9], BOPP (biaxially oriented polypropylene) films have been proposed as the thermoplastic film type. Due to availability issues with this film type in small quantities, it was necessary to use other practical film types that were available on the market. Thereby, four alternative types of film were examined for their properties and subsequently assembled and tested as HASEL actuators.

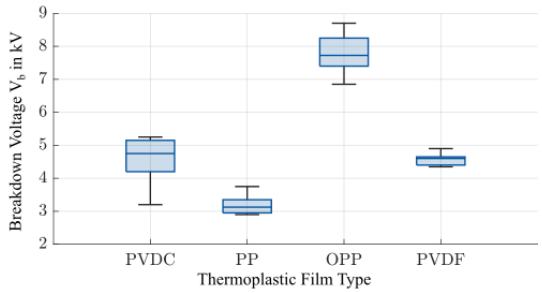

Figure 2 Boxplot diagram showing the determined breakdown voltages of the examined thermoplastic films.

In **Figure 2**, the investigated film types are depicted along with their breakdown voltages in a boxplot. The breakdown voltage was experimentally determined by coating the films on both sides with overlapping electrodes made of graphite paint (Cramolin Graphit, Cramolin, Germany). Subsequently, the electrodes were connected to an electrical high-voltage source (Ultravolt 5HVA24-BP1, Advanced Energy Inc., USA), and the voltage was gradually increased by 50 V increments until electrical breakdown occurred. This experiment was conducted six times for each type of film to gain insights into the behavior of the films. Partial larger fluctuations in breakdown voltages are observed, attributable to tolerance variations in film thickness. Consequently, the electrode spacings are locally reduced, resulting in premature electrical breakdown.

To determine the breakdown strength E_b, the averaged breakdown voltage of each film type was divided by its respective film thickness (**Table 1**).

Table 1 Characteristics of the examined thermoplastic films.

Type of Film	d_f in µm	ε_r	V_b in V	E_b in $\frac{V}{\mu m}$
PVDC	10	3.5 – 4.5	4550	455
PP	18	2.2	3200	178
OPP	20	2.2	7775	389
PVDF	25	9	4583	183

The comparative analysis of various film types according to **Table 1** reveals that PVDC (polyvinylidene chloride) film exhibits the best electrostatic properties. However, in practice, it has been found that this type of film was not practical due to increased self-adhesion. This necessitated significant restoring forces to return the actuator to its initial position. The PVDF (polyvinylidene fluoride) film is highly intriguing due to its high relative permittivity for generating significant actuator forces. However, the considerable thickness of the film led to instabilities during actuation, resulting in unpredictable twitches. There were no issues observed during the actuation of the HASEL actuators with PP (polypropylene) and OPP (oriented polypropylene) films. Due to the lower breakdown strength of the PP film, the OPP film was chosen for further manufacturing of the actuators.

2.2 Valve Design

Given the application of the valve within the scanning area of the MRI and thus in close proximity to the patients, the valve design was conceived as a vacuum valve. By venting the valve from vacuum to ambient pressure, the pressure surge is directed into the valve rather than out of the valve, thereby ensuring improved sterility and acceptance by the patient.

Figure 3 depicts the CAD design of the valve head along with the HASEL actuators used for actuating the valve stem. The sectional view on the left side of **Figure 3** demonstrates the valve logic.

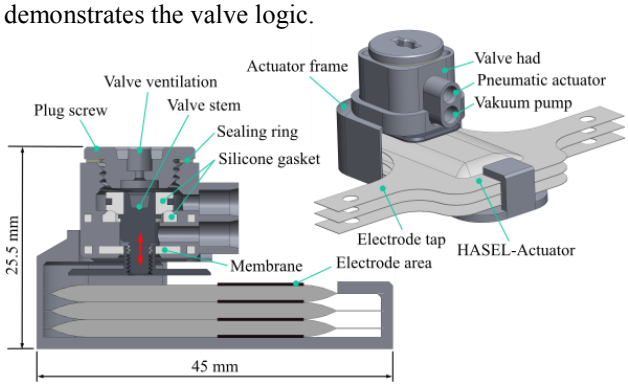

Figure 3 Pneumatic Vacuum Valve Design

The HASEL actuators feature a rectangular contour, with electrodes applied half sided on both sides and led outward through tabs (see **Figure 3**, right). To achieve increased actuator force and stroke, three actuators were stacked on top of each other. When an electrical voltage is applied to the

electrodes, they contract, pushing the dielectric liquid underneath the valve stem and causing it to move upward. In doing so, the valve ventilation is closed, causing the upper valve port to be subjected to vacuum. The structurally rigid components of the valve were fabricated using SLA printing (Form 3, Formlabs, USA) with Clear resin and a layer resolution of 25 µm. The threaded connections of the valve stem and the valve plug screw were created during the printing process, reliably achieving thread sizes as small as M3. To seal the thread of the valve plug screw, a sealing ring made from Formlabs Elastic 50A was 3D printed and attached to the valve plug screw using the same resin and subsequent UV curing. The internal seals and the membrane for the valve stem's return spring were produced using silicone casting (Ecoflex 00-30, Smooth on, USA) (**Figure 4**).

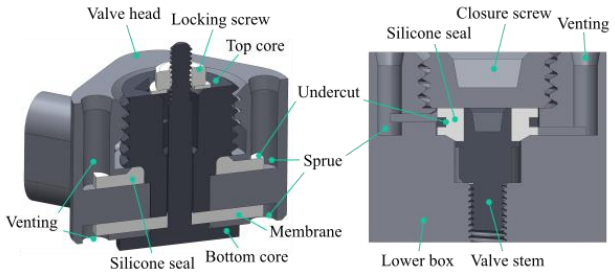

Figure 4 Casting molds for silicone seals in the valve head and on the valve stem

For the silicone seals of the valve head (**Figure 4**, left), upper and lower cores were designed and secured to the housing with a locking screw. Sprue and venting were achieved through channels in the valve head. The silicone seal on the valve stem was produced using a separate casting mold (**Figure 4**, right). Undercuts were incorporated into the components to secure the encapsulated silicone seals.

3 Experiments

3.1 Test Bench Setup

For conducting the experimental tests, a test setup was constructed to evaluate the valve under its maximum achievable vacuum conditions. The block diagram in **Figure 5** illustrates the individual components and their electrical and pneumatic interconnections.

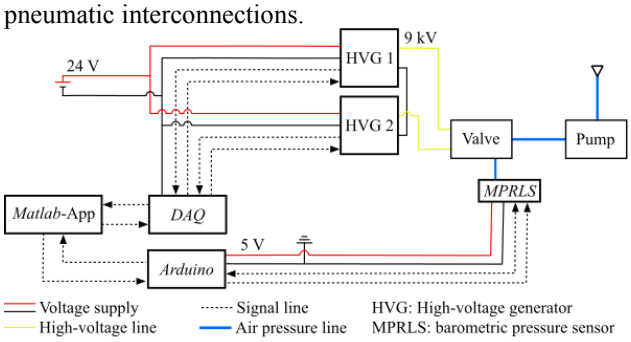

Figure 5 Block diagram of the test rig setup

For the visualization and communication of electrical voltage, current, and pressure signals, a Matlab app was developed. Pressure measurement was conducted using a barometric pressure sensor (MPRLS, Adafruit, USA) connected to the output of the pneumatic valve. Communication with the pressure sensor was achieved via the I^2C interface of an intermediary microcontroller (Arduino Mega 2560, Arduino, Italy). The high voltage supply for the HASEL actuators was provided by two high voltage generators (as described in Section 2.1), each generating 5 kV, connected in series to achieve a total voltage of 10 kV. The HASEL-Actuators themselves, were then supplied with 9 kV. Signal processing for the control and monitoring of the high-voltage generators was performed using a data acquisition (DAQ) device (NI PXI-6255, National Instruments, USA). The valve's vacuum supply was provided by a metering pump (DX-250, Metcal, USA) connected to a compressed air source operating at 5 bar.

3.2 Results

The experiments comprised a total of four individual trials with varying differential pressures set at the vacuum pump. **Table 2** presents the measured valve switching pressures at the valve outlet and the valve switching delays during activation and deactivation for each experimental series.

Table 2 Valve switching pressures and valve switching delays depend on the set differential pressure at the vacuum pump.

Δp_D in kPa	Δp_S in kPa	Δt_{on} in s	Δt_{off} in s
1.2	0.85	0.2	1.95
5	2.14	0.18	1.28
10	4.7	0.12	2.35
15	4.76	0.1	2.37

The HASEL-actuated pneumatic valve demonstrated reliable switching across all differential pressure levels, confirming the actuators performance capability. However, upon analyzing the valve switching pressures Δp_S in **Table 2**, significant deviations from the specified differential pressures Δp_D were observed. Additionally, it was noted that above a differential pressure of 10 kPa, there was only a minor increase in the valve switching pressure. This behavior was attributed to system leaks, allowing vacuum to escape through the ventilation port in the valve. **Figure 6** illustrates the valve in its non-actuated state (left) and actuated state (right). The lines before and after actuation indicate the position of the valve stem, a noticeable tilt. As a result, the valve stem seal did not uniformly press against the ventilation port, leading to inadequate sealing. Even guides that had been integrated into the valve stem could not compensate for the uneven force distribution of the HASEL actuators on the valve stem.

Figure 6 The tilting of the valve stem during actuation. Left without actuation and right with actuation.

The switching delays of the HASEL actuators during valve activation Δt_{on} significantly decreased with increasing differential pressure, while the delay Δt_{off} during deactivation markedly increased. This behavior was attributed to residual electrode charging, maintaining residual actuator force even at 0 kV. A brief reversal of the electrode polarity (-3 kV for 0.5 s) partially alleviated this effect; however, some residual charge persisted. This behavior is depicted in **Figure 7**, where the valve switching pressures Δp_S are plotted against time t at a differential pressure Δp_D of 10 kPa. The abrupt pressure change in **Figure 7** by off switching the valve is attributed to the polarity reversal, resulting in another brief actuator displacement.

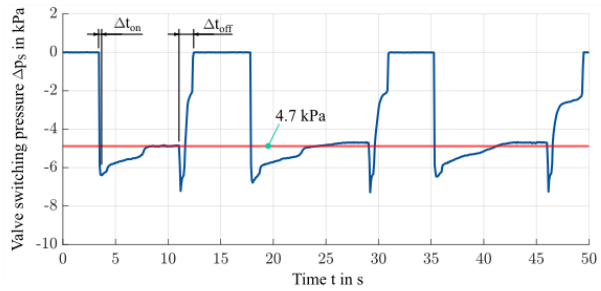

Figure 7 Valve switching operations with an applied differential pressure of 10 kPa.

The initial experiments with an expansion HASEL actuator in the scanning field of a 3-Tesla MRI (Siemens, Magnetom Skyra, Germany) demonstrated artifact-free imaging in the activated state (**Figure 8**). For the assessment of image quality, a bottle phantom [10] is used that is clearly visible in the MRI image, thereby making image artifacts apparent (**Figure 8**, left) . The dielectric liquid of the HASEL actuator is visible in the image, indicating its activated state as the liquid is pushed to the edge of the actuator (**Figure 8**, right).

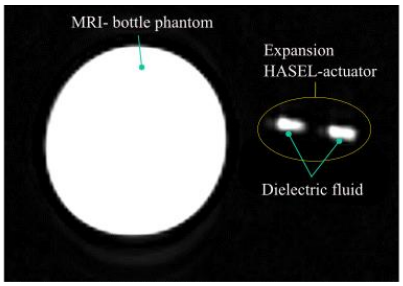

Figure 8 MRI cross section of an expansion HASEL actuator with an MRI phantom bottle for image quality assessment.

4 Discussion

In this work, a HASEL-actuated pneumatic valve was successfully developed and tested. Given the procurement difficulties with the currently recommended actuator film, experiments were conducted using available thermoplastic films. It was found that OPP film represents a viable alternative. The experiments demonstrate significant potential of the actuators with the opportunity of further optimisation. Future optimisation of the valve design aim to reduce existing leaks to enable higher valve switching pressures. Additionally, measures to mitigate prolonged off-switch delays due to residual electrode polarization will be further developed. The HASEL actuator was successfully tested under MRI imaging within the direct scanning field. The test confirmed that the actuator's electric field in this arrangement does not affect the MRI's magnetic field signals. The visibility of the actuator in the MRI image also enables the possibility of controlling the actuator positions based on the image data. Therefore, this work motivates further development of these actuators for integration into biopsy robot systems under MRI imaging.

5 Literature

[1] Iguchi, T., Hiraki, T., Tomita, K., Gobara, H., Fujiwara, H., Sakurai, J., Matsui, Y. u. Kanazawa, S.: Simultaneous biopsy and radiofrequency ablation of T1a renal cell carcinoma. Diagnostic and interventional imaging 97 (2016) 11, S. 1159–1164

[2] Fichtinger, G., Troccaz, J. u. Haidegger, T.: Image-Guided Interventional Robotics: Lost in Translation? Proceedings of the IEEE 110 (2022) 7, S. 932–950

[3] Acome, E., Mitchell, S. K., Morrissey, T. G., Emmett, M. B., Benjamin, C., King, M., Radakovitz, M. u. Keplinger, C.: Hydraulically amplified self-healing electrostatic actuators with muscle-like performance. Science (New York, N.Y.) 359 (2018) 6371, S. 61–65

[4] Suo, Z.: Theory of dielectric elastomers. Acta Mechanica Solida Sinica 23 (2010) 6, S. 549–578

[5] Pirozzi, I., Kight, A., Han, A. K., Cutkosky, M. R. u. Dual, S. A.: Circulatory Support: Artificial Muscles for the Future of Cardiovascular Assist Devices. Advanced materials (Deerfield Beach, Fla.) (2023), e2210713

[6] Washington, A., Su, J. u. Kim, K. J.: Actuation Behavior of Hydraulically Amplified Self-Healing Electrostatic (HASEL) Actuator via Dimensional Analysis. Actuators 12 (2023) 5, S. 208

[7] Kirkman, S., Rothemund, P., Acome, E. u. Keplinger, C.: Electromechanics of planar HASEL actuators. Extreme Mechanics Letters 48 (2021), S. 101408

[8] Mitchell, S. K., Wang, X., Acome, E., Martin, T., Ly, K., Kellaris, N., Venkata, V. G. u. Keplinger, C.: An Easy-to-Implement Toolkit to Create Versatile and High-Performance HASEL Actuators for Untethered Soft Robots. Advanced science (Weinheim, Baden-Wurttemberg, Germany) 6 (2019) 14, S. 1900178

[9] Rothemund, P., Kellaris, N., Mitchell, S. K., Acome, E. u. Keplinger, C.: HASEL Artificial Muscles for a New Generation of Lifelike Robots-Recent Progress and Future Opportunities. Advanced materials (Deerfield Beach, Fla.) 33 (2021) 19, e2003375

[10] MedSpares: Bottle Phantom Large -Siemens MRI Symphony Sonata 5512608. https://www.medspares.com/products/bottle-phantom-large-siemens-mri-symphony-sonata-5512608, abgerufen am: 12.04.24

Improving dynamic accuracy of closed loop bandwidth of piezo mechanisms with advanced control laws and embedded eddy current position sensors

Clément Cote, Alexandre Pagès, Olivier Sosnicki, Mathieu Castruccio, Timoteo Payre, Guillaume Mansuy, Xavier De Lepine, Cedrat Technologies, Meylan, France.
alexandre.pages@cedrat-tec.com

Abstract

Fast Steering Mirrors (FSM) play an important role in diverse optical applications for beam stabilization, image sharpening or dynamic beam steering. These applications require the FSM to have a precise response across a large frequency range, thus the need of a dynamic controller. But the controller is ultimately limited, among other factors, by the performance of the sensor: its ability to measure accurately the required physical value and with a sufficient bandwidth. The compact, dynamic and precise embedded Eddy Current Sensors (ECS) developed by Cedrat Technologies, combined with a model-based controller allow a two and a half times improvement on the bandwidth compared to current sensing technology, while being more precise overall.

1 Introduction

The need to increase the dynamic accuracy of Fast Steering Mirrors (FSM) is limited by multiple factors : the mechanical resonance frequency of the mechanism, the observability of the sensor or the performance of the control loop.
CEDRAT TECHNOLOGIES (CTEC) usually embeds Strain Gauges (SG) in its actuators and mechanism. SG measure the strain of actuating piezoelectric ceramics, which is an indirect estimation of the mechanism position. SG sensors have the advantages of being compact, accurate and easily integrable. Nevertheless, as SG give an in-direct measure, their dynamic response is somewhat different from the one of the mechanism positions, especially around and above the first resonance frequency of the mechanism. This lack of observability can be detrimental to the performance or the dynamic precision of the controlled mechanism.
CTEC has developed and embedded new position sensors to overcome these difficulties. A prototype of its tip-tilt mechanism TT60SM is integrated with Eddy Current Sensors (ECS) to measure the position of its mirror. To fully use the improved observability given by the new sensors, it is possible to use full state feedback controllers to improve the bandwidth and dynamic precision of the closed-loop controlled system.

2 System description

2.1 Mechanism

The TT60SM is a standard Tip-Tilt mechanism of CEDRAT TECHNOLOGIES (CTEC), that has a stroke of 20 mrad on its axis.

Figure 1 TT60SM-ECS and its CAD model

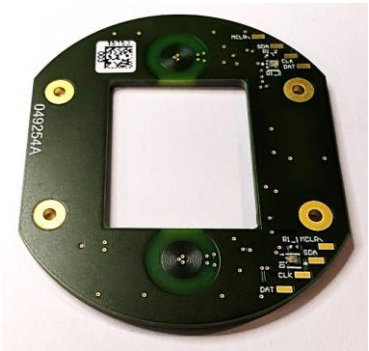

Figure 2 PCBA of the embedded ECS

2.2 Driver

This mechanism can be driven by the CCBu40, a standalone driver for piezoelectric mechanism, that can supply up to 500 mA between -20 and +150 V. With this configuration, a dynamic up to a few hundreds of Hertz can be reached.

2.3 Sensor conditioning

This prototype TT60SM is equipped with embedded Eddy Current Sensors (ECS) in addition to the SG sensors.
The SG sensors are conditioned by the embedded conditioner of the CCBu40.

These sensors are conditioned by a dedicated custom-made electronic prototype, the ECSF. It consists of a self-oscillating coil probe that generates a signal whose frequency varies based on the inductance value of the probe coil.
This technology offers several key advantages. Firstly, it enhances system observability, allowing for better monitoring and control. Secondly, it provides adjustable nanometer resolution, although this may come at the cost of reduced bandwidth. Moreover, it offers redundancy capabilities in degraded mode, which depend on the system's topology. Finally, as a result of its digital design, this technology is capable of operating at a low voltage (5Vdc), enhancing its efficiency and compatibility with a wide range of power systems.
However, the ECSF prototype comes with a significant drawback: its susceptibility to cable movement between the probe and the conditioner. To address this issue, CTEC is developing a new sensor prototype. This updated design consists of two primary components: the probe segment integrates a digital front-end to isolate the measurement part, while the conditioning segment manages data acquisition, linearization, and user interface functionality for the sensor.

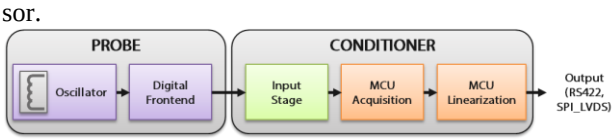

Figure 3 New ECS sensor architecture

2.4 Test setup

The rest of the test setup is composed of a Software-In-the-Loop (SIL) Speedgoat platform, used to acquire data and compute the control law in real time, and a high speed autocollimator to get the true mirror position of the mechanism.

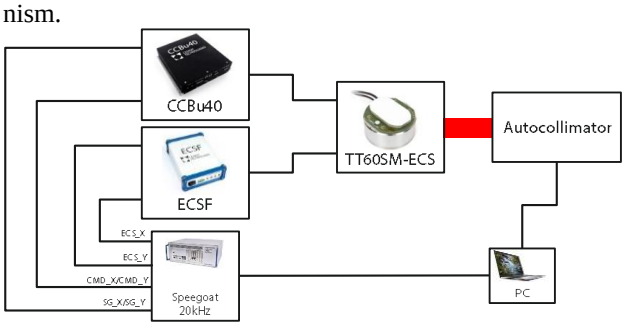

Figure 4 Test setup schematic

3 System characterisation

First, the system needs to be characterized in open loop, with the objective to obtain a model of the whole system.
The frequency response of the system has been estimated using a white noise as the input signal.

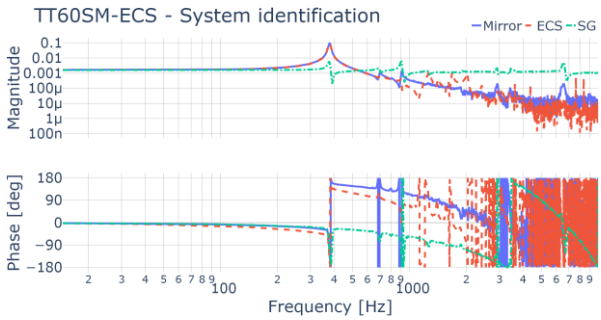

Figure 5 Estimated frequency response of the system

The main resonance frequency of the system is at 375 Hz. Around the resonance frequency, it is possible to see the lack of observability of the SG compared to the mirror position. The ECS are way closer to the real position of the mirror, up to 900 Hz.
A zero-pole-gain model is fitted on this experimental data, and is used to synthesize and tune the advanced controller.

4 Closed loop performance and robustness evaluation

The main closed loop performance criterion is the -3 dB bandwidth, which corresponds to the frequency at which the gain of the closed loop transfer function goes below -3 dB.

Robustness is characterised according to [1].
Phase and gain margin are two well known ways to characterize robustness. They represent the minimal phase variation (respectively gain variation) that destabilise the system. Good stability margins are usually above 40° and 3 dB respectively.
The infinity norm of the sensitivity function is another approach of robustness. With L the open loop transfer function, we know that the closed loop becomes unstable as trace of L in the complex plane goes from one side to the other of the critical point $-1 + 0 \cdot j$ (with j the complex variable such as $j^2 = -1$). A good way of defining the robustness is then to characterise the minimum distance between the open loop transfer function L and the critical point. This distance is called the modulus margin, and its value is $\min_{\omega}|1 + L|$. With the sensitivity function defined as S=1/(1+L), this point becomes:
$\|S\|_\infty = max|1/(1 + L)|$
Thus, to assure a robust control, one does not want the modulus margin to go below a certain value, corresponding to a maximum value for $\|S\|_\infty$. Usual values are that $\|S\|_\infty$ should be below 2 to 3. This criterion has the advantage of taking into account variation of gain and phase of the system at the simultaneously, thus better representing the robustness of the controlled system.

5 Standard achievable bandwidth

CTEC usually implement PID + filters controllers in its electronics. This PID controller uses the SG sensor to close

the loop. The first controller is implemented to get a baseline of current CTEC abilities.

5.1 Controller architecture

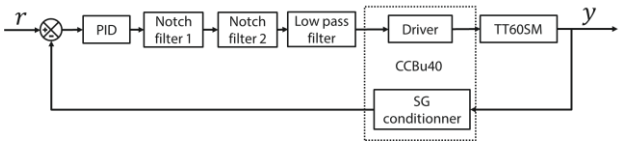

Figure 6 Standard control loop architecture

This architecture is the standard architecture implemented in CCBu20 or CCBu40 electronics, enhanced with an additional low pass filter to further improve stability margins of the closed loop.
The notch and low pass filters frequency are tuned in regard to the system identification.
The PID parameters are tuned with a trial and error method on the real system.

5.2 Controller performance

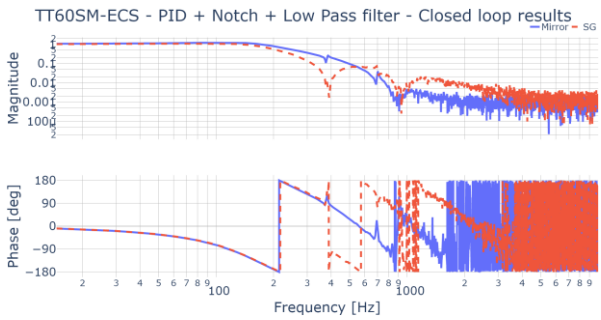

Figure 7 Standard control performance

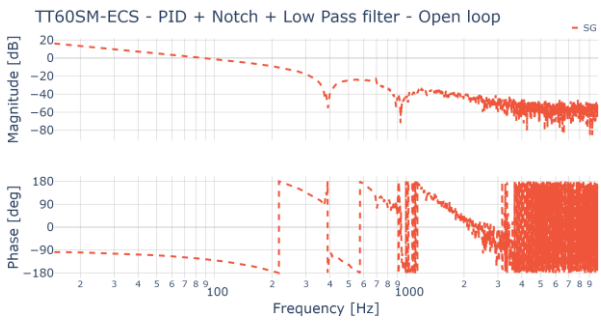

Figure 8 Standard control open loop frequency response

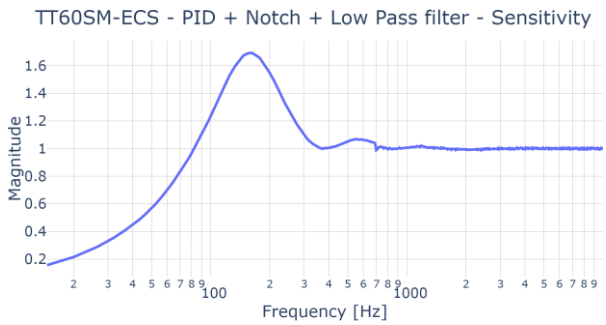

Figure 9 Standard control sensitivity function

With this architecture, it is possible to achieve 179 Hz of bandwidth (about half of the first resonance frequency) at the SG sensor with 55° of phase margin, 10 dB of gain margin and $\|S\|_\infty = 1.7$.

An error between the measured value at the SG and the real position of the mirror is visible on the Bode diagram.

6 Advanced controller

To further improve the bandwidth and to take advantage of the increased observability given by the ECS, a advanced model based controller has been implemented.

6.1 Controller architecture

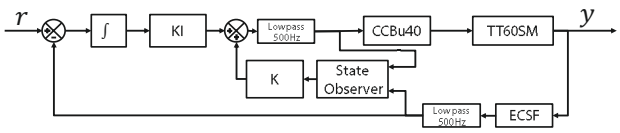

Figure 10 Advanced control loop architecture

This controller has a full state feedback with a state observer, and an integrator to reduce the static error to zero. Two additional low pass filters at 500 Hz are in the loop, to mitigate the effect of higher resonance frequency.

6.2 Controller performance

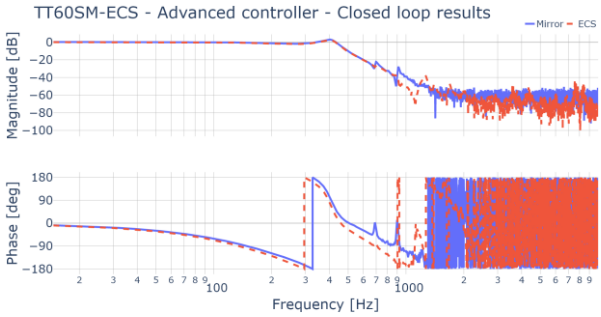

Figure 11 Advanced control performance

This controller is able to achieve a bandwidth of 448 Hz on the ECS, above the first resonance frequency at 375 Hz.

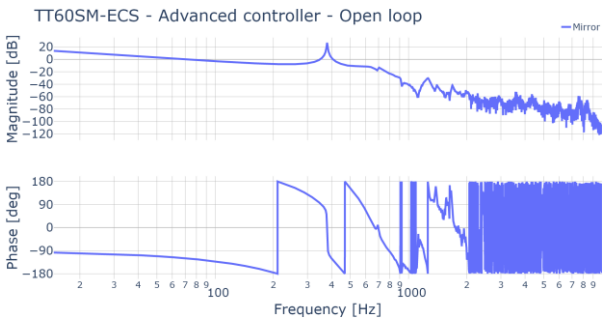

Figure 12 Advanced control open loop frequency response

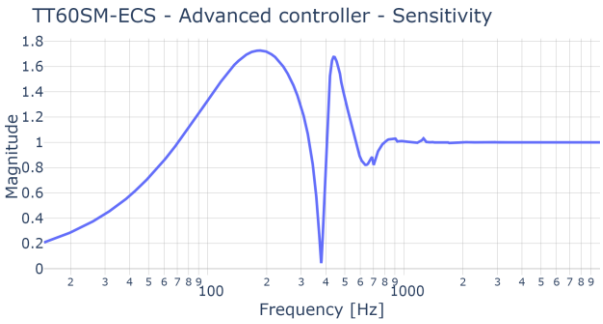

Figure 13 Advanced control sensitivity function

This performance is achieved with stability margins of 7.7 dB for the gain and 53° for the phase. $\|S\|_\infty = 1.7$, so the increased bandwidth is achieved with the same robustness margin as the standard controller.

Here the response measured by the ECS is a better image of the real displacement of the mirror. The better observability given by the ECS allow the control at higher bandwidths, after the first resonance frequency. Moreover, the advanced control loop provides active damping, which is not possible with the standard control architecture, as the controller as a lower bandwidth and the notch filter prevents any action at the resonance frequency.

7 Conclusion

The use of ECS on the TT60SM improves the controllability of the mechanism on several aspects.
This sensor gives a better representation of the mirror displacement compared to the usual SG sensor.
This improved measurement allows the efficient use of advanced model-based control law, which can control the mirror position accurately above the resonance frequency of the mechanism.
This results in a two and a half times improvement of the bandwidth without significative reduction in robustness margins.

	SG + PID	ECS + Advanced control
Bandwidth	179 Hz 0.5 x fr	448 Hz 1.2 x fr
Gain margin	10 dB	7.7 dB
Phase margin	55°	53°
$\|S\|_\infty$	1.7	1.7

The authors are grateful for the support of the French government that fund part of the work presented in this paper within the frame of CLEOPATRE project and FRANCE 2030.

8 Literature

[1] S. Skogestad et I. Postlethwaite, Multivariable feedback control: analysis and design, 2. ed., Repr. Chichester: Wiley, 2010.

Measurement of the High-Power Quality Factor for Piezoelectric Transducers Based on the Electrical Harmonic Steady-State Response

Alexej Wischnewski, Physik Instrumente (PI) GmbH & Co. KG, Karlsruhe, Germany
Email: a.wischnewski@pi.de

Abstract

The mechanical quality factor is an important parameter of piezoceramics and piezoceramic components. When designing new compositions of piezoceramics or new piezoceramic devices, it is important to know the value or the characteristic curve of the mechanical quality factor in power applications. The method for the quality factor determination conventionally used in low-power applications and valid for linear oscillators cannot be used in power applications. In this article, the author shows why determining the mechanical quality factor of piezoceramics in power applications using the model for a linear oscillator is inappropriate. Furthermore, a nonlinear model of the piezoceramic oscillator and a new measurement method for determining the mechanical quality factor are presented. Results of quality factor determination of a piezoceramic component and piezoceramic materials are shown as an example.

1 Introduction

Components made of hard piezoelectric ceramics are widely used as electromechanical power converters in electronic devices such as ultrasonic transmitters, transformers, actuators, and ultrasonic motors. Piezoceramic materials in these applications operate under high mechanical stress. All the electromechanical parameters of piezoceramics exhibit a nonlinear trend and deteriorate. The mechanical quality factor Q_m is an important parameter of piezoceramic materials and piezoceramic devices. Electromechanical parameters of ultrasonic transducers depend on the Q_m factor of the piezoceramic material used. When designing new compositions for piezoceramics or new piezoceramic devices, it is important to know the change in the Q_m factor in high-power applications. Many publications from the last 30 years present the results of attempts to determine the Q_m factor of piezoceramic devices or piezoceramics in high-power applications based on the decay of a piezoceramic oscillator and with reference to the relationships that apply to a linear oscillator [1]-[2]. However, this method is unsuitable for determining the Q_m factor in piezoceramics because the Q_m factor of piezoceramic oscillators is highly nonlinear. The Q_m factor differs greatly under high mechanical stress versus under low stress and can decrease by a factor of 20.

2 Conventional Model of a Piezoelectric Oscillator

Conventionally, the oscillation behavior of a piezoelectric transducer near resonance is described using the model shown in Figure 1. The model consists of the input capacitance C_0, dielectric loss resistance R_p, and transformer with a force factor A, as well as the equivalent mechanical stiffness, equivalent mass, and equivalent loss resistance C_m, L_m, R_m connected in series.
The C_m, L_m, R_m form the mechanical oscillator. The oscillation behavior of a free linear damped harmonic oscillator

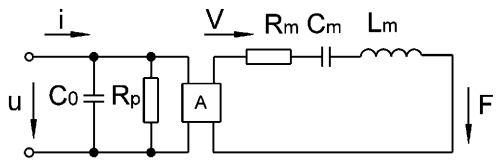

Fig. 1. Simplified model of a linear piezoelectric ultrasonic transducer

is described by the following differential equation for the oscillator:

$$\ddot{i} + \beta\dot{i} + \omega_0^2 i = 0 \tag{1}$$

where i is the current, $\beta = 2R_m/L_m$ is the decay coefficient, and $\omega_0 = (1/(L_m C_m))^{1/2}$ is the natural frequency.

3 Determining the Quality Factor

The Q factor of a damped oscillator is defined as the ratio of the energy W_0 stored in the oscillator at the beginning of the oscillation period to the energy W_l converted into heat at the loss resistance R_m per this oscillation period T.

$$Q = \frac{W_0}{W_l} \tag{2}$$

In a linear harmonic oscillator, R_m is a constant magnitude. The energy W_l converted into heat at the R_m per period T is proportional to the energy W_0 present in the oscillator at the beginning of the period. Therefore, a free-swinging damped linear harmonic oscillator decays according to an e-function:

$$i = A_i \sin(\omega t) = i_0 e^{-\beta t} \sin(\omega t) \tag{3}$$

Equation (3) is a solution for the differential equation (1). Here, the amplitude A_i of the oscillation decreases exponentially with decay coefficient β. Q_m is a constant magnitude in the case of a linear oscillator. The Q_m factor of a

linear damped oscillator is determined from the resonance curve according to the relationship

$$Q_m = \frac{f_r}{\Delta f} \tag{4}$$

where f_r is the resonance frequency and Δf is the 3 dB bandwidth at resonance frequency.
Determining the Q_m factor according to (4) is possible for a piezoceramic oscillator only in a low-power application. Low-power applications, e.g., in components for a sensory application, have very low mechanical deformation and low mechanical stress in the piezoceramic and very low electrical current through the piezoelectric transducer. Piezoceramics are highly nonlinear in high-power applications such as ultrasonic motors or transformers. The stiffness C_m and the mechanical loss R_m change based on oscillation amplitude. The resonance curve shows strong distortion due to high power excitation. The Δf and Q_m cannot be determined.
Furthermore, it is possible to determine the Q_m factor of a linear oscillator from its decay. Because the loss resistance R_m in a linear oscillator is constant, the ratio of two successive oscillation amplitudes $\varepsilon(t_1)$, $\varepsilon(t_2)$ is also constant. By measuring of the amplitudes of two successive oscillations and the corresponding times t_1, t_2, the Q_m factor of a linear oscillator can be determined from the decaying oscillation using the decay coefficient β:

$$Q = \frac{\omega_r}{2\beta} \tag{5}$$

Determining the Q_m factor of a piezoceramic transducer in high-power applications from its decay according to equation (5) based on the electrical transient response method, also called the burst method, is known from [2]. However, determining Q_m according to equation (5) is generally unsuitable for piezoelectric ceramics because this nonlinear oscillator does not decay exponentially. Equation (5) yields an invalid result when measuring the Q_m factor of a nonlinear oscillator. In high-power applications, the quality factor of piezoceramics has a strong nonlinear dependency on deformation, mechanical stress and the electrical current. The energy W_l converted into heat in the oscillator at R_m per period T is not only proportional to the energy present in the oscillator at the beginning of the period, as in a linear oscillator, but rather also depends on R_m. $W_l = f(W_0, R_m)$. R_m changes nonlinearly in the piezoceramic oscillator according to the oscillation amplitude. The ratio of successive amplitudes, or rather β, is not a constant quantity. Therefore, the decay of the piezoceramic oscillator is not exponential. The Q_m factor cannot be determined.

4 Piezoceramic as a Nonlinear Harmonic Oscillator

Ultrasonic transducers with or without a small hysteresis loop, manufactured from a piezoelectric ceramic or a single crystal can be considered as a nonlinear harmonic oscillator with variable C_m and R_m in a wide range of excitation levels. Figure 2 shows the equivalent circuit of the transducer.

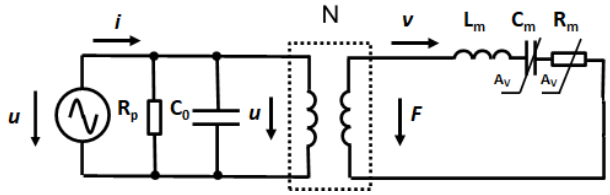

Fig. 2. Simplified model of a piezoceramic ultrasonic transducer

When changing the oscillation amplitude from one level to another, C_m and R_m of the oscillator change. This occurs in a certain transition time τ, which can be more than one oscillation period. Figure 3 schematically illustrates the transition between the oscillation amplitudes of a piezoceramic oscillator oscillating in resonance with different amplitudes.

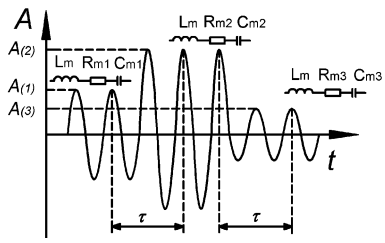

Fig. 3. Piezoceramic ultrasonic transducer at different oscillation levels

After the transition time τ, the piezoceramic transducer oscillates harmonically with the new oscillator parameters R_m and C_m corresponding to this oscillation level until the deformation amplitude changes. During steady oscillations, the piezoelectric oscillator is a harmonic oscillator with constant L_m, C_m, R_m. Measurements of the total harmonic distortion (THD) of the current at very high vibration amplitudes, close to the ceramic fracture limit, on a free-swinging plate or ring transducer made of the hard piezoceramic PIC181 show a maximum value of 2 %. Measurements of the current-vibration velocity dependence made with a laser vibrometer on a freely vibrating piezoceramic transducer show a constant correlation. This enables us to apply the method proposed in Section 6 for measuring the Q_m factor with the accuracy determined by THD.

5 Modeling of the Oscillator

A mathematical model was developed that describes piezoceramic oscillator behavior near resonance and under high-power excitation. According to the model, the loss resistance R_m and stiffness C_m of the piezoceramic material depend on the deformation amplitude. The well-known model of a linear damped harmonic oscillator was adapted to account for this type of nonlinearity as follows:

$$\ddot{x} + R_m(A)\dot{x} + C_m(A)x = 0 \tag{6}$$

Here, the loss resistance R_m and the stiffness C_m are polynomial functions second order of the deformation amplitude A_d:

$$R_m = a_1 + a_2 A_d + a_3 A_d^2 \,;\; C_m = a_4 + a_5 A_d + a_6 A_d^2$$

The model of nonlinear piezoceramic harmonic oscillator described in Figure 2 was solved numerically in the Matlab/Simulink program for a piezoceramic plate oscillator. The piezoceramic plate is the actuator of the ultrasonic motor [3], has the dimensions 25 x 11 x 4 mm^3 and is made of the hard piezoceramic PIC181 manufactured by PI Ceramic in Lederhose, Germany. The parameters L_m, C_m, R_m used in the simulation were measured with impedance analyzer Agilent 4294A. The polynomial coefficients $a_1 - a_6$ were created using curve fitting, where the measurement points were carried out according to the proposed method (see Section 6). Figure 4 shows the Simulink model of the piezoceramic oscillator.

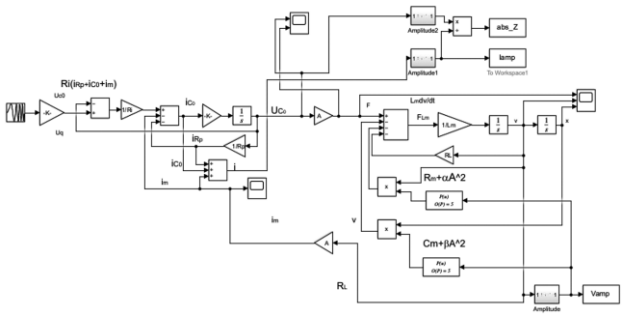

Fig. 4. Simulink model of the piezoceramic oscillator

The model was excited with down frequency sweep and the amplitude of the current was recorded. Figure 5 illustrates the current and oscillation velocity waveforms through the piezoceramic transducer, which were calculated using the model, in the range of 180 to 140 kHz for small-signal and large-signal excitation.

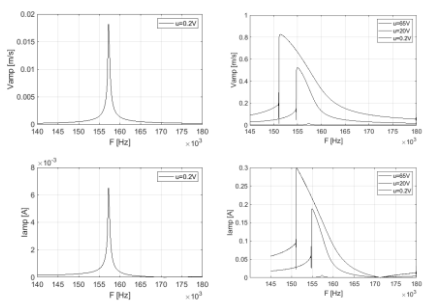

a) b)

Fig. 5. Numerically calculated resonance curves of a piezoelectric transducer a) Small-signal resonance curves; b) Large-signal resonance curves

Due to the nonlinear dependence of the stiffness C_m on the oscillation amplitude, a parametric oscillation occurs in the piezoceramic oscillator near resonance as a result of the abrupt change in stiffness, which is similar to the effect seen in a Duffing oscillator [4] and is often referred to as jumping and dropping phenomena in the literature.

The resonance curves of the small-signal excitation in Figure 5a are narrow and symmetrical. The large-signal resonance curve in Figure 5b shows that the resonance frequency depends on the amplitude of the electrical current or the deformation and mechanical stresses, which is typical for piezoceramics. As the current amplitude increases, the resonance frequency of the oscillator becomes lower and lower.

Figure 6 illustrates a comparison of the measured current resonance curve of the piezoceramic plate and the numerically calculated curve based on the model in Figure 4.
It is clear from the figure that the model created for the piezoceramic oscillator precisely represents the behavior of the piezoceramic plate near the resonance frequency.

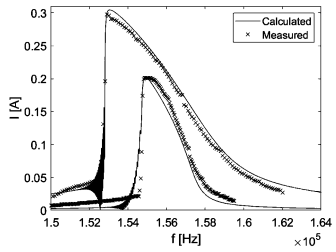

Fig. 6. Large-signal resonance curves

6 Proposed Measurement Method

The proposed method for determining the Q_m factor of piezoceramic transducers with large-signal excitation uses the steady-state harmonic response of piezoceramic transducers and is based on the model (6). Even though the piezoceramic transducer is a nonlinear oscillator, its Q_m factor can be measured quite simply since it is a harmonic oscillator during steady-state oscillations.
The Q_m factor of a linear harmonic oscillator is also defined as a ratio of reactance to active resistance:

$$Q_m = \frac{\omega_r L_m}{R_m} \tag{7}$$

Because a sinusoidally driven piezoceramic transducer is a harmonic oscillator for any given amplitude value of the current, the following relationship can be established for Q_m at high power excitation Q_{hpe} and low power excitation Q_{lpe} :

$$Q_{hpe}/Q_{lpe} = \frac{\omega_{r_hpe} L_m}{R_{hpe}} \Big/ \frac{\omega_{r_lpe} L_m}{R_{lpe}} \tag{8}$$

where *hpe* and *lpe* mean “high-power excitation” and “low-power excitation” respectively.

When changing the excitation level of a piezoceramic transducer, its mode shape does not change. Therefore, its equivalent mass L_m does not change either. It follows from (8) that

$$Q_{hpe} = \frac{\omega_{r_hpe} Q_{lpe} R_{lpe}}{\omega_{r_lpe} R_{hpe}} \tag{9}$$

This means that the mechanical quality factor with large-signal excitation can be calculated by determining the mechanical quality factor of the small-signal excitation, the internal resistances of the piezoceramic transducer at high- and low-power excitations, and the resonance frequencies on both excitation levels.

At the resonance frequency of a piezoceramic oscillator, the phase-shift angle between the current and the voltage is 0°. The resonant circuit has a pure ohmic resistance at the resonance frequency because the inductance and capacitance compensate for each other. This characteristic resistance R can be determined from the voltage u and the current i:

$$R = \frac{u}{i} \tag{10}$$

In the first step of the proposed measurement method, the small-signal measurement is performed. The down frequency sweep excitation is performed by a signal generator with a low sinusoidal voltage value, and the current through the oscillator is measured and saved. Then, the mechanical small-signal quality factor Q_{lpe} is calculated from the measured values according to equation (4) and at the resonance ω_{r_lpe}, and the characteristic resistance R_{lpe} is calculated according to (10).

In the second step, the large-signal measurement is performed. Here, the oscillator is excited with an electrical sine wave voltage of a large amplitude. The frequency is changed from a higher to a lower value, and the current through the oscillator is measured and saved. At the resonance frequency ω_{r_hpe}, i.e., at a phase angle of $\varphi = 0°$ between the voltage U_{hpe} and the current i_{hpe}, the characteristic resistance R_{hpe} of the high-power excitation is calculated according to (10). Finally, the mechanical large-signal quality factor Q_{hpe} is determined according to (9).

To be able to compare the properties of piezoceramic materials, it is advisable to perform the measurements on ring-shaped test specimens with excitation of radial vibration modes. In the radial vibration mode of a ring, the mechanical stresses are almost constantly distributed over the entire volume of the resonator [5], so that the measured characteristic values can be related to the resonator volume and thus the parameters can be determined as specific properties of the piezoceramic material.

The determination of the nonlinear dependence of the mechanical quality factor Q_m, resistance R_m, and resonance frequency f_r on the current amplitude was performed on the piezoceramic plate transducer and a ring-shaped resonator with dimensions OD:ID:H 30 x 26 x 6.5 mm^3 made of the piezoceramics PIC181 and CTBS3 using the proposed method. Figure 7 illustrates the parameter nonlinearity of piezoceramic plate resonator (left) and the ring-shaped resonators (right) under power excitation.

Figure 7a shows current resonance curves for the piezoceramic plate when excited under different excitation voltages with frequency sweep. Below the resonance frequency, the current drops abruptly due to the abrupt change in stiffness (dropping phenomena). 7b, 7c and 7d show a strong nonlinear progression of the parameters f_r, R_m, Q_m.

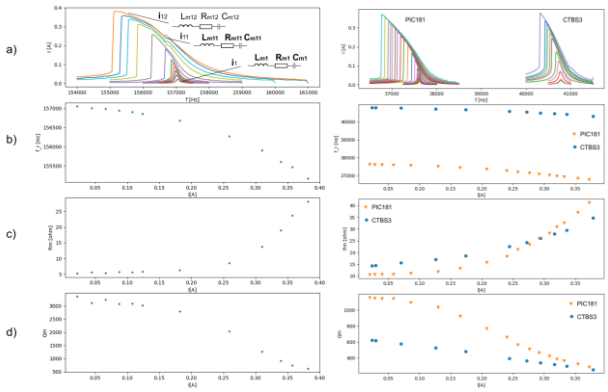

Fig. 7. Nonlinearity of parameters of a piezoceramic plate transducer under power excitation. a) Dependence of current amplitude I_A on excitation frequency; b) Dependence of resonance frequency f_r on current amplitude I_A; c) Dependence of loss resistance R_m on current amplitude I_A; d) Dependence of mechanical quality factor Q_m on current amplitude I_A;

L_m, C_m, R_m elements are marked in Figure 7 to make it clear that the piezoceramic plate at any current amplitude in is a harmonic oscillator with parameters corresponding to this current amplitude.

7 Conclusion

The presented measurement method enables simple determination of the mechanical quality factor, the characteristic resistance, and the frequency shift of piezoceramic actuators. This makes it possible to compare the properties of piezoceramic actuators made from different types of piezoceramics or different production batches of the same ceramic. Furthermore, the method enables determination of the above-mentioned piezoceramic parameters as specific material properties. This is important for developing new types of piezoceramics.

8 Literature

[1] M. Umeda, Kentaro Nakamura, Sadayuki Ueha, “The Measurement of High-Power Characteristics for a Piezoelectric Transducer Based on the Electrical Transient Response”, Jpn. J. Appl. Phys. Vol. 37 (1988) pp. 5322-5325, Part 1, No. 9B, Sep. 1998.

[2] Husain Shekhani, Timo Scholehwar, Eberhard Hennig, K. Uchino, “High Power Characterization of Piezoelectric Materials Using the Burst/Transient Method with Resonance and Antiresonance Analysis”, Journal of the American Ceramic Society, May 2016

[3] O. Vyshnevskyy, S. Kovalev, and W. Wischnewskiy, “A Novel, Single-Mode Piezoceramic Plate Actuator for Ultrasonic Linear Motors”, IEEE Trans. on Ultrasonic Ferroelectrics and Frequency Control, Vol. 52, No. 11, Nov. 2005

[4] G. Duffing, “Erzwungene Schwingungen bei veränderlicher Eigenfrequenz” (Forced vibration with variable natural frequency). F. Vieweg, Braunschweig, 41/42, (1918)

[5] Warren P. Mason, “Physical Acoustics, Principle and Methods”, Vol.1, Methods and Devices, Part A, Academic Press, New York and London, 1964

Inertial & Inchworm piezoelectric motors: Design and Motorization selection key aspects

Nabil Bencheikh, Nicolas Bourgeot, Alexandre Pagès, Gérald Aigouy, Jocelyn Rebufa, Etienne Betsch, Frank Claeyssen.
CEDRAT TECHNOLOGIES, 38240 Meylan, FRANCE, nabil.bencheikh@cedrat-tec.com

Abstract

Piezoelectric motors have gained increasing prominence in various applications due to their unique capabilities and advantages. These motors are adapted for applications which require non-magnetic and radiation compatibility, high force/volume ratio, good unpowered stall force and low power consumption. Cedrat Technologies (CTEC) have developed inertial and inchworm motorization for a wide range of application such as Space, Defense and Nuclear. Each motorization solution has its own advantages and disadvantages which are discussed in this paper. Key aspect for the design and key element for the motorization selection are presented below.

1 Operating principle

1.1 Inertial motor

These motors are composed of a fixed Amplified Piezo Actuator (**APA®**) and a spring providing a preload between the actuator and the payload. (Figure 1-1). This preload allows to transmit motion or force through **friction** to drive a payload in either a linear or a rotational motion depending on the guiding.

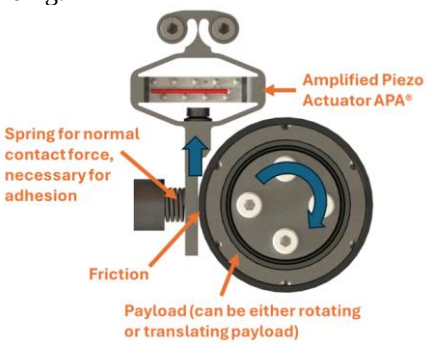

Figure 1-1: Modular Stepping Piezo Actuator (MSPA)

As the guiding is performed outside the Modular Stepping Piezo Actuator (MSPA) module, the friction track can be scaled to provide the required full stroke. This makes the MSPA highly versatile as the same actuator can be used to provide displacement on **rotary** or **linear** motors of **any stroke.**

The **stick slip** operation principle is illustrated in the Figure 1-2, it is composed of the following phases:

1. Piezo actuator is in a neutral state with no voltage applied.
2. Stick phase: The voltage is slowly increased. Piezo actuator slowly contracts. As long as the resulting acceleration force remains smaller than the static friction force between the parts, they stick and move together.
3. Slip phase: The voltage is rapidly decreased. The resulting acceleration force is higher than the friction force. Thus, the actuator comes back to neutral position whereas the mobile mass remains in place.

A displacement in the opposite direction is obtained by inversing the slow-fast voltage sequences in the actuation signal.

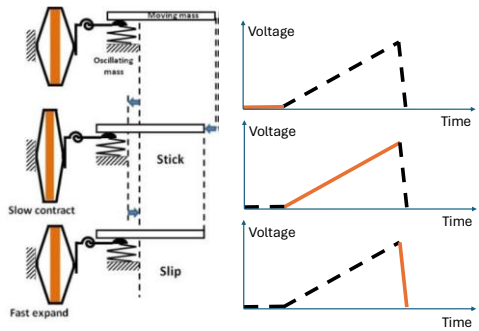

Figure 1-2: Stick-slip actuation of inertial piezo motors [1]

The stick-slip actuation can be combined with **the piezo deformation mode to obtain high resolution**: by staying in the stick mode, the smallest obtained displacement is only limited by the resolution of the electronic supplying the piezo voltage. Thus these motors offer high resolution motions together with high speed.

1.2 Inchworm motor

One possible architecture for inchworm motor is to use 2 pairs of actuators. For each pair, one actuator is the clamp, the other one is the extender (provides stroke to the payload).

The operating principle is displayed Figure 1-3.

1. 1st actuator pair clamping phase
2. 1st actuator pair stroke phase
3. 2nd actuator pair clamping phase, followed by the 1st pair unclamping phase
4. 2nd actuator pair stroke phase, with 1st pair retraction

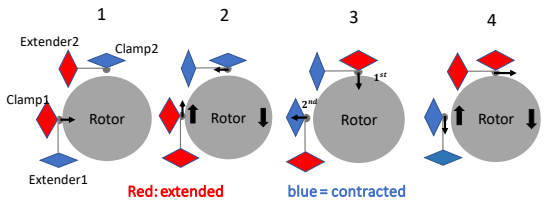

Figure 1-3: Inchworm motor operating principle

2 Mechanical design

2.1 Model and simulation

Both inchworm and inertial piezo motors provide **holding force when not powered.** The holding force when the actuator is not supplied is:

$$F_{holding} = \mu_S F_N$$

For both motors, during the stick phase, the following condition is verified:

$$F_f(t) \leq \mu_S F_N$$

F_N and F_f are the normal force applied by the preloading spring and the friction force respectively. $\mu_s$is the static friction coefficient force.

If a resistive force F_{res} is acting on the payload, the friction force between the actuator and payload is:

$$F_f(t) = m_{MM}\ddot{x}_{MM}(t) + F_{res}$$

It corresponds to the force transmitted by the actuator to the payload. $m_{MM}, \ddot{x}_{MM}$ being the masse and acceleration of the mobile masse.

For inertial motor only, during the slip phase, the acceleration is such that there is no more adhesion between the actuator and payload:

$$m_{MM}\ddot{x}_{MM}(t) > \mu_S F_N$$

For a more precise modelling of the dynamical behaviour of the inertial motors, a Lumped Parameter Model has been developed. (Figure 2-1). Typical results of the simulation are presented Figure 2-2.

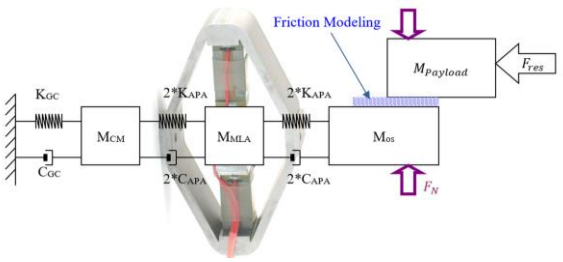

Figure 2-1: Lumped Parameter Model of MSPA motors

The lumped model allows to simulate the dynamic behaviour of the motor such speed and stroke.

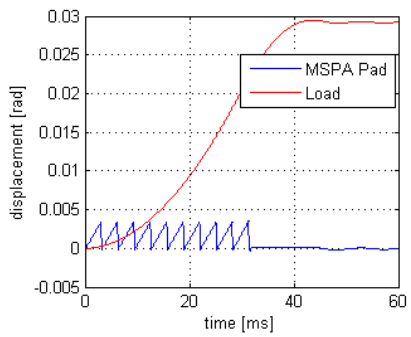

Figure 2-2: Typical simulated displacement versus time

2.2 Tribological aspect

CTEC has experience in the use of several pair of materials for both inertial and inchworm applications in several environment (ambient, vacuum) and temperature (-180 to 70°C).
The choice of these materials is based on a compromise between a high coefficient of friction, enabling high force to be transmitted, and wear limitation.

It is known that the tribological properties of material can change drastically depending on pressure (ambient/vacuum) and temperature. CTEC heritage in this domain is a key knowledge to develop piezo electric motors for harsh environments. The contact geometry is also designed to reduce wear and improve performance stability.

Figure 2-3 presents results of a study performed by UNIROMA in a previous project on a test bench codesigned between UNIROMA and CTEC. Homogenous wear and stable friction coefficient was observed after 20 million cycles. [2]

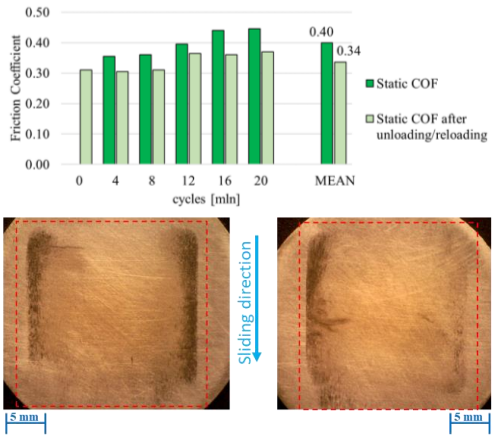

Figure 2-3: Friction coefficients and Microscope images after 20mln cycles [2]

3 Driving strategy

3.1 Driving signals

In the case of inertial motors, the signal is based on sawtooth signal (Figure 1-2). The performance of the motor can be optimised by changing the rising, falling time and the amplitude of the voltage. The rising time corresponds to the stick phase (the load is moving), the falling time corresponds to the slip phase (the load stays in place).

The falling time must be short in order to generate slippage. Nevertheless, the falling time is constrained by the current limitation on the driver.

$$I = C_p \frac{dU}{dt}$$

Typical signals used for inchworm motors are given Figure 3-1. They correspond to the working principle described Figure 1-3.

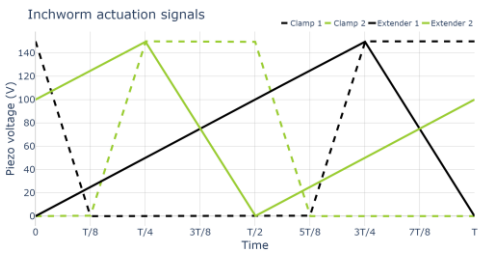

Figure 3-1: Typical signals used for inchworm motors

3.2 Backlash behaviour

Inertial and inchworm motors are based in step accumulation. Irregularities of torque, displacement and speed are an intrinsic properties of stepping motors. The optimization of driving signals is key to enhance the performance of the motors. Specific driving signals are developed for both motorizations in order to reduce the backlash.

The Figure 3-2 presents the impact of signal optimization on the speed of an inchworm motor. The green curve presents the results obtained on the speed after optimisation. The discontinuity of the speed between the steps is reduced (spikes are related to backlash).

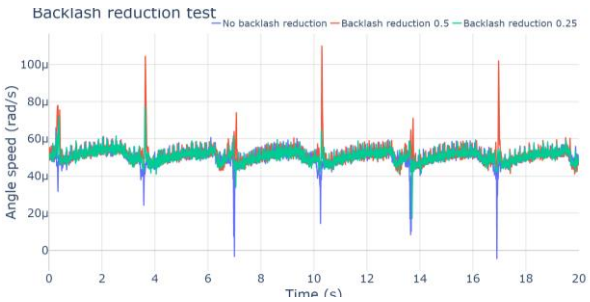

Figure 3-2: Backlash compensation effect on speed

On the Figure 3-3, one can see that the angular displacement obtained is more linear on the green curve.

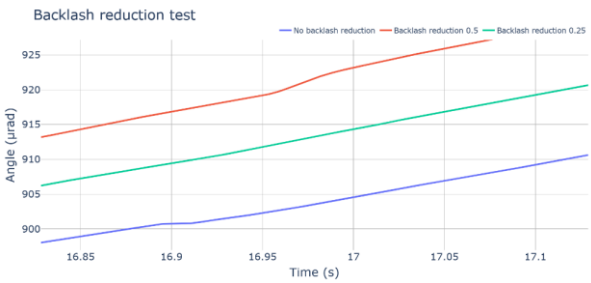

Figure 3-3: Backlash compensation effect on displacement

On the Figure 3-4, only the backlash (parasitic displacement) is plotted for another motor. One can see that the amplitude of the backlash is reduced by almost 70 % (red curve compared to blue curve).

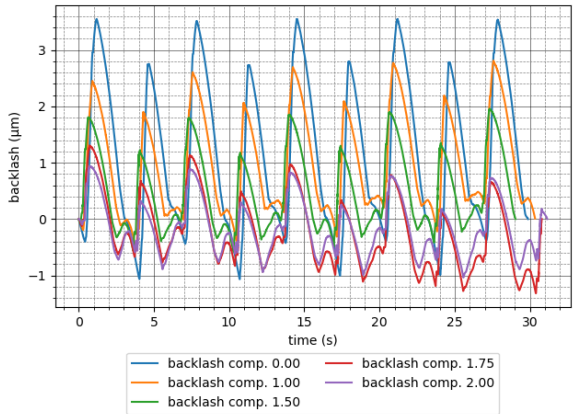

Figure 3-4: Typical results obtained after backlash compensation

3.3 Self-heating

The environment temperature is an important constraint to withstand for some application besides the motor self-heating. For some environmental condition (high temperature, vacuum…) and motor duty cycle, thermal draining is imperative to ensure the motor performance and to not damage the motor and especially the piezoelectric material.

Thermal draining solutions are designed to dissipate the self-heating. These solutions are designed to respond to the thermal constraint with limited impact on mechanical performance (stroke, speed, lifetime, wear compensation ...).

The dissipated power on the ceramic is driven by the formulation hereafter.

$$P = \frac{\pi}{4} . f . C_p . \tan(\delta) . U_p^2$$

with:
$\tan(\delta)$: The dielectric dissipation factor,
C_p: The capacitance of the piezoelectric material,
f: The operational frequency,
U_p: The Peak-Peak amplitude of the applied voltage.

A thermal drain designed for an inertial motor allowed to reduce the thermal resistance by half in vacuum configuration compared to a version without drain. ().

Parameter	Units	Case 1	Case 2
Dissipated power	W	0.47	0.72
Temperature rise	°C	52	39
Thermal resistance	°C/W	111	54
Thermal draining	/	No	Yes

Table 3-1. The temperature on motor with and without drain

The thermal drain carries heat away from the ceramic (Figure 3-5).

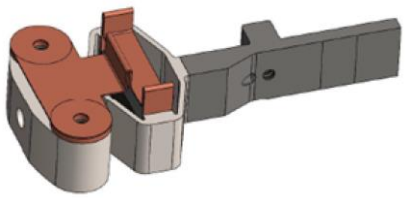

Figure 3-5: Thermal draining solution design

4 Motor performance

Several motors have been developed by CTEC based on both motorizations previously described on this paper, such as the inchworm motor prototype presented below (Figure 4-1).

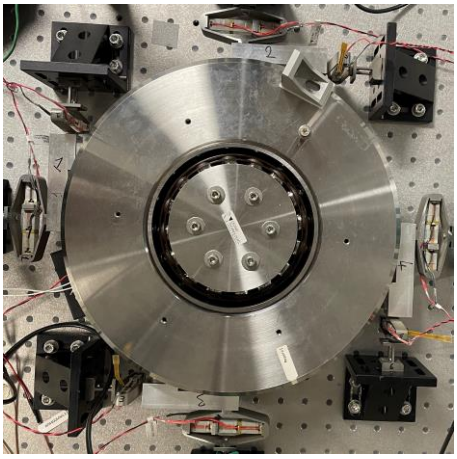

Figure 4-1: Inchworm motor prototype (Inchworm#1 - 300mm diameter)

The performances of some inchworm and inertial motors developed by CTEC are summarized in the following tables.
The static performances of the motors are given in the table (Table 4-1) corresponding to the holding torque of each motors.

Type	Rotor lever arm [mm]	Holding Torque at rest [N.m]
Inertial #1	35	0.3
Inertial #2	17	0.1
Inchworm #1	150	29
Inchworm #2	85	20
Inchworm #3	600	100
Inchworm #4	320	3.3

Table 4-1. Static performances of the motors

The dynamic performances of the motors are given the table below (Table 4-2). In the stick mode, the smallest obtained displacement is only limited by the resolution of the electronic supplying the piezo voltage. For the inertial motor, two values of resolution are given. The first values (indicated by *) corresponds to the resolution in slip mode. In this case, the indicated resolution (in mrad) is obtained at the given speed.

Type	Speed [RPM]	Torque [N.m]	Resolution Slip mode(*) / stick mode
Inertial #1	3.8	0.1	4.7mrad(*) / < 1 nrad
Inertial #2	8.6	0.026	1.3 mrad(*) / < 1 nrad
Inchworm #1	quasistatic	> 11	< 1 nrad
Inchworm #2	quasistatic	> 4	< 1 nrad
Inchworm #3	quasistatic	50	< 1 nrad
Inchworm #4	quasistatic	2.5	< 1 nrad

Table 4-2: Motors Performances

5 Conclusion and Know-how

The development and the design of inertial and inchworm motors require transversal knowledge:
Tribology for better evaluation of the transmitted force.
Signal processing for driving signal optimisation.
Mechanical design for the thermal and dynamic behaviour.

Motors are characterized by the following features:
Both inchworm and inertial motors provide blocking force at rest, severe environment compatibility options and resistance to external forces (shock, vibrations).

Inchworm motors provide better resolution and greater holding force/torque. They are therefore suitable for pointing and position holding applications. They also display reduced generated micro vibration and wear.

Inertial motors allow for higher speeds and good resolution. In addition, they are compact and require only one channel input to be controlled. They are more suitable for scanning applications, miniaturisation, wide temperature range and reduced series costs.

6 Acknowledgement

CTEC received funding from Eurostars under the PROOFED 2361 Consortium Agreement. The Eurostars Program is powered by EUREKA and the European Community. The Coordinator CTEC is supported by BPI FRANCE and the French state within the “France 2030” program.

7 Literature

[1] F. Dubois, F. Barillot, V. Thiebaud, C. Belly, T. Porchez, M. Barraja, A. Saulot, Y. Berthier. *Module Stepping Piezoelectric Actuator - A versatile way of micro-positioning actuation*, ACTUATOR 2016

[2] E. Betsch, J. Gauthier, N. Bencheikh, A Pagès *High power density Piezo motors for critical environments* ACTUATOR2022.

Targeted acoustic positioning of various objects

Alexander Backer*, Sandro Krempel, Benedikt Stromer, Klaus Stefan Drese
Institute of sensor and actuator technology, University of applied sciences Coburg, Am Hofbräuhaus 1b, 96450 Coburg
Alexander.Backer@hs-coburg.de, Sandro.Krempel@hs-coburg.de, Benedikt.Stromer@hs-coburg.de, Klaus.Drese@hs-coburg.de

Abstract

The precise positioning of objects (especially on a flat surface), is crucial in numerous industrial applications, from large object movement in machine tools to precise alignment in optical microscopes. This paper focuses on targeted movement and positioning of smaller objects on a flat surface using piezoelectric actuators. Specifically, it investigates the stick-slip motor principle for achieving high-speed transport and high-resolution positioning. The stick-slip motor utilizes the friction between objects and surfaces to generate motion. The experimental setup includes a piezoelectric actuator inducing asymmetric vibrations in a glass plate (stator), resulting in controlled movement of a slider (the object). An asymmetrical excitation signal, generated by superimposing two sinusoidal waves, is applied to the piezoelectric actuator. The influence of the different parameters of the excitation signal on the object speed is examined in more detail. The results demonstrate successful movement and precise positioning of various objects. It concludes that the developed stick-slip motor can efficiently move objects of different materials and sizes, offering a versatile solution for precise object positioning in confined spaces.

1 Introduction

The precise positioning of objects (especially on a flat surface) plays an important role in many industrial applications. This applies to both the movement of large objects over long distances (e.g. in machine tools, sorting of parts) and the movement of small objects in very small dimensions, e.g. in optical microscopes for the alignment of specimens to be examined. The positioning systems used are based on a wide variety of principles. These range from classic mechanical actuators, vibration motors, magnetic linear motors, and inertial motors to guided acoustic wave actuators. With most mechanical drives, the object to be moved moves with the base. This can take up a lot of space. The work here relates to the targeted movement and positioning of smaller objects on a flat surface. The aim is to achieve both a high speed in the range of several mm/s during transport and a high resolution in the range of a few micrometres during positioning with the system. With already known acoustic systems such as the inertia motor (often also called stick-slip motor [1]) or the travelling wave motor [2], smaller objects or masses can easily be moved in a circle or on a line (e.g. camera lens, rod drive, tangential drive) [3, 4, 5]. Two-dimensional object movement using a stick-slip motor has already been implemented by Shimizu et al. with a movement range of ±1 x ±1 mm^2 [6]. The aim of this work is initially to move and precisely position various small objects over a long distance in one dimension. This is achieved with the help of the stick-slip principle.

2 Materials and Methods

As the name stick-slip motor implies, this motor utilizes the static and sliding friction of objects on surfaces. The components required are shown below.

2.1 Mechanical design and mode of operation

The motor can be divided into three main components, which are shown in Figure 1. The stator, the slider, and the actuator. The slider is the object to be moved, which is in frictional contact with the stator. The stator is the part of the motor that is moved by the piezo. The asymmetrical oscillation of the stator required for a directed movement is realized by the actuator and, in this specific case, by the electrical control of the piezo. This alternately pushes the stator away and then pulls it back at different speeds. The asymmetrical movement of the stator is transmitted to the slider via friction and ultimately ensures the directed motion of the slider.

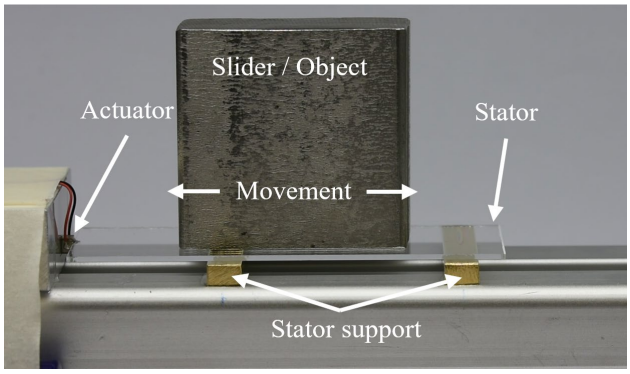

Figure 1: Components of the stick-slip motor

A 76 mm long, 26 mm wide and 1 mm high glass plate resting on two brass bars was used as the stator for the assembled motor. A rectangular stack piezo - PL033.31 from PiCeramic - with an edge length of 3 mm and a height of 2 mm was used as actuator. At a maximum permissible voltage of +100 V, it deflects by 2.2 µm. The

slider is the object to be moved, which is, in the example shown below, a piece of metal weighing 195 g.

2.2 Excitation signal

A sawtooth signal, for example, could be used as an asymmetrical theoretical excitation signal. The abrupt retraction of the stator would maximize the ratio of the speeds between the push-off and retraction. In practice, this movement of the stator must be generated by the piezo. The maximum transmittable forces are limited and can lead to the destruction of the piezo if they are exceeded.
For this reason, an excitation signal is required that is asymmetrical on the one hand and minimizes the forces acting on the piezo on the other.
A signal that fulfils this requirement can be achieved by superimposing two sine waves as described by the formula (1) below.

$$U(t) = \hat{U}\left(\sin(\omega t) + \frac{1}{Q}\sin(2\omega t + \Phi)\right) \qquad (1)$$

$\hat{U}$ is the maximum voltage of the fundamental oscillation and ω is the angular frequency. The second superimposed sinusoidal oscillation has twice the angular frequency. The proportion of the superimposed oscillation can be set via factor Q and the phase shift via Φ. The signal form originates from the Fourier series of a sawtooth signal. Figure 2 shows an example of two excitation signals with a fundamental frequency of 1 kHz, a phase shift of π and the Q factors 2 and 7. A sawtooth signal is also shown for comparison.

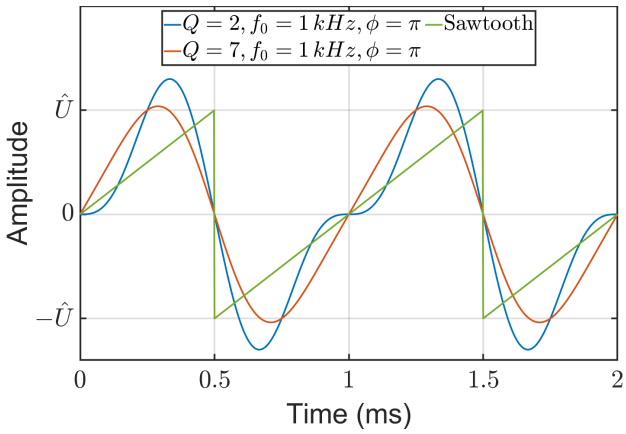

Figure 2: Excitation signal of the stack piezo

The excitation signal described by formula (1) was generated in the experiments by an Agilent 33521A function generator and amplified by a DYNACORD PAA 880 audio amplifier. A voltage offset of +40 V was used to ensure that the piezo was operated in the centre of its permissible voltage range of -20 V to +100 V.

3 Results and Discussion

Objects of different materials, sizes and weights were examined with the stick-slip motor set up, which can be seen in Figure 3. The respective material and weight are listed in Table 1.

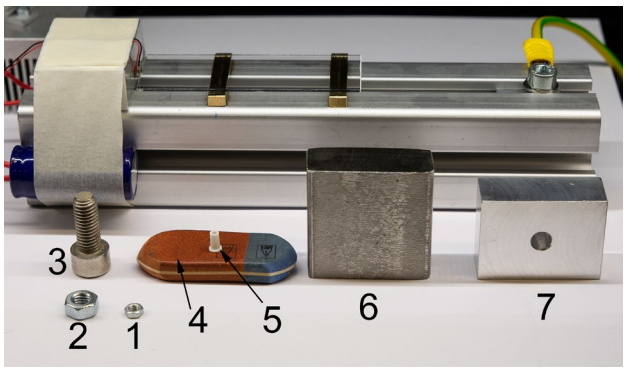

Figure 3: Experimental setup and seven different test objects

Table 1: Weight and material of the sliders used

Slider-Number	Material	Weight in g
1	Steel	0.32
2	Steel	2.13
3	Steel	12.75
4	Rubber	11.31
5	Plastic	0.0339
6	Steel	194.66
7	Aluminium	46.23

The movement of the objects is shown as an image sequence in Figure 4 using the example of slider 6 at an excitation frequency of 1.8 kHz and an excitation voltage of 90 V_{PP}.

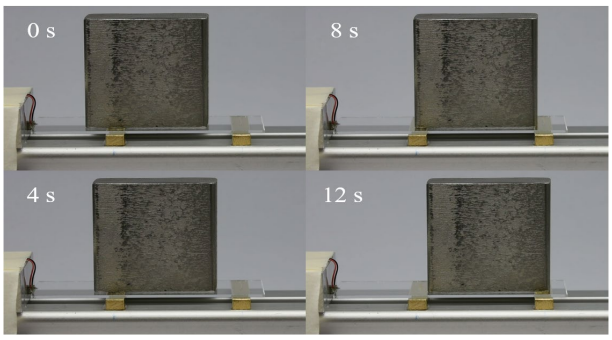

Figure 4: Images sequence of slider 6 in motion in 4 second time steps, Q = 7, Φ = π, U_{PP} = 90 V, f_0 = 1.8 kHz

During the tests, the object movement was visualized using the PSV-400-M laser scanning vibrometer from Polytec. The measured speed and the corresponding object displacement over time for slider 7 are shown in Figure 5..
At a relatively low excitation frequency of 600 Hz, the object moved forward but then slid back a little within each oscillation period. This can also be seen in the graph at the top left, where the object velocity is both positive and negative. The distance travelled by the object during each oscillation was approximately 250 nm. As the frequency increases, the distance slid back by the slider is decreased and a smooth object motion is achieved. This can be seen in the permanently positive object speed shown at the top right. The higher the frequency, the higher the maximum speed

achieved. Above 3 kHz, however, the natural resonances of the glass plate used as a stator increase, leading to an abrupt and sometimes uncontrolled change in the object speed. Conversely, if the excitation frequency is too low, below 400 Hz in the case of this slider, the adhesion of the slider to the stator cannot be overcome and the object therefore does not start moving. This results in a lower and an upper operating frequency.

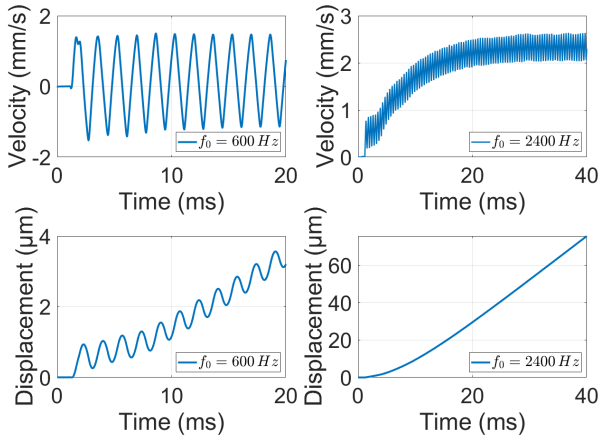

Figure 5: Slider 7, Q = 7, Φ = π, U_{PP} = 90 V for 600 Hz (left) and 2400 Hz (right)

In addition to the excitation frequency, the excitation voltage, the phase angle, and the Q-factor can also be varied. The influence of the excitation voltage on the piezo is shown in Figure 6. As with all other evaluated objects, a minimum necessary excitation voltage was also observed for slider 7. In this case, the forces occurring at a voltage of 7.5 V_{PP} were high enough to overcome the adhesion and set the object in motion. Above this voltage value, a directly proportional and almost linear relationship between excitation voltage and object speed was observed.

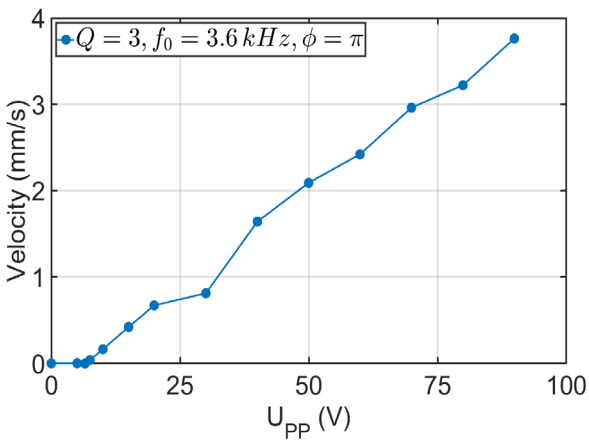

Figure 6: Slider 7, Voltage-dependent object speed

Figure 7 shows how the phase shift between the two superimposed sinusoidal oscillations affects the object velocity. It was shown that the object velocity can be altered by changing the phase position at a constant excitation voltage and frequency. However, this relationship is not linear, as with the excitation voltage, but sinusoidal.

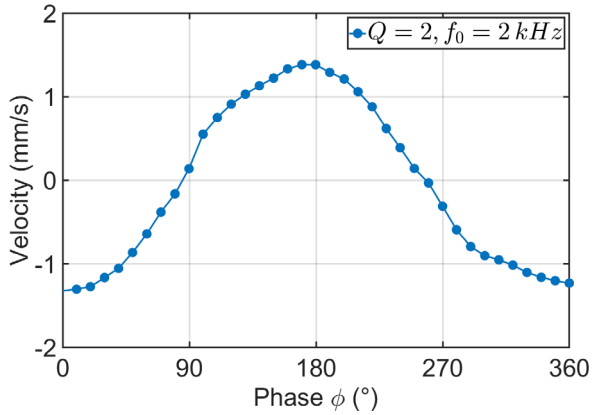

Figure 7: Slider 7, Phase-dependent object speed, U_{PP} = 90 V

With regard to the last adjustable parameter in the excitation signal, the Q-factor, it can be said that no significant differences were observed between a Q-factor of 2 and 7. Only at values above 10 the asymmetry of the signal, and thus the stator movement, was no longer sufficient to set the object in motion. Taking into account the maximum forces acting on the piezo, the highest possible Q-factor, which is 7 for the developed stick-slip motor, is therefore preferable.

Based on the experiments carried out, it can be said that each of the objects examined could be moved on the slider. There were only slight differences in the maximum speed and the minimum required excitation frequency or excitation voltage of the piezo. For example, the voltage had to be slightly higher for slider 4.

Variable object speeds of up to several mm/s in combination with a step width of a few hundred nm make it possible to align objects both quickly and precisely. This opens a wide range of possible applications when it comes to the precise positioning of objects where space is limited.

4 Conclusion and Outlook

In this work it could be shown that it is possible to position with an accuracy of 250 nm with the help of the developed stick-slip motor. The main factors that influence the movement are the frequency and excitation voltage. Superimposed sinusoidal oscillations were used as the excitation signal in order to reduce the acceleration and thus the forces exerted on the piezo element. It turned out that the so-called Q-factor between the two sine waves can be very large and a value of 7 provides a satisfactory result. In the end, a movement speed of up to 4 mm/s was achieved.

Based on the results of the experiments, the principle of one-dimensional object movement is to be extended to two dimensions with a significantly larger range of movement. The prototype is shown in Figure 8. In the centre is the 150 x 150 mm^2 stator, which is held by elastic hinges, which in turn are bolted to a solid steel frame. Pre-stressed

stack piezos with a maximum deflection of 30 µm are attached to two orthogonal sides of the stator. Springs generate a counterforce on the other two sides. The elastic hinge allows the stator to be moved in one dimension without affecting the second dimension. This should make it possible to move objects in two dimensions in the future and thus extend the potential field of application of the developed positioning unit.

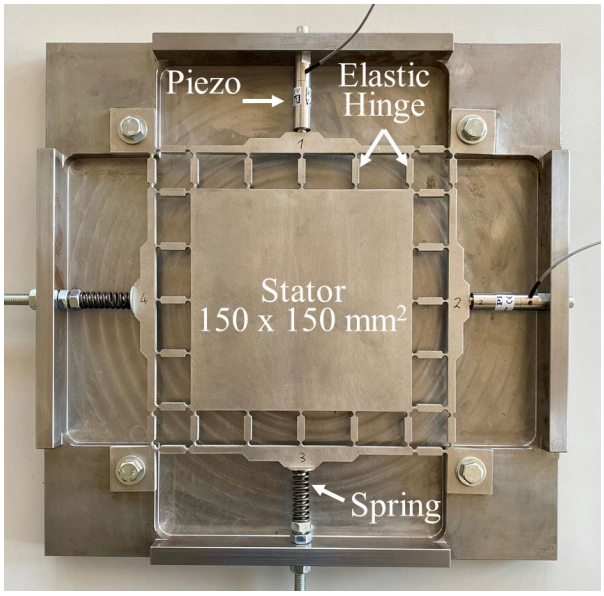

Figure 8: Experimental setup for 2D acoustic positioning of objects

5 Literature

[1] Piezoelectric Inertia Drives: https://www.physikinstrumente.com/en/expertise/technology/piezoelectric-drives/piezo-inertia-drives, Access: 23.04.2024

[2] M. Hermann, W. Schinköthe: Piezoelektrische Wanderwellenmotoren für lineare Bewegungen, VDI-Berichte 1269, S. 301-314, 1996

[3] M. Hunstig: Konzeption, Ansteuerung und Eigenschaften schneller piezoelektrischer Trägheitsmotoren - Schriften des Lehrstuhls für Mechatronik und Dynamik 2, Shaker Verlag, Aachen 2014, ISBN: 9783844028355

[4] T. Hemsel: Untersuchung und Weiterentwicklung linearer piezoelektrischer Schwingungsantriebe, HNI-Verlagsschriftenreihe, Band 101, 2001. Zgl. Dissertation, Universität Paderborn, 2001, ISBN 3-935433-10-7

[5] Q. Chang, W. Chen, S. Zhang, J. Deng, Y. Liu: Review on Multiple-Degree-of-Freedom Cross-Scale Piezoelectric Actuation Technology, Advanced Intelligent Systems, 2024, 10.1002/aisy.202300780

[6] Y. Shimizu, Y. Peng, J. Kaneko, T. Azuma, S. Ito, W. Gao, T. Lu, Design and construction of the motion mechanism of an XY micro-stage for precision positioning, Sensors and Actuators A: Physical, Volume 201, 2013, Pages 395-406, ISSN 0924-4247, 10.1016/j.sna.2013.08.012

Investigations of additively manufactured SMA high-load actuator elements

Andrea Böhm[1], Christian Weck[2], Andreas Hofer[1], Kenny Pagel[1], Welf-Guntram Drossel[1]
[1] Fraunhofer Institute for Machine Tools and Forming Technology IWU, Dresden, Germany
[2] Fraunhofer Institute for Manufacturing Technology and Advanced Materials IFAM, Bremen, Germany
andrea.boehm@iwu.fraunhofer.de

Abstract

Additive Manufacturing techniques like laser powder bed fusion process allow for the manufacturing of NiTi shape memory elements. The additive produced hollow samples are in the low-temperature phase in the martensitic state at room temperature. The reversible, martensitic-austenitic phase transformation results in a shape memory effect. The additional heat treatment makes the hollow cylinders suitable for cyclic use as actuator material. Microstructure, phase transformation temperatures, and cyclic behavior were investigated. In addition, a high-load actuator element is presented.

1 Introduction

NiTi alloys are the most commonly used shape memory alloys (SMA) due to their excellent functional properties. NiTi alloys are conventionally produced via casting, metal forming or via powder metallurgy processes. Research and development should be done on bulk SMA-actuators to apply their advantages to higher forces. There are plenty of potential applications demanding higher forces (kN-range) that cannot be generated by SMA-wires [1, 2].
Additive Manufacturing techniques like laser powder bed fusion process (PBF-LB/M) on the other hand allow for the manufacturing of NiTi shape memory elements (SME) into complex geometries with little or no machining and properties comparable to conventionally parts [3, 4]. Furthermore, with PBF-LB/M, cost-effectiveness can be achieved even in small batches. Hence, a PBF-LB/M-process for high-load actuator elements has been developed and the material behavior of additively manufactured samples investigated.

2 Experimental

The additive manufactured samples were fabricated using PBF-LB/M. The powder was produced from a $Ni_{45.0}Ti_{50.0}Cu_{5.0}$-ingot (at. %) by the Ingpuls GmbH. The atomized resulting powder had a D_{90} of 61 µm. The printing of the samples was performed on a TruPrint 1000 (TRUMPF SE + Co. KG) [5].
The local transformation behavior of the material was investigated by means of dynamic differential scanning calorimetry, DSC.
Systematic investigations of the microstructure were carried out. The microstructure investigations were also done by scanning electron microscopy (SEM).
All compression tests were performed utilizing a custom build SMA-test-bench [5]. The need for measuring high forces (kN range) and small strokes (µm range) requires a specifically high stiffness. To achieve this, the test-bench is based on a solid steel frame. Moreover, free movement with minimal friction is obtained using linear bearings.

3 Results and Discussions

3.1 Microstructural investigations

The shape memory specimens could successfully be printed with densities over 98 % using a laser power of 100 W, a scanning speed of 450 mm/s, a hatching distance of 60 µm and a layer thickness of 30 µm. The resulting volumetric energy density was 123 J/mm^3. The manufactured element had a height of 7.8 mm, an inner diameter of 13.8 mm and an outer diameter 15 mm. **Figure 1** shows an example of the optical microscopic results of an additively manufactured NiTiCu hollow sample after application of the PBF-LB/M process.

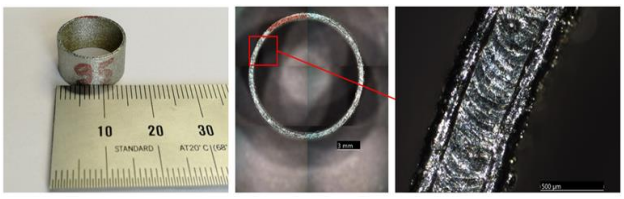

Figure 1 Images of an additively manufactured NiTiCu hollow sample using the laser powder bed fusion processing

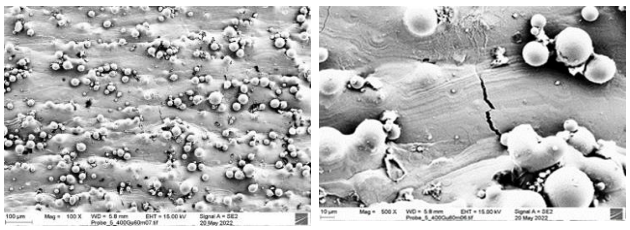

Figure 2 SEM results of an additively produced sample

Electron microscopic investigations showed that the shape memory elements produced using PBF-LB/M exhibited significant residual porosity and cracks on the outer and front surfaces **(Figure 2)**. After evaluating the cracks it can be assumed that these are due to the thermal stresses in the printing process. In addition to the laser parameters (laser power, hatching distance, scanning speed), the sequence of the laser exposure processes plays a decisive role for the

geometry to be produced. A software-based optimization of the exposure for the element to be produced was carried out. SEM analyses showed that the cracking of the samples could be significantly reduced by adjusting the exposure strategy.

3.2 Thermal investigations and cyclic behavior

As part of the work, the thermal characterization of the differently produced test specimens was carried out using DSC measurements and the phase transformation temperatures were determined. For the actuator technology, it is important that a relatively high martensite finish temperature M_f is present so that a complete transformation back into martensite from the high-temperature phase austenite is achieved and thus suitable material with very good functional properties is available. The initial results of the manufactured PBF-LB/M samples showed M_f temperatures, which were still clearly too low. For PBF-LB/M elements in particular it is known that subsequent heat treatment can influence the transformation temperatures over a wide range [6].

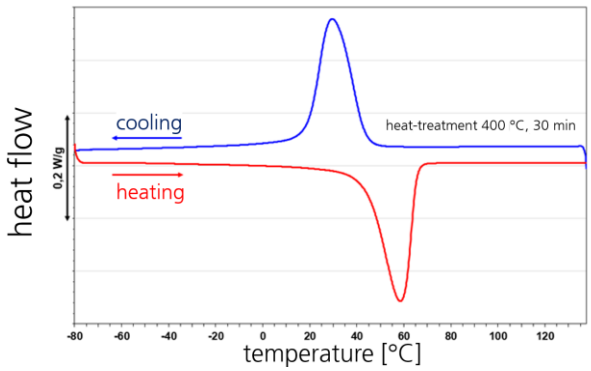

Figure 3 DSC measurement result of a heat-treated (400 °C, 30 min) sample

In this context, additive manufactured cylinder samples were produced and subjected to different heat treatments by varying the temperature, holding time and cooling conditions. In principle, the PBF-LB/M samples exhibited a one-step transformation behavior and higher transformation temperatures after heat treatment at 400 °C **(Figure 3)**.

In further work, the cyclic behavior of compression-loaded shape memory elements (125 MPa) manufactured using an additive PBF-LB/M process was also investigated. The specimens were cycled up to 1,000 **(Figure 4)**. The function of the shape memory elements has been proven. Thus, a high-load shape memory elements that has been developed is presented. On a heat-treated (400 °C) and then cycled hollow specimen (1,000 cycles), only a small reduction in transformation temperatures was observed.

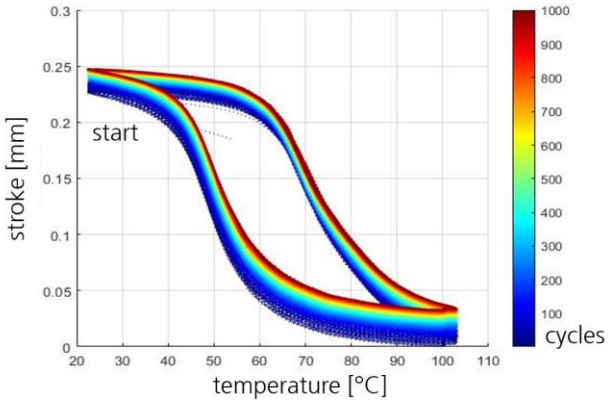

Figure 4 Cyclic behavior of compression-loaded shape memory element (1,000 cycles)

4 Summary

The additively produced PBF-LB/M samples are in the low-temperature phase in the martensitic state at room temperature. Due to the reversible, martensitic-austenitic phase transformation, there is a one-step shape memory effect. The additional heat treatment makes the hollow cylinders suitable for cyclic use as actuator material. Microstructure, function, and phase transformation temperatures were determined. A high-load actuator element will be presented.

Acknowledgement

The authors wish to thank the Fraunhofer-Gesellschaft (FhG) for the financial support. All presented findings were obtained in the project “HochPerForm”, which was financed by the FhG.

5 Literature

[1] Maiwald, D.; Bucht, A., Zorn, W., Drossel, W.-G.: Proceedings of the ASME 2020 Conference on Smart Materials, SMASIS 2020, Sept. 15, 2020, Virtual, Online

[2] Böhm, A.; Maiwald, D.; Pagel, K.; Drossel, W.-G.: ACTUATOR 2022, June 29 - 30, 2022, Mannheim, ISBN 978-3-8007-5894-4, S. 194

[3] Chekotu, J.C.; Goodall, R.; Kinahan, D.; Brabazon D.: Materials & Design, 2022, pp. 218, https://doi.org/10.1016/j.matdes.2022.110715

[4] Dadbakhsh, S.; Speirs, M.; Van Humbeeck, J.; Kruth, J.-P.: MRS Bulletin, 41, 2016, pp. 765-774, https://doi.org/10.1557/mrs.2016.209

[5] Thüsing, D.; Hofer, A.; Pagel, K., Weck, C.; Drossel, W.-G.: Proceedings of the ASME 2023 Conference on Smart Materials, SMASIS 2023, Sept. 11-12, 2023, Austin

[6] Saedi, S., Turabi, A.S., Andani M.T., Haberland, C., Karaca, H., Elahinia, M.: J Alloy Compound, 2016, 677, 204–10

Modular Gripping Mechanism for Collaborative Robotic Endoscopic Lumbar Decompression (ELD) surgery

Giovanni Battista Regazzo[1], Ayoob Davoodi[1], Yuyu Cai[1], Fabio Carrillo[2], Christoph J. Laux[3], Philipp Fürnstahl[2], Emmanuel Vander Poorten[1].

[1] KU Leuven, Department of Mechanical Engineering, Robot-Assisted Surgery Group (RAS), 3000 Leuven, Belgium.

[2] Research in Orthopedic Computer Science (ROCS), University Hospital Balgrist, University of Zurich, 8008 Zurich, Switzerland.

[3] University Spine Center Zurich, University Hospital Balgrist, University of Zurich, 8008 Zurich, Switzerland.

Abstract

Endoscopic Lumbar Decompression (ELD) is a minimally invasive surgical procedure to remove the herniated disc material within the spinal canal. In a traditional approach, the clinician holds the endoscope and inserts the instruments into its lumen to reach the surgical window and perform the decompression surgery. Some steps, such as opening ligamentum flavum, benefit from the help of an assistant who can hold the endoscope while the surgeon is handling the working-sleeve to partially resect the ligament directly neighboring neural structures. This approach can be time-consuming and uncomfortable. To overcome this drawback of traditional ELD, a robotic approach using a collaborative robot to hold the endoscope is explored. It is essential that such system is modular and can be quickly coupled and released without harming the patient or damaging expensive endoscopes. In this context, a gripper with a dedicated actuation system that is safe, reliable and lightweight is proposed. This paper describes this novel mechanism for manual actuation of the gripper. The system offers the surgeon full control over the applied gripping force on the endoscope, omitting the need for an assistant to perform this task while handling the plurality of instruments involved in the procedure.

1 Introduction

ELD is increasingly gaining popularity as a safe and effective form of minimally invasive surgery (MIS) for lumbar disc herniation [1]. In comparison to conventional open surgery, percutaneous endoscopic lumbar surgery offers advantages such as reduced hospitalization duration, shorter incisions, minimal blood loss, and lower levels of back pain [2]. In the past decades, the use of robotics has achieved success in various surgical sub-specialties. Also in spine surgery, there is a growing interest in using robotics to facilitate MIS approaches, enhancing ergonomics and effectiveness. Given the challenge of reliably maneuvering endoscopic instruments with millimetric spatial resolution and long lever arms, this work proposes a collaborative approach for robotically supporting the endoscope during ELD procedures. As the intervention takes place at a critical region of the body, in the vicinity of the spinal canal, the robotic instruments and their actuation system should be safe and dependable. This novel manual mechanism provides clinicians with complete control over the grasping force applied by the gripper to the endoscope.

2 Materials and Method

The design of the mechanical actuator revolves around a flexible sleeve-based gripper that is used to grasp the endoscope. This type of gripper, that was previously used to drive catheters [83], is based on the idea that by pulling two collars at both ends of a cylindrical flexible sleeve apart along the sleeve's longitudinal axis, the internal diameter of the sleeve reduces. The endoscope tube inserted into the sleeve forms a constraint for further contraction. The distributed normal pressure that subsequently arises generates a frictional force between endoscope body and sleeve that resists relative displacements of the endoscope. In this new design, the collars are pulled apart by exploiting the surgeon's input force. Hereto, the wedge cam mechanism, shown in **Figure 1**, converts the tangential lever motion to the axial motion of the mechanism.

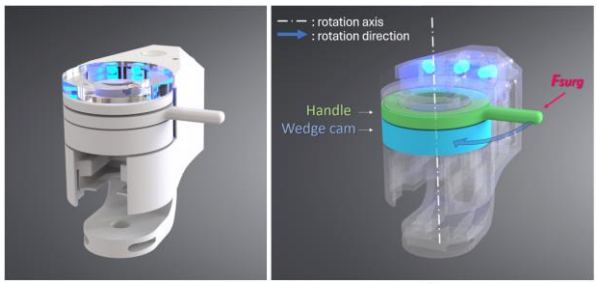

(a) (b)

Figure 1 (a) Graphic representation of the end-effector. (b) Handle and wedge cam of the mechanical actuator highlighted in the end-effector design together with the axis and direction of the rotation.

The cylindrical mechanism shown in **Figure 1** is also shown in a planar view in **Figure 2**. After inserting the endoscope tube into the sleeve, the surgeon rotates the handle, applying a tangential force F_{surg} to it. A compliant mechanism inside the handle transmits the force to a wedge cam, which converts it into an axial force on the basis of the wedge cam angle α and of the friction coefficient μ in the contact surface, and thus pushes the lower sleeve apart from the upper sleeve attached to the end-effector frame. Therefore, as the handle and the wedge cam are rotated around the axis shown in **Figure 1.B**, the sleeve increasingly stretches and the reaction force exerted to the tip of the compliant mechanism increases. This determines

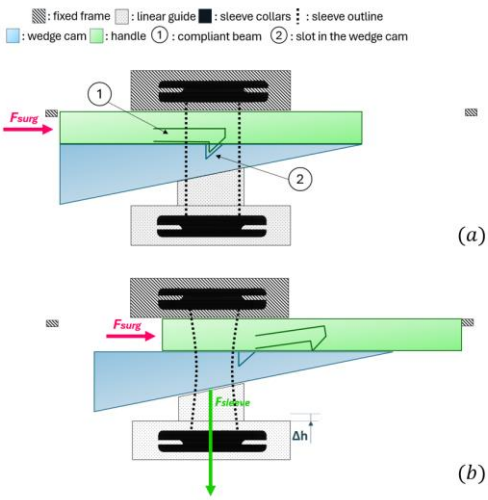

Figure 2 Planar representation of the mechanism with the same color pattern as in Figure 1. (a) Mechanism at null force configuration. (b) Mechanism at maximum force configuration with compliant mechanism fully detached and handle at the end of its stroke.

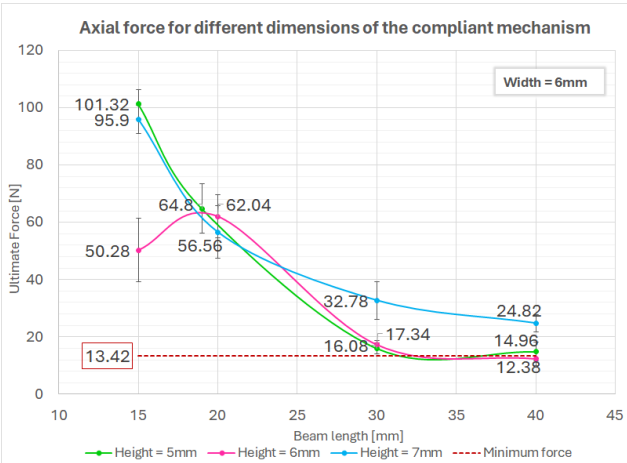

Figure 3 Axial grasping force provided by the system to the endoscope for different dimensions of the compliant mechanism (beam length and height).

its bending deformation. The force rises until it is large enough to cause a sufficient displacement to its tip such as to lift it completely out of its slot on the wedge cam, thus disengaging the coupling system. As a consequence, the force transmission stops once a maximum force value is reached, which depends on the structural characteristics of the compliant mechanism.

$$\eta = \frac{\tan(\alpha - \arctan(\mu))}{\tan(\alpha)} \qquad (1)$$

To prevent the reaction force of the sleeve from causing uncontrolled retrograde motion, the angle of the wedge cam is chosen to nullify the efficiency of such motion in (1), thus allowing the surgeon to apply any force between null and a preferred maximum to restrain the movement of the endoscope. This could be beneficial for adjusting the endoscope constraints to a desired level in situations where a certain degree of rotation is required and the endoscope cannot be completely immobilized, such as during the identification of neural structures. In this design, μ is assumed to be 0.5 and α is set to 8°.

The compliant mechanism is designed as a curved beam that follows the circular shape of the handle and has a chamfered tip. Twelve handles with beams of different sizes were manufactured to assess the capabilities of the actuation system. For dimensional reasons, the width was kept constant at 6mm, while the height and length were varied. The entire mechanism was 3D printed in PLA.

Performance was assessed by attaching the end-effector to a frame, inserting the endoscope, activating the mechanism to maximum force, and using a digital dynamometer to measure the maximum axial force required to overcome static friction between the endoscope and the gripper. For each beam configuration, the test was repeated five times.

2 Results and Discussion

Figure 3 shows the results of the test for 3 groups of samples having same beam height but different lengths. The majority of samples were able to provide a force greater than the minimum required to lock the endoscope both axially and rotationally. A peak force of 101N was measured. The force trend increases with shorter beams but not with bigger beam cross areas, contrary to expectations. The reason for this may be due to the anisotropy of the 3D printed PLA samples tested, the manufacturing quality, and the high friction at the contact point at the beam tip. The overall mass of the actuator was 80g, making it suitable for implementation in robotic applications requiring lightweight end-effectors. The end-effector and the actuator system for the gripper were validated by an orthopedic spine surgeon (co-author CJL) through a functionality test that investigated maneuverability, grip strength, and user friendliness (**Figure 4**).

(a) (b)

Figure 4 (a) Functionality test of the proposed gripping mechanism. (b) Setup for the robot-assisted ELD procedure.

3 Literature

[1] Y. Ahn, “A historical review of endoscopic spinal discectomy,” World Neurosurgery, vol. 145, pp. 591–596, 2021.

[2] Kotheeranurak, Vit, et al. "Full-endoscopic lumbar discectomy approach selection: a systematic review and proposed algorithm." *Spine* 48.8 (2023): 534-544.

[3] Al-Ahmad, Omar, et al. "Force control with a novel robotic catheterization system based on braided sleeve grippers." *IEEE Transactions on Medical Robotics and Bionics* (2023).

Custom Voice Coil Actuator for flexure-based electromechanical RF switch

Daniel Grivon, CSME, Rue de l'Observatoire 51B, Neuchâtel, Switzerland

daniel.grivon@csem.ch

Abstract

In electromechanical RF switches the rotor is moved between stable angular positions using a DC motor sustained using ball bearings. For space applications, compliant mechanisms may overcome the well-known drawbacks of ball bearings. Nevertheless, high reluctant forces in conventional motors prevent using them as actuators for compliant mechanisms. The design of an actuator to minimize the impact of radial forces and ease the mate with flex mechanisms is presented.

1 Introduction

The usually preferred actuating solution for flexures-based mechanisms are Voice Coil Actuators (VCA) because their actuating principle, which relies on Lorentz' force, minimizes the parasitic forces, i.e. the forces arising in any direction other than the motion direction. This is particularly important because compliant mechanisms suffer from low transversal rigidity, especially at the end of their motion stroke. Moreover, COTS solutions have usually a large footprint, to maximize the output torque. For these reasons a custom design has been developed by CSEM (in the frame of the ESA project WAVEGUIDE) to build a slender VCA (having a footprint ≤38mm x 38mm) able to provide up to 54mNm of output torque when supplied with 500mA, with an angular stroke of ±45° and for an operating temperature range of -35° to +75°C.

1.1 Electromagnetic modelling and design

1.1.1 High-Fidelity Magnetic Equivalent Circuit

A High Fidelity Magnetic Equivalent Circuit (HFMEC)[1] is built as an initial design tool to explicitly define the relations between the main quantity interest (torque) and the other geometrical and magnetic parameters.

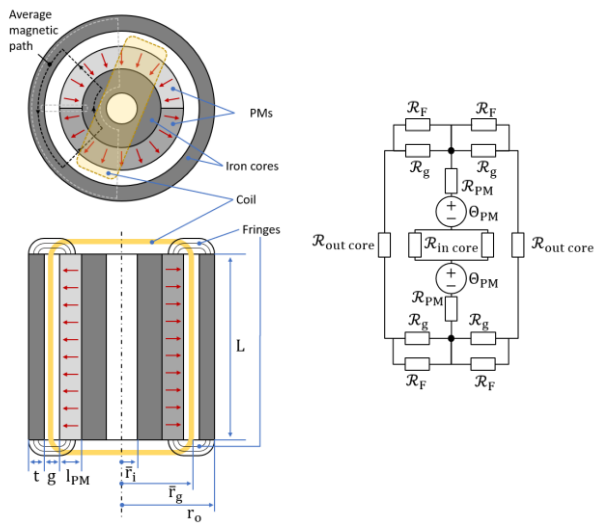

Figure 1 Schematic representation of the actuator and main geometrical parameters and associated HFMEC

1.1.2 Finite element modelling

1.1.2.1 Induction in the airgap and torque

A finite element (FE) model of the actuator is built to validate the inductions in the middle of the airgap and the working point of the magnets predicted by the HFMEC.

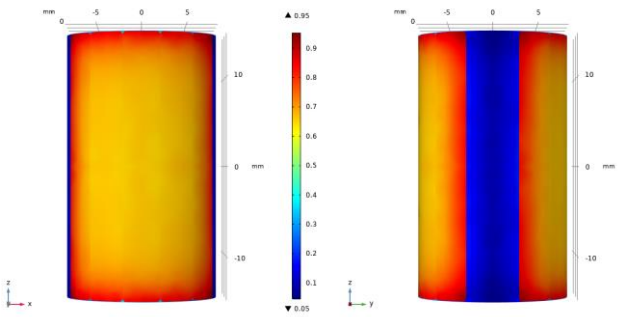

Figure 2 Magnetic density distribution in the middle of the PMs (units are [T])

1.1.2.2 Parasitic forces

The FE model allows to estimate the parasitic forces over the whole angular range (**Figure 3**). Due to the low radial stiffness of the compliant mechanism, even small radial forces imply large (non-acceptable) displacements. To solve this problem, PMs are arranged on both the airgap sides, so to compensate the border effects and to minimize the tangential component of the magnetic induction is minimized (**Figure 4**). As a results, non-uniformity in the induction distribution in the middle of the airgap and due to the saliency related to the discrete magnet

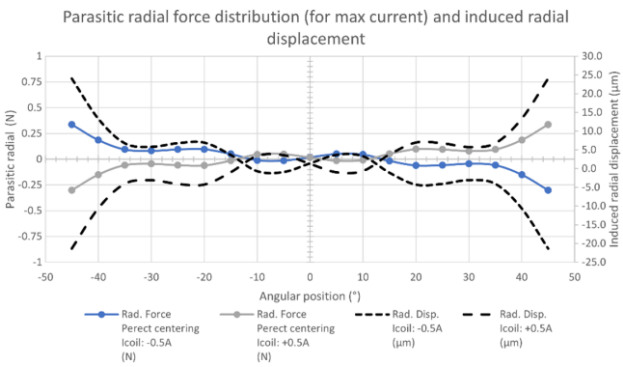

Figure 3 Assembled EM model of the VCA

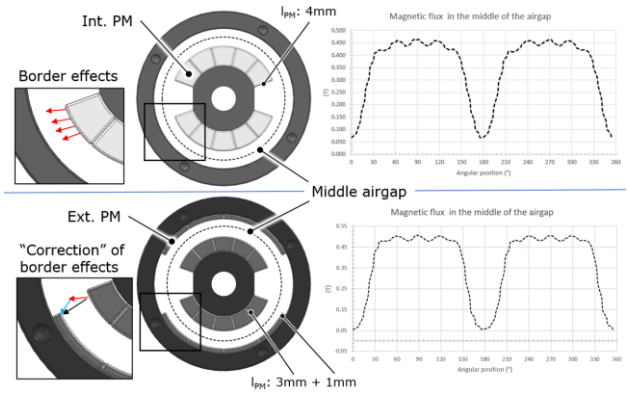

Figure 4 Assembled EM model of the VCA

The following figure shows the reduction of radial displacement due to parasitic forces obtained with the new magnets disposition.

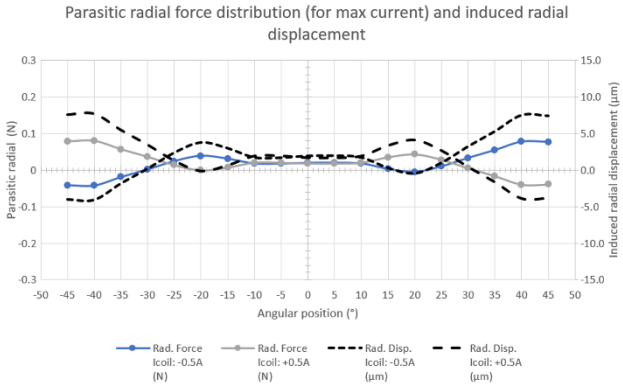

Figure 5 Assembled EM model of the VCA

2 Experimental validation

Two Engineering Models (EM) of the VCA have been manufactured to be successively integrated on the complete RF switch (**Figure 6**).

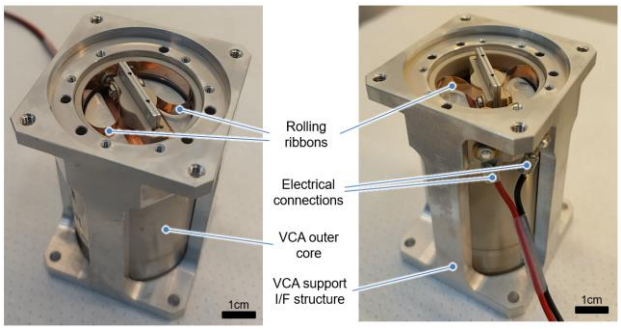

Figure 6 Assembled EM model of the VCA

2.1 Torque

The actuator output torque is the main quantity of interest to validate the overall design. **Figure 7** shows that measurements agree with the simulated value (<7% relative error over the whole angular span).

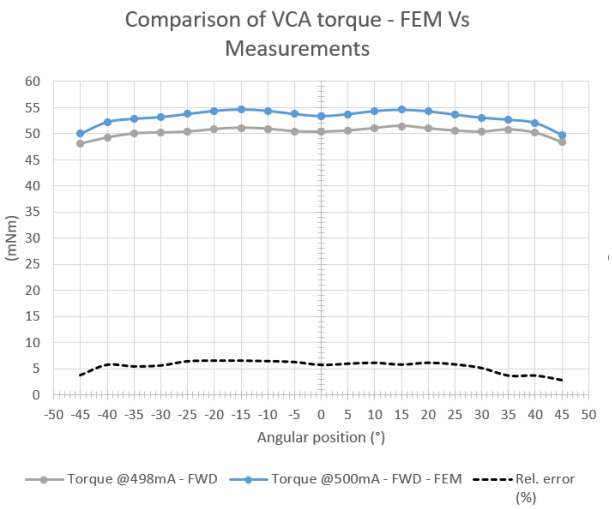

Figure 7 Comparison between simulated and measured torque.

2.2 Radial forces

As mentioned, the minimization of radial forces has been one of the main goals of the proposed design which led to the characteristic topology described in Section 1.1.2.2. A dedicated setup is currently under development to measure them and validate the final design.

3 Conclusion

The presented paper comprehensively describes the design, modelling and characterisation of a voice coil actuator used for space RF waveguide switches based on compliant mechanisms. The design methodology is presented and features the initial use of a High Fidelity Magnetic Equivalent Circuit which is then validated against FEM results. The minimization of radial parasitic forces being a driving parameter for the design of this actuator, a dedicated magnetic topology is proposed to fulfil these requirements. Its validity is proven against FEM results. Finally, measurements are performed to assess the actual values for moving and latching torques and to ultimately validate the overall design.

4 Literature

[1] Grivon, D.: Design, Modelling and Sensing Possibilities of Magneto-Rheological Based Devices, PhD Thesis, EPFL, 2017.

Modelling of an ice protection system based on icephobic and piezoelectric technologies, for WT demonstration.

Luigi Mangiacrapa[1], Nadine Rehfeld[2], Filomena Piscitelli[1], Salvatore Ameduri[1], Antonio Concilio[1], Giuseppe Mingione[1]

[1]Centro Italiano Ricerche Aerospaziali, CIRA, Capua, Italy

[2]Fraunhofer-Institut für Fertigungstechnik und Angewandte Materialforschung IFAM, Bremen, Germany

Corresponding author: l.mangiacrapa@cira.it

Abstract

Icing represents a serious problem for the aeronautic sector for its impact on the aerodynamic efficiency, the engine life and the authority of the aerodynamic surfaces. Conventional ice protection systems assure a safe and adequate protection, but present some drawbacks: they are power consuming and invasive. Moreover, with the emergence of new aircraft concepts, based on electrical propulsion or with a large use of electrical power, classical Ice Protection Systems (IPSs), based on hot-air spilled from engine, cannot be used. For this reason, attention is paid to novel approaches. This work focuses on the design of an innovative IPS based on piezo-electrics and superhydrophobic (SHC) coating, applied to a wing section demonstrator that will be tested in the ice wind tunnel facility of Fraunhofer IFAM. The paper starts with an overview on similar applications. Then the requirements of the proposed concept are critically discussed and, on this basis, the layout of the system is sketched. A dedicated numerical model, that was realized in order to adequately describe the action of the piezoelectric transducers, in charge of driving mechanical waves to detach the ice, is described. The work ends with an overview of the results achieved, expressed in terms of percentage of the amount of ice detached at the interface with the skin element.

1 Introduction

Icing represents a serious problem for the aeronautic sector, mainly because accreted ice reduces aerodynamic efficiency and engine life. Different technologies are used to remove ice or prevent its accumulation, assuring a safe and adequate protection, but they result power consuming and invasive. So, new approaches focus on more energy efficient solutions. IPSs can be divided in three mainly groups: anti-icing systems, that prevent the accreting of ice, de-icing systems, that remove accreted ice and hybrid systems, that prevent the accreting of ice and remove the accreted amount. Furthermore, IPSs can be divided into active systems, which require power, and passive systems, which do not. Different principles have been used to design IPSs as thermal, thermo-mechanical, but also electro-mechanical, pneumatic (de-icing boot), and chemical (e.g., icephobic coatings) [1]. For classical commercial medium- and long-range aircraft, wing ice protection system is obtained by heating the leading edge with hot-air spilled from the engine. This solution requires and oversizing of the engine, causing an increase in fuel consumption and emission and, of course, is not applicable for new electrical based propulsion systems. For these reasons, new innovative ice protection systems are addressed within the Clean-Aviation "UP wing" Project coordinated by AIRBUS. The Ultra Performance Wing project ("UP wing") will validate, down select, mature and demonstrate key technologies and provide the architectural integration of high aspect ratio wing concepts for targeted ultra-efficient Short/Medium Range aircraft (SMR), i.e. ~150-250 PAX and ~1000-3700km (~500-2000nm) range [2].

Looking for future sustainable aviation, low-energy-demanding IPSs, based on ultrasonic waves, has been being under investigation. Mechanical waves can be generated within the structural element causing shear at the interface between the structure and the ice. The accreted ice layer will be shed off if magnitude of this shear exceeds ice adhesion strength. Piezo-electric transducers appear capable of exciting ultrasonic waves with sufficient power [3].

Hybrid IPSs, which combine active IPSs with passive superhydrophobic/icephobic coatings, able to prevent, delay, and/or reduce the ice accretion, might represent a valuable solution, reducing the energy consumption and the CO_2 emissions [4].

For the demonstration of this technological approach, tests in representative environmental conditions are required. The test campaign will be conducted in the ice wind tunnel at Fraunhofer IFAM. In this closed loop test facility, wind speeds of up to 95m/s and supercooled water droplets can be generated to accrete ice formations on aerodynamic profiles. These parameters are the pre-requisite to assess the de-icing performance of the designed hybrid ice protection system in this study. Section 2 will be dedicated to IWT scenario and requirements, which have constituted a guideline for modelling of IPS demonstrators. Moreover, the system itself will be described and the role of superhydrophobic technology will be discussed. Within section 3 the modelling of the demonstrators is described. The results of structural analysis and the evaluation of IPS performance, with and without superhydrophobic coating, are discussed in the section 4 paragraph. The paper ends with concluding remarks, future steps and the acknowledgments.

2 IWT demonstration

The object of this work is a demonstrator whose naked view is illustrated in **Figure 1**. It reproduces a NACA 0012 airfoiled segment with a chord of 310 mm and a span of 150 mm. Two lateral ribs connected to a rear and a front spar constitute its main structure. Three skins (0.5, 0.8 and 1 mm thick) will be screwed on these ribs. At the leading-edge zone and on the interior surface of the skin, a total of 12 PZT transducers (6 on the top and 6 on the bottom) will be bonded. Their scope is to drive in- and out-of-plane shear actions at the interface with the ice layer accreted during the test in the icing wind tunnel. These transducers are made of PIC 255 composition, selected as good compromise between hardness and transmittable strain.

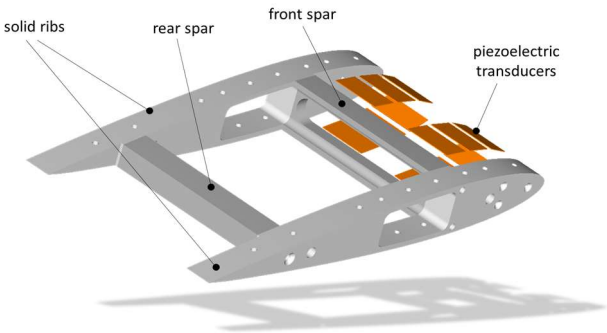

Figure 1 – Wind tunnel model

For the demonstration of the de-icing performance of the designed system, a closed loop ice wind tunnel is used (**Figure 2**). The demonstrators are equipped with the electromechanical de-icing system, attached to the skin of an aerodynamic NACA0012 model. The Aluminium skin is optionally equipped with a superhydrophobic surface and allows the direct comparison of the de-icing performance with unmodified surfaces. For the tests, ice is accreted in a pre-defined process, followed by the activation of the active de-icing system and the evaluation of the de-icing efficiency. For this purpose, ice shapes prior to and after the de-icing process are measured and compared to each other.

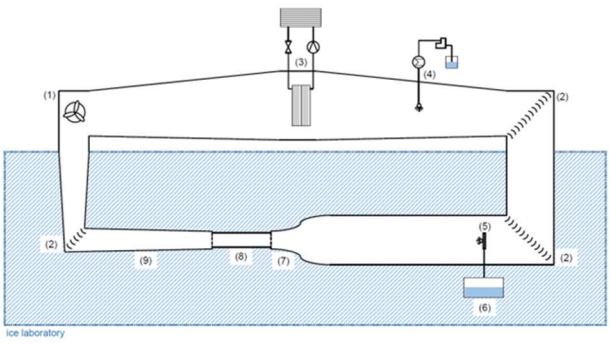

Figure 2 – Fraunhofer IFAM ice wind tunnel with a fan drive system (1), turning vanes (2), heat exchanger of refrigeration system (3), humiditystat (4), water spray bar (5), water reservoir and pumps (6), test section entrance (7), test section (8), and diffusor (9)

For the ice wind tunnel tests at Fraunhofer IFAM, static air temperatures in the range of -4°C to -20°C and velocities from 80 m/s to 95 m/s will be considered. The cloud characteristics include an MVD of 20µm and an LWC up to 0.6 g/m^3. The angle of attack is set at 0°. Half demonstrators will be coated with a SHC developed at CIRA [5],[6] able to significantly reduce the wettability of surface. In order to improve the coating adhesion, the metallic surface will be sand abraded at 3 bar to achieve a roughness Ra of about 3 µm. The wettability of surface before and after the application of the coating will be assessed through Contact Angle (CA) measurements and Surface Free Energy (SFE), in compliance with the ASTM D7490-13 standard [7], with 3µL of water (H_2O), diiodomethane (CH_2I_2), and formamide ($HCONH_2$). The SFE will be calculated according to the Owens-Wendt (OW) method, for which the surface energy of a solid is the sum of two components, a dispersive and a polar one [8],[9]. To give an idea of the coating performances, in **Figure 3** results in terms of morphology and wettability of reference (R) and coated with the SHC (C) sample of metallic surface performed in a previous work [10] are reported.

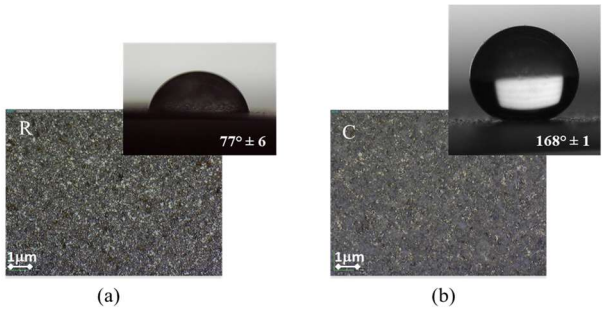

Figure 3 – Micrography image of metallic surface before (a) and after (b) the application of the SHC developed at CIRA [10].

3 Modelling of Ice Protection System

Numerical analyses, based on FEM, were carried out to verify the strength and the dynamic behaviour of the system. The modelled parts are the skin, the front spar, the rear spars and the ribs. Shell elements were adopted to model the skin, while solid elements for the front spar, the rear spar and the ribs. The adopted materials were aluminium alloy for the skin, the rear spar and the ribs and steel alloy for the front spar. In the following table, the main mechanical properties are summarized.

Material	E [GPa]	ν	Yield Strength [MPa]
Alum. 7075-T6	71.7	0.33	503
Steel AISI 310	210	0.30	275

Table 1 – Material main mechanical properties

Single Point Constraint (SPC) were used to fix the structure in correspondence of the four lateral holes; Rigid Body Elements were used to link the hole boundary nodes to the SPCs, (**Figure 4**). To verify the strength of the structure, XFOIL software was adopted to obtain the aerodynamic load, under the following most critical conditions: airflow speed = 90 m/s and AoA = 12°. An additional model was also realised to estimate the impact of the piezoelectric transducers when excited for detaching the ice layer. Due to the small wavelength of the ultrasounds, an adequate refinement level was necessary. The leading-edge zone was modelled by using more solid elements along the thickness of the skin to describe the

evolution of the wave along this direction. The spanwise symmetry was exploited to halve the computational weight. A detail of the model is illustrated in **Figure 5**.

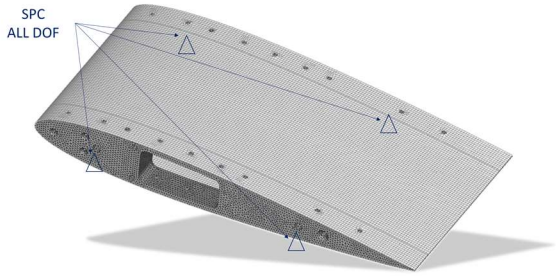

Figure 4 – Full model and constraints scheme.

The model was used both to estimate the shear at the interface with the ice and to verify that the ultrasound generation would not affect the structural integrity of the skin, of the piezoelectric patches and of the bonding layer.

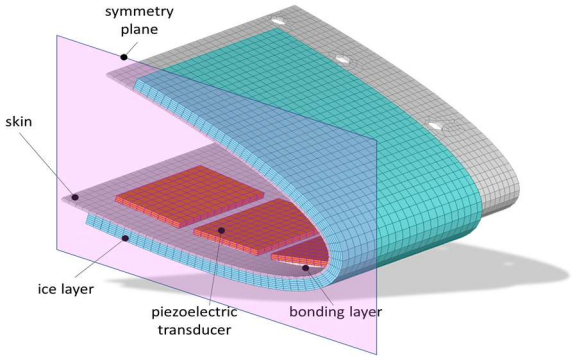

Figure 5 – Leading-edge refined model.

4 Results

Von Mises Stress was taken into account to verify the strength of the structure and to calculate the safety factor (SF), as the ratio between the yield stress and the working stress. As expected, the stress peak is localized on the skin (**Figure 6**) and, an SF greater than 3 was obtained in all the structure. Then, the dynamic behavior was characterized. The first three modes of the structure were calculated by means of a normal mode analysis; they resulted respectively: $f_1 = 494$ Hz, $f_2 = 570$ Hz, $f_3 = 615$ Hz.

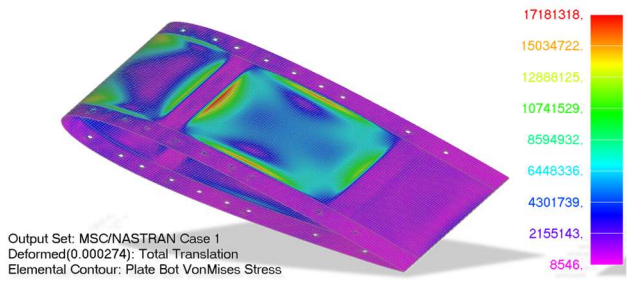

Figure 6 – Von Mises Stress map over the skin.

A dynamic analysis in the frequency domain was implemented with the aim of finding the maximum peaks of excitation. This value was in fact assumed as nominal working condition to compute the stress level in the different parts and verify its compliance with the structural safety. Two peaks were identified for the most critical configuration (thinnest skin of 0.5 mm integrated with piezo patches 0.6 mm thick); 12.9 and 41.5 kHz. At first the impact of the excitation with an amplitude of 100 V was investigated in terms of structural solicitation. In **Figure 7** the stress level achieved in the skin is shown for both the peaks of excitation. The first peak resulted the most critical, with a maximum von Mises stress level of 25 MPa, in any case significantly lower the yield strength of the material.

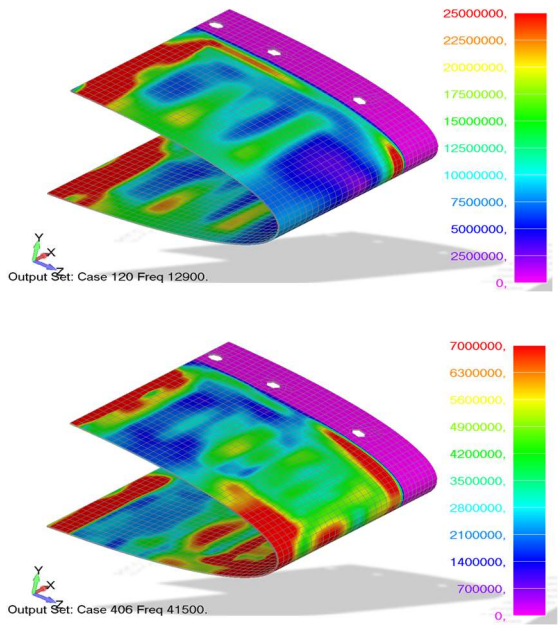

Figure 7 – Stress level produced in the skin by the piezoelectric for excitation at 12.9 (top) and 41.5 kHz (bottom).

Then the stress level in the piezoelectric transducers and in the adhesive layer was also investigated (**Figure 8**). The maximum solicitation for the transducers occurred at 41.5kHz (50MPa) while, for the adhesive layer, at 12.9kHz (7MPa). Both these levels result significantly lower than the strength limits of the piezo compound (650MPa) and of the adhesive layer (Master Bond EP21LV, 17.2 MPa - shear strength).

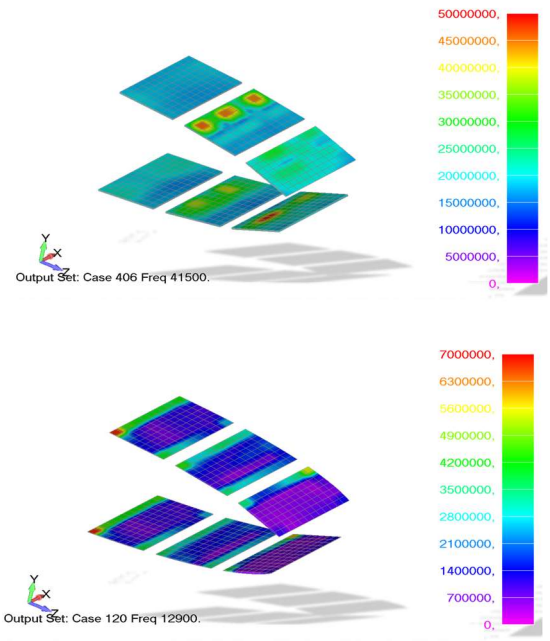

Figure 8 – Stress level in the piezo transducers (top) at 41.5 kHz and in the adhesive layer (bottom) at 12.5 kHz.

Finally, the impact of the excitation on the shear at the interface with the ice was also estimated. To this scope, an ice layer 3 mm thick was considered. in-plane and out of-plane shear actions were estimated. In the plots of **Figure 9**, the maximum actions produced in-plane (top, 12.9 kHz) and out-of-plane (bottom, 41.5 kHz) are illustrated. These actions cross the threshold ice strength, assumed in a conservative way of 0.568 MPa [11], on a wide part of the interface. The presence of the superhydrophobic/icephobic coating will also dramatically abate this value [12], in this sense further facilitating the work of the piezo-actuators.

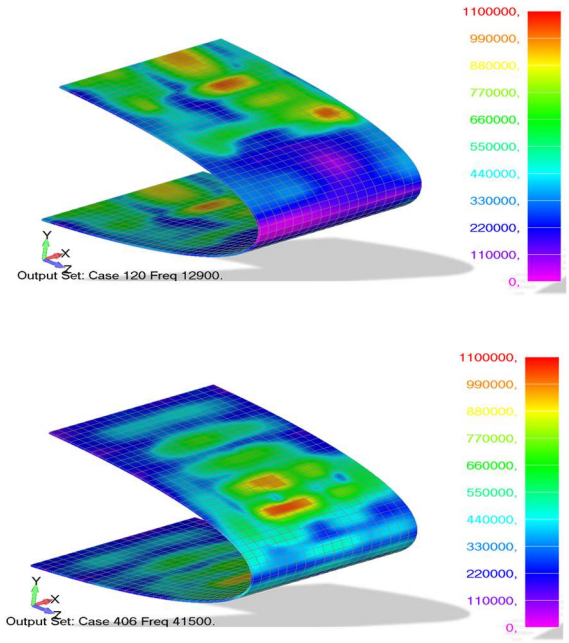

Figure 9 – In-plane (top) and out-of-plane (bottom) shear actions produced at the interface with the ice at 12.9 and 41.5 kHz, respectively.

5 Concluding remarks and future steps

A description of piezo-electric and ice-phobic coating based IPS was modelled. The device proved to be widely compliant with the wind tunnel safety requirements, from one side, and capable to drive shear actions, from the other side, with enough magnitude to detach ice accretions. The work herein illustrated represents a first step of an investigation focusing on the combined action of two ice protection technologies, ultrasounds driven by piezoelectric patches and superhydrophobic/icephobic coating. Dedicated demonstrators are under constructions. Their experimental characterization will be then executed, first, in the laboratories at CIRA (functionality, commissioning) and, then, in the wind tunnel of IFAM (final tests in representative environment).

6 Acknowledgments

The Project Ultra Performance Wing (UP Wing, project number: 101101974) is supported by the Clean Aviation Joint Undertaking and its members.

7 Disclaimer

Co-Funded by the European Union. Views and opinions expressed are however those of the author(s) only and do not necessarily reflect those of the European Union or Clean Aviation Joint Undertaking. Neither the European Union nor the granting authority can be held responsible for them.

8 Literature

[1] Yamazaki, M.; Jemcov, A.; Sakaue, H. A Review on the Current Status of Icing Physics and Mitigation in Aviation. Aerospace 2021, 8, 188. https://doi.org/10.3390/aerospace8070188

[2] https://cordis.europa.eu/project/id/101101974

[3] Vladislav Daniliuk et al., Feasibility Study of Ultrasonic De-Icing Technique for Aircraft Wing Ice Protection, 10.2991/aviaent-19.2019.15

[4] Piscitelli, F. Special Issue "Superhydrophobic and Icephobic Coatings as Passive Ice Protection Systems for Aeronautical Applications". Appl. Sci. 2024, 14, 1288. https://doi.org/10.3390/app14031288

[5] F. Piscitelli, Italian Patent N. IT102021000032444, "Rivestimento superidrofobico e ghiacciofobico di un substrato, metodo per il suo ottenimento e substrato così rivestito", 23 December 2021.

[6] F. Piscitelli, F. Substrate superhydrophobic and icephobic coating, method for obtaining it and substrate thus coated, International Patent Application N° PCT/IB2022/062672, 22 December 2022.

[7] ASTM D7490-13; Standard Test Method for Measurement of the Surface Tension of Solid Coatings, Substrates and Pigments Using Contact Angle Measurements. American Society for Testing and Materials: West Conshohocken, PA, USA, 2013.

[8] Owens, D.K.; Wendt, R.C. Estimation of the Surface Free Energy of Polymers. J. Appl. Polym. Sci. 1969, 13, 1741–1747.

[9] Zenkiewicz, M. Methods for the Calculation of Surface Free Energy of Solids. J. Achiev. Mater. Manuf. Eng. 2007, 24, 137–145.

[10] Piscitelli, F.; Volpe, A. Superhydrophobic Coatings for Corrosion Protection of Stainless Steel. Aerospace 2024, 11, 3. https://doi.org/10.3390/aerospace11010003

[11] Ameduri, S.; Concilio, A.; Brindisi, A.; Galasso, B. An Ice Protection System Based on Phased Piezoelectric Transducers. Actuators 2024, 13, 158. https://doi.org/10.3390/act13050158

[12] Tetteh, E.; Loth, E. Reducing Static and Impact Ice Adhesion with a Self-Lubricating Icephobic Coating (SLIC). Coatings **2020**, 10, 262. https://doi.org/10.3390/coatings10030262

Co-funded by the European Union

CLEAN AVIATION

Easy access to smart materials data and models using an ontology-based data and model access approach

Robert Courant[a], Jana Mertens[a], Mena Leemhuis[b], Özgür Özçep[b], Martin Dahlmann[c], Sebastian Stark[d], Andrea Böhm[e], Kenny Pagel[e], Maximilian Hinze[g], Daniel Pinkal[f], Michael Wegener[f], Martin Wagner[g], Holger Neubert[d], Thomas Sattel[c], and Jürgen Maas[a]
[a]Technische Universität Berlin, Berlin, Germany
[b]University of Lübeck, Lübeck, Germany
[c]Technische Universität Ilmenau, Ilmenau, Germany
[d]Fraunhofer Institute for Ceramic Technologies and Systems IKTS, Dresden, Germany
[e]Fraunhofer Institute for Machine Tools and Forming Technology IWU, Dresden, Germany
[f]Fraunhofer Institute for Applied Polymer Research IAP, Potsdam, Germany
[g]Technische Universität Chemnitz, Chemnitz, Germany

Abstract

Smart materials can be used as bidirectional transducers responding to various physical fields (e.g. electrical, magnetic, and thermal fields), eanbling a use as sensors, actuators, and generators. One challenge in developing smart material transducers is the access to material data and models. Different working principles, measurement and analysis methods, as well as data storage approaches often lead to heterogeneous and partly inconsistent datasets. However, easy and multiscale access to material data and models enables efficient research and development with regard to the selection of the materials and their optimization towards specific applications. Therefore, we developed a system build on the ontology-based data access (OBDA) approach, a method to access such heterogeneous datasets easily and quickly. This approach is extended in our multidisciplinary work to incorporate a model access, enabling material models to transform material data across multiple scales to compute new responses beyond stored data. The advantages are demonstrated using exemplary use cases for four subclasses of smart material: thermal and magnetic shape memory alloys, piezo-electric ceramics, and dielectric elastomers.

1 Introduction

Smart materials research is a young and dynamic field encompassing many topics within materials science. An overview of smart materials is given in [1, 2, 3]. The material properties are constantly being optimized and adapted to applications. They can be modified by changing the chemical composition or by using different processing methods and properties. With continuous research and further development of functional materials, large amounts of data are generated and the access to this data is decisive for an efficient and application-oriented material development and selection. Furthermore, fast and comprehensible data processing is required. In the course of digitalization, ontology-based data access (OBDA) turns out as an effective method and is gaining significance in materials science [4, 5, 6]. In particular, this approach allows access to heterogeneous databases using a common vocabulary stored in the ontology without requiring in-depth knowledge of the queried data. In our contribution, we present an extension of this OBDA approach, the ontology-based data and **model** access (OBD**M**A). The system is being developed for four exemplary smart material classes: thermal shape memory alloys (SMA) [7], magnetic shape memory alloys (MSMA) [8], piezo-electric ceramics (PC) [9], and dielectric elastomers (DE) [10]. Further, the system can be applied to other materials as well.

One distinctive feature of OBDA is, that the data remains stored in conventional databases and is accessed by using the predefined vocabulary stored in the ontology. The extension to a model access enables data conversion considering multiple scales and generating new data. With this, the developed OBDMA system increases the interchangeability and enables variable datasets, which is essential, especially for dynamic research fields like smart materials. In this contribution, the working principle of the developed OBDMA system is first presented in general and then in more detail for a specific use case of the maximum blocking stress. This common use case for all four smart material subclasses employs completely different material specific models under the hood and yet it can be queried through the same common ontological vocabulary. It is followed by an overview of the wide range of use cases showcasing further distinct capabilities of our OBDMA system.

2 OBDMA-System

An ontology is a structure to store knowledge in an organized way. It consists of a terminological box (*TBox*) and an assertion box (*ABox*). The simplified principle of

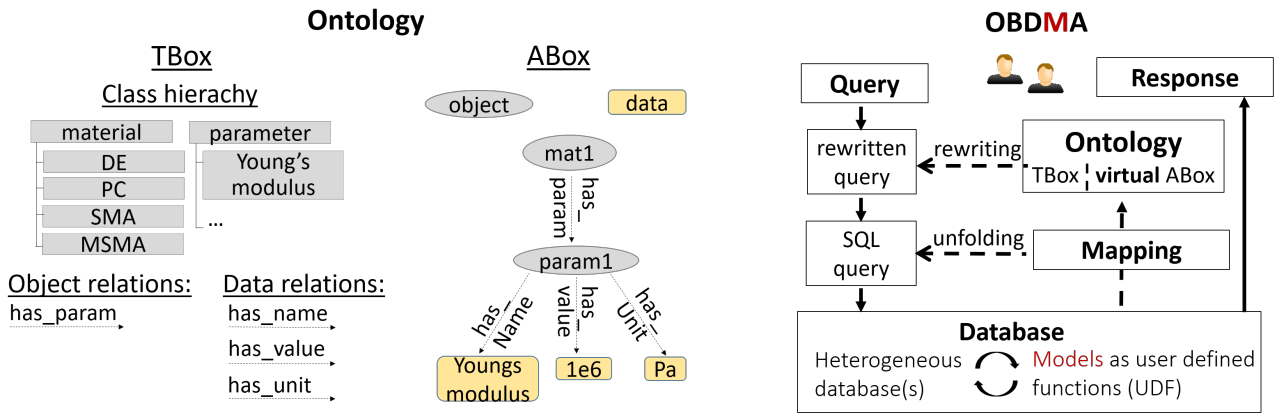

Figure 1 Working principle of an ontology (left) and the OBDMA system (right).

an ontology is demonstrated in **Figure 1**. The main aim of the *TBox* is to store vocabulary in form of classes and relations. To generate the *ABox*, objects from the classes are combined with the relations. The link of two objects with one relation is called triple, several triples are called RDF-graph. Is *mat1* an object of the class *material* and *param1* an object of the class *parameter*, [*mat1 - hasParam - param1*] is a triple and stored as a fact in the *ABox*. In addition to such object relations, data relations enable to link an object with data knowledge. In the example of **Figure 1**, "param1" is linked to name, value and unit. To access this knowledge, the *TBox*-vocabulary is used to access the knowledge stored in the *ABox*.

To use ontologies for existing data stored in conventional database, two main options exist. First, there are several tools to convert the database to an ontology structure and store the data in the *ABox* as an RDF-graph. Second, one can use the ontology-based data access (OBDA) approach, which we use in our contribution. The working principle of OBDA is demonstrated in **Figure 1** on the right. Here, the data is still stored in the conventional database. For the query, the vocabulary stored in the *TBox* is used. Knowledge stored in the *TBox*, for example DE is a material, is included in the query by rewriting the query. With the help of so called mappings, the *TBox* vocabulary is translated to the database vocabulary. Consequently, the most simple mappings store, where to find the queried data information in the database. This step is called unfolding and generates a SQL-query. Based on this, a virtual *ABox* is generated with the data information of the database and the knowledge stored in the *TBox*, resulting in a response table. One of the main advantage of OBDA is the common access to heterogeneous databases using the vocabulary of the *TBox*. In our example, we access data of four different subclasses of smart materials. To combine this data access with calculations, we extend this approach to an ontology-based data and model access (OBDMA). In our approach, the models are stored on database level as user defined functions (UDF). The access to these functions from the ontology level is described in the mappings. Thus, the developed OBDMA system combines data access with calculations in one system.

The languages used on all four system levels are standards of the world wide web consortium (W3C) [11]: SPARQL for the query, OWL2QL for the ontology, R2ML for the mappings and SQL as the database language. As SPARQL is not widely used in the engineering sector, we have also developed a user interface for an easy access to our system. This allows the user to select the parameters or characteristics to be queried via a drop-down menu and the corresponding SPARQL query is automatically generated in the background. The developed system is published on GitHub under the following URL: `https://github.com/SmaDi-OBDMA/SmaDi-OBDMA-system`.

3 Use Cases

In this section, the principles of the OBDMA system are explained using the example of the maximum blocking stress, followed by a wider range of applications with their corresponding queries.

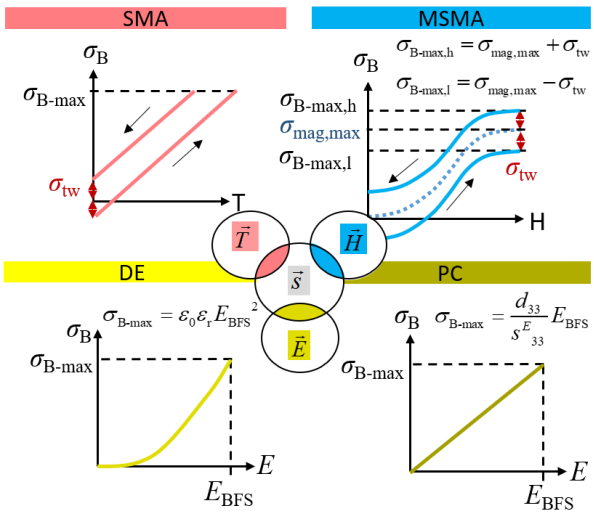

Figure 2 Definition of the maximum blocking stress for the four considered material subclasses.

The maximum blocking stress is defined for all four material subclasses and arises by applying the appropriate

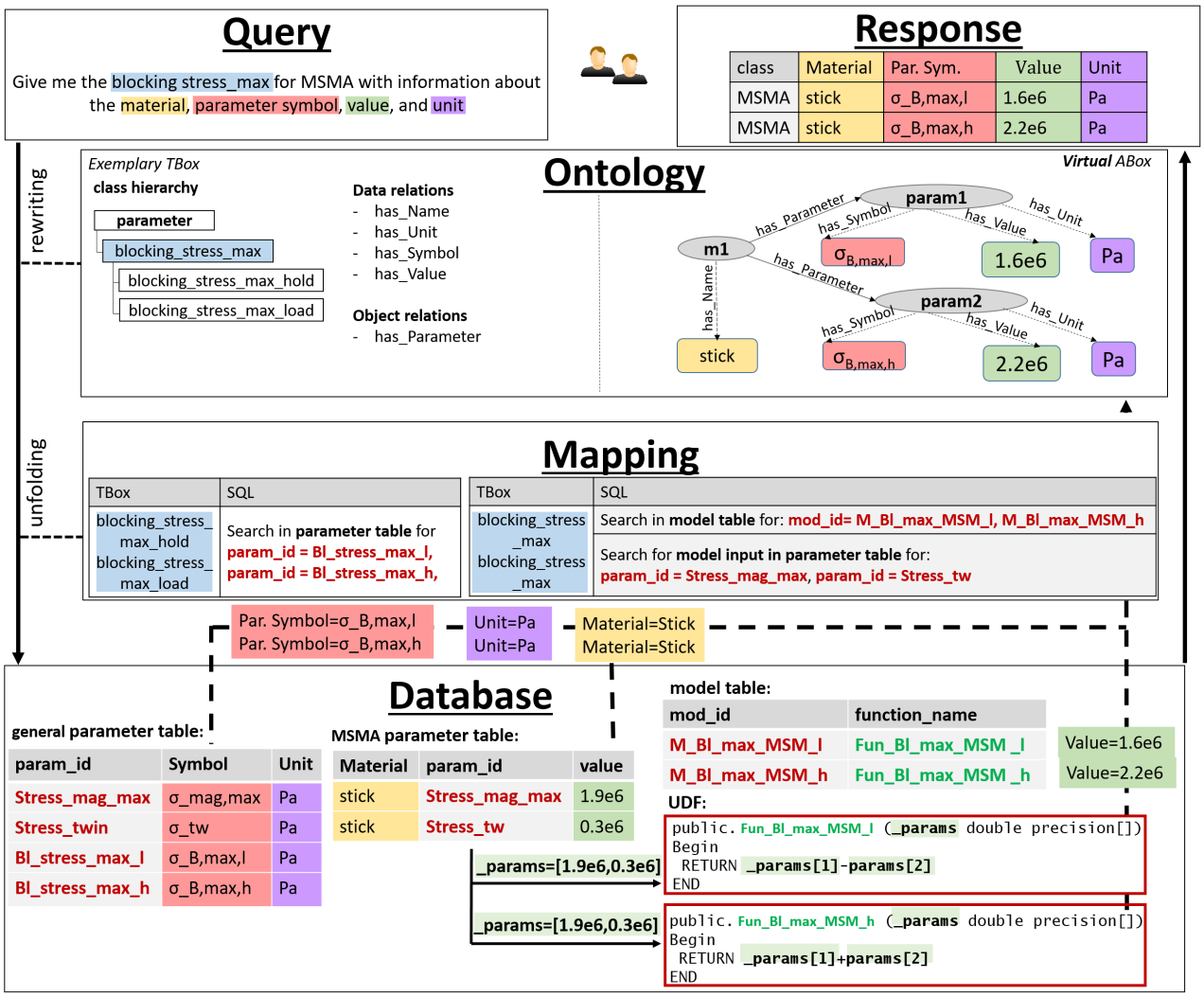

Figure 3 Working principle of OBDMA-system shown the use cases of maximum blocking stress of MSMA.

physical field while deformation is prevented simultaneously. It is one of the characteristic values on transducer level, that helps to decide which material is appropriate for a specific application. An overview of the definitions of the maximum blocking stress for the four subclasses used in our system is given in **Figure 2**. For the SMA, the value is stored directly in the database, for the other three material subclasses simple equations are defined to calculated the maximum blocking stress. One unique property of the MSMA is that the hysteresis behavior results in two definitions for the maximum blocking stress, one for the holding and one for the loading direction. As this particular knowledge can be stored in the *TBox*, the working principle of OBDMA is demonstrated for the case of the MSMA in **Figure 3**. In the ontology box on the left, an extension of the *TBox* including the class hierarchy and relations is shown. By defining the *maximum_blocking_stress_load* and *maximum_blocking_stress_hold* as subclasses of *maximum_blocking_stress*, both classes are automatically requested by querying the parameter *maximum_blocking_stress*. Thus, the user does not need to know, that two parameters are defined for the MSMA and still receives both values. With the vocabulary of the *TBox* the query is formulated according to the query box of **Figure 3** on the top left. This natural query must be formulated in SPARQL, which can be done by the user or in the background if a user interface is available.

The next step is the mapping, storing the corresponding parameter IDs and function names in the database for the required data and calculation functions. The information about the queried calculated values, the parameter symbol, the unit and the material name is returned to the ontology and the *ABox* is generated virtually to create the response table.

The wide range of uses cases is illustrated using several exemplary queries, grouped by type. The basic use case of the classical OBDA is the access to parameters, characteristics and matrices based on the database entries. The extension to model access enables calculations generating new data, for example for parameter identification, dataset transformation and transducer calculation.

- Access parameter, characteristics and matrix element based on the database entries
  - Give me the (martensite content−temperature) curve for SMA materials.

  - Give me the interpolation points of the stored hysteresis model [12].

- Model based parameter identification
  - Give me the Yeoh parameters for the stress-strain curve corresponding to a specific DE. To solve this query, the system internally uses an optimization algorithm to minimize the error in a specified identification range.

- Model based dataset transformation
  - Give me the magnetic curve of an MSM material in the form $B - \mu_r$ based on the stored $H - M$ curve. This is done using

$$B = \mu_0 \mu_r H = \mu_0 (H + M) = \mu_0 H + J. \quad (1)$$

  - Give me all entries of the piezoelectric voltage constant g, based on the piezoelectric charge constant d and the permittivity at constant mechanical stress ε^T. This internally uses

$$g = {\varepsilon^T}^{-1} d. \quad (2)$$

- Model based transducer calculation
  - Give me the maximum blocking force for a cross-sectional area of $A = 0.1\,\mathrm{mm}^2$. The result is calculated following

$$F_B = \sigma_B A, \quad (3)$$

    with the stresses σ_B calculated recursively according to **Figure 2**.
  - Give me the maximum stroke for a transducer length of $l = 10$ mm. This uses

$$x_{\max} = \varepsilon_{\max} l, \quad (4)$$

    with the free strokes $\varepsilon_{\max}$ calculated individually for the different material sub classes.

Further details corresponding to the OBDMA system and the use cases including a journal publication under review will be continuously added to the project website [13].

4 Conclusion

The proposed OBDMA approach outlines a system designed to offer easy access to heterogeneous data and models, while providing the flexibility for adaptable modifications and expansions within the database structure. This is achieved through the utilization of a general vocabulary defined on ontology level, ensuring independence from the underlying database framework. Our extension of the well-known OBDA approach to the OBDMA system enables the combination of data access with data manipulation, facilitating parameter conversion and parameter identification in particular. This enhancement allows for efficient material development and selection tailored to specific applications. Furthermore, this approach holds significant relevance across diverse engineering challenges, particularly in scenarios necessitating streamlined data access coupled with transformation capabilities.

5 Acknowledgements

This contribution is accomplished within the project SmaDi funded by the German Federal Ministry of Education and Research under grant number 13XP5124A-E.

6 Literature

[1] Mukesh V Gandhi and BD Thompson. *Smart materials and structures*. Springer Science & Business Media, 1992.

[2] Donald J Leo. *Engineering analysis of smart material systems*. John Wiley & Sons, 2007.

[3] W-G Drossel, Holger Kunze, André Bucht, Linda Weisheit, and Kenny Pagel. Smart3–smart materials for smart applications. *Procedia Cirp*, 36:211–216, 2015.

[4] A. Poggi, D. Lembo, D. Calvanese, G. De Giacomo, M. Lenzerini, and R. Rosati. Linking data to ontologies. In *Journal on data semantics X*, pages 133–173. Springer, 2008.

[5] D. Calvanese, G. De Giacomo, D. Lembo, M. Lenzerini, A. Poggi, M. Rodriguez-Muro, and R. Rosati. *Ontologies and databases: The DL-Lite approach*. Springer, 2009.

[6] Thomas Schneider and Mantas Šimkus. Ontologies and data management: a brief survey. *KI-Künstliche Intelligenz*, 34(3):329–353, 2020.

[7] D. C. Lagoudas. *Shape Memory Alloys - Modeling and Engineering Applications*. Springer New York, NY, 2008. doi: 10.1007/978-0-387-47685-8.

[8] U. Gaitzsch, R. Chulist, L. Weisheit, A. Böhm, W. Skrotzki, C.-G. Oertel, H.-G. Brokmeier, T. Lippmann, I. Navarro, M. Pötschke, J. Romberg, C. Hürrich, S. Roth, and L. Schultz. Processing routes toward textured polycrystals in ferromagnetic shape memory alloys. *AEM*, 14(8):636–652, 2012. URL `https://doi.org/10.1002/adem.201200084`.

[9] T. Ikeda. *Fundamentals of Piezoelectricity*. Oxford science publications. Oxford University Press, 1990. ISBN 9780198563396. URL `https://books.google.de/books?id=FW14QgAACAAJ`.

[10] Federico Carpi, Danilo De Rossi, Roy Kornbluh, Ronald Edward Pelrine, and Peter Sommer-Larsen. *Dielectric elastomers as electromechanical transducers: Fundamentals, materials, devices, models and applications of an emerging electroactive polymer technology*. Elsevier, 2011.

[11] `https://www.w3.org/`.

[12] R. Courant and J. Maas. Bridging the scales between twin level and component level models of magnetic shape memory alloys. In *ASME 2022 Conference on Smart Materials, Adaptive Structures and Intelligent Systems*. American Society of Mechanical Engineers, sep 2022. URL `https://doi.org/10.1115/smasis2022-91681`.

[13] `https://www.materialdigital.de/project/10`.

Design and simulation of negative-stiffness thermoplastic biasing mechanism for dielectric elastomer actuators

Saverio Addario*[1], Alberto Priuli*[1], Jonas Hubertus[3], Günter Schultes[3], Stefan Seelecke [1,2], Gianluca Rizzello[1]
[1.] Saarland University, Department of Systems Engineering, Saarbrücken, Germany.
[2.] Smart Material Systems, Center for Mechatronics and Automation Technology - ZeMA gGmbH, Saarbrücken, Germany.
[3.] Department of Sensors and Thin Films, University of Applied Sciences of Saarland, Saarbrücken, Germany.

Abstract

Dielectric elastomer actuators (DEAs) are soft transducers consisting of thin and highly stretchable polymeric membranes coated with compliant electrodes. DEAs can work in an out-of-plane configuration by properly coupling the membrane with a mechanical biasing system whose force-displacement behavior is designed to match the one of the dielectric membranes. In this paper we propose an approach for fabrication, modelling, and optimization of a DEA biasing system consisting of a thermoformed PET buckling beam. The buckling response of the PET beam presents a less hysteretic behavior than silicone-based counterparts, while still being based on polymeric material. To better design the biasing system with the goal of integration within a DEA, a finite element model and a geometric optimization routine are developed.

1 Introduction

Dielectric elastomer actuators (DEAs) consist of thin and highly stretchable dielectric membranes coated with compliant electrodes, which react to an applied high voltage with a controllable mechanical deformation [1]. DEAs can be used to convert an applied electric voltage into a controllable deformation. Their features include lightweight, flexibility, and high compliance, thus making them suitable for a wide spectrum of applications, including smart wearables [2] and soft robots [3].

DEAs can feature both in-plane and out-of-plane actuation, by properly coupling the membrane with a mechanical biasing system, whose force-displacement behavior is designed to match the one of the transducers. Common solutions are based on coupling the DE membranes with elements as linear springs, while other approaches involve the use of negative-stiffness nonlinear mechanisms, such as pre-compressed metal beams, to increase the actuation stroke [4]. These beams are subjected to high inherent stresses, and thus are not well suited for integration into soft structures. Alternative negative-stiffness mechanisms such as silicone-based buckling domes are in principle fitting for this task, but also show several drawbacks such as their limited repeatability, elaborated manufacturing process, and large hysteresis [5].

To overcome these issues, this work investigates novel DEA biasing mechanisms based on thermoplastic polymers. The proposed biasing components exhibit the required negative stiffness, and are well suited for miniaturized, soft, and fully polymeric DEA systems. In comparison to silicone biasing mechanisms, they exhibit less hysteretic losses while showing higher compliance and flexibility than metal-based biasing elements. Inspired by the latter, they can also be designed in a simple beam shape with a stress-free configuration, due to the adopted thermoforming process. Their mechanical characteristics thus mainly depend on the thermoforming process parameters, as well as on their shape and dimensioning [6]. This paper first explores the thermoforming manufacturing process of the biasing element through a setup solution, in which most of the components are either commercially available or 3D printed. A finite element model of the nonlinear biasing system is also developed, to identify the material parameters after the thermoforming procedure with the support of the experimental data. Envisioning the use of the biasing system in a complete DEA system, the identified model, as well as existing 1D approximations found in the literature, will be used as a numerical tool to develop a design optimization routine. The optimization metric is defined as the as the total stroke of the DEA. The work is organized as follows. In section 2 the geometric design and the fabrication process are explained. Section 3 presents the results of the experimental test and a comparison with a silicone-based solution in terms of hysteretic behavior. In section 4 a finite element model of the buckling beam is developed to identify the material parameters is presented as well as an example of optimization of the biasing system geometry over the total stroke of a DEA.

2 Design and fabrication

In this study, the limitations of polymeric NBS domes prompted the exploration of alternative materials for the production of flexible biasing systems. Thermoplastic A-PET was chosen for this purpose due to its favorable characteristics, including good stiffness, cost-effectiveness and established recycling processes [7]. This semi-crystalline polymer has a glass transition temperature (T_G) of 75°C, a cold crystallization temperature (T_C) of 135°C and a melting temperature (T_M) of 250°C. The study employs Euler-Bernoulli out-of-plane beam theory to assess the suitability as a negative-stiffness biasing element. When the strip is pre-compressed and buckled, it

behaves as a bistable system capable of transitioning between two stable states. Within this transitional region, it exhibits the negative stiffness characteristics necessary for the NBS. According to Euler-Bernoulli theory, when subjected to axial compression surpassing a critical value, the beam buckles into its first buckling mode. This behavior is described by the equation [8]

$$w(x) = \frac{h}{2}\left[1 - \cos\left(\frac{2\pi x}{l}\right)\right], \tag{1}$$

where x is the beam axial coordinate, $w(x)$ represents the average deviation of the beam from a straight line connecting its endpoints, h denotes the initial height of the beam's vertex, and l indicates the current length of the beam, as shown in **Figure 1**.

The manufacturing process of the A-PET strip for the thermoplastic biasing system involves several steps. Initially, the thermoplastic strip is cut and clamped using a fused filament fabrication (FFF) process [9]. Then, the strip undergoes thermoforming inside an oven, where it is shaped around a core plug (positive mold) to fill the space between the plug and the negative mold. The thermoforming temperature is set at 140°C to soften the material within the cold crystallization range, enabling easier deformation without reaching the melting temperature. The thermal process involves heating the clamped strip in the oven for 20 minutes, followed by a rapid forming process lasting approximately 30 seconds .

The forming tool used includes 4 compression springs with a stiffness of 7.97N/m, compressed by applying a predefined displacement in order to know the forming pressure applied. After forming, the specimen is cooled for 20 minutes under load in a temperature-controlled chamber to maintain the new geometry. The specimen, shown in **Figure 1**, is subsequently removed from the forming tool and subjected to testing and measurements on a test bench, in **Figure 2**. These tests are performed under quasi-static conditions, to disregard dynamic viscoelastic effects. During each test, a linear motor deforms the A-PET strip according to a predefined displacement profile, while a load cell measures the reaction force.

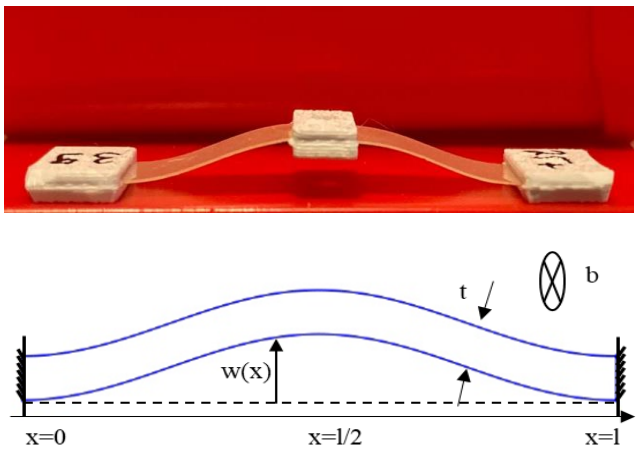

Figure 1 Thermoformed A-PET strip (upper part), sketch of the buckling beam with dimensions (lower part).

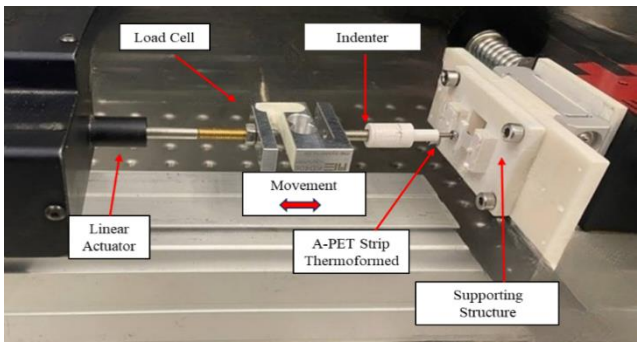

Figure 2 Experimental setup.

3 Experimental results

In this section, an evaluation of the mechanical behavior of silicone dome and A-PET strip subjected to constant deformation (relaxation test) over 72 hours is carried out. This test aims to assess the stability of the biasing system and stroke of the resulting DEA (Dielectric Elastomer Actuator) over time. The resulting curves are shown in the figure (normalized graph), with the red and blue solid lines indicating the tests conducted 72 hours apart, and the dashed lines representing the average cycle between the round trips. The metric used to describe the relative amount of hysteretic losses of both materials in a normalized fashion is defined through the Material hysteretic parameter (*MHP*), defined as the ratio between the hysteresis cycle area (dissipated free energy over a cycle) and the area subtended by the average curve representing reversible contribution of stored elastic free energy during loading path, i.e.,

$$MHP = 100 \times \frac{\text{Hysteresis Cycle Area}}{\text{Stored System Energy}}. \tag{2}$$

The thermoformed strips proved to be more energy efficient, with a value of 6.25% compared to 9.30% for the silicone domes.

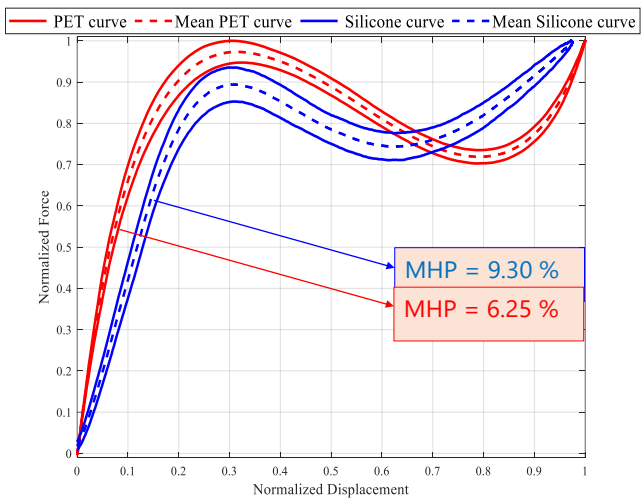

Figure 3 Comparison between normalized force-displacement curves measured before and after a 72-hours relaxation test.

4 Modelling and simulation

A finite element model of the system is implemented in COMSOL Multiphysics, by defining a 2D geometry whose characteristic dimensions mirror the one chosen in the design phase of the work. The model is defined under quasistatic conditions, , i.e., no inertial and viscoelastic effects are considered, due to the slow speed at which the experimental tests have been conducted. Since the system undergoes large deformations and its envisioned working temperature of the system is expected to be much lower than the glass transition temperature, the constitutive equations of the material are defined starting from an isotropic linear elastic model where the second-order components of the finite strain tensor are considered and not neglected. The boundary conditions on the system are composed of two fixed boundary constraints corresponding to the location of the printed clamping on the beam, and an imposed displacement along a direction orthogonal to the beam applied on the upper flat surface. The simulation is run by controlling the displacement of the end-effector section of the beam to capture the principal, ideal buckling mode of the beam and describing it with a well-conditioned system of equation, which would not be possible by controlling the applied force up after reaching the buckling load. The displacement is quasi statically, gradually applied in steps up to a maximum value corresponding to two times the pre-deflection of the beam, namely

$$u_{y,max} = 2h. \tag{3}$$

According to finite element simulations making use of common values for the material parameters that can be found in the literature [10], i.e., $E = 2$GPa and $\nu = 0.35$, the actuated thermoformed system with the described geometry presents equivalent stresses that are higher than the yield stress of the PET material, causing partial plastic deformation during the first actuation cycles. However, since the regions in which such stresses are reached are small and localized close to the corners of the fixed boundaries, the influence of the plastic deformation on the force-displacement characteristic after the first cycle is negligible. This has been observed with the aid of preliminary finite element simulations exploiting a linear, isotropic hardening model for the linear elastic material. Once the model is set up, the material parameters for the model are calibrated on a set of experimentally collected measurements, by using them as free variables in an optimization routine where the objective function to be minimized is defined as the absolute error between the experimental and simulated force-displacement curves. The calibrated material parameters after the procedure assume the values of $E^* = 2.23$ GPa and $\nu^* = 0.32$.

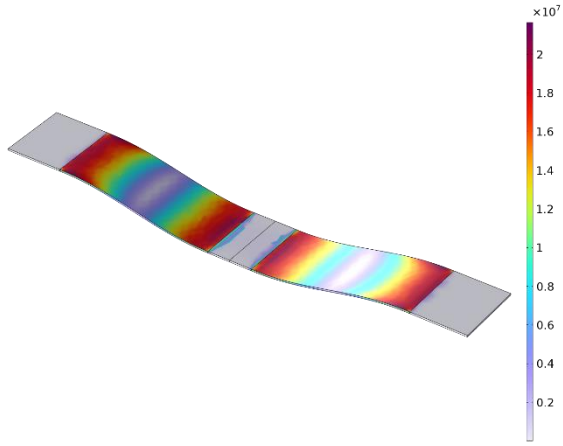

Figure 4 Finite element model of the biasing system in a deformed configuration. Scale: Von Mises stress [N/m^2].

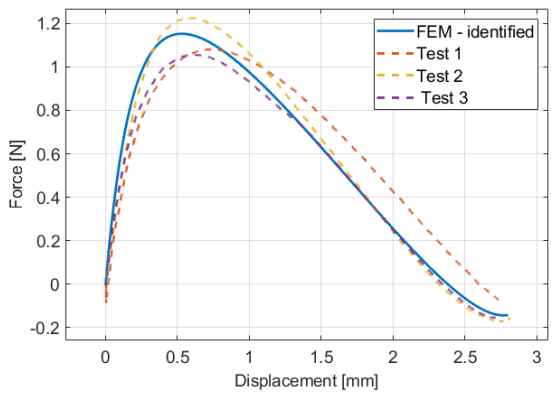

Figure 5 Experimental and simulated force-displacement response after the identification of the material parameters.

In parallel to the finite element modelling, an optimization routine is set up to find a set of geometric parameters of the biasing system that ensures a local optimum with respect to the overall stroke of a DEA. Since the stroke depends on the intersection of the biasing force-displacement characteristics with those of a DE under minimum and maximum voltage actuation, a simple 1D Neo-Hookean model of a DE membrane with arbitrarily fixed geometric and material parameters is considered. The biasing system is initially chosen as random. The biasing system force-displacement characteristic is also modeled as a 1D system which only undergoes the first buckling mode as in [8]. The optimization objective to be maximized is set as the absolute difference between the displacement values of the first two intersection points, while constraints are considered to keep the optimization variables in reasonable ranges (e.g. positive lengths). Due to the highly nonconvex nature of the optimization problem, the constraints are lifted in the cost function by means of a penalty formulation. The optimization variables are chosen as follows:

Variable	Description
t	Thickness [mm]
Q	Height to thickness ratio [-]
l	Length [mm]
x_0	Biasing system spacing [mm]
b	Width [mm]

The embedded MATLAB function *fminsearch* used to solve the optimization problem exploits a Nelder-Mead simplex method. **Figure 6** shows the force-displacement response of a biasing system before and after imposing the optimal geometric parameters from the solution of the optimization problem. The resulting DEA design appears as feasible.

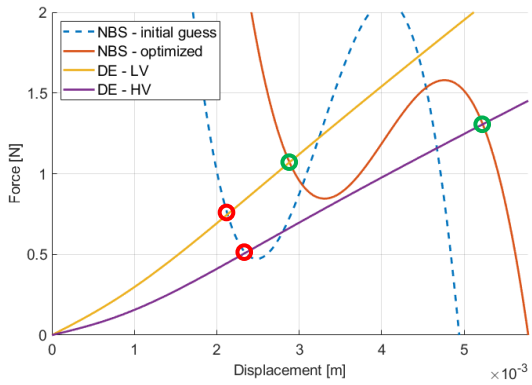

Figure 6 Initial and final force-displacement characteristics resulting from the optimization routine. Initial (red) and final (green) working points of the DEA.

5 Conclusions

In this work, a nonlinear biasing system fabrication, modelling and optimization solution for a DEA is presented. The system is composed of a thermoformed PET buckling beam, motivated by the highly hysteretic behavior of silicone biasing systems that were previously considered. After investigating the change in the force-displacement response of the two types of system by means of a 72-hours relaxation test, it can be noted that thermoformed PET beam samples present a lower relative stored hysteretic energy. This ensures a lower variation of force values during loading-unloading working cycles and, as such, the working points of the DEA vary less during actuation. The 2D finite element model of the buckling beam is used to identify the material parameters. An optimization routine is set up, successfully returning an optimal solution, albeit local, for the geometric parameters of a buckling beam for a DEA.
Future studies will envision further experiments with different system geometries, to validate the material parameters identified with the finite element model. The optimization routine will also be experimentally checked with the development of a DEA prototype, to be later serially embedded in a small-scale cooperative DEA matrix.

6 Funding

The authors gratefully acknowledge the support of the Deutsche Forschungsgemeinschaft (DFG, German Research Foundation) through Priority Program SPP 2206 ‘Cooperative Multistage Multistable Microactuator Systems’ (Projects: RI3030/2-2, SCHU1609/7-2, SE704/9-2).

7 Literature

[1] Chiba, S. (2019). Dielectric elastomers. *Soft Actuators: Materials, Modeling, Applications, and Future Perspectives*, 259-273.

[2] Huang, B., Li, M., Mei, T., McCoul, D., Qin, S., Zhao, Z., and Zhao, J., *“Wearable stretch sensors for motion measurement of the wrist joint based on dielectric elastomers,”* Sensors 17(12), 2708 (2017).

[3] Soleti, Giovanni, et al. *"Energy based control of a bi-stable and underactuated soft robotic system based on dielectric elastomer actuators."* IFAC-PapersOnLine 56.2 (2023): 7796-7801.

[4] Hodgins, M., York, A., and Seelecke, S., *“Experimental comparison of bias elements for out-of-plane deap actuator system,*” Smart Materials and Structures 22(9), 094016 (2013)

[5] Neu, J., Hubertus, J., Croce, S., Schultes, G., Seelecke, S., & Rizzello, G. (2021*). “Fully Polymeric Domes as High-Stroke Biasing System for Soft Dielectric Elastomer Actuators*”. Frontiers in Robotics and AI, 8, 695918.

[6] Throne, Jim. "*Thermoforming*." Applied plastics engineering handbook. William Andrew Publishing, 2024. 449-480.

[7] Zhang, J. (2004), “*Study of polytrimethylene terephthalate as an engineering thermoplastics material.”* J. Appl. Polym. Sci., 91: 1657-1666.

[8] Qiu, J., Lang, J., and Slocum, A., “A curved-beam bistable mechanism,” Journal of Microelectromechanical Systems 13(2), 137–146 (2004).

[9] Singh, Sunpreet, et al. *"Current status and future directions of fused filament fabrication."* Journal of Manufacturing Processes 55 (2020): 288-306.

[10] Bin, Y., Oishi, K., Yoshida, K., & Matsuo, M. (2004). Mechanical properties of poly (ethylene terephthalate) estimated in terms of orientation distribution of crystallites and amorphous chain segments under simultaneous biaxially stretching. *Polymer journal*, *36*(11), 888-898.

Miniaturization of HASEL Actuators for Next-Generation Applications

Ashwani Sharan Tripathi[1], Chen Jiao[1], Andreas Lars Peter Hubracht[2], Georgi Paschew[1], Uwe Marschner[1], E.-F. Markus Henke[1,3], Jürgen Maas[2], and Andreas Richter[1]

[1]Institute of Semiconductors and Microsystems, Technische Universität Dresden, 01062 Dresden, Germany

[2]Mechatronic Systems Lab, Technische Universität Berlin, Hardenbergstraße 36, 10623 Berlin, Germany

[3]Biomimetics Lab, Auckland Bioengineering Institute, The University of Auckland, 70 Symonds St, Auckland 1010, New Zealand

Abstract

Hydraulically Amplified Self-Healing Electrostatic (HASEL) actuators have emerged as a promising technology due to their exceptional performance characteristics, including high force output, large displacement, and low power consumption. However, the bulky size of conventional HASEL actuators has hindered their integration into miniaturized devices, limiting their applicability in various domains. This paper explores the miniaturization of HASEL actuators through a synergistic combination of microfabrication techniques and flexible materials and introduces a novel rapid production method. Microfabrication techniques, offer the precision and control necessary to create miniaturized HASEL actuators with intricate features and enhanced performance.

1 Introduction

Collaborative multi-actuator systems are poised to become indispensable components in future applications, spanning domains like robotics, medical appliances, and advanced user interfaces [1]. Their versatility spans across scales, from the infinitesimal realm of the nanoscale, where fundamental phenomena originate, to the more tangible micro- and macroscales, where technical demands closely resemble human capabilities. As these systems undergo expansion, they must demonstrate the ability to autonomously navigate through intricate sequences of movements and tasks, adeptly perceive their surroundings, and dynamically adapt to changing environmental conditions. Achieving the vision of entirely soft bio-inspired robots necessitates the development of fully soft electronic circuits. Goal of the joint project CALMAR (DFG, 512586089) is the development of a collaborative multi-actuator system, combining the advantages of Dielectric Elastomer Transducers (DETs), Dielectric Elastomer Switches (DESs) and HASELs.

This contribution introduces the first results of our HASEL developments. HASEL actuators are soft actuators that generate motion using electrostatic forces [2]-[6]. They comprise a polymer shell, a dielectric liquid layer, and embedded electrodes. Voltage application polarizes the liquid, causing electrode movement and polymer deformation, resulting in motion. HASEL actuators offer large force output, self-healing capabilities, and have diverse applications. Figure 1 illustrates the operational concept of miniaturized symmetric HASEL actuators [7]. Both actuator chambers are partially filled with the dielectric liquid in the inactive state, with none of the cavities in an active state.

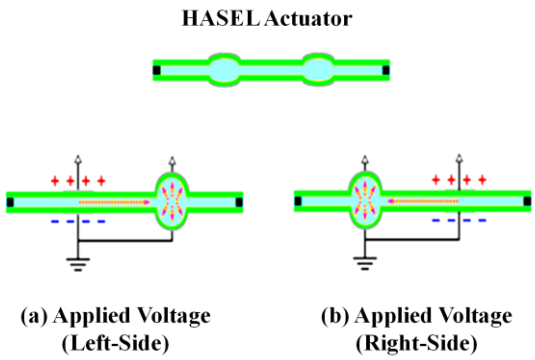

Figure 1 Working principle of miniaturized HASEL actuator.

Upon applying voltage to the electrodes on the left actuator, a Maxwell pressure occurs between both electrodes the electrodes that causes attracting forces between the upper and the lower electrode. This force causes the cavity between the electrodes attempting to close, pushing liquid through the channel to the right side, resulting in expansion on the right cavity and vice versa.

The electrostatic force, caused by the Maxwell pressure (F) for the HASEL actuator can be expressed as follows [4]:

$$F = \frac{1}{2}\frac{\varepsilon_0 \varepsilon_{\text{fluid}} A V^2}{\left(\frac{\varepsilon_{\text{fluid}}}{\varepsilon_{\text{polymer}}} t_{\text{polymer}} + t_{\text{fluid}}\right)^2} \qquad (1)$$

Whereas $\varepsilon_{\text{fluid}}$ and $\varepsilon_{\text{polymer}}$ represent the dielectric permittivity of the dielectric fluid and the polymer (shell), respectively and ε_0 the permittivity of vacuum. The variables t_{fluid} and t_{polymer} denote their respective thicknesses. A represents the active area of the electrodes, and V is the operating voltage. In the scenario where the thickness of the polymer shell, is significantly smaller than the thickness of the fluid medium, the term t_{polymer} can be discarded. This simplifies equation (1) to equation (2):

$$F = \frac{1}{2}\frac{\varepsilon_0 \varepsilon_{\text{fluid}} A V^2}{(t_{\text{fluid}})^2} \qquad (2)$$

2 Materials and Methods

The production process that has been used in this contribution is based on the methods described in [8]. However, here we describe an improved production process that reduces the number of required steps and the complexity of the production process. A schematic of fabricated HASEL actuator is shown in Figure 2 (a) as a top and as a sectional view. Figure 2 (b) illustrates the novel fabrication process that has been developed step by step.

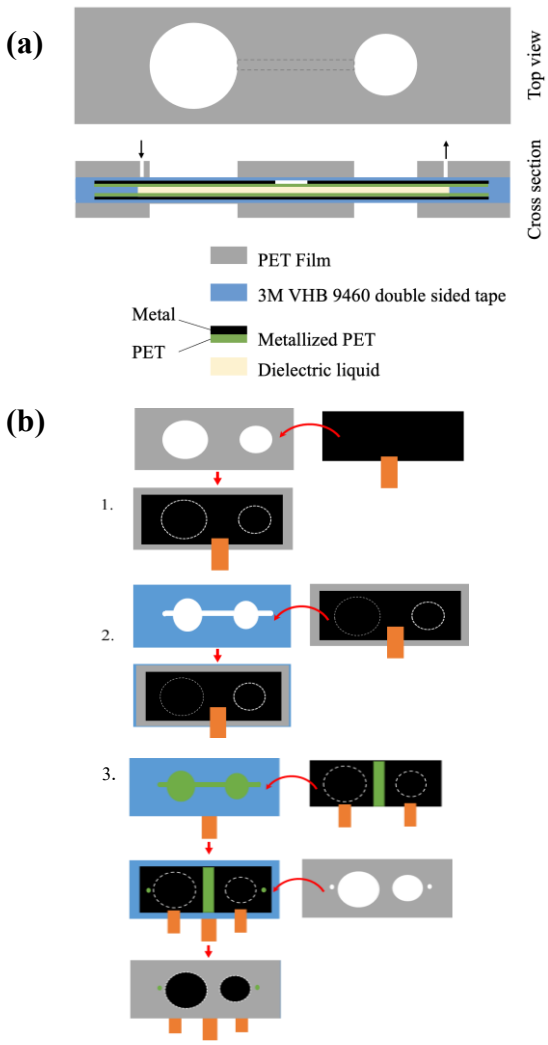

Figure 2 Fabrication of HASEL actuator: (a) schematic of fabricated HASEL actuator, (b) step-by-step illustration.

In a first step, the bottom substrate was created using a 100 µm thick PET film, cut precisely with a Trotec Speedy100 laser. Afterwards, a 14 µm metalized PET film was glued atop the PET film, using 50 µm thick VHB 4905 tap by 3M, ensuring the metallized layer faced outward, forming the base of the device. In step 2, cavities for the dielectric liquid were formed by laser cutting a 50 µm thick VHB 4905 tape, which was then affixed to the bottom substrate prepared in the previous step. This tape served as a spacer, facilitating the creation of a micro-fluidic channel with circular cavities. The channel had a width of 2 mm and a length of 20 mm, with circular cavities of 12 mm and 8 mm diameters positioned at both ends. Notably, the adhesive surface of the VHB tape simplified electrode attachment on either side of the micro-fluidic channel. Finally, in the last step, another metallized PET layer was etched to form two individual electrodes. This layer was then bonded atop the VHB tape from the top, subsequently covered with an additional 100µm thick PET film. This 100-micron thick PET film served as an outer frame, supporting the HASEL structure. Two holes were additionally created on the top PET film using a laser cutter, functioning as entry points for injecting the dielectric liquid into the micro-fluidic channel. To ensure proper electrical conductivity throughout the actuator, connections to the electrodes were created using copper tape, prior to adding the top PET film. Vegetable oil was chosen as the dielectric liquid due to its compatibility and availability [9],[10]. The injection of the dielectric liquid into the channel ensured proper functioning of the actuator.

2.1 Setup for Actuation Measurement

Actuation measurement of HASEL was performed using a setup as shown in Figure 3. A square wave voltage ranging from 0 to 3000 V at a frequency of 0.5 to 2 Hz was applied to the HASEL samples. Voltage readings were continuously recorded using LabVIEW interfaced with an NI-9205 module (DAQ, National Instruments GmbH) to ensure accurate data acquisition.

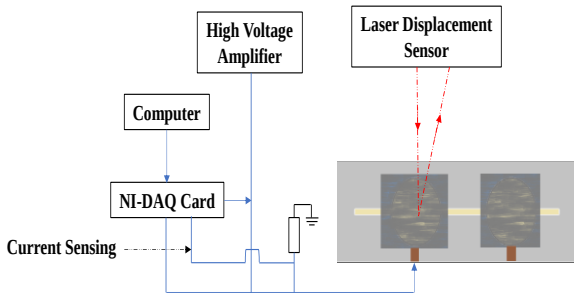

Figure 3 Schematic of actuation measurement setup.

To measure the actuation displacement response, a displacement laser (ILD 1420-10, Micro-Epsilon) was used. This laser system provided actuation measurements necessary for capturing the subtle movements of the HASEL. The laser was positioned above the HASEL samples to record displacement changes from the top, offering a better

understanding of the actuation behavior. Throughout the experiment, voltage and current are measured by the high-voltage measurement box. The integration of data acquisition and the displacement laser system facilitated precise measurements, enabling a thorough analysis of the HASEL actuation performance.

3 Results and Discussion

Actuation testing was conducted over five repetitive cycles spanning from 0 to 3000 volts step voltage. The visual depiction of the actuation response for both the left and right-side circular electrode cavities is illustrated in Figure 4 (b) and (c).

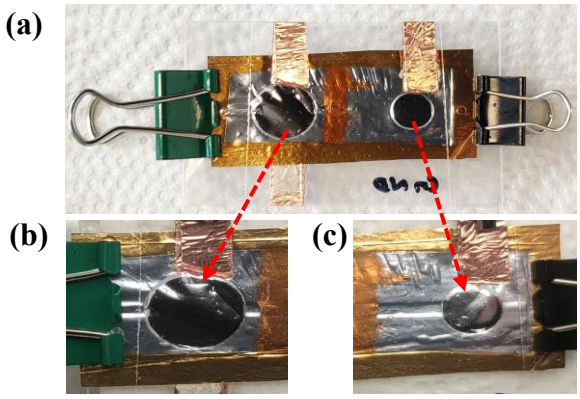

Figure 4 Visual representation of actuation response: (a) resting state, (b) actuated left electrode, and (c) actuated right electrode.

Traditionally, HASEL actuators operate within a higher voltage range of 4-10 kV (Kilovolts). However, in this study, the voltage limit for actuation was kept lower. This limitation was imposed to align with potential future applications involving the integration of HASEL with Dielectric Elastomer Switches (DES), which typically function within lower voltage ranges 2-5 kV.

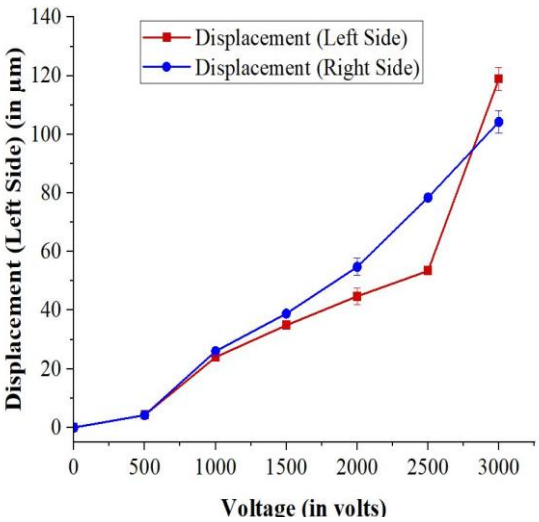

Figure 5 Actuation response of HASEL (voltage vs. displacement).

The measured displacement for both the left and right-side cavities is depicted in Figure 5. From the actuation response of left side cavity, it can be observed that within the lower voltage range (0 to 2500 volts), the actuation response demonstrates a relatively linear behavior. However, at 3000 volts, there is a notable exponential increase in actuation response. A maximum average displacement of 119 µm and 104 µm for both the left and right-side cavities respectively was achieved at 3000 volts. The right-side cavity exhibited a comparatively lower displacement than the left cavity due to its smaller circular diameter, which limits fluid storage. This suggests that by minimizing the overall thickness of the HASEL actuator, the voltage requirement for actuation can be optimized. These findings highlight the potential for tailoring the design of HASEL actuators to achieve desired actuation performance while minimizing energy consumption and optimizing compatibility with other electromechanical systems.

4 Conclusion

In this paper, we introduced a novel, rapid production technology for miniaturized HASEL actuators, and have successfully tested a first demonstrator. The obtained results significantly validate a reduction in the voltage requirement for actuation, highlighting the efficacy of miniaturization strategies. The miniaturization of HASEL actuators using flexible materials, compliant electrodes, and microfabrication techniques opens up new frontiers for their application in microfluidic systems. The development of miniaturized HASEL actuators with enhanced actuation performance, reliability, and integration capabilities will enable the creation of innovative microfluidic devices with enhanced functionality and reduced environmental impact, revolutionizing the field of microfluidics and paving the way for future advancements.

5 Acknowledgement

Funded by the Deutsche Forschungsgemeinschaft (DFG, German Research Foundation)-512586089 and 418669083.

6 References

[1] Rizzello, G., “A Review of Cooperative Actuator and Sensor Systems Based on Dielectric Elastomer Transducers,” *Actuators*, **12**(2), p. 46, 2023.

[2] A. J. Veale, S. Q. Xie, and I. A. Anderson, “Characterizing the Peano fluidic muscle and the effects of its geometry properties on its behavior,” *Smart Materials and Structures*, vol. 25, no. 6, p. 065013, May 2016, doi: 10.1088/0964-1726/25/6/065013.

[3] N. Kellaris, V. Gopaluni Venkata, G. M. Smith, S. K. Mitchell, and C. Keplinger, “Peano-HASEL actuators: Muscle-mimetic, electrohydraulic transducers that linearly contract on activation,” *Science Robotics*, vol. 3, no. 14, Jan. 2018, doi: 10.1126/scirobotics.aar3276.

[4] M. Taghavi, T. Helps, and J. Rossiter, “Electro-ribbon actuators and electro-origami robots,” *Science Robotics*, vol. 3, no. 25, Dec. 2018, doi: 10.1126/scirobotics.aau9795.

[5] P. Rothemund, N. Kellaris, S. K. Mitchell, E. Acome, and C. Keplinger, “HASEL Artificial Muscles for a New Generation of Lifelike Robots—Recent Progress and Future Opportunities,” *Advanced Materials*, vol. 33, no. 19, Nov. 2020, doi: 10.1002/adma.202003375.

[6] M. R. O’Neill *et al.*, “Rapid 3D Printing of Electrohydraulic (HASEL) Tentacle Actuators,” *Advanced Functional Materials*, vol. 30, no. 40, Aug. 2020, doi: 10.1002/adfm.202005244.

[7] R. Uramune, H. Ishizuka, T. Hiraki, Y. Kawahara, S. Ikeda, and O. Oshiro, “HaPouch: A Miniaturized, Soft, and Wearable Haptic Display Device Using a Liquid-to-Gas Phase Change Actuator,” *IEEE Access*, vol. 10, pp. 16830–16842, 2022, doi: 10.1109/access.2022.3141385.

[8] E. Leroy, R. Hinchet, and H. Shea, “Multimode Hydraulically Amplified Electrostatic Actuators for Wearable Haptics,” *Advanced Materials*, vol. 32, no. 36, Jul. 2020, doi: 10.1002/adma.202002564.

[9] M. Rafiq *et al.*, “Use of vegetable oils as transformer oils – a review,” *Renewable and Sustainable Energy Reviews*, vol. 52, pp. 308–324, Dec. 2015, doi: 10.1016/j.rser.2015.07.032.

[10] Y. Wang, Y. Wang, R. T. Mushtaq, and Q. Wei, “Advancements in Soft Robotics: A Comprehensive Review on Actuation Methods, Materials, and Applications,” *Polymers*, vol. 16, no. 8, p. 1087, Apr. 2024, doi: 10.3390/polym16081087.

Miniaturized Dielectric Elastomer Switch with the Potential as Bricks of Cooperative Multi-Actuator System

Chen Jiao[1], Ashwani Sharan Tripathi[1], Andreas Hubracht[2], Uwe Marschner[1], Jürgen Maas[2], and Andreas Richter[1], E.-F. Markus Vorrath[1,3]

[1]Institute of Semiconductors and Microsystems, Technische Universität Dresden, 01062 Dresden, Germany

[2]Mechatronic Systems Lab, Technische Universität Berlin, Hardenbergstraße 36, 10623 Berlin, Germany

[3]Biomimetics Lab, Auckland Bioengineering Institute, The University of Auckland, 70 Symonds St, Auckland 1010, New Zealand

Abstract

Collaborative multi-actuator systems will become important in future applications such as robotics, medical devices, and advanced user interfaces. Combining several multi-functional dielectric elastomers (DEs) with Hydraulically Amplified Self-Healing Electrostatic actuators (HASELs), enable multi-actuator networks that combine HASEL's performance and DE's multifunctionality. The core to multifunction DEs are dielectric elastomer switches (DESs). These devices enable signal processing capabilities, directly embedded into soft circuitry. In this contribution, we present the application basic DE-circuitry, to combine and intrinsically control multiple DE actuator-DE switch (DEA-DES) unit cells. We raise a mathematical model for such unit cells and networks capable of complex actuation tasks. We predict the multiple outputs of a single input pulse voltage for a highly integrated inverter system through simulation and present first experimental result, to proof the model.

1 Introduction

Collaborative multi-actuator systems are poised to become indispensable components in future applications, spanning domains like robotics, medical appliances, and advanced user interfaces [1]. Their versatility spans across scales, from the infinitesimal realm of the nanoscale, where fundamental phenomena originate, to the more tangible micro- and macroscales, where technical demands closely resemble human capabilities. As these systems undergo expansion, they must demonstrate the ability to autonomously navigate through intricate sequences of movements and tasks, adeptly perceive their surroundings, and dynamically adapt to changing environmental conditions. Achieving the vision of entirely soft bio-inspired robots necessitates the development of fully soft electronic circuits. Goal of the joint project CALMAR (DFG, 512586089) is the development of a collaborative multi-actuator system, combining the advantages of Dielectric Elastomer Transducers (DETs), Dielectric Elastomer Switches (DESs) and HASELs.

This contribution introduces the first results of our DES simulations and experimental investigations. Dielectric elastomers (DEs) are electroactive polymers with multifunctional properties. They are typically composed of a compliant elastomeric matrix sandwiched between compliant, conductive electrodes [2],[3]. This unique composition enables them to undergo substantial deformations when subjected to electric fields. When an electric field is applied across the electrodes, the elastomer experiences electrostatic forces that cause it to contract. This electrostatic actuation is reversible, allowing for precise control over the deformation of the material. Also, this response to electrical stimulation is similar to that of human muscle, enabling functionalities such as actuation, sensing, energy harvesting, and basic logic functions. Their versatility positions DEs as crucial components within collaborative multi-actuator systems envisioned for revolutionary applications in robotics, medical devices, and advanced user interfaces. For miniaturized systems, the challenge of independently performing complex sequences of tasks, sensing the environment, and acting autonomously is greatly magnified due to functional, technical, and size limitations.

Within this context, DE transducers form multi-actuator systems that harness cooperative synergies. By harnessing the remarkable capabilities of DEs to deform in response of electrical stimuli, these transducers play a pivotal role in enabling collaborative interactions between multiple actuators within a system, finding applications ranging from grippers in soft robotics to innovative uses like membrane loudspeakers [4]. During the last two decades manifold applications of DE have been reported, such as soft energy harvesters [5], soft-computers [6], stretchy sensors [7] or logic gates [8]. In cooperative multi-actuator systems, DE transducers serve as key components for actuation, sensing, and energy harvesting, facilitating seamless coordination and synchronization among individual actuators. Their inherent compliance and versatility allow for the creation of agile and adaptive systems capable of executing complex tasks with precision and efficiency. Nevertheless, the majority of DE arrays currently necessitate intricate external multi-channel high-voltage control systems to drive each DE actuator (DEA) individually. Our objective is to pioneer the development of sophisticated multi-actuator DEA

arrays equipped with internal control mechanisms. Such innovative systems have the potential to autonomously execute complex tasks by leveraging integrated bioinspired logic operations to drive the entire DEA array [9]. However, accurately predicting the behavior of these collaborative systems is a major challenge.

In response to this challenge, we introduced a mathematical framework for modeling DE-based multi-actuator networks, capitalizing on the versatile nature of DEs as actuators, digital switches, capacitors, and resistors. This model facilitated the creation of intricate actuator systems endowed with logic operation capabilities. Leveraging insights gained from our initial investigations into DEs, sensors, oscillators, and pacemakers for soft robots, we amalgamated diverse DE components to simulate sophisticated multi-actuator networks [10]. We first investigated the effect of different thickness and contents of carbon black-based (CB) electrodes on the resistance of DE switch (DES). To simulate the piezoresistive performance of DES, the resistance in the original and stretched states were measured for evaluation. Simultaneously, based on a simple unit cell mathematical model that has been experimentally validated, a model for more complex multi-actuator networks was derived. Using traditional electronic design methods such as pass transistor logic [11], we laid out larger electronic networks and simulate their behavior using SIMULINK. In addition, we described the derivation of a DE array with logic functionality based on predefined actuation patterns and introduced the model to lay out the system, which was validated by initial experimental results on parts of a complex multi-actuator system. This dynamic control mechanism effectively governs the actuation pattern of individual artificial muscles within the network, allowing for the selection of the most suitable actuation pattern as required.

2 Materials and methods

2.1 Modelling DE circuitry

A DEA can be represented as a compliant capacitor, consisting of an elastic dielectric membrane, sandwiched between two compliant electrodes. When a high input voltage V_{in}, is applied, opposite charges attract while, creating Maxwell's pressure, causing expansion in-plane and contraction in thickness. The in-plane expansion is here used to compress a DES directly positioned next to the DAE. This combination has been reported as a digital logic inverter [3],[6]. In the initial state, no actuation occurs, as no voltage is applied to the DEA, and DES conductive particles are dispersed at low density, high electric resistance (>10^9 Ohm) preventing current flow (**Figure 1**a). When the DEA is actuated, it expands in x_1 direction, the DES compressed, increasing the density of conductive particles, sharply dropping its resistance (**Figure 1**b), thus, lowering the output voltage. This set-up is similar to a classic digital inverter: a low input signal yields a high output, and vice versa. Thus, these inverters, consisting of a DEA and DES pair, function as a unit or gate.

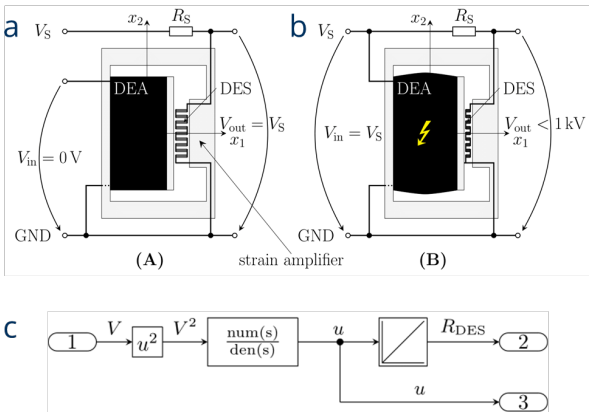

Figure 1 Working principle of a single inverter in (a) low input state and (b) high input state. The black rectangle represents the DEA, while the meander pattern symbolizes the DES. (c) Block diagram of a single inverter. SIMULINK sub-system to calculate the actuator displacement u based on V_{in} and further calculate the resulting V_{out} of voltage divider R_{DES}.

The DE multi-actuator networks were modeled using a SIMULINK model introduced by Henke et al. [12]. It combines a hyper-viscoelastic material model for the dielectric membrane with electrostatic field equations (**Figure 1**c). The model enables the connection of individual units into logic gates [8], complex circuitry [13], and oscillators [12]. By accurately predicting the actuation state of each inverter stage, it can simulate the behavior of complex multi-actuator systems constructed from digital DE gates. To simulate the behavior of collaborative multiactuator systems, arrays of several inverters have been studied for this contribution. Each inverter stage was connected to different inverters, forming a cooperative system where individual actuation states depend on those connected. The goal was to calculate the output voltage of each inverter, V_{out}, with a SIMULINK subsystem designed to calculate actuator displacement u based on V_{in} and determine resulting V_{out} of voltage dividers $R_{S\,i}$ and $R_{DES\,i}$ for each stage i. Each inverter was an electrically independent and identical circuit that could be interconnected in various configurations. The aim was to simulate methods of switching between different stable actuation patterns of cooperative multi-actuator systems, such as rows and arrays of actuators, with just a limited number of inputs.

2.2 Experimental set-up

The individual logic gates are applied to pre-strained VHB 4905 (by 3M) membranes. A logic gate consists of a DE actuator and a DE switch positioned next to it. Both components require different, and specific, membrane pre-strains for proper functionality. They are therefore produced in individual steps. For the DE membrane, a piece of VHB 4905 is supported in an iris-like device and pre-strained to an intermediate pre-strain of λ = 1.9. The switching grease, consisting of a 5:1 mixture by weight of

Molykote 44 Medium grease to Cabot Vulcan XC72 carbon, is applied to a PDMS stamp (Sylgard 184, by Dow Corning) by using a size zero soft taper point color shaper. The coated stamp is then pressed on the top of the membrane, against a flat counter mold from the bottom of the membrane, for at least 30 s to ensure a proper transfer of the switching grease. Afterwards, the membrane is further strained to a final pre-stretch of $\lambda = 3.5$. After pre-straining the membrane, it is glued to a laser-cut PMMA frame. During this step, it must be ensured that the membrane and the frame are positioned accurately with respect to each other. To ensure a proper switching by the DES, the individual DESs have to be placed as near as possible to the adjunct frame edge. For an uniaxial compression of the individual switches, narrow PMMA stiffener bars are also attached to the membrane from underneath. Finally, the electrodes for the DEAs are hand brushed to the membrane by using Nyogel 756G carbon grease and all necessary conductive tracks are hand brushed onto the top of the device. As voltage supply, a Peta-pico-Voltron EAP controller [14], developed by EPFL's soft transducer's lab, remotely controllable was used. It is a 4-channel high-voltage signal generator (maximal 5000V), remotely controlled by a LabView software application. Voltage measurements were performed with a self-developed, high-resistance voltage divider combined with a pre-amplifier to step down the high voltages to low-voltage signals, which were measured by a National Instruments NI-9205 analog to digital converter unit and processed by LabView.

3 Results and discussion

3.1 Modelling multi-actuator systems

Combinational circuits responded to a single input signal, driving system changes. **Figure 2**a shows a circuit with four inverters arranged consecutively. Except for the initial inverter controlled by V_{in}, all DEAs receive the output voltage of the preceding inverter stage V_{i-1} and a constant supply voltage V_{CC}. V_{in}, a one-bit input, controlled the entire four-bit output vector. V_{CC} remained constant at 3500 V. The DES resistors R_{DES}, along with serial charging resistors R_S, regulated signal levels at the output. SIMULINK accurately simulated the four output voltages V_1-V_4 using the model from **Figure 2**a with V_{in} = 0 V or V_{in} = 3250 V, as shown in **Figure 2**b and c for an alternating input voltage:

$$\{0\} \Longrightarrow \{1\ 0\ 1\ 0\} \Longleftrightarrow \{1\} \Longrightarrow \{0\ 1\ 0\ 1\}.$$

Throughout the 100-second duration, the input voltage accurately reflected its inversion at the output. Specifically, V_1 and V_3 exhibited a phase opposition to the V_{in} pulse, while V_2 and V_4 are aligned with it. The actuation pattern was described using high and low voltage levels denoted as 1 and 0, respectively. In this study, thresholds of 0.5 and 2.5 kV were selected. Here, 0 and 1 represent the logic voltage values corresponding to the static state and active state of the DEA. Voltage values below 0.5 kV were considered logic 0, while those above 2.5 kV were regarded as 1. It was demonstrated that a single-bit input could control four output values between two states. Additionally, the model accurately reproduced the delayed feedback of DES. As the voltage pulse propagated, V_{out} gradually underwent a phase shift due to the time required for the response of DEA actuation, indicating the simulation's overall accuracy. SIMULINK calculates that V_4 exhibited a delayed response of 3 s compared to V_{in}. The value of this delay was determined by the time constant $\tau = R_1 C_{\mathrm{DEA}\ i+1}$.

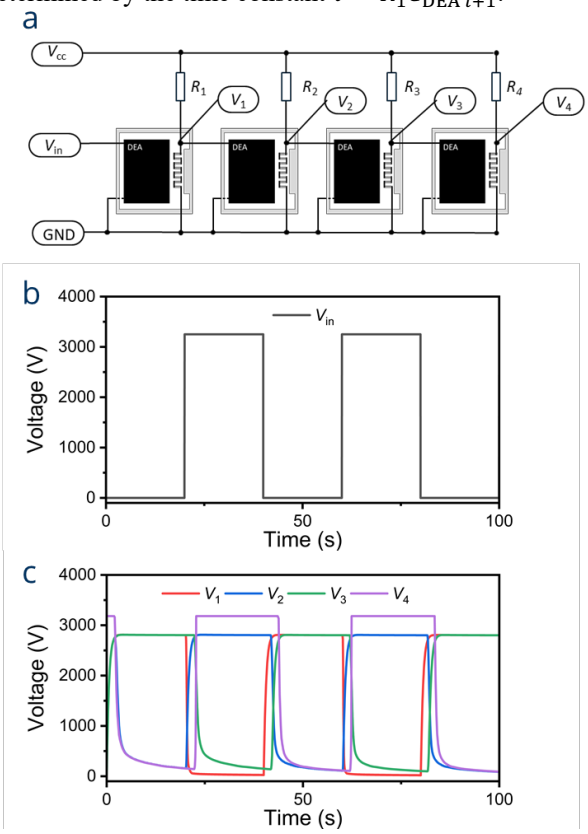

Figure 2 (a) Design of four inverters in a row with a single input supply. Simulation results of (b) input and (c) four output voltage for four inverters in a row with a single input over the entire measurement time of 100 s.

3.2 Experimental results

Based on the theoretical guidance of SIMULINK simulation, a circuit with four consecutively arranged inverters (**Figure 3**a) has been built. Except for the initial inverter controlled by V_{in}, all DEAs received the previous inverter stage's output voltage V_{i-1} as signal input and the constant supply voltage V_{CC} as supply. In order to obtain a significant inverter effect, V_{CC} was chosen constant at 3250 V, with either V_{in} = 0 V or V_{in} = 3000 V to drive the DEA with a square wave of 0.01 Hz frequency. The AC input voltage V_{in} and the four output voltages V_1-V_4 are shown in **Figure 3**b and **Figure 3**c respectively.

The output voltage accurately reflected the inversion at the input for the entire 250 s duration. Consistent with SIMULINK predictions, V_1 and V_3 appeared opposite phase to the V_{in} pulse, while V_2 and V_4 align with it. Unlike the simulated results, all four output voltages took a longer time to reach the plateau, which was why the frequency of the AC input voltage was chosen to be reduced from 0.025 Hz to 0.01 Hz. On the other hand, V_1 and V_2 showed a large stable voltage difference under AC-driven DEA,

and the stable voltage at logic 0 was lower than 0.5 kV, while the stable voltage at logic 0 of V_3 and V_4 was still higher than 1 kV. It illustrated that as the number of series connections increases, the conversion effect of the inverter decreased. The delayed feedback results of DES were consistent with SIMULINK predictions.

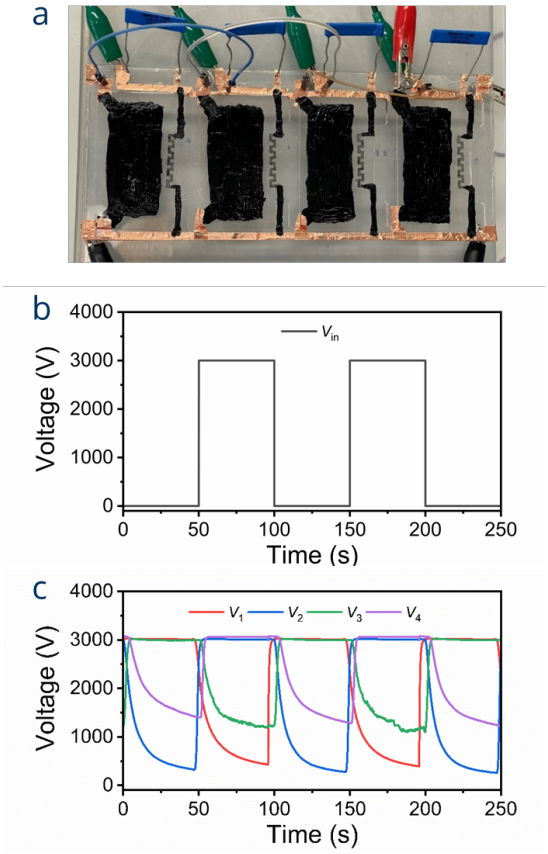

Figure 3 (a) Photo of four inverters in a row with a single input supply. Experimental results of (b) input and (c) four output voltage for four inverters in a row with a single input over the entire measurement time of 250 s.

4 Conclusion

In conclusion, a mathematical model was used to analyze multi-actuator networks, allowing for logic functionality. By integrating different DE components, we simulated networks capable of switching between pre-defined actuation patterns. The model accurately inverted the square wave pulse input voltage in each stage, replicating the delayed feedback of DES. The approach can be extended to model more complex systems, validated through experimentation. It established the foundation for advanced multi-actuator systems in soft robotics and beyond, offering intelligent solutions for various challenges.

5 Acknowledgement

Funded by the Deutsche Forschungsgemeinschaft (DFG, German Research Foundation)-512586089 and 418669083.

6 Literature

[1] Rizzello, G., “A Review of Cooperative Actuator and Sensor Systems Based on Dielectric Elastomer Transducers,” *Actuators*, **12**(2), p. 46, 2023.

[2] Pelrine, R., Kornbluh, R., Pei, Q., et al. “High-Speed Electrically Actuated Elastomers with Strain Greater Than 100%,” *Science*, V. 287, No. 5454, 2000.

[3] Suo, Z., “Theory of Dielectric Elastomers,” *Acta Mechanica Solida Sinica*, **23**(6), pp. 549–578, 2010.

[4] Anderson, I. A., Gisby, T. A., McKay, T. G., et al. “Multi-functional dielectric elastomer artificial muscles for soft and smart machines,” *Journal of Applied Physics*, V. 112, No. 4, p. 41101, 2012.

[5] McKay, T. G., O’Brien, B. M., et al. “Soft generators using dielectric elastomers,” *Applied Physics Letters*, V. 98, No. 14, p. 142903, 2011.

[6] O’Brien, B. M., and Anderson, I. A. “An artificial muscle computer,” *Applied Physics Letters*, V. 102, No. 10, p. 104102, 2013.

[7] O’Brien, B., Gisby, T., and Anderson, I. A. “Stretch sensors for human body motion.” *Proc. SPIE 9056*, p. 905618, 2014.

[8] Wilson, K. E., Henke, E.-F. M., Slipher, G. A., et al. “Rubbery logic gates,” *Extreme Mechanics Letters*, V. 9, pp. 188–94, 2016.

[9] Henke, E.-F. M., Schlatter, S., and Anderson, I. A. “Soft dielectric elastomer oscillators driving bioinspired robots,” *Soft Robotics*, 2017.

[10] Wang, Y., Ding, H., Zhao, J., and Li, R., “Neural Network-based Output Synchronization Control for Multi-actuator System,” *International Journal of Adaptive Control and Signal Processing*, 36(5), pp. 1155–1171, 2022.

[11] Ciarella, L., Richter, A., and Henke, E.-F. “Digital electronics using dielectric elastomer structures as transistors,” *Applied Physics Letters*, V. 119, No. 26, 2021.

[12] Henke, E.-F. M., Wilson, K. E., and Anderson, I. A., “Modeling of Dielectric Elastomer Oscillators for Soft Biomimetic Applications,” *Bioinspiration & Biomimetics*, **13**(4), p. 046009, 2018.

[13] Ciarella, L., Wilson, K. E., Richter, A., et al. “A model for dielectric elastomer based electronics,” *IFAC-PapersOnLine*, V. 55, No. 20, pp. 588–93, 2022.

[14] Schlatter, S., Illenberger, P., and Rosset, S., “Peta-pico-Voltron: An open-source high voltage power supply” *HardwareX*, V. 4, pp. e00039, 2018.

A bistable pneumatic actuator based on flexible metamaterials

Anagha Navale, Ritika Gupta, Hugo de Souza Oliveira, Viacheslav Slesarenko, Edoardo Milana
Department of Microsystems Engineering - IMTEK, University of Freiburg, Freiburg, Germany
Cluster of Excellence *liv*MatS @ FIT, University of Freiburg, Freiburg, Germany
E-mail address: edoardo.milana@imtek.uni-freiburg.de

Abstract

In this work, we combine the programmable mechanical response of flexible mechanical metamaterials with pneumatic actuation, with the aim of constructing soft machines with mechanically programmed actuation patterns. We design and fabricate flexible metamaterials that undergo snap-through instabilities under tension, enabled by the unit cell comprising double-clamped curved beams. Specifically, we test snapping metamaterials with cylindrical topologies, each composed of a repeating array of four unit cells along the circumferential direction. These metamaterials are fabricated using FDM 3D printing with NinjaFlex filament (TPU 85A), and their nonlinear mechanical response under tension is characterized using a uniaxial testing machine. We design a linear actuator by coupling the flexible metamaterial with a pneumatic single-acting cylinder, thereby placing the nonlinear elasticity of the metamaterial in parallel with the piston. The actuators are characterized in terms of their snapping pressures using a measurement setup comprising a motorized syringe pump for controlled inflation and a pressure sensor.

1 Introduction

Future robots are expected to operate in highly unstructured environments, where unforeseen interactions with the external world may occur, or even be necessary. This presents challenges to current control algorithms, which need to possess a consistent level of adaptivity. Conversely, adaptivity appears easy and natural for the biological organisms that abound in our world. The adaptivity of biological organisms arises from the intelligent use of the physical properties of their bodies, a crucial aspect enabling them to embody low-level control schemes and thrive in unstructured environments [1].

Inspired by this concept, a paradigm shift is underway in robotics, where control schemes are not solely programmed within the high-level abstraction of algorithms but are also embodied into the physics of the materials used to construct the hardware [2]. This shift is particularly evident in the field of soft robotics, where traditional control schemes struggle due to the infinite parameters of their configuration space [3]. However, the complex mechanics of soft robots, while challenging from an algorithmic perspective, can offer advantages from a physical standpoint.

Many mechanical nonlinearities present in soft materials have been utilized to achieve functionalities that would otherwise require numerous bulky and rigid components, such as solenoid valves, pumps, compressors, and microcontrollers. Soft valves, utilizing snapping membranes as mechanisms [4], [5], can induce pneumatic self-oscillation and incorporate fluidic logic gates to generate fluidic digital circuits [6]. Such circuits have been employed to control the walking gait of soft robots in open-loop configurations [7]. One advantage of the high deformability of soft materials is the ability to create monolithic mechanisms that do not require component assembly and can thus be easily 3D printed. Recently, an entirely soft robot, including its self-oscillatory pneumatic logic circuit, has been fully designed and printed as a single piece [8]. Beyond self-oscillation and logic, the mechanical nonlinearities of soft materials have been harnessed to implement another type of control scheme: sequential actuation. Many snapping inflatable actuators—actuators with a non-monotonic response—can be interconnected to the same pressure supply in an underactuated configuration and driven in a discrete sequence. This is achieved by designing each actuator with different snap-through pressure thresholds or by implementing flow restrictors between actuators to generate pressure drops. This method can generate underactuated motion asymmetries (e.g., metachronal waves [9] or walking gaits [10]) or even complex sequential patterns (e.g., playing a melody [11]).

This work is situated in such a context and presents preliminary results towards a new design of a semi-soft pneumatic actuator, which leverages the nonlinearities of flexible mechanical metamaterials [12]. The objective is to explore the large design space of mechanical metamaterials and their fabrication space in terms of 3D printing parameters, such as infill density and geometry, which can impact the mechanical characteristics. By expanding the design and fabrication space of nonlinear soft actuators, more complex control schemes can be integrated into soft robotic systems.

In particular, we focus on mechanical metamaterials that exhibit bistability. We realize a bistable semi-soft actuator by placing a bistable metamaterial in parallel with a single-acting pneumatic cylinder. We first introduce the design of the metamaterial and its assembly into an actuator, and describe the manufacturing process, as well as the experimental setups. Furthermore, we present and discuss the results obtained from the mechanical characterization of the metamaterials, as well as the pressure snapping points characterization of the bistable actuator.

2 Design and Fabrication

2.1 Snapping metamaterial with cylindrical topology

The design of the semi-soft bistable actuator consists of a mechanical metamaterial with a cylindrical topology placed in parallel to a single-acting cylinder used in entertainment toys (Lego Technic pneumatic piston). The low force required to deform the metamaterial (< 5N) makes the "toy" piston a suitable actuator for the scope of this research. The cylinder's chamber has a cross-section area of 26.45 mm^2.

The key requirement for the metamaterial is to exhibit a non-monotonic force-displacement curve under tension, which means it undergoes a snap-through instability when a local force peak is reached, switching between two stable configurations (bistability). We opt for a flexible metamaterial composed of a unit-cell made of double-clamped curved beams. Such beams have a snapping transition analogous to the von Mises Truss. This family of flexible nonlinear metamaterials have been already reported by several authors [13], [14], [15], [16]. To have a symmetric design, we adopt a cylindrical topology composed of an array 1x4 of unit cells and placed the single-acting cylinder in the middle, so that the axis of the metamaterial and the piston coincide. In this way, the force is exerted in the middle point of the cross-section, avoiding bending deformations of the metamaterial.

The curved beams are parametrized using the trigonometric function $y(x) = h/2[1 - \cos(2\pi x/l)]$ in the interval $[-l/2,0]$, as reported in [17]. The design parameters are reported in Table 1 and depicted in Figure 1A. The other subfigure (1B) displays the 3D design of the metamaterial, where we additionally increase the wall height of 10 mm above and below the architected structure to improve mechanical stability. The overall size of the metamaterial is 34 mm in height and 37 mm in diameter.

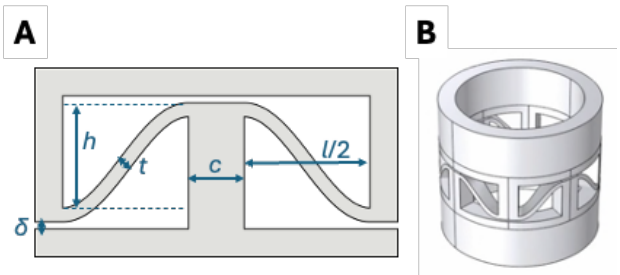

Figure 1. A) Design parameters of the metamaterial unit cell in plane. B) CAD design of the final metamaterial with cylindrical topology.

2.2 Fabrication process

The flexible metamaterials are fabricated via FDM 3D printing (Prusa MK4) using flexible TPU filament (NinjaFlex TPU Shore 85A from NinjaTek). The sample is printed with the cylinder axis of the metamaterial perpendicular to the print bed, using support of the same material, which is subsequently cut out. We use honeycomb infill geometry and print samples with two different infill density (40% and 80%) to check whether the infill density influences the snapping force thresholds. As the curved beams are only 1 mm thick, the infill density only affects the mechanical properties of the thicker support beams and walls. Figure 2A shows a picture of metamaterial in the two stable states.

Additional holders to assemble the metamaterial with the piston are printed using PLA. Figure 2B depicts the components of the assembly of the bistable actuator.

Parameters	Dimensions (mm)
l	18
c	4
t	1
h	7.5
δ	0.5

Table 1. Dimensions of the unit cell

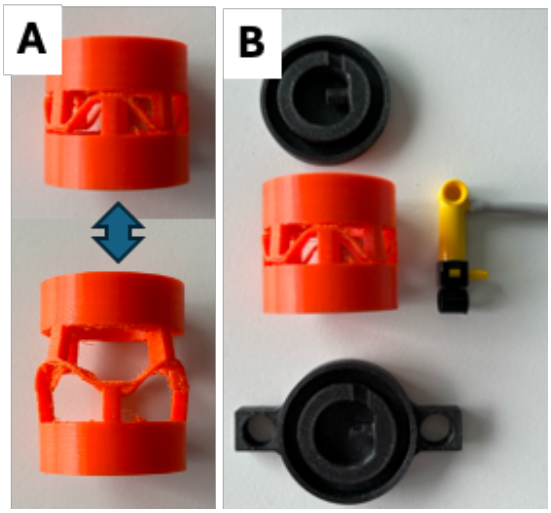

Figure 2. A) Metamaterials in the two stable states. B) Components of the bistable actuators: metamaterial, single-acting cylinder, and holders.

3 Experimental setups

3.1 Force-displacement test

The metamaterials are tested under tension using a universal testing machine (zwickiLine from ZwickRoell, with load cell 50 N). The test consists in a prescribed linear displacement of 15 mm to ensure the tests finish in the post-snapping configuration and a return travel back to the starting position. In the full experiment the test is cycled 5 times at a displacement rate of 30 mm/min.

3.2 Pressure snapping test

The bistable actuators, composed by assembling in parallel the metamaterial and the piston, are characterized in terms

of snapping pressure. The setup consists of a motorized syringe pump driven by a stepper motor (NE-501 OEM Syringe Pump from KF Technology) to generate a controlled air compression in the actuator and a pressure sensor (DRMOD-I2C-R6B for positive pressure and DRMOD-I2C-RV1 for negative pressure from B+B Thermo-Technik GmbH) in between the actuator and the syringe to measure the pressure. The data from the pressure sensor are acquired with an Arduino Uno board.

4 Results and discussion

The results of the characterization of the mechanical metamaterials are depicted in Figure 3. Both samples have a clear non-monotonic force displacement curve, and the snapping thresholds can be accurately determined. All curves cross the zero-force line, which indicates that both samples are consistently bistable over the multiple cycles. As expected by soft materials, large hysteresis loops form during the loading-unloading cycle.
We refer to the positive force peak of the loading cycle as the snap-through point, where the transition occurs from the designed configuration to the metastable. We call snap-back point the force valley of the unloading cycle, where the sample goes back into the original configuration. We observe that the sample with 80% infill density has ~30% higher snap-through, and ~60% higher (in absolute values) snap-back points compared to the one with 40% infill density. As mentioned, the infill density only affects the stiffness of the support structures of the metamaterial, as the thin curved beams are completely filled by the few layers of TPU. Nevertheless, the support stiffness significantly affects the snapping points due to changes in the boundary conditions of the thin beams.

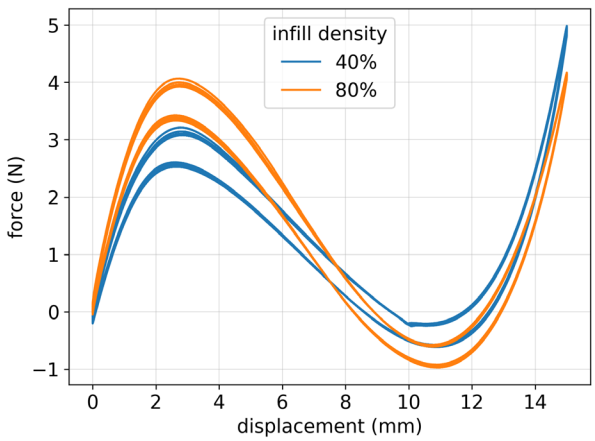

Figure 3. Force-displacement curves of the metamaterial with infill density 40% and 80%.

Further, considering the cross-section area of the piston's chamber, we compute the snap-through and snap-back forces into pressures and compare them with the pressure thresholds measured in the pressure snapping test. The results are reported in Figure 4. The calculated expected values align with the measured values. The slightly higher

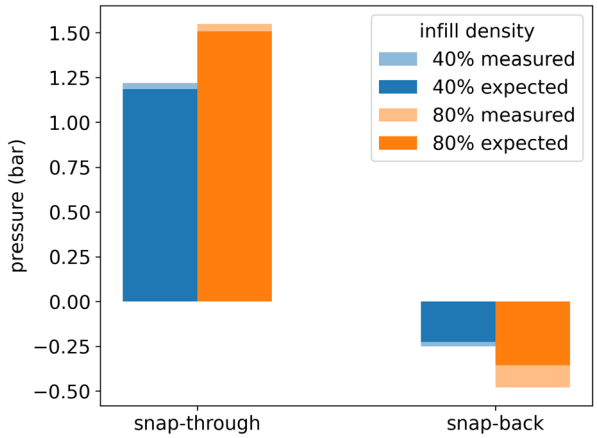

Figure 4. Snap-through and snap-back pressures of the actuators featuring the metamaterials with infill density 40% and 80%, both measured and expected from the force-displacement curves.

measured values can be attributed to friction in the piston and viscous losses in the tubing.
Our bistable actuator behaves as follow; when the piston is pressurized, a normal force is exerted on the metamaterial. If the force exerted by the piston is below the snap-through point, the displacement of the actuator is minimal and the elasticity of the metamaterial drives back the piston when the cylinder is depressurized, acting as a linear spring. However, when the force exceeds the threshold, the metamaterial snaps and the actuator has a quick and large displacement. As the metamaterial is bistable, the actuator remains in the metastable configuration (Figure 4B) even when the piston is depressurized, and an external force or negative pressure is needed to snap the back to the initial state (Figure 4A).

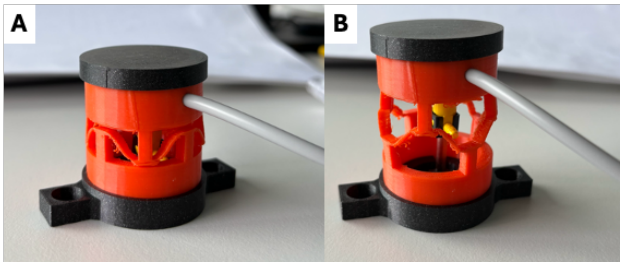

Figure 4. The bistable pneumatic actuator in the two stable configurations: the designed (A) and the metastable (B) ones.

5 Conclusion

These preliminary results demonstrate that it is possible to realize bistable and in general nonlinear actuators by harnessing the large design opportunities offered by 3D printed flexible mechanical metamaterials. We also show that for a fixed geometry, the snapping pressure thresholds can be tuned by the infill density chosen during the printing process, offering new strategies for tuning nonlinear mechanical response of soft actuators.

Next steps will include replacing the rigid piston with a soft inflatable segment, to have an entirely soft bistable actuator. At this stage, the selection of the single-acting cylinder was driven by the absence of a spring or elastic reaction inherent in this type of actuator. In contrast, typical soft inflatable extending actuators, typically made of rubber, possess their own intrinsic elastic reaction, which combines with the elastic reaction of the metamaterial. This cumulative stiffness tends to linearize the overall system response, counteracting the bistable effect we aim to achieve. Therefore, further research is necessary to develop zero-stiffness inflatable soft segments that do not compromise the nonlinearity of the metamaterial. Promising work goes towards wrinkled pouches [18].
Further, we will implement multiple nonlinear actuators in a single fluidic circuit, to generate physically controlled motion sequences in soft robotic systems.

Acknowledgment

This work was funded by the Deutsche Forschungsgemeinschaft (DFG, German Research Foundation) under Germany's Excellence Strategy – EXC-2193/1 – 390951807 and under Walter Benjamin Programme – MI 3063/1-1 – 505075715.

6 Literature

[1] R. Pfeifer and J. Bongard, “How the Body Shapes the Way We Think,” in *How Body Shapes W. We Think*, The MIT Press, 2006. doi: 10.7551/mitpress/3585.003.0018.

[2] C. A. Aubin *et al.*, “Towards enduring autonomous robots via embodied energy,” *Nature*, vol. 602, no. 7897, Art. no. 7897, Feb. 2022, doi: 10.1038/s41586-021-04138-2.

[3] D. Rus and M. T. Tolley, “Design, fabrication and control of soft robots,” *Nature*, vol. 521, no. 7553, pp. 467–475, May 2015, doi: 10.1038/nature14543.

[4] P. Rothemund *et al.*, “A soft, bistable valve for autonomous control of soft actuators,” *Sci. Robot.*, vol. 3, no. 16, p. eaar7986, Mar. 2018, doi: 10.1126/scirobotics.aar7986.

[5] L. C. van Laake, J. de Vries, S. Malek Kani, and J. T. B. Overvelde, “A fluidic relaxation oscillator for reprogrammable sequential actuation in soft robots,” *Matter*, vol. 5, no. 9, pp. 2898–2917, Sep. 2022, doi: 10.1016/j.matt.2022.06.002.

[6] D. J. Preston *et al.*, “Digital logic for soft devices,” *Proc Natl Acad Sci U A*, vol. 116, no. 16, pp. 7750–7759, Apr. 2019, doi: 10.1073/pnas.1820672116.

[7] D. Drotman, S. Jadhav, D. Sharp, C. Chan, and M. T. Tolley, “Electronics-free pneumatic circuits for controlling soft-legged robots,” *Sci. Robot.*, vol. 6, no. 51, p. eaay2627, Feb. 2021, doi: 10.1126/scirobotics.aay2627.

[8] S. Conrad *et al.*, “3D-printed digital pneumatic logic for the control of soft robotic actuators,” *Sci. Robot.*, vol. 9, no. 86, 2024, doi: 10.1126/scirobotics.adh4060.

[9] E. Milana, B. Van Raemdonck, A. S. Casla, M. De Volder, D. Reynaerts, and B. Gorissen, “Morphological Control of Cilia-Inspired Asymmetric Movements Using Nonlinear Soft Inflatable Actuators,” *Front. Robot. AI*, vol. 8, p. 788067, Jan. 2022, doi: 10.3389/frobt.2021.788067.

[10] B. Gorissen *et al.*, “Hardware Sequencing of Inflatable Nonlinear Actuators for Autonomous Soft Robots,” *Adv Mater*, vol. 31, no. 3, pp. 1–7, 2019, doi: 10.1002/adma.201804598.

[11] B. Van Raemdonck, E. Milana, M. De Volder, D. Reynaerts, and B. Gorissen, “Nonlinear Inflatable Actuators for Distributed Control in Soft Robots,” *Adv. Mater.*, vol. 35, no. 35, p. 2301487, 2023, doi: 10.1002/adma.202301487.

[12] K. Bertoldi, V. Vitelli, J. Christensen, and M. van Hecke, “Flexible mechanical metamaterials,” *Nat. Rev. Mater.*, vol. 2, no. 11, Art. no. 11, Oct. 2017, doi: 10.1038/natrevmats.2017.66.

[13] S. Shan *et al.*, “Multistable Architected Materials for Trapping Elastic Strain Energy,” *Adv. Mater.*, vol. 27, no. 29, pp. 4296–4301, 2015, doi: 10.1002/adma.201501708.

[14] D. Restrepo, N. D. Mankame, and P. D. Zavattieri, “Phase transforming cellular materials,” *Extreme Mech. Lett.*, vol. 4, pp. 52–60, Sep. 2015, doi: 10.1016/j.eml.2015.08.001.

[15] H. Yang and L. Ma, “Multi-stable mechanical metamaterials by elastic buckling instability,” *J. Mater. Sci.*, vol. 54, no. 4, pp. 3509–3526, Feb. 2019, doi: 10.1007/s10853-018-3065-y.

[16] F. Wenz, D. Schönfeld, S. C. L. Fischer, T. Pretsch, and C. Eberl, “Controlling Malleability of Metamaterials through Programmable Memory,” *Adv. Eng. Mater.*, vol. 25, no. 3, p. 2201022, 2023, doi: 10.1002/adem.202201022.

[17] H. Yang and L. Ma, “1D and 2D snapping mechanical metamaterials with cylindrical topology,” *Int. J. Solids Struct.*, vol. 204–205, pp. 220–232, Nov. 2020, doi: 10.1016/j.ijsolstr.2020.08.023.

[18] S. Rahman, L. Wu, A. El Elmi, and D. Pasini, “Zero-Power Shape Retention in Soft Pneumatic Actuators with Extensional and Bending Multistability,” *Adv. Funct. Mater.*, vol. 33, no. 49, p. 2304151, 2023, doi: 10.1002/adfm.202304151.

Axially Distributed Fluidic Actuators for Steerable Minimally Invasive Surgical Device Applications

Bob Lathrop[a], Mouloud Ourak[a], and Emmanuel Vander Poorten[a]
[a]Department of Mechanical Engineering, KU Leuven, Celestijnenlaan 300B, 3001 Leuven Belgium

Abstract

Recent advancements in the design of miniature fluidic actuators have enabled the development of novel actuation schemes suitable for use in a wide range of minimally invasive surgery (MIS) applications. Due to their high force production, high bandwidth, and potential for miniaturization, research has been ongoing to integrate fluidic muscles in steerable catheters. In previous work, intrinsically actuated steerable surgical catheters have been built using an arrangement of $2-4$ fluidic artificial muscles antagonistically connected in parallel within a bending segment at or near the distal tip of the catheter. This configuration necessitates a larger catheter diameter to accommodate the actuators without any interference between the pressurized actuators or catheter interior walls. In this study a novel design is presented which distributes actuators along the length of the catheter to ensure that only one actuator takes up cross sectional space at any point along the device. This enables significant reduction in diameter with comparison to the state-of-the-art. A proof of concept prototype has been built using 2.0 mm diameter pneumatic artificial muscles to actuate a 3.3 mm diameter steerable catheter bending segment beyond a $+/-90°$ range of motion in a tortuously constrained space.

1 Introduction

Steerable catheters are a key enabling technology used in the diagnosis and treatment of a wide range of pathologies [1, 2]. Progress in the development of miniature pneumatic artificial muscles (PAMs) has presented an opportunity for the design of novel intrinsic actuation schemes to enable smaller, more capable flexible steerable devices for minimally invasive surgery (MIS). PAMs are a variety of fluidic actuator well suited for use in medical device applications due to their high power-to-weight ratio, compliant components, inexpensive material cost[3], and demonstrated functional utility at diameters as low as one millimeter[4]. Small diameter actuators are ideal for integration into long, thin MIS devices such as surgical catheters and endoscopic devices, which can range from 7 to less than 2 mm in diameter [5, 6] to enable access to remote anatomic regions.
Previously introduced steerable fluidically actuated catheter designs such as the 7.0 mm diameter device of Devreker et al [7] use $2-4$ PAMs connected in parallel inside a bending segment to produce multiple degree of freedom (DOF) movement, as shown in Fig. 1a. Miniaturization of this design is desirable to expand the potentially addressable clinical applications, but challenging due to the need to maintain enough cross-sectional area for each of the actuators to radially expand during pressurization without interfering with one another. A new design is proposed here which distributes PAMs along the length of the steerable catheter, reducing the overall cross-sectional area needed. Each actuator is suspended between a different point along the perimeter of the distal tip and an anchor cable fixed to the proximal end of the catheter. This enables antagostic steering of of the bending segment.

This study evaluates a proof of concept prototype of the proposed axially distributed embedded PAM actuation scheme. The 3.3 mm diameter prototype is constructed as a simplified version of the design shown in Fig. 1b, using one pair of antagonistic actuators to steer in positive and negative directions along a single degree of freedom. Bending performance is evaluated in different constrained conditions, to mimic the confined anatomic spaces which must be navigated by steerable surgical catheters.

2 Methods and Materials

Miniature pneumatic artificial muscles with 50 mm functional length were constructed using the following materials:

- Pneumatic bladder: 1.9 mm outer diameter silicone tubing (Dow Corning, USA)
- Braid: 1.7 mm woven polyimide (Bossert Kast, Germany)
- End connectors: 2.2 mm outer diameter stainless steel tubing (Salomon Metalen, Netherlands)
- Adhesive: 204-CTH-F UV-cure adhesive (Dymax, USA)

The polyimide braid was woven from 24 0.07 mm diameter filaments with a resting 30° braid angle with respect to the longitudinal axis at 1.7 mm overall diameter. The components were assembled and pneumatically sealed using the UV-cure adhesive, then fixed to 0.2 mm diameter steel cables at each end. The cables were then connected to different points along the perimeter of a 3.3 mm diameter

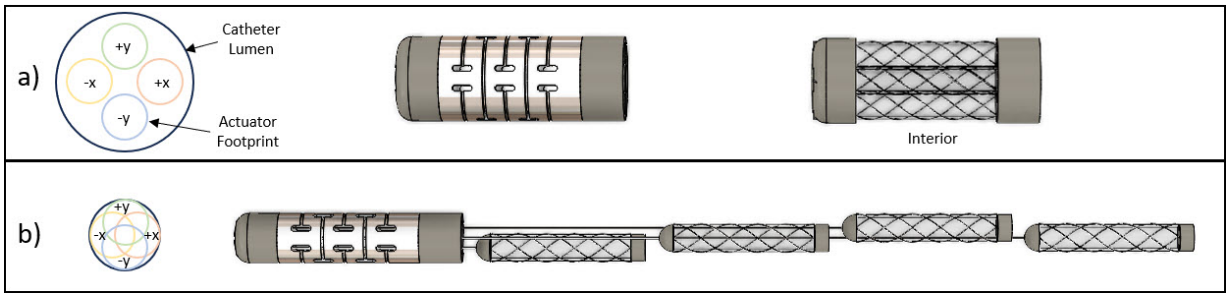

Figure 1 Comparison of tip embedded fluidic actuation schemes for steerable MIS devices: a) Previously developed catheter with 4 parallel pneumatic artificial muscles shown in cross-section, exterior, and interior view, and b) Axially distributed design and cross-section showing radial overlap of actuator footprints. Proximal connections and sheathe not pictured.

Figure 2 Bending segment range of motion when constrained within a) a straight 4 mm wide channel and b) a tortuous path of 25 mm radius turns

nitinol bending segment and a fixed base point as shown in Fig. 1b. Care must be taken to prevent any twisting or tangling of cables during the construction process. It is also important to ensure consistent pretensioning of the bladders and braids during construction, to avoid any bias in the position of the catheter at rest. Initial bending characterization was performed by actuating the PAMs in different configurations and measuring the resultant bend angle, to examine the device's capability to navigate in free space as well as highly constrained conditions. As shown in Fig. 2, the prototype was placed into two 4.0 mm wide channels, one straight and the other a tortuous series of 25 mm radius curves. The proximal end of the bending segment was clamped in place to the fixture, and the anchor cable connected to the proximal PAM ends was fixed at the end of each channel. Images were taken from a camera mounted directly above the test fixture at variable pressure levels for each of the actuators. Bend angle measurements were made via image analysis using ImageJ software to determine the angle between the distal tip of the actuated bending segment and the longitudinal axis of the device.

3 Experiments and Discussion

After mounting the prototype device in the constraint channels as shown in Fig. 2, bending was assessed by independently actuating each PAM over a range of $0-5$ bar of pressure. This resulted in the bending angles shown in Fig. 4. When constrained in the straight channel, the prototype achieved a maximum bend angle of 103.6 degrees when driven by the distal PAM and 101.8 degrees in the opposite direction when driven by the proximal PAM. Similarly, when constrained in the tortuous channel, the prototype achieved a maximum bend angle of 104.7 degrees when driven by the distal PAM and 91.7 degrees when the proximal PAM was actuated.

Several trends arise from analysing these results. Overall performance of the prototype, producing over 90 degrees of bending, is well within the range of clinical relevance for many steerable surgical catheter applications. The bending produced by the proximal actuator is generally slightly less than that produced by the distal actuator at the same pressure, potentially due to interference between the driving cable and the distal PAM. This is particularly visible in the tortuous test condition, with the proximal PAM requiring 5 bar of pressure to produce similar bending to the distal

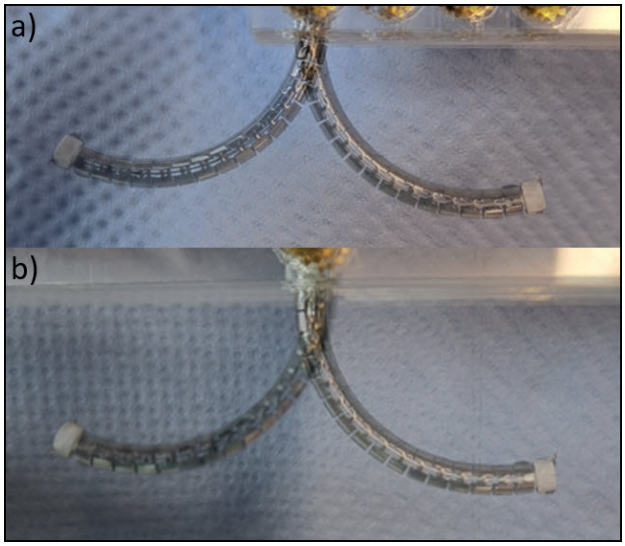

Figure 3 Bending segment range of motion when constrained within a) a straight 4 mm wide channel and b) a tortuous path of 25 mm radius turns.

PAM at 3 bar. This behavior should be addressed with future design improvements to minimize risk of interference between components, such as the use of lengths of multi-lumen tubing to isolate and maintain order of the actuation cables.

Further design work should focus on the development of higher-DOF instruments using additional actuators and targeted to specific clinical applications. The extent to which axially distributed actuators have the potential to interfere with one another is largely determined by the constraints of the space they are navigating, which necessitates functional testing under conditions specific to the target anatomy and the catheter access pathway. The lower cross-sectional area required by this actuation scheme may also be useful for the development of catheters targeted at procedures which require large working channels. This scheme may also be useful in the production of small-diameter catheters that have higher stiffness than current designs, opening up new possibilities for the development of therapeutic devices that benefit from stiffness at the point of tissue contact.

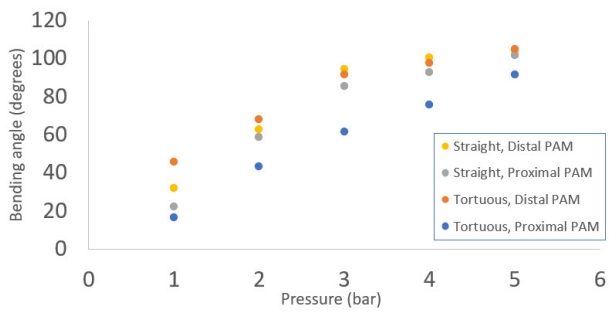

Figure 4 Bend angles produced by actuating the prototype in straight and tortuous configurations

4 Conclusion

The results of the initial proof-of-concept evaluation show that the proposed design can be used to produce clinically relevant steering motion at a significantly smaller diameter than previous fluidically actuated catheters. Antagonistic actuation was achieved over 90° in the tested constrained conditions, with a 3.3 mm diameter footprint that could be used to access significantly smaller anatomic regions than previous 7 mm diameter catheters. Initial tests show some reduction in performance of actuators located further from the device tip due to interference between the actuators and drive cables, which may limit the application of this design for navigating highly tortuous pathways. This behavior should be minimized in future designs, or compensated for via closed loop control of the catheter bending position. An evaluation of bending hysteresis and the forces produced on surrounding tissues in clinically relevant configurations will also be important for development of functional steerable catheters. Further testing should be done to expand to multiple degree of freedom actuation and evaluate performance of a functionalized catheter for specific clinical applications.

Acknowledgments

This project received funding from a KU Leuven internally funded project FLEXFET (3E200384).

5 Literature

[1] Fu, Y. et al.: Steerable catheters in minimally invasive vascular surgery,: The International Journal of Medical Robotics and Computer Assisted Surgery. Vol. 5, 2009

[2] Hu, X. et al.: Steerable catheters for minimally invasive surgery: a review and future directions,: Computer Assisted Surgery. Vol. 23, No. 1, 2018

[3] De Volder, M. et al.: Pneumatic and hydraulic microactuators: a review,: Journal of Micromechanics and Microengineering. Vol. 20, No. 1, 2010

[4] Lathrop, R. et al.: Miniature Pneumatic Artificial Muscles for Use in Surgical Devices, Actuator, 2022 , pp. 1-4

[5] Vander Poorten, E et al.: Cognitive Autonomous CAtheters Operating in Dynamic Environments,: Journal of Medical Robotics Research., 2016

[6] Lange,R et al..: Diagnostic Cardiac Catheterization,: Circulation., 2003 Vol. 107, pp 111–113

[7] Devreker, A. et al.:Fluidic actuation for intra-operative in situ imaging,: IROS, pp. 1415-1421

A toolchain for deployment of concentric tube continuum robots as curved cannulae in stereotactic neurosurgery

Julian Mühlenhoff[a], Matthias K. Hoffmann[b], Dörthe Keiner[c], Mohamed Henia[c], Joachim Oertel[c], Kathrin Flaßkamp[b], and Thomas Sattel[a]
[a]Mechatronics Group, Technische Universität Ilmenau, Ilmenau, Germany
[b]Systems Modeling and Simulation, Saarland University, Saarbrücken, Germany
[c]Department of Neurosurgery, Saarland University Medical Center and Faculty of Medicine, Homburg, Germany

Abstract

In this paper, we present a methodology and toolchain for deploying concentric tube continuum robots as curved cannulae in stereotactic neurosurgery. We aim towards performing a whole robotic surgery procedure on a phantom head with artificial target and obstacle markers under clinical conditions. At first, a computed tomography scan of the head with applied localization markers – defining the patient's coordinate system – is generated. Based on this, we identify and label the skull, entry and target regions, as well as obstacles inside the imaging data. Path planning is carried out by manual and automatic approaches using state-of-the-art cannula models. For the resulting path, the target parameters of the stereotactic head frame are calculated. The robot is then attached to the head frame and actuated according to the planning.

1 Introduction

For treating various diseases of the human brain, e.g. tumors, lesions, parkinsonism, or dystonia, it is important to reach varying and partially deep-sited neurological target areas with high precision at low medical risks while simultaneously avoiding eloquent, i.e. functionally critical, parts of the brain. In the field of stereotactic neurosurgery, these interventions are carried out by use of a stiff frame, on which the patient's head is mounted via fixation screws. This defines a global coordinate system to enable repeatable and predictable movements of cannulae via an additional aiming device, as shown in **Figure 1**. To date, stereotactic devices are limited to the use of straight cannulae, which can increase surgical risks or prohibit the whole surgery when the straight path between a target point and feasible entry points is near to eloquent brain parts. It is assumed that curved insertion paths would be a major step towards safer neurosurgical interventions [1].

So called continuum robots (CRs) –mechanical structures with a continuously deforming backbone – are seen as a promising solution for various minimally invasive surgical applications [2]. While numerous publications care for design, manufacturing, modelling, measurement, and control of these robots, research on their applicability to surgical demands and adaption to clinical circumstances is still in its infancy. Publications proposing new designs of medical CRs usually lack the integration in a clinical context and thorough studies on assumed medical benefits. Moreover, in the field of stereotactic neurosurgery, there is no CR system known which integrates into the total stereotactic procedure consisting of medical imaging, path planning, calculation of the aiming system's target coordinates, path validation and surgery. In [3], a specific CR design aimed towards neurosurgery is tested in-vivo on sheeps together with path planning and control algorithms, though without the usage of a stereotactic frame. In contrast to that, we assume a rigid stereotactic approach together with a stiffer type of CR with less degrees of freedom to achieve higher accuracies, especially in soft and gel-like brain tissue.

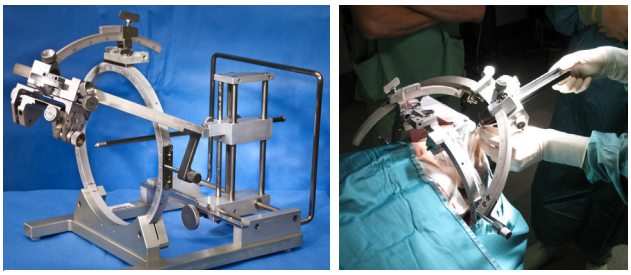

Figure 1 Riechert-Mundinger stereotactic device consisting of a base ring and a 4-DoF aiming arm in a target point simulator (**left**) and used for biopsy (**right**)

Therefore, this paper contributes with development and implementation of a complete toolchain for integrating a concentric tube continuum robot (CTCR) into a stereotactic procedure. Prior studies on mechanical design, path planning, optical measurements and radiological compatibility establish a basis for this work [1,4].

2 Workflow definition

The proposed workflow is visualized in **Figure 2**. The idea is to transform the complete conventional stereotactic surgical procedure to an application of CTCRs. Therefore, we start with the making of an artificial phantom head, which acts as a replacement for the real patient, simulating different radiological densities for skull, brain tissue and obstacles. As in the usual stereotactic procedure, the head is mounted in the stereotactic frame (here: Riechert-Mundinger type frame from *inomed Medizintechnik GmbH*) and radiological localization markers are applied. A subsequently computed tomography (CT) scan provides a 3D voxel data set in the DICOM format containing head and localization set.

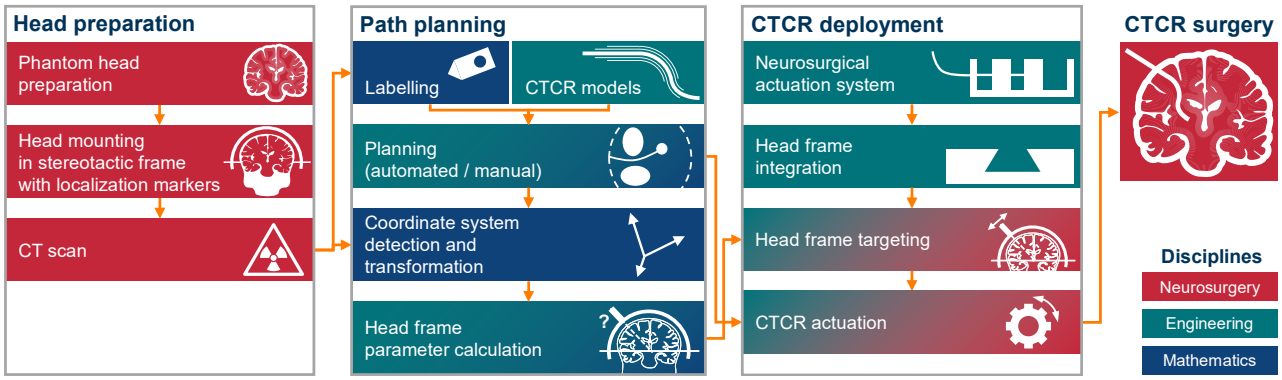

Figure 2 Proposed workflow for a stereotactic surgery of a phantom head using a CTCR

In contrast to the conventional approach, we now label different regions of the brain inside the DICOM data, including skull, hemisphere, feasible entry regions, obstacles, and the target region. Together with state-of-the-art mechanical models for CTCRs, we conduct a planning both by manual and automated approaches, making use of different parameter set for different exchangeable tubes. The result of the planning is visualized for the neurosurgeons with a possible iteration loop of the planning itself. In case of a feasible path, we continue with detection of the radiological localization set to establish the patient's coordinate system and transforming the planned path into it. To finish the planning phase, the aiming system's coordinates must be calculated in such a way, that the CTCR – being different to conventional devices w.r.t. geometrical properties – aims in the planned direction of the path.
For the surgery itself, we incorporate a CTCR prototype, which was designed specifically for the demands of this stereotactic application study, allowing precise movements of two tubes both in rotation and translation. The robot is mounted via a dovetail joint on the stereotactic aiming system, which is put onto the already prepared head and frame combination. The aiming system's coordinates are set, followed by clamping the selected tubes. After setting the tubes' rotation, we insert both tubes inside the phantom brain and observe the final configuration via a second CT scan.

3 Component development

3.1 Phantom head preparation

The phantom head serves as a model for the real patient's head in all stages of the workflow and, therefore, needs to reproduce different physical and radiological properties. This includes stiffness and tensile strength of the skull, reacting forces and stability of the brain-tissue-like gel and visibility as well as distinguishability of different head parts in the CT scan. Also, markers are needed for modelling obstacle and target regions. In [5], a standardized cranial phantom is described, which is taken as a starting point here.
For the skull, we start with commercially available plaster skull models designed for validation of cranial implants. After plugging holes in the skull, the head is filled up with 10% agar upside-down via the foramen magnum in layers. During this process, small spheres of bone cement are placed at different positions inside the agar, serving as target or obstacle markers. Finally, the foramen magnum is plugged and the phantom is cooled until application.
As a starting point for the CTCR surgery, the phantom head is mounted inside a conventional stereotactic ring in the surgery room in dorsal position, as shown in **Figure 3**. The localization set are fitted. A CT scan validates the resulting quality of the phantom head, where skull, brain tissue and targets/obstacles should be clearly visible. This CT scan is also the base for all following steps of path planning.

3.2 Labelling

In this step, we identify and label different parts of the brain as a base for path planning. We start with the raw DICOM data set, which gives a voxelized representation of the brain. In this, we define various labels as well as the set of voxels belonging to each label. The *Matlab Volume Segmenter* software is used here, offering different interpolation and labelling methods in order to avoid a time-consuming pixel-wise marking for each layer of the scan.

3.3 Manual path planning

To enable manual neurosurgical plannings of curved cannulae by medical personnel, a software tool with a graphical user interface (GUI) is developed. Its usability is inspired by state-of-the-art commercial software tools for conventional straight cannulae, which usually present three scrollable intersection views of the head – axial, sagittal and coronal view – combined with a probe view, where the

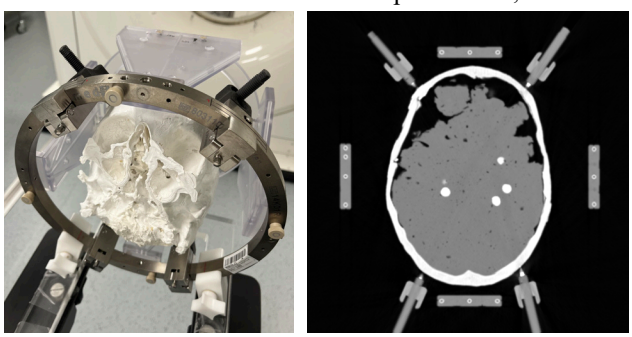

Figure 3 Phantom brain mounted in the stereotactic base ring with the translucent localization set (**left**) and one example slice of a CT scan of that same arrangement (**right**)

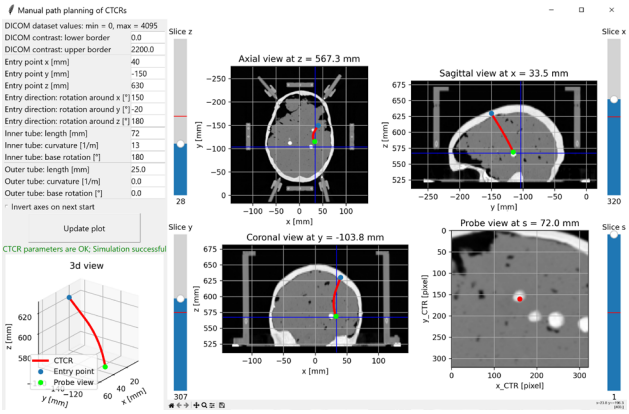

Figure 4 Exemplary screenshot of the manual path planning tool with loaded phantom brain data set: parameter input (top left), 3D visualization of the cannula (bottom left), main intersection views with sliders (mid), and a probe view at adjustable depths (bottom right)

intersection orthogonal to the cannula at selectable cannula backbone points is shown, enabling an endoscopic look "through the cannula". Since CTCRs exhibit greater complexity than straight cannulae, we also add a 3D view, where just the cannula itself is shown in the stereotactic coordinate system. For reduced complexity, we decided to limit the CTCR's parameter input to two tubes. We also used a simplified circular-arcs-model for the CTCR, in order to get rid of material parameters and diameters of the tubes. However, parameters and model can be easily extended in future, if necessary.

The overall GUI is shown in **Figure 4**. The implementation is done in *Python* and *tkinter* for platform-independence. For DICOM data support, the *pydicom* module is used, which reads in the 3D voxel image and cares for metadata like information on the coordinate system's position and pose. For the three main views, the robot is projected onto the intersection view. The probe view's is based on an interpolation of the voxel image at a given position with given orientation, defined by the cannula and the slider for the probe view's depth.

3.4 Automated path planning

While the manual planning tool allows the surgeons for a better understanding and controllability of the curved cannulae principle, the amount of parameters and their combinations hinders a time-efficient planning. To overcome this, a software toolchain for automated path planning using optimization techniques has been developed, as described in [4]. The automated path planning approach has been integrated into the stereotactic toolchain described here, using the labelled data as input and determining the cannula's path w.r.t. the stereotactic coordinate system.

3.5 Coordinate system transformation

The stereotactic localization set depicted in **Figure 3** contains 12 metallic rods arranged in 4 planes around the head in a certain known position and rotation relative to each

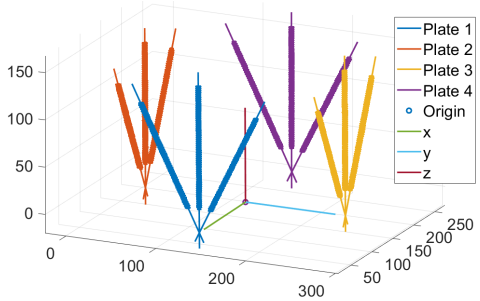

Figure 5 Plot of the clustered metal rods with fitted lines and the resulting coordinate system, expressed in mm

other. Additionally, a 13th rod marks the remaining orientation left to right. These rods are defining the stereotactic coordinate system, which is identified in this step.

The coordinate system is computed using the same CT scan from above. Since the head's position is known roughly, the voxels belonging to the head are cut off by defining static regions of interest. Next, all brightness values below 1230 and above 1800 are cut off, as they do not correspond to metallic material, leaving only the metal rods contained in the localization set and further metal parts of the head ring. Application of the DBSCAN clustering algorithm with a minimum squared Euclidean distance of 2 separates the rods from other parts. To differentiate between these, lines are fit to each cluster via singular value decomposition and filtered for the largest error. Since the rods are slender, the perpendicular distance to the fitted line is less than 4 voxels, whereas for the bulky metal parts the maximum distance is much higher. The remaining 13 clusters are matched to the localization set planes and their intersection points are computed as the point that minimizes the perpendicular distances to all three fitted lines.

Finally, the patient coordinate system is computed. The plate marked with a double rod corresponds to the positive x-direction. The z-direction is approximated as the mean of the directions of the middle, vertical rods. The y-direction is then computed as the vector product of z- and x-direction. The origin is set to the mean of the four intersection points. The results are shown in **Figure 5**.

3.6 Calculation of stereotactic coordinates

With the CTCR's path being determined and being expressed in the stereotactic coordinate system, the final step of the planning process is to find the four coordinates for the stereotactic aiming system displayed in **Figure 1**, which are azimuth, elevation and two tilting rotations. In [6], the geometrical dependencies for this type of stereotactic frame are described, which was used as a base for the implementation done here.

The stereotactic coordinate system from the last step is taken as the starting point. From there, the kinematics of the Riechert-Mundinger aiming system can be described by alternating translation and rotations of this coordinate system, until the transformed new coordinate system is identical to the CTCR exit point and orientation from the path planning. Additionally to conventional stereotactic procedures, the geometric relations introduced by the

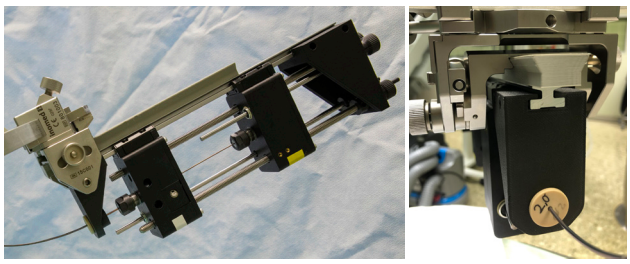

Figure 6 Two-tube manual actuation system mounted in the Riechert-Mundinger stereotactic system

CTCR actuation system, which differs in the relative position of the cannula's exit point, need to be incorporated. Besides geometrical constants coming from the stereotactic system, the four aiming system's coordinates arise as unknown variables. Also, the actuation system's insertion depth is an unknown coordinate introduced by the curving of the cannula. In total, these five coordinates can be found by solving the nonlinear system of equations under the condition of identical position and orientation of the CTCR at the actuation system's exit point.

3.7 Actuation system

A CTCR's actuation system fulfills the role of precisely setting the tubes' translation and rotation, while making measurements of the actuation quantities possible. For testing the complete workflow, we used the manually driven actuation system depicted in **Figure 6**, which is capable of driving two tubes with repetition accuracies of 200 µm and 2 °, respectively. In order to reduce weight and increase stiffnesses, housing parts are manufactured additively from PLA-CF. making use of stiffener and honeycomb structures. The tubes are mounted via a clamping mechanism [1]. Tribological plastics together with aluminium guides and spindles care for friction-stressed parts. In order to achieve self-blocking, high gear ratios, the rotations from the handwheels are translated via spindles and worm gears, respectively. An actuation can be measured by counting the number of rotations on the handwheels, supported by a rotating scale for finer reading.
For incorporation of the actuation system into stereotactic frame systems, the low maximum dimensions have to be considered in the design of the CTCR. Also, a dovetail guide is needed to mount the CTCR on the aiming arm. ON the dovetail, scales are representing the actuation system's insertion depth as calculated before.

3.8 Cannula insertion

At first, the tubes selected via the path planning have to be mounted in the actuation system. Afterwards, the rotations' zero point has to be set by estimating the position where the tubes' curvatures are only located in the x-z-plane. The rotations from the planning are set by the handwheels with a known gear ratio. For setting the zero point of the translations, the tubes have to be put in that position, where the tubes' distal ends is on the exit point of the actuation system. Afterwards, the tubes are actuated in the same way as the rotations, with the outer tube starting due to higher stiffness in order to minimize follow-the-leader-deviations.

4 Outlook

For the first time, the authors have developed a surgical intervention procedure for CTCR-driven curved cannulae for stereotactic neurosurgery. The approach has been validated to be viable with typical stereotactic equipment in clinical circumstances, however, a thorough investigation of reached target point accuracies as well as follow-the-leader deviations is left for future work, which can be done by CT-scanning the whole system after cannula insertion.
Starting from this, we aim towards more studies on the design of the actuation system itself, enabling an easier use by medical personnel, reduced dimensions, increased actuation accuracy, and a better compatibility with medical standards. The two path planning approaches could also be combined for more effective plannings incorporating neurosurgeons' knowledge. Open questions in the medical field are potential effects of curved cannulae on human brain tissue, the quantification of assumed benefits from this new type of surgery, and further steps towards a final medical application.

5 Acknowledgements

Fabian Rabel (Mechatronics Group, Technische Universität Ilmenau) has contributed to the mechanical design of the CTCR actuation system, depicted in **Figure 6**.
Funded by the Deutsche Forschungsgemeinschaft (DFG, German Research Foundation) – 501928699; 461953135.

6 Literature

[1] Mühlenhoff, J. et al.: A manually actuated continuum robot research platform for deployable shape-memory curved cannulae in stereotactic neurosurgery, ACTUATOR 2022, Mannheim, Germany, 2022

[2] da Veiga, T. et al.: Challenges of continuum robots in clinical context: a review, Prog. Biomed. Eng. 2.3 (2020), DOI: 10.1088/2516-1091/ab9f41

[3] Secoli, R. et al.: Modular robotic platform for precision neurosurgery with a bio-inspired needle: System overview and first in-vivo deployment, PLOS ONE 17.10 (2022), DOI: 10.1371/journal.pone.0275686

[4] Hoffmann, M.K. et al.: Path Planning for Concentric Tube Robots: A Toolchain with Application to Stereotactic Neurosurgery, IFAC-PapersOnLine 56.2 (2023), pp. 2871–2876, DOI: 10.1016/j.ifacol.2023.10.1403

[5] Krüger, M.T.: Development of a Standardized Cranial Phantom for Training and Optimization of Functional Stereotactic Operations, Stereotact. Funct. Neurosurg. 96.3, pp. 190-196, DOI: 10.1159/000489581

[6] Birg, W. et al.: Computer calculations of target parameters for a stereotactic apparatus, Acta Neurochir. 29 (1973), pp. 123–129, DOI: 10.1007/BF01414622

Inverse pneumatic artificial muscles with implantable vascular graft

Laura Galassi[1,2], Lucrezia Lorenzon[1,2], and Matteo Cianchetti[1,2]
[1]The BioRobotics Institute, Scuola Superiore Sant'Anna, Pisa, Italy.
[2]Department of Excellence in Robotics & AI, Scuola Superiore Sant'Anna, Pisa, Italy.
{laura.galassi, lucrezia.lorenzon, matteo.cianchetti}@santannapisa.it

Abstract

This study aims to design Inverse Pneumatic Artificial Muscles (IPAMs) integrating a commercial implantable vascular graft as deformation-guiding element. Mechanical characterization tests revealed reliable behavior, maximum elongation and contraction up to 160% and -60%, respectively, and a tensile force up to 23 N. The proposed IPAM offers design flexibility for different application related requirements, such as force, dimensions and strain. This study represents an initial step toward a fully soft and biocompatible IPAM suitable for implantable soft robotic applications.

1 Introduction

Traditional Pneumatic Artificial Muscles (PAMs) suffer from low energy conversion efficiency, due to radial expansion, limiting their effectiveness and operational range.[1] Recently, IPAMs were studied, offering enhanced performances and wider operational ranges compared to PAMs, up to 300% strain. This type of actuator operates in a reverse modality to traditional PAMs: when subjected to pressure, the IPAM extends, while reducing the internal pressure, it contracts.[2] IPAMs typically are characterized by an inflatable elastomeric air chamber, externally reinforced with inextensible fibers that guide the deformation upon inflation.[3],[4] The external reinforcing structure aims to constrain radial expansion and prevent the ballooning effect.[5] Current IPAMs face issues such as material properties mismatch, and interface problems due to the presence of rigid components, with related implantability limitations.[6]-[8] In this work, we propose an IPAM incorporating a soft and biocompatible reinforcing structure composed of a commercial vascular graft. The employed vascular graft has previously been used in a minimally invasive surgery (MIS) manipulator.[9] In general, MIS manipulators come into close contact with internal organs and tissues while approaching the surgical site. Thus, ensuring a safe interaction with the body is crucial.[10] The development of soft robotics technologies, driven by the use of compliant and highly deformable materials, offers a potential solution to address safety concerns in constrained environments. [11]-[13] The compliance of these materials allows soft devices to be intrinsically safe and adaptable, particularly in unstructured working environments.[14]

2 Materials and Methods

2.1 Design of an IPAM with integrated vascular graft

The proposed IPAM is composed of three components: an internal pneumatic chamber, an external reinforcing structure and two end-caps at the extremities (**Figure 1**). The pneumatic chamber has an external diameter of 9 mm and a length of 60 mm. It is characterized by a hollow central channel for the air, of diameter equal to 2 mm. Two pneumatic chambers were fabricated of two typologies of silicones (Smooth-on, Inc.), having different stiffnesses: Ecoflex 00-30 (EF30) and Dragon Skin 10 (DS10). EF30 is characterized by shore hardness 00-30 and 100% modulus equal to 10 psi, DS10 has shore hardness 10 A and 100% modulus equal to 22 psi. The external reinforcing structure is made of a commercial knitted polyester vascular graft (Vaskutek Inc., Terumo Company, UK), of length 35 mm, internal diameter of 10 mm, and external diameter of 12 mm. The reinforcing structure has the function of giving the direction of the elongation: pure elongation is caused by applying positive pressure to the pneumatic chamber, it constrains the actuator radial expansion and drives the deformation along its principal axis. In addition, it prevents the ballooning effect and provides a protective sheath to the silicone. The actuator's extremities are characterized by the presence of two cylindrical end-caps, one allowed the connection to the air supply, the other sealed the actuator. The end-caps are fabricated in Smooth-Sil 950 (Smooth-on, Inc.). In addition, they allow to couple the elastomeric chamber with the reinforcing structure, by embedding them. The design specifications are summarized in **Table 1.**

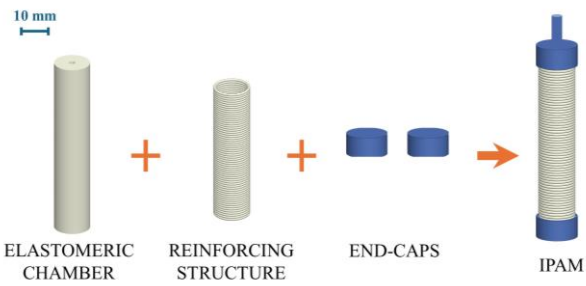

Figure 1 IPAM's components: internal elastomeric chamber, external reinforcing structure, two end-caps at the extremities. One end-cap is sealed, the other can be connected to the air supply.

Table 1. Design specifications of IPAM's components.

	Pneumatic chamber	**Reinforcing structure**	**End-caps**
Internal diameter [mm]	2	10	2
External diameter [mm]	9	12	14
Length [mm]	60	35	8
Material	Ecoflex 00-30 / Dragon Skin 10	Vascular graft	Smooth-Sil 950

2.2 Manufacturing procedure of the IPAM

The manufacturing procedure of the IPAM is illustrated in **Figure 2**. The elastomeric chamber was fabricated by injection molding and the hollow channel was created by inserting a metallic rod in the cylindrical mold (step 1 and 2). After the demolding of the elastomeric chamber (step 3), the end-caps were cast one at a time. To ensure proper integration between the components, the vascular graft was placed coaxial with the elastomeric chamber and dipped in the liquid silicone which was poured in the mold to create the end-cap (step 4 and 5). This procedure guaranteed the bonding between the vascular graft, the elastomeric chamber and the end-cap. The procedure was repeated for the second end-cap on the other extremity. In the end, a flexible tube for pneumatic actuation, with an external diameter equal to 4 mm, was inserted in one of the holes at the two extremities and it was fixed with silicone glue (Sil-Poxy, Smooth-On Inc.). The hole in the other extremity was sealed with a small amount of Smooth-Sil 950.

2.3 Mechanical Characterization of the IPAMs

Mechanical characterization of the IPAMs included cyclic and until burst strain-pressure experiments, and unidirectional tensile force-strain experiments.

2.3.1 Strain-pressure experiments

At first, the strain-pressure experiment was performed until burst, and then, on different samples, in a cyclic modality. Both tests were conducted with one IPAM prototype in EF30 and one in DS10. The experiment was made by measuring the actuator's active length, at different levels of pneumatic pressure applied to the pneumatic chamber. The active length is the portion of the actuator that undergoes elongation and contraction when pressurized and depressurized. This length is in between the two end-caps. A compressor (Fiac Air Compressors, Leonardo) provided the continuous air supply and an electronic valve (CAMOZZI, K8P0-D522-08) controlled the supplied pressure. A digital manometer (CAMOZZI, SWCN-P10-P3-2) connected to the actuator continuously monitored its internal pressure. The actuator length was measured at each pressure step using a caliper, and the strain was computed as:

$$\varepsilon = \frac{L_a - L_0}{L_0}. \quad (1)$$

where L_a is the actual active length of the actuator, and L_0 is its rest length at 0 bar. The maximum elongation and the maximum contraction were calculated as:

$$\varepsilon_e = \frac{L_{max} - L_0}{L_0}, \quad (2)$$

$$\varepsilon_c = \frac{L_o - L_{max}}{L_{max}}. \quad (3)$$

where L_{max} is the maximum achieved actuator length at the maximum applied pressure.

2.3.1.1 Strain-pressure experiments until burst

Firstly, to define the operative range of the two typologies of IPAMs, the strain-pressure experiments were performed until burst. The inflation pressure for the EF30 actuator was set from 0 bar up to 1 bar, in 0.2 steps. On the other hand, due to the higher stiffness of the elastomeric chamber, DS10 IPAM was tested up to 3.2 bar with 0.4 bar of increment.

2.3.1.2 Cyclic strain-pressure experiments

Regarding the strain-pressure experiments in the cyclic modality, the actuators underwent three cycles of loading and unloading at 13 pressure levels, ranging from 0 bar to 0.6 bar in 0.05 steps for the EF30 prototype, and up to 2.4 bar with 0.2 bar of increment for the DS10 IPAM. To reduce the influence of the Mullin's effect on the results, the first cycle was discarded from the data analysis.

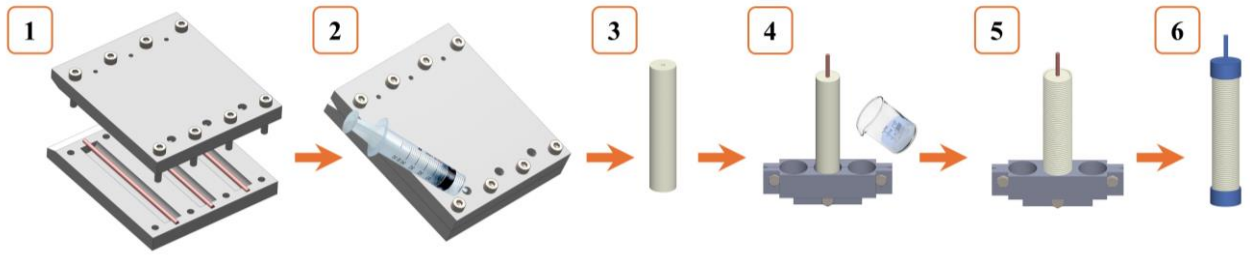

Figure 2 IPAM manufacturing procedure: 1) Mold used for the fabrication of the elastomeric chamber; 2) injection molding step; 3) demolding of the elastomeric chamber; 4) casting of one end-cap; 5) positioning of the vascular graft in the mold; this step is repeated for the other end-cap; 6) prototype of the IPAM with vascular graft.

2.3.2 Force-strain experiments

The force-strain characterization employed a Universal Testing Machine (INSTRON 5965, Norwood, MA, USA), equipped with 1 kN load cell. A tensile test was performed on one EF30 and one DS10 IPAM, up to 150% of strain at a rate of 50 mm/min. The test was repeated at different actuator's internal pressure. For EF30 IPAM the force was recorded at 0, 0.2, 0.4 and 0.6 bar and for DS20 IPAM at 0, 0.8, 1.6 and 2.4 bar. For each pressure level, the cross-bar of the testing machine was manually moved to reach the zero force and the tensile test was repeated. Taking into account the Mullin's effect, the first loading curve at null pressure was excluded.

3 Results and discussion

3.1 IPAM prototype with integrated vascular graft

The designed and fabricated IPAM with vascular graft is shown in **Figure 3 (a)**. Due to the limited availability and high costs of the commercial vascular grafts, we fabricated prototypes, one for each material typology.

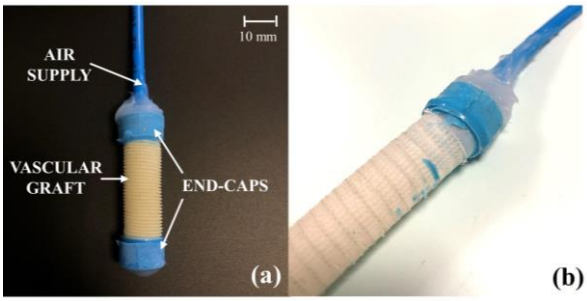

Figure 3 (a) IPAM prototype with integrated vascular graft; (b) observed delamination at the interface between vascular graft and end-cap during the strain-pressure experiment until burst.

3.2 Mechanical characterization

3.2.1 Strain-pressure experiments

The strain-pressure experiments until burst allowed to determine the operative pressure range of the prototypes. EF30 and DS10 IPAMs reached the maximum elongation at 1 bar and 3.2 bar, respectively (**Figure 4**). Experimental evidence showed that the maximum elongation of the actuators was determined by the maximum axial elongation of the employed vascular grafts. At the end of the experiment until burst, the IPAMs exhibited delamination at the end-caps, as shown in **Figure 3 (b)**. The computation of the maximum elongation and contraction revealed that EF30 IPAM allowed larger elongation (161%) and contraction (-62%) than the DS10 IPAM (139% and -58%) due to the different elasticity of the materials.

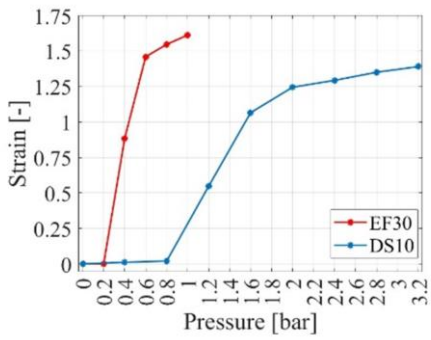

Figure 4 Strain-pressure experiment until burst for EF30 IPAM (red curve) and DS10 IPAM (blue curve).

For setting an appropriate pressure range during the cyclic experiments, the operative pressure range was evaluated. In particular, to avoid the risk of delamination and bursting, the maximum pressure was set two steps before the maximum pressure used in the experiment until burst, thus, at 0.6 bar and 2.4 bar for EF30 and DS10 IPAMs, respectively. As expected, the strain-pressure relationships of both the EF30 and DS10 IPAMs are non-linear and show hysteresis (**Figure 5**). Additionally, the plots present similar trends: an initial offset is related to the fact that the actuator's length only slightly changes at low pressures. This occurs because, at low pressures, the elastomeric chamber undergoes minimal radial expansion. With the increasing pressure, the external surface of the elastomeric chamber gets contact with the inner wall of the vascular graft, and the elongation of the actuator starts. Furthermore, both the plots are characterized by a linear path at intermediate actuation pressures, and a final plateau, when the actuator gets close to its maximum length.

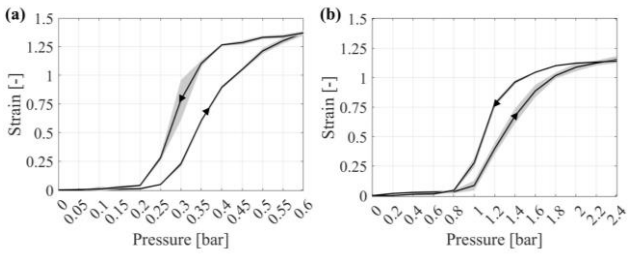

Figure 5 Cyclic strain-pressure experiments: (a) EF30 IPAM, (b) DS10 IPAM.

3.2.2 Force-strain experiments

The force-strain characterization demonstrated the ability of the IPAMs to exert variable pulling force for a fixed actuator length, depending on both the material of the elastomeric chamber and the inflating pressure. At atmospheric pressure, the EF30 prototype achieved a maximum pulling force of 7 N and the DS10 prototype of 23 N (**Figure 6**). Both IPAM typologies showed the same trend: increasing the pressure, the behavior approaches the linearity, the initial length increases, the final force decreases and the stiffness increases. Indeed, the slope of the different curves increases with the pressure. The results of this experiment

demonstrated that, for a fixed actuator length, given by the requirements of the envisioned application, it is possible to obtain different tensile forces by changing the pressure in the actuator. In addition, with slight modifications to the actuator design, such as the geometry (internal and/or external elastomeric chamber diameter) or the stiffness of the constitutive material of the elastomeric chamber, it is possible to tune the actuator's characteristics of maximum elongation/contraction and pulling force.

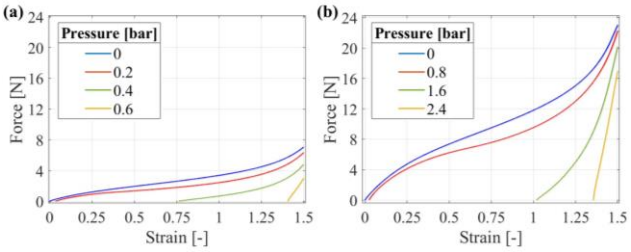

Figure 6 Tensile force-strain experiments: (a) EF30 IPAM, (b) DS10 IPAM.

4 Conclusions

The proposed IPAM prototype demonstrated adaptability to application requirements. Future investigations should focus on the performance of IPAMs, with changes in geometric features of the elastomeric chamber, constitutive materials, and vascular graft length at rest. Indeed, the vascular graft is a bellow and the number of crests in the active length of the IPAM significantly impacts the actuator's elongation. At equal active length, by incorporating a compressed segment of vascular graft, thus having a higher number of crests, the axial deformation range of the IPAM will be widened. In this preliminary study, the experiments were performed on a single prototype for each material typology; thus, to increase the statistical significance, the results should be verified across multiple samples. In our expectations, the standardized fabrication procedure that we have described here, will give consistent and repeatable outcomes. Additional experiments will be required to test the durability of the IPAMs too. Based on the results obtained from this study, the delamination at the end-caps noticed at high pressures represents the major concern. However, it was observed at high pressure only, and at the extension limits of the employed vascular graft, while a safe operational range was still wide (up to 0.6 bar and 2.4 bar for the EF30 and the DS10 IPAM, respectively). In addition, a stronger bonding of the vascular graft to the elastomeric chamber and the end-caps could be achieved by optimizing the fabrication procedure and, for example, externally reinforcing the interface through heat shrink sleeves. In future studies, biocompatible silicone materials (e.g., Elkem Silicones France SAS) will be used to manufacture the elastomeric chamber and the end-caps, thus creating a fully implantable IPAM for biomedical applications. Here, the presented IPAM is the first proof-of-concept of a fully soft and (possibly) implantable actuator, which has the potential to be an implantable actuation system for medical devices, artificial organs and prostheses.

5 Literature

[1] Skorina, E. H. *et al.*: Reverse pneumatic artificial muscles (rPAMs): Modeling, integration, and control,*PLOS ONE*, vol. 13, no. 10, p. e0204637, Oct. 2018.

[2] Hawkes, E. W. *et al.*: Design and implementation of a 300% strain soft artificial muscle, in *2016 IEEE International Conference on Robotics and Automation (ICRA)*, May 2016, pp. 4022–4029.

[3] Sridar, S. *et al.*: Hydro Muscle - a novel soft fluidic actuator, in *2016 IEEE International Conference on Robotics and Automation (ICRA)*, May 2016, pp. 4014–4021.

[4] Zhu, M. *et al.*: Fluidic Fabric Muscle Sheets for Wearable and Soft Robotics,*Soft Robotics*, vol. 7, no. 2, pp. 179–197, Apr. 2020.

[5] Elsayed, Y. *et al.*: Crimped braided sleeves for soft, actuating arm in robotic abdominal surgery, *Minimally Invasive Therapy & Allied Technologies*, vol. 24, no. 4, pp. 204–210, Jul. 201.

[6] Yukisawa, T. *et al.*: Modeling of extensible pneumatic actuator with bellows (EPAB) for continuum arm, in *2017 IEEE International Conference on Robotics and Biomimetics (ROBIO)*, Dec. 2017, pp. 2303–2308.

[7] Lorenzon, L. *et al.*: Modelling and characterization of a Soft Inverse Pneumatic Artificial Muscle, in *ACTUATOR; International Conference and Exhibition on New Actuator Systems and Applications 2021*, Feb. 2021, pp. 1–4.

[8] Roche, E. T. *et al.*: A Bioinspired Soft Actuated Material, *Advanced Materials*, vol. 26, no. 8, pp. 1200–1206, 2014.

[9] Gerboni, G. *et al.*: Modular soft mechatronic manipulator for minimally invasive surgery (MIS): overall architecture and development of a fully integrated soft module, *Meccanica*, vol. 50, no. 11, pp. 2865–2878, Nov. 2015.

[10] Cianchetti, M. *et al.*: Soft Robotics Technologies to Address Shortcomings in Today's Minimally Invasive Surgery: The STIFF-FLOP Approach, *Soft Robotics*, vol. 1, no. 2, pp. 122–131, Jun. 2014.

[11] Majidi, C. *et al.*: Soft Robotics: A Perspective—Current Trends and Prospects for the Future," *Soft Robotics*, vol. 1, no. 1, pp. 5–11, Mar. 2014.

[12] Laschi, C. *et al.*: Soft Robotics: New Perspectives for Robot Bodyware and Control, *Front. Bioeng. Biotechnol.*, vol. 2, Jan. 2014.

[13] Paternò, L. *et al.*: Soft robotics in wearable and implantable medical applications: Translational challenges and future outlooks," *Front. Robot. AI*, vol. 10, Feb. 2023.

[14] Ranzani, T. *et al.*: A bioinspired soft manipulator for minimally invasive surgery, *Bioinspir. Biomim.*, vol. 10, no. 3, p. 035008, May 2015.

An origami-based fluidic actuator for Minimally Invasive Surgery

Le Gall Alexia, Scuola Superiore Sant'Anna, Italy, Alexia.LeGall@santannapisa.it
Dangel Théo, Scuola Superiore Sant'Anna, Italy, Theo.Dangel@santannapisa.it
Chen Zixi, Scuola Superiore Sant'Anna, Italy , Zixi.Chen@santannapisa.it
Cianchetti Matteo, Scuola Superiore Sant'Anna, Italy, Matteo.Cianchetti@santannapisa.it

Abstract

Minimally Invasive Surgery (MIS) has transformed surgery by reducing invasiveness and post-operative pain. Traditional pneumatic actuators, while effective, often suffer from high-pressure range and complex fabrication steps. This paper introduces a compact origami-based actuator optimized for elongation within the MIS-size range. Our study demonstrates a strain within the range of 130%, offering more efficient surgical tools.

1 Introduction

1.1 Minimally Invasive surgery and pneumatics

Minimally Invasive Surgery (MIS) has long been the gold standard for reducing patient trauma but its progress is impeded by the lack of development of new surgical tools that can interact safely with human tissues. Soft actuators in MIS must meet specific requirements, including small size and safety. Although soft robotics offers numerous actuation solutions easily down-scalable, they require high current or temperatures, damageable to human tissues. Pneumatics, though bulky, is favoured [1] for its high output force and inherent safety. In an effort to reduce the bulkiness of the whole fluidic circuit, we designed a soft fluidic chamber working at a lower range of pressure by deploying instead of deforming [2] thanks to origami folding. Its optimal dimensions are a diameter D = 11mm for a maximum height of H = 8mm.

1.2 Origami and soft robotics

Origami structures allow for the folding and deployment of a seemingly bigger area in a smaller volume and thus while adopting different kinematic behaviors like extension with a Yoshimura's pattern [3] or twisting with a Kresling's pattern[4]. In the context of a fluidic chamber, which require enclosure, we focus on origami bellows [5] as a subset of origami patterns. Multiple works, showcased in **Erreur ! Source du renvoi introuvable.**, already explore the use of origami for large deformations in compliant bodies through a large range of fabrication methods. Our work builds upon this foundation by proposing a novel approach to fabricate normally folded origami to deploy upon pressurization. Injection molding allows for the creation of complex shapes while keeping precise dimensions without the need for labor-intensive processes like folding, sewing, heat sealing, or layer casting [2]. Furthermore, the process is scalable and allows for a wide range of materials to be used: overall, it offers the versatility and precision needed. As a first approach, we limited our actuator to a 1DoF (extension) movement based on Yoshimura's pattern.

2 Methods

2.1 Yoshimura's pattern and parametrization

A tessellation can be defined as the repetition of a cell. Based on [5], we define one cell of Yoshimura's pattern as in 2b. Deployment is based on the height h of a cell which defines the height of the unfolded origami h_t as a multiple of the number of unit cells deployed. Before studying our origami, we add two geometrical constraints:

• Our bellows is circumscribed in a circle of diameter D as to maintain stability during the deployment.

• We maintain two planar symmetries to ensure a 1DoF extension.

We can therefore describe the cell with the following model:

$l_{n_x} = D * sin\left(\frac{\pi}{n_x}\right)$, the length of the polygon's side

$h = D * cos\left(\frac{\pi}{n_x}\right)$, the height of the unit cell

Name	Author	Year	Strain	Pressure [kPa]	Fabrication
A Compact Soft Robotic Wrist Brace With Origami Actuators	Liu et al	2021	0,31	185	Blow molding
Deployable Soft Pneumatic Networks (D-PneuNets) Actuator With Dual-Morphing Origami Chambers for High-Compactness	Woongbae et al	2022	1,63	10	Layer Stacking Molding
Origami-Inspired Soft Pneumatic Actuators: Generalization and Design Optimization	Zaghloul A.	2023	0,46	-80	3D printing
Elastomeric Origami: Programmable Paper-Elastomer Composites as Pneumatic Actuators	Martinez et al	2012	2,5	15	Overmolding Paper
This work		2023	1,35	15	Injection

Table 1 State of the Art of different Yoshimura's based soft fluidic actuators for medical applications.

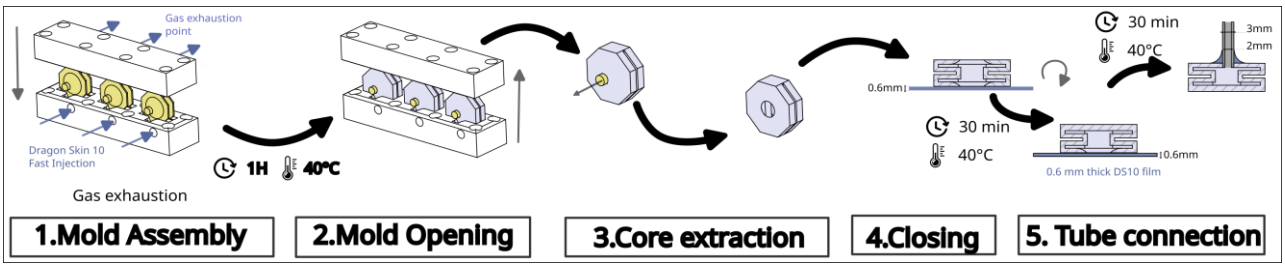

Figure 1 Fabrication of the chambers

Therefore for a set diameter, increasing the number of sides n_x will reduce the maximum height of each unfolded cell.
The minimum number of sides to ensure enclosure is n_x=3 [5]: in our work, we will choose $n_x = 4$ to ensure stability during the unfolding.
As we aim to work at lower scales, the precision of the fabrication method could begin to interfere with the design of the actuator molds and be a source of imprecision if not accounted for. Therefore we propose a modification of the pattern as illustrated in **Figure *3***, and define by the following parameters:

- t_g, the thickness of the chamber;
- t_v, the minimal thickness of the walls of the molds;
- $t_m = t_v + 2*t_g$, the minimal thickness of the mountain folds.

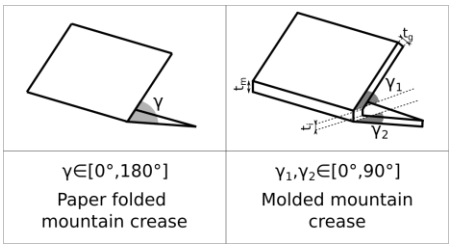

Figure 2 Modification of the creases to account for fabrication limitations.

2.2 Manufacturing of the chambers

All prototypes are injection-molded using Dragon Skin 10 Fast and cured at 40°C for 60 minutes. Molds were 3D printed in PLA via FDM (RAISE 3DE2 - Creality) with a precision of $0.1 * 0.1 * 0.1$mm. The fabrication of a chamber is illustrated in **Figure *1***.
Three chambers, one of each type were fabricated and then characterized. To compare the modified and optimized patterns, it was decided to scale the size of the actuator by two for practical considerations related to the ease and precision of characterization. A real-scale chamber of the optimized version was then compared to the scaled version to ensure the coherence of the comparison despite the scaling.

3 Results

3.1 Original pattern optimization

To optimize the extension, we will be studying the strain of the two patterns.
To account for the thickness of the wall, we model each crease of the flat pattern as a thick crease following **Figure *2*** parametrization and introduce different values for the different thicknesses, based on the fabrication method chosen:

- t_v = 0.4mm, minimal thickness of a wall in FDM
- t_g = 0.6mm, minimal wall thickness of silicone
- t_m = 1.6mm

As a first approach, we keep the framework of a regular, n-sided polygon and we get the following model with $n_x = 8$:

$$l_{n_x} = D * sin(\pi/8) = 4.2mm$$
$$h = l_{n_x}/\sqrt{2}$$
$$h_{t,f} = 2 * h + \mathrm{h_{t,0}}$$
$$h_{t,0} = 2 * \mathrm{t_m} + \mathrm{t_v} = 3.6mm$$
$$\Delta h = \frac{h_{t,f} - h_{t,0}}{h_{t,0}} = \frac{\sqrt{2} * l_{n_x}}{h_{t,0}} \approx 1.65$$

Transformation is illustrated in **Figure *3***. Without any optimization, one of the origami chambers should showcase a strain of 165%.
To optimize the strain of our model, we will break the assumption of a n-sided polygon as shown in **Figure *4***.
From the geometric model we obtain the prospective strain :

$$l_{n_x} = D * sin\left(\frac{\pi}{4} - asin\left(\frac{t_m}{D}\right)\right) \approx 6.6$$
$$h = \frac{l_{n_x}}{sqrt(2)} \approx 4.7$$
$$h_{t,f} = 2 * h + h_{t,0} = l_{n_x} * \sqrt{(2)} + h_{t,0}$$
$$h_{t,0} = 2 * t_m + t_v = 3.6mm$$
$$\Delta h = \frac{2 * h}{h_{t,0}} \approx 2{,}6$$

We expect a strain of 260 % for the optimized version of the origami pattern.

3.2 Characterisation

Characterization of a modified pattern and optimized pattern were conducted and are presented in **Figure *4***. Experimental results are compared to the theoretical value.
All three samples present similar behaviour when pressurized: a first fast, linear slope followed by a second flatter slope. Both scaled-up versions peak around 15 kPa, whereas the scaled-down version peaks around 7kPa, but at a similar strain to its counterpart.

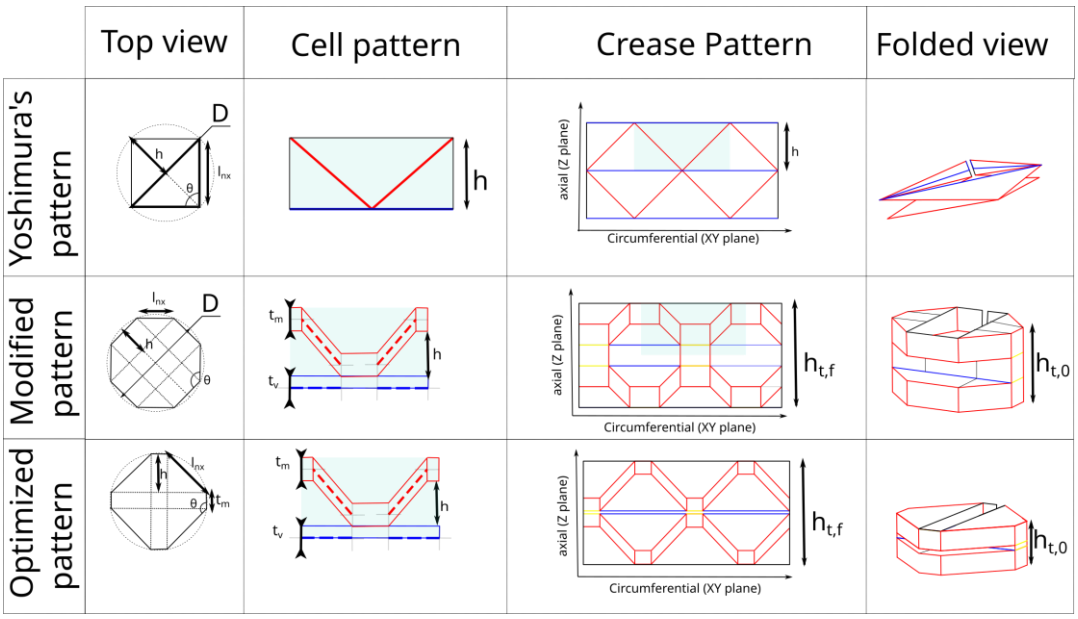

Figure 3 Different views and parametrization of the three patterns studied in this work.

Both the optimized chambers have a maximum strain of 135% whereas the solely modified chamber has a maximum strain of 90%.
However, if this strain is enough to make the actuators comparable to the state of the art, all chambers fall short of their theoretical maximum: fault may lay in the boundary conditions, the tubing stopping the proper deployment of the pattern, or in the unwanted deformation of the chamber walls.

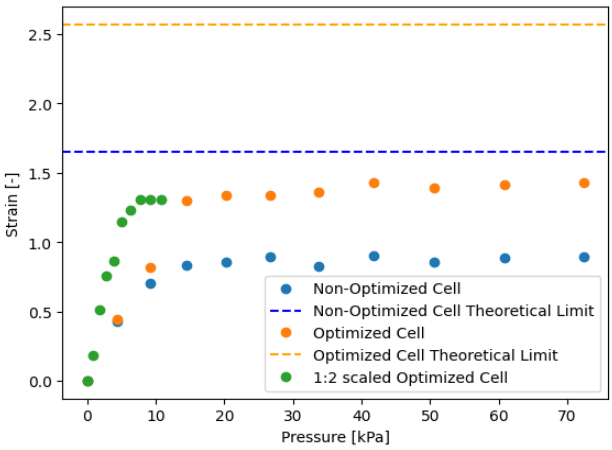

Figure 4 Strain of the different fluidic chambers tested for an input pressure (kPa) compared to their theoretical maximum value.

4 Discussion

In this study, we have introduced the design, geometric optimization, and fabrication of a fluidic chamber based on a Yoshimura pattern. If progress can be made to take advantage of the full range of motion offered by the origami, our actuator deploys within 130% of its initial size, at less than 20 kPa, despite being in the size range of MIS. Future work will focus on further characterization of the fluidic chambers and their behavior, by in silico or experimental means.

5 Literature

[1] M. Runciman, “Soft Robotics in Minimally Invasive Surgery,” Soft Robotics, vol. 6, pp. 423–443, Aug. 2019.

[2] W. Kim, “Bioinspired dual-morphing stretchable origami,” Science Robotics, vol. 4, no. 36, Nov. 2019.

[3] H. Jiang, “Parametric design of developable structure based on Yoshimura origami pattern,” Sustainable Structures, vol. 2, 2022.

[4] B. Kresling, “Origami-structures in nature: Lessons in designing ”smart” materials,” MRS Proceedings, vol. 1420, Jan. 1, 2012.

[5] A. Reid, “Geometry and design of origami bellows with tunable response,” Physical Review E, vol. 95, no. 1, p. 013 002

[6] H. Hummler,“Impact of Tablet Size and Shape on the Swallowability in Older Adults”, Pharmaceutics, vol.15, no. 4, p.1042

Biomimetic Hygromorphic Actuator Systems

Jürgen Rühe, University of Freiburg, IMTEK – Department of Microsystems Engineering, Freiburg, Germany, ruehe@imtek.de

Abstract

In this contribution we demonstrate how hygromorphic actuators can be generated based on the biological example of the pinecone. The actuation principle in the technical system is similar to the pinecone as the bending is caused by a hygroscopic layer which takes up water and swells upon rising relative humidities. The technical system, however, bends upon drying rather then swelling. We will also present ideas and first results of cooperative systems which include a second stimulus for swelling and deswelling.

1 Biological concepts as guide for systems design

Cooperative and synchronized actuators and actuator fields are found in many different types in biological systems. Two examples are cilia fields [1] used for transport purposes and pine cones which open or close their wings depending on humidity [2]. These two examples cover two very different length scales as well. Researchers now look for ways to mimic such systems and to build complex actuator fields which react to multiple stimuli both in a linear and non-linear fashion.

In this contribution we report on research that aims at the generation of actuators and actuator fields in which the individual actuators may eventually react to multiple stimuli such as alternating magnetic fields and humidity. Our methods are based on thermal and photochemical fabrication schemes which use C,H insertion crosslinking (CHic) reactions to generate surface-attached polymer networks. This chemical strategy can be combined with various methods for microstructuring such as 3D printing, molding, and coating techniques.

Here, we focus mainly on biomimetic hygromorphic systems derived from the pine cone. In this system it is not just a bilayer mechanism based on an actuating (swellable) layer and an restrictive (non- or lesser swellable) fiber tissue layer but a delicate interplay of the mechanical and hydraulic properties of each structural component. Investigations of the exact mechanism using also micro-computed tomography (µ-CT) investigations (see Figure 1) along with finite element simulations have yielded a model that describes both the pinecone actuation principles and serves as a guide for the development of biomimetic hygromorphic systems [2].

2 Hygromorphic actuators

Based on the studies on biological actuator examples we have designed a hygromorphic actuator that bends open or closed upon change of humidity. One key learning of the pine cone studies was that the pinecone bends during water uptake because the elongation of the sclereid cells proceeds along the passive layer. Based on this finding we have designed a bilayer system that is fully stretched in the swollen state and bends upon drying. The bending is driven by the force that a hydrogel layer exerts on a underlying passive layer.

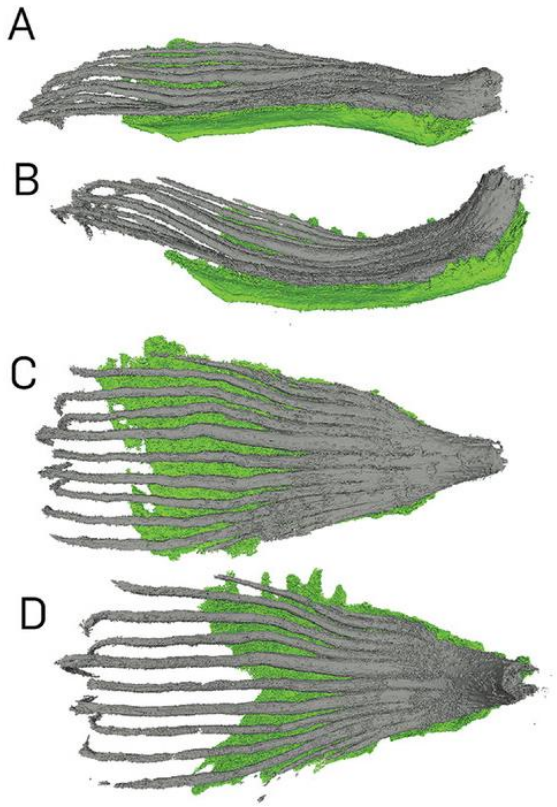

Figure 1 Tissues of a scale of P. sylvestris reconstructed based on µ-CT-scanning. In the dry state, the lateral view shows a straight scale, where the sclerenchyma fiber strands (gray) lies on the sclereid layer (green) A). The lateral view of the scale in the wet state shows a bent scale in upwards direction B). The top view of the dry state shows the sclerenchyma fiber strands spreading in the scale C). In the dry state, the differentiation between sclereid layer and brown tissue was not always possible, which is why the sclereid layer looks so different from C) to D). The top view of the wet state D).

The hydrogel layer was generated on top of the passive layer from polydimethylacrylamide (PDMAA) precursor polymers that contained a few percent of a crosslinker for C,H insertion crosslinking (Chic) as described here [3,4, 5]. The copolymer used in this study was prepared by free-radical polymerisation from DMAA and the crosslinker monomer. The synthesis of the crosslinker monomer is described in detail in reference [5].

Figure 2 shows the chemistry behind the layer formation and also provides typical fabrication parameters. It should be noted that the crosslinking does not only occur between the PDMAA chains but also across the interface to the substrate polymer. In this way a very strong chemical adhesion is established which is needed to avoid delamination during actuation.

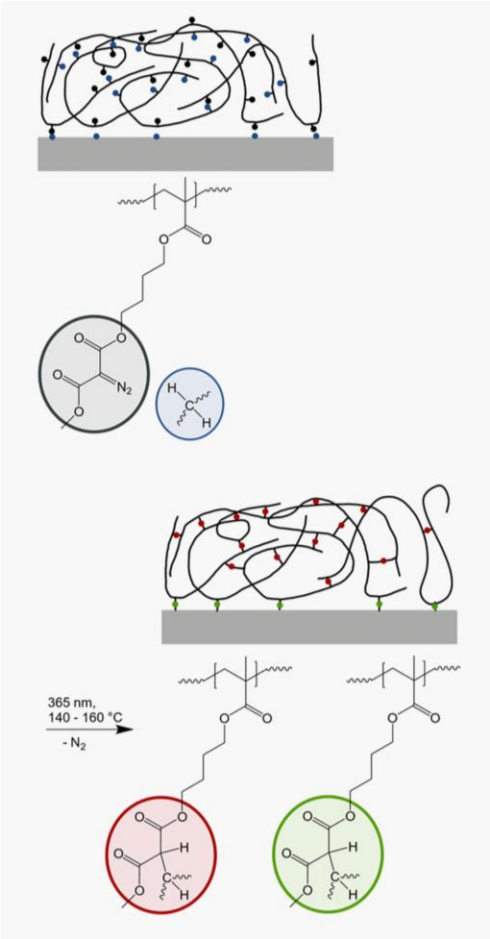

Figure 2 Mechanism of layer formation via Chic crosslinking. Upon thermal or photochemical activation the corsslinker forms a reactive species which inserts into a C,H group of a neighboring polymer chain which may be another PDMMA chain or one from the substrate.

Figure 3 shows the working principle of an actuator based on this system. Two situations are shown. In both cases the temperature was approximately identical (22 - 23°C). However the relative humidity was set to 30% in image A and to 76% in image B.

So far this system is actuated exclusively by the stimulus humidity which causes swelling or shrinking of a layer deposited on a passive carrier foil. Many of the features of the pinecone example are translated into this technical scheme but an extension to a cooperative system is envisioned.

To do so a second stimulus needs to be integrated. This stimulus may be provided by a third component or integrated with the components already used. Here, we study the use of hydrogels or hydrogel layers which show an LCST (lower critical solution temperature) behaviour. The swelling of such layers is then not only depending on the humidity but also on the temperature and a short rise in temperature may trigger a collapse of the layer even at high humidity.

A

B

Figure 3 Bilayer system at room temperature and A) 30% rel. humidity and B) at 76% rel. humidity. The strip straightens up upon swelling of the hydrogel layer deposited on a passive layer.

3 Literature

[1] Belardi, J.: Schorr, N.: Prucker, O.: Rühe, J.: Artificial: Generation of Magnetice Actuators in Microfluidic Systems. Advanced Functional Materials, 21 (2011), 3314-3320. DOI: 10.1002/adfm.201100787.

[2] Eger, C.J.: Horstmann, M.: Poppinga, s.: Sachse, R.: Thierer, R.: Nestle, N.: Bruchmann, B.: Speck, T.: Bischoff, M.: Rühe, J.: The Structural and Mechanical Basis for Passive-Hydraulic Pine Cone Actuation. Advanced Science (2022) 2200458. DOI: 10.1002/advs.202200458

[3] Pandiyarajan, C.K.: Prucker, O.: Ruhe, J.: Humidity Driven Swelling of the Surface-Attached Poly(N-alkylacrylamide) Hydrogels. Macromolecules 49 (2016), 8254-8264. DOI: 10.1021/acs.macromol.6b01379.

[4] Prucker, O.: Brandstetter, T.: Rühe J.: Surface-attached hydrogel coatings via C,H-insertion crosslinking for biomedical and bioanalytical applications (Review). Biointerphases 13 (2018) 010801. DOI: 10.1116/1.4999786

[5] Kost, J.; Bleiziffer, A.; Rusitov, D.; Rühe, J.; Thermally Induced Cross-Linking of Polymers via C,H Insertion Cross-Linking (CHic) under Mild Conditions; J. Am. Chem. Soc. 143 (2021) 10108. DOI: 10.1021/jacs.1c02133)

Development of a 3D-Bendable soft Robotic Segment actuated by Rolled Dielectric Elastomer Actuators

Julian Kunze[1], Giovanni Soleti[2], Daniel Bruch[2], Gianluca Rizzello[2], Paul Motzki[1,2]
[1]ZeMA - Center for Mechatronics and Automation Technology,
Depart. Smart Material Systems, Saarbrücken, Germany
[2]Saarland University, Depart. Systems Engineering, Saarbrücken, Germany

Abstract

Soft robotic technology has the potential to improve safety in human-robot collaboration, as well as increasing the possibilities of using robots in unstructured environments. Our research presents a compact soft robotic arm segment, actuated by silicone-based rolled dielectric elastomer actuators (RDEAs), in combination with a central ball-joint, which features multi-directional bending. RDEAs utilize an electrostatic actuation principle and are well suited for this application due to their inherit compliance and high work density. We created a simplified model of the system employing an energy-based approach, which supported the selection of suitable geometric parameters. The realized segment relies on PCBs as structural material and utilizes a custom, low friction ball joint. Experiments show a bending angle of up to 25° in all directions.

1 Introduction

With increased applications of robots cooperating with humans, soft robotics emerged as a promising alternative to classical rigid robots. Due to their inherent compliance, they can decrease the risk of injuries and offer advantages in unstructured environments by passively adapting to their surroundings. One central part of soft robots is their actuation system. Typical principles include pneumatic [1] and hydraulic actuators [2], for example pistons or bladders, the use of electric motors with tendons [3], shape-memory alloys (SMAs) [4] and dielectric elastomer actuators (DEAs) [5].
In this work, we present a novel articulated soft robotic module driven by rolled dielectric elastomer actuators (RDEAs).

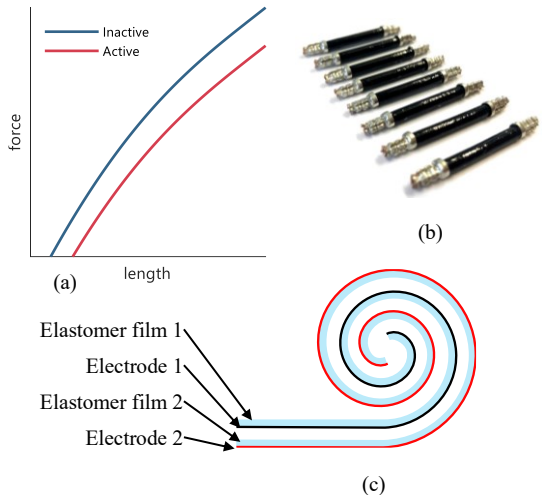

Figure 1: Qualitative force displacement curve of the RDEAs without applied voltage (Inactive) and with applied voltage (Active) (a). Picture of several RDEAs (b). Schematic of the layered structure of an RDEA (c)

Our RDEAs, which are described in detail in [6] and shown in Figure 1 (b) and (c), consist of two sheets of thin silicone elastomer films, interleaved by two flexible, screen-printed electrodes. The electrical as well as the mechanical connection is realized by crimping wire-end ferrules to the end of the rolls and filling them with conductive glue. By applying a high voltage to the electrodes, their force-displacement characteristic changes according to (a).
This phenomenon can be utilized to develop actuator systems. In our case, we present a 3D-bending module, which is intended to be stacked to create a soft-robotics tentacle arm. It is an extension into the third dimension of our previous work on a 2D-bending module, presented in [7] and modeled in [8]. In this 2D-bending module, the movement was constrained to a plane and consists of two rigid platforms connected by a sheet of spring steel and two opposing RDEAs.
The following chapters describe the concept, a brief modeling overview, the realization of the segment as well as initial experimental results and a conclusion including an outlook on future work.

2 Concept

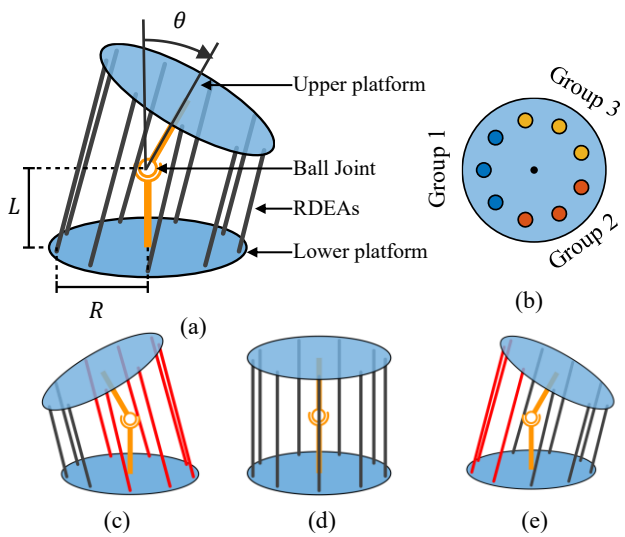

Figure 2: Schematic of the segment (a). The two design parameters are the distance between the ball joint and the platform L and

the radial distance of the RDEAs R. Depending on the voltage applied to the groups of RDEAs (b), the segment bends in the desired direction. Activated RDEAs are depicted in red (c-e).

The segment consists of two circular rigid platforms, which are connected by a custom low-friction ball joint and nine RDEAs around their circumference, as shown in Figure 2 (a) and (b). By strategically applying voltages to specific RDEAs, their force is lowered and the opposing RDEAs pull the segment in their direction, illustrated in (c), (d) and (e).

3 Model Overview

A simplified, quasi-static model is developed to support the design process. It utilizes an energy-based approach, whereby the total energy of the system is expressed as the sum of the elastic and electrostatic energies of the RDEAs according to [9], and the gravitational potential energy of the top segment. The viscoelastic properties of the RDEAs as well as inertial effects are neglected. The total energy is then minimized with respect to the bending angles Φ, which denotes the direction of bending, and θ, which denotes the amount of bending as shown in Figure 2 (a). The angles related to the minimum of this are the desired equilibrium angles. Since the energy depends solely on 2 pose-related variables, it can be visualized in a polar surface plot. An example of such a plot is shown in Figure 3 (b). A more detailed description of the model is presented in [10].

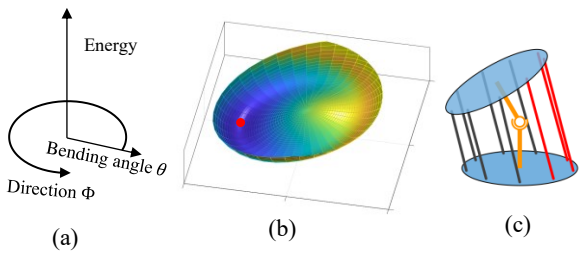

Figure 3: Exemplary diagram of the energy-landscape, with the total energy of the system dependent on the bending direction Φ and the bending angle θ. Coordinate system (a); actual energy landscape with minimum (b); schematic of segment with activated RDEAs in red (c).

Since the geometry of the RDEAs is set due to their manufacturing constraints, only the geometric parameters of the segment remain as design parameters. Those are the distance of the center of the ball joint to platform L and the distance of the center of the platform to the RDEA-attachment points R. In initial parameter studies, two operating regimes have been identified, which differ in the possible ranges for the bending angle θ. For a constant value of $R = 12$ mm, if $L < 15.5$ mm, the model predicts bending angles between 0° and 15°, depending on the applied voltages. We termed this behavior mode A. If $L > 15.5$ mm, only the maximum bending angle of 31° is predicted, independent of the applied voltages, which means, that even if no voltage is applied, the segment is in a bent state, whereby its directional angle θ is arbitrary. This behavior is termed mode B.

4 Realization

The platforms of the segment are constructed from milled printed circuit boards (PCBs) due to their excellent stiffness and manufacturing properties. The beams connecting the ball joint to the platforms are made from threaded rods to aid with adjustability. As for the ball joint, various commercial and 3D-printed components were considered. Their internal friction, however, is too high in comparison to the achievable forces of the RDEAs. As such, a custom ball joint has been designed: it consists of a cone-shaped bore at the ends of the threaded rods, onto which Teflon tape is attached. A 2.9 mm steel ball is clamped between the two bores by the tension of the surrounding RDEAs. Their electrical connection is realized by copper-traces on the PCBs.

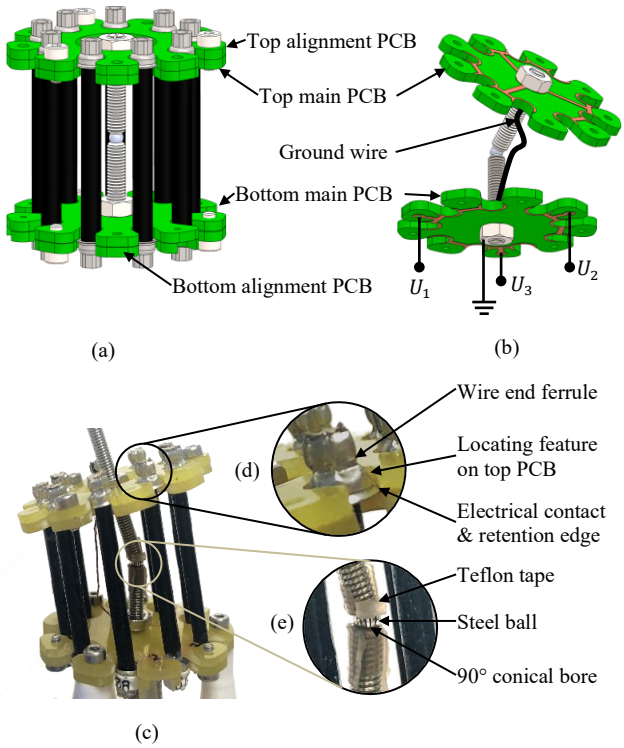

Figure 4: Overview of the CAD model (a), (b) as well as the realized segment (c) with a detailed view of the RDEA-attachment point (d) and the custom ball-joint (e).

5 Initial Experimental Evaluation

The segment was connected to a 3-channel high-voltage amplifier (3x HiVolt model HA3B3-S in 1x HAR42-4 Mainframe). The voltage signals are chosen so that the square of the voltages, which is proportional to the force of the RDEAs, changes in a trapezoidal way. The signals to the three groups of RDEAs are phase-shifted 120° to each other. The segment is recorded with a camera, and the bending angle θ is extracted for some frames. In Figure 5 the bending of the segment set up for mode B under electrical activation is shown.

Both modes which have been predicted by the model could be observed in the realized segment. However, the maximum achievable angle in the experiments was 7° for mode A and 24° for mode B. Additionally, while the segment set

up for mode A allowed for fast movements, the segment set up for mode B could only be moved slowly in a reliable way. Additionally, asymmetries in the movement of the segment could be observed. It was determined that this is due to inconsistencies in the manufacturing process of the RDEAs. The viscoelastic behavior of the RDEAs could also play a role in this regard.

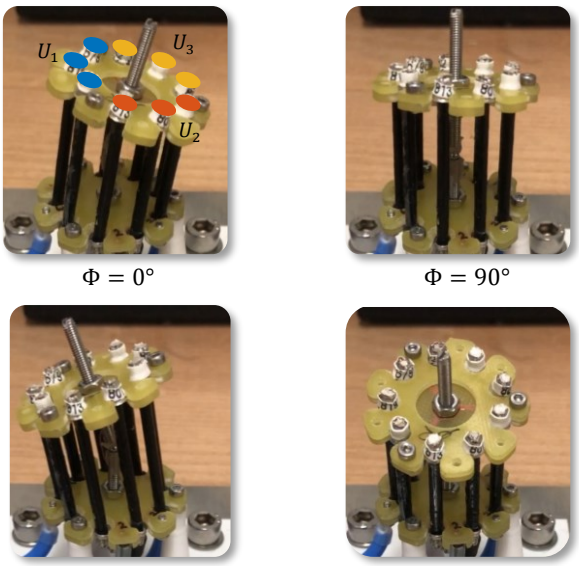

Figure 5: still frames of the segment set up for mode B. Different bending directions Φ could be achieved with a bending angle θ of up to 25°. The colored RDEAs in the top left picture shows the grouping of the RDEAs.

6 Conclusion and Outlook

We showed the feasibility of a 3D-bending segment actuated by RDEAs. By independently activating the groups of RDEAs, the segment bends in the desired direction depending on the magnitude of the applied voltages. Two different actuation modes have been identified, mode A with a larger bending range at the expense of the maximum angle, and mode B with a higher bending angle at the expense of the bending range.

While the qualitative behavior explored in the initial experiments is similar to the predicted movement determined from a simplified quasistatic model, this work is only the first step to a fully 3D-soft-robotic tentacle arm. Future work will include detailed modeling of the system by incorporating viscoelastic effects of the RDEAs, as presented in [11], as well as inertial effects, and validate the model by performing thorough experimental parameter studies. We also plan to investigate polymeric alternatives to the central ball joint. Finally, multiple of those segments should be stacked and a 3D soft-robotic tentacle arm will be constructed.

7 Literature

[1] J. Walker *u. a.*, „Soft Robotics: A Review of Recent Developments of Pneumatic Soft Actuators“, *Actuators*, Bd. 9, Nr. 1, Art. Nr. 1, März 2020, doi: 10.3390/act9010003.

[2] H. Shi, K. Tan, B. Zhang, und W. Liu, „Review on Research Progress of Hydraulic Powered Soft Actuators“, *Energies*, Bd. 15, Nr. 23, Art. Nr. 23, Jan. 2022, doi: 10.3390/en15239048.

[3] B. Deutschmann, J. Reinecke, und A. Dietrich, *Open Source Tendon-driven Continuum Mechanism: A Platform for Research in Soft Robotics*. 2022, S. 61. doi: 10.1109/RoboSoft54090.2022.9762144.

[4] M. A. Mandolino, Y. Goergen, P. Motzki, und G. Rizzello, „Design and Characterization of a Fully Integrated Continuum Robot Actuated by Shape Memory Alloy Wires“, in *2022 IEEE 17th International Conference on Advanced Motion Control (AMC)*, IEEE, Feb. 2022, S. 6–11. doi: 10.1109/AMC51637.2022.9729267.

[5] J. H. Youn *u. a.*, „Dielectric elastomer actuator for soft robotics applications and challenges“, *Applied Sciences (Switzerland)*, Bd. 10, Nr. 2, S. 1–31, 2020, doi: 10.3390/app10020640.

[6] J. Kunze *u. a.*, „Design, Manufacturing, and Characterization of Thin, Core-Free, Rolled Dielectric Elastomer Actuators“, *Actuators*, Bd. 10, Nr. 4, S. 69, März 2021, doi: 10.3390/act10040069.

[7] M. Baltes, J. Kunze, J. Prechtl, S. Seelecke, und G. Rizzello, „A bi-stable soft robotic bendable module driven by silicone dielectric elastomer actuators: design, characterization, and parameter study“, *Smart Materials and Structures*, Bd. 31, Sep. 2022, doi: 10.1088/1361-665X/ac96df.

[8] J. Prechtl, J. Kunze, S. Nalbach, S. S. Seelecke, und G. Rizzello, „Soft robotic module actuated by silicone-based rolled dielectric elastomer actuators: modeling and simulation“, in *Electroactive Polymer Actuators and Devices (EAPAD) XXII*, Y. Bar-Cohen, I. A. Anderson, und H. R. Shea, Hrsg., SPIE, Apr. 2020, S. 79. doi: 10.1117/12.2557736.

[9] J. Prechtl, J. Kunze, G. Moretti, D. Bruch, S. Seelecke, und G. Rizzello, „Modeling and experimental validation of thin, tightly rolled dielectric elastomer actuators“, *Smart Materials and Structures*, Bd. 31, Nr. 1, S. 015008, Jan. 2022, doi: 10.1088/1361-665X/ac34be.

[10] J. Kunze *u. a.*, „Development and Experimental Evaluation of a Compact 3D Bending Module actuated by Rolled Dielectric Elastomer Actuators“, *Electroactive Polymer Actuators and Devices (EAPAD)*, Bd. XXVI, März 2024.

[11] G. Rizzello, „Energy-based modeling of rate-independent hysteresis and viscoelastic effects in dielectric elastomer actuators“, *Smart Materials and Structures*, 2024.

Integrated manufacturing of small-scale dielectric elastomer transducers with rigid structures

Andreas Hubracht[a], Albert Thelemann[a], Chen Jiao[b], Ashwani Sharan Tripathi[b], Uwe Marschner[b], Andreas Richter[b], E.-F. Markus Vorrath[b], and Jürgen Maas[a]
[a]Mechatronic Systems Lab, Technische Universität Berlin, Hardenbergstraße 36, D-10623 Berlin
[b]Institute of Semiconductors and Microsystems, Technische Universität Dresden, Nöthnitzer Str. 64, D-01062 Dresden

Abstract

The manufacturing of dielectric elastomer transducers (DET) poses some ongoing challenges. In addition to the widespread manufacturing by hand, there exist automated processes and even the commercial availability of DET stacks is emerging. In order to test new materials and to enable design flexibility (so-called rapid prototyping), the production using a 3D printer was investigated. In total, three materials with different properties have to be combined in a structured way: A rigid frame for connection or handling, and for the fundamental function of a DET, a conductive and stretchable electrode as well as an insulating but also stretchable dielectric. The fuse filament fabrication (FFF) process is used for processing the rigid frame, the electrode is applied using a droplet-based method and the dielectric is dispensed using direct ink writing (DIW). All processes are integrated in one system and supported by additional peripherals such as a precise layer thickness sensor, an infrared heater and a camera. 16 integrated produced DET were built using 3D printing. With the exception of two outliers, the capacitive evaluation showed good results (28.21 pF $\pm$ 4.4 pF). Furthermore, a transversal displacement of almost 200 µm at 3 kV was achieved. This corresponds to an electric field of around 45 V/µm. These results show the feasibility of a fully integrated production of DET by additive manufacturing.

1 Introduction

The interest in small, versatile and soft transducers is continuing to grow. Dielectric elastomer transducers (DET) belong to this category, as they have dimensions in the mm-range, are comparatively free in their design and contain exclusively stretchable materials. In general, DET consist of a flexible dielectric material sandwiched between two compliant electrodes. Both materials are usually polymer-based. By applying a high voltage, an electrostatic pressure is generated by the attraction of opposing charges. This can be used to generate forces or perform work. With a layer thickness of 20−50 µm and breakdown field strengths of around 50 V/µm, the required electrical voltage lies in the range of 1−2.5 kV. [1]

In addition to the advantages already mentioned and beyond the bare usage as actuator DET fulfill an intrinsic sensor function and can even be used as a generator [2]. DET are used in a wide variety of areas, such as the emerging field of soft robotics [3]. They are used as actuators in various forms such as planar, rolled, multi-layer stacked, balloon, cone-shaped or minimum energy structures [3]. Another application, without any claim to completeness, use planar DET with the buckling principle as loudspeakers [4]. DET can also be integrated into cooperative actuators and sensor systems [5].

Besides the still common manual production method, there are promising approaches to further process an industrially prefabricated film automatically [6]. This promises a high level of quality, but is at least restrictive in terms of the choice of materials. The availability of entire DET on the market is also becoming increasingly serious [7], but severely restricts design and material diversity. Manufacturing processes that use versatile liquid raw materials, such as 3D printing, are therefore ideal for ensuring design freedom. Research is also currently being carried out on the optimization of materials explicitly for 3D printing of DET [8]. Several potential 3D printing technologies exist that could be used in the context of DET production, including inkjet, extrusion, laser-induced, and stereolithography [9]. For example, DET have already been manufactured using the inkjet printing technology [10].

Within the joint project CALMAR (DFG, 512586089) the goal is to develop a collaborative multi-actuator system, combining the advantages of DET, dielectric elastomer switches (DES) and hydraulically amplified self-healing electrostatic (HASEL) actuators. This contribution focuses on the production of DET using a 3D printing system realized for this purpose including three printing technologies: fused filament fabrication (FFF), a droplet-based micro-dispensing system and direct ink writing (DIW) [11]. Moreover, measurement equipment and temperature control options are available. The aim is to produce DET completely in one single process. A DET-design should be chosen that allows easy electrical contacting, a layer thickness well below 100 µm and a functional test.

The contribution is structured into two main parts. Section 2 describes the target design of the DET. Furthermore, the printing process including the three different printing technologies and the used materials are presented. Section 3 points out the practical results, containing an electrical characterization, mechanical investigations and electromechanical results.

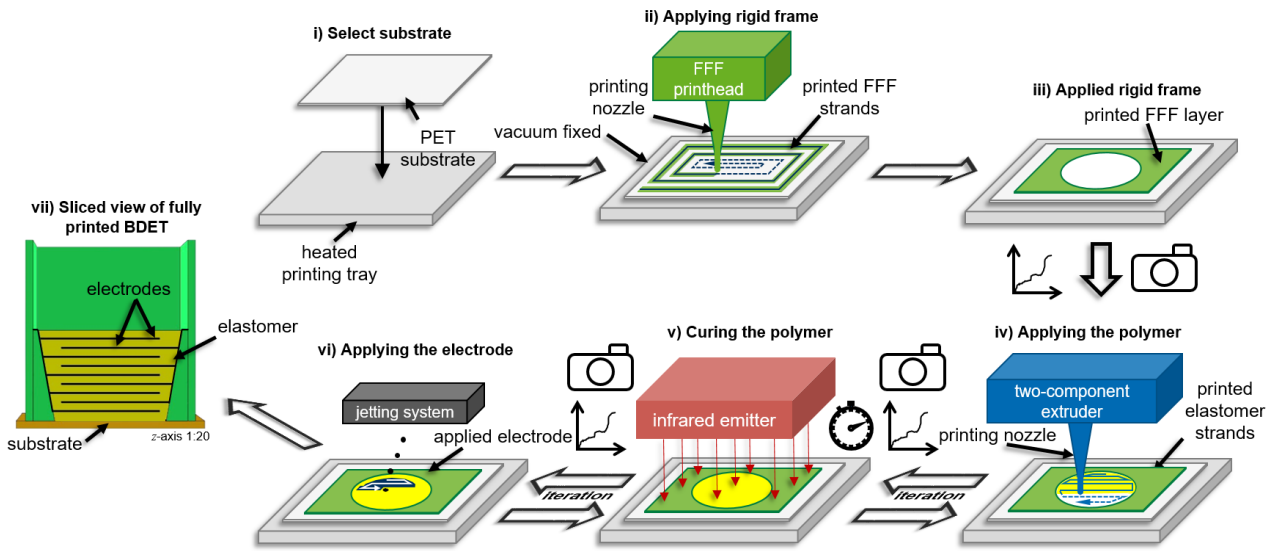

Figure 1 Target design of the dielectric elastomer transducer (vii) and schematic overview of the processing (i-vi).

2 DET design and printing process

A DET-design and appropriate materials are required for the production of fully integrated DET. In general, at least two compliant materials are necessary for proper functioning, one electrically conductive (electrode material) and the other one electrically isolating (dielectric material). In addition, a rigid material can be useful for mechanical connections, to support the shape, to facilitate electrical contacting or as a simple frame. In order to produce fully integrated dielectric elastomer transducers it is important to arrange the three materials in a way, which i) allows the production according to the used techniques and ii) enables the proper operating of the transducer.

Figure 1 (vii – on the left side) is showing schematically the proposed target design pursued in this contribution. On the substrate a polymer layer acts as base with the main characteristic to enable a non-destructive removing of the finished DET in the end. Above, the two main materials, electrode (black) and dielectric (yellow), are stacked in an alternating manner. The active part is surrounded by the rigid frame (green). One key is to have the electrical contacting in mind from the beginning. In this case, the approach is to extend the electrodes on both sides alternating beyond the edge of the rigid frame. Therewith, a reliable electrical contacting should be possible from the top layer to the layers below.

The printing process consists of the three main production steps: 1. FFF printing of the rigid frame, 2. DIW dispensing of the dielectric layer, and 3. droplet-based application of the electrode layer. The repetition of these production steps in an appropriate sequence enables the step-by-step build-up of the DET. For the actual approach the procedure is as follows.

As substrate material a common PET-film is positioned on the heated tray and fixed using vacuum (see Figure 1 i). The temperature of the tray is kept constant at $T = 45\,°C$ during the entire production and all samples. The second production step is the application of the rigid frame using the FFF printing technology (see Figure 1 ii & iii). The filament-material is commercially available, strand-based, white PLA (polylactic acid). The printer's control unit requires a G-code for the execution of the production task. This G-Code can be generated by the special software provided with the printer, but was developed by ourselves due to efficiency and individualization reasons. The printing path and a photo after printing of the rigid frame are shown in Figure 2 i.

The next step is applying the first polymer layer on the bottom using the two component extruder (see Figure 1 iv). The processed material is the room temperature curing silicone rubber ELASTOSIL ® RT 625 A/B (Wacker Chemie AG, Germany) [12]. The component A is solved 50:50 in a linear silicone fluid WACKER ® AK 1 (Wacker Chemie AG, Germany) [13]. The polymer is applied with the two component extruder and heated using an infrared emitter (see Figure 1 v). The printing nozzle has a diameter of 580 µm. The printing path and a photo after printing of the first polymer layer are shown in Figure 2 ii. A special aspect is the neutralization path, which ensures that the material flowing out is in a steady state, and thus, enhancing the layer quality.

In order to add the electrode layer, a droplet-based jetting system was used and cured after printing again with the infrared emitter (see Figure 1 v & vi). The printing path and the corresponding photo after curing are shown in Figure 2 iii. The electrode ink [14] is, besides additives, a mixture of the linear silicone fluid WACKER ® AK 1 (Wacker Chemie AG, Germany) [13] and ELASTOSIL ® LR 3162 A/B [15].

After every process step a photo was taken and the thickness measured using a confocal laser sensor (CL-P015G, Keyence). For reaching more layers, the presented process parts can be combined (see Figure 2 iv - vi). Finally, the PET-film serves as carrier to handle the printed samples until the DET is removed for the targeted application.

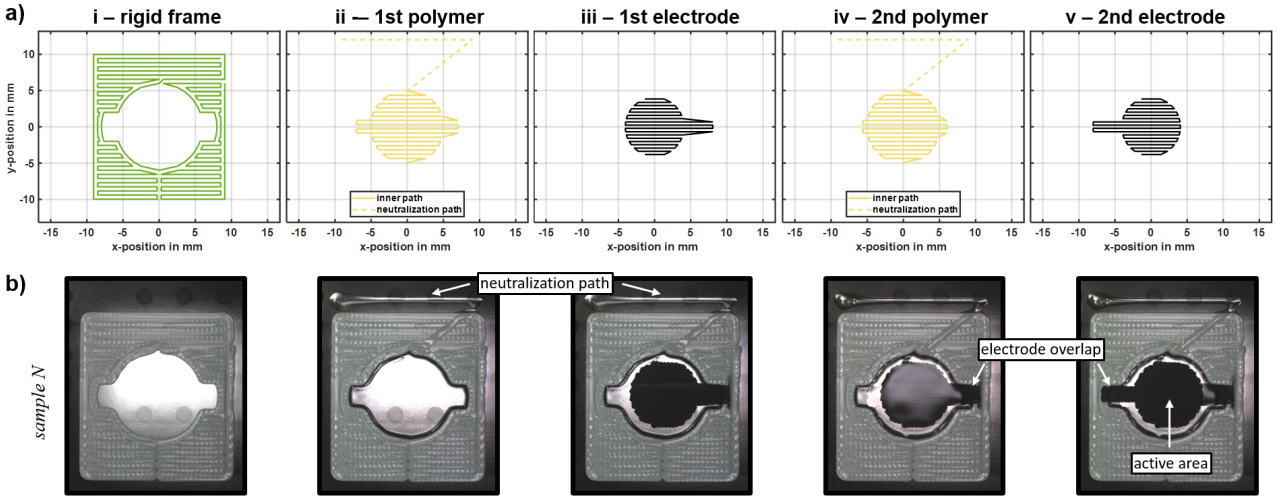

Figure 2 Printing path of the three materials and in-process photographs of sample "N": a) G-Code based printing path of the relevant layers and b) in-process photographs after the respective production step.

3 Results

Several DET samples were printed using various parameters and settings. After eliminating obvious failed samples by visual inspection a total number of 16 samples remained. In order to not exceed the scope of this article, not all samples were investigated mechanically and electromechanically, but the capacitance was analyzed for all to give an impression of the overall printing quality.

The electrical capacitance is a simple and sufficient way of evaluating the manufactured DET, because geometry and the known material parameters are influencing it. Due to the parallel arrangement, the individual capacitances in the non-deformed state simply sum up. Table 1 contains the capacitance measurements of the 16 samples ("A"–"P") using a LCR-meter (GW Instek LCR-817). The individual layer capacitance can not be measured straightforward, but the total capacitance. The capacitance per layer can be specified using the respective number of active layers N_a. This enables comparability between the samples with different number of layers. A box plot is depicted in Figure 3 a including outliers and the mean value of 28.21 pF. It can be seen, that only two outliers ("G" and "I") are present and also the multilayer samples are in a comparable range. The standard deviation is 4.4 pF.

For the electromechanical test sample "L" was selected, because it has a measured capacitance close to the mean value and the visual inspection of the photo during the production was showing a dielectric layer without any visual air inclusion. The latter is important to ensure a high electric breakthrough field strength. Due to the pre-strain-free configuration a simple connection to a high voltage source, is not useful. Therefore, similar to the buckling principle [4], a mechanical pre-deformation is realized (see Figure 3 b) and the transversal displacement was measured using a laser triangulation sensor (optoNCDT 2220-20, Micro-Epsilon Messtechnik GmbH & Co. KG, Germany). The quasi-static measured transversal displacement with an applied DC voltage up to 3 kV is shown in Figure 4 a. The voltage was increased in steps of 100 V us-

Table 1 Produced samples with measured capacitance.

Sample	Layer N_a	C_{meas} in pF	C_{meas}/N_a in pF
A	1	29.6	29.6
B	1	26.8	26.8
C	1	30.5	30.5
D	1	34.4	34.4
E	1	33.0	33.0
F	3	97.2	32.4
G	1	18.4	18.4
H	1	26.9	26.9
I	1	19.5	19.5
J	1	27.8	27.8
K	3	77.4	25.8
L	1	29.6	29.6
M	1	30.7	30.7
N	1	31.7	31.7
O	5	134.1	26.8
P	5	137.4	27.5
		mean (std) = 28.21 (±4.4)	

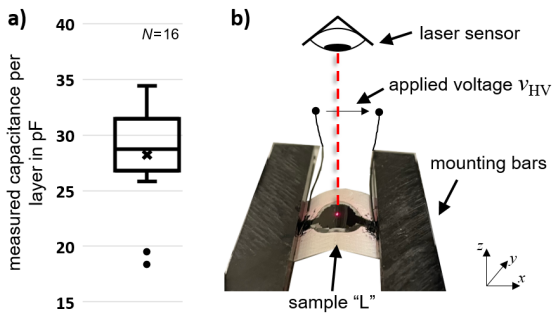

Figure 3 a) Statistical analysis of the measured capacitance per layer and b) measurement set-up for investigating the transversal displacement in z-direction.

ing a high voltage amplifier including the module "BPp 30 105 12" (iseg Spezialelektronik GmbH, Germany). The measured points are marked with a cross. The maximum transversal displacement is reached, as expected, at 3 kV with 191.7 µm.

The in-process measurements of the individual layer heights from sample "L" are depicted in Figure 4 b & c. The relevant thickness of the active polymer reaches from the upper edge of the 1st electrode to lower edge of the 2nd polymer. The average thickness and its standard deviation is 66.6 µm ± 3.5 µm and 67.3 µm ± 3.7 µm in x- and y-direction, respectively. The line-measurement was positioned in the middle of the sample. With the measured average layer thickness, the electric field can be specified as about $E \approx 3000\,\mathrm{V}/66\,\mu\mathrm{m} \approx 45\,\mathrm{V}/\mu\mathrm{m}$. For comparison, typical values found in the literature are in the range of 20 - 200 V/µm [16]. A detailed analysis of the breakthrough field strength remains open.

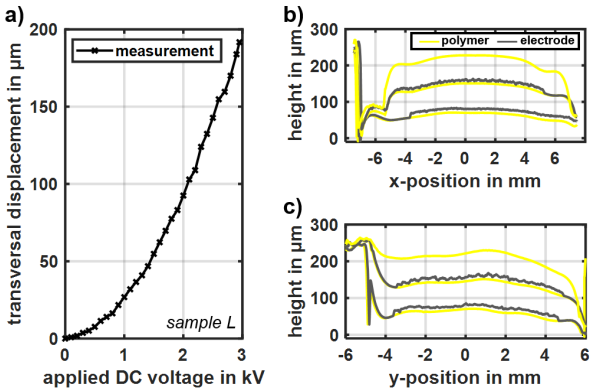

Figure 4 Sample "L": a) measured quasi-static displacement up to 3 kV, b) in-process measured layer heights in x-direction, and c) in y-direction.

4 Conclusion

In this article, a fully integrated dielectric elastomer transducer was produced using a 3D printing system. Three different materials with their individual properties were applied. The solid frame was printed using fused filament fabrication (FFF), the conductive electrode with a droplet-based micro-dispensing system and the dielectric with the direct ink writing (DIW) technique. During the process, photos were taken and the layer thickness was measured. A total of 16 samples was produced, some of which were multilayer samples. The electrical capacitance was measured (28.21 pF ± 4.4 pF) as an indicator of the dimensional accuracy of the production. The transversal strain for one sample "L" reached almost 200 µm at 3 kV. With a measured layer thickness of about 66 µm the electric field results in 45 V/µm. Analytical modeling as well as FEM investigation of the transversal displacement, a study regarding the breakthrough field strength, and the exploration of new materials are part of future work. In summary, 3D printing is a promising manufacturing approach to be suitable for producing fully integrated, functioning dielectric elastomer transducers in one single process.

Acknowledgement

This contribution was created as part of the joint project *CALMAR* - German Research Foundation (512586089). We thank Wacker Chemie AG for providing material.

Literature

[1] F. Carpi et al. *Dielectric Elastomers as Electromechanical Transducers*. Amsterdam, NL: Elsevier, 2008.

[2] Y. Zhao et al. "Review of dielectric elastomers for actuators, generators and sensors". In: *IET Nanodielectrics* (2020).

[3] Y. Guo et al. "Review of Dielectric Elastomer Actuators and Their Applications in Soft Robots". In: *Advanced Intelligent Systems* (2021).

[4] M. Gareis and J. Maas. "Buckling Dielectric Elastomer Transducers as Loudspeakers". In: *Journal of the Audio Engineering Society* (2022).

[5] G. Rizzello. "A Review of Cooperative Actuator and Sensor Systems Based on Dielectric Elastomer Transducers". In: *Actuators* 12.2 (2023).

[6] T. Krüger, O. Çabuk, and J. Maas. "Manufacturing Process for Multilayer Dielectric Elastomer Transducers Based on Sheet-to-Sheet Lamination and Contactless Electrode Application". In: *Actuators* (2023).

[7] Dätwyler Holding AG. `https://datwyler.com/de/media/news/innovative-collaboration-for-dielectric-elastomer-actuators`. Accessed: (08.05.2024). 2024.

[8] P. M. Danner et al. "Polysiloxane Inks for Multimaterial 3d Printing of High-Permittivity Dielectric Elastomers". In: *Advanced Functional Materials* 34.17 (2024), p. 2313167.

[9] H. Zhang et al. "3D printing dielectric elastomers for advanced functional structures: A mini-review". In: *J. Appl. Polym. Sci.* (2024).

[10] G. Gallucci et al. "Fully inkjet-printed dielectric elastomer actuators". In: *EAPAD XXVI*. Vol. 12945. SPIE, 2024, p. 129450I.

[11] A. Hubracht and J. Maas. "Manufacturing of dielectric elastomer transducers using 3D printing". In: *Proceedings: MikroSystemTechnik Kongress* (2023).

[12] Wacker Chemie AG. *ELASTOSIL ® T 625 A/B*.

[13] Wacker Chemie AG. *WACKER ® AK 1*.

[14] O. Çabuk and J. Maas. "Investigation of a deposition method for the application of electrode layers for dielectric elastomer transducers". In: *EAPAD XXIII*. Vol. 11587. SPIE, 2021, 115871Q.

[15] Wacker Chemie AG. *ELASTOSIL ® LR 3162 A/B*.

[16] J. Kunze et al. "Design, Manufacturing, and Characterization of Thin, Core-Free, Rolled Dielectric Elastomer Actuators". In: *Actuators* 10.4 (2021).

Miniature Piezo Fast Steering Mirror for Optical Communication in NanoSats and CubeSats

Sylvain Chardon, Timotéo Payre, Mathieu Thomachot, Hugo Grardel, Yann Quentel, Gérald Aigouy, Frank Claeyssen
CEDRAT TECHNOLOGIES, 38240 Meylan, FRANCE, mailto:frank.claeyssen@cedrat-tec.com

Abstract

Access to data has become vital and strategical for individuals and nations, Earth planet preservation and monitoring, and mobility applications. In this context, the number of satellite constellations projects is growing drastically worldwide and is a next generation challenge of the New Space cost efficient industry.
To replace radio frequencies (RF) communications, space optical communication will be the new trend, addressing both very high speed and as secured encrypted communication improvements.
Fast Steering Mirrors (FSM) are a key component used in optical communication, and for a large field of functions such as Point Ahead Mechanisms (PAM), Raster Scanning, Beam Steering Mirrors (BSM), Fine Pointing Mechanisms (FPM) and Line of Sight stabilization (LOS).
The following paper presents test results of CEDRAT TECHNOLOGIES piezoelectric mini-FSM and associated CCBu20 driving electronics.

1 Introduction

Free Space Optical communication offer a solution to provide both very high data rate and highly secured encrypted communication. This revolutionary concept has passed a big step of feasibility thanks to the successful communication links established in 2023 with the PSYCHE NASA mission, noting that for this mission CEDRAT TECHNOLOGIES (CTEC) has delivered the PAM30 [1] [2], steering the laser beam of the communication link.
Starting from this space heritage CTEC has achieved the design and qualification of a piezoelectric mini-FSM for 3U CubeSats, targeting an undisclosed constellation composed of several hundreds of satellites, with cost and reliability being the main drivers. The highest reliability and small size APA® Amplified Piezo Actuator reference from CTEC optronics heritage was selected, having demonstrated zero failure over more than 5000 piezo mechanisms produced in the last 20 years. The FSM mechanical parts number was reduced as far as possible choosing an all-in-one patented mirror holder ensuring flexure bearing, mirror flexible interface mounting, and flexural pivots. By this innovation and former test approach from optronics recurrent manufacturing, the total MAIT time for this device has been reduced to less than 2 days, while providing 100% testing to insure zero defect at customer level.
The design of this mini-FSM and the first test results are presented in [3]. This mechanism gives the capacity, in a very small size, to withstand very high vibration and shock while keeping high angular stroke capacity, and resolution. The present paper presents final results and perspectives.

1.1 Design and performances summary

The main specifications for this product are to ensure a ±6 mrad angular stroke (@25°C) in a miniature volume (30mm diameter / 20 mm height). The mechanism must move a 6mm diameter mirror with a 500 Hz control bandwidth.

Performance	Value
Mechanism's diameter	30mm
Mechanism's thickness	20mm
Mirror's mass	Up to 0.1g
Angular stroke	±6.5mrad
Control bandwidth	>550 Hz
First resonance frequency	1700Hz
Rise time	0.4ms
Settling time	1.1ms

The Miniature FSM is a tip tilt platform based on four CEDRAT TECHNOLOGIES APA35XS® as in [4]. It is composed of the following parts:

- A stainless steel frame baseplate on which each APA is fixed. The central cylinder is fastened on this baseplate.
- Two housing parts (in aluminium)
- 4 APA35XS-SG with stainless steel shell: They provide the required displacement and are fixed to the frame and to the guiding blade. The APAs are equipped with strain gage (SG) sensors.
- A guiding blade (stainless) welded onto the central cylinder that stiffens radially the assembly and prevents parasitic motions during actuation.
- A mirror holder in aluminium.
- 4 arms (in stainless) are welded onto the guiding blade.
- The mirror

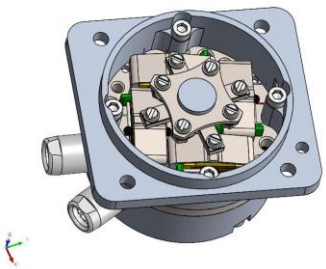

Figure 1 Miniature Piezo FSM overview

The APA® are patented compact space-qualified Amplified Piezo Actuators from CTEC based on a low voltage multilayer piezo ceramic (MLA) and a shell ensuing both MLA pre-stressed and amplification of the MLA displacement. They include strain gages (SG) for sensing the stroke. The APA® offers a stroke proportional to the voltage, in closed loop control with SG. The APA35XS are based on 2x5x10mm3 piezo MLA. Their stroke is about 40µm, while the MLA stroke is 10µm. Driving the APA® in push pull by opposite pairs, this Tip-tilt allows deflections of the mirror around X and Y axis.
The observability of the mirror position is assured by embedded strain gages onto MLA ceramics. Theses sensors will be used with the controller to measure the real position of the FSM and reach the desired accuracy. Nevertheless, such a solution is not optimal because the angular position of the mirror is not accurately observed at high frequency, impacting the controllability of the FSM.

To embed such a technology in the mechanism, a particular attention is given to the internal electrical connection with multiples signals, high amplitude voltage or ultra-low amplitude signals. Two printed circuit boards are proposed to connect the two separate sensors and piezo output pigtails.

2 Miniature FSM Tests results

Several mechanisms were manufactured in 2022 and 2023. Main tests results are presented here above.

2.1 Modal frequencies measurements

The mechanism stiffness and associated modal landscape is evaluated with an admittance sweep. With that method, only the piezo coupled modes are visible, hence the vertical pumping mode (cancelled from piezo point of view) is not visible. The minimal first mode frequency on the prototypes is 1700 Hz. This allows to have a bandwidth higher than 550 Hz.

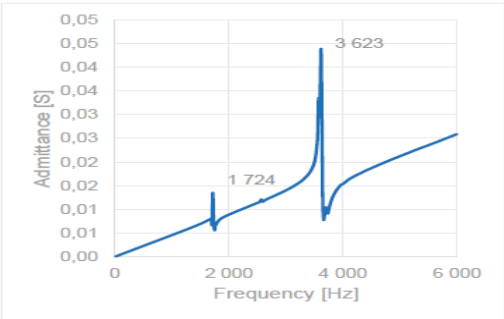

Figure 2 typical admittance versus frequency

2.2 Closed loop control performance

The mini-FSM was tested with a CCBu20 controller, rugged for NewSpace applications, using the embedded strain gauges position sensors (SG). This controller has a peak output current limitation of 0.2A and an RMS maximum output current of 35mA per axis.

Figure 3 Rugged version of CCBu20 Drive Electronics

With Proportional Integral controller associated with notch filters, bandwidths greater than 550 Hz were measured.

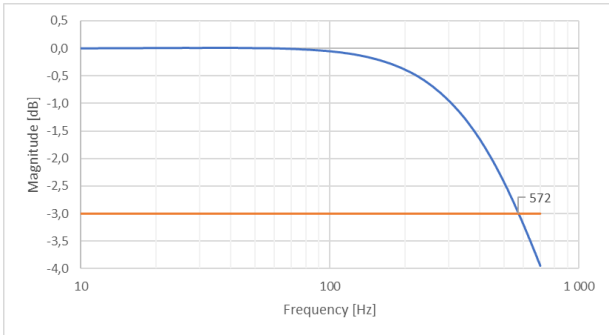

Figure 14. Typical closed loop bandwidth

This performance allows a rise time about 0.4ms and a settling time about 1.1ms, measured on a 3mrad (50% of full stroke) step.

3 Raster scan pattern

The raster scan is used to establish an optical communication between 2 satellites. The goal of the raster scan is to explore the whole FSM solid angle, until the target laser is detected. Once the target is detected, the FSM points toward the target and turns into tracking mode, where the FSM's role is to maintain the target in the line of sight, by compensating external perturbation such as flywheels or compressors' vibrations.

3.1 Pattern implementation

The raster scan is implemented in the rugged version of the CCBu20 controller. When enable the controller run this mode until the user stop it.

The scan pattern is driven by the following equation:

$$X = Mag1 * \sin(2\pi f_1 t) * \sin\left(2\pi f_2 t + \frac{\pi}{2}\right)$$
$$Y = Mag2 * sin(2\pi f_1 t) * sin\,(2\pi f_2 t)$$

The magnitudes Mag1 and Mag2 and the frequencies f1 and f2 are user configurable. (f1 is limited to 500Hz and f2 to 450 Hz).

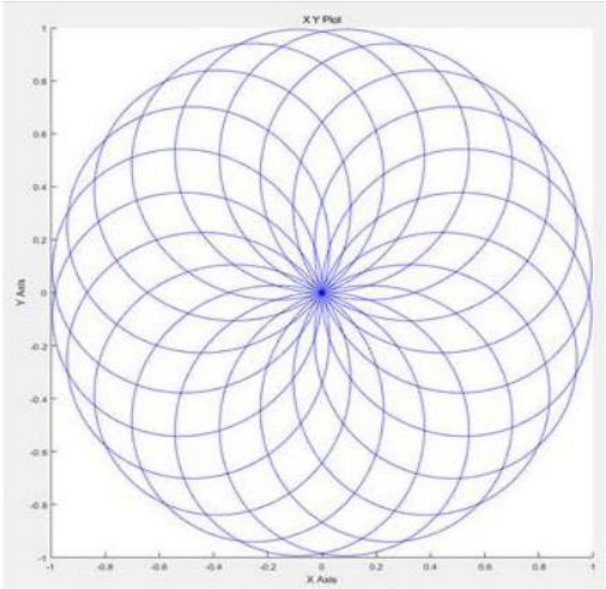

Figure 4 Example of pattern for f1=500Hz, f2=450Hz

3.2 Raster scan consumption

The scan mode is very power demanding (about 30W for the pattern of **figure 4**) while the stabilization mode generally asks only few watts.
Design a controller to handle this extra power will increase the controller volume, weight, and heat dissipation.
Instead, the controller is in "overheating" mode. The temperature of some components is always increasing. Of course, these temperatures are monitored to avoid any damages.
This implies that the raster scan mode cannot exceed 1 or 2 minutes, which is large enough to detect the target.

3.3 Laser distortion and strain gauge observability

On each axis, the rosace pattern driving signal is made of a sine signal A with a frequency fa, multiplied by another sine signal B with a frequency fb. The resulting signal has a spectrum with 2 peaks at f1 = fa + fb and f2 = fa – fb, with its negative counterpart.
On the other side, the FSM mechanism has a given admittance, with principal resonance modes and their harmonics. If the driving signal spectrum has some peaks that are close to one or several FSM modes, these modes will be excited, and the mirror movement will be different from the one seen by the strain gauge.

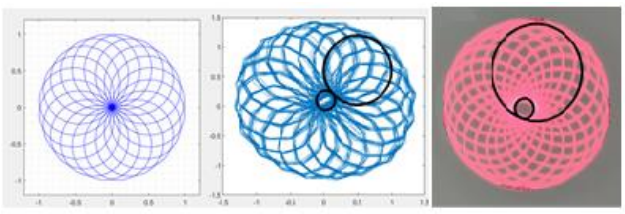

Figure 13. Comparison between order, SG feedback and real laser pattern

To observe this phenomenon, the FSM was installed on a setup with a PSD sensor that monitors the real mirror movement and allows to measure it. The frequency was set at f1 = 500 Hz and f2 = 450 Hz.

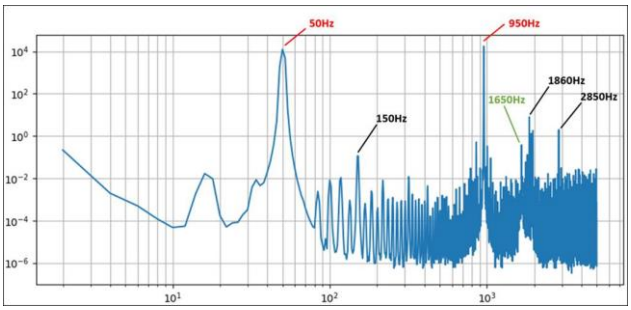

Figure 5 PSD of a laser movement

This spectrum shows:

- The 2 mains harmonics of the driving signal: 50 Hz (500 Hz – 450 Hz) and 950 Hz (500 Hz + 450 Hz).
- The system's resonance frequency at 1650 Hz.
- Other peaks (150 Hz, 1860 Hz and 2850 Hz) look like harmonics of the driving signal.

The fact that the FSM's resonance frequency peak is present confirms that somehow, this resonance frequency is excited by one of the driving signal harmonics. This subharmonic excitation phenomena are due to piezo non-linearities as presented in detail by theory and test in [5]. It explains why the laser movement is different from the SG signal, especially at particular frequencies.
Conversely, when there is no interference between the driving signal and the FSM harmonics, no deformation of the scanning signal is observed: The laser movement corresponds with the SG signal.

3.4 Reproducibility and robustness of the mechanism's performances during scan pattern

The previous chapter explained that the driving signal harmonics can excite resonance modes of the FSM.
These resonant modes can change:

- Between each FSM manufactured.
- With FSM aging.
- With FSM's load.

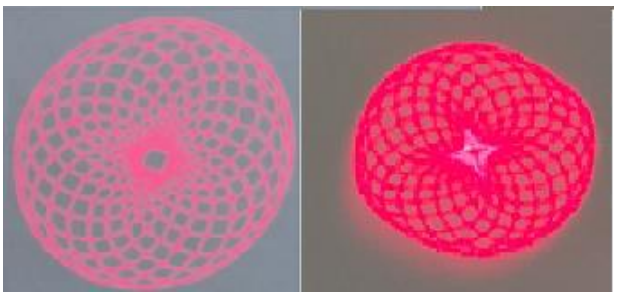

Figure 6 laser figure on two different FSM

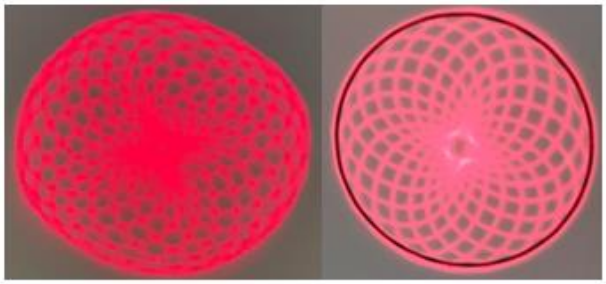

Figure 7 laser figure between test and final mirror

Because of the natural variability of the FSM's resonance frequency, it seems difficult to define a common tuning that will be suitable for all the mechanisms. A specific tuning method must be considered taking each FSM modal signature into account.

4 Possible control improvements

To enhance the controllability of the FSM up to the mirror level itself, one solution is to have a sensor that directly describes the position of the mirror. A solution is to place a PSD sensor in the optical terminal design, and to use the PSD sensor signal instead of the SG signal in the closed loop controller. In this case, the control loop will damp the principal resonant mode to avoid parasitic excitation.

Another solution could consist in using eddy current sensors (ECS) to monitor the mirror movement as done successfully in CTEC magnetic SM [6] and some piezo FSM [7]. But the integration of ECS in this miniature piezo FSM is not straightforward at all due to its small dimensions.

To improve controllability, the mini FSM stiffness could also be increase. This would shift the excitation modes to higher frequencies and reduce the risk of exciting them with the control signal. However, doing this would reduce the FSM stroke.

Other patterns could also be implemented to reduce the harmonic frequency.

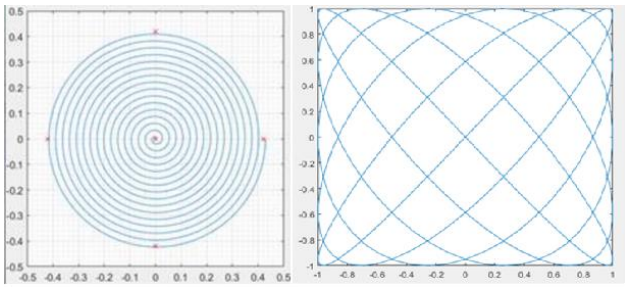

Figure 8 other possible patterns

5 Conclusion

The development of the Piezo Mini-FSM for an optical communication constellation has been successfully achieved. A rugged version of the CCBu20 electronics has been delivered with the Mini-FSM. Both have passed the qualification tests including the vibration tests. Control with strain gages have shown precision limitations in dynamics but these can be circumvented.
Because of this promising results and market, CTEC is committed in the CONECS project, funded in FRANCE 2030 framework. The goal of this project is to develop a complete piezo FSM system qualified for New Space applications. This system will include the FSM piezo mechanism, its mirror and the associated CCBu20 New Space controller.

6 Literature

[1] A. Guignabert, T. Maillard, F. Barillot, F. Claeyssen Point Ahead Mechanism for Deep Space Optical Communication – Development of a new Piezo-Optical Tip-tilt mechanism, Proc AMS, Houston, 2020

[2] A. Guignabert, T. Maillard, A. Baillus, G. Aigouy, Fine Steering Mirror based on piezo actuators: Point Ahead Mechanism for Deep Space Optical Communication for PSYCHE mission, Proc. ICSO, Feb. 2021

[3] T. Payre, S. Chardon, M. Thomachot, H. Grardel, Miniature Piezo Fast Steering Mirrors (FSM) for Space Optical Communication in NanoSats and CubeSats, ESMATS, 2023

[4] G. Aigouy, A. Guignabert, E. Betsch, C. Cote, Large stroke Fast Steering Mirror for Free-Space Optical Communication, Proc. ICSO, February 2021

[5] F. Claeyssen, C. Belly, R. Le Letty, Dynamic strain limits of Amplified Piezo Actuators, Proc Actuator 2010, Pub Messe Bremen (G), June 2010

[6] E. Betsch, A. Bedek, N. Bourgeot, A. Barnique, Magnetic Fast Steering Mirror for Inter-satellites and Feeder Link Optical Communication, Proc Actuator 2024, June 2024

[7] C. Cote, A. Pagès, O. Sosnicki, M Castruccio, Improving dynamic accuracy of closed loop bandwidth of piezo mechanisms with advanced control laws and embedded eddy current position sensors, Proc Actuator 2024, June 2024

Transient response control of the ultrasonic motor with adaptive frequency sweep

Tatsuki Sasamura[1], Norio Sashida[3] and Takeshi Morita[1,2]
[1] Graduate School of Frontier Sciences, The University of Tokyo, Kashiwanoha 5-1-5, Kashiwa, Chiba, Japan
[2] Graduate School of Engineering, The University of Tokyo, Hongo 7-3-1, Bunkyo-ku, Tokyo, Japan
[3] SHINSEI CORPORATION, 2-1-8, Kasuya, Setagaya-ku, Tokyo, Japan 157-0063,

Abstract

This study investigates the transient response of the traveling wave ultrasonic motor (TWUSM) with varying frequency sweep speeds to identify limitations in response times. Simplifying the system for analysis, the stator was isolated from the rotor and modeled using an equivalent circuit that incorporated nonlinear capacitance and resistance. This model effectively captured both static and dynamic behaviors of the TWUSM stator.

To optimize the start-up response, the Soft Actor Critic (SAC) deep reinforcement learning algorithm was employed within the simulated environment defined by the equivalent circuit model. The SAC model demonstrated superior performance, achieving faster responses than traditional constant frequency sweeps during simulations. However, when applied in a real control system, the SAC model's performance was hindered by delays in inference calculation, leading to suboptimal results compared to the simulated outcomes.

Future work will focus on minimizing the discrepancy between simulation and real-world application by optimizing real-time inference processes and expanding the model to include rotor-stator interactions. Additionally, comprehensive dynamic modeling of the entire motor system under varying operational conditions will be pursued to enhance the robustness of frequency control using advanced reinforcement learning techniques.

1 Background

Traveling wave ultrasonic motors (TWUSMs) are distinguished by their rapid responsiveness, which facilitates swift and precise control of position and speed. However, these motors typically exhibit a longer response time during startup compared to stopping. For instance, the USR60-E3T model by SHINSEI CORPORATION has a stop time of 1 ms and a startup time of 50 ms[1]. This discrepancy is primarily due to the need to adjust the driving frequency downward at startup, a process complicated by the significant nonlinearity of TWUSMs' vibration and the hysteresis in the resonance curve.

The research presented here offers two main contributions:

1) A combined experimental and theoretical analysis of the startup response time
2) A method to accelerate the stators' vibrations using reinforcement learning.

2 Experimental analysis

2.1 Experiment setup

As depicted in **Figure 1**, the experimental system used in this study includes a control circuit managed by a microcontroller (ESP32-S3-DevKitC-1-N8, Espressif Systems). This circuit features four Direct Digital Synthesizers (DDSs) (WS-251S3, NF Corp.). Two DDS channels control the TWUSM, USR60-E3T (labeled as Phase A and Phase B), while the other two channels generate the DDS reference signals (COS and SIN). The driving signals from the DDSs are amplified through bipolar amplifiers (HSA4052, NF Corp.) and 1:5 transformers to enable driving voltages up to 180 Vp. The driving currents for both Phase A and Phase B are transformed by 1:500 transformers (AS-104, Nuvotem Talema) and 1kΩ resistors to achieve a sensitivity of 2V/A. These voltages are processed into in-phase and quadrature components using Phase Sensitive Detectors (PSDs), with the DDS's COS and SIN signals multiplied by the current signals. The resulting signals are then smoothed by low-pass filters. The system also incorporates a rotary encoder interface to measure the TWUSM's rotation speed using its built-in rotary encoder.

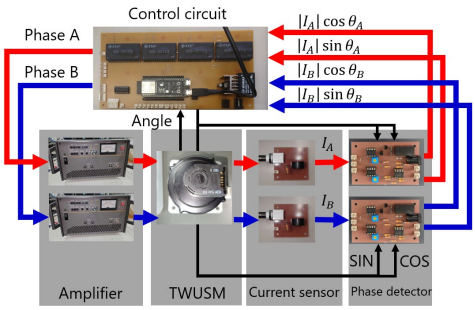

Figure 1 Experiment setup

2.2 Response measurement of the TWUSM

2.2.1 The static response measurement

Figure 2 illustrates the rotation speed of the TWUSMs when the frequency is swept up and down between 39 kHz and 45 kHz over a 500 ms period. This measurement

highlights the hysteresis in the frequency characteristics of the TWUSM, emphasizing the need for down-sweeping during resonance driving.

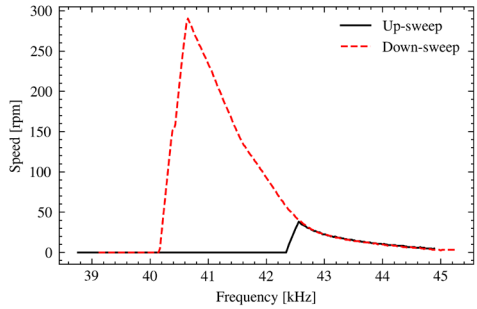

Figure 2 Measured rotation speed of USR60-E3T with frequency sweep between 39 kHz and 45 kHz

2.2.2 The transient response measurement

The start-up response of the TWUSM, captured in **Figure 3**, was analyzed by varying the sweep duration from 45 kHz down to 41 kHz over different periods: 0 ms (direct jump), 1.5 ms, 2 ms, and 5 ms, with a driving voltage amplitude of 140 Vp. The results show that a 2-ms sweep duration results in a quicker start-up than a 5-ms period, while a sweep of 0 ms and 1.5 ms initiates rotation faster, approximately 2 ms after the start. These findings suggest that adjusting the frequency sweep speed adaptively from fast to slow can achieve a faster response.

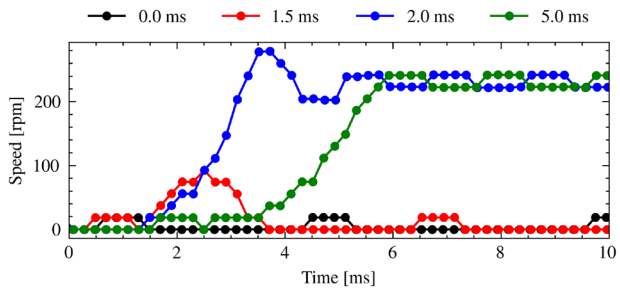

Figure 3 Measured transient response of rotation speed, current, and its mechanical factor, with varying sweep duration, 0, 1.5, 2.0, 5.0 ms

The nonlinearity observed in the ultrasonic motor stems from two primary factors: the interaction between the stator vibration and the contact force from the rotor[2], and the nonlinear viscoelasticity of the stator[3]. Despite their similar effects, the contact force is more complex and heavily influenced by the mechanical condition of the load. For simplicity, and to prioritize foundational understanding and preliminary studies of optimal frequency control, subsequent chapters will focus on the stator's nonlinear viscoelasticity.

3 Simulation model

3.1 Nonlinear vibration models

The stator vibration is represented by an equivalent circuit as shown in **Figure 4**, where L, R, and C correspond to the equivalent mass, viscosity, and compliance, respectively. The compliance and viscosity exhibit nonlinear behavior as follows[3]:

$$R = R_0 + \eta {i_m}^2 \tag{1}$$

$$C^{-1} = {C_0}^{-1} + \xi {q_m}^2 \tag{2}$$

Here, η and ξ are the nonlinear viscosity and compliance parameters, respectively. The variable q_m is the integral of the mechanical branch current i_m, calculated as $q_m = \int i_m \, dt$.

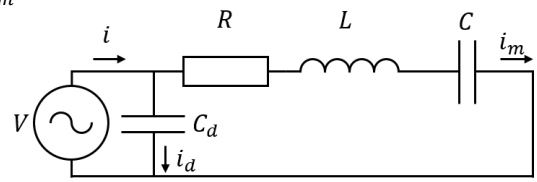

Figure 4 Equivalent circuit model with nonlinearity

The dynamics of the equivalent circuit are governed by three key relationships:

$$V = L\frac{di_m}{dt} + R_0 i_m + \eta {i_m}^3 + {C_0}^{-1} q_m + \xi {q_m}^3 \tag{3}$$

$$V = {C_d}^{-1} q_d \tag{4}$$

$$i = i_m + i_d \tag{5}$$

In these equations, C_d represents the static capacitance, i_d and q_d are current and charge of the static capacitance, respectively. The total driving current of the stator is denoted by i.

3.2 Parameter identification

To isolate the effects of the contact force, the TWUSM was disassembled and tests were conducted solely on its stator. Only the Phase-A electrode was activated, and its driving current was recorded. The static response of the stator's driving current was measured across a frequency sweep from 39.7 kHz to 40.2 kHz with both upward and downward sweeps, using a driving voltage range of 5 to 15 Vp as shown in **Figure 5**. It was observed that hysteresis becomes more pronounced as the driving voltage increases.

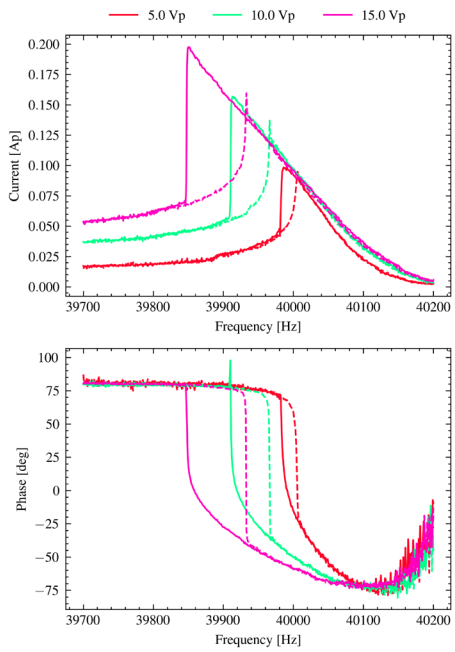

Figure 5 Frequency characteristics of the stator in measurement

The model parameters $L, R_0, C_0, C_d, \eta, \xi$ were estimated as presented in **Figure 6** using a least squares approach with the trust region reflective algorithm, implemented in

the Python library SciPy[4]. The results shown in **Figure 6**, show that the calculated current closely matches the measured current, accurately depicting the frequency characteristics observed in **Figure 5**.

Table 1 Elasticity parameters of prototype rotors

R_0	C_0	L	η	ξ	C_d
48.4 Ω	84.7 pF	186 mH	815 Ω A^{-2}	2×10^{20} $F^{-1}C^{-2}$	8.8 nF

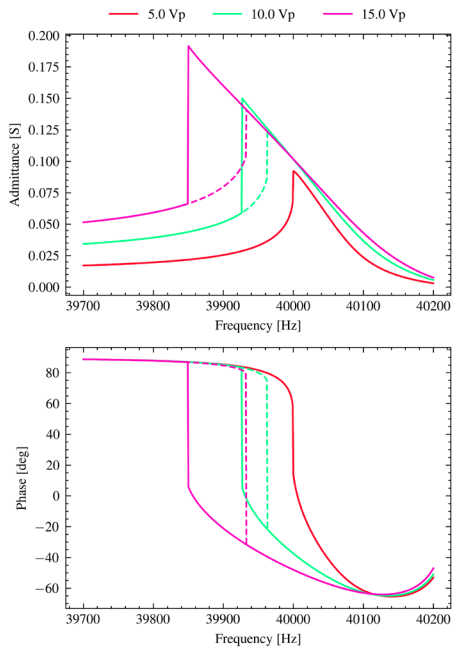

Figure 6 Frequency characteristics of the stator, calculated by nonlinear equivalent circuit model

4 Reinforcement learning

4.1 Reinforcement learning formulation

To optimize the frequency control for the fastest startup response, the task has been framed as a reinforcement learning challenge.

4.1.1 Environment

The state s and the action a in the environment are defined as:

$$s = (I_{real}, I_{imag}, f_{drv}) \tag{6}$$

$$a = \Delta f_{drv} \tag{7}$$

Here, I_{real} and I_{imag} represent the in-phase and quadrature components of the driving current i, respectively. f_{drv} is the current driving frequency, and Δf_{drv} indicates the frequency change for the next step.
The reward r is defined as the amplitude of the driving current

$$r = \sqrt{{I_{real}}^2 + {I_{imag}}^2} \tag{8}$$

The agent's goal is to maximize the cumulative reward, which is expected to facilitate the fastest startup of the resonance drive.

4.1.2 Agent

The agent employs the Soft Actor Critic (SAC) algorithm[5] and includes both an actor and a critic, each comprising a neural network with a middle layer of 64 nodes.

4.2 Training in Simulation

The agent underwent training through 100 episodes of interaction with the simulation model, with each episode consisting of 50 steps. **Figure 7** illustrates the simulated startup response managed by the trained agent compared to a constant frequency sweep, ranging from 1 ms to 40 ms.

Although the constant sweep response rises faster with shorter sweeping periods over 10 ms, it fails to start at 4 ms or less, similar to the speed response observed in Section 2. In contrast, the trained agent successfully initiates the driving current quicker than any constant sweep method without failure, using a strategy that starts with a fast sweeping speed and then decelerates, as shown in **Figure 7**.

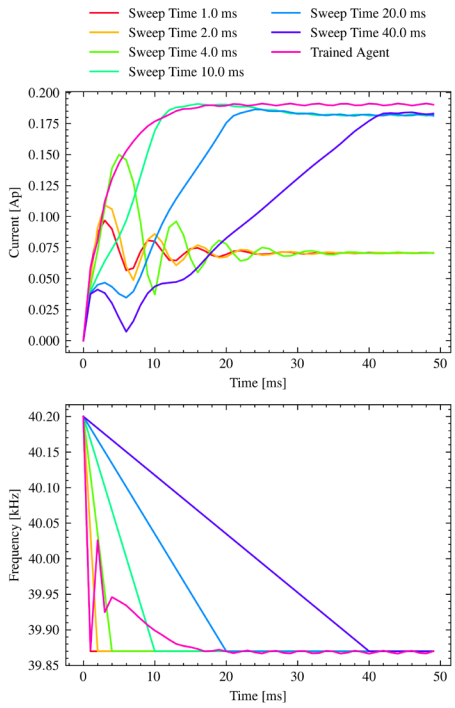

Figure 7 Start-up response of trained agent control and fixed step sweeping control

4.3 Experiment evaluation

The trained agent was implemented in the experimental setup and evaluated alongside the constant sweep under the same conditions as described previously.

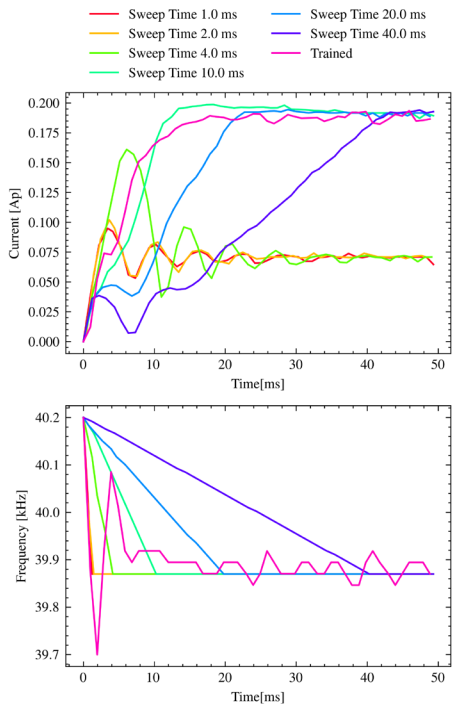

Figure 8 The start-up in real measurement

The results, depicted in **Figure 8**, demonstrate that the constant frequency sweep responses closely match those simulated in **Figure 7**, affirming the high fidelity of the equivalent circuit model. However, the responses of the trained agents were slower than the simulated results, likely due to the inference delay of the actor network, which takes about 500 µs, significant in comparison to the 1 ms control period.

5 Conclusion

This study has evaluated the transient response of the TWUSM's rotation speed under different frequency sweep speeds, highlighting the inherent limitations in response time. For simplicity, and without losing the nonlinearity of the system, the stator was isolated from the rotor and successfully modeled using an equivalent circuit that accounted for nonlinear capacitance and resistance. This model accurately reproduced both the static and dynamic behaviors of the TWUSM stator.

Utilizing this equivalent circuit model as a training environment, the Soft Actor Critic (SAC) deep reinforcement learning algorithm was applied. The trained SAC model surpassed all tested constant frequency sweeps in terms of response speed. When deployed in a real control system, however, the SAC model underperformed relative to its simulation predictions, likely due to delays from inference calculations.

Our future research will focus on two main objectives:

1) Reducing Discrepancies:
We aim to minimize the performance gap between simulations and actual conditions. This involves optimizing the real-time inference implementation to reduce delays. Additionally, incorporating these delays within the simulation itself could improve the real-world performance.

2) Modeling and control of whole TWUSM:
Currently, our model only includes the stator without the rotor. Going forward, we will expand our measurements and modeling to include the rotor-stator interactions to create a more comprehensive model of the entire motor. This will involve adjusting the model to capture the complex dynamics introduced by these interactions. We will also explore advanced control strategies that can effectively manage the full dynamics of the TWUSM, integrating sensory signals such as rotation speed or temperature into the reinforcement learning framework to enhance control robustness.

By addressing these areas, we hope to refine our control models and achieve closer alignment between simulated predictions and real-world performance, paving the way for fast-response and reliable ultrasonic motor control.

6 Literature

[1] Shinsei corporation. (2023). https://www.shinsei-motor.com/en/product/standard/index.html (accessed November 8, 2023).

[2] H. Storck, J. Wallaschek, The effect of tangential elasticity of the contact layer between stator and rotor in traveling wave ultrasonic motors, Int. J. Non. Linear. Mech. 38 (2002) 143–159.

[3] S. Miyake, T. Kasashima, M. Yamazaki, Y. Okimura, H. Nagata, H. Hosaka, T. Morita, Quantitative evaluation method for nonlinear characteristics of piezoelectric transducers under high stress with complex nonlinear elastic constant, Jpn. J. Appl. Phys. 57 (2018) 07LB14.

[4] M. A. Branch, T. F. Coleman, and Y. Li, A Subspace, Interior, and Conjugate Gradient Method for Large-Scale Bound-Constrained Minimization Problems, SIAM Journal on Scientific Computing, 21(1999), 1-23.

[5] T. Haarnoja, A. Zhou, P. Abbeel, S. Levine, Soft Actor-Critic: Off-Policy Maximum Entropy Deep Reinforcement Learning with a Stochastic Actor, arXiv [cs.LG]. (2018).

Micro magnetomechanical systems (MAMS)

Kari Ullakko, Ville Laitinen, Andrey Saren, Hu Hao, Aditya Kumthekar, Meysam Inally
Material Physics Laboratory, Lappeenranta-Lahti University of Technology LUT, Lappeenranta 53850, Finland
E-mail address: kari.ullakko@lut.fi

Abstract

Micro magnetomechanical systems (MAMS) represent the next generation of electromechanical devices. These devices are made from adaptive materials, like magnetic shape memory alloys, that exhibit actuator and sensor functions. MAMS devices do not have separate actuators or sensors but they are integrated in the adaptive material chip. The MAMS devices can be manufactured from adaptive material wafers using lithography and etching or by additive manufacturing. In this paper, the first steps in fabricating the MAMS devices will be presented.

1 Inroduction of MAMS concept

Many functions that can be performed in conventional electromechanical machines using components like electric motors, gears, shafts, and pulleys, cannot be used in micro-scale devices. In this presentation, we introduce for the first-time micro magnetomechanical systems (MAMS), made from magnetic shape memory (MSM)[1] alloys, in which actuation is generated in properly treated and shaped zones. Other zones of the MAMS devices are treated and shaped to have functions other than actuation. These functional zones are integrated in the MAMS devices (Fig. 1) analogous to integration of electronics components in integrated electric circuits.

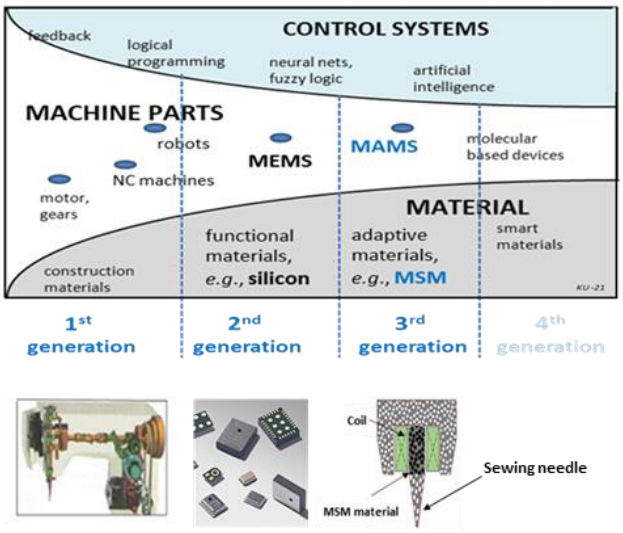

Figure 1. MAMS will replace separate machine parts and miniaturize electromechanics.

In evolution of electromechanics (Fig. 1), role of materials and software increase at the expense of separate components, like in evolution of electronics has happened. Conventional electromechanical machines are named here the **1st generation devices**. **MEMS** made from functional silicon material are examples of the **2nd generation**, and **MAMS** made from adaptive or responsive materials represent the **3rd generation**. MAMS technology significantly differs from MEMS technology because, unlike passive silicon, MSM material is an active material whose shape can be changed, *e.g.* elongated, contracted or bent even several per cent, by applying a magnetic field to it. The conceptual difference between the 1st and 3rd generation devices is illustrated by a sewing machine: conventional sewing machine needs tens of separate machine parts for moving the needle, while the 3rd generation machine could be fabricated from an MSM material (except coil).

Due to outstanding characteristics of the MSM materials (strains of 6% even in 0.5 µs, actuating velocity of 5.5 m/s, and acceleration of over 200 000 g^2), the MAMS devices are expected to exhibit superior dynamics. While MEMS devices are manufactured from a single crystalline silicon wafer, MAMS devices can be made from MSM material wafers. MAMS devices include motion-generating and other functional zones in the structure, which is not possible for MEMS. For instance, a MAMS lab-on-a-chip with fluid channels, chambers, filters, pumps and valves can be fabricated.

2 Operating principle of MAMS

MAMS devices are composed of **active zones** and **passive zones**. Active zones, or actuating zones, strain even several percent when a magnetic field is applied to them. Active zones can act as grippers, switches, pumps, valves or manifolds. Passive zones do not strain in the applied magnetic field but they have other functions, such as a magnetic flux path, spring, latch of a valve, fluid channel or housing of the device. As a conceptual illustration of different functions of the zones, Fig. 2 shows a gripper. This gripper contains an active zone (1) and two passive zones that act as a spring (2) and a magnetic flux path (3). Spring keeps the gripper open (Fig. 2a). Because the active region is then elongated, short crystallographic c-axes are aligned in vertical direction. When the magnetic field is applied to the active zone, c-axes, which is also easy direction of magnetization, align along the magnetic field direction (horizontal) resulting in contraction of the active zone and closing the gripper (Fig. 2b). In the example shown in Fig. 2, twin boundaries in the passive zones (black) are immobilized by implantation (or laser treatment), which introduces lattice

defects. The active zones are masked and are not affected by the flux of ions.

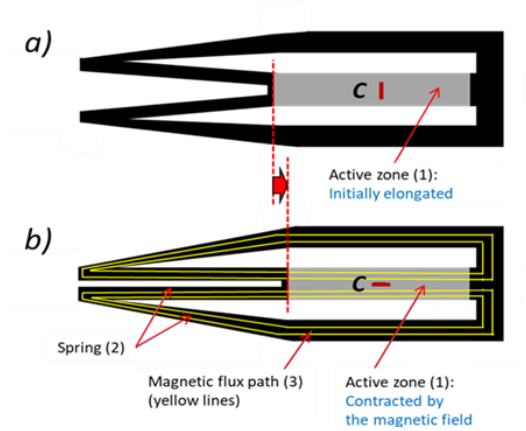

Figure 2. Example of a MAMS device containing three functional zones: Active zone (1) is marked with grey color, and passive zones spring (2) and magnetic flux path (3) are marked with black. Magnetic flux lines are shown as yellow lines.

Ion implantation is a method for providing an additional degree of control since, depending on the intensity of ion flux, twin boundaries can be immobilized either entirely or to a desired value of switching field. (Switching field is defined as the magnetic field level at which the twin boundaries start moving). Ultrafast MSM microgrippers potential applications in biomedical engineering, for instance, gripping microbes.

3 Manufacturing of MAMS

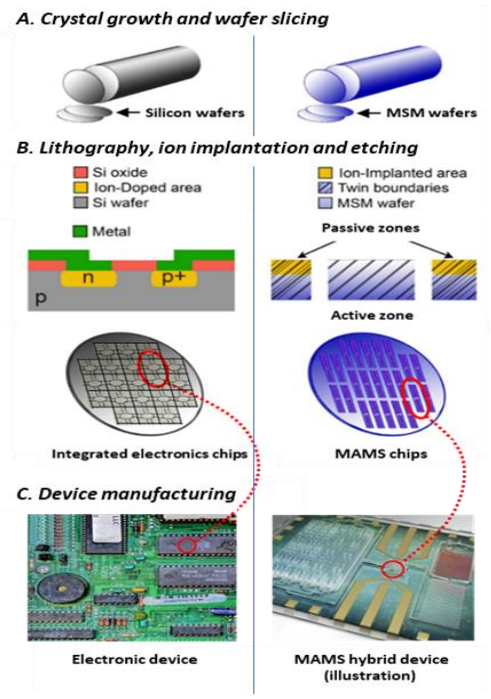

Figure 3. Manufacturing steps of an electronic device and a hybrid MAMS device.

These hybrid chips may contain an electronic chip made from silicon. The electronic chip may contain coils for driving the active zones of the MAMS chips, power electronics, control electronics and other devices required for the application, for instance, flow sensors. A microfluidic hybrid chip, *e.g.*, lab-on-a-chip, may also incorporate a plastic chip with fluid channels and chambers.

An alternative method of fabricating MAMS devices is additive manufacturing. This method alloys making complicated structures. We developed etching of MAMS chips and additive manufacturing of single crystalline Ni-Mn-Ga samples.

4 Results and discussion

We took the first steps of demonstrating the MAMS concept: 6% magnetic-field-induced strain was measured in an active zone of a 3D printed polycrystalline Ni-Mn-Ga sample[3]. Figure 4 shows magnetic-field-induced strain for three sequential measurements (black curve) and the applied magnetic field (red curve) *vs*. time. Based on our heat flow model, indicating that printing of single crystalline Ni-Mn-Ga is possible[4], we develop techniques of manufacturing MAMS devices containing active and passive zones.

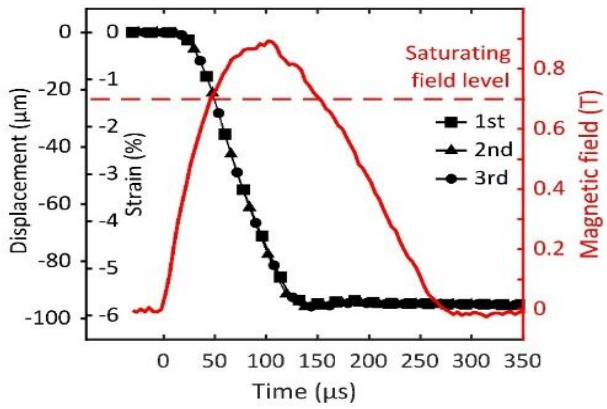

Figure 4. Magnetic-field-induced strain of 4D printed Ni-Mn-Ga sample[3].

5 Literature

1. Ullakko, K., Magnetically controlled shape memory alloys – a new class of actuator materials, Journal of Materials Engineering and Performance, Vol 5 (3), pp. 405-409, June 1996
2. Musiienko, D., Saren, A., Straka, L., Vronka, M., Kopecek, J., Heczko, O., Sozinov, A. and Ullakko, K. Ultrafast actuation of Ni-Mn-Ga micropillars by pulsed magnetic field, Scripta Mater. 162 (2019) pp. 482-485.
3. Laitinen, V., Saren, A., Sozinov, A. and Ullakko, K., Giant 5.8% magnetic-field-induced strain in additive manufactured Ni-Mn-Ga magnetic shape memory alloy, Scripta Mater., Vol. 208, 1 February 2022, 114324
4. Ullakko, K., Sozinov, A., and Järvinen, J., Is it possible to make single crystalline Ni-Mn-Ga devices by 3D printing?, 5th Int. Conf. on Ferromagnetic Shape Memory Alloys, September 5–9, 2016, Sendai, JAPAN

Chemofluidics – an autonomous Lab-on-Chip concept based on smart material components

Andreas Richter[1*], Mario Menschikowski[2], Markus Friedemann[2], Denise Gruner[1,2], Anthony Beck[1], Mohammed Sahadha[1], Franziska Obst[1], Paula Kalenczuk[1], Stefan Grünzner[1], Alexander Kutscher[1], Andreas Voigt[1], Uwe Marschner[1]

[1] Institute of Semiconductors and Microsystems, Technische Universität Dresden, Nöthnitzer Str. 64, 01062 Dresden, Germany,

2 Institute of Clinical Chemistry and Laboratory Medicine, University Hospital Dresden, Fetscherstr. 74, 01307 Dresden, Germany

During the COVID-19 pandemic, many people have more or less consciously come into contact with microfluidics in the form of rapid tests for the first time. However, hardly anyone knows that microfluidics plays a significant role in around 70% of all medical decisions and that modern medical molecular diagnostic methods are based on it. Similar to microelectronics, circuit concepts, so-called labs-on-a-chip (LoC), have great automation potential for microfluidic processes. However, their widespread use is being held back by the fact that it is currently not possible to combine all system components on a chip. Instead, they are complex computer-controlled microelectromechanical systems (MEMS) without feedback to the (bio)chemical information carriers, which are too expensive or too inefficient for many potential applications. Microfluidic integrated circuits based on smart materials, so-called chemofluidic LoCs, have a completely different functional principle that solves key problems of MEMS LoCs. The smart material components are self-powered by the chemical energy of the process liquids and have feedback functions to the process-relevant (bio)chemicals. Combined into logical circuits, the smart material components control the complex circuit processes autonomously thanks to their material-inherent sensor-actuator functions. They therefore completely replace the complex MEMS-LoC systems in functional terms, despite being completely electronics-free. The central components are chemofluidic transistors, which have decision-making functions for process-relevant chemical and physical parameters. We introduce two basic types of chemofluidic transistors, the membrane-isolated chemofluidic volume-phase transition transistor (MIS-CVPT) and the chemofluidic volume-phase transition transistor (CVPT) [1], and discuss helpful analogies to microelectronic transistor concepts. We then outline the fundamentals of discrete and analogue chemofluidic circuits (Figures 1 and 2) [2], [3] and dicuss basic fabrication concepts of chemofluidic circuits printing [4]. Using specific point-of-care tests, including a rapid test for respiratory infections, we discuss the potential of chemofluidics and demonstrate that, despite its early stage of development, chemofluidics is already relevant to practice. We show how the test protocols to be automated are translated into specific circuit designs. We then present how the chemofluidic circuits autonomously and feedback-controlled by the process media containing the detection chemistry and the patient samples calculate and execute the specific analysis procedure. We also compare the results obtained with the gold standards.

Keywords: smart material, lab on a chip, chemofluidics, chemofluidic transistors, microfabrication, point-of care testing.

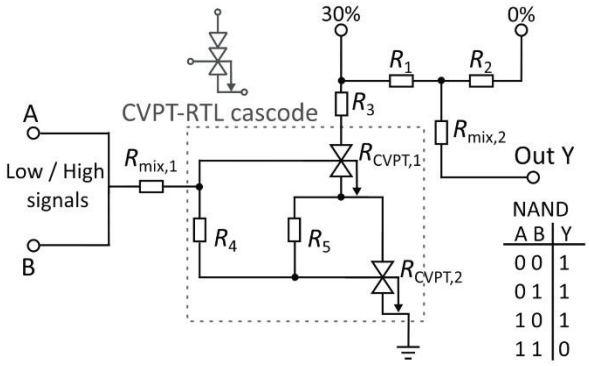

Figure 1: Schematic of a chemofluidic cascade based on CVPTs.

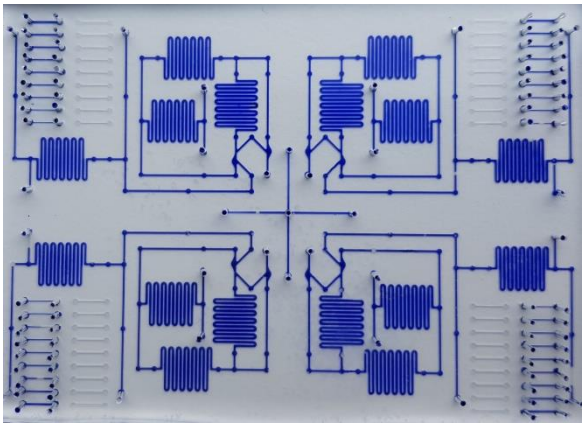

Figure 2: Chemofluidic chip with four cascodes.

References

1. A. Beck, et al., "Fundamentals of Hydrogel-Based Valves and Chemofluidic Transistors for Lab-on-a-Chip Technology: A Tutorial Review," Adv. Mater. Technol., 2023, 8, 2200417
2. Frank, P., et al., "Autonomous Integrated Microfluidic Circuits for Chip-Level Flow Control Utilizing Chemofluidic Transistors," Adv. Funct. Mater., 2017 27, 1700430
3. A. Beck, et al., "Logic Circuits Based on Chemical Volume Phase Transition Transistors for Planar Microfluidics and Lab-on-a-Chip Automation," Adv. Mater. Technol., 2022, 7, 2200185
4. Kutscher, A., et al., "Fabrication of Chemofluidic Integrated Circuits by Multi-Material Printing", Micromachines, 2023, 14, 699

Adaptive Hydrogel Microactuators

H.B. Duc Tran, [1,2] Christoph A. Spiegel, [1,2] Eva Blasco[1,2]

[1]*Institute of Organic Chemistry (OCI), Heidelberg University, 69120 Heidelberg, Germany*

[2] *Institute for Molecular Systems Engineering and Advanced Materials (IMSEAM), Heidelberg University, 69120 Heidelberg, Germany*

Soft robotics is a growing field in the engineering sciences.[1] Active materials including liquid crystal elastomers (LCEs), dielectric-elastomer-based actuators (DEAs), ionic-polymer-based actuators (IPAs), or conjugated polymers (CPs) are key for the development of soft-robotics and actuators.[2] Despite these well-established approaches at the macroscale, there is an increasing demand for novel materials and design concepts to accomplish effective actuation at various scales, particularly at the sub-millimeter scale. The accurate shaping of microactuators is a significant challenge and requires a versatile method with highly accurate spatial precision. Recent developments in additive manufacturing have resulted in an incredible increase in 3D structure potential. Direct laser writing (DLW), also known as two-photon lithography, has evolved into a potent technology for printing precise and advanced 3D designs at the micro and nanoscale scale (Figure 1a). Stimuli-responsive hydrogels are a great material for making soft robotics or microactuators in aquatic environments, including biological experiments.[3,4] The development of DLW-printable stimuli-responsive hydrogels has become an emerging field with great promise. The most often used materials for such stimuli-responsive systems are DLW-printable hydrogels based on acrylamides or acrylates, while the integration of OEGMA polymers remains unexplored.[5]

This project explores the intersection of stimuli-responsive hydrogels and the fabrication of thermoresponsive systems using alternative thermoresponsive monomers. Specifically, we delve into the novel approaches to design and engineer hydrogel structures with switchability in response to changes in temperature with high precision. So far, PNIPAM is one of the most well-studied and well established thermo-responsive polymers exhibiting an LCST close to body temperature.[6] PNIPAM exhibits a lower critical solution temperature (LCST) at around 32°C (Figure 1b). Below this temperature, it is hydrophilic and soluble, while above this temperature, it becomes hydrophobic and insoluble. However, this transition is limited to a narrow temperature range (32-37 °C) (Figure 1b). Thus, our main goal was to explore alternative materials based on soft oligomers such oligo(ethylene glycol), whose phase transition temperature can be tailored on demand within a broader temperature range.[7] To this aim, we have synthesized a library of oligomers with different molecular weights and compositions and tested their printability and response. The temperature-switchable nature of these

hydrogel structures opens up new possibilities for controlled drug release, tissue engineering, and the development of microdevices for diagnostics. Special attention will be paid to their biocompatibility in the near future.

In summary, our work has focused on the alternative and more controlled printable thermoresponsive systems. The precise control afforded by DLW and macromolecular design enhances their potential for customization and adaptability, making it a very valuable approach. This research paves the way for a new era of functional and responsive hydrogel materials with applications in different fields, especially in soft microrobotics.

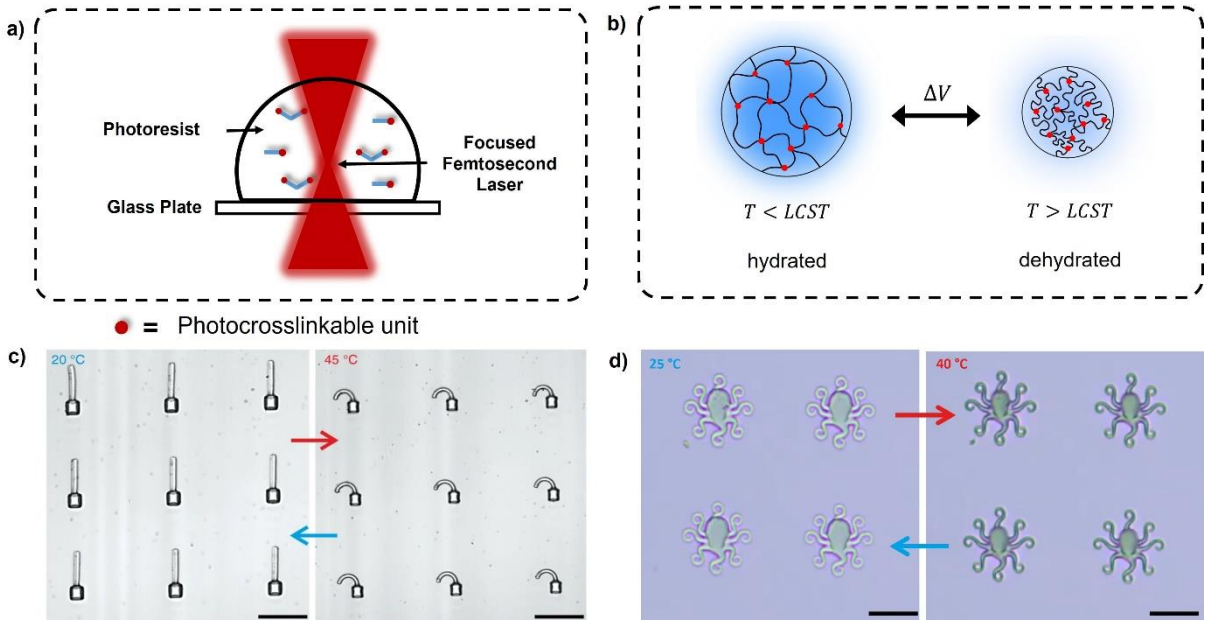

Figure: 1a) Schematic representation of the two-photon lithography process. A NIR pulsed laser is used to initiate two-photon-polymerization of a photocrosslinkable resin; b) Schematic representation of the actuation of thermoresponsive hydrogels; c) PNIPAM based monomers employed as DLW photoresists. Temperature-triggered actuation with hetero-microstructures based on pNIPAM. T = 20 °C and T = 45 °C are the two temperatures that are indicated in blue and red, respectively.[5]; d) OEGMA based polymers employed as DLW photoresists. Temperature-triggered actuation with hetero-microstructures based on OEGMA. T = 20 °C and T = 45 °C

[1] D. Rus, M. T. Tolley, *Nature* 2015, *521*, 467–475.

[2] Q. M. Zhang, M. J. Serpe, *ChemPhysChem* 2017, *18*, 1451–1465.

[3] M. del Pozo, C. Delaney, C. W. M. Bastiaansen, D. Diamond, A. P. H. J. Schenning, L. Florea, *ACS Nano* 2020, *14*, 9832–9839.

[4] S. Turunen, T. Joki, M. L. Hiltunen, T. O. Ihalainen, S. Narkilahti, M. Kellomäki, *ACS Appl. Mater. Interfaces* 2017, *9*, 25717–25730.

[5] M. Hippler, E. Blasco, J. Qu, M. Tanaka, C. Barner-Kowollik, M. Wegener, M. Bastmeyer, *Nat. Commun.* 2019, *10*, 232.

[6] L. Tang, L. Wang, X. Yang, Y. Feng, Y. Li, W. Feng, *Prog. Mater. Sci.* 2021, *115*, 100702.

[7] J.-F. Lutz, Ö. Akdemir, A. Hoth, *J. Am. Chem. Soc.* 2006, *128*, 13046–13047.

Conference: Actuator 2024, International Conference and Exhibition on New Actuator Systems and Applications
Session : Cooperative Multistage Multistable Microactuator Systems (KOMMMA)
Application: Oral

In-Plane Bistable Microdevice in Silicon Technology

Gowtham Arivanandhan[1], Maximilien Kiegerl[l], Elaheh Akbarnejad[2], Zixiong Li[1], Alfred Ludwig[2] and Manfred Kohl[1]

[1]Institute of Microstructure Technology, Karlsruhe Institute of Technology (KIT), Karlsruhe, Germany

[2]Institute for Materials, Ruhr University Bochum (RUB), Bochum, Germany

We present the design, fabrication and characterization of an in-plane microdevice capable of lateral movement between two stable states that has been developed within the framework of the DFG Priority Program KOMMMA. This research is motivated by the need of ultra-small actuators allowing for large strokes in the order of several percent of actuator size that are compatible with silicon technology. In particular, bidirectional and bistable actuations are highly attractive for Si micromechanical and Si photonic devices. Although the concept of in-plane bi-stable actuation based on buckling bridges has been successfully demonstrated at the macro scale, significant challenges arise upon miniaturization to micrometer dimensions and below due to fabrication limitations and lack of actuation mechanisms for switching. Here, we explore the down-scaling of an in-plane bistable mechanism to the micro scale using silicon technology and investigate the limits of bistability of a first demonstrator device.

Layout and limits of bistability: The design of the bistable device comprises a central moving platform that is suspended by bridges with narrow hinges of widths w_h as shown in Fig. 1. The bridges are designed with a pre-deflection offset x_o. By applying an external load to the central platform along x-direction, the platform is displaced from its initial equilibrium position (state 1) and the hinges are axially compressed, which eventually results in switching to the second equilibrium position of the device (state 2). Fig. 2 shows simulated characteristics of reaction force versus displacement of the bistable device for different pre-deflection offsets x_o corresponding to different Q ratios ($Q = x_0/w_h$). Increasing the Q ratio leads to negative stiffness behavior associated with a negative force region. Above a critical Q ratio, the reaction force becomes negative indicating bistability. Fig. 3 shows minimum force values obtained for different hinge widths w_h and pre-deflection offsets x_0 demonstrating that bistability is achieved for Q ratios above 2.3.

Fabrication: The fabrication process flow is summarized in Fig. 4. It comprises electron-beam lithography (EBL), wet etching and reactive ion etching (RIE) making use of the ultra-high precision of the silicon cryo-etching process. The process flow includes the deposition of a shape memory alloy (SMA) layer (Fig. 4e) to enable self-actuation of the device. Fig. 5 depicts SEM images of an in-plane bistable micro-device in its two stable states. To overcome the challenges of mechanical loading and characterization, adaptor structures on either end of the microdevice are developed (Fig. 5) to transfer the mechanical load of a nanomanipulator to the bistable microdevice.

Characterization: Fig. 6 shows experimental and simulated characteristics of reaction force versus displacement of the bistable microdevice. The characteristics reveal the force barrier that needs to be overcome for bistable switching as well as the negative stiffness behaviour. Both, the maximum reaction force and the corresponding critical displacement are well reproduced by the simulations. The deposition of an additional SMA layer on the silicon microdevice opens up the potential to generate the force required for bistable switching through local Joule heating. Thus, the presented results provide a basis for the development of in-plane bistable SMA microactuators that self-actuate between the equilibrium states with large stroke.

Acknowledgements:
This research was funded by the German Research Foundation within the Priority Program “Cooperative Multistage Multistable Microactuator Systems” (SPP2206).

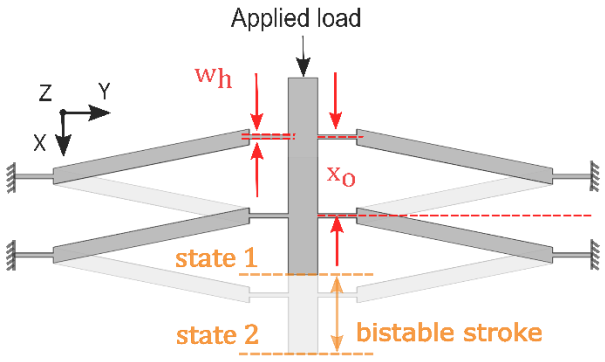

Fig. 1: Schematic of the bistable microdevice, which is actuated by a mechanical load along x-direction. The central platform is connected to bridges with narrow hinges of width w_h and a pre-deflection offset x_o, which allow for two stable positions (states 1 and 2).

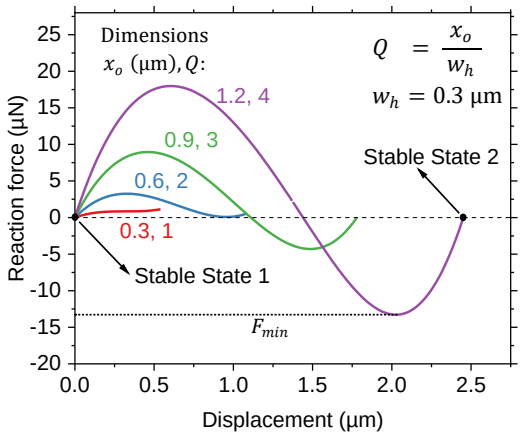

Fig. 2: Simulation of the reaction force versus displacement of a silicon bistable microdevice for different pre-deflection offsets x_o and a hinge width w_h of 0.3 µm. The minimum reaction force F_{min} is indicated for the case $x_o = 1.2$ µm.

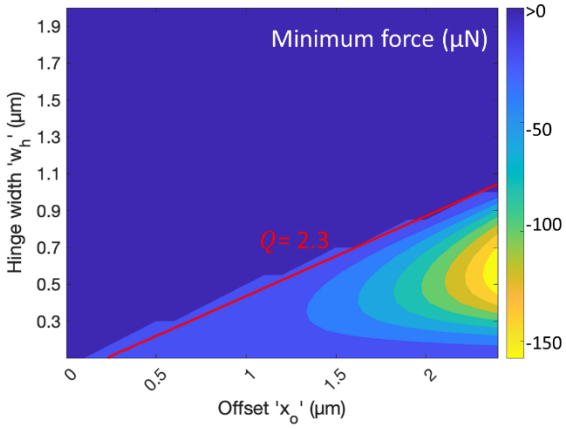

Fig 3. Simulation of the minimum reaction force F_{min} for various hinge widths w_h and pre-deflection offsets x_o to analyze bistability. A critical value $Q = x_0/w_h$ of 2.3 is required for bistability, which defines the red line.

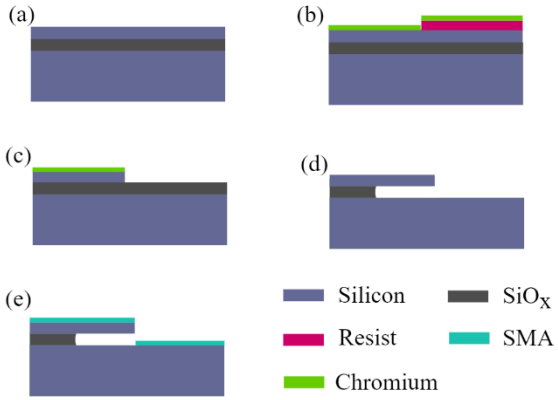

Fig. 4: Schematic process flow for fabrication of a bistable device consisting of a SMA/Si composite layer. (a) SOI-wafer with 2.5 µm device layer, (b) patterning of a 50 nm thick chromium layer using EBL and lift-off, (c) cryogenic RIE etching of silicon, (d) chromium stripping and wet etching of SiO_2 sacrificial layer, (e) DC magnetron sputtering of SMA layer.

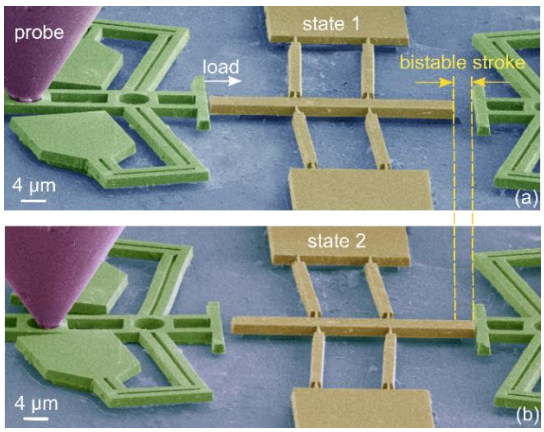

Fig. 5: SEM images of a bistable silicon microdevice and two silicon adaptor structures on either end of the micro-device for bidirectional actuation by the mechanical load of a nanomanipulator (see conical probe). (a) and (b) display the bistable positions (states 1 and 2).

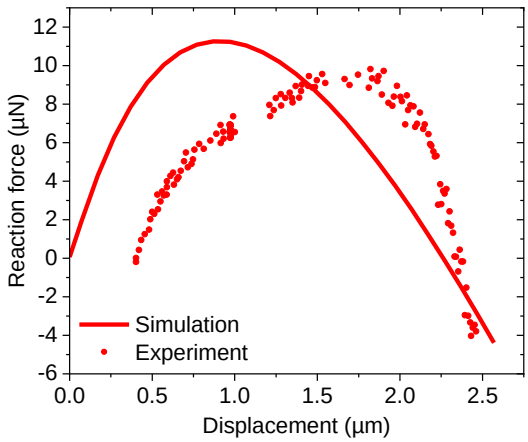

Fig. 6: Experimental and simulated reaction force versus displacement of a bistable silicon microdevice (w_h= 0.3 µm, x_o= 3 µm). The experimental data are determined by subtracting the reaction force of the adaptor structure from the total reaction force.

Conference Focus: Cooperative Multistage Multistable Microactuator Systems (KOMMMA)

Application: Oral

Development of a Re-Programmable Micro Origami Device

Vincent Gottwald[1], Lena Seigner[1], and Manfred Kohl[1]
[1]Institute of Microstructure Technology, Karlsruhe Institute of Technology (KIT), Karlsruhe, Germany

We report on the design, fabrication, and characterization of a re-programmable micro origami device within the framework of the DFG Priority Program KOMMMA. The device is characterized by origami-inspired self-folding from an initial flat shape to two alternative 3D shapes, including reversible magnetic latching on demand and self-unfolding. This research aims at the development of re-programmable micro-matter consisting of many micro-scale tiles being homogenous at the human length scale to enable the reversible formation of various 3D shapes on demand. Previous work mainly focused on macro-sized concepts demonstrating origami-inspired self-folding actuation for applications, e.g., in robotics and aerospace. Here, we transfer this concept to the micro-scale by designing a network of shape memory alloy (SMA) hinge actuators of Ti-Ni-Cu films for bi-directional self-folding that are initially shape-set by local Joule heat-treatment and subsequently operated through local Joule heating. In addition, we present reversible magnetic latching comprising heatable soft-magnetic pads of Ni-Mn-Ga films.

The Ti-Ni-Cu and Ni-Mn-Ga films are fabricated by magnetron sputtering. Fig. 1 displays the temperature-dependent electrical resistance of a Ti-Ni-Cu film of 10 µm thickness after rapid thermal annealing at 700 °C for 15 minutes and after a local Joule heat treatment at a current density of 0.325 mA/µm^2 for 1 minute. The additional local Joule heat treatment leads to a decrease in absolute electrical resistivity and an increase in electrical resistivity change of the Ti-Ni-Cu film. Furthermore, the phase transformation temperatures increase.

The layout of the re-programmable micro origami device consists of four triangular tiles being interconnected by the Ti-Ni-Cu hinge actuators and Ti-Ni-Cu conduction tracks for Joule heating as sketched in Fig. 2 (a). Wing-like geometries of the hinge actuators improve temperature homogeneity and allow for additional pulling motion during bidirectional actuation. Underneath the soft-magnetic Ni-Mn-Ga pads with a thickness of 5 µm, the conduction track is designed as a heater to induce a ferromagnetic transition in the Ni-Mn-Ga pad and, thus, to switch the magnetic attraction force between the pad and a miniature permanent magnet placed above. As illustrated in Fig. 2 (b, c), the micro origami device is designed for reversible folding and unfolding to adopt the shapes of either a pyramid or a table.

Fabrication of the micro origami device involves sputter deposition and micromachining of the SMA films and polymer tiles by optical lithography as sketched in Fig. 3. Subsequent steps are device release and local Joule heat treatment. The SMA hinge actuators allow for bidirectional self-folding angles up to ±85°, which are enhanced by additional magnetic latching forces. Fig. 4 (a) shows the micro origami device after Joule heating the protagonist hinge actuators and magnetic latching with a miniature Nd-Fe-B magnet to adopt the pyramid shape. After unlatching and Joule heating the antagonist hinge actuators, a table shape is adopted, as shown in Fig. 4 (b).

A series of electrical and mechanical measurements have been performed to characterize the functional properties of the device. Fig. 5 shows an electrical resistance characteristic of the outer conduction track showing a sequence of phase transformations of the micro-scale heater at the heating power of 4 mW and of the antagonist hinge actuator at 7 mW. The well-separated range of heating power allows for selective heating of the Ni-Mn-Ga pad without affecting the hinge actuator. Furthermore, the sharp phase transitions enable control with optimal electrical power to minimize thermal cross-coupling. Fig. 6 shows a series of measurements of the maximum blocking torque, which reaches a maximum of 122 µNmm at an electrical power of 13 mW. These results mark an important milestone in the development of re-programmable micro-matter, which includes upscaling the number of tiles and addressing the challenge of further miniaturization.

Acknowledgements:
This research was funded by the German Research Foundation within the Priority Program “Cooperative Multistage Multistable Microactuator Systems” (SPP2206).

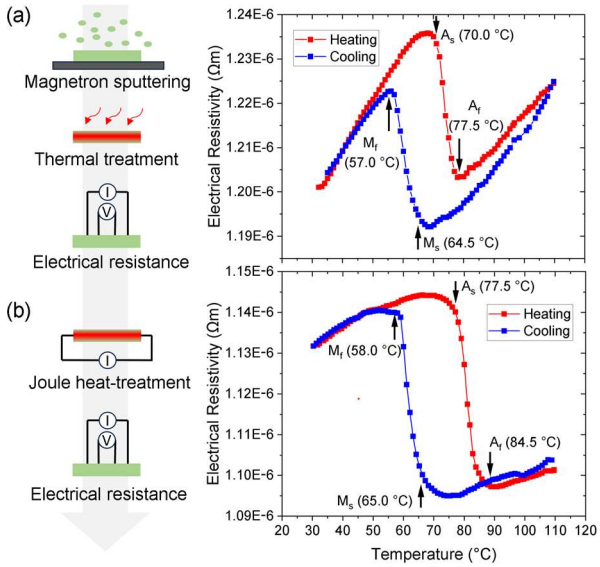

Fig. 1: Schematics of Ti-Ni-Cu film preparation process, experimental setup, and corresponding film resistivity versus temperature characteristics (a) after rapid thermal annealing at 700 °C for 15 minutes, (b) after an additional Joule heat treatment at a current density of 0.325 mA/µm^2 for 1 minute.

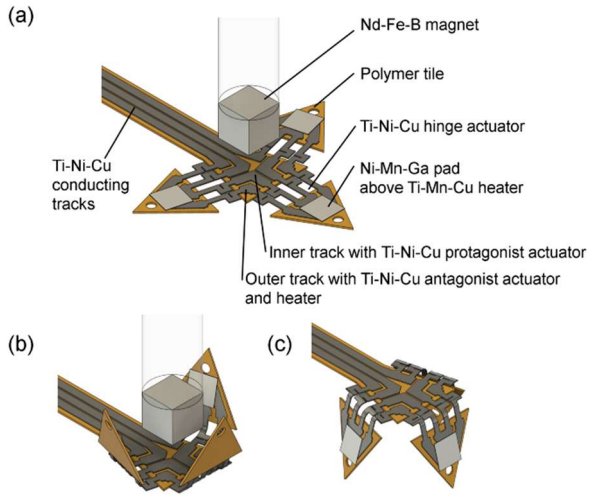

Fig. 2: Layout of the re-programmable micro origami device. (a) Schematic of functional units, (b) 3D shape after self-actuation by the protagonist Ti-Ni-Cu hinge actuators and before magnetic latching, (c) 3D shape after active unfolding and self-actuation by the antagonist Ti-Ni-Cu hinge actuators.

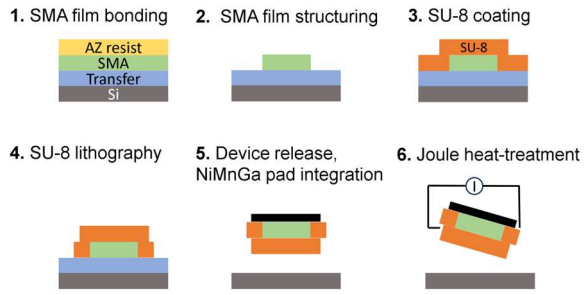

Fig. 3: Fabrication sequence of the re-programmable micro origami device.

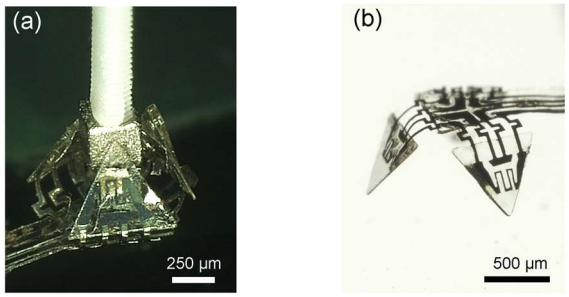

Fig. 4: Photos of the re-programmable micro origami device in (a) pyramid configuration, latched with a miniature permanent magnet, and (b) table configuration.

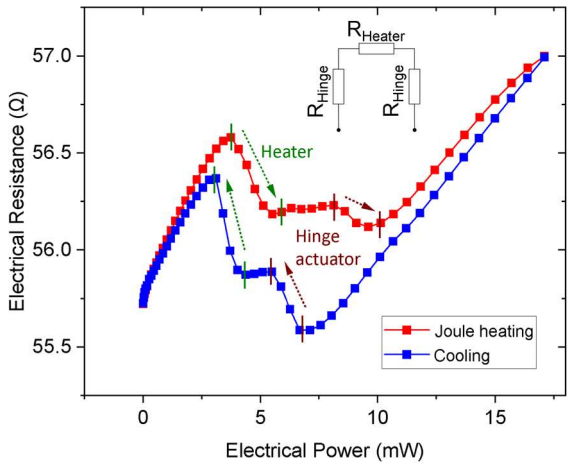

Fig. 5: Electrical resistance versus electrical power applied to the outer conduction track (see Fig. 2 (a)) consisting of Ti-Ni-Cu antagonist hinge actuator and heater as indicated in the inset.

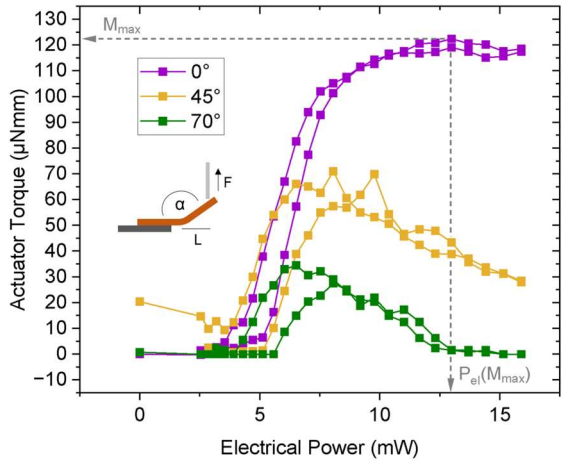

Fig. 6: Blocking torque of the Ti-Ni-Cu protagonist hinge actuator at different angular positions as indicated in the inset. Decrease in torque at higher electrical power due to thermal cross-coupling with the antagonistic hinge actuator.

-Hold it together-
Micro-actuator latching mechanism

Martin Heyer, Jürgen Rühe

Latching mechanisms are found all over in nature, a great example are pine cones. They contain between their scales an oil resin which evaporates in a warm and dry external temperature, allowing for the unlocking of the closed scales and hence, allow for their seeds to be disbursed. This unlocking is an extremely quick process which causes a cracking sound to be heard. However, locking of the scales can also be achieved through the oil resin hardening and through its tacky properties locks the scales in place, to prevent seed disbursing. This locking mechanism occurs when the external temperatures are cold and damp. This opening and closing, or unlatching and latching of the pine cones occurs passively, meaning no energy is required to either keep a locked state or an unlocked state. However, one draw back of the pine cones is that these mechanisms do not occur unless seed have fully matured, making the process not controllable until the seeds have matured. Hence, a mechanism which can be controlled at any point in time using an external stimulus such as temperature can be of interest for programable and transformable micro-actuators.

Here we present two mechanisms, the first a heat-activated and the second a passive one. Figure 1 illustrated the heat-activated mechanism. It consists out of a container, filled with a filling-substance such as wax and a plunger which is dipped into the filling-substance. In the unlocked (open) state, the plunger is not within the container and its filling-substance. In order for the mechanism to move from open to closed, the filling-material will need to get molten in order for the plunger to be inserted and then allowed to cool down so the filling-material is hardened. In this state the latching mechanism is in a energy-free state and can only be unlatched through re-heating of the filling material, decreasing the unlocking force in order to pull the plunger.

Figure 1

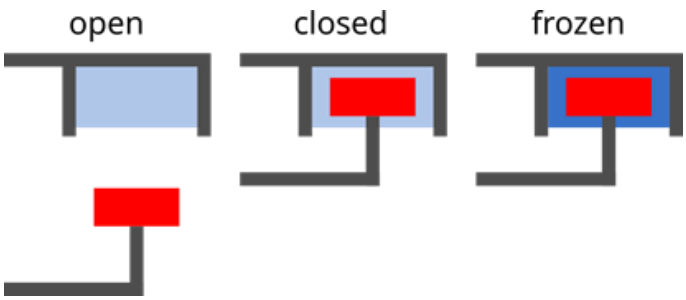

The second mechanism which we are trying to investigate is as previously mentioned a passive one (see figure 2). Instead of relying on an external stimulus to reduce the unlocking force, ‘brute-force’ is applied in order to move from a latched to unlatched state. Figure 2 shows an upper surface, which contains a sticky patch which can vary from pressure sensitive adhesives (PSAs) to tacky polymers. In this mechanism both surfaces need to come into contact to allow for a latched state to occur. In order to unlatch this mechanism, a force greater than the adhesive force from the sticky patch must be applied, hence ‘brute-force’. This principle is similar to opening and closing cupboard doors. A sufficient force is required to open it and requires no energy when closed.

Figure 2

Here we showed two initial mechanisms which rely on an energy-free latched state. The first mechanism is heat=activated whilst the second relies upon ‘brute-force’. Further mechanisms have been considered for future investigations. The overall goal for these mechanisms is to remain energy-free when latched, however, secondary goals such as size ranges below 100µm and thermostability of temperatures up to 100°C are considered for the latching of programmable and transformable micro-actuators.

GMM-Fachberichte

Die Beiträge der GMM-Fachtagungen und -Workshops sind in den GMM-Fachberichten dokumentiert. Die von Programmausschüssen selektierten und zumeist reviewten Beiträge stellen aktuelle Entwicklungen aus der Mikroelektronik, Mikrosystem- und Feinwerktechnik vor.

VDE VERLAG

Technik. Wissen. Weiterwissen.

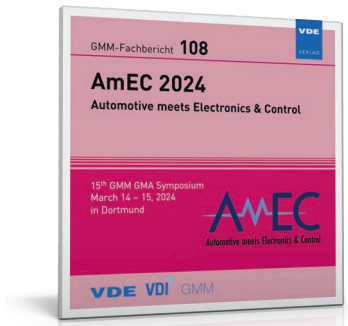

GMM-Fachbericht Band 108

AmEC 2024

Automotive meets Electronics & Control

15. GMM GMA Symposium, March 14 – 15, 2024 in Dortmund

▶ The first core field to mention is on applications of artificial intelligence/machine learning (AI/ML) to many different domains. The second core field is trajectory planning, where of course a strong interaction exists with AI/ML. Additional topics cover reliability, fuel cells, sensor technology and new computer architectures which become important for automotive.

2024, 94 Seiten, 140 x 124 mm, Slimlinebox, CD-ROM

54,– €

ISBN 978-3-8007-6284-2 (CD-ROM) ISBN 978-3-8007-6285-9 (E-Book)

Titel / Untertitel	Jahr	Seiten	Buch/CD/E-Book	ISBN-Nummer	Preis
GMM-Fachbericht Band 107 EBL 2024 – Elektronische Baugruppen und Leiterplatten 12. GMM/DVS-Tagung, 05. – 06. März 2024 in Fellbach	2024	316	- / + / +	978-3-8007-6265-1 (CD-ROM) 978-3-8007-6266-8 (E-Book)	148,-
GMM-Fachbericht Band 106 AmE 2023 – Automotive meets Electronics 14. GMM-Symposium, June 15 – 16, 2023 in Dortmund	2023	113	- / + / +	978-3-8007-5990-3 (CD-ROM) 978-3-8007-5991-0 (E-Book)	49,-
GMM-Fachbericht Band 105 Mikro-Nano-Integration Beiträge des 9. GMM-Workshops, 21. – 22.11.2022 in Aachen	2022	131	- / + / +	978-3-8007-5990-3 (CD-ROM) 978-3-8007-5991-0 (E-Book)	82,-
GMM-Fachbericht Band 104 AmE 2022 – Automotive meets Electronics 13. GMM-Symposium, September 29 – 30, 2022 in Dortmund	2022	104	- / + / +	978-3-8007-5955-2 (CD-ROM) 978-3-8007-5956-9 (E-Book)	67,-
GMM-Fachbericht Band 103 IKMT 2022 – Innovative Kleinantriebs- und Kleinmotorentechnik Innovative Small Drives and Motors, Beiträge der 13. GMM/ETG-Fachtagung, 14. – 15. September 2022, Johannes Kepler Universität Linz, Österreich	2022	310	- / + / +	978-3-8007-5938-5 (CD-ROM) 978-3-8007-5939-2 (E-Book)	161,-
GMM-Fachbericht Band 102 EASS 2022 – Energieautonome Sensorsysteme 2022 Beiträge der 11. GMM-Fachtagung, 5. – 6. Juli 2022 in Erfurt	2022	82	- / + / +	978-3-8007-5896-8 (CD-ROM) 978-3-8007-5897-5 (E-Book)	59,-
GMM-Fachbericht Band 101 ACTUATOR 2022 International Conference and Exhibtion on New Actuator Systems and Applications June 29 – 30, 2022 in Mannheim	2022	369	- / + / +	978-3-8007-5894-4 (CD-ROM) 978-3-8007-5895-1 (E-Book)	192,-
GMM-Fachbericht Band 100 Elektromagnetische Verträglichkeit in der Kfz-Technik Beiträge der 8. GMM-Fachtagung, 31. Mai – 1. Juni 2022, Schwieberdingen	2022	100	- / + / +	978-3-8007-5697-1 (CD-ROM) 978-3-8007-5698-8 (E-Book)	67,-
GMM-Fachbericht Band 99 AmE 2021 – Automotive meets Electronics 12. GMM-Symposium, March, 10 – 11, 2021, Online Event	2021	80	- / + / +	978-3-8007-5487-8 (CD-ROM) 978-3-8007-5488-5 (E-Book)	46,-

Sämtliche Veröffentlichungen der GMM-Fachberichte können auch im Abonnement bezogen werden. Preisänderungen und Irrtümer vorbehalten.

Bestellen Sie jetzt: (030) 34 80 01-222 oder www.vde-verlag.de/gmm-fachberichte

Tagungsbände online

Erwerb von einzelnen Tagungsbeiträgen im PDF-Format

Der VDE VERLAG publiziert jährlich rund 30 Tagungsbände mit mehr als 1.500 Fachbeiträgen. Diese können Sie auch einzeln erwerben. Zurzeit stehen Ihnen mehr als 29.000 Fachbeiträge im PDF-Format zum Download zur Verfügung. Die Kosten pro Beitrag betragen 15,– €.

Recherchieren Sie auf www.vde-verlag.de in einer täglich wachsenden Zahl von technisch-wissenschaftlichen Fachbeiträgen und erwerben Sie diese im direkten Download mit bequemen Bezahlmöglichkeiten per Kreditkarte oder PayPal.

Weitere Informationen: www.vde-verlag.de/buecher/proceedings/beitraege-suchen.html

Preisänderungen und Irrtümer vorbehalten.